OCT 28 1949

THE PHYSICAL REVIEW

VOLUME 76 *Second Series* NUMBER 8

OCTOBER 15, 1949

Published for the

AMERICAN PHYSICAL SOCIETY

by the

AMERICAN INSTITUTE OF PHYSICS
Incorporated

LANCASTER, PA., AND NEW YORK, N. Y.

THE PHYSICAL REVIEW

A journal of experimental and theoretical physics established by E. L. Nichols in 1893

Published by the American Institute of Physics for the

AMERICAN PHYSICAL SOCIETY

Officers

President

F. W. Loomis
University of Illinois
Urbana, Illinois

Vice-President

I. I. Rabi
Columbia University
New York, New York

Secretary

K. K. Darrow
Bell Telephone Laboratories
Office:
Columbia University
New York 27, New York

Treasurer

G. B. Pegram
Columbia University
New York 27, New York

Local Secretary for the Pacific Coast

J. Kaplan
University of California at Los Angeles
Los Angeles, California

Managing Editor

John T. Tate
University of Minnesota
Minneapolis, Minnesota

BOARD OF EDITORS

Editor

John T. Tate

Assistant Editor

J. W. Buchta

Associate Editors

H. A. Bethe — S. A. Goudsmit — W. E. Lamb, Jr.
L. A. Ridenour — E. M. Purcell — R. G. Herb
W. H. Zachariasen — V. F. Weisskopf — J. Bardeen

Manuscripts for publication should be submitted to John T. Tate, University of Minnesota, Minneapolis, Minnesota. The authors' institutions are requested to pay a publication charge of $4 per page which, if honored, entitles them to 100 free reprints. Instructions will be sent with galley proofs.

Proof and all correspondence concerning papers in the process of publication should be addressed to the Publication Manager, American Institute of Physics, 57 East 55 Street, New York 22, New York.

Subscription Price

United States and Canada.....$25.00
Elsewhere.....$27.00

Back Numbers[1]

Yearly back number rate when complete year is available:
Prior to 1949: $20.00
Thereafter: $27.00
Single copies: $2.00 each, prior to July, 1929;
$1.00 each, July, 1929–December, 1941;
$2.00 each, January, 1942–December, 1946;
$1.00 each, January, 1947–December, 1948.
Current issues: $1.25 each.
General index, 1893–1920: $4.00.

Subscriptions and orders for back numbers should be addressed to Prince and Lemon Streets, Lancaster, Pennsylvania, or to the American Institute of Physics, 57 East 55 Street, New York 22, New York.

Changes of address in the case of members of the American Physical Society should be addressed to the Treasurer; in the case of other subscribers to the Business Manager, American Institute of Physics.

[1] For Series 1 inquire of Physics Department, Cornell University, Ithaca, New York.

The Physical Review is published semi-monthly at Prince and Lemon Streets, Lancaster, Pennsylvania.

Entered as second-class matter March 6, 1947, at the Post Office at Lancaster, Pennsylvania, under the Act of March 3, 1879.

Acceptance for mailing at special rate of postage provided for in paragraph 4, section 538, P. L. & R., authorized January 27, 1933.

THE
PHYSICAL REVIEW

A journal of experimental and theoretical physics established by E. L. Nichols in 1893

SECOND SERIES, VOL. 76, NO. 8 OCTOBER 15, 1949

A Preliminary Directional Study of Cosmic Rays at High Altitude.* I. Apparatus and Procedure

W. G. STROUD, J. SCHENCK, AND J. R. WINCKLER
Palmer Physical Laboratory, Princeton University, Princeton, New Jersey
(Received June 9, 1949)

To study the effects of secondary particles on the measurement of the primary directional intensity at high altitudes, a preliminary study has been carried out. Geiger counter telescopes at selected zenith angles from 0° to 90°, utilizing Pb filters up to 17 cm, have been sent up to 100,000 feet using constant-level Pliofilm balloons. Counting rates, temperature, pressure, and azimuthal orientation were radioed to the ground by means of a 15-channel f-m telemetering system. This paper describes in detail the electronic and mechanical features of the apparatus.

A description of the data and their interpretation are given in the following paper.

INTRODUCTION

IN view of the long-standing lack of information about the directional asymmetry of the primary cosmic radiation, and because of the importance of this information for an understanding of many cosmic-ray phenomena, a study of the directional distribution of primary rays and its dependence on latitude has been undertaken.

A large amount of data on the east-west and other asymmetries has been collected at sea level and at mountain elevation,[1] and a small effect is observed. The interpretation of these results is difficult, as most of the particles measured are secondaries produced in the atmosphere and no adequate information is available relating the direction of the secondary particles to that of the primaries.

Recent experiments[2–4] at intermediate altitudes (18 cm Hg pressure) with aircraft indicate a large east-west asymmetry of up to 35 percent, but there still remains the problem of relating these measurements to the primary particles because of the some 240 g/cm² of air above the equipment. If one assumes an absorption coefficient of 1/160 g^{-1} cm^2 in air for the primary particles, one would expect to observe not more than 20 percent of the incoming primaries in the vertical direction at this atmospheric depth, and even fewer at larger zenith angles. Cloud-chamber observations at similar altitudes show that fewer than 1/30 of the particles have energies greater than 2.0 Bev and support this conclusion.[5] Also, barometric and atmospheric temperature effects seem to be most troublesome at these intermediate altitudes.[6] The fact that the observed asymmetry is so large and increases for increasing hardness of radiation indicates that the high energy secondaries probably preserve the direction of the primaries to a large degree.

The only measurement of the E-W asymmetry at high altitudes[7] gives a seven percent effect at 100-g/cm² depth. This low value is in apparent contradiction with the above-mentioned results but may find an explanation in the accuracy with which the azimuthal direction of the recorded cosmic-ray particles was known. Also, the total intensity was measured in these experiments at an atmospheric depth where low energy secondary particles are most numerous and might cause a washing out of the primary asymmetry because of their angular divergence.

The recent development of constant-level high altitude balloons[8] provides the possibility of making

* Assisted by the joint program of the AEC and the ONR.
[1] T. H. Johnson, Rev. Mod. Phys. **10**, 193 (1938); Vallarta, Perusquía, and de Oyarzábal, Phys. Rev. **71**, 393 (1947).
[2] Schein, Yngve, and Kraybill, Phys. Rev. **73**, 928 (1948).
[3] W. C. Barber, Phys. Rev. **75**, 590 (1949).
[4] Biehl, Neher, and Roesch, Phys. Rev. **75**, 688 (1949).
[5] Adams, Anderson, Lloyd, Rau, and Saxena, Rev. Mod. Phys. **20**, 334 (1948).
[6] Swann, Morris, and Seymour, Phys. Rev. **75**, 1317 (1949).
[7] T. H. Johnson and J. G. Barry, Phys. Rev. **56** 219 (1939).
[8] Spilhaus, Schneider, and Moore, J. Meteorology **5**, 130 (1948).

directional intensity studies at small atmospheric depths where most of the particles observed might be primary particles. Even at these maximum balloon altitudes, however, there are still about 13 g/cm² of air above a vertical counter telescope, which may reduce the primary intensity by as much as 10 percent. In addition, measurements of the primary directional distribution might be distorted by secondary particles moving upward through the atmosphere, by the multiplication of the primaries at large zenith angles where the air path is longer, and by charged secondary particles trapped in the earth's magnetic field above the atmosphere. Accordingly, an investigation of these effects has been made at one latitude (56°N geomagnetic), preliminary to the main asymmetry study planned for a series of geomagnetic latitudes.

The initial flights were made at Princeton in February of 1948 using the Dewey and Almy Type J-2000 Neoprene balloons, carrying from 30 to 40 pounds of equipment.[9] It became apparent that these balloons were inadequate for keeping the equipment within a few percent of the top of the atmosphere for extended periods of time. At this time the Office of Naval Research made available through Project Skyhook the large constant-level balloons developed by General Mills, Inc.,[10] which proved capable of carrying payloads of 90 pounds to altitudes approaching 100,000 feet and remaining at constant level for extended periods. Geiger counter telescopes were designed for measuring the directional distribution, and in June, 1948, a series of six flights was carried out at Camp Ripley, Minnesota (geomagnetic latitude of 56°N), using the Project Skyhook facilities there.

I. COUNTER GEOMETRY

The counter geometry used during the main part of this series is shown in Fig. 1. There were five threefold telescopes, their axes pointing to zenith angles of 0°, 22½°, 45°, 67½°, and 90°, respectively. Thus, counters 1, 0, and 1 made up the vertical telescope; 2, 0, and 2, the 22½° unit; and so on—counter 0 being common to all telescopes. The 1.9-cm and 7.6-cm Pb filters could be inserted in quadrants within this geometry, but as the dotted circles show, the first counter in each telescope had to be moved out to accommodate the 16.7-cm Pb filter. The method of connecting the counters to the coincidence circuit is shown in Fig. 2. The angles subtended were 21° perpendicular and 48° parallel to the plane of the counters' length for the 0, 1.9-cm, and 7.6-cm Pb filters, and 14° and 37°, respectively, for the 16.7-cm filter. Because of the decreased cross section presented by the telescope to particles off the axis, the effective angular aperatures are about half these values.

Showers

Counters of 6-in. length were provided in the geometries to detect air showers and possibly bursts and multiple events in the lead. Referring to Fig. 1, detection was provided in the following manner: considering the vertical threefold telescope, a coincidence between this telescope and counters 10 and/or 12 was considered a shower of two or more particles associated with the vertical direction. The few such showers detected all occurred in the lower atmosphere (below 15 cm Hg pressure), no events being observed at maximum altitude. This latter observation was a little disturbing

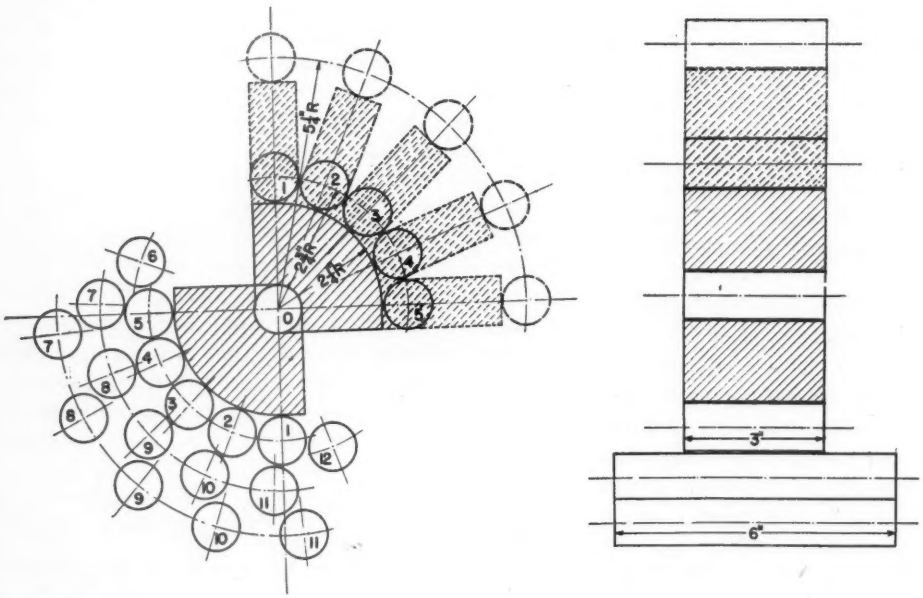

FIG. 1. Counter geometry.

[9] J. R. Winckler, Phys. Rev. 74, 1214 (1948).
[10] The inflation and launching techniques for this type of balloon are described in detail in reports on constant-level balloons of the Research Division, College of Engineering, New York University, A. F. Spilhaus, Director.

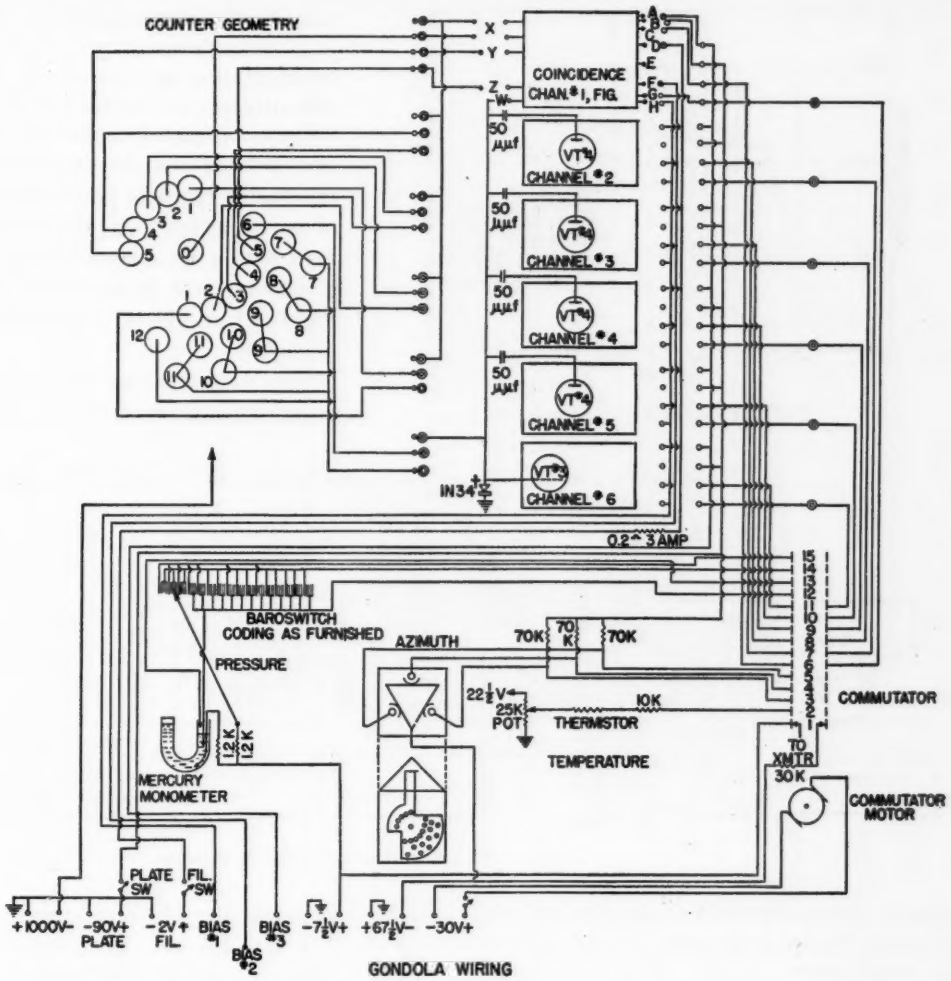

FIG. 2. Gondola wiring diagram.

since meson production events such as those observed by Schein and collaborators[11] might be expected. We have no explanation for this failure to observe such events other than that the shower channels did not work properly for some undetermined reason, or that the shower geometry was relatively inefficient for narrow bursts.

II. COUNTERS

A sketch of the Geiger-Müller counters used in the gondolas is shown in Fig. 3. A typical plateau is shown in Fig. 4. Although the geometric effective length was 3 inches, a measurement of the effective length similar to that used by Greisen and Nereson[12] gave a value of 2.75 inches.

III. DESCRIPTION OF GONDOLA AND COMPONENTS

The coincidence circuits (Fig. 5) were of the conventional threefold Rossi type, with a fourth tube forming a two-position stable flip-flop, regenerating through the screens of the first three tubes. The remaining four tubes on each channel were necessitated by the time-division properties of the telemetering

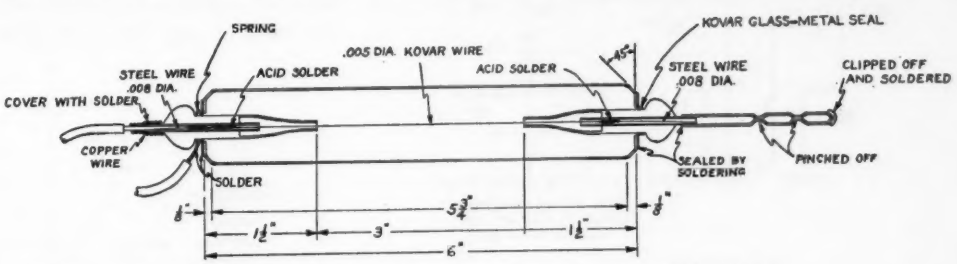

FIG. 3. Geiger-Müller counter construction.

[11] Schein, Jesse, and Wollan, Phys. Rev. **60**, 615 (1941); Schein, Iona, and Tabin, Phys. Rev. **64**, 253 (1943).
[12] K. Greisen and N. Nereson, Phys. Rev. **62**, 316 (1942).

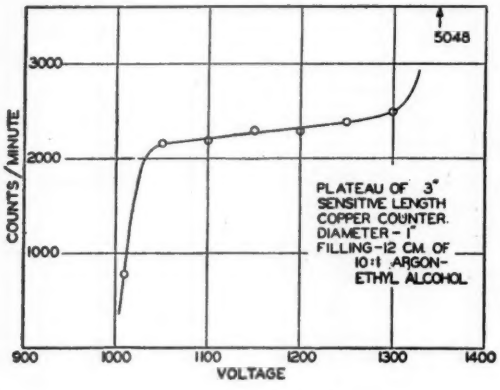

FIG. 4. Typical counter plateau.

sampling by the commutator were held over until the next cycle. "Partial" pulses which might be of doubtful interpretation on the record were thus avoided. One difficulty of the circuits was that each of the three bias voltages on each channel had to be selected with some care so that the circuit would work properly over a reasonable range of plate voltages. The resolving time of the coincidence circuit was better than 10 μsec., and tests with a Ra source nearby to give counting rates similar to those at maximum altitude showed that the effects of accidental coincidences and deadtime were negligible.

The pressure was measured by an aneroid baro-switch with coded contacts, supplemented by a small,

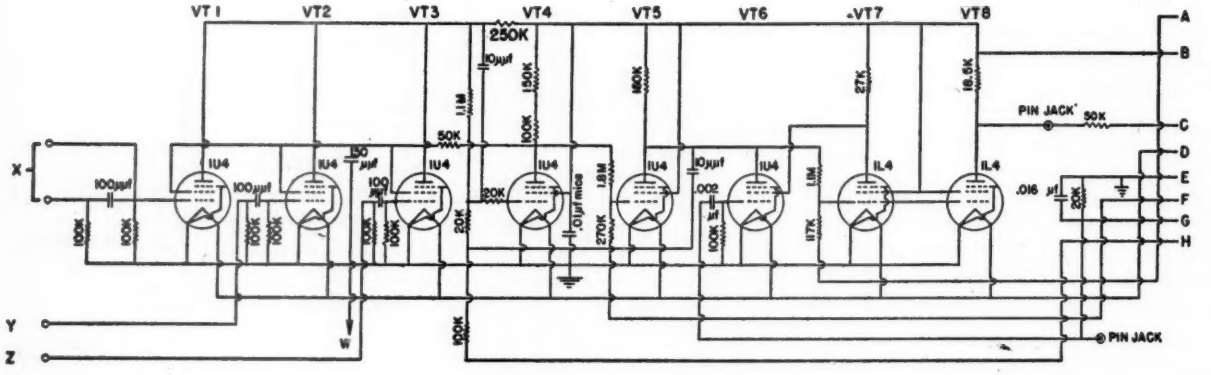

FIG. 5. Coincidence channel circuit diagram.

scheme, and constituted a second coincidence between the stored Geiger-coincidence count and the arrival of the commutator on that channel. Thus, events which occurred on a particular channel after the start of

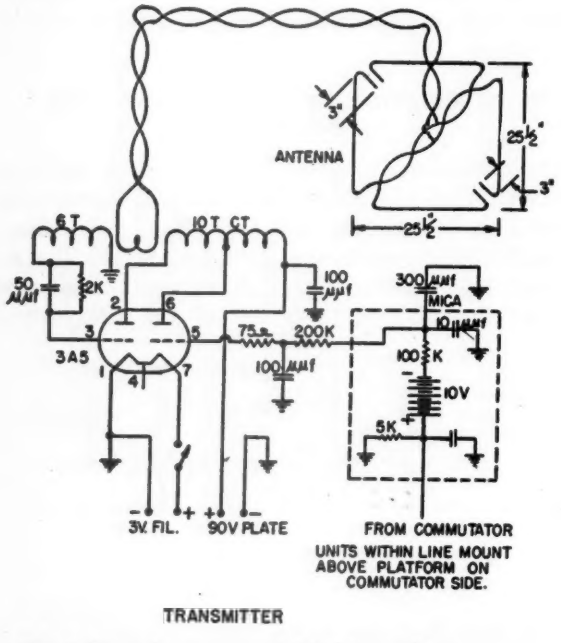

FIG. 6. 76-mc frequency-modulated transmitter.

non-spillable Hg manometer with contacts at about 1.0 and 1.5 cm. Temperatures were recorded by a resistive element (thermister). This "end" instrument, providing a continuously varying signal, could not be recorded on the flight film and had to be checked by occasionally measuring the pulse height on the temperature channel as shown on the monitoring oscillograph during flight. A pre-flight calibration of this pulse height made the measurement reliable to about ±5°C.

The azimuthal orientation of the gondola was determined by means of three banks of photo-cells, each placed on a side of an equilateral triangle and viewing a 180° sector. Thus, by forming combinations of the three photo-channels, we were able to obtain six azimuthal bearings of the gondola. It was found necessary to calibrate the photo-cell array with relation to the time of day for each flight. The photo-cells were

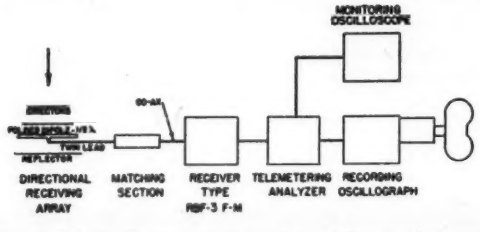

FIG. 7. Block diagram of ground receiving equipment.

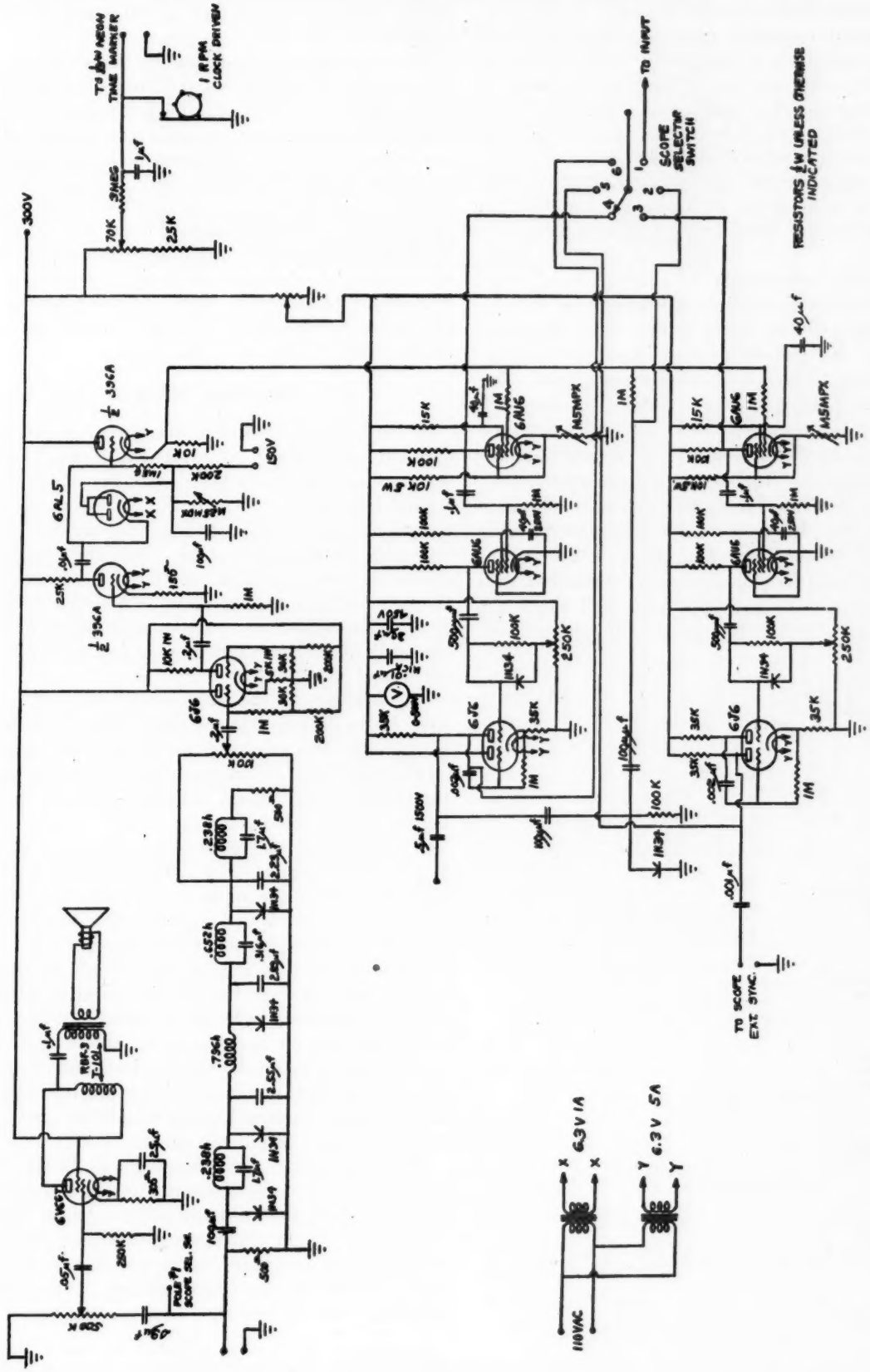

FIG. 8. Circuit diagram of telemetering analyzer.

shielded from reflected light from the balloon in order to obtain satisfactory azimuthal bearings. In flight the gondola rotated irregularly, often remaining at a fixed azimuthal position for a long period. Similar behavior was observed with clusters of Neoprene balloons in flights at Princeton. The addition of a jet-rotator with seven-foot arms operated by means of a cylinder of Freon refrigerant produced a uniform rotation of the gondola at high altitudes. Our experience indicates that without some such device to insure constant rotation the interpretation of the azimuthal data becomes very difficult.

All these end instruments, 15 channels in all, were fed into a time-division system of telemetering (Fig. 2). A small motor-driven wiper switch or commutator made contact successively to the 15 separate terminals at the rate of 10 complete samples per second. The information appearing on each terminal was either "on" or "off" and the frequency of a small reactance-tube modulated r-f oscillator (Fig. 6) was deviated accordingly by about 30 kc (carrier at approximately 76 mc). The r-f output of the transmitter was about 0.1 watt and was radiated by means of an Alford array, being concentrated in the horizontal plane. Even at this power output, little difficulty was experienced with signal strength, the signal still being well above the noise level when the equipment was 250 miles away at 40,000 feet. Apparently at 100,000-foot altitude, the signals would be satisfactory at 400 miles, the optical horizon.

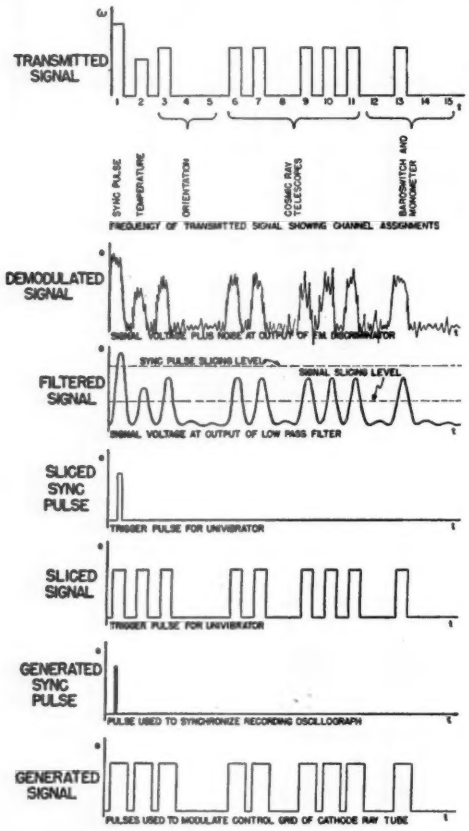

FIG. 9. Diagram of the telemetering process.

The gondola was constructed of Dow metal angles with aluminum sheet floor and ceiling; dimensions were 19 in.×19 in.×54 in. It contained, from top to bottom, photo-cells, counter array and temperature device, coincidence circuits, commutator and pressure instruments, batteries, transmitter, and antenna. The completed weight without lead but with enough battery power for about twelve hours of flight was 45 pounds. To keep the equipment at a reasonable temperature, 30° to 50°C, the gondola was completely covered with lightweight black paper, then one-third of the area covered with aluminum foil, and finally the whole gondola with two layers of Cellophane.

Receiving Scheme

A block diagram of the receiving and recording apparatus is shown in Fig. 7. The directional antenna fed through a $\lambda/4$ impedance matching section to the RBF-3 f-m receiver.[13] The output of the receiver was passed through a telemetering analyzer and into a recording oscillograph whose horizontal sweep (10 cycles/sec.) was synchronized with the commutator in the gondola by a master pulse transmitted once each cycle. The cathode-ray tube was photographed continuously by a 35-mm film moving at a rate of $\frac{1}{10}$ inch per second.

The functions of the telemetering analyzer (Fig. 8) were (1) to differentiate the signal from the noise, (2) to provide synchronizing pulses for the recording oscillograph, and (3) to modulate the control grid of the recording cathode-ray tube according to the intelligence of the received signal.

A diagram of the telemetering process is given in Fig. 9. All the graphs are plots of voltage *vs.* time with the exception of the topmost, which is frequency *vs.* time. The diagram is to a large degree self-explanatory; however, it should be noted that pulses applied to the cathode-ray tube modulated the *Z*-axis so that the camera saw the base line of the lowest graph at all times. A portion of a record is reproduced in Fig. 10. Note that each channel was blank unless "yes" information was given out by the end instrument, then the channel was filled in. Thus, a line appearing across any of the channels assigned to the cosmic-ray circuits was interpreted as a cosmic-ray count.

The system had the advantages of being able to transmit many pieces of information in a simple way, of having excellent discrimination against noise, of meeting the weight requirements of balloon equipment, and of giving a compact, easily readable record. However, it suffered the disdavantage of limiting the counting rate unless the commutating speed were

[13] Loaned by the U. S. Navy Underwater Sound Laboratory, New London, Connecticut, through the kindness of Captain William L. Pryor, Jr., Commanding Officer.

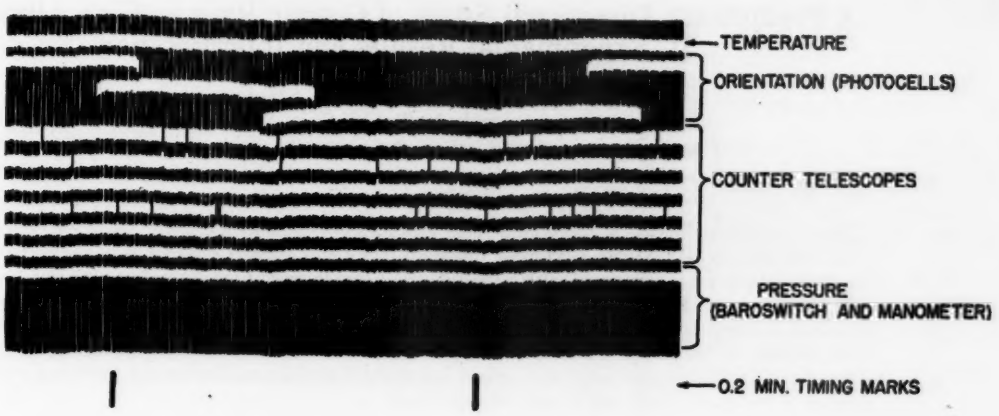

FIG. 10. Section of telemetering record.

increased,[14] and of requiring that random information be stored.

Calibration

The counter telescopes and coincidence circuits were calibrated by operating them at sea level over a long enough period to get 10,000 counts; i.e., about 1 percent statistics. Because of the long time required—the ground rate was about 1 count per minute without lead —two channels were run simultaneously by mounting the two adjacent telescopes so that each had a zenith angle of $11\frac{1}{4}°$. The counting rates thus obtained were corrected to the vertical rate without lead using the well-established $\cos^2\theta$ law. The results are given in Table I.

TABLE I. Calibration data summary.

Gondola No.	Amount of Pb cm	Vertical rate on ground without Pb—counts/min. (zenith angle during flight) 0°	22½°	45°	67½°	90°
V[a]	No Pb and 7.6	0.944±0.015	1.045±0.009	0.931±0.012	1.015±0.008	0.958±0.012
VI[b]	1.9	0.974±0.010	0.939±0.009	1.015±0.010	0.985±0.012	0.994±0.012
VII	7.6	0.932±0.009	0.955±0.008	1.031±0.010	1.017±0.008	1.000±0.011
VIII[c]	16.7	0.492±0.007	0.505±0.006	0.476±0.006	0.443±0.005	0.487±0.008
IX[d]	——	1.045±0.014	1.002±0.010	1.028±0.014		

[a] Two flights made with this gondola, one with no Pb, the other with 7.6 cm.
[b] Two flights made with this gondola with 1.9 cm Pb (one unsuccessful).
[c] At Princeton, modified to have 1.9 cm Pb in 0° and 22½° telescopes, no Pb in 45 telescope during flight.
[d] Gondola VIII had smaller solid angle to accommodate 16.7 cm of Pb (see Fig. 1). One flight.

Complete calibration data were taken at Minnesota ($\lambda = 56°$N, altitude 1100 feet). It is interesting to compare this to the Princeton data ($\lambda = 51°$N, 100 feet) by means of the ratio, average rate all telescopes at Minnesota/average rate all telescopes at Princeton, which equaled 1.059±0.004. This increased rate can be accounted for by the altitude difference, which was estimated to produce a 5 percent effect.[15]

Calibration data were taken after flights wherever possible and were in agreement with the pre-flight values.

ACKNOWLEDGMENT

We give our sincerest thanks to the many people who have contributed to this venture—in particular to Mr. D. B. Davis, head, and Messrs. E. G. Card and F. Schwarz of the shop staff for construction of gondolas and telemetering equipment; Miss H. Maginnis for construction of the counters; and Mr. E. L. Church for help in calibration of the units and analysis of data.

[14] The average deadtime introduced by the commutator was 0.05 sec. so that the counting rate loss at the maximum observed rate of 0.5 counts/sec. was about 2.5 percent. Since the losses were even less at the highest altitudes, no corrections were made.

[15] B. Rossi, Rev. Mod. Phys. **20**, 540 (1948).

A Preliminary Directional Study of Cosmic Rays at High Altitude.* II. Experimental Results and Interpretation

J. R. WINCKLER AND W. G. STROUD
Appendix by T. J. B. SHANLEY
Palmer Physical Laboratory, Princeton University, Princeton, New Jersey
(Received June 9, 1949)

The zenithal distribution of particles at high altitudes observed with counter telescopes has been compared with simple calculations concerning the multiplicity and angular divergence of secondary particles. The observations are in agreement with a sharply collimated forward type of production event, and disagree with the wide angle type of production of hard secondaries. The azimuthal distributions and zenithal distributions indicate a nearly isotropic primary flux, in agreement with geomagnetic considerations at geonetic latitude 56°N. The effects of the atmosphere on directional asymmetry measurements at 13-g/cm² atmospheric depths are concluded to be small, especially if lead filters of a few cm thickness are used. The number of low energy particles is small at this depth.

I. EXPERIMENTAL RESULTS

THE data obtained in the series of experiments described in the previous paper may be presented in four ways:

(1) Counting rate *vs.* atmospheric depth for various lead filter thicknesses at each zenith angle (average of all azimuths).
(2) The zenithal distribution for various filter thicknesses at several atmospheric depths (average of all azimuths).
(3) The integrated flux at various atmospheric depths.
(4) The azimuthal distribution (successfully measured for 45°, 67°, and 90° with 7.6 cm-lead filter only at approximately 1.5 cm Hg pressure).

The curves in category (1) are shown in Fig. 1. We have chosen to plot the pressure on a logarithmic scale as this accentuates the high altitude portions. Also, such a scale makes the ordinate nearly linear in the height, and thus permits a comparison of the curves on a basis of air path. Each curve has been normalized to the vertical ground counting rate of the same telescope with the lead filters removed, at Princeton. Absolute flux values may be obtained if the ground flux is known.[1]

During the period of the flights, a high counting rate telescope was used to monitor the ground intensity and, in addition, the Cheltenham ionization chamber data** were examined. No large fluctuations of intensity were present.

The curve with 1.9 cm of lead in the vertical and 22° zenith directions, and the no lead curve at 45° were obtained at Princeton (geomagnetic latitude 51°N) on November 30, 1948 (shown with heavy lines). All the other data were obtained at Camp Ripley, Minnesota (geomagnetic latitude 56°N) during the period May 22–July 4, 1948. The 7.6-cm values are an average of two flights, while all the others represent a single flight for each thickness of lead. The experiment carrying the 16.7-cm thickness of lead reached a height of 2.5 cm Hg, while the others all reached the 1.0-cm point.

The total vertical intensity curve is about the same as that obtained by Pfotzer[2] and more recently by Biehl *et al.*[3] The vertical curves with large amounts of lead resemble the data obtained by Schein,[4] showing a continual increase of intensity to the highest altitude reached (the convex upward shape is due to the logarithmic scale of pressure!). A large amount of the secondary radiation responsible for the peak in the total intensity may be removed with 1.9 cm of lead, but even the curve with this thickness shows a flat maximum at about the same point as the total intensity maximum. Data similar to this in the vertical direction have been obtained by Pomerantz[5] with filter thicknesses up to 8 cm. His results do not differ significantly from the present data.

A table of the energies necessary to penetrate the counters and the various thicknesses of Pb used in the telescopes is given in Table I.

Data on the zenith angle distribution of intensity obtained by Swann[6] with no lead filtering to pressure heights of 4 cm are in essential agreement with these results except for the horizontal intensity. Swann's horizontal value reaches about the same magnitude as the vertical intensity. In the present experiments (Fig. 1), the horizontal component is in general considerably lower than previously reported, with the exception of the measurement with 1.9 cm Pb, which increases with altitude to about the vertical value. Our other horizontal measurements with no or 7.6 cm lead (the latter from two flights) show a low value, the intensity with a 16.7-cm filter being extremely low (5 percent of the vertical). The very sharp dependence of intensity on zenith angle near the horizontal as shown

* Assisted by the joint program of the AEC and the ONR.
[1] E.g., the value $1.14 \cdot 10^{-2}$ particle/cm²/sec. given by B. Rossi (Rev. Mod. Phys. 20, 537 (1948)). Within the accuracy of this experiment, this flux may be assumed constant, provided no severe solar disturbances or magnetic storms occurred. (See previous paper for calibration procedure.)
** Furnished through the kindness of Dr. S. E. Forbush, Carnegie Institution of Washington.

[2] G. Pfotzer, Zeits. f. Physik **102**, 23, 41 (1936).
[3] Biehl, Montgomery, Neher, Pickering, and Roesch, Rev. Mod. Phys. **20**, 360 (1948).
[4] Schein, Jesse, and Wollan, Phys. Rev. **59**, 615 (1941).
[5] M. Pomerantz, Phys. Rev. **75**, 69 (1949).
[6] Swann and co-workers, Nat. Geo. Soc. Contributed Tech. Papers, Stratosphere Series No. 2.

by the present results (see Fig. 2) would make the observed intensity very sensitive to the angle included by the telescope, or to the leveling of the instrument.

Because of the important connection between angular divergence of secondary particles and the horizontal intensity, this measurement has been repeated by T. J. B. Shanley, of this laboratory, using a telescope with a small angular operation (12:1). (See Appendix.) His results show a *large* horizontal intensity with no lead, about equal to our measured vertical value, and therefore in agreement with Swann's data. The drop of intensity with lead filtering for horizontal particles, which is in contrast to what is observed in the vertical direction at high altitude indicates that the horizontal flux is of a non-penetrating secondary nature, in agreement with an analysis presented later in this paper.

The peak total intensity, and in fact all the other curves with various filter thicknesses, shift towards greater heights as the zenith angle is increased. This effect is apparently connected with the greater air path seen at low zenith angles, as first pointed out by

TABLE I. Energies necessary to penetrate the counters and the various thicknesses of Pb used in the telescopes.

Minimum energy required by various particles to traverse telescope					Electrons[c]	
Thickness of material in counter telescope		Min. energy in Mev required to traverse[a]		Shower units of material	Energy of incoming electrons (ev)	Probability of finding no electrons under material
cm Pb	g/cm²	mesons[b]	protons			
0.29[d]	3.3[d]	15.0	38.0	0.81	7×10^7	0.07
					5×10^8	0.006
					4×10^9	0.0006
2.2	24.8	53.0	130.0	6.1	7×10^7	0.19
					5×10^8	0.04
					4×10^9	0.003
7.9	89.3	140.0	270.0	22.0	7×10^7	1.0
					5×10^8	0.7
					4×10^9	0.09
17.0	192.0	245.0	430.0	47.5	7×10^7	practically 1
					5×10^8	practically 1
					4×10^9	practically 1

[a] From curves prepared by E. P. Gross, Princeton University, December, 1947.
[b] Meson of mass 200 m_e is considered.
[c] N. Arley, *Stochastic Processes and Cosmic Radiation* (G.E.C. Gads Forlag, Copenhagen, 1943).
[d] g/cm² of Cu—obtained by considering only the counter walls.

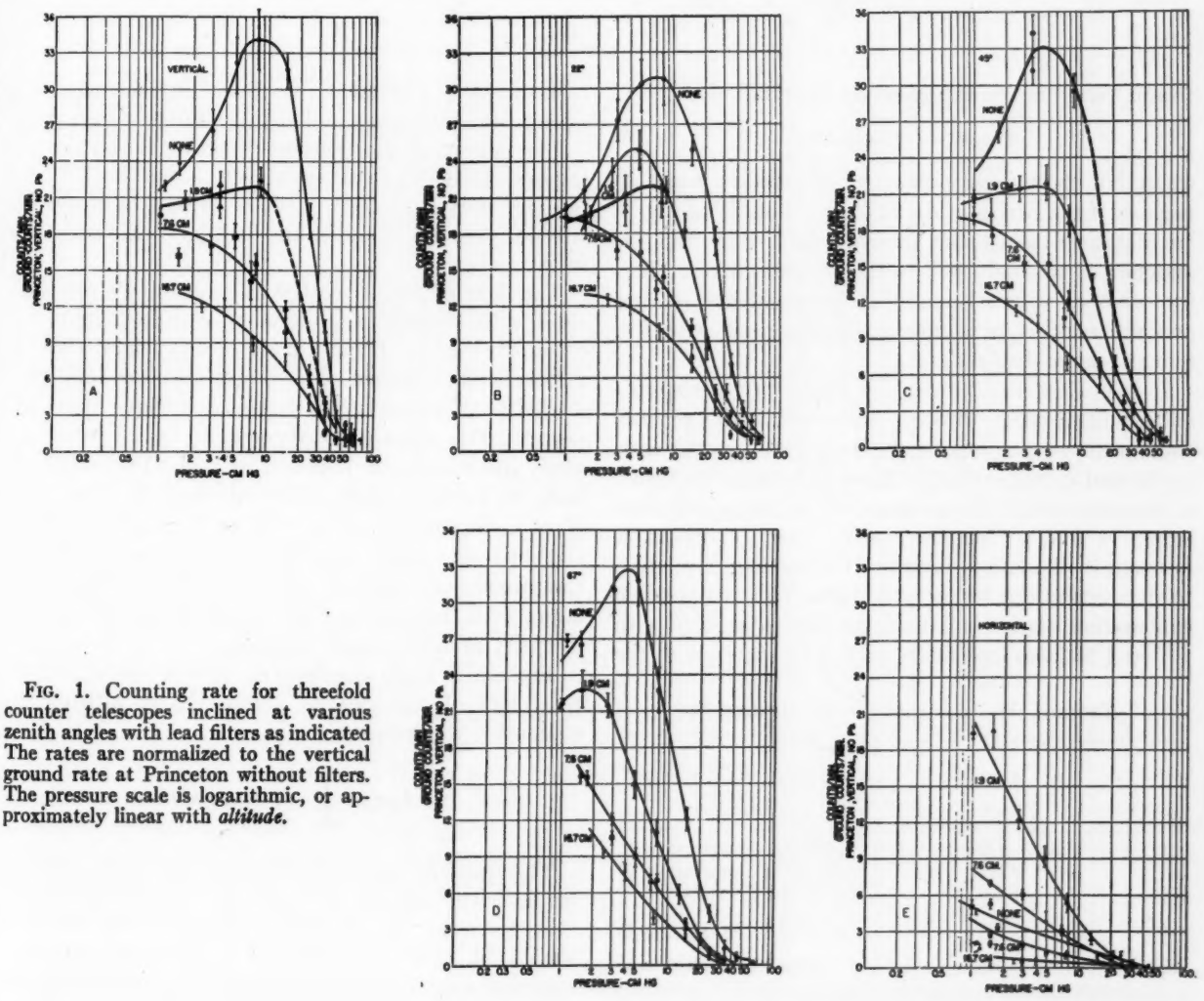

FIG. 1. Counting rate for threefold counter telescopes inclined at various zenith angles with lead filters as indicated The rates are normalized to the vertical ground rate at Princeton without filters. The pressure scale is logarithmic, or approximately linear with *altitude.*

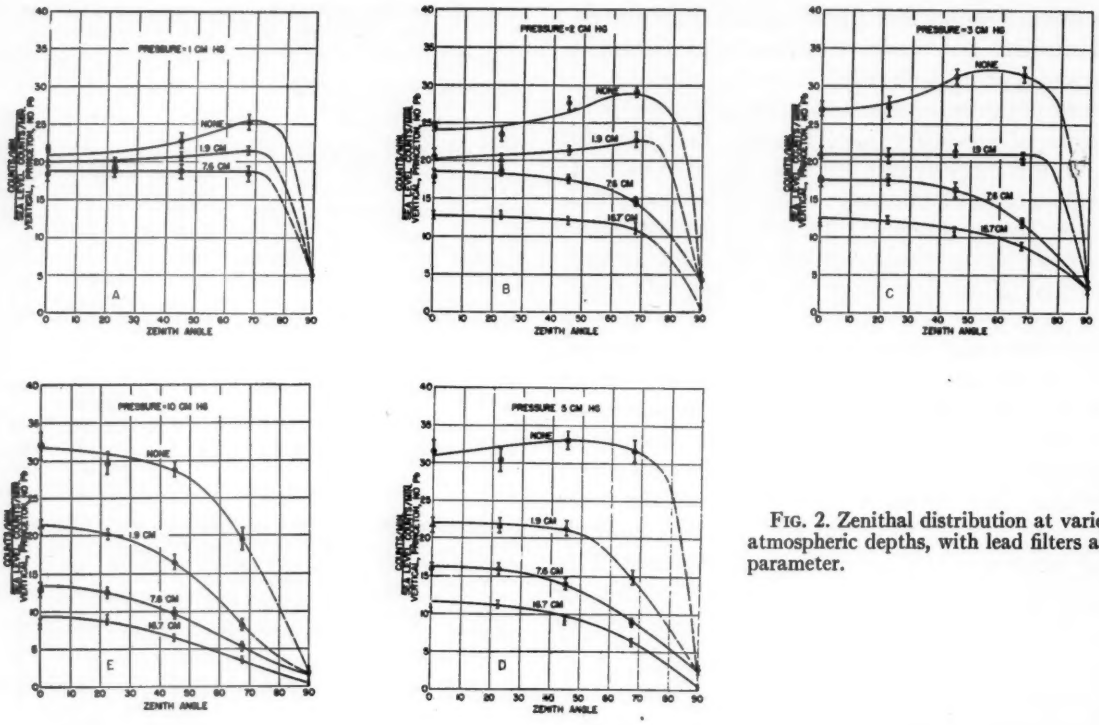

FIG. 2. Zenithal distribution at various atmospheric depths, with lead filters as a parameter.

Swann,[6] and may be expressed by the relation

$$I(p, \theta) = I(p \sec\theta, 0),$$

where I is the intensity observed at pressure p and at angle θ. If the curves at $\theta = 22\frac{1}{2}°$, 45°, and 67° of Fig. 1 are displaced along the pressure axis, they can be matched surprisingly well to the vertical curves. Then the ratio of values brought into coincidence on the pressure scale is in approximate agreement with the $\sec\theta$ as seen in Table II.

It is evident that the entire cosmic-ray absorption and multiplication process observed with vertical counter telescopes can be duplicated at lower zenith angles and correspondingly higher altitudes. This result is not surprising if the primary flux of particles is isotropic in free space. One would expect, however, a decrease in the meson intensity for low angles relative to the vertical due to decay in flight. This is a possible explanation of the fact that the curves at $67\frac{1}{2}°$ with 7.6- and 16.7-cm lead filters cannot be matched to the corresponding vertical curves by a displacement, but have a lower intensity and slightly different curvature.

TABLE II. Test of relation $I(p, \theta) = I(p, \sec\theta, 0)$.

θ	$\sec\theta$	Pressure scale ratios to match intensity-height curve at θ to value indicated
$22\frac{1}{2}°$	1.08	1.0±0.1 matched to 0°
45°	1.41	1.6±0.1 matched to 0°
$67\frac{1}{2}°$	2.60	2.2±0.1 matched to 0°
$22\frac{1}{2}°$	$\sec 45/\sec\theta = 1.3$	1.5±0.1 matched to 45°
$67\frac{1}{2}°$	$\sec 45/\sec\theta = 1.9$	2.0±0.1 matched to 45°

The important question as to whether the secant law implies a large degree of persistence of direction between primary and secondary particles cannot be answered without detailed analysis, and will be considered later in this paper.

The data of Fig. 1 plotted as zenith angle distributions with various lead filters at various heights are given in Fig. 2. These curves clearly show that at atmospheric pressures of 5 cm or less the unfiltered intensity at larger zenith angles is greater than the vertical. This effect is greatly reduced by a 1.9-cm lead filter, and completely removed by larger thicknesses of lead. At 1-cm pressure, a filter of about 3 cm or more gives a constant intensity with zenith angle nearly to the horizontal where the sharp drop is observed. But as the atmospheric depth is increased, the telescopes with larger lead thicknesses show a continuous decrease of intensity as zenith angle increases.

The zenith angle distributions enable one to find the total flux of particles as a function of altitude by evaluating the integral

$$J_2 = 2\pi \int_0^{\pi/2} I(\theta) \sin\theta d\theta.$$

This quantity has been plotted in Fig. 3, in which the sea-level vertical flux at Princeton was assumed to be that given by Rossi.[1] This omnidirectional flux, J_2, should be that measured by a spherical ionization chamber with walls equivalent to 2.6 g/cm² of Cu, and

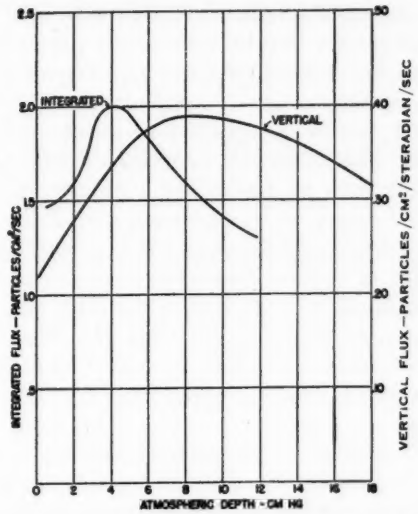

FIG. 3. The omnidirectional flux, as determined from counter telescopes without lead (2.6 g/cm² counter wall). Shown for comparison is the vertical flux (particles/cm²/sec./steradian note omission in drawing).

it can be seen from the figure that the sharp maximum at 4 cm pressure occurs at the same place as the ion chamber or single counter measurements.[7] The vertical counter telescope, on the other hand, gives the much broader maximum peaking at about 8 cm Hg.

The azimuthal distribution measured at 1.5-cm Hg height is given in Fig. 4. A nearly uniform rotation of the equipment was achieved on one of the flights with 7.6-cm lead filtering on all telescopes for a period of about four hours. The data have been summed in each 45° sector at zenith angles of 45°, 67½°, and 90°, and are entirely consistent with an isotropic primary flux. A similar result was obtained by Swann without lead filters,[6] although at lower altitude where secondary particles are more numerous.

II. INTERPRETATION

It is probable that even at the heights reached by high altitude balloons an appreciable fraction of the primary rays have undergone absorption in the atmosphere, and have multiplied into secondary rays which may diverge in direction from the primary rays. The angular divergence of secondaries may obscure an azimuthal asymmetry measurement at fixed zenith angle, and the multiplication and absorption processes give an erroneous relation between primary intensities at different zeniths because of the changing air path. The horizontal intensity observed in these experiments indicates that the angular divergence of penetrating secondaries is not large, but the multiple production of forward-moving secondaries is shown even at the highest altitudes reached by the increase of intensity with zenith angle at angles as large as 70°.

To give a more quantitative meaning to these experiments, several kinds of assumptions about the angular divergence and multiplicity of secondary particles have been made, and in each case the expected zenithal distribution was calculated for comparison with experiment.

An isotropic primary flux of intensity I_0 particles/sec./cm²/per steradian was assumed. These particles are absorbed in the atmosphere according to the relation

$$I' = I_0 e^{-\mu x \sec\psi}, \qquad (1)$$

where x is the atmospheric depth in g/cm², μ the absorption coefficient in cm²/g, and ψ the zenith angle of the ray. Secondary particles are produced by a catastrophic event with an angular distribution in the laboratory system given by a function, $f(\theta_{12})$, of the angle θ_{12} between the primary and secondary directions. Consider those secondaries produced by a primary entering an atmospheric layer of thickness dx (see Fig. 5) at zenith angle ψ and azimuth ϕ, where $\phi=0$ is in the plane passing through the vertical and the direction of observation. The layer dx is at depth x and the secondary particles travel at a zenith angle θ toward the point of measurement located at atmospheric depth y. The secondary particles are also assumed to be absorbed exponentially with coefficient ν according to the relation

$$I'' = I_0'' e^{-\nu|y-x|\sec\theta}. \qquad (2)$$

The multiplicity N (number of secondaries/primary) is given by

$$N = 2\pi \int_0^\pi f(\theta_{12}) \sin\theta_{12} d\theta_{12}. \qquad (3)$$

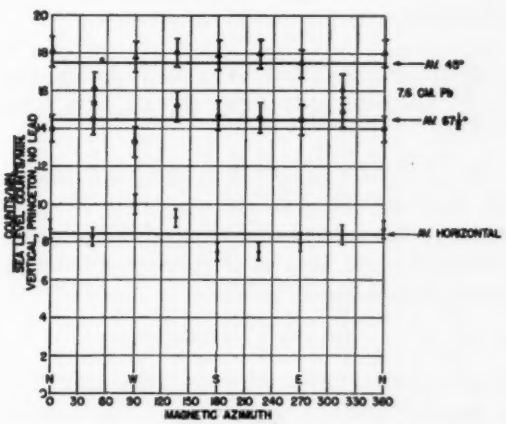

FIG. 4. The azimuthal distribution at about 1.5 cm Hg atmosphere depth with 7.6-cm Pb filter, at 45°, 67½°, and 90° zenith angles.

The intensity $I(y, \theta)$ is then given by the sum of primaries and secondaries reaching the depth y at zenith angle θ:

$$I(y,\theta) = I_0 e^{-\mu y \sec\theta} + \mu I_0 \sec\theta \int e^{-\mu x \sec\psi} \times \sin\psi e^{-\nu|y-x|\sec\theta} f(\theta_{12}) d\psi d\phi dx. \qquad (4)$$

[7] Millikan Neher, and Pickering, Phys. Rev. **61**, 397 (1942).

Equation (4) includes both upward and downward moving particles if the absolute value of the secondary path length, $y-x$, is preserved in the integration.

Consider three kinds of secondary distributions:

Case 1: $f(\theta_{12})=0$.

This corresponds to the experimental condition that the secondaries have been completely absorbed by filters in the apparatus, and that only the primary rays are detected, their intensity being given by the first term of Eq. (4).

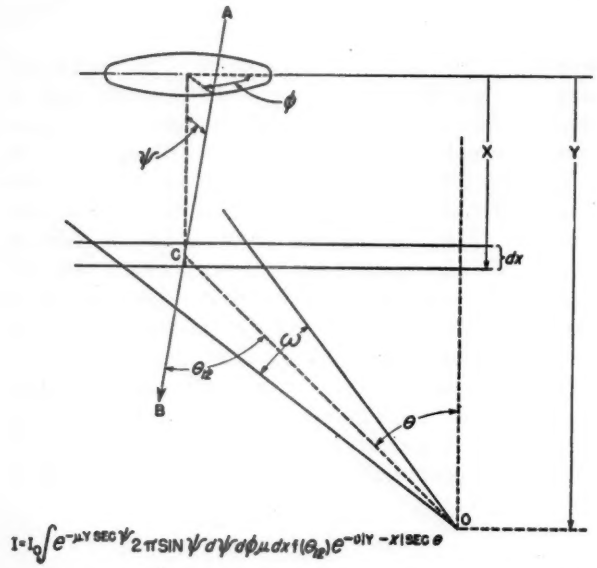

FIG. 5. The geometry considered in Eq. (4). AB is the path of a primary ray, making an angle ψ with the vertical and an angle ϕ, in the horizontal plane, with the plane through the vertical and the direction of observation CO. Secondaries produced in a layer dx at atmospheric depth x with an angle of divergence θ_{12} from AB are observed at 0 at a depth y by a telescope of solid angle ω at a zenith angle θ.

Case 2: $f(\theta_{12})=0$ when $\theta_{12}\neq 0$, $f(\theta_{12})=N$ when $\theta_{12}=0$ which has the physical meaning that N secondary particles continue in the direction of the primary after the absorption of the latter. (These secondaries are detected as individual particles.)

Case 3:
$$f(\theta_{12})=c(1+\cos\theta_{12})^n. \tag{5}$$

This gives a distribution of secondaries with an adjustable angular divergence. For $n=1$, the intensity at $\theta=\pi/2$ is 50 percent of that at $\theta=0$, but at this same angle drops to about 5 percent for $n=4$. A large horizontal and upward flux results from so broad an assumed distribution.

In Fig. 6 are plotted the calculated depth-zenith angle distribution in Case 1, Eq. (4) being reduced to:

$$I(y,\theta)=I_0 e^{-\mu y \sec\theta}. \tag{6}$$

For comparison with experiment, one observes that the vertical intensity at 1 cm pressure where secondaries are not numerous is reduced very little by a 7.6-cm lead filter. At greater depths where secondaries are more numerous, the same filter has a very large effect. Thus this 7.6-cm filter seems to approximate the ideal filter of Case 1, which is supposed to select only primary particles. The observed intensities using this filter agree best with an absorption coefficient μ of 1/275 cm²/g and appear to be consistent with the interpretation that these particles are primary rays. However, the possibility of equally *penetrating* secondaries produced with a multiplicity near unity is not ruled out. Also, the observed horizontal flux at 10-cm Hg depth with the 7.6-cm Pb filter is too high to consist of primary particles, whose intensity, as given by Eq. (6), would be very low.

Case 2, in which N secondaries continue in the direction of the primary ray after the catastrophic absorption of the latter, results in a simplification of Eq. (4) to

$$I(y,\theta)=I_0 e^{-\mu y \sec\theta}+\mu N I_0 \sec\theta \int_{x=0}^{y} e^{-\mu x \sec\theta} e^{-\nu|y-x|\sec\theta} dx$$

$$=I_0\left\{\left[1+\frac{\mu N}{\nu-\mu}\right]\exp(-\mu y\sec\theta) - \frac{\mu N}{\nu-\mu}\exp(-\nu y\sec\theta)\right\}. \tag{7}$$

Formula (7) is plotted in Fig. 7.

The best fit with the unshielded telescope data (see Fig. 2) at $y=13.5$ g/cm² and $y=135$ g/cm² is obtained with N close to 3, $\mu=1/275$ cm²/g and ν between 1/100 and 1/150 cm²/g.

If the effect of the earth's curvature is taken into account at the highest altitude, the calculated horizontal flux I/I_0 is raised both in Case 1 and Case 2 to about 0.3, in agreement with experiment at 13.5 g/cm². This point is discussed more fully in a later section.

Equation (7) has been compared with the *unshielded* telescope data, as the effects of lead absorbers on secondary particles at various points in their range is difficult to estimate. The exponential, rather than the range type of absorption was chosen for secondaries because of their probable distribution in energy and nature.

Assume now a wide angular divergence for secondaries given by Eq. (5) with $n=1$. The multiplicity of secondary production in terms of c is given by

$$N=2\pi c\int_0^{\pi}(1+\cos\theta_{12})\sin\theta_{12}d\theta_{12}, \tag{8}$$

which leads to the normalization $c=N/4\pi$. Using the relation

$$\cos\theta_{12}=\cos\theta\cos\psi-\sin\theta\sin\psi\cos\phi,$$

the angles being defined in Fig. 5, the ratio of observed

to primary flux is given by the equation

$$I/I_0=e^{-\mu y\ \sec\theta}+(\mu N/4\pi\cos\theta)\int\exp[-\mu x\sec\psi]$$
$$\times\exp[-\nu|y-x|\sec\theta]\sin\psi(1+\cos\theta\cos\psi$$
$$-\sin\theta\sin\psi\sin\phi)d\psi d\phi dx. \quad (9)$$

The integration is first carried out with respect to the azimuth θ over a 2π-interval. The integration with respect to the atmospheric depth x is carried out from $x=0$ to $x=y$ for downward moving secondaries, and from $x=y$ to $x=y_0$ for upward moving secondaries, where y is the depth of the point of observation and y_0 is the lower limit of the atmosphere. For upward particles, the distribution function $f(\theta_{12})$ must be replaced by $f(\pi-\theta_{12})$.

The downward moving flux, including primaries, is given by the relation

$$I_{\text{down}}/I_0=\exp(-\mu y\sec\theta)+\frac{N}{2}(I_1+I_2), \quad (10)$$

where

$$I_1=[-E_i(-\mu y)][(\mu/\nu)^3\cos^3\theta+(\mu/\nu)^2\cos\theta-(\mu/\nu)\mu y$$
$$-(\mu/\nu)^2\mu y\cos^2\theta+\tfrac{1}{2}(\mu/\nu)(\mu y)^2\cos\theta]$$
$$-[E_i(\nu y\sec\theta-\mu y)][e^{-\nu y\ \sec\theta}(-(\mu/\nu)^2\cos\theta$$
$$-(\mu/\nu)^3\cos^3\theta)]+e^{-\mu y}[\mu/\nu+(\mu/\nu)^2\cos^2\theta$$
$$+\tfrac{1}{2}(\mu/\nu)\cos\theta-\tfrac{1}{2}(\mu/\nu)\mu y\cos\theta],$$

$$I_2=-e^{-\nu y\ \sec\theta}\{\log_e[1-(\nu\sec\theta/\mu)]$$
$$\times[(\mu/\nu)^3\cos^3\theta+(\mu/\nu)^2\cos\theta]$$
$$+\mu/\nu+\tfrac{1}{2}(\mu/\nu)\cos\theta+(\mu/\nu)^2\cos^2\theta\}.$$

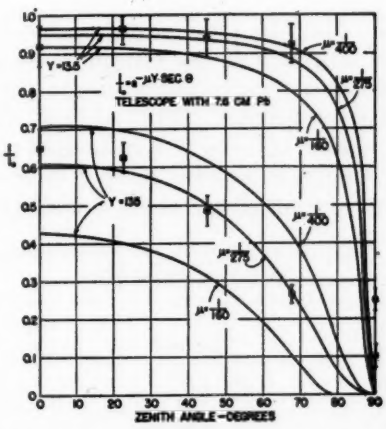

FIG. 6. Plot of $I/I_0=e^{-\mu y\ \sec\theta}$ *vs.* zenith angle θ, for absorption coefficients of $\mu=1/400$, $1/275$, and $1/160$ cm²/g, respectively, at atmospheric depths given by $y=13.5$ and 135 g/cm². The squares represent the experimental data obtained under 7.6 cm Pb at these two atmospheric depths.

The upward flux is

$$I_{\text{up}}/I_0=\frac{N}{2}\{[-E_i(-\mu y)]$$
$$\times[-(\mu/\nu)^3\cos^3\theta-(\mu/\nu)^2\cos\theta$$
$$-(\mu/\nu)\mu y-(\mu/\nu)^2\mu y\cos^2\theta-\tfrac{1}{2}(\mu/\nu)\mu^2y^2\cos\theta]$$
$$+[-E_i(-\{\mu y+\nu y\sec\theta\})]e^{\nu y\ \sec\theta}$$
$$\times[(\mu/\nu)^2\cos\theta+(\mu/\nu)^3\cos^3\theta]$$
$$+e^{-\mu y}[\mu/\nu+(\mu/\nu)^2\cos^2\theta-\tfrac{1}{2}(\mu/\nu)\cos\theta$$
$$+\tfrac{1}{2}(\mu/\nu)\mu y\cos\theta]\}. \quad (11)$$

For the special case $\theta=90°$, these expressions reduce to

$$I/I_0=\frac{N\mu}{2\nu}\{e^{-\mu y}-\mu y[-E_i(-\mu y)]\}, \quad (12)$$

which includes the contributions to the horizontal flux from both directions. E_i is the integral-exponential function, tabulated, for example, in the W.P.A. Mathematics Tables.***

The contributions to the observed intensity from upward and downward moving particles are listed in Table III, and the total intensity is plotted in Fig. 8 for a range of values of θ at atmospheric depths $y=13.5$ and $y=135$ g/cm². In one case it was assumed $N=3$, $\mu=1/275$, and $\nu=1/125$, and in a second case $N=10$, $\mu=1/275$, and $\nu=1/60$. The consequences of the assumed distribution $f(\theta_{12})=c(1+\cos\theta_{12})$ are, as shown in Fig. 8, a high horizontal particle flux, and a vertical intensity at $y=135$ g/cm² which is *less* than that at $y=13.5$ g/cm². The latter fact is in complete disagreement with experiment (e.g., the Pfotzer maximum). The over-all intensity for $N=10$ is too high at 13.5 g/cm² atmospheric depth. However, for $N=3$, the

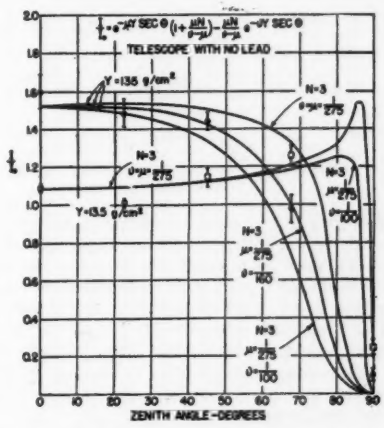

FIG. 7. Zenithal distribution of particles under the assumption of a sharply collimated forward burst of multiplicity N. Ordinate ratio of total flux to incident primary flux.

*** *Tables of Sine, Cosine, and Exponential Integrals* (U. S. Works Projects Administration, 1940) Vol. 2.

horizontal intensity is about correct to agree with our most recent measurement, as well as that of Swann.[6] Best agreement with the experimental results would evidently be obtained by a production event combining Case 2 and Case 3, that is, a penetrating bundle of forward moving particles (mesons?) and a wide angle burst of low energy particles (electrons, nucleons?), which can be absorbed in a few cm of lead.

In all the computations so far in this paper, the earth's atmosphere was assumed to be flat, corresponding to an earth of infinite radius. The effect of the finite curvature at high altitude and low zenith angles is to shorten the air path, and to make its value finite even in the horizontal direction. If $\rho(r-r_e)$ is the atmospheric density at a radius r, where r_e is the earth's radius, the total air mass in the vertical direction above a point $r=r_0$ is

$$m_0=\int_{r_0}^{\infty}\rho(r-r_e)dr. \tag{13}$$

The air mass seen from the point r_0 obliquely at a zenith angle θ is given by

$$m=\int_{r_0}^{\infty}\frac{\rho(r-r_e)rdr}{(r^2-r_0^2\sin^2\theta)^{\frac{1}{2}}}. \tag{14}$$

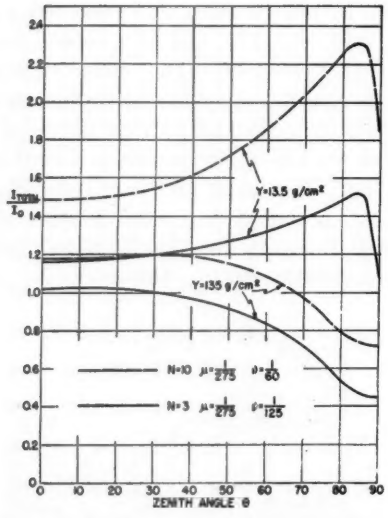

FIG. 8. Zenithal distribution of particles at two atmospheric depths calculated from an assumed wide-angle burst of secondaries. The lack of increase with depth for vertical particles (Pfotzer maximum) is in disagreement with experiment for both $N=3$ and $N=10$. For $N=10$ the over-all intensity at 13.5 g/cm² depth is too high. The horizontal intensity at this depth for $N=3$ agrees with our most recent measurement, and the data of Swann for unshielded telescopes. These results suggest penetrating *forward* moving particles and a wide-angle burst of low energy particles as the typical production event.

If we take for ρ the function $\rho=\rho_0\exp[-\alpha(r-r_e)]$ which corresponds to the earth's atmosphere with r and r_e in kilometers and $\alpha=0.12$ and make the substitution $\delta=r-r_e$, we find for the ratio P of the vertical-to-the-oblique air mass, the value

$$m/m_0=P=0.12(r_0/2)^{\frac{1}{2}}\int_0^{\infty}\frac{e^{-0.12\delta}d\delta}{((r_0/2)\cos^2\theta+\delta)^{\frac{1}{2}}}. \tag{15}$$

In this expression, we have neglected δ in comparison with r_0 because of the rapid falling off of the integrand with δ. In the case $r_0/2\cos^2\theta\gg\delta$ corresponding to values of θ between 0 and 70°, P reduces to $\sec\theta$. The behavior of P as compared with $\sec\theta$ is given in Table IV. P is insensitive both to the atmospheric depth and the value of α in the atmospheric density function. It is not possible to take account of this air path correction exactly in the type of secondary angular distribution assumed in Case 3, but because of the weak directional correlation between primary and secondary particles the effect on the calculations is very small. However, in Cases 1 and 2 the correction may be applied. The actual air path at $\theta=90°$ and at an atmospheric depth of 13.5 g/cm² is the same as the secant law air path at 88°. Accordingly, I/I_0 (secant law, 88°)$=I/I_0(90°)$. This correction brings the calculation into apparently good agreement with the horizontal measured value in both Case 1 and Case 2.

TABLE III. Directional distribution of particles, assuming widely diverging secondaries $[f(\theta_{12})=c(1+\cos\theta_{12})]$.

Zenith angle degrees	Particle flux I/I_0: $N=3$, $\mu=(1/275)$ cm²/g, $\nu=(1/125)$ cm²/g, Atmospheric depth 13.5 g/cm² Down	Up	135 g/cm² Down	Up	$N=10$, $\mu=(1/275)$ cm²/g, $\nu=(1/60)$ cm²/g, Atmospheric depth 13.5 g/cm² Down	Up	135 g/cm² Down	Up
0	1.05	0.11	0.98	0.04	1.25	0.24	1.10	0.08
40	1.05	0.17	0.90	0.07	1.26	0.35	1.06	0.13
70	1.06	0.32	0.59	0.14	1.42	0.61	0.73	0.25
80	1.06	0.42	0.35	0.18	1.52	0.74	0.49	0.30
85	1.02	0.49	0.27	0.20	1.49	0.82	0.41	0.33
90	0.57	0.57	0.23	0.23	0.91	0.91	0.36	0.36

III. CONCLUSIONS

The results of these experiments are in accord with a mean free path for primary rays in air of 275 g/cm², with a rather large uncertainty due to the effects of penetrating secondaries. The zenithal distribution curves considered in the light of an analysis of secondary particle production indicate sharply forward moving secondaries of multiplicity about 3 and with a mean

TABLE IV. Comparison of air paths. Flat atmosphere (secant law) *vs.* curved atmosphere.

Zenith angle degrees	Secant θ	Relative air path—P
0	1.0	1.0
45	1.41	1.41
70	3.08	3.00
80	5.75	5.25
85	11.46	9.45
89	57.1	25.4
90	∞	27.0

free path of from 100 to 150 g/cm². These conclusions are supported by other recent results[8] which indicate that the east-west asymmetry is preserved to a large extent at considerable atmospheric depths. The horizontal flux is a very sensitive measure of the angular divergence of secondary rays. A large angular divergence produces a large horizontal and upward moving flux. The experimental results indicate that the widely divergent particles responsible for the horizontal flux have low energy and are easily observable as such.

The theoretical assumptions are certainly an oversimplified picture of the complex cosmic-ray processes at the top of the atmosphere. Nevertheless, these results show that the effects of the atmosphere at 13 g/cm² depth on a projected study of the primary directional asymmetry are not large. The small effect of lead absorbers on vertical rays at this depth rules out any appreciable number of electrons or photons of low energy trapped in the earth's magnetic field above the atmosphere. The multiplication of primaries into secondaries is noticeable as an increase of intensity at large zenith angles where the air path is larger, but lead filters of a few cm thickness reduces the apparent multiplicity to near unity. Finally, the analysis shows that those secondary rays are sharply collimated, and therefore asymmetry measurements should not be in error due to secondary effects.

ACKNOWLEDGMENT

The writers wish to express their indebtedness to Professor J. A. Wheeler, who first interested the senior author (J. W.) in this problem, and who has provided support and encouragement at every step in the way. Thanks are due to Mr. Kenneth Ford for evaluating some of the integrals.

APPENDIX ON REDETERMINATION OF HORIZONTAL INTENSITY WITH NO LEAD FILTER

In view of the anomalous result obtained for the horizontal intensity with no lead filter (see Fig. 1E), a threefold horizontal Geiger counter telescope was sent to 78,000 feet, counting rate and pressure being radioed to the ground by an f-m telemetering system. The counters had an effective length of 12 inches, one inch diameter, and were filled with a mixture of argon and ethelyne. End counters were separated by 12 inches, giving an effective angular opening of about 4°. Counter pulses were fed into a threefold Rossi coincidence circuit with a resolving time of 2×10^{-5} sec. The vertical ground counting rate of the counter telescope was 1.986±0.021 counts per minute. This apparatus was launched from Princeton on May 14, ascended to an altitude of 2.3±0.2 cm Hg (~78,000 feet) at an average rate of about 800 feet per minute. It remained at this altitude for 153 minutes, then descended at approximately the same rate and was recovered. Radio contact with the equipment was maintained throughout the flight. After the flight the vertical ground counting rate was 1.90±0.04 counts per minute, the decrease being attributable to a considerable misalignment of the counter telescope when the equipment struck the ground.

TABLE V. Counting rate vs. pressure in cm Hg. Each counting rate shown in the second column is an average value over the corresponding pressure range indicated in the first column, corrected for counter inefficiency. The third column gives the ratio of the actual counting rates to the ground counting rate of the telescope in a vertical position. Data marked with an asterisk was obtained during the descent, all other data during the ascent.

Pressure range in cm Hg	Average counting rate, counts per min.	Normalized counting rate
21.2–12.7	6.8±0.9	3.4±0.5
12.7–6.8	11.2±0.8	5.6±0.4
6.8–5.6	25.0±2.0	12.6±1.0
5.6–4.1	33.4±2.0	16.8±1.0
4.1–3.1	37.2±2.0	18.7±1.0
3.1–2.5	42.5±2.1	21.4±1.1
2.5–2.1	42.84±0.25	21.57±0.13
*2.5–3.4	39.6±2.2	20.0±1.1
*3.4–4.4	33.4±2.0	16.8±1.0
*4.4–5.9	30.4±1.9	15.3±1.0
*5.9–7.1	22.6±2.0	11.4±1.0
*7.1–12.1	18.6±1.1	9.4±0.6

The results are given in Table V, corrected for counter inefficiency. No shower correction was applied. The correction for accidental threefold coincidences is negligible.

These results show that the no lead horizontal counting rate exceeds all horizontal counting rates with lead filters between the counters. We here obtain 21.57 counts/min. at 2.2 cm Hg with no lead, compared to 14.6 counts/min. at the same altitude with a 1.9-cm Pb filter (see Fig. 1e).

Comparison of counting rate at 2.1 cm Hg with various thicknesses of lead absorbers give an absorption coefficient of 1/56 $(\text{gram/cm}^2)^{-1}$ for horizontal particles if they are absorbed exponentially. Fifty-six grams/cm² is the range in lead of 200-Mev protons. The exponential absorption coefficient in lead for the vertical flux is 1/274 $(\text{gram/cm}^2)^{-1}$ at the same altitude. It is clear that most of the horizontal praticles are secondaries.

[8] Stroud, Schenck, and Winckler, Phys. Rev., preceding paper.

The Lateral Structure of Cosmic-Ray Air Showers

G. Cocconi, V. Cocconi Tongiorgi, and K. Greisen
Cornell University, Ithaca, New York

(Received June 2, 1949)

The lateral distributions of the electrons and penetrating particles in extensive cosmic-ray air showers have been measured directly, and as a function of the size of the showers. No evidence was found for multiple cores in the showers. The lateral distribution of the electrons was found to agree well with that calculated by Molière, taking into account only Coulomb scattering of the electrons. The density of penetrating particles at a given distance from the core was found to be proportional to that of the electrons. The ratio of p.p. to electrons seems to increase slowly with distance from the core, but changes only by a factor of about 2 between 5 and 100 m from the core, while the electron density decreases by a factor of about 100.

Evidence was obtained that most of the penetrating particles reached the apparatus as single, independent particles from the air, but that about ¼ of the events in which p.p. were detected involved groups of particles that were probably locally produced in the lead.

I. INTRODUCTION

THE discoveries of penetrating ionizing particles and of neutrons in the extensive air showers of cosmic rays, the discovery that electrons are rare or non-existent among the primary cosmic rays, and the discovery that heavy or "penetrating" particles can with large cross section produce bursts of cascade radiation associated with showers of penetrating particles, have led to new speculation about the mechanisms by which the large air showers are initiated. An important clue in the unraveling of these complex phenomena is the scattering or space-distribution of the particles in the showers.

For instance, if the showers are originated by primary electrons, one must expect each shower to have a single, narrow core, and to find that the Coulomb scattering of the electrons governs the lateral distribution of the particles about the core of the shower. For this particular case, the lateral distribution function has been calculated by Molière.[1] If the showers originate from electromagnetic radiation of heavier primary particles such as protons, one may expect an appreciable scattering of the original high energy photons, so that the core may be less concentrated, or there may be multiple cores separated by distances of the order of several tens of centimeters. On the other hand, if the cascade particles are secondaries of heavy particles that are produced with high multiplicity in nuclear interactions, one may expect original scattering angles of the order of $(M/E_0)^{\frac{1}{2}}$ (M and E_0 being the rest energy and kinetic energy of the primary particle), so that one should expect showers to have multiple cores separated by distances of the order of several tens of meters near sea level. If, as has been suggested, the showers are caused by the arrival of dust particles or collections of photons on the atmosphere, the absence of a single core should be even more pronounced.

Until the present, there has been no direct measurement of the lateral distribution of the particles in extensive air showers, with the exception of the recent experiment of R. W. Williams,[2] in which a detailed analysis was possible in about 40 cases of individual showers of 10^6–10^8 particles that struck within 40 meters of his apparatus. The Molière theory gave reasonable consistency in the interpretation of his results. By the simultaneous use of four ionization chambers, Williams also proved that the showers do not have multiple cores, unless the cores are separated by less than a meter or more than about 20 meters, or unless one core is much more dense than all the others. Except for this experiment of Williams, the interpretation of experiments on the lateral distribution of air showers has in general required (*a*) an arbitrary assumption about the height of origin of the shower and the nature of the primary, (*b*) the assumption of constancy of the space-distribution function of the showers, (*c*) an integration of the showers over all distances from the shower cores, and (*d*) an integration over the energy spectrum of the primaries. Blatt[3] has shown that as a consequence of these integrations the experimental results have been very insensitive to the precise shape of the space-distribution function.

From previous shower experiments, it has been concluded that the primary cosmic rays contain individual particles with energies as high as 10^{16}–10^{17} ev. This conclusion has been indirectly reached and strongly contested. What has been proved, in fact, is that a few counters, either of small area and a few meters apart or of larger area and hundreds of meters apart, have been discharged simultaneously with an appreciable frequency. If there are not multiple cores or local condensations in the showers, if the structure function is as calculated by Molière, if the primaries are single particles and if the assumed primary energy spectrum is right, then some of the observed coincidences are due to such high-energy primaries (i.e., a significant portion of the integrals referred to above lies above 10^{16} ev primary energy). Until now, all of

[1] G. Molière, *Cosmic Radiation*, edited by W. Heisenberg (Dover Publications, New York, 1946).

[2] R. W. Williams, Phys. Rev. 74, 1689 (1948).

[3] J. M. Blatt, Phys. Rev. 73, 1252 (1948) and 75, 1584 (1949).

the above-mentioned points in the argument have been debatable.

About the production of the heavy particles observed in the extensive showers, very little is known. Some indication of the nature of these processes may be found in information about the scattering of the penetrating particles, but until now, there have been no direct data on this subject.

For these reasons, we devised an experiment last year with the following intentions: (1) to look for evidence of uniqueness or multiplicity of the shower cores, (2) to measure the space distribution of particles in individual showers, and to see whether or not it is the same from one shower to another, (3) to compare the lateral distribution with that calculated by Molière on the basis of multiple Coulomb scattering only, (4) to see how the absorbability of the penetrating particles varies with distance from the shower core, and (5) to compare the lateral distribution of the penetrating particles with that of the electrons.

A schematic diagram of the layout of the various pieces of apparatus in a horizontal plane is shown in Fig. 1, and a more detailed discussion of the individual parts is given below. Firstly, it was necessary to have a "core selector" (abbreviated C.S. below) so that the distances from the other detecting apparatus to the cores of the showers should always be known. The use of five C.S. separated by distances from one to 36 meters served three purposes: to increase the counting rates almost five fold, to test with what precision the core was determined by the C.S., and to give indication of the existence of multiple cores.

The existence of multiple cores or local condensations was also expected to show up as a variation, greater than experimental errors, in the relative electron densities at two fixed distances from a core selector. Hence we had two electron density detectors (abbreviated E.D. below) at different distances from the line of C.S. In part of the experiment, one of the E.D. was at 48 meters while the other was at 96 m; in another part, one was at 96 m while the second was at 200 m; and in the third part, one was at 48 m while the other was at about 2 m from C.S. #4. In the last position, the distances from the various C.S. were 15, 5, 3, 2 and 21 m respectively, while in the other positions, the distances from all five C.S. to a given E.D. were about equal.

If, as it turned out, the relative electron densities at two fixed distances were constant within the uncertainty of measurement, the records of the two E.D. could yield the relative electron density at each pair of distances from the shower core; i.e., the lateral distribution function could be directly determined for distances from 2 to 200 meters. The limits on shower size (i.e., total number of particles) were set by the limits of sensitivity of the E.D.

The apparatus labeled *M* in Fig. 1 detected penetrating particles simultaneously under three different thicknesses of lead and iron. It was always placed near one of the E.D., so that the density of penetrating particles relative to that of electrons could be determined directly and as a function of electron density. The distance from the C.S. was varied from 2 to 96 meters (by moving the 12-ton absorber a few times), so that the above ratio could be determined also as a function of distance from the core.

Still another associated piece of apparatus was a cloud chamber, permanently located near the line of C.S., and shielded on all sides with lead. The cloud chamber was triggered on every pulse from any of the C.S. and was intended to give information on the nature of the penetrating particles in the showers. The present article confines its attention to the counter data, while the cloud-chamber pictures are discussed in detail in an accompanying article by Brown and McKay.[4]

The experiment was performed at Echo Lake Colorado, elevation 3260 m, average pressure 708 g/cm². The various pieces of equipment were housed in tents or Celotex boxes, kept at moderate temperature, and interconnected by many long cables. Daily extensive checks were made that all the counters and circuits were behaving properly and that there were no induction effects between the cables or within the circuits. By use of a telephone system, it was possible to have one person introduce artificial pulses at various points in a circuit 200 meters away while another observed the effects at the central recording station.

The magnitude of the experiment was such that it was necessary to have assistance from several persons

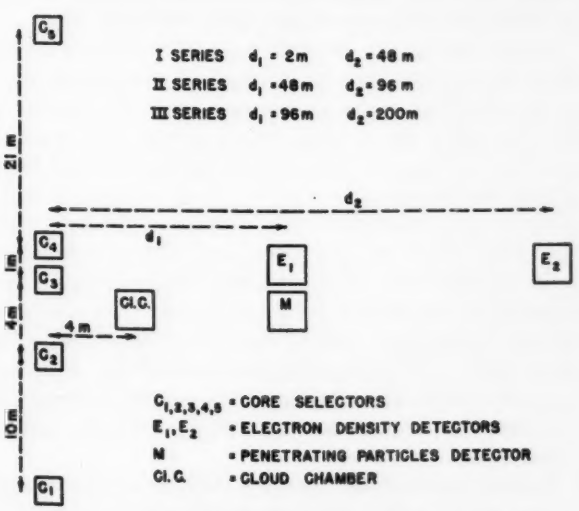

FIG. 1. Arrangement of apparatus in a horizontal plane.

in addition to the authors of this paper. In particular, help was given in the construction and running of the apparatus by Dr. W. Kraushaar and E. D. Palmatier, A. S. McKay, W. W. Brown, and Dr. W. D. Walker,

[4] W. W. Brown and A. S. McKay, Phys. Rev. 76, 1034 (1949).

who were graduate students at Cornell University.* Help in the tabulation of the data was given by Mrs. Ada Tongiorgi. The facilities of the Inter-University High Altitude Laboratory at Echo Lake were used in the performance of the experiment, and financial support was given by the Research Corporation of America. For all this assistance we give our thanks.

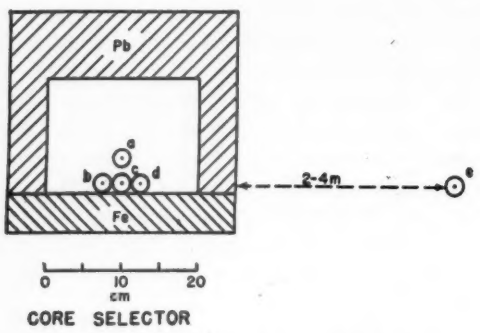

FIG. 2. Cross section of core selector.

II. THE CORE SELECTORS

A cross-sectional diagram of a C.S. is shown in Fig. 2. A fivefold coincidence of the four counters *a*, *b*, *c*, and *d* inside the shield and the one unshielded counter *e* a few meters away was interpreted as indicating a shower core striking nearby. The counters were each of area 98 cm², and the shield was 9-cm Pb on top, 5-cm Pb on the sides and at the ends, and 5-cm Fe underneath the counters. Since most of the showers are nearly vertical, the effective thickness of the shield was 9-cm Pb.

Our contention in interpreting a fivefold coincidence *abcde* as a shower core is as follows. Coincidences *abcd* of the shielded group of counters may be caused in general either by a high energy electron or photon striking the lead, or by a local shower generated by a meson or nucleon. The latter type of shower is in general not associated with extensive showers,[5] and therefore would not be associated with a coincident pulse in counter *e*; whereas all high energy electrons and photons in the air are accompanied by a rather dense shower of electrons, one of which is very likely to hit the counter *e*. Fivefold coincidences therefore represent extensive showers containing high energy electrons or photons, that cannot be scattered far from the core of the shower.

Indeed, the cascade theory predicts that the energy of a cascade particle that produces, on the average, a shower of 3 electrons under 9-cm Pb is equal to or greater than about 6 Bev. The R.M.S. distance of such particles from the core of a shower should be only about 1.3 meters at Echo Lake. Such a computation is of course meaningless without taking into account the fluctuations in the cascades, because particles of lower energy are much more numerous and spread over a larger area in the showers. However, it is very unlikely for a cascade particle of less than 1/5 of the above energy to produce a shower of 3 particles under the lead, and a shower of so few particles has only a small chance to strike the four counters. Hence, if the coincidence is due to a single electron or photon striking the lead, one might expect that the core of the shower lies with great probability within about five to ten meters of the detector.

In principle, a core selector requiring high energy particles is better than one requiring many particles, because in a large shower, a high particle density may occur far from the core, whereas high energy cascade particles should not be found far from the core, even in large showers.

TABLE I. Association of C.S. signals with pulses in E.D. at various distances.

Distance R (meters)	No. of C.S. signals	Percent of C.S. signals not accompanied by pulse in E.D.
2	329	4
3	381	4
5	360	8
15	350	9
21	325	9
48	3819	24
96	4638	48
200	2318	80

TABLE II. Counts in the individual core selectors.

C.S.	Counts in 1284 hours
#1	1794
#2	1874
#3	1837
#4	1704
#5	1746
47 m	not measured
95 m	not measured
200 m	not measured

TABLE III. Ratio between the coincidence rate of two core selectors and the average counting rate of each core selector, as a function of the separation. The data include showers of all sizes.

Separation of C.S. (meters)	Ratio of coincidences to single counts (percent)
1	27.2
4	17.2
5	14.4
10	7.6
14	3.8
15	3.5
21	1.6
22	1.3
26	0.94
36	0.90
47	0.65
95	0.13
200	0.00

* Dr. Kraushaar is now in the Physics Dept. of M.I.T., and E.D. Palmatier is at the University of North Carolina.

[5] G. Cocconi and K. Greisen, Phys. Rev. **74**, 62 (1948); and J. Tinlot and B. Gregory, Phys. Rev. **75**, 520 (1949).

Because of the long ranges of low energy photons in lead, however,[6] our C.S. did not really require high energy cascade particles. If a sufficient number of low energy electrons and photons strike the lead, there is a significant probability that the "tails" of the cascades will discharge the shielded counters. The requirement of a multiple coincidence minimizes this effect, except for very dense incident showers.

Therefore we expect that our C.S. signals usually indicate the core of a shower within a distance of 5 to 10 meters, except for extremely large showers which may strike at greater distances.

Because of the qualitative nature of the above arguments and the questionable assumptions involved, the real test of the effectiveness of the C.S. lies in the experimental data. First, one may check that the coincidences indicate extensive showers by observing whether or not other counters, placed a few meters away, are struck every time there is a C.S. signal. This information is given by the E.D. (electron density detectors, consisting of 27 unshielded counters with total surface 0.88 m², as described in Section III below). In Table I we list the number of C.S. signals obtained at distance R from an E.D., and the percentage of these signals *not* accompanied by pulses in any of the counters of the E.D. It is apparent from the numbers in Table I that at most, only four percent of the C.S. signals are not associated with extensive air showers; and that the likelihood of shower particles being at a distance R from the detector is a decreasing function of R even at the smaller distances.**

The precision with which a C.S. determines the location of the shower core is further indicated by the decoherence curve of the C.S.; i.e., the variation of the coincidence rate between two of the C.S. as a function of their separation. The use of five C.S. in fixed positions gave such data for 10 separations varying from 1 to 36 meters. During part of the experiment, similar C.S. were set up at 47, 95 and 200 meters from the line of five permanent C.S. The data on the coincidences between the C.S. are presented in Table III. (In Table II the numbers of counts in the individual C.S. are presented as evidence that the various detectors were equally efficient.)

It is apparent that the coincidence rate falls off rapidly with separation so that 90 percent of the coincidences between two C.S. occur at separations less than about 15 meters. In order to understand the long tail of the decoherence curve, however, we have made a further division of the data according to the size of the showers. From the response of the E.D. at 48 m or 96 m from the C.S., we have divided the showers into three groups, group I being showers of small size, group III being very large showers, and group II being those of intermediate size. (See Section III below for method of shower size determination.) The decoherence curves for the three groups of showers are presented in Fig. 3, so normalized that the extrapolated intercepts at zero separation are equal to 100.

Group I represents 347 C.S. coincidences in 4241 showers, or one per 12 showers; group II represents 552 coincidences in 1680 showers, or one per 3 showers; while group III represents 122 coincidences in 102 showers, or 1.2 per shower (more than one C.S. coincidence could occur in a shower because there were more than two core selectors).

In Fig. 3 one sees, as explained qualitatively above, that the coincidences between distant C.S. occur practically only in the very great showers, which were few in number. The curves of Fig. 3 are exponential in shape. For the group of smallest showers, 90 percent of the coincidences occur with separations less than 10 meters; for the intermediate group, 90 percent have separations less than 15 meters; while even for the group of largest showers, most of the coincidences occur between C.S. less than 30 meters apart.

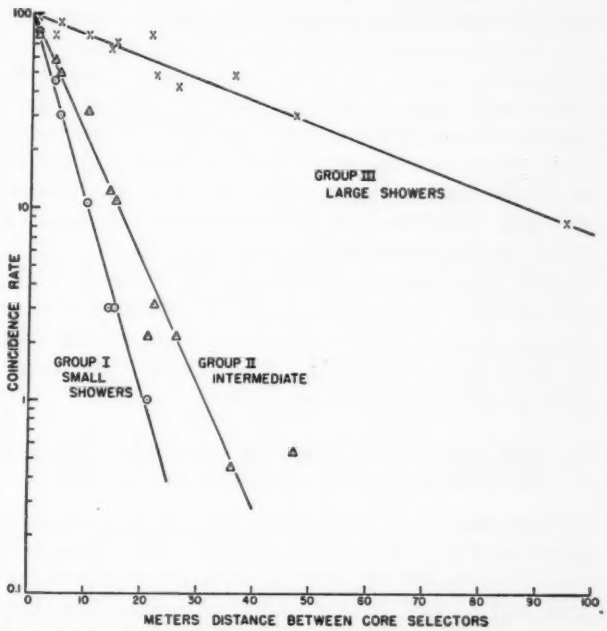

FIG. 3. Decoherence curves of the core selectors for showers of different sizes. Group I represents showers with less than 8 particles/m² at 48 m from the C.S.; group III represents showers of more than 128 particles/m² at this distance; and group II represents the showers of intermediate size. According to the Molière distribution, the number of particles is less than 3.6×10^5 in the showers of group I, between 3.6×10^5 and 5.8×10^6 in the showers of group II, and more than 5.8×10^6 in the showers of group III.

The decoherence curves of the C.S. establish, for use in interpreting the other data of this experiment, that

[6] K. Greisen, Phys. Rev. **75**, 1071 (1949).

** The four percent of the C.S. signals that are apparently not accompanied by extensive air showers are about double the expected number of chance coincidences between a local shower under the lead (a knock-on shower of a meson or a local penetrating shower) and an unassociated pulse in the unshielded counter a few meters away. This makes clear the importance of the distant unshielded counter of the core selector, since the great majority of the fourfold coincidences under the lead are due to phenomena not associated with extensive air showers.

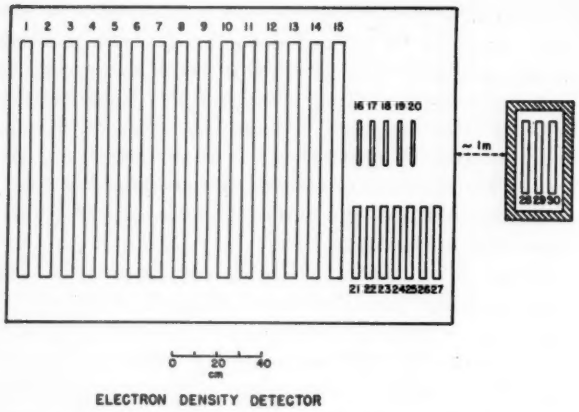

FIG. 4. Cross section of electron density detector viewed from above. The sensitive areas were 530 cm² for counters 1–15, 98 cm² for counters 21–30, and 29 cm² for counters 16–20. Total sensitive area of the 27 unshielded counters was 0.88 m².

the core of a shower strikes usually within a few meters of a C.S. that gives a signal. The curves also give some information about the structure of the showers. If, instead of a single sharp core, each shower had a large number of cores distributed over a distance of the order of R' meters, the decoherence curve of the C.S. should be nearly flat for separations R less than R'. Instead, our data indicate, even at the smallest distances, a rapidly falling decoherence curve, the shape of which is at least approximately that which is expected if the showers have a single sharp core. Therefore, if a large number of cores or a "smeared-out" core region exist in the showers, the radius over which they are spread must be less than about two meters.

III. THE RECORDING SYSTEM AND THE THEORY OF THE ELECTRON DENSITY DETECTORS

A drawing of one of the E.D., viewed from above, is shown in Fig. 4. It contains 15 large counters, each of sensitive area 530 cm², 7 medium size counters of 98-cm² area, and 5 small counters of 29-cm² surface. The three counters under lead, numbers 28, 29 and 30, constituted one of the "core detectors" that were set up at large distances from the five permanent C.S., as mentioned above. These three counters were not used in determining the electron densities, nor were they able to generate the "master pulses" described below.

Each of the five fixed C.S. generated a signal whenever it registered a fivefold coincidence of all its counters. The signals from the five C.S. were fed into a mixing circuit, which generated a "master pulse" upon receipt of any signal from a C.S. The master pulse was sent down separate cables, driven by separate cathode followers, to each of the other pieces of apparatus. A master pulse itself was sufficient to trip the cloud chamber. At the E.D. boxes, the master pulse was put in simple twofold coincidence with each of the counters. A coincidence occurring within a resolving time of about 25 microseconds caused a thyratron to pass current and discharge a condenser connected to the plate of the tube. Upon extinction of the thyratron, the condenser was recharged through a long cable and a neon bulb located in the central recording set. Thus, although the neon bulb remained on for about 0.1 second, the coincidence resolving time was only 25 microseconds. The charging currents of the condensers were so small that no induction effects were experienced in spite of the length of the unshielded cables to the neon bulbs, and the whole apparatus was remarkably trouble-free.

A camera at the central station took photographs of the array of neon bulbs, and automatically advanced the film. An example is shown in Fig. 5. The two columns of ten bulbs, on the extreme right and left sides, were always triggered by the master pulse alone, and served only as fiducial marks. In the second row from the left, the upper five bulbs indicate which core selectors were struck; in this case, we had C.S. number 3 and number 4 which were one meter apart. The third row indicates which counters in the penetrating-particle detector were discharged. Rows 4 to 6 indicate which counters were struck in one of the E.D., and rows 7 to 9 give the same information for the second E.D. The example shown in Fig. 5 was a very dense shower, since it discharged 22 counters in the nearer E.D. and 14 counters in the more distant one. Rare showers were actually observed, however, that were so large as to strike *all* the counters in the set, even when it was 100 meters from the core selector.

The counters used in the E.D. had brass walls 0.5-mm thick. In the walls, some electrons of the showers are absorbed and some of the photons are materialized.

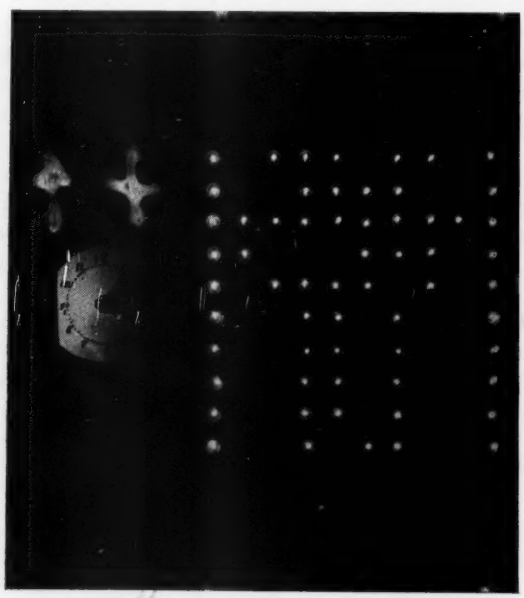

FIG. 5. Example of a photographic record of a shower. Columns 1 and 10 are fiducials, while the other neon bulbs indicate which core selectors triggered the event, and which counters were struck in the electron density detectors and the penetrating particle detector.

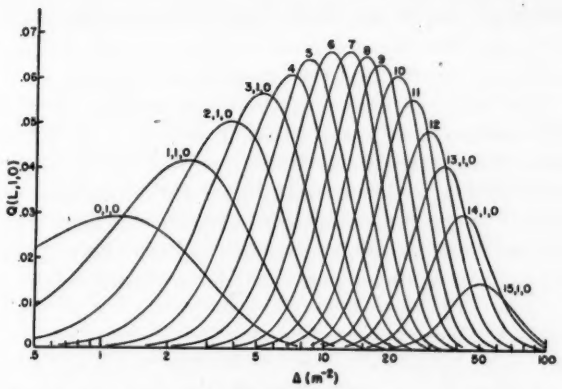

FIG. 6. Probabilities Q, as a function of shower density Δ, for zero small counters to be discharged, one medium counter, and various numbers of large counters L from 0 to all 15.

E. D. Palmatier has shown experimentally*** that for brass wall thicknesses from zero to 1.5 mm, the net absorption effect is practically zero for the extensive showers.

In the E.D., the counters were separated from each other so that except for very inclined showers, the surfaces were independent. When a shower of Δ-particles per square meter strikes the E.D., the probability $Q(\Delta, L, M, S)$ that L out of 15 large counters will give pulses coincident with the master pulse, and M of 7 medium counters and S of 5 small counters will also give pulses, while the remaining counters do not, is:

$$Q(\Delta, L, M, S)=(P_L)^L(P_M)^M(P_S)^S(1-P_L)^{15-L}$$
$$\times(1-P_M)^{7-M}(1-P_S)^{5-S}\cdot C_{15}{}^L C_7{}^M C_5{}^S, \quad (1)$$

where $C_K{}^i=[K!/i!(K-i)!]$ and the P's are the probabilities for individual counters to give pulses.

In evaluating P_L, P_M, and P_S, which are functions of Δ, it is important in this experiment to take into account the inefficiencies of the counters and the probabilities of chance coincidences, even though these are small. Hence $P(\Delta)$ has the form

$$P(\Delta)=(1-e^{-A\Delta})E+(e^{-A\Delta})N\tau, \quad (2)$$

where A is the area of the counter, E its efficiency, and $N\tau$ the probability of a chance coincidence with a given master pulse. The inefficiencies were calculated from the deadtimes and counting rates of the counters, while the chance coincidence rates were determined by direct measurement. For the three different counter sizes, the constants in Eq. (2) were as follows:

Area A	Efficiency E	Chance $N\tau$
0.0530 m²	0.97	1.5×10^{-3}
0.0098	0.995	3×10^{-4}
0.0029	0.998	1×10^{-4}

Figure 6 shows a graph of a family of curves of Q *versus* Δ, representing Eq. (1) for $S=0$, $M=1$ and values of L from 0 to 15. It is apparent that most of the probability curves are very steep on both sides of the maximum, so that only a shower within a rather narrow density range has an appreciable probability to produce a particular type of coincidence.

On the average, the half-width of these curves at half-maximum is equal to a factor 1.7. For the types of coincidences in which only 0, 1 or 2 counters are struck, or only 0, 1 or 2 counters are missed, the probability curves are less steep than for the other combinations, and the uncertainty is accordingly greater in determining the shower density Δ. The curves corresponding to 5 or more counters struck and 5 or more missed are the steepest curves, and have a half-width at half-maximum equal to a factor of 1.4 to 1.6.

For each photographic record of a shower, it was desired to determine the most probable electron density, within a constant logarithmic interval, corresponding to the type of coincidence observed in each of the E.D. Such a determination requires in principle a knowledge of the *a priori* probability $f(\Delta)d\Delta$ that a shower, selected by the core selector, strikes at the E.D. with density Δ to $\Delta+d\Delta$. For a coincidence of given L, M and S, the probability that the responsible shower had a density between Δ and $\Delta(1+\epsilon)$, if $\epsilon\ll1$, is

$$G(\Delta)=\epsilon\Delta f(\Delta)Q(\Delta, M, L, S). \quad (3)$$

The problem was to determine the maximum of $G(\Delta)$ for each combination L, M, S at each distance from the C.S.

From other experiments on extensive showers, it was expected that the quantity $\Delta f(\Delta)$ could be represented by an expression of the form const. $\Delta^{-\gamma}$ over quite large ranges of Δ, with $\gamma<1.5$ because of the action of the core selector. Over the range of densities and distances with

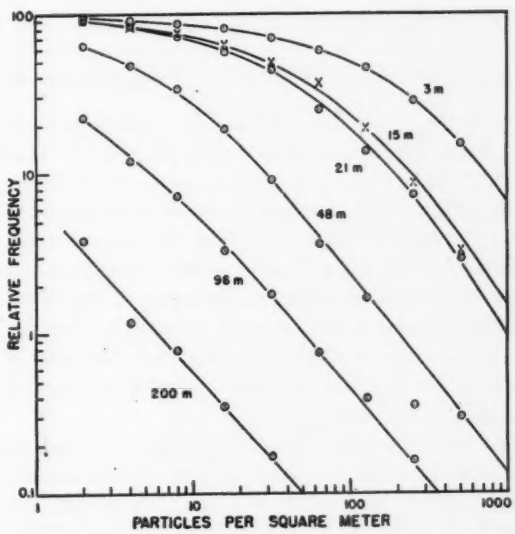

FIG. 7. Integral distribution curves of the shower densities recorded at 3 m, 15 m, 21 m, 48 m, 96 m and 200 m from the core selectors. The ordinate gives the percent of the showers having density greater than Δ.

*** We are indebted to Mr. Palmatier for making these data available to us.

TABLE IV. Numbers of showers detected in the various density intervals at 200 m and 96 m from the C.S.

DENSITIES AT 200 m

DENSITIES AT 96 m (m^{-2}) \ (m^{-2})	0 2	2 4	4 8	8 16	16 32	32 64	64 128	128 256	256 512	> 512
0-2	1774	10								
2-4	235	7								
4-8	107	12								
8-16	84	12								
16-32	17	13	4							
32-64	7	5	5	3	1					
64-128	3	1		7						
128-256		2			2					
256-512						3	1			
> 512					1					

which we are concerned, γ is also never less than -2. Hence, $\Delta f(\Delta)$ is slowly varying compared with $Q(\Delta)$ except within a short range of the maximum of Q (for almost all combinations of L, M and S); and the maximum of $G(\Delta)$ is near that of $Q(\Delta)$. Therefore as a first approximation, we assumed the maxima of Q and G to be identical, and identified each of the recorded showers with a most probable density, determined from curves like those of Fig. 6. At each distance from the core selectors, we thereby deduced integral frequency-distribution curves similar to those in Fig. 7. From the slopes of these curves, the function $f(\Delta)$ could be found, and values of γ could be calculated for all ranges of Δ and distances from the core selector.

By setting the derivative of Eq. (3) equal to zero and substituting Eq. (1) for Q, and $\Delta^{-\gamma}$ for $\Delta f(\Delta)$, one obtains the following condition for the most probable density:

$$\frac{P_L'(L-15P_L)}{P_L(1-P_L)}+\frac{P_M'(M-7P_M)}{P_M(1-P_M)}+\frac{P_S'(S-5P_S)}{P_S(1-P_S)}=\frac{\gamma}{\Delta}. \quad (4)$$

Each of the terms on the left side of this equation was calculated for all values of L, M and S, and for $\Delta=0, 2, 4, 8, \cdots, 256, 512, \infty$ particles/m². For any combination L, M, S, there is a pair of adjacent values among these densities such that for one of them the right side of Eq. (4) exceeds the left, while for the other value of Δ the inequality is reversed. Thus, we could quickly determine the interval (of width a factor 2) in which the most probable density lies. Because of the width of the probability curves, a more accurate determination is not worthwhile.

The least accurate determinations, corresponding to only 0 or 1 counters struck or zero or one missed, fall in the extreme intervals 0 to 2 or 512 to ∞ particles/m². Therefore these intervals are not further subdivided.

The approximation of neglecting the *a priori* probabilities $f(\Delta)$ essentially amounts to setting $\gamma=0$ in Eq. (4). The refinement of considering the correct values of γ in no case shifted the most probable density by more than one interval (*a* factor 2), and in many cases had no effect on the grouping of the results.

The integral density-distribution curves, obtained from such an analysis of the E.D. data at each distance from the core selectors, are represented on logarithmic scales in Fig. 7. The data in Fig. 7 are normalized with respect to the total number of showers recorded, which was set equal to 100, so that the ordinates give directly the percent of the showers that have density above Δ.

TABLE V. Numbers of showers detected in the various density intervals at 96 m and 48 m from the C.S.

DENSITIES AT 96 m

DENSITIES AT 48 m (m^{-2}) \ (m^{-2})	0 2	2 4	4 8	8 16	16 32	32 64	64 128	128 256	256 512	> 512
0 - 2	775	10								
2 - 4	309	14								
4 - 8	225	36	3	1						
8 - 16	199	79	29	3						
16 - 32	48	62	35	27	3					
32 - 64	10	16	21	27	13	3		1		
64 - 128			2	11	12	9	2			
128 - 256			1	3	4	8	1			
256 - 512					1		1			
> 512						1	1	5		2

Because of the uncertainty in the distance to the core of the showers, the measurements at 2 m, 3 m, and 5 m from the core selectors have been lumped together in Fig. 7 (and in Table VIII below) and labeled "3m." We have also approximated as equal the distances from all five C.S. to the E. D. at 48 m, because the maximum variation among these distances was only 4 m.

IV. RESULTS OF THE ELECTRON DENSITY MEASUREMENTS

The electron densities were always determined simultaneously at two different distances from the core selectors. In Tables IV to VIII the results are portrayed. The horizontal rows and vertical columns represent density intervals at the two stations, and the number in each square is the number of showers recorded with most probable densities in the corresponding pair of intervals.

The density measurements below 4 particles/m² were much less accurate than the measurements of higher densities, so that in examining Tables IV to VIII one should focus one's attention on the intervals 4–8 m^{-2} and higher. It appears that for a given density interval at one distance d_1, there is a distribution of densities obtained at a second distance d_2. A typical example, taken from Table V and shown in Fig. 8, is the densities recorded at 48 m corresponding to those between 8 and 16 particles/m² at 96-m distance. The breadth of the distribution curve may be due to (*a*) error in the

density measurement at 48 m, (*b*) error in the measurement at 96 m, (*c*) variations in the actual distances to the cores of the showers, (*d*) existence of multiple cores in the showers, or local condensations of particles, or (*e*) variations in the lateral distribution function from one shower to another. Since the known uncertainties in the density measurements are about a factor two in either direction at both stations, the errors (*a*) and (*b*) are alone enough to account for the width of the distribution curve.

Similar distributions picked from Tables VI and VII are equally narrow as the one shown in Fig. 8. In Table VIII, the distributions are somewhat wider, but this fact can be accounted for by the larger percentage errors in determining the distance from the E.D. at 3 m to the core of the shower.

In no case is the distribution so wide that one must assume multiple cores in the showers, or local condensations, or variations in the lateral structure function in order to account for the results.

Tables IV to VIII may be treated as three-dimensional graphs with logarithmic coordinates in the plane of the paper (except for the highest and lowest density intervals). On each of these graphs we have drawn a diagonal line which connects as closely as possible the peaks of all the distributions. These lines represent logarithmic graphs of most probable density at distance d_1 against most probable density at distance d_2.

TABLE VI. Numbers of showers detected in the various density intervals at 48 m and 21 m from the C.S.

DENSITIES AT 48 m

DENSITIES AT 21 m (m^{-2}) \ (m^{-2})	0–2	2–4	4–8	8–16	16–32	32–64	64–128	128–256	256–512	>512
0–2	28	2								
2–4	22	3								
4–8	26	6	1	1						
8–16	16	16	10	2						1
16–32	8	13	13	7	1					
32–64	1	8	21	23	6	1				
64–128		1	4	17	9	3	1			
128–256				1	12	5	2			
256–512				2	1	4	4	3		
>512						3	2	4		

It should be noted that of the 6023 entries in the tables, only 2 or 3 deviate from any of the diagonal lines by more than can be explained by the likely errors in density and distance measurement. Indeed, the average logarithmic deviation of the entries in the tables from the diagonal lines (neglecting entries below 2 or above 512 particles/m²) is equivalent to a factor 1.7 in Table IV, 1.5 in Table V, 1.6 in Table VI, 1.6 in Table VII and 1.9 in Table VIII. These deviations are close to the expected errors in density measurement. The two or three exceptional cases may represent rare instances when the coincidence in the core selector was not caused by electrons or photons of the extensive shower, but by a local shower made by another type of particle far from the main shower core.

From these tables, therefore, we draw the following conclusions:

(1) Within the accuracy of our data (average error in particle density about a factor 2), there is a unique correlation between the particle density at one distance from the shower core and the particle density at any other distance.

(2) The lateral structure function, for the showers we detected and within our accuracy of measurement, is independent of the shower size. That is, there is a constant ratio between the densities at any two fixed distances from the shower core.

(3) There is no evidence in our data for appreciable local condensations of the shower particles, or multiple cores.

(4) Some showers occur of such greatness that the particle density even at 100 meters from the core is more than 500 particles per square meter. When such showers occur, the density is not this large only at the one detector, but over all the region within a radius of 100 m from the core of the shower.

The diagonal lines drawn in Tables IV to VIII may also serve to determine the average ratios of particle densities at the various pairs of distances. Thereby we can construct a table of densities, all relative to the particle density at 48 m from the core. The results of this treatment are given in the second column of Table IX.

An independent method of finding the average relative densities at different distances is to use the distribution curves of Fig. 7 as follows. If the lateral structure function is unique, as it seems to be, all the showers that at distance d_1 have density above Δ_1 will at another distance d_2 have density above Δ_2, where Δ_1/Δ_2 is the ratio between the densities of the showers at d_1 and d_2. For these two densities the integral frequencies at d_1 and d_2 must be equal.

Therefore, the separations between the curves of Fig. 7 for equal ordinates (i.e., the horizontal separations) give the relative densities at the different dis-

TABLE VII. Numbers of showers detected in the various density intervals at 48 m and 15 m from the C.S.

DENSITIES AT 48 m

DENSITIES AT 15 m (m^{-2}) \ (m^{-2})	0–2	2–4	4–8	8–16	16–32	32–64	64–128	128–256	256–512	>512
0–2	32	1								
2–4	24	3								
4–8	20	2		1						
8–16	24	11	4	1						
16–32	19	15	11	3	1					
32–64	8	12	14	8	1					
64–128	2	4	16	21	13	1	2			
128–256			3	8	16	5	1	2		
256–512			2	4	4	7		1		
>512					1	3	4	3		

tances. The values so deduced, relative to the density at 48 m, are given in the third column of Table IX.**** The results obtained by the two methods are in good agreement, and the means of the two determinations have been plotted in the graph of Fig. 9.

TABLE VIII. Numbers of showers detected in the various density intervals at 48 m and "3 m" (i.e., 2m, 3m or 5 m) from the C.S.

DENSITIES AT 48 m

DENSITIES AT 3 m (m^{-2}) \ DENSITIES AT 48 m (m^{-2})	0 – 2	2 – 4	4 – 8	8 – 16	16 – 32	32 – 64	64 – 128	128 – 256	256 – 512	> 512
0 – 2	59		1							
2 – 4	36	1								
4 – 8	37	7		1						
8 – 16	48	8	3	2			1			
16 – 32	68	21	8	1	2	1				
32 – 64	65	43	11	5	3	1				
64 – 128	29	47	33	19	8	2				
128 – 256	9	37	33	58	24	14	1	1		
256 – 562	3	12	29	33	35	16	6	3		
> 512	2	3	6	18	54	46	13	14		1

The smooth curve in Fig. 9 represents the theoretical calculations of Molière,[1] normalized at 48 m. In applying Molière's numerical results, we have substituted for the characteristic length r_1, 114 meters, which is the value of r_1 at 10°C and at an altitude about one radiation length higher than Echo Lake.

Figure 9 shows that there is complete agreement between our results and the Molière calculations at distances from 3 m to 200 m from the shower core and within the accuracy of our data (i.e., within a factor of about 2 in the relative density between 3 and 200 m).† Since the only scattering process considered in the Molière calculations is the Coulomb scattering of the electrons, we are led to conclude that all other processes contributing to the lateral separations of the particles are comparatively insignificant. Our results are in particular disagreement with the predictions of the symmetrical pseudoscalar meson theory of Lewis, Oppenheimer, and Wouthuysen,[7] according to which, at the origin of a shower, large angular separations should occur between the photons arising from decay of the neutral mesons.

Our experimental results are in complete agreement with those of R. W. Williams,[2] with respect to the absence of multiple cores and the agreement of the lateral distribution with the calculations of Molière. Williams' results are most reliable at smaller distances (2 to 20 m) from the shower core, while ours are most accurate at larger distances (5 to 200 m).

We are, therefore, justified in using the Molière theory to calculate the total numbers of particles in the showers which we detected. The largest showers had a density of about 500 particles/m^2 at 100 m from the core; this corresponds to a total number of particles equal to 10^8. The smallest showers in which the densities were measured had a density of about 4 particles/m^2 at 3 m from the core, which corresponds to a total number of particles equal to 4000.

The primary energies responsible for these showers cannot be determined without knowing the height of the origin, the number of particles at the origin, and the fraction of the energy given to particles not in the soft component (i.e., to mesons, neutrons, neutrinos, etc.). However, the *minimum* energy that could be responsible for the largest showers can be estimated by assuming that the showers were detected at their maximum development, and that all the energy was in the soft component. On this basis, the minimum energy for the largest showers is 10^{17} ev.

In all of the above discussion, we have neglected the zenith-angle distribution of the showers and assumed that they all arrived in the vertical direction. We think this is justified because of our method of selection of the showers, which did not require coincidences between distant detectors in order that the showers be recorded. In order to generate a master pulse, it was only necessary that a core selector be tripped. Therefore, we had no bias in favor of inclined showers, and the angular

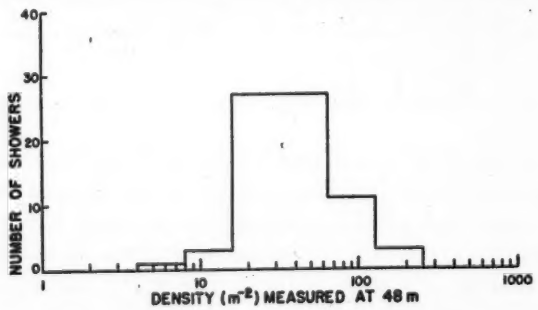

FIG. 8. Frequency distribution of particle densities measured at 48 m from the C.S., for showers of measured density between 8 and 16 particles/m^2 at 96 m.

**** Actually, the horizontal separations in Fig. 7 are almost but not exactly constant, as the curves converge gradually with increasing shower size. This is because of the fact that the cores of larger showers may strike farther from the core selector than the cores of small showers. This produces a greater decrease of particle density at an E.D. near the core selector than at one much farther away. Indeed, for sufficiently large showers, thousands of times greater than those we detected, all of the E.D. would on the average be equally close to the cores of the showers and the frequency-density curves would be independent of the presence or location of the core selectors. Fortunately, this effect does not introduce much ambiguity in determining the relative densities from the curves of Fig. 7 because most of the showers we detected were small enough so that the shower cores had to be near the core selectors (see Table III and Fig. 3); and the curves in Fig. 7 are nearly parallel. For best accuracy in determining the relative densities, we used the curve separations at the lowest densities consistent with accurate density measurement.

† The point at 3 m is brought into perfect agreement with the curve by taking into account that the shower cores did not strike exactly at the core selector, so that the average distance to the shower core was about 5 m rather than 3 m. The experimental points then lie all within a factor 1.5 of the theoretical curve.

[7] Lewis, Oppenheimer, and Wouthuysen, Phys. Rev. **73**, 127 (1948).

TABLE IX. Particle densities at various distances from the core, relative to the density at 48 m.

Distance from core	Relative density deduced from lines in Tables IV–VIII	Relative densities deduced from curves in Fig. 7
200 m	0.037	0.023
96	0.25	0.20
48	1.0	1.0
21	5.2	6.6
15	8.0	8.2
3	26.0	27.0

distributions that have been measured with cloud chambers[8] should apply to our showers. All of the angular distributions show a strong maximum in the vertical direction, even for very large showers, compatively few having axes inclined more than 30°.

When a shower struck our apparatus with an inclined axis, the distances from *both* of the E.D. to the core of the shower were smaller, by the same factor, than the horizontal distances that we have reported. The error thus introduced in the *ratio* of the particle densities at the two distances is of second order, and less than the other uncertainties in our measurements. It therefore does not influence the agreement between our results and the Molière theory. The error enters directly, however, in the computation of the total numbers of particles in the largest showers, and makes this computation somewhat unreliable. If the shower axes of the largest showers were inclined 60° relative to the zenith, the error nevertheless would be less than a factor 5 in the computed size of the largest showers.

V. THE PENETRATING PARTICLE DETECTOR (M.D.)

The penetrating particles in the showers are only one or two percent of the total number of ionizing particles; therefore, it was considered impossible to measure the densities of p.p. in the individual showers as was done by the E.D. for the total ionizing particle density. Thus we were led to use statistical interpretations in order to obtain the densities of penetrating particles.

The detector is shown in Fig. 10. The counters were connected in six groups, with parallel connection between the five adjacent counters of each group. Each counter had an effective area of 500 cm². Thus at each of the three depths in the absorber, there were two independent counter trays, each of surface 2500 cm². Each of the six trays was put in coincidence with the master pulses from the C.S., and coincidences were indicated by neon bulbs as explained in Section III.

In the illustrative example of Fig. 5, the shielded trays that were discharged were trays a_1, b_1, and c_1. This probably indicates that a single penetrating particle crossed all three of the trays in a direction close to the vertical. No particle crossed trays a_2, b_2, or c_2. A large fraction of the records of penetrating particles showed this type of coincidence.

During part of the experiment, the M.D. was placed at 48 m from the core selectors and within a few meters of an electron density detector. For another time interval, it was placed at 96 m from the C.S. and also near an E.D. The third position was about 2 m from C.S. number 2. Here it was 10 m from C.S. number 1, about 5 m from C. S. number 3 and number 4, and 26 m from C.S. number 5. In this position also, it was a few meters from an E.D. The locating of the M.D. always near an E.D. makes it possible, in the treatment of data below, to determine the average densities of penetrating particles for showers of known total-particle density.

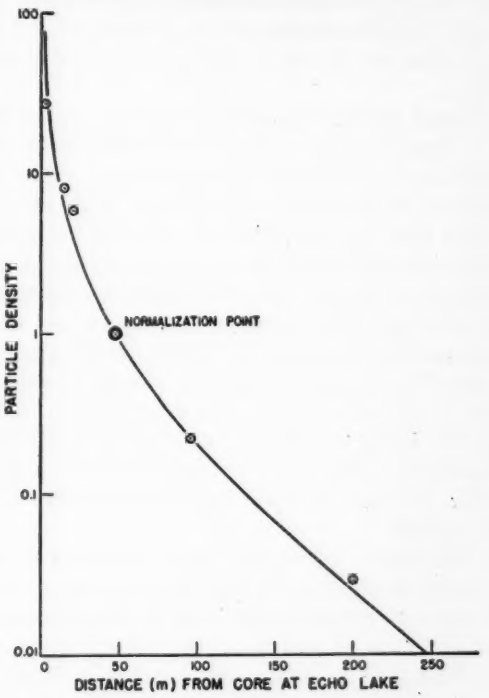

FIG. 9. Particle density in the showers *vs.* distance from the core. Densities are given relative to that at 48 m. The points enclosed in circles were deduced from the experiments; the smooth curve represents the Molière theory.

The first question that we wish to discuss is that of the absorbability of the penetrating particles, and how this varies with distance from the shower core. For this purpose, we shall not subdivide the showers according to total particle density, but consider all sizes together. We also consider trays a_1 and a_2 as a single tray, a, of 5000 cm² surface; and likewise trays b_1 and b_2, and c_1 and c_2. While the M.D. was at 48 m or 96 m from the core selectors, the absorber above tray a was 7 inches lead; the absorber between trays a and b was 8 inches iron, and that between b and c was also 8 inches iron. In 2646 films with the M.D. at 48 m, 203 films showed counts in tray a, 188 showed counts in tray b, and 157 showed counts in tray c. These numbers are in the ratio $a/b/c = 100/93/77$. In 2318 films with the M.D. at 96 m,

[8] J. Daudin, J. de phys. et rad. 6, 302 (1945); M. Deutschmann, Zeits. f. Naturforschung 2, 61 (1947); see also references 2 and 4.

we had 106 with counts in a, 98 with counts in b and 86 with counts in c, giving the ratio $a/b/c=100/92/81$.

The identical absorbers and counter trays were also used by the authors in another experiment[9] in which extensive showers were selected by three trays of unshielded counters placed within a few meters of the M.D. In this situation, the average distance to the core of the showers was less than 48 m; most likely about 20 m. In that experiment, it was found that the relative numbers of particles reaching trays a, b and c was $a/b/c=100/90/79$ (with statistical errors of about ± 2). This ratio and the corresponding ratios at 48 and 96 m from the core are all equal within the statistical uncertainties.

The small absorption, about 20 percent, in the 40 cm of iron between trays a and c shows that most of the particles that strike even the uppermost tray are truly penetrating in character and are most likely μ-mesons. The fact that the absorption is roughly the same at 96 m from the core as at 48 m or at an average distance of about 20 m indicates that the energy spectrum of the penetrating particles far from the core is not on the average much softer than that of the particles nearer to the core. This statement applies, of course, only to a limited range of energies, not exceeding by a large factor the energy required to penetrate the absorbers. The momentum limits set by the absorbers for μ-mesons were 3.4, 5.8, and 8.3×10^8 ev/c, respectively, for the trays a, b and c.

An absorption curve has been measured at Echo Lake for penetrating particles irrespective of air showers by Rossi and collaborators.[10] With a permanent absorber of 18 cm of lead as in the present experiment, they found that an additional absorber of 40-cm iron reduced the intensity by 27 percent, which is a somewhat larger reduction than we have found for the penetrating particles in air showers.

When our penetrating particle detector was placed close to the core selectors, the absorber thicknesses were not kept the same as at the larger distances but were varied according to the needs of another experiment that was being performed simultaneously. Hence at the shorter distances from the core, we have used only the data given by the bottom trays of counter, c_1 and c_2. These were always under a thickness of at least 6 inches lead plus 8 inches iron, with a maximum thickness of 5 inches lead plus 14 inches iron. If the absorption of penetrating particles is like that observed at the other distances from the core, this variation of the absorber thickness affects the number of penetrating particles by no more than 7 percent, which is negligible in the treatment of data given below. The mean thickness was about equal to that above trays b_1 and b_2 when the detector was at 48 or 96 m from the core selector.

The smallness of the absorption also allows us to average together, in the 48-m and 96-m data, the counts obtained in the three pairs of trays a, b and c. This improves the statistical accuracy a little. The mean results apply most accurately to particles that can penetrate the mean absorber thickness, which was practically the same at all distances of the M.D. from the core selectors.

The data from the M.D. and the nearby E.D. are collected in Tables X to XIII. In column 2 of these tables we list the number of showers recorded with total particle density in the intervals listed in column 1. The third column gives the total number of coincident pulses observed in all the trays of shielded counters (6 trays at 96 m or 48 m, 2 trays at the smaller distances). The correction for chance coincidences was appreciable only for the low density showers at the larger distances. In the last column the mean density of penetrating particles, Δ, is calculated by the formula

$$\frac{\text{counts per tray}}{\text{no. of showers}}=1-e^{-S\Delta},$$

where $S=\frac{1}{4}$ m^2 is the area of each counter tray. Blanks are left in the last column where the calculation would be completely meaningless because of statistical error.

Because of the comparatively small numbers of showers recorded at the smaller distances, we have combined the results at 10 and 26 m from the core selectors and have also combined the results at 2, 4 and 5 m from the C.S. Such averaging helps to correct for the fact that the distances from the E.D. and M.D. to the same C.S. were not exactly identical (i.e., the E.D. was 5 meters closer than the M.D. to C.S. number 5, but 5 meters farther than the M.D. from C.S. number 1).

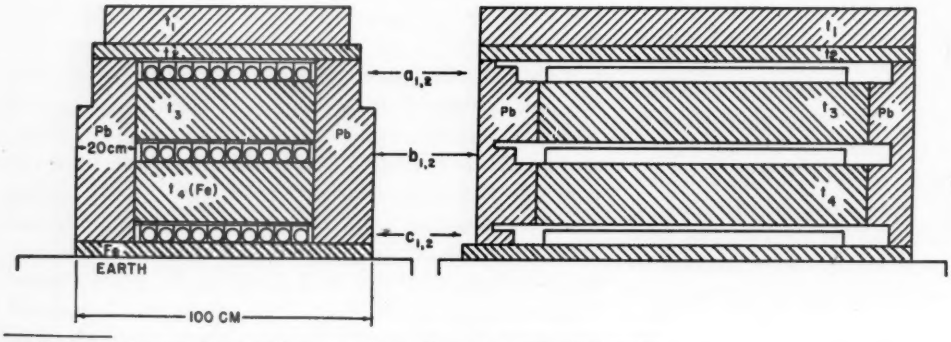

FIG. 10. Arrangement of counters and absorbers in the penetrating particle detector, M.D.

[9] Cocconi, Cocconi Tongiorgi, and Greisen, Phys. Rev. **75**, 1063 (1949).
[10] Rossi, Greisen, Stearns, Froman, and Koontz, Phys. Rev. **61**, 675 (1942).

The results of this treatment of the data at 48 m and 96 m from the core are plotted in Fig. 11. It is apparent from the graph that the number of penetrating particles is proportional to the number of electrons. The proportionality is verified over a range greater than a factor 100 in the densities of the particles or in the size of the showers; and over this range, the maximum variation in the ratio of p.p. to electrons is a factor less than 2. However, the ratio is not the same at the two distances. At 96 m from the core, the p.p. are about 2.5 percent of the total density, while at 48 m the p.p. are only 1.5 percent of all the particles.

At the smaller distances, 2 to 26 m from the C.S., the interpretation is less certain than at the larger distances. The calculated densities of penetrating particles had no statistical significance below electron densities of 16 particles/m². At higher densities, it seems that the density of p.p. is not quite proportional to that of the electrons, but this could be an instrumental effect due to the fact that the M.D. and E.D. were not exactly in the same position. In the showers of highest measured electron density, the E.D. was likely closer to the core, on the average, than the M.D.

Regardless of these uncertainties, it is clear from the data that the relative number of penetrating particles and electrons undergoes no very large change between about 5 m and 100 m from the core of the shower. The p.p./electrons ratio may be about twice as great at 96 m as at 5 m from the core, but the electron densities at these distances have a ratio greater than 100. Therefore, the decoherence curve of the penetrating particles is very similar to that of the electrons.

If the penetrating particles were chiefly produced locally in the absorbers by the incident electrons and photons, one would have to expect that the p.p./electron ratio decreases with distance from the core since the mean energy of the photons and electrons decreases with distance. The fact that the p.p./electron ratio does not decrease, but actually increases with distance, proves that most of them, at least, are not locally produced in this manner.

Indeed, it is significant that the penetrating particles even at 96 m from the core have a mean energy large compared with 8×10^8 ev as indicated by the absorption data. From cloud-chamber photographs of meson production, it is known that such energetic secondary particles travel nearly parallel to their primary. Therefore, on the average, the penetrating particles must originate at a height more than 1000 m, probably several thousand meters, above the point of detection. The mean range of μ-mesons before decay (13,000 m for a meson of 2 Bev) is long enough to allow such distances of travel, but π-mesons would decay in flight. Therefore, even if, as is very likely, the mesons directly produced in the showers are π-mesons, those detected are likely to be μ-mesons.

The authors have previously measured the ratio of penetrating particles to electrons in the showers at Echo Lake,[9] with much better statistical accuracy than in the present experiment, but averaged over all distances from the core and a wide range of shower sizes.

TABLE X. Density distribution of penetrating particles at 96 m.

Shower density (m^{-2})	No. of showers	No. of p.p. signals	Expected by chance	Residual no. per tray	Mean p.p. density (m^{-2})
0–2	1784	92	13	13.1	0.029
2–4	242	47	2	7.5	0.13
4–8	119	19	1	3.0	0.10
8–16	96	42	1	6.8	0.29
16–32	34	22	0	3.7	0.46
32–64	21	31	0	5.2	1.1
64–128	11	27	0	4.5	2.1
128–256	4	17	0	2.8	4.8
256–512	4	22	0	3.7	10.0
512–∞	1	4	0	0.7	...

TABLE XI. Density distribution of penetrating particles at 48 m.

Shower density (m^{-2})	No. of showers	No. of p.p. signals	Expected by chance	Residual no. per tray	Mean p.p. density (m^{-2})
0–2	767	19	6	2.2	0.011
2–4	322	23	2	3.4	0.042
4–8	264	46	2	7.3	0.11
8–16	303	70	2	11.3	0.15
16–32	174	74	1	12.1	0.29
32–64	90	90	1	14.8	0.72
64–128	36	62	0	10.3	1.4
128–256	17	37	0	6.2	1.8
256–512	2	11	0	1.8	10.0
512–∞	9	51	0	8.5	12.0

TABLE XII. Density distribution of penetrating particles at 10 and 26 m.

Shower density (m^{-2})	No. of showers	No. of p.p. signals	No. per tray	Mean p.p. density (m^{-2})
0–2	45	0	0	...
2–4	40	1	0.5	...
4–8	41	4	2.0	...
8–16	63	4	2.0	...
16–32	69	15	7.5	0.46
32–64	74	26	13.0	0.77
64–128	73	44	22.0	1.4
128–256	36	23	11.5	1.5
256–512	21	24	12.0	3.4
512–∞	14	18	9.0	4.1

TABLE XIII. Density distribution of penetrating particles at 2–5 m.

Shower density (m^{-2})	No. of showers	No. of p.p. signals	No. per tray	Mean p.p. density (m^{-2})
0–2	46	0	0	...
2–4	31	3	1.5	...
4–8	35	2	1	...
8–16	49	3	1.5	...
16–32	76	18	9	0.5
32–64	97	51	25.5	1.2
64–128	100	64	32	1.5
128–256	135	120	60	2.3
256–512	99	110	55	3.3
512–∞	123	167	83.5	4.5

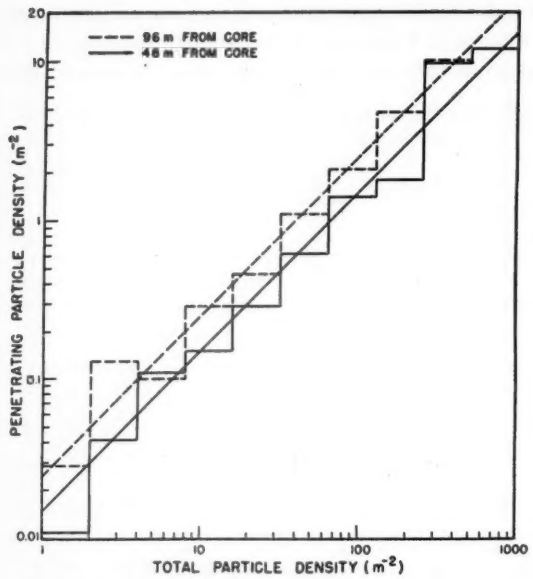

FIG. 11. Density of penetrating particles *vs.* total particle density at two distances from the core selectors.

The ratio was found to vary from 0.7 to 1.4 percent depending on the mean size of the showers. The present results seem on the average to indicate a slightly higher ratio, possibly because of the greater emphasis on large distances from the core; but in view of the uncertainties in both experiments, the difference is not significant. Likewise, the variation of the p.p./electron ratio found in the previous experiments (a factor 2 over a range of a factor 200 in shower size) is so small that it may have been obscured in the present data by statistical and systematic errors.

It is noteworthy that the results of these experiments indicate very great numbers of mesons in the largest showers. As explained above, the largest showers that we recorded had about 10^8 particles, of which about 1.5 percent are mesons. This implies 1.5×10^6 mesons in the shower at the time of detection. Since some of the mesons must decay in flight through the air, the number of mesons *produced* in the largest showers must exceed 1.5 million by an unknown factor depending on the energy spectrum of the mesons produced. Our absorption data indicate that the mean energy of the observed mesons is at least 2 Bev. Therefore, a minimum estimate of the combined energy of the mesons produced in such showers is about 10^{16} ev, or 10 percent of the minimum estimate of the total energy of the showers.

VI. INDEPENDENCE OF THE PENETRATING PARTICLES RECORDED WITH THE M.D.

One may check the statistical calculation of densities of the penetrating particles, and at the same time test the independence of the particles, by comparing the number of coincidences of two adjacent trays with the number of pulses in each tray. Indeed, if n_1 is the number of p.p. recorded by one tray and the p.p. are independent, the number of coincidences n_2 should be $n_2=n_1(1-e^{-S\Delta})$, where $S=\frac{1}{4}$ m² is the area of a tray and Δ is the density of the penetrating particles.

In Tables X to XIII the mean values of n_1 are listed for electron showers of various densities. Using these values of n_1, and values of Δ taken from the smooth lines drawn in Fig. 11, we have calculated the expected values of n_2 for the showers of various densities. In Table XIV we list the calculated numbers n_2 and those which were actually observed (summed over all three pairs of trays). The agreement appears to be satisfactory. Because of the width of the density intervals, the mean densities of penetrating particles should be slightly greater in the showers in which at least one p.p. is recorded than it is in unselected showers of the same density range. This could well account for the slight excess of observed coincidences over the calculated ones.

The apparent independence of the penetrating particles, however, may be due to the large area of our counter trays since a group of particles created locally in the absorber might frequently strike only one of the two adjacent trays. In order to investigate further the associations of the penetrating particles, we rearranged the counters of the M.D. Under a thickness of 8-inch lead, 12 counters were placed in a single row. Parallel connection was made between counters 1 and 7, 2 and 8, 3 and 9, etc., so that there were 6 pairs of counters but the two members of each pair were widely separated. Each counter was 2 inches in diameter and 40 inches long. With this geometry, an average lateral spread of one inch was sufficient so that a group of particles would not be recorded as only a single particle. The absorber was located in the close position to the core selectors.

The data corresponding to this arrangement are collected in Table XV. In the small showers, one sees that usually there are no penetrating particles recorded or else only one counter pair is struck. Only in the large showers, in which one must expect many particles to be incident from the air, is the probability high for a multiple coincidence.

TABLE XIV. Calculated and observed numbers of coincidences, n_2, between shielded trays.

Shower density (m^{-2})	96 m		48 m		10–26 m		3–5 m	
	Exp.	Obs.	Exp.	Obs.	Exp.	Obs.	Exp.	Obs.
0–2	0.25	1	0	0	0	0	0	0
2–4	0.4	3	0.1	0	0	0	0	0
4–8	0.3	0	0.5	1	0.06	0	0	0
8–16	1.4	0	1.4	1	0.1	1	0.1	0
16–32	1.4	1	3	6	1	2	1	6
32–64	4	6	7	13	3	5	5	19
64–128	6	5	9	12	7	10	11	13
128–256	6	5	9	5	5	7	27	35
256–512	10	10	4	5	7	6	32	38
512–∞	2	1	24	24	6	7	57	73
Total	32	32	58	67	29	38	133	184

TABLE XV. Distribution of coincidences observed between 6 counter pairs under 8 inches of lead.

Total particle density (m^{-2})	Counter pairs struck 0	1	2	3	4	5	6	Total
0–2	24	1						25
2–4	12	1		1				14
4–8	11	1						12
8–16	20	2	1	1				24
16–32	24	5		1			3	33
32–64	18	12	2	1	2	1		36
64–128	21	9	3	1	1	2		37
128–256	10	5	4	1	1	1	2	24
256–512	4	8	4	5	0	2	4	27
512–∞	1	4	2	2	5	0	9	23
Total	145	48	16	13	9	6	18	255

TABLE XVI. Calculated distribution of coincidences between 6 shielded counter pairs.

Total particle density (m^{-2})	Counter pairs struck simultaneously 0	1	2	3	4	5	6	Total
0–2	24.7	0.3	...	...	...	...	...	25
2–4	13.5	0.5	...	...	...	...	...	14
4–8	11	0.8	0.03	...	...	...	...	12
8–16	21	3	0.2	0.01	...	...	...	24
16–32	25	7	0.9	0.06	...	...	...	33
32–64	20	12	3	0.4	0.03	...	...	36
64–128	14	15	6.5	1.5	0.2	0.015	...	37
128–256	5.4	9	6.4	2.4	0.5	0.06	0.003	24
256–512	3.3	8	9	5	1.5	0.3	0.02	27
512–∞	1.5	5	7.5	6	2.6	0.6	0.06	23
Total	139	61	34	15	5	1.0	0.1	255

A more quantitative evaluation of these data may be made on the basis of calculations of the expected distribution of multiplicity among the coincidences. By using the p.p. densities given in Fig. 11 for various total particle densities, we have calculated the relative number of times one should expect to have zero counter pairs struck or 1, 2, 3, 4, 5 or all 6 counter pairs struck simultaneously. The results were normalized to the total number of events recorded in each interval of electron-density and are displayed in Table XVI.

Comparison of Tables XV and XVI shows that there are indeed some cases when coincidences of high multiplicity are observed in excess of the expectation on the assumption that the particles are independent. Only about 10 percent of the showers fall in this class, however; namely, the cases when all 6 counter pairs were struck and some of the cases when 4 or 5 pairs were struck. Otherwise, the Poisson distribution accounts well for the observed distribution of coincidences. The unusual cases are about 20 to 25 percent of the showers in which any penetrating particles were recorded.

These events cannot easily be accounted for by knock-on electrons of mesons because the frequency is too great and the number of cases in which all 6 counter pairs are struck is too large compared with the number in which one was missed. Nor can rays traveling in nearly the horizontal direction explain the coincidences because the counters were shielded by eight inches of lead on the sides and form a narrow telescope in that direction. Mesons traveling in such a limited direction could hardly occur in 20 percent of the showers in which *any* penetrating particles were detected! Low energy photons penetrating the lead are also incapable of explaining the sixfold coincidences. The total width of 6 counters was more than 13 inches. Photons found that far apart certainly must have originated from different particles striking the absorber and would therefore be independent, having the same effect on the rates as a slight increase in the number of independent penetrating particles. Their presence would not affect the relative number of times when different numbers of counters are struck.

It is likely that these unusual events are instances of the local production of groups of penetrating particles in the absorber and are an indication of the presence in the showers of particles capable of producing such nuclear interactions. The cloud-chamber pictures described in the accompanying article[4] also show the occasional occurrence of a local penetrating shower. This should not be surprising, since the observation of large numbers of penetrating particles implies that interactions giving rise to them occur frequently. Therefore a small number of local events of this type must be expected.

A Cloud-Chamber Study of Extensive Air Showers at 3260 Meters Elevation

W. W. BROWN AND A. S. MCKAY
Cornell University, Ithaca, New York
(Received June 2, 1949)

The penetrating particles in extensive air showers have been observed in a cloud chamber under 6 inches of lead at an elevation of 3260 meters. If a group of air showers is selected in such a way that their cores mostly land between 4 and 24 meters from the chamber, the penetrating particles are seen to consist mainly of μ-mesons which have been produced in the air above the apparatus. If a group of air showers is selected so that their cores are mostly <6 meters from the chamber there are again many μ-mesons and in addition there is evidence for local production of penetrating particles in mixed showers and high energy nuclear disintegrations produced by both neutral and ionizing penetrating particles. Thus we have evidence that high energy neutral particles and highly interacting ionizing particles make up an appreciable portion of the penetrating particles in the cores of air showers. There are more cascades of energy $>10^8$ ev under the lead shield than can be accounted for by the radiation and knock-on processes of the observed number of mesons.

I. INTRODUCTION

IN the preceding article[1] an experiment is described in which the soft and penetrating components of extensive cosmic-ray air showers are studied by means of various counter arrays. The showers were selected by requiring their cores to be detected by one of the five core selectors located at the positions marked C_n (Fig. 1 of I). In conjunction with this experiment a cloud chamber, located near core selectors number 2, 3 and 4 as shown in the diagram, and surrounded by thick lead, was triggered in coincidence with these showers. Expansions were also triggered by various coincidences of a system of counters above and below the chamber (Fig. 1), which generally required the core of an air shower to land nearby. The present article is an analysis of the two sets of cloud-chamber pictures thus obtained.

II. EXPERIMENTAL

A cylindrical cloud chamber of 11 inches diameter and $3\frac{1}{4}$ inches depth was used with argon at a pressure of 17 cm Hg above atmospheric pressure, which was 51 cm Hg, and a vapor mixture of alcohol and water. The chamber also contained 5 horizontal lead plates (7 in.$\times 3\frac{1}{4}$ in.$\times\frac{1}{2}$ in.) to serve as a means of distinguishing penetrating and soft particles. The chamber was surrounded by a lead house with 3-inch walls and a 6-inch roof, and some lead and iron beneath. Two perpendicular sections of the arrangement are shown to scale in Fig. 1. Photographs (non-stereoscopic) were taken through the 6 in.$\times$6 in. aperture, with a Sept camera at f 5.6 to 8. Illumination was achieved by triggering two G.E. FT-126 flashtubes, supplied by 50 μf at 1500 volts, 0.1 second after the expansion. The thin covering L (0.5 g/cm^2) surrounding the apparatus served both to keep extraneous light from entering the camera, the shutter of which remained open during operation, and as an insulator to simplify the temperature regulation of the interior which was maintained at 87°F. The apparatus was housed in a canvas tent during the full period of operation at Echo Lake (el. 3260 meters). The counters at X, Y, and Z some of which are connected in pairs as indicated in the diagram, have effective dimensions $\frac{1}{2}$ in.$\times$10 in., 1 in.$\times 2\frac{3}{4}$ in., and 1 in.$\times$16 in. respectively. The four neon bulbs situated at S, P, C, and A indicate the type of counter coincidence causing each particular expansion and were photographed simultaneously with the cloud chamber. The clock T (Fig. 1) was synchronized with that used in I where all the data were recorded by photographing neon bulbs.

The expansion of the chamber was triggered whenever a master pulse was generated by one of the following events:

(a) A coincidence in any one of the core selectors C_n (Fig. 1 of I), referred to hereafter simply as a C event if not associated with the other types of counter coincidence listed below. The occurrence of this event was indicated by the lighting up of neon bulb C. As described in more detail in I (see Fig. 2 of I for geometry) this type of coincidence usually indicates that the core of an air shower has landed near the core selector. C event pictures thus yield information about the penetrating component to be expected at distances up to about 25 meters from the core of an air shower. From the photographic records in I both the distance to the core selector which caused a particular expansion, and the particle density Δ_d of the shower at 44 or 92 meters from the cloud chamber could be determined.

(b) A sixfold coincidence of the counters at X, indicated by neon bulb S, and referred to hereafter as simply an S event if it was not associated with an air shower.

(c) Any one of the counters at X, in coincidence with any two of the pairs at Y, indicated by neon bulb P, and referred to hereafter as a P event if not associated with an air shower.

(d) An eightfold coincidence of S with the two pairs at Z, indicated by simultaneous lighting of neon bulbs S and A and referred to as SA. These events are associated with air showers and, as will be explained below, happen most frequently for showers whose cores land near the chamber ($<$5–10 meters away). Indeed the geometry is very similar to that of a core selector except that a greater thickness of lead surrounds the shielded counters in the present experiment and a larger number of coincidences are required in both the shielded and unshielded counters.

[1] Cocconi, Tongiorgi, and Greisen, Phys. Rev. **76**, 1020 (1949) (hereafter referred to as I).

(e) A fivefold coincidence of P with the two pairs at Z, indicated by simultaneous lighting of neon bulbs P and A, and referred to as PA. These coincidences also indicate the presence of an air shower.

Chance coincidences of the above events were negligible.

The numbers of the above events, together with various coincident combinations, that were recorded over a period of 871 hours of operation are given in Table I. In the last column of the table are the numbers of these events recorded in 118 hours with the lead roof and walls removed but the lead and iron surrounding the Y counters retained.

The S and P events, which are not associated with air showers of at least sufficient density to trip the Z counters, will be analyzed in a subsequent paper.

As was mentioned earlier the arrangement of counter trays described in I permitted the measurement of the particle density Δ_d of each individual shower at at least one of two places 44 and 92 meters away from the cloud chamber. These places were 48 and 96 meters away from and in a direction perpendicular to the line of the C selectors. These data were used to divide the C events into a high density group and a low density group as indicated in the table.

For a short period shower particle densities were simultaneously measured near the cloud chamber (~6 meters away) and 44 meters away. From these data the integral frequency of C-selected showers as a function of particle density and distance from the C selector has been given in I (see Fig. 7 of I). Considering C selectors 2, 3, and 4 to be at an average distance of 4.5 meters from the chamber, and C_1 and C_5 at distances of 12 and 24 meters respectively, the differential frequency spectrum per logarithmic density interval at the cloud chamber was determined by interpolation from these curves. The spectrum is plotted in Fig. 2 (Curve A) normalized to a total of 4125. The differential curve beyond $\Delta_0 = 512$ m^{-2} was plotted according to a distribution proportional to $\Delta_0^{-1.6}$ normalized to the integral curve at $\Delta_0 = 512$ m^{-2}. The exponent was determined from direct density measurements with the cloud chamber on the 746 showers involving C coincidences observed during the 118 hours the lead shield was removed. The measurements were made by counting the number of particles observed in the top and side sections of the chamber and calculating the density assuming an effective area of 150 cm^2 for these compartments. Though the absolute density values are uncertain because of the effective area not being known too well, the relative values are good (see Fig. 3), and show that the frequency of high density C-selected showers is proportional to $\Delta_0^{-1.6}$.

From further analysis of the original data of I the logarithmic density distribution of C-selected showers at the chamber, under the condition that the density at 48 meters from the C selector $\Delta_{48} > 50$ m^{-2}, was also obtained. This distribution normalized to a total of 221 is plotted in Fig. 2, curve B, and again was assumed to go as $\Delta_0^{-1.6}$ beyond $\Delta_0 = 512$ m^{-2}. The difference between these distributions, indicated by the dotted line C in Fig. 2, is the density distribution at the chamber of C-selected events under the condition $\Delta_{48} < 50$ m^{-2}.

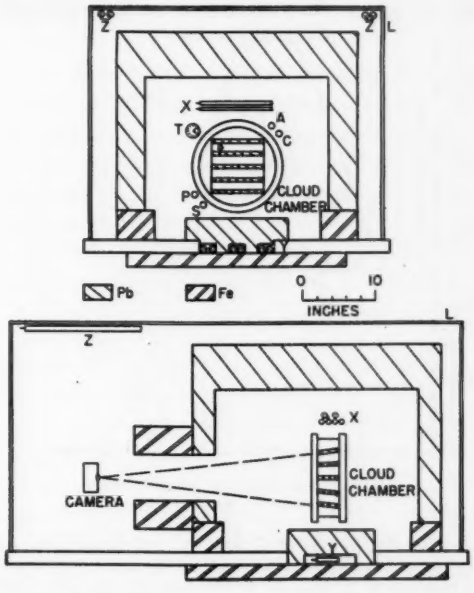

FIG. 1. Two perpendicular sections showing the disposition of absorber and counters about the cloud chamber. The chamber is triggered by various coincidences in the counters at X, Y, and Z as well as by coincidences in the more distant C selectors shown in Fig. 1 of I.

The coincidence of the Z counters with about 40 percent of the C events is consistent with the fraction of coincidences expected from the density distribution of curve A, Fig. 2, and is further evidence that C events are associated with air showers.

III. CLASSIFICATIONS OF EVENTS SEEN IN THE CLOUD CHAMBER

In many of the air shower events occurring under lead the cloud-chamber photographs showed the presence of:

TABLE I. The number of times each type of counter coincidence triggered the cloud chamber in 871 hours under lead and in 118 hours without the lead over the cloud chamber. The last three types are not associated with dense air showers and will be analyzed in a subsequent paper.

Type of triggering coincidence	Number of events observed in 871 hours with lead	Number of events observed in 118 hours without lead
C ($\Delta_{48} < 50$ m^{-2})	3864	686
C ($\Delta_{48} > 50$ m^{-2})	214	
SC	1	0
PC	0	1
SCA	17	26
PCA	10	10
$SPCA$	19	23
SA	44	21
PA	27	36
SPA	18	6
S	3551	15
P	1245	96
SP	153	1

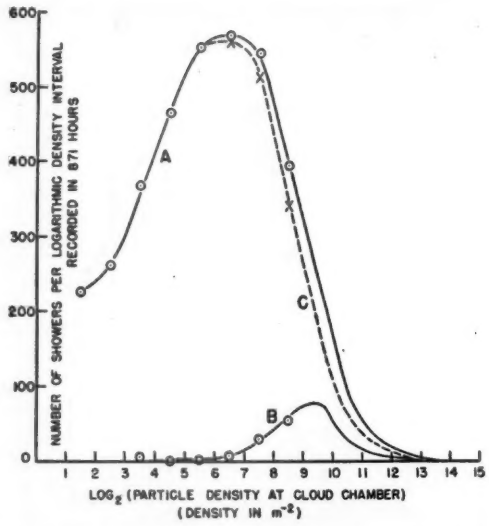

FIG. 2. Number of showers observed per logarithmic density interval (log to base 2) at the cloud chamber. *A*, distribution of all 4125 *C*-selected events. *B*, distribution of the 221 *C*-selected events for which $\Delta_{48}>50$ m^{-2}. *C*, the difference between *A* and *B*. The curves are derived from the integral density distributions of Fig. 7 in the preceding article and from the distribution given in Fig. 3.

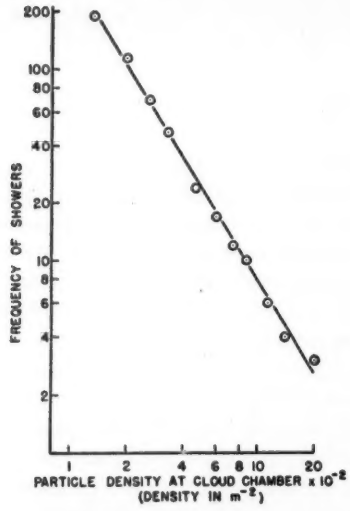

FIG. 3. Integral distribution of high density showers obtained by counting particles seen in pictures taken when *C*-selected showers triggered the expansion of the unshielded chamber. The above results give a shower frequency proportional to $\Delta_0^{-1.6}$.

(1) Penetrating particles, most of which did not produce secondaries in the lead plates. A particle was called penetrating if it was observed to pass through at least one lead plate without multiplication and was visible over a path length of at least ½ inch in the compartments above and below the plate. Eighty percent of these particles were observed to cross at least two plates without multiplication so that the identification of a penetrating particle was usually more certain than would be indicated by the minimum requirement.

(2) Fast electrons (of energy $>10^8$ ev) as evinced by the production of at least 5 electrons emerging from a lead plate.

(3) Slow electrons (of energy $<10^8$ ev)—tracks of minimum ionization showing neither penetration nor multiplication, and tracks above minimum ionization with very devious paths. Except for electrons the only known particles that might exhibit low ionization and not penetrate a lead plate are mesons in a very narrow energy interval—so narrow that the observation of many such particles is improbable.

(4) Nuclear disintegrations—events showing at least two heavy particles (either heavily ionizing or both lightly ionizing and penetrating) radiating from a common point in a lead plate. Both ionizing and non-ionizing particles were observed to produce these events, though identification of the latter type of originating particle was sometimes doubtful because of the absence of stereoscopic vision.

(5) Single heavily ionizing particles.

Two of the above events sometimes occurred in the same picture. In order to show the frequency of occurrence of this association, whenever it exists, the data are presented as indicated in Table II. The headings of the four rows and first four columns of the table represent the events (1) to (4) respectively, and the four pairs of numbers entered in a given square are the numbers of pictures of that type belonging to the corresponding four groups of triggering coincidences listed in the squares of column five.

For instance, the top number of the square in the third column and third row, 132, means that there were 132 pictures in the low density *C* events ($\Delta_{48}<50$ m^{-2}) in which penetrating particles alone were observed; while the fourth number in the square belonging to row 3, column 1 indicates that there were 25 pictures in which both penetrating particles and low energy electrons were observed simultaneously in all of the events designated by *SA*, *PA*, and *SPA*. Reference to Table I gives the total number of low density *C* events, and the sum of *SA*, *PA*, and *SPA* events as 3864 and 89 respectively. The percentages of these totals in the above two examples are, then 3.4 and 28, respectively. These numbers have been entered in parentheses in Table II after the 132 and 25, respectively. The remaining numbers and corresponding percentages give the frequency of occurrence of all other observed associated events of the four groups.

In many cases a picture showed no visible tracks. The number and percentage of times this occurred in each of the four groups are given in the square occupying the upper right-hand corner of the table. The square in row 2 column 2, has been left empty since high energy electrons were always accompanied at least by the low energy electrons they produced by the cascade process in the lead plates. The other vacant squares just represent repetitions of the combinations already treated in the lower left-hand part of the table.

In the total of 4214 pictures associated with air showers there were 57 cases (1.4 percent) in which the single heavily ionizing particles mentioned in (5) above occurred. These cases are not included in Table II.

Only those tracks which appeared to be of counter age were counted in constructing the above table. In addition there were many tracks composed of droplets noticeably underdeveloped. The particles causing these tracks were assumed to have entered the chamber

sometime after the initiation of the expansion and hence are incoherent or "post-expansion" particles. Random expansion experiments conducted at 260 m elevation, but otherwise under operating conditions similar to those at the higher altitude, and using the same arbitrary method of classifying the tracks, indicated that half of the random penetrating tracks appeared to be of counter age and half post-expansion. Hence the frequency of occurrence of post-expansion penetrating tracks at 3260 meters (118 tracks in 4125 pictures or (2.9 ± 0.3) percent) may be considered as equal to the background of incoherent penetrating tracks of apparent counter age.

The tracks of particles entering the chamber prior to the expansion were separated by the clearing field (+74 volts on alternate plates) and not counted.

It has been found convenient, in the following discussion, to group the air showers in various ways. Seven methods of grouping are listed below and will be referred to hereafter by the letter G with the appropriate subscript.

G_1: Showers causing coincidences only in C selectors and having $\Delta_{48}<50$ m^{-2}.
G_2: Showers causing coincidences only in C selectors and having $\Delta_{48}>50$ m^{-2}.
G_3: Showers causing coincidences *SCA*, *PCA*, and *SPCA* (in 7 of these events $\Delta_{48}>50$ m^{-2} while in the other 40, $\Delta_{48}<50$ m^{-2}).
G_4: Showers causing coincidences *SA*, *PA*, and *SPA*.
G_5: All low density showers having $\Delta_{48}<50$ m^{-2} (consisting of G_1+40 from G_3). The density distribution of these at the chamber is given in Fig. 2, curve *C*.
G_6: All high density showers having $\Delta_{48}>50$ m^{-2} (consisting of G_2+7 from G_3). See Fig. 2, curve *B*, for the density distribution at the cloud chamber.
G_7: All showers involving C events ($G_1+G_2+G_3$). See Fig. 2, curve *A*, for the density distribution at the cloud chamber.

IV. PARTICLES SEEN UNDER 6 IN. OF LEAD IN *C* EVENTS

The increase in the number of electrons and penetrating particles seen in the cloud chamber with the shower density measured 44 m away is quite evident from a comparison of groups G_1 and G_2 in Table II, and establishes the true association of these events with extensive air showers.

It is remarkable that in the table there are more than twice as many cases, triggered by C-selectors (groups $G_1+G_2+G_3$) in which, under 6 inches of lead electrons alone are seen, as there are cases in which penetrating tracks are observed regardless of their association with other events. This is in qualitative agreement with Greisen's calculation[2] in which it is shown that many of the particles counted under thick lead absorber (4 to 8 inches) are low energy electrons produced by photons of several Mev energy. The picture of Fig. 4a triggered by *SCA* is a good example of this type of electron production. Many low energy electrons are seen to be produced in the lead plates.

More specifically the calculations predict that the number of electron cascades of one or more particles expected under 6 inches of lead when a shower of density Δ_0 is incident on the surface is about $0.004\Delta_0$, a number which has been verified experimentally[3] with G-M counters. The cloud chamber is more efficient for the detection of these photons than a counter would be. A semi-quantitative comparison of the cloud chamber results with the above prediction can be made by calculating the number of times in which one or more electrons would be expected in one compartment of the chamber (indicated by D in Fig. 1) in the 221 high density showers of G_6. If this compartment has an

TABLE II. Showing the association of different types of events as they occur together in the cloud chamber for four groups of triggering events. These events were observed in the shielded chamber.

	Low energy electrons ($<10^8$ ev) (1)	High energy electrons ($>10^8$ ev) (2)	Penetrating particles (3)	Nuclear disintegrations (4)	Triggering events	Number of pictures with zero tracks present
Low energy electrons ($<10^8$ ev) (1)	484(12.5)				G_1 (C, $\Delta_{48}<50$ m^{-2})	3200(82.8)
	47(22)				G_2 (C, $\Delta_{48}>50$ m^{-2})	136(64)
	15(33)				G_3 (*SCA*, *SC*, *PCA*, *SPCA*)	8(17)
	32(36)				G_4 (*SA*, *PA*, *SPA*)	12(13)
High energy electrons ($>10^8$ ev) (2)	8(0.02)				G_1	
	2(0.9)				G_2	
	3(6.5)				G_3	
	8(9)				G_4	
Penetrating particles (3)	35(0.9)	1(0.003)	132(3.4)		G_1	
	7(3.3)	1(0.5)	20(9.3)		G_2	
	14(30)	2(4)	1(2)		G_3	
	25(28)	6(7)	2(2)		G_4	
Nuclear disintegrations (4)	1(0.003)	0(0)	1(0.003)	2(0.005)	G_1	
	0(0)	0(0)	1(0.5)	0(0)	G_2	
	3(7)	0(0)	1(2)	0(0)	G_3	
	1(1)	1(1)	2(2)	0(0)	G_4	

[2] K. Greisen, Phys. Rev. **75**, 1071 (1949).
[3] Cocconi, Cocconi Tongiorgi, and Greisen, Phys. Rev. **75**, 1063 (1949).

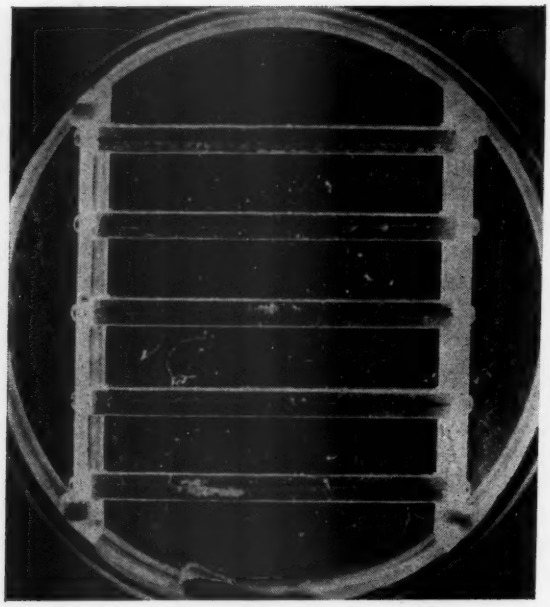

(a)

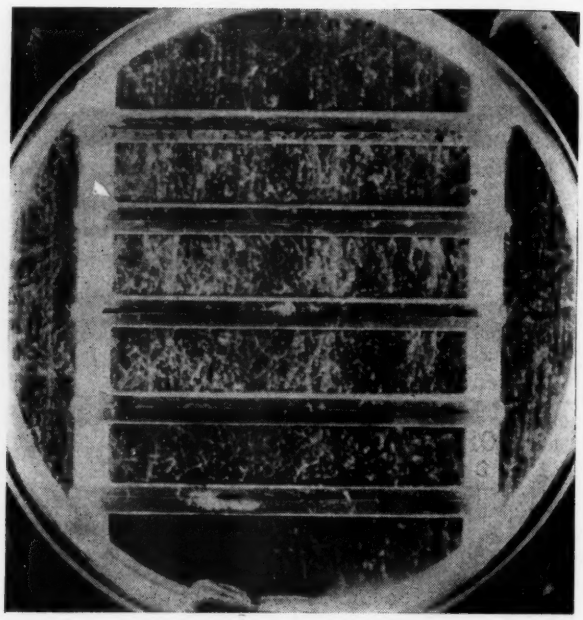

(c)

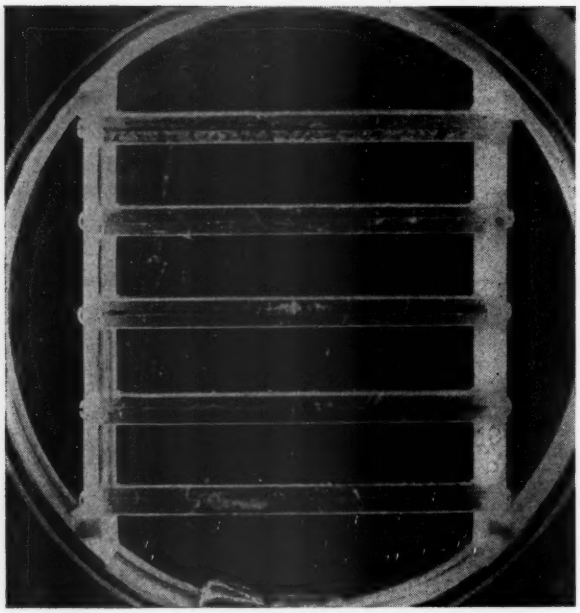

(b)

FIG. 4(a). The particles in the above picture, most of which are electrons are associated with an air shower which triggered the expansion of the cloud chamber by the coincidence *SCA*. The existence of so many low energy electrons under the thick lead shield surrounding the chamber is accounted for by the long mean free path in lead of photons of energy $\sim 10^7$ ev. The core of the air shower struck in the neighborhood of the cloud chamber and core selectors 2 and 3. The measured particle density 96 meters away was 4 m^{-2}.

FIG. 4(b). Four nearly parallel penetrating particles are visible in this picture. A measurement of their angular divergence shows they could not have been produced in the lead surrounding the chamber, but were made more than one meter above the lead. They are associated with an air shower which triggered the chamber expansion by a *C* event. The shower core was detected at C_2 (Fig. 1 of I), 5 meters from the cloud chamber. The particle density 48 meters from C_2 was 30 m^{-2}.

FIG. 4(c). This picture, taken with the unshielded chamber, shows the appearance of a small section of a large air shower. Some idea of the magnitude of the shower is obtained by noting that the triggering event, *SPCA*, consisted of coincidences in C_1, C_2, C_3 and C_4 as well as in counters around the chamber. An estimate of a total of 60 particles in the top and side compartments corresponds to a particle density of 4000 m^{-2} at the chamber.

effective area A square meters, the probability that one or more electrons will appear in this compartment when a shower of density Δ_0 is incident on the surface of the 6-inch lead absorber above the chamber is $[1-\exp(-R_s\Delta_0 A)]$, where $R_s=0.004$ is the ratio of the number of cascades of one or more electrons detectable under the 6-inch absorber to the number of ionizing particles incident on it. In the present calculation R_s is assumed to be independent of the size of the shower and the distance away from the core, although these assumptions have been shown to be not strictly valid.[3] For the shower spectrum $F(\Delta_0)$ at the chamber given by curve *B*, Fig. 2 the total number of such events expected is therefore

$$\int_0^\infty F(\Delta_0)[1-\exp(-R_s\Delta_0 A)]d(\log_2\Delta_0).$$

Assuming $A=0.014$ m^2 for one compartment, numerical integration gives 5 percent as the fraction of pictures in

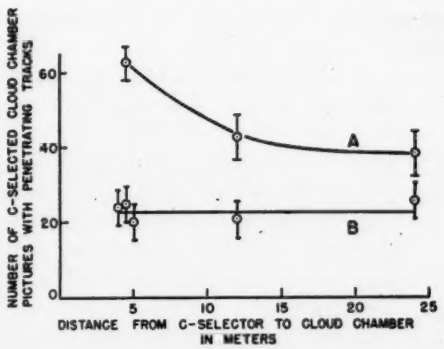

FIG. 5. Dependence of the frequency with which penetrating particles are observed in the cloud chamber on the distance between cloud chamber and C selector. A, includes all pictures triggered by C events in which counter age penetrating particles occurred. B, includes all C event pictures in which post-expansion penetrating particles occurred and shows the incoherence of these particles.

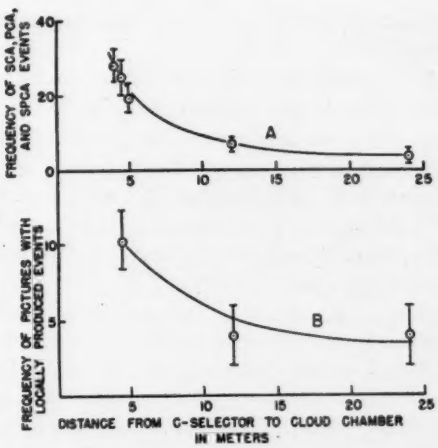

FIG. 6. Dependence of the frequency of events of local origin on the distance between C selector and cloud chamber. A, the frequency dependence of the counter coincidences in group G_3 (all SCA, PCA, $SPCA$ events). B, frequency dependence of local events seen in the cloud chamber.

which electrons are expected to be seen in the single compartment. Electrons were actually observed in compartment D (see Fig. 1) in (8.5±2) percent of this group of pictures. The difference is hardly significant in view of the uncertainty as well as the different methods of shower selection and the consequent differences in shower spectra and average distance from the shower cores. The cloud chamber results may be considered as a direct verification of the presence of the comparatively large number of low energy electrons under 6 inches of lead and associated with air showers.

V. VARIATION OF THE NUMBER OF PENETRATING PARTICLES WITH DISTANCE FROM THE CORE

The frequency of occurrence of penetrating particles in pictures belonging to group G_7 is plotted in Fig. 5 (curve A) as a function of the distance of the cloud chamber from the core selectors. The distribution is also plotted for the incoherent post-expansion penetrating particles (curve B). The latter are seen to be uniformly distributed whereas counter age tracks occur more frequently near the chamber. In curve A a background about equal to curve B is expected (see Section II). After subtraction of this background the frequency shows a strong dependence on the distance between cloud chamber and core selector. Therefore, a large fraction of the penetrating particles either must travel very closely parallel to the shower core, or must be produced in or near the detecting apparatus. If the latter alternative is correct, the producers of the penetrating particles must have a strong concentration in the shower core. These results agree with those of I, in which it was found that the density of penetrating particles falls off with distance from the core almost as fast as the density of electrons.

TABLE III. Data to show the variation of the numbers of the penetrating particles of air showers, seen in the cloud chamber, with the electron density.

Electron Δ_{48} / Density Δ_{88}	0–50 m^{-2} / 0–10 m^{-2}	50–200 m^{-2} / 10–40 m^{-2}	>200 m^{-2} / >40 m^{-2}	>50 m^{-2} / >10 m^{-2}	Total >0 / >0
Number of pictures	3904	190	31	221	4125
Number of penetrating tracks observed	189±14	29±5.4	11±3.3	40±6.3	229±15
Number of chance tracks expected	112±10	5.4±0.5	0.89±0.08	6.3±0.7	118±10
Corrected number of penetrating tracks	77±17	23.6±5.6	10.1±3.3	33.7±6.4	111±18
Number of penetrating tracks per 100 pictures	1.97±0.43	12.4±2.9	32.5±10	15.2±2.9	2.7±0.5

VI. VARIATION IN THE NUMBER OF PENETRATING PARTICLES WITH THE DENSITY OF THE SHOWERS

As was previously pointed out from a comparison of G_1 and G_2 in Table II, penetrating particles occur more frequently in pictures belonging to the denser shower group. However the data of Table II are uncorrected for chance coincidences. In Table III the densities have been divided into smaller intervals and the data include all pictures belonging to G_7 (i.e., all events in which C selector coincidences played a part). After the 2.9 percent correction for chance tracks is made it is seen that the probability of a penetrating particle traversing the chamber increases uniformly with the shower density. It is also evident that in showers having $\Delta_{48}>50$ m^{-2}, about 85 percent of the observed penetrating particles are certainly associated with the extensive air showers.

VII. THE ORIGIN AND NATURE OF IONIZING PENETRATING PARTICLES IN AIR SHOWERS

If the penetrating particles in air showers are of local origin one would expect to observe more pictures with 2 or more tracks than if their origin were some distance away. In the latter case a Poisson distribution is

expected for the penetrating particles in showers of a given total density.

The 221 pictures of air showers for which $\Delta_{48}>50$ m^{-2} (group G_6) have been classified in Table IV in accordance with the number of penetrating particles observed in each picture. It must be emphasized that G_6 demands the presence of a C coincidence irrespective of whether S or P coincidences occur simultaneously, and hence there is no bias introduced by the counters under the lead around the cloud chamber.

An explicit calculation of the number of penetrating tracks expected to traverse the cloud chamber in this group of high density showers can be made from the results of the experiment of Cocconi, Tongiorgi and Greisen.[3] They give the fraction of penetrating particles in air showers of mean density Δ_0 as $R_p=0.016\Delta_0^{-0.13}$. Assuming a Poisson distribution of the penetrating particles, the probability of observing n penetrating particles to traverse a cloud chamber of effective area A in a shower of density Δ_0 is

$$\frac{(AR_p\Delta_0)^n \exp(-AR_p\Delta_0)}{\Gamma(n+1)}.$$

The total number of cases expected in G_6 (for which the density spectrum $F(\Delta_0)$ at the chamber is given by Fig. 2, curve B) is thus

$$\int_0^\infty F(\Delta_0)\frac{(AR_p\Delta_0)^n \exp(-AR_p\Delta_0)}{\Gamma(n+1)}d(\log_2\Delta_0).$$

An effective area $A=0.0225$ m^2 for the cloud chamber has been calculated on the assumption of a $\cos^3\theta$ zenith angular dependence of the penetrating particles and taking into account the requirement that the particles penetrate at least one plate.

The results of numerical integrations for $n=0$, 1, 2 and >2 are given in the last row of Table IV where they are compared with the observed number of cases in which 0, 1, 2, and >2 penetrating tracks were seen in the 221 dense showers of G_6. Corrections to the observed numbers were made on the basis of the (2.9±0.3) percent chance background as determined above. No normalizing factor (except the total number of pictures taken) was used in the calculation. Since the results of the counter experiment and the above calculation are based on a Poisson distribution for the penetrating particles, the agreement with the cloud-chamber observations in both the distribution and the total number of particles shows that the major portion of the observed ionizing penetrating particles associated with this selected group of air showers are indeed independent of each other and therefore probably not of local origin—though this method may not be very sensitive to the detection of a small fraction (like 10 percent) of locally produced penetrating particles, and the conclusion rests on the assumption that locally produced penetrating particles would occur usually in groups rather than singly.

Of five cases in which there were two observed penetrating particles in the cloud chamber, two of the pictures contained tracks that were too nearly parallel to have come from a point in the lead. This is further evidence that the penetrating particles do not all originate in local showers generated in the lead. Of the remaining three pictures two contained a fast particle and a slow one going in a different direction and stopping in a lead plate. In these cases it is not clear whether the particles might have had a common origin. In the fifth picture there are two fast particles seen moving in different directions which could be divergent from a point in the lead. In one unusual case (see Fig. 4b) four nearly parallel penetrating tracks associated with an air shower of moderate density can be seen. These tracks do not diverge from a common point in the lead.

In the experiment of Cocconi, Tongiorgi, and Greisen[3] it has been concluded from absorption measurements that the ionizing penetrating particles associated with air showers are mostly μ-mesons. The following cloud-chamber observations lend further support to this conclusion: (1) in the total observed path of 1140 grams per cm^2 of lead traversed by the penetrating particles of G_6 no nuclear interactions were observed—indicating a mean free path greater than the 160 to 300 grams per cm^2 attributed to highly interacting particles.[4,5]

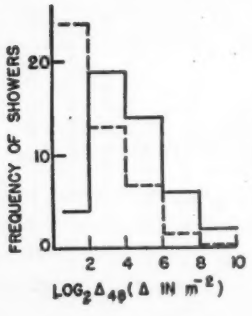

FIG. 7. Frequency of occurrence of showers of group G_3 per logarithmic density interval at 48 meters from the C selectors (full line histogram), compared to the distribution of all C events (broken line histogram), normalized to the same area.

TABLE IV. The number of times 0, 1, and 2 penetrating particles appear in the cloud chamber in group G_6.

	Number of times n penetrating particles appear in the cloud chamber				Total number of penetrating tracks
	$n=0$	$n=1$	$n=2$	$n>2$	
Observed number of cases	186±14	30±5	5±2	0	40±6
Correction for chance coincidences	+6±0.6	−5±0.6	−0.6±0.1	0	6.3±0.7
Observed number corrected for chance coincidences	192±14	25±5	4.4±2	0	34±6
Calculated* number	194±14	23±4	3±1	1.2±0.6	33±4

* Calculations were based on the results of Cocconi, Tongiorgi, and Greisen (see reference 3).

[4] L. Janossy and D. Broadbent, Proc. Roy. Soc. **A190**, 497 (1947); **A191**, 517 (1947); **A192**, 364 (1948).

[5] B. Rossi, Rev. Mod. Phys. **20**, 537 (1948); G. Wataghin, Nature **161**, 91 (1948); E. P. George and P. T. Trent, Nature **161**, 248 (1948); G. Cocconi and K. Greisen, Phys. Rev. **74**, 62 (1948); G. Cocconi, Phys. Rev. **75**, 1075 (1949).

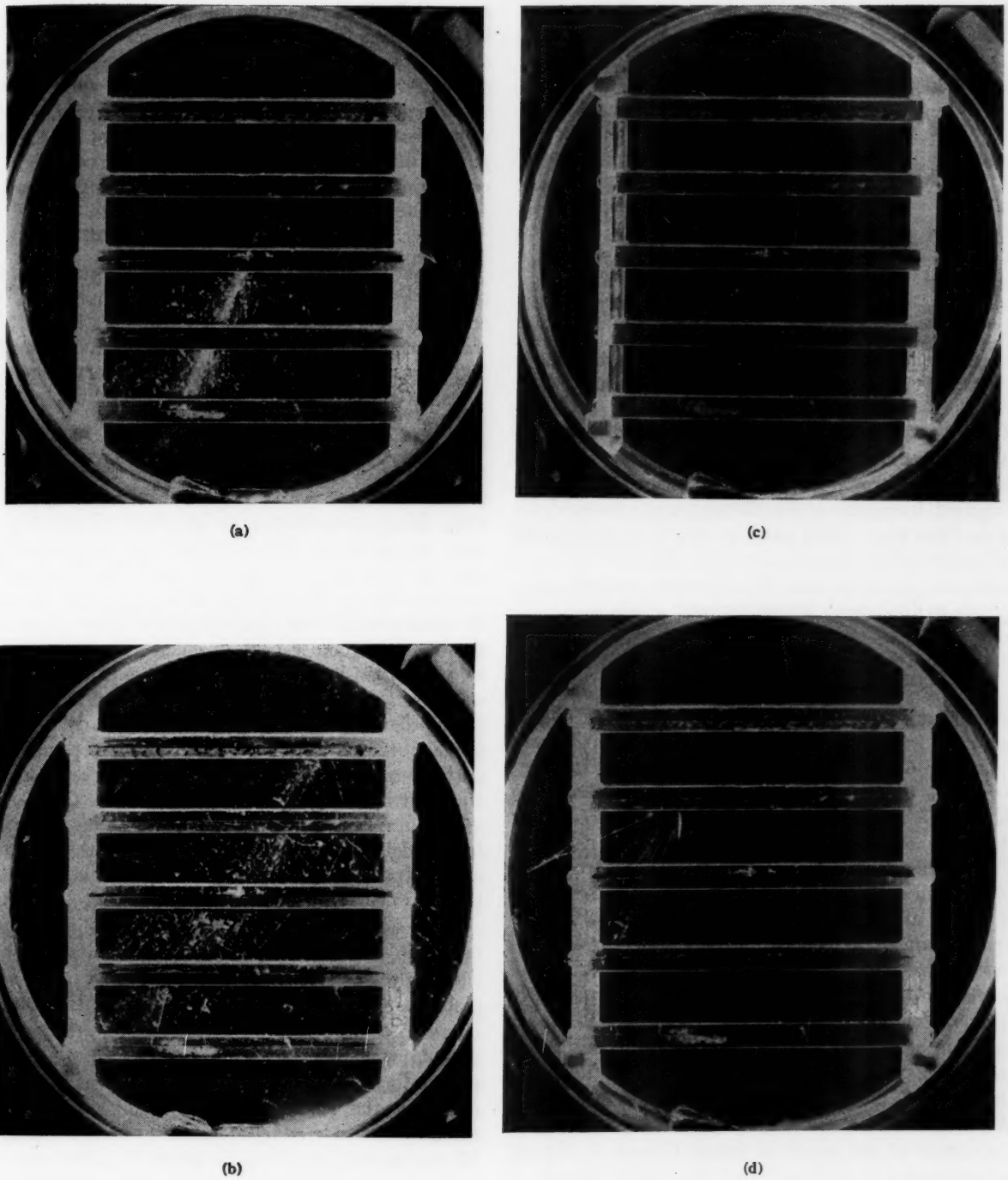

FIG. 8. Local events associated with extensive air showers: (a) A cascade produced in the chamber. No penetrating secondaries are distinguishable. An event of this type could not be produced directly by the electrons and photons of the air shower incident on the 6-inch Pb absorber surrounding the chamber. The frequency of these cascades is greater than can be accounted for by the radiation or knock-on processes of μ-mesons. There are more than 50 particles at the maximum of the shower development indicating a primary energy of $\sim 10^{10}$ ev. Simultaneous coincidences in C_2, C_3, and C_4 and in the counters around the chamber indicate that the shower core was located nearby. The measured particle density in the air 6 meters from the chamber was >500 m^{-2} and 48 meters away it was about 50 m^{-2}. (b) A mixed shower originating in the lead above the chamber. At least four penetrating particles traverse the first two plates. The chamber was triggered by coincidence SA. (c) A nuclear disintegration probably produced by a neutral particle. It is associated with an extensive air shower the core of which landed near C_3. One of the particles ejected in the forward direction penetrates the fourth plate while the four backward ejected particles must penetrate about $\frac{1}{2}$ inch of lead before emerging from the third plate. A lower limit for the primary particle energy is 10^9 ev. The particle density 48 meters from C_3 was about 80 m^{-2}. (d) A nuclear disintegration of neutral origin in which 17 particles emerge from the second lead plate. The core of the air shower with which this event is associated was detected by C_2. The particle density in the air 6 meters from the cloud chamber was ~ 10 m^{-2}.

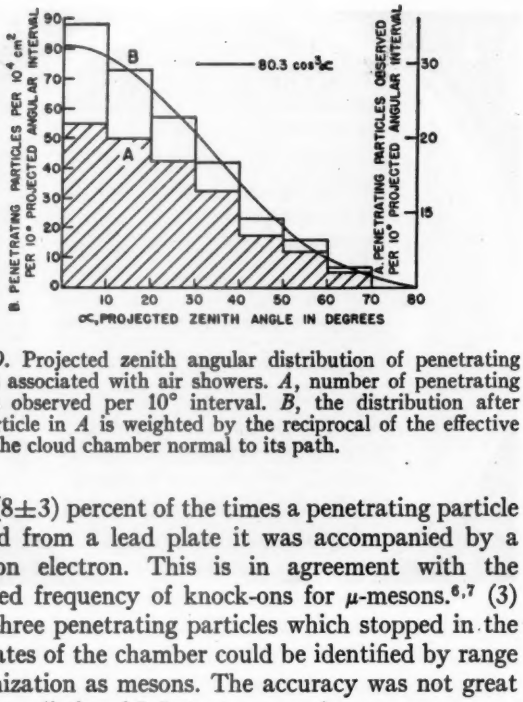
B, PENETRATING PARTICLES PER 10^4 cm² PER 10° PROJECTED ANGULAR INTERVAL
A, PENETRATING PARTICLES OBSERVED PER 10° PROJECTED ANGULAR INTERVAL
B
A
80.3 cos³α
α, PROJECTED ZENITH ANGLE IN DEGREES

FIG. 9. Projected zenith angular distribution of penetrating particles associated with air showers. A, number of penetrating particles observed per 10° interval. B, the distribution after each particle in A is weighted by the reciprocal of the effective area of the cloud chamber normal to its path.

(2) In (8±3) percent of the times a penetrating particle emerged from a lead plate it was accompanied by a knock-on electron. This is in agreement with the measured frequency of knock-ons for μ-mesons.[6,7] (3) In G_6 three penetrating particles which stopped in the lead plates of the chamber could be identified by range and ionization as mesons. The accuracy was not great enough to distinguish between π- and μ-mesons.

VIII. EVENTS IN WHICH COUNTERS AROUND THE CLOUD CHAMBER ARE DISCHARGED

The group G_3 of Table II is selected from the C events (group G_7) by requiring various counter coincidences under the 6 inches of lead surrounding the chamber. Group G_3 therefore represents air showers similar to those of G_7 except that there is stronger bias in favor of those showers striking closer to the cloud chamber. This is shown by the graph in Fig. 6 where the frequency with which each C selector contributes to these events is plotted as a function of distance from the C selector to the chamber. It is apparent that a large fraction of the cores of these showers land in the neighborhood of C selectors 2, 3, and 4 which were within 5 meters of the cloud chamber. The group of pictures G_4 is similar to G_3 in requiring the coincidence of the unshielded counters Z with a counter group under the lead, but the events G_4 did not trigger any of the five C selectors. We believe that there is no fundamental difference in the nature of the events of groups G_3 and G_4. Indeed in reference 1 it is shown that the major fraction of showers which trigger one core selector fails to trigger the other core selectors nearby. It may also be seen from the classification of events in Table II that the phenomena occurring in group G_3 are the same as those occurring in group G_4 and occur with equal probabilities.

The logarithmic spectrum of the particle densities measured 48 meters from the C selectors is given for group G_3 by the full line histogram in Fig. 7 and for group G_7 by the broken line histogram which is normalized to the same area. The comparison shows that the showers of group G_3 (and hence of G_4) are of greater average size than those of G_7. Since in addition the showers of G_3 and G_4 strike on the average closer to the cloud chamber than those of G_7 we may expect the particle density at the cloud chamber to be considerably greater in the showers of G_3 and G_4 than in those of G_7.

IX. LOCALLY PRODUCED EVENTS

Though local production of multiple secondaries by penetrating particles in air showers appears to be relatively rare, there were a few instances in which it was observed. These events take the form of cascades and nuclear disintegrations—mixed showers, penetrating showers, and stars. Examples are shown in Figs. 8a, b, c, and d. The manner in which the sum of the frequencies of such events observed in G_3 depends on the distance of the cloud chamber from the core selector is shown in Fig. 6 (curve B). The decrease of frequency with distance by the factor of about 2.5 shows that most of the events at least were not just coincident with air showers by chance but were truly associated with air showers. Furthermore if an appreciable fraction of these events were coincident by chance with air showers one would expect an equal number to appear as post-expansion events. No post-expansion events were seen.

In order to make an unbiased comparison of the number of local events with the number of penetrating particles of a given shower group all the pictures triggered by C coincidences are used (i.e. $G_7=G_1+G_2+G_3$). In G_4 the method of triggering is more efficient for the detection of local events than for the detection of penetrating particles of non-local origin, therefore the group G_4 is not included in the present analysis.

Reference to Table II shows that in G_7 there are four events in which both penetrating particles and high energy electrons (cascade producing) occur in the same picture. In two of these events the penetrating particle is not associated with the point of production of the cascade, while the other two pictures indicate that the penetrating particles and cascades have a common origin in the lead above the chamber. These two events are considered to be mixed showers. From Table III we see that in this same group G_7 there were 111 penetrating particles observed in the chamber (after correction for 118 chance coincident tracks). None of these particles was observed to produce mixed showers or penetrating showers, or any type of nuclear disintegration while they traversed a total of 4000 g/cm² of lead. It thus appears that while in the air showers there do exist some particles capable of this type of interaction either they are few in number compared with all other penetrating particles, or else the cross section for this type of interaction is very small.

Of the remaining 15 cascades observed in G_7 without

[6] W. E. Hazen, Phys. Rev. **64**, 7 (1943).
[7] Brown, McKay, and Palmatier, Phys. Rev. **76**, 506 (1949).

distinguishable penetrating particles, 13 had primary energies in the range 10^8 to 10^9 ev and 2 were $>10^9$ ev. Since they were unaccompanied by many low energy electrons (other than those developed in the lead plates by the cascade itself) they are more likely to be the product of some local interaction in the lead within or just above the chamber than descendents of the cascade radiation incident on top of the lead.

At sea level the experimentally measured total probability for the production of cascade showers of energy $>10^8$ ev by mesons in lead, either by a knock-on or radiation process, is $\sim 10^{-4}$ per g/cm^2.[7,8] The total number of penetrating tracks observed in G_7 (including background) is 229. For each track there was on the average a path length of only 50 g/cm^2 in which a cascade with this appearance could be generated. Hence if the penetrating particles are all μ-mesons only $229\times 50\times 10^{-4}\approx 1$ shower of this type would be expected. Since 15 were observed, it is practically certain that they were produced by some other type of particle. Other possible processes which could account for these cascades have been considered theoretically.[9]

In G_7 eight nuclear disintegrations were observed. Three of these eight were observed in the 221 pictures of large showers while the other five occurred among the 3904 showers of smaller size. This strong dependence of the probability of observation on the shower size shows that these events are truly associated with air showers and not just coincident by chance.

All eight of these nuclear disintegrations appeared to be of neutral origin—though the true nature of the originating particle is rendered uncertain by the lack of stereoscopic vision. Five contained particles capable of penetrating a lead plate (see Fig. 8, c and d) and total energies probably in excess of 500 Mev. The nuclear disintegrations must occur in the chamber if their existence or the nature of their originating particle is to be determined. Hence in this case it is assumed that each potential initiating particle crosses 3 plates (40 g/cm^2 Pb) on the average, like the penetrating particles. If the mean free path is 300 g/cm^2 the above events indicate $5(1-e^{-40/300})^{-1}=40$ for the number of high energy strongly interacting neutral particles traversing the chamber in G_7.

Though neutrons of moderate energy (3–15 Mev) have been observed previously[10] the presence of high energy neutrons has only been inferred from indirect evidence. The present observations indicate that high energy neutrons do exist in air showers and it may be estimated from the above calculation that they are of the order of 40 percent as frequent as the ionizing penetrating particles in these air showers.

From Table II it is seen that the local events occur more frequently in G_3 than in G_2+G_1. As explained in Section VIII the former group consists of showers of greater average size and with cores nearer to the cloud chamber, than the group G_1+G_2.

Similar types of local production are observed in G_4 with the exception that two of the four nuclear disintegrations were caused by ionizing particles. Hence in the showers of G_3 and G_4 where 74 ionizing penetrating particles were observed to traverse a total of 2800 g/cm^2 of lead in the chamber, one would expect only about 20 percent of these to be strongly interacting particles (m.f.p.$=300$ g/cm^2 Pb). This is in spite of the fact that the groups G_3 and G_4 were selected by demanding a local counter coincidence under the lead and so favored strongly the observation of this type of particle. Hence we may conclude that (a) strongly interacting, ionizing, heavy particles probably exist in the air showers but (b) they are only a small fraction of the total number of penetrating particles.

In G_3 and G_4 four particles were observed to stop in the chamber. Three of these could be identified by range and ionization as mesons, and one as a proton. The 74 penetrating particles of these groups emerged from lead plates 146 times and produced knock-on electrons in (7 ± 2) percent of these cases, exactly as expected for μ-mesons.

X. ZENITH ANGLE DISTRIBUTIONS OF AIR SHOWERS AND THEIR PENETRATING PARTICLES

The projected zenith angular distribution of the penetrating particles in the large air showers of G_2, G_3, and G_4 is shown in the shaded histogram A of Fig. 9. Events PA containing penetrating particles have been omitted since this type of counter coincidence would tend to introduce a bias in favor of the vertical direction. When each particle is given a statistical weight equal to the reciprocal of the effective area of the lead plates

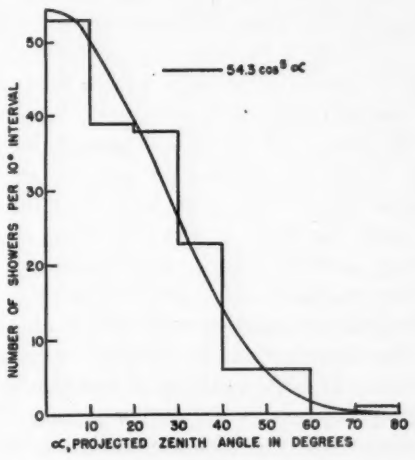

FIG. 10. Projected zenith angular distribution of air showers seen with the unshielded chamber

[8] A. C. Lovell, Proc. Roy. Soc. **172**, 568 (1939).
[9] R. J. Finkelstein, Phys. Rev. **72**, 415 (1947); R. F. Christy and J. R. Oppenheimer, Phys. Rev. **60**, 159 (1941); M. M. Mills and R. F. Christy, Phys. Rev. **71**, 275 (1947).
[10] V. Cocconi Tongiorgi, Phys. Rev. **75**, 1532 (1949).

normal to its path, the distribution takes the form of the unshaded histogram B of Fig. 9. It is apparent from the figure that an empirical law of the form $\cos^3\alpha$ fits the data satisfactorily. The effective area normal to the path of a given particle was determined by measuring the projected zenith angle α seen by the camera in the vertical plane of the chamber, and estimating the projected zenith angle β in the vertical plane perpendicular to the plane of the chamber by observing the particle's point of entry into and emergence from the sensitive volume of the chamber. Knowing α and β the area of the lead plates as seen by the particle can be calculated. The angles α could be measured to the nearest degree, while β may be in error by as much as 10°.

If the zenith angle distribution is of the form $\cos^n\theta$ where θ is the zenith angle, the projected zenith angle distribution also follows a cosine law with the same exponent. From this and the above experimental results it is seen that the zenith angle distribution is of the form $\cos^3\theta$.

For a short time the lead shield over the chamber was removed and the distribution in projected zenith angle of the air showers themselves was measured. All events other than those triggered only by P coincidences were counted. Angles were measured to the nearest degree. To ensure that measured tracks were associated with an air shower, each picture measured was required to have either at least three parallel tracks or a cascade developed in the lead plates with a well-defined core plus one other track parallel to the core. The effective area of the chamber was assumed not to vary with the projected zenith angle. This assumption is justifiable if the zenith angle distribution is of the form $\cos^n\theta$. In this case the projected angular distribution is also of this form. The measured distribution (Fig. 10) is satisfactorily fit by a $\cos^5\alpha$ empirical law.

The greater steepness of the angular distribution of the air showers compared to that of the penetrating particles associated with them and detected near the cores, suggests that some of the penetrating component is produced locally in the lead by particles in the shower core, and is produced at large angles relative to the paths of the primaries. This observation has been made earlier.[11] However, the inclusion of penetrating particles of group G_4 in the distribution and the influence of scattering of the particles in the lead above the chamber may account for some of the difference—though all penetrating particles which were obviously of local origin were excluded. The influence of the different methods of shower selection employed in obtaining the two angular distributions is expected to be small for two reasons: (1) both methods of selection demanded high density showers, $\sim$100 m^{-2} or greater, (2) it has been shown that the altitude variation of shower frequencies is almost independent of the shower size over a wide range.[12]

[11] G. Cocconi and C. Festa, Nuovo Cimento **3**, 293 (1946).

XI. COMPARISON WITH OTHER EXPERIMENTS

The results of this experiment substantiate or contradict many of the results which have been previously obtained by others who used the more indirect methods of counter observations. For instance, we observe even more slow electrons under 6 inches of lead than is predicted by Greisen[2] and observed by Cocconi, Tongiorgi, and Greisen.[3] We conclude that most of the ionizing penetrating particles associated with air showers are non-locally produced μ-mesons in agreement with the tentative conclusion of Cocconi, Tongiorgi, and Greisen[3] which was based on absorption measurements.

On the other hand this conclusion is contrary to that of Janossy and McCusker[13] who claim that the penetrating particles in air showers are highly unstable and are produced locally in the first few centimeters of lead. Their observed decrease in counting rate with the addition of 1.7 cm of lead in a plane 50 cm above the 15-cm lead shield above their counters could be due to a decrease in the number of times that the shielded counters are triggered by soft electrons. The addition of 20 g/cm^2 of brick above the 15-cm lead shield would have comparatively little effect on the high energy electrons and photons that impinge on the lead shield. Thus local production is not necessarily implied by their results.

We see some local production of penetrating particles and cascades under 6 inches of lead with the cores of air showers nearby. The complexity and unknown features of this local production make it difficult to interpret quantitatively the counter experiments of others[4,14] on the basis of our observations although it is readily understood that they should observe some effects of the local production of groups of penetrating particles associated with extensive showers.

Our value of $\cos^3\theta$ for the zenith angle dependence of the intensity of the ionizing penetrating particles associated with air showers is steeper than the $\cos^2\theta$ dependence obtained by Greisen[15] for all ionizing penetrating particles at this altitude. However, the penetrating particles we observed are within about 24 meters of the cores of air showers and so there is a bias in the directions of the cores themselves. We find that the air showers have a steeper zenith angle dependence of $\cos^5\theta$. Daudin[16] observed a somewhat steeper zenith-angle distribution for air showers at

[12] G. Cocconi and V. Cocconi Tongiorgi, Phys. Rev. **75**, 1058 (1949).

[13] L. Janossy and C. B. H. McCusker, Nature **163**, 181 (1949).

[14] Auger, Daudin, Freon, and Maze, Comptes Rendus **226**, 169 (1948); J. Daudin, Comptes Rendus **227**, 1094 (1948); G. Salvini and G. Tagliaferri, Phys. Rev. **73**, 261 (1948); Phys. Rev. **75**, 1112 (1949).

[15] K. Greisen, Phys. Rev. **61**, 212 (1942).

[16] J. Daudin, J. de phys. et rad. **6**, 302 (1945).

2000 meters elevation, going about as $\cos^8\theta$. Deutschmann[17] also observed about the same zenith-angle dependence as Daudin. Williams[18] observed a very steep distribution at 3050 meters. Only 2 showers out of a total of 100 had projected zenith angles greater than 30 degrees. In the showers we observed, 36 out of 166 had projected zenith angles greater than 30 degrees. Some of this disagreement may be attributed to the different methods of shower selection that were used in the two experiments.

V. Cocconi Tongiorgi[10] has concluded from counter studies of the moderate energy (3–15 Mev) neutrons associated with air showers that there should be a fast nucleonic component of air showers with an intensity of the order of magnitude of 2 to 3 percent of the intensity of the electronic component of the showers (i.e. about double the intensity of ionizing penetrating particles in the showers). We have fairly reliable direct evidence that a high energy neutron component can exist in air showers in numbers roughly 0.5 percent of the intensity of the electronic component when the cores are mostly from 4 to 24 meters from the place of observation. Both of these estimates assume a mean free path of 300 g/cm^2 for nuclear interaction of nucleons in lead. Our results indicate that there are more high energy neutral particles than energetic highly interacting ionizing particles associated with air showers.

The authors wish to thank Professors K. Greisen and G. Cocconi for suggesting this experiment and for their generous help both in solving experimental problems and in discussions of the results. They are grateful to the Research Corporation for a grant which covered the expense of performing this experiment. The cost of constructing the apparatus was provided through an ONR contract. The facilities of the Inter-University High Altitude Laboratories were of great help in performing the experiment.

[17] M. Deutschmann, Zeits. f. Naturforschung **2**, 61 (1947).
[18] R. W. Williams, Phys. Rev **74**, 1689 (1948).

PHYSICAL REVIEW VOLUME 76, NUMBER 8 OCTOBER 15, 1949

Cosmic-Ray Mesons near Sea Level

WILLIAM L. KRAUSHAAR*
Cornell University, Ithaca, New York
(Received June 20, 1949)

The differential and integral intensities of mesons have been studied using delayed coincidence, anticoincidence, and coincidence methods. It is shown that the differential range spectrum of slow mesons is nearly flat out to 100 g cm^{-2} of air-equivalent at sea level and at Echo Lake (3240 meters). The zenith angle distribution of slow mesons has been measured, and can be expressed by $\cos^{3.4}\theta$ at Ithaca and $\cos^{3.1}\theta$ at Echo Lake. Three independent measurements of the differential intensity of mesons lead to a value of $(6.0\pm0.15)\times10^{-6}$ sterad^{-1} g^{-1} sec.$^{-1}$ at a range of 105 g cm^{-2} of air-equivalent at Ithaca, New York (260 meters). The sea level electron intensity is considered, and it is concluded that this intensity is consistent with the electron-2 neutrino decay scheme for the μ-meson provided there is a source in addition to mesons contributing electrons with a very steep zenith angle distribution.

I. INTRODUCTION

THE present measurements were undertaken originally as part of an attempt to evaluate accurately the sea level electron intensity. As is well known, meson decay and collision processes are responsible for a large fraction of the sea level electron component. Other sources of electrons (meson radiation, nuclear interactions, proton collision processes, etc.) contribute the remainder. The subject has been discussed frequently.[1–3] Reliable methods have been developed for calculating the intensity of electrons that should arise from the decay and collision processes of mesons. On the other hand, the experimental determination of the electron intensity is beset by troublesome complicating factors. Low energy electrons predominate and as a result the apparent electron intensity is a very sensitive function of the geometric details of the detecting apparatus.

One procedure has been to measure the total ionizing cosmic-ray intensity, and to subtract from this quantity the meson intensity. In this connection, the slow meson intensity and zenith angle distribution have been uncertain, and indirect methods have been used to evaluate that portion of the soft component due to these slow mesons.

Frequently, wide discrepancies have been reported between the observed and predicted intensities. At the time this investigation was started, it was believed that the decay products of a meson at rest were a neutrino and a 50-Mev electron. Under this assumption, it was

* Now at Physics Department and Laboratory for Nuclear Science and Engineering, Massachusetts Institute of Technology, Cambridge, Massachusetts. The work was done in partial fulfillment of the requirements for a Ph.D. at Cornell University.
[1] Bernardini, Cacciapuoti, and Querzoli, Phys. Rev. **73**, 328, 335 (1948).
[2] K. Greisen, Phys. Rev. **63**, 326 (1943).
[3] B. Rossi, Rev. Mod. Phys. **21**, 104 (1949).

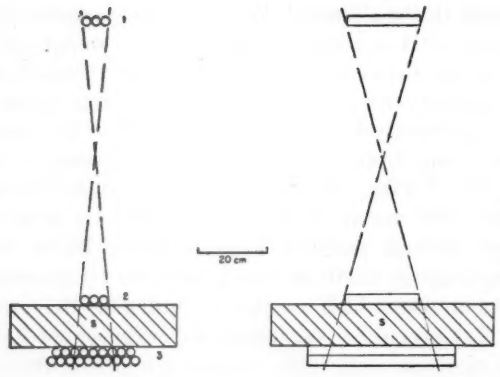

FIG. 1. Telescope geometry for experiment I: Absolute vertical intensity of mesons having a range greater than 80 g cm^{-2} of air equivalent.

difficult to understand the frequent result that there were *fewer* electrons than should arise from meson processes alone. Further, the zenith angle and altitude dependence of electrons near sea level is stronger than that of the mesons, implying that there are additional sources contributing significantly to the sea level electron intensity. It therefore seemed desirable to reexamine the problem. Mr. E. D. Palmatier of Cornell has made a careful measurement of the total cosmic-ray intensity using thin-wall aluminum Geiger counters. These results will be reported by him in a later paper. The present measurements bearing on this subject have been concerned largely with the slow meson intensity. The method of delayed coincidences has been used to study the shape of the low energy end of the meson spectrum, and the zenith angle distribution of these slow mesons. Because of the complicated geometry and uncertainty in the range of the decay electron, it was not possible to obtain accurate absolute intensities from this experiment alone. The measurements were therefore normalized to coincidence and anti-coincidence measurements of the differential intensity. Different experimenters have found widely varying values for the differential intensity of mesons, and it is believed that most of the difficulty has been due to scattering. Particular attention has been focused on this source of error, and the results of three independent measurements are shown to be in agreement.

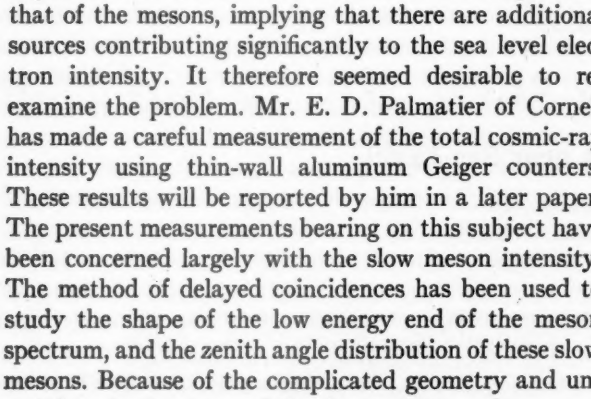

FIG. 2. Telescope geometry for experiment II: Anti-coincidence measurement of the number of mesons in a given range interval.

These experiments complete those intended to aid in evaluating the sea level electron component. Other experiments designed to study certain aspects of the meson component as such were performed at Echo Lake, Colorado. At this altitude (3240 meters) the differential range spectrum and zenith angle distribution of slow mesons have been measured. Some of our data have permitted a rough estimate of the slow proton intensity.

Finally, a short discussion has been devoted to a reevaluation of the sea level electron intensity, using the slow meson information as obtained from these experiments and the total cosmic-ray intensity as measured by Greisen.[2]

II. DESCRIPTION OF EXPERIMENTAL EQUIPMENT AND PRESENTATION OF RESULTS

Several different counter geometries were used in the course of the experiments to be described. Common to all was the use of all-metal Geiger counters of the self-quenching variety with brass walls 0.5 or 0.6 mm thick. The pertinent dimensions are evident from the figures.

The errors reported are standard statistical errors. Where experimental conditions have permitted, the data have been taken so that lack of internal consistency would be evident. In the measurement of the shape of the low energy end of the meson spectrum, and the zenith angle dependence of slow mesons, for instance, the measurements were interlapped, running under one condition for about two days at a time, where the total running time for a given condition was 10 or 12 days. The internal consistency was satisfactory in all cases except one, which will be pointed out.

The integrated intensities J that are reported refer to the number of particles crossing a sphere of unit cross-sectional area.

A. Experiment I. Absolute Vertical Intensity of Mesons Having a Range Greater Than 80 g cm^{-2} of Air-Equivalent

The telescope geometry in which threefold coincidences were recorded is shown in Fig. 1. It is to be noticed that the telescope differs from the usual cosmic ray telescope in that there is no absorbing material between the counters which define the solid angle. This has a twofold purpose. In the first place, the presence of a dense material near a counter has the effect of increasing the effective area of the counter, in that some 7 percent of the mesons emerging from thick layers of a dense material, such as lead, are accompanied by electrons of energy greater than 2 Mev. Hence an incident meson not in the solid angle defined by the telescope may cause a count to be recorded through the effect of its knock-on electrons, and the absolute rate tends to be over estimated. Secondly, in a material of high atomic number, the scattering even of reasonably fast mesons is a large effect. If lead is between the counters

of a telescope, the effective solid angle is in general distorted in a complicated way. Some of the mesons originally in the solid angle are scattered out, while some originally out of the solid angle are scattered in. In the special case of a most simple telescope, one counter tray above and one below the lead, this effect can be shown to cancel in very good approximation. In more complicated geometries, involving three or more separated counters, this cancellation is destroyed.

The third coincidence tray was covered with lead in such a way that the recording of threefold coincidences due to incident electron showers should be very rare.

In an experiment such as this where there is a tray containing a large number of counters there is always an uncertainty about the efficiency of the tray. This is especially serious when the counters are connected in parallel since then the pulse heights are reduced by the extra capacity introduced by the other counters in the tray, and further, the voltage on the other counters is reduced when one or more counters are discharged. A clamp circuit was therefore devised that prevented coincidences from being recorded for a 400-microsecond interval following any detectable pulse from tray 3. In this way a larger inefficiency has been introduced, but it can be evaluated with an accuracy limited only by how well the length of the 400-microsecond interval and pulse rate from the tray in question can be measured.

The threefold coincidence rate, corrected only for the intentionally introduced inefficiency of tray 3 (0.74 percent), was 1.865 ± 0.010 min.$^{-1}$. The geometric factors for converting this rate to units of absolute intensity have been obtained from expressions deduced by Greisen,[4] and our result for the absolute vertical intensity is $I_v(R)=(0.880\pm0.005)\times10^{-2}$ cm^{-2} sterad^{-1} sec.$^{-1}$. Our result is very insensitive to the exact value of R, the minimum range set for mesons by the apparatus. As is shown in subsequent sections, about 0.04 percent of the meson component is stopped per g cm^{-2} of lead. It is clear that no large errors are involved in taking R as just the measured thickness of absorbing material, equivalent here to 138 g cm^{-2} of lead or 80 g cm^{-2} of air-equivalent.

It is possible that the 12 days during which this experiment was being run were non-typical, because of barometric fluctuations, etc. This question can be at least partially answered by considering some data obtained by E. D. Palmatier, who had a twofold coincidence wide-angle telescope operating continuously in Ithaca during the months of April and May, 1948. The average rate of this equipment during the 12-day period was 168.2 counts per minute, whereas for the two month period the average was 169.8 counts per minute. The correlation with barometric pressure was excellent. It therefore seems reasonable that the present value of I_v be increased in the ratio 169.8/168.2, giving $I_v(R)=(0.887\pm0.005)\times10^{-2}$ cm^{-2} sterad^{-1} sec.$^{-1}$. Since the observed zenith angle dependence of these mesons is $\cos^{2.09}\theta$ just multiplying by $2\pi/3.09$ gives $J(R)$, the number crossing a sphere of 1 cm^2 cross-sectional area per second. Hence $J(R)=(1.801\pm0.011)\times10^{-2}$ cm^{-2} sec.$^{-1}$.

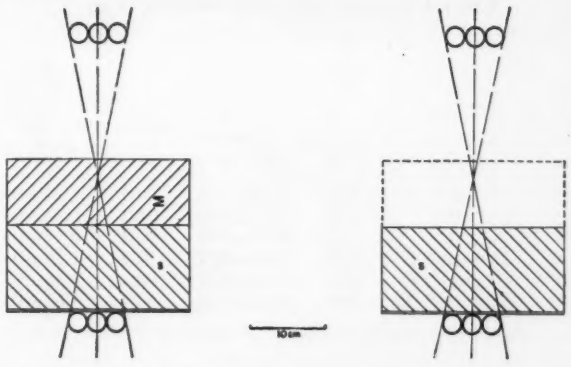

FIG. 3. Telescope geometry for experiment III: Coincidence measurement of the number of mesons in a given range interval.

It should be pointed out that only five of the six counters defining the solid angle were measured for effective length. The sixth one failed in the course of another experiment before the lengths of the counters were measured. The maximum variation among the effective lengths of the five counters was $\frac{1}{4}''$, and if the sixth one was not outside these limits, our results can not be affected by more than 0.5 percent by assuming its length to be the average of the others. We estimate that the telescope dimensions were measured to an accuracy such that the result could be in error by as much as 0.25 percent from this cause alone. Considering these two sources of error and the statistical uncertainty, we may state the result as $J(R)=(1.801\pm0.014)\times10^{-2}$ cm^{-2} sec.$^{-1}$ averaged over April and May, 1948, at Ithaca (elevation 260 m).

B. Experiment II. Anti-Coincidence Measurement of the Number of Mesons in a Given Range Interval

The number of mesons in a given range interval has frequently been measured by simple absorption curves

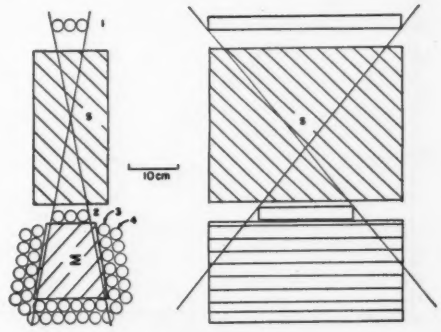

FIG. 4. Telescope geometry for experiments IV and VI: Shape of the low energy end of the meson spectrum and slow meson zenith angle dependence by delayed coincidences.

[4] K. Greisen, Phys. Rev. **61**, 212 (1942).

TABLE I. Delayed coincidence counting rates.

θ	S	Delayed coincidences Total	Rate, hr^{-1}	Accidental rate, hr^{-1}	Rate corrected for accidentals and geometry, hr^{-1}
0°	0	443	1.26±0.06	0.03	1.27±0.06
30°	0	140	0.75±0.06	0.02	0.74±0.06
60°	0	27	0.14±0.03	0.01	0.12±0.03
0°	25 g cm^{-2} C	479	1.52±0.07	0.02	1.54±0.07
0°	50 g cm^{-2} C	419	1.53±0.07	0.01	1.56±0.07
0°	82 g cm^{-2} Al	398	1.63±0.08	0.01	1.67±0.08

(provided enough absorber is used to eliminate electrons) and by anti-coincidence methods. The results by the two methods have usually not been in agreement.

The pitfalls in an anti-coincidence measurement are many and varied. The more striking ones will be taken up one at a time, together with their relative importance in the present geometry, shown in Fig. 2.

First there are "side showers" which we may define as two or more genetically related cosmic-ray particles that may give rise to spurious coincidences. It is customary to obtain a background anti-coincidence rate in experiments of this kind by removing the absorber between the last coincidence tray and the anti-coincidence tray, and to subtract the background from the measured rate with the absorber in place. It is likely, however, that the shower background does not stay the same, since the absorber above the anti-coincidence counters serves to protect them from soft particles. In the present experiment there were two features tending to reduce the number of spurious counts due to side showers. In the first place, coincidence tray 3 was well protected by lead so that only a very energetic electron or a particle traveling horizontally could get at it. Secondly, the anti-coincidence counters presented a large unshielded area, and this area was changed only slightly when the lead Σ was removed. Hence it is unlikely that a shower could cause a threefold coincidence, and even more unlikely that it could cause a threefold coincidence and not have

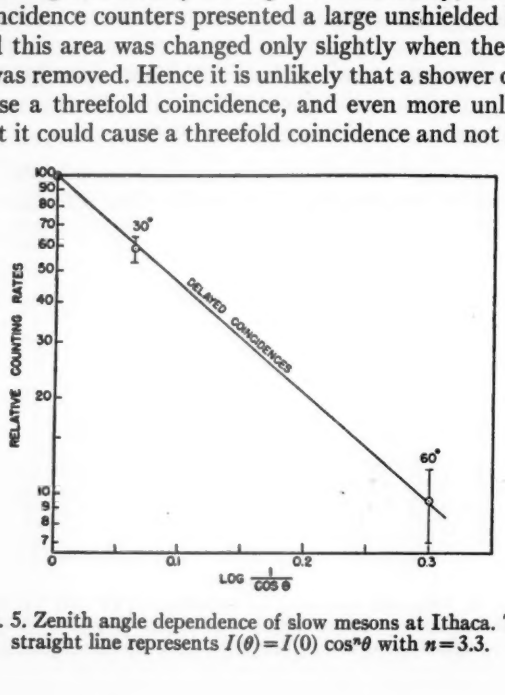

FIG. 5. Zenith angle dependence of slow mesons at Ithaca. The straight line represents $I(\theta)=I(0)\cos^n\theta$ with $n=3.3$.

any of its particles strike the large area presented by the anti-coincidence counters.

Here again, as in simple coincidence measurements, there are unfortunate consequences if one places an absorber between the coincidence counters that define the telescope solid angle. The effective area of the counter below the lead is increased, but not equally so for all mesons. Usually ~100 g cm^{-2} of lead is used above the anti-coincidence counters, so that the maximum momentum that a meson destined to stop in the lead can have in passing through the last coincidence counter is $\sim 2.2\times 10^8$ ev/c. This sets an upper limit on the energy that its knock-on electron can have at 5 Mev, which is about the energy limit set by the counter walls for electrons. Hence the effective area of the counter is increased only for the fast mesons, and it is usually the ratio of number of anti-coincidences to number of coincidences that is of interest. This source of error has been largely eliminated in the present experiment by defining the solid angle with no absorber except the counter walls between the sensitive counter volumes.

A serious source of discrepancy has arisen in the past out of attempts to reduce the anti-coincidence background rate; i.e., the anti-coincidence rate with the lead Σ removed. This rate is usually subtracted directly from the observed anti-coincidence rate with Σ in, and so the natural inclination is to make it as small as possible.

Let us consider some of the sources of this background rate. If we assume that shower effects have been made small there remain: (1) dead time inefficiency of the anti-coincidence tray which may be ~1 percent depending upon the size of the anti-coincidence counters, (2) particles stopping in the counter walls; i.e., real anti-coincidences, (3) large time delays in the anti-coincidence counters, (4) chance anti-coincidences, and (5) insufficient coverage of the meson beam emerging from the telescope array by the anti-coincidence counters. Direct subtraction of the background anti-coincidence rate due to causes (1) through (4) can lead to only small errors in the evaluation of the true number of mesons stopping in a given range interval. It is (5) which we wish to emphasize.

Some of the particles emerging from the last coincidence counters have been badly scattered in the layer of absorber S above them. In fact, as is seen from an expression given by Rossi and Greisen[5] for the mean square angle of emergence, even those mesons that can penetrate halfway down into absorber Σ emerge from S with $\langle\theta^2\rangle^{\frac{1}{2}}\approx 25$ degrees. If, as has usually been the case, the anti-coincidence counters cover little more than the solid angle defined by the telescope array, some of these particles will be recorded as anti-coincidences whether or not Σ is in place. If the resulting high background rate is subtracted from the anti-coincidence rate with Σ in place, the number of particles stopping

[5] B. Rossi and K. Greisen, Rev. Mod. Phys. 13, 240 (1941).

in Σ is underestimated, because the badly scattered particles referred to above have, in general, low energy and would be stopped in Σ.

Since the high background rate is not desirable, it has often been reduced by methods which in effect redefine a solid angle for the particles emerging from the first absorber. This can be done either by judicious placement of a second group of anti-coincidence counters, or by the use of what amounts to a second coincidence telescope. An example of this method of attack is to be found in experiment IV. In either method it is clear that the low energy particles are being discriminated against. It should be pointed out that these methods are perfectly satisfactory for most of the purposes for which the measurements were intended. For instance, meson lifetime measurements have sometimes been concerned with the ratio of two anti-coincidence measurements at different altitudes, or angles with the zenith. In these cases there is only a second-order error involved, due to a possible change in the shape of the incident meson spectrum. Discrepancies arise when experiments using methods such as these are compared in order to arrive at the absolute number of mesons in a given range interval.

The present experiment, it is believed, has avoided a large portion of the discrepancies due to scattering. This was accomplished by placing anti-coincidence counters in positions such that with the lead Σ removed they would be in the path of practically all of the badly scattered mesons emerging from the lead above coincidence tray 3, and at the same time not interfere with the stopping of these particles while Σ is in place.

The threefold coincidence rate was 440 ± 2 hr.$^{-1}$. The background anti-coincidence rate (with Σ removed), corrected only for the small artificial inefficiency, was 2.4 ± 0.2 hr.$^{-1}$, or 0.5 percent of the coincidence rate. (The artificial inefficiency was introduced by a clamp circuit, as in experiment I, which rendered the recording circuit inoperative for a period of 500 microseconds after any pulse from the anti-coincidence tray.) Of this background, about 40 percent is due to residual inefficiency of the anti-coincidence tray, and about 30 percent can be accounted for by mesons stopping in the counter walls. The remainder is probably due to a combination of side showers and scattering, and is too small to affect our results significantly.

The anti-coincidence rate with Σ in place was 20.8 ± 0.4 hr.$^{-1}$, or 4.7 ± 0.1 percent of the coincidence rate. Subtracting the background, and including a geometric factor of 1.02 arising because of the different zenith angle distributions of fast and slow mesons (investigated in experiments IV and V below), we find $(4.26\pm0.10)\times10^{-2}$ for the fraction of the particles in the vertical direction that can penetrate S but not $S+\Sigma$.

The absorber Σ had a vertical thickness of 93.4 g cm^{-2} of lead plus 5 g cm^{-2} of iron, and the total is equivalent to 99.3 g cm^{-2} of lead. The absorber S was equivalent to 131 g cm^{-2} of lead, which includes the 5 g cm^{-2} of iron and the counter walls.

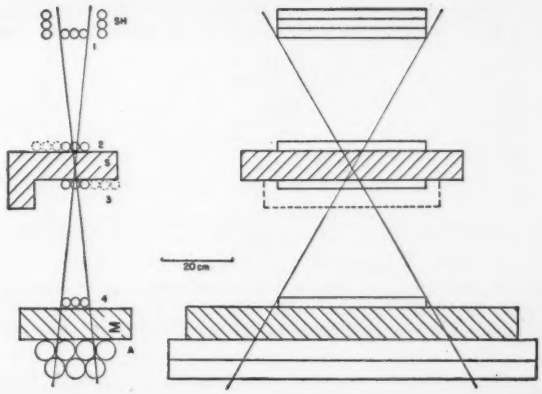

FIG. 6. Telescope geometry for experiment V: Anti-coincidence measurement of the number of mesons in a given range interval as a function of zenith angle.

It is often convenient to have the results in a slightly different form.[6] Of the mesons traveling vertically that can penetrate at least 180 g cm^{-2} of lead (0.044 ± 0.001) percent are stopped per g cm^{-2} of lead.

We prefer not to translate these quantities into other units such as g cm^{-2} of air-equivalent or momentum because there is some question about the effect of multiple scattering in the lead, and that discussion is taken up later.

C. Experiment III. Coincidence Measurement of the Number of Mesons in a Given Range Interval

The measurement of the number of mesons in a given range interval by the coincidence or absorption curve method suffers from one striking disadvantage; namely,

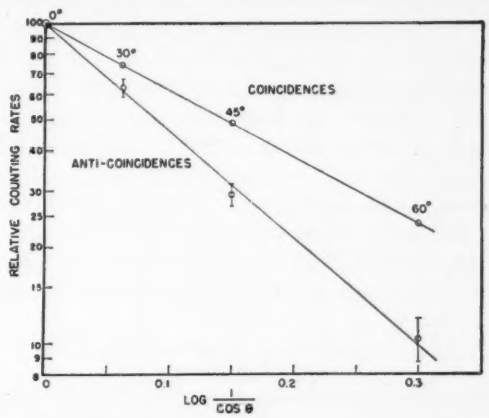

FIG. 7. Zenith angle dependence of mesons with ranges between 94 and 188 g cm^{-2} of lead at Ithaca. The straight lines follow $\cos^n\theta$ with $n=2.09$ and 3.3.

[6] Because the absorbers Σ are often rather thick, it is desirable to define an absorber $S'=S+\frac{1}{2}\Sigma$, and a coincidence rate $N'=N-\frac{1}{2}$ A.C. The fractional number of particles stopped is then A.C. rate/$N'\Sigma$ per g cm^{-2} at a range S'. The extension of this to coincidence measurements is obvious.

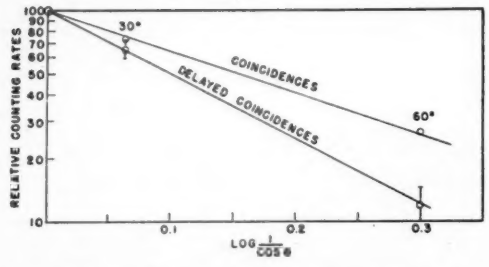

FIG. 8. Zenith angle dependence of mesons able to penetrate 170 g cm^{-2} of lead but not an additional 25 g cm^{-2} of carbon at Echo Lake. The straight lines follow $\cos^n\theta$ with $n=2.0$ and 3.1.

it is required to find the slope of the absorption curve, which inherently involves being concerned with a small difference between two or more relatively large counting rates measured independently. Small changes in the experimental conditions such as would result in 1 percent changes in counting rates introduce 25 percent errors or more in the quantity being measured. The rates for two different thicknesses of absorber cannot be measured at the same time on the same piece of equipment, so that fluctuations in the barometric pressure introduce errors, unless such effects are carefully taken into account. On the other hand, the method as we have used it has some rather striking advantages, in that most of the spurious effects with which we were concerned in the anti-coincidence method cancel, and so leave the measured result in a form not subject to much question.

Consider the effect of side showers. In a simple coincidence experiment such as that used and shown in Fig. 3, the vulnerability of the counters to side showers is virtually unchanged when an additional absorber is placed between the counters. Hence when the rates are subtracted the same number of spurious side showers is included in both rates, and the difference is unaffected.

The effect of the scattering of mesons in the lead absorbers can be shown to be small by the following considerations. If the mesons incident upon the apparatus are isotropic, the scattering into and out of the telescope solid angle cancel, so that the measured coincidence rate is in very good approximation equal to the number of mesons incident in the telescope solid angle, with a minimum range as determined by the absorber thickness. This cancelation is only slightly disturbed by a $\cos^3\theta$ zenith angle distribution. Further, however, the differential range spectrum of mesons is essentially flat (see Fig. 10) so that for different absorbers whatever scattering errors there may be are the same with both thicknesses, and so the errors cancel in the difference of the counting rates.

TABLE II. Portions of the data bearing on the meson range spectrum.

	$\Sigma=8.3$ g cm^{-2} of carbon		$\Sigma=57.5$ g cm^{-2} of lead	
S	D.E. Rate, hr^{-1}	A.C. Rate, min^{-1}	D.E. Rate, hr^{-1}	A.C. Rate, min^{-1}
0	7.1 ±0.4			
8″ Pb	6.1 ±0.4	1.31±0.04	1.96±0.15	5.34±0.05
20½″ Pb	4.2 ±0.4	0.64±0.09	1.44±0.22	2.99±0.05
Ratio $\frac{8''\text{ Pb}}{20\frac{1}{2}''\text{ Pb}}$	1.45±0.17	2.04±0.29	1.36±0.23	1.78±0.03

A certain fraction of the mesons emerging from an absorber is accompanied by electrons, and some of these electrons may pass through one of the bottom counters, while the meson does not. The resulting coincidence is of course indistinguishable from a meson passing through the telescope in the normal fashion. These knock-on electrons are in equilibrium with the meson beam, however, and once again the effect cancels in the subtraction of the rates.

In order to minimize the effect of barometric fluctuations, the experiment was run using two identical pieces of apparatus, operating side by side. The absorber was shifted from one telescope to the other every day for 22 days.

Corrected for chance coincidences, the fractional absorption in Σ was $(4.19\pm0.39)\times10^{-2}$ from the data of one telescope and $(3.55\pm0.40)\times10^{-2}$ from the other. Assuming the difference between the absorption as deduced from the two telescopes has arisen from non-canceling barometric fluctuations and statistical fluctuations, we may consider the two values to be of equal validity, and take the average. By doing this we get $(3.87\pm0.28)\times10^{-2}$ for the fractional absorption. The absorber Σ in this experiment was 93.4 g cm^{-2} of lead, and S was equivalent to 131 g cm^{-2} of lead. The solid angle as defined by this experiment was the same as that in experiment II, and the appropriate geometric factor for correction to the zenith direction is the same, 1.02. Our result then is that of the mesons traveling vertically that can penetrate at least 178 g cm^{-2} of lead, (0.042 ±0.003) percent are stopped per g cm^{-2} of lead.

D. Experiment IV. Shape of the Low Energy End of the Meson Spectrum and Slow Meson Zenith Angle Dependence by the Method of Delayed Coincidences

The preceding three experiments have been concerned with mesons with ranges greater than some 130 g cm^{-2} of lead. Smaller thicknesses of lead permit an increasing number of electrons to get through, but the method of delayed coincidences serves very effectively to separate the mesons from the electrons. The telescope geometry is shown in Fig. 4. The absorber Σ was composed of graphite.

The following type of event was recorded as a delayed coincidence: a coincidence 1, 2 at time $t=0$, accompanied by no count from trays 3 or 4 from $t=-15$ microseconds to $t=1$ microsecond, but followed by a coincidence between trays 3 and 4 in the interval $t=1$ to $t=7$ microseconds. This 6-microsecond interval was split into three channels, 1 to 3, 3 to 5, and 5 to 7 microseconds, and a comparison of the number of counts

in the three channels served as a check on the operation of the equipment, since the mean life of the meson is known to be about 2.2 microseconds. The delay discriminator was similar to that of Sands.[7]

The pertinent results are given in Table I. The geometric correction was necessary because of the finite resolution of the telescope. Corrected for accidentals, the distribution of delayed events in the three channels 1–3, 3–5, and 5–7 microseconds was 1194, 516, and 196 respectively. For a 2.15-microsecond lifetime the ratio between adjacent channels should be 2.5 and is seen to be 2.3±0.1 and 2.6±0.2.

The geometry of the decay electron counter trays did not lend itself to an accurate determination of the absolute detection efficiency, hence these are relative measurements, and require normalization. The largest thickness of absorber used, 82 g cm^{-2} of aluminum, is in the range accessible to anti-coincidence measurements, and the normalization may be made at this point.

Figure 5 shows the observed zenith angle dependence of the lowest momentum group of mesons measured, those that could penetrate the counter walls of the telescope, but not the counter walls plus 25 g cm^{-2} of carbon plus one of the counter walls comprising tray 3. Of course, the exact distribution could hardly be expected to follow so simple a function as $\cos^{3.3}\theta$, but this function gives a good empirical fit within the accuracy of the data.

E. Experiment V. Anti-Coincidence Measurement of the Number of Mesons in a Given Range Interval as a Function of Zenith Angle

The geometry for experiment V is shown in Fig. 6. Anti-coincidences (1, 2, 3, 4)—SH and anti-coincidences (1, 2, 3, 4)—SH—A were recorded.

The lead above and to the side of coincidence tray 3 and the anti-coincidence counters near tray 1 served to keep the effects of side showers very small. The absorbers S and Σ each had a thickness of 93.4 g cm^{-2} of lead, plus the counter walls.

It will be noticed that counter trays 3 and 4 serve to redefine a solid angle for mesons emerging from S. This does not affect the detection of fast mesons, but definitely discriminates against the slower mesons which tend to be scattered in passing through S. The measurement is therefore unsatisfactory for determining the absolute intensity of mesons in a given range interval, but should be satisfactory for measuring the relative number of mesons in a given range interval as a function of zenith angle. In principle, scattering could influence even this relative measurement if the shape of the incident meson spectrum were very different at different angles with the zenith, but the present experiments have shown that the shape of the spectrum is not a sensitive function of the zenith angle.

[7] M. Sands, M.I.T. thesis (1948).

TABLE III.

Σ	Anti-coincidence rate, hr^{-1}	Decay electron rate, hr^{-1}
40.0 g cm^{-2} Fe	281±4	3.45±0.28
57.5 g cm^{-2} Pb	320±3	1.96±0.15
8.3 g cm^{-2} C	78±2	6.15±0.40

Because the extreme counters of the telescope were separated by a distance large compared to the width of the telescope trays, there are no geometric corrections large enough to apply here. In order to be certain that the influence of side showers was not large, trays 2 and 3 of the telescope were displaced as shown in Fig. 6. This, it was assumed, did not change the vulnerability of the equipment to side showers, and made it most improbable for a single particle to go through the necessary counters and be recorded. Under these conditions the anti-coincidence rates were in all cases less than the statistical errors in the results with the counters in line. Further, at least some of these events were subtracted with the background, obtained with Σ removed, and therefore no special correction for side showers has been made.

The present experiment provides a good example of the sort of scattering difficulties one may encounter in such an anti-coincidence measurement. Absorber Σ here was about the same as the corresponding absorbers in experiments II and III, and the number of anti-coincidences was only 2.35 percent of the number of coincidences, as compared to 4 percent in the other experiments.

Figure 7 shows the coincidence and anti-coincidence rates as a function of $1/\cos\theta$, plotted on a log-log scale. Both measurements are seen to be well expressed by $\cos^n\theta$, with $n=2.09$ for the integral or coincidence data, in general agreement with many other measurements, and $n=3.3$ for the anti-coincidences, the same exponent found in the measurement of the lowest momentum group of experiment IV.

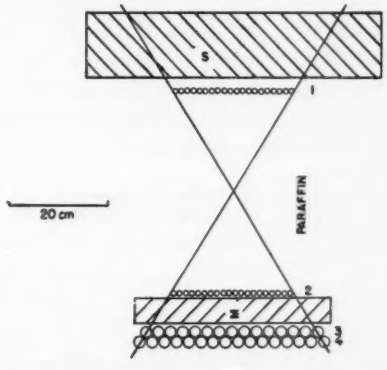

FIG. 9. Telescope geometry for experiments VII and VIII: Anti-coincidence and delayed coincidence measurements at Echo Lake and at Ithaca.

TABLE IV. Comparison of the data taken at Echo Lake and at Ithaca.

	$\Sigma=8.3$ g cm^{-2} carbon		$\Sigma=40$ g cm^{-2} iron	
	D.E., hr^{-1}	A.C., min^{-1}	D.E., hr^{-1}	A.C., min^{-1}
Ithaca $S=158$ g cm^{-2} of Pb	2.4±0.2	0.417±0.015	1.38±0.11	1.55±0.02
Echo Lake $S=230$ g cm^{-2} (8″) of Pb	6.1±0.4	1.31 ±0.04	3.45±0.28	4.68±0.06
Ratio, Echo Lake/Ithaca	2.6±0.2	3.14 ±0.15	2.5 ±0.3	3.02±0.06

F. Experiment VI. Measurement of the Number of Mesons in a Given Range Interval as a Function of Zenith Angle at Echo Lake, by the Method of Delayed Coincidences

The experiment used the same telescope and detecting equipment as were used for experiment IV. The absorber S was 170 g cm^{-2} of lead, and the data were taken at Echo Lake, Colorado.

The distribution of delayed events in the three channels 1–3, 3–5, 5–7 microseconds was 267, 104, and 45, respectively, and if the expected numbers of accidentals are subtracted, we get 262, 99, and 40. The expected ratio between the number of counts in adjacent channels is about 2.5 for an assumed meson lifetime of 2.15 microseconds, and the above data are consistent with this.

The data normalized to 100 for $\theta=0$ have been plotted in Fig. 8. The zenith angle distributions of both the coincidence counting rate and delayed counting rate are seen to be practically the same as those of the corresponding quantities at Ithaca.

Since the telescope geometry was the same as that used in experiment IV at Ithaca, the relative rates of both coincidences and delayed coincidences can be compared at the two altitudes. Making a small correction for the difference in the absorbers S as used at the two places (118 g cm^{-2} of lead-equivalent at Ithaca, 170 g cm^{-2} at Echo Lake) we find for the integral intensity, I_v (170 g cm^{-2} Pb) at Echo Lake/I_v (170 g cm^{-2} Pb) at Ithaca$=1.71\pm0.02$. For the slow mesons, there is no appreciable correction due to the change in the absorbers, and we find for the differential intensity, i_v at Echo Lake/i_v at Ithaca$=2.0\pm0.2$.

TABLE V. Comparison of number of mesons in a given range as given by three different experiments.

Experiment	S' in g cm^{-2} of Pb	Σ	% stopped per g cm^{-2} of Σ	% stopped per g cm^{-2} of Pb corrected for multiple scattering
II, Anti-coincidence	180	Pb	0.044±0.0010	0.040±0.0010
III, Coincidence	180	Pb	0.042±0.003	0.038±0.003
VIII, Anti-coincidence	184	Fe	0.060±0.003	0.041±0.002

G. Experiment VII. Measurement of the Differential Range Spectrum of Mesons by the Method of Delayed Coincidences at Echo Lake

This was actually a part of another experiment (performed in collaboration with V. T. Cocconi) designed to investigate the neutrons associated with the stopping of mesons in various materials. Figure 9 shows the geometry of the experiment pertinent to this discussion.

The events recorded were coincidences 1, 2; anti-coincidences (1, 2)—(3 or 4); and delayed coincidences (1, 2), (3, 4). The detecting equipment was the same as used in experiments IV and VI, except for the addition of an anti-coincidence circuit similar to that used in experiment II.

It will be noticed from Fig. 9 that in this experiment the solid angle has been defined after the particles have passed through the first absorber, S. Scattering in S will not affect the detection of the fast mesons. For the slower mesons, the scattering should have the effect of making the angular distribution below the absorber more nearly isotropic than it was above it. An evaluation of the vertical intensity of mesons stopping in Σ requires a knowledge of their angular distribution incident upon the telescope, but the dependence of the result upon this angular distribution is slight. In treating the data we have assumed that the angular distribution of the slow mesons is one power of $\cos\theta$ greater than that of the fast mesons, as indicated approximately by the zenith angle experiments IV, V, and VI.

A possible source of error in this experiment is the effect of knock-on electrons. Imagine a fast meson incident upon the absorber S, passing through counter tray 1 but missing tray 2. It may be accompanied by a secondary electron that passes through tray 2 but stops in the absorber Σ and so causes an anti-coincidence, indistinguishable from one caused by a meson stopping in Σ. Because of the low mean energy of the secondary electrons, those that strike tray 2 must be produced mostly in the paraffin above tray 2 and can never emerge from the paraffin far from the trajectory of the meson. Therefore such an event occurs only for a small fraction of the mesons that traverse tray 1 and pass near tray 2 without striking it. From reported experimental determinations of the magnitude of similar effects[2,8] we estimate that our anti-coincidence rates in this experiment may be 5 or 10 percent too high. There are no errors arising from this effect in the delayed coincidence measurements, and only second-order errors in the comparison of anti-coincidence measurements at different altitudes or with different absorbers in positions S and Σ.

Experiments VII and VIII were run using the same apparatus. The portions of the data bearing on the meson range spectrum at Echo Lake are given in

[8] C. Milone and V. Tongiorgi, Phys. Rev. **72**, 735 (1947).

Table II. Accidental coincidences and anti-coincidence background rates have been subtracted.

One point regarding the reliability of the data should be mentioned. In considering the distribution of delayed events in the three timing channels, 1–3, 3–5, and 5–7 microseconds, we find 625, 232, and 123 counts, respectively, corrected for accidentals. The ratio of the number of counts between adjacent channels should be 2.5, and is seen to be 2.69 ± 0.21 and 1.89 ± 0.21, the latter rather far outside the standard error. Similar data, not pertinent to the present discussion but taken under the same conditions, showed the same tendency with more statistical accuracy. This was of concern, and the apparatus was tested thoroughly many times in attempts to find some reason. Perhaps the most convincing checks were the following: random pulses from large trays of counters were fed into the circuits in such a way that there were a large number of accidental delayed counts, and no real ones. The distribution of accidental counts in the three channels was 527, 562, and 538 counts whereas the expected number for channels of 2 microseconds width was 536 per channel. As a further test, tray 2 was placed under trays 3 and 4, so that any particle passing through trays 1 and 2 must have passed through trays 3 and 4 also. In this condition no delayed counts were observed in 22 hours. It must be stated frankly that the reason for the distribution observed is not understood. In the other experiments IV, VI, and VIII, in which the same delay discriminator was used, the distribution of counts in the three channels was quite normal.

By comparing the ratios of the rates with 8 inches of lead to those with 20.5 inches of lead, it is seen that the two delayed coincidence measurements are in agreement with each other, as are the two anti-coincidence measurements. The delayed coincidence measurements are not in good agreement with the anti-coincidence measurements, however, and they should be, under the hypothesis that both represent only mesons. The reasons for the disagreement are not certain, but the effect is in a direction which would support the hypothesis that there are significant numbers of slow protons at Echo Lake, with rapidly increasing numbers under smaller thicknesses of absorber.

To a fairly good approximation, the mesons emerging from a slab of lead some 200 g cm^{-2} thick are distributed rather uniformly in range, at least for ranges up to an additional 60 g cm^{-2} of lead. This permits us to interpret the anti-coincidence data from experiments VII and VIII, in terms of the relative efficiency of lead and iron per g cm^{-2} for removing or absorbing mesons from the beam. While there are certainly some particles other than mesons capable of penetrating the 8 inches of lead used in this experiment, they are a small fraction of the total, and further the dependence of the ionization losses upon the atomic number is not at all a sensitive function of the mass of the particle in question.

The necessary data are included in Table III. All

TABLE VI.

A. At Ithaca
I_v (80 g cm^{-2} air) $=(0.887\pm0.005)\times10^{-2}$ cm^{-2} sterad^{-1} sec.$^{-1}$
J (80 g cm^{-2} air) $=(1.801\pm0.011)\times10^{-2}$ cm^{-2} sec.$^{-1}$
i_v (105 g cm^{-2} air) $=(6.0\pm0.15)\times10^{-6}$ sterad^{-1} g^{-1} sec.$^{-1}$
j (105 g cm^{-2} air) $=(8.7\pm0.2)\times10^{-6}$ g^{-1} sec.$^{-1}$
$I_\theta(R)=I_v(R)\cos^{2.09}\theta$ $\quad(R=60$ g cm^{-2} air$)$
$i_\theta(R)=i_v(R)\cos^{3.3}\theta$ $\quad(R=90$ g cm^{-2} air$)$
$i_\theta(R)=i_v(R)\cos^{3.3}\theta$ $\quad(R=15$ g cm^{-2} air$)$
B. At Sea Level
I_v (80 g cm^{-2} air) $=0.845\times10^{-2}$ cm^{-2} sterad^{-1} sec.$^{-1}$
J (80 g cm^{-2} air) $=1.71\times10^{-2}$ cm^{-2} sec.$^{-1}$
i_v (105 g cm^{-2} air) $=5.5\times10^{-6}$ sterad^{-1} g^{-1} sec.$^{-1}$
j (105 g cm^{-2} air) $=8.0\times10^{-6}$ g^{-1} sec.$^{-1}$

were taken under an absorber S consisting of 8 inches (230 g cm^{-2}) of lead.

Let us first note that for ionization losses alone, on the basis of the calculations of Wick,[9] 40 g cm^{-2} of iron are equivalent to 57.5 g cm^{-2} of lead, where g cm^{-2} means distance as measured along the path of the particle. Hence it might first be expected that the anti-coincidence rates should be equal, while in fact they are in the ratio $\mathrm{Pb/Fe}=1.14\pm0.02$.

Now the decay electrons emitted by mesons stopping in the absorbers must certainly have an effect of the above ratio. The operation of the circuits was such that after a twofold coincidence, any pulse in either of trays 3 or 4 up to 8 microseconds later was recorded as a particle passing all the way through the absorber. For a decay electron to be recorded, it was required to pass through both trays 3 and 4, during a 6-microsecond interval starting at 1 microsecond. If the decay electron rates are increased so as to include those decay electrons emitted from 0 to 1 and from 7 to 8 microseconds, we get 5.7 hr^{-1} and 3.2 hr^{-1} for the iron and lead respectively (and 10.2 hr^{-1} for the carbon). The anti-coincidence rates must be increased by at least this much. But then the question arises as to how many decay electrons pass through either one of trays 3 or 4 but do not pass through both of these trays. In order to bring the anti-coincidence results into agreement it would be necessary to assume that 16 times as many decay electrons pass through either tray 3 or 4 as pass through trays 3 and 4. This is an improbably large factor, and indeed would have the effect of increasing the detection efficiency for the decay electrons in carbon to a value considerably above unity, even disregarding a factor ~2.5 due to the comparatively small solid angle covered by the decay electron trays.[10]

So far, the effect of multiple Coulomb scattering in the absorbers has been neglected. Koenig[11] has treated

[9] G. Wick, Nuovo Cimento **1**, 302 (1943).

[10] We have neglected here the possibility that the decay electrons emerging from the carbon have a higher average energy than those emerging from the iron and lead. This is undoubtedly the case since the vertical thickness of the carbon is less than the expected range of the decay electron. The basic argument is, however, unchanged.

[11] H. Koenig, Phys. Rev. **69**, 590 (1946).

TABLE VII.

Author	S	Stopping material	Percent absorption per g cm^{-2} of air-equivalent at 100 g cm^{-2} of air-equivalent (sea level).
	Anti-coincidence measurements		
Koenig[11]	160 g cm^{-2} Pb	Pb	0.057±0.002
	160 g cm^{-2} Pb	Fe	0.051±0.002
	160 g cm^{-2} Pb	Al	0.049±0.004
	160 g cm^{-2} Pb	H_2O	0.047±0.002
Addario and Cocconi[12]	310 g cm^{-2} Pb	Pb	0.046±0.002
	113 g cm^{-2} Pb + 105 g cm^{-2} H_2O	Pb	0.052±0.002
Sands[7]	167 g cm^{-2} Pb	C	0.045
Exp. II	125 g cm^{-2} Pb	Pb	0.066±0.002
Exp. VIII	158 g cm^{-2} Pb	Fe	0.068±0.002
	Coincidence measurements		
Nielson, *et al*[13]		Pb	0.082±0.008
Rossi, *et al*[14]	187 g cm^{-2} Pb	C	0.058±0.008
	144 g cm^{-2} Pb	Pb	0.057±0.008
Sands[7]	167 g cm^{-2} Pb	Pb	0.063
Exp. III	125 g cm^{-2} Pb	Pb	0.064±0.004

this problem on the basis of the scattering theory of Williams, and finds that to a good approximation the vertical thickness of anti-coincidence absorbers should be increased by the following factors: lead 1/0.907, iron 1/0.975, aluminum 1/0.986. We have repeated Koenig's calculation for lead absorbers from 50 to 180 g cm^{-2} thick and find that the correction is, to a very good approximation, linear. If the iron and lead absorbers used here are increased in accordance with the above factors we find they are equivalent to 41 g cm^{-2} of iron and 63.5 g cm^{-2} of lead.

Turning again to Wick's range-momenta data we find that 41 g cm^{-2} of iron are equivalent to 58 g cm^{-2} of lead, so that we would expect the anti-coincidence rates to be in the ratio 58:63.5 or 1:1.095, assuming the effect of the decay electrons to have been evaluated accurately. Now to bring the observed data into agreement we find that the number of decay electrons passing through trays 3 or 4 must be 4±2 times the number passing through 3 and 4, a much more acceptable factor. This argument simply serves to show that Koenig's multiple scattering factors are reasonable, and we propose to use them further in the section below.

H. Experiment VIII. Second Anti-Coincidence Measurement of the Number of Mesons in a Given Range Interval at Ithaca

This experiment is the same as experiment VII, except that it was run at Ithaca, and the data are not as complete. It serves as an independent check on the number of mesons in a given range interval, and permits an evaluation of the increase in the number of mesons at Echo Lake over those at Ithaca.

In Table IV are listed the Ithaca data, together with the Echo Lake data suitable for comparison. Because the differential range curve is so mild a function of the range, there is very little error in comparing differential measurements under slightly different thicknesses of absorber at the two altitudes.

As seen from the table, the anti-coincidence measurements are in agreement in the sense that both the iron and carbon data increased by compatible factors in going from Ithaca to Echo Lake. The decay electron measurements are in similar internal agreement,[15] but the decay electron and anti-coincidence data differ from each other, the decay electron events increasing by a smaller factor than the anti-coincidences. This is in the same direction as the similar effect noted in comparing the Echo Lake data under different thicknesses of absorber—there seem to be too many anti-coincidences (or too few delayed coincidences) at Echo Lake under the 230 g cm^{-2} of lead absorber. It should be noted however, that these observations are not independent in the case of carbon, the same data (Echo Lake, 8.3 g cm^{-2} of carbon under 230 g cm^{-2} of lead) having entered both considerations. Some further discussion of this disagreement is to be found in Section III B where the Echo Lake measurements are considered in more detail.

This experiment permits another evaluation of the number of mesons in a given range interval at Ithaca. In the preceding section a comparison was made of the number of particles stopping in iron and lead at Echo Lake, the telescope geometry being the same as was used here. It was found that the results were in agreement with the known ionization losses in these materials provided multiple scattering and a reasonable assumption about the effect of the decay electrons were taken into account. We have taken these factors into account in treating the data obtained at Ithaca, and find the fractional absorption at 184 g cm^{-2} of lead to be $(0.041\pm0.002)\times10^{-2}$ per g cm^{-2} of lead.

I. Summary of Intensity Measurements

In this section a comparison will be made of the present experimental evaluations of some of the quantities measured in more than one way. Where possible a best value will be selected and used in the subsequent discussions.

[12] M. Addario and G. Cocconi, Nuovo Cimento 4, 1 (1947).
[13] Nielson, Ryerson, Nordheim, and Morgan, Phys. Rev. 59, 547 (1941).
[14] Rossi, Hilberry, and Hoag, Phys. Rev. 57, 461 (1940).

[15] Negative μ-mesons decay in carbon, but are captured in iron. Negative π-mesons are believed to be captured in both iron and carbon. Positive π- or μ-mesons decay in iron and carbon. Now positive π-mesons could conceivably contribute to our delayed coincidence counting rates by stopping in our absorbers and decaying into a μ-meson which promptly decays into an electron. However, our delayed coincidence rates increased for carbon and for iron absorbers by equal factors in going from Ithaca to Echo Lake. Either the relative number of π- and μ-mesons is the same at the two altitudes, (which is most unlikely) or the number of π-mesons at Echo Lake is such that our rates are not affected appreciably. We shall assume the latter.

Three measurements have been made of the number of mesons in a given range interval at Ithaca. They are given in Table V in a form suitable for comparison.

These are seen to be in satisfactory agreement. Two things about experiment VIII should be recalled. First, the agreement between absorption in iron and lead has essentially been forced, though on a reasonable basis, at Echo Lake. Hence the agreement of experiment VIII with the others at sea level should not be interpreted as an indication of the validity of the assumed relative ionization losses of mesons in iron and lead. Rather, it bears only on the evaluation of the number of mesons in a given range interval at Ithaca. Secondly, we have remarked that there may be some spurious effects attributable to knock-on electrons contributing to this anti-coincidence measurement. We have proceeded believing the effect to be small, but must regard this measurement with less confidence than the others.

The result of experiment II will be adopted as the "best result" for further use, because its sfatistical error is smaller than the others and the method is believed to be sound.

It remains to convert this result into suitable units of absolute intensity. Our absorber S' was 180 g cm^{-2} of lead, and this is equivalent to 105 g cm^{-2} of air. Under the conditions of our experiment, (dense) air is 1.73 times as effective as lead for stopping mesons. Hence of the mesons that can penetrate 105 g cm^{-2} of (dense) air, (0.069 ± 0.002) percent are stopped per g cm^{-2} of air. Now the result of experiment I may be corrected from 80 to 105 g cm^{-2} of air, $(25\times0.069=1.7$ percent correction), to give us the absolute vertical intensity at this range, and we find I_v(105 g cm^{-2} of air) $=(0.872\pm0.005)\times10^{-2}$ cm^{-2} sterad^{-1} sec.$^{-1}$. The differential vertical intensity is then $(6.0\pm0.15)\times10^{-6}$ sterad^{-1} g^{-1} sec.$^{-1}$, at 105 g cm^{-2} of air-equivalent. (In all cases, absorber thicknesses are measured along the actual path of the particle.)

Some of the useful results are tabulated in Table VI, where the errors are the standard statistical errors, not including estimates of the systematic errors, which are believed to be smaller than the statistical uncertainties.

The intensity measurements may be corrected to sea level by an extrapolation of our data on the altitude variation, and some data recently compiled by Rossi.[16] For slow mesons, $i_v(R)$ at 1007 g cm^{-2}/$i_v(R)$ at 1035 g cm^{-2} $=1.09$. The corresponding factor for the hard component is 1.05.

III. COMPARISON WITH OTHER MEASUREMENTS AND CALCULATIONS

A. Measurements at Ithaca

So far as we know, the only other measurement of the absolute integrated intensity of the hard component suitable for comparison with the present result is that of Greisen.[2] Here the minimum range set by the apparatus was 71 g cm^{-2} air-equivalent (of lead). Our present result has been corrected to this range, using the differential intensity of mesons as found in experiment II.

Greisen: J(71 g cm^{-2} of air) $=(1.803\pm0.012)\times10^{-2}$ cm^{-2} sec.$^{-1}$.

Experiment I: J(71 g cm^{-2} of air) $=(1.806\pm0.014)\times10^{-2}$ cm^{-2} sec.$^{-1}$.

The agreement is seen to be excellent. Both measurements were made at Ithaca (1007 g cm^{-2}).

Ithaca is appreciably above sea level (260 meters) and the present experiments cannot fairly be compared with others without taking this into account. As stated previously, our results may be transformed to sea level intensities by decreasing the hard component by 1/1.05, and decreasing the slow meson intensity by 1/1.09.

First let us consider the experiments measuring the percentage of particles stopped per g cm^{-2} of absorber. Different experimenters have stopped the mesons in different materials, so it is convenient to refer the measurements to g cm^{-2} of air, taking the multiple scattering into account in each case. The zenith angle dependence of the stopped mesons has been taken as one power of $\cos\theta$ greater than that of the hard component. It has been assumed that 113 g cm^{-2} of lead (19 radiation lengths) reduces the number of electrons detected to a negligible amount.

The actual absorber S was in general different for each experiment listed in Table VII. The percentage of stopped particles has been corrected so that the different results can be compared at 100 g cm^{-2} of air-equivalent. In doing this, the differential range spectrum has been assumed to be flat, and only the hard component as measured by the apparatus has been adjusted.

It is seen that the coincidence measurements tend to give results higher than the anti-coincidence measurements (except in the case of the present measurements), in agreement with the hypothesis put forth previously,

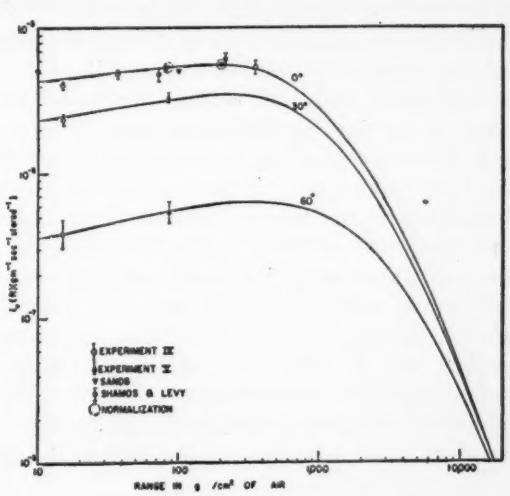

FIG. 10. Differential range spectrum of mesons at sea level in the vertical direction and at zenith angles of 30° and 60°.

[16] B. Rossi, Rev. Mod. Phys. **20**, 537 (1948).

that most anti-coincidence measurements have in the past discriminated in one way or another against the slow mesons.

Simple counter experiments, such as the coincidence and anti-coincidence methods that have been described, have been interpreted at sea level in terms of mesons since the relative number of other penetrating particles is believed to be small. It should be pointed out that the direct evidence for the intensity of penetrating particles other than mesons at sea level is scanty. On the basis of cloud-chamber studies by a number of experimenters, the penetrating component at sea level is believed to be composed of ~1 percent fast protons, and ~0.2 percent slow protons such as might stop in an apparatus like ours (see Rossi[16] and Janossy[17]). No attempt will be made to correct our data for this; the estimates of proton intensity are entirely too tentative.

The other measurements that were made at sea level were concerned with relative meson intensities and are best presented in the form of curves. The zenith angle distributions of two slow meson groups have already been presented in Figs. 5 and 7 and as far as we know there are no measurements with which they may be compared. The zenith angle distribution of the fast mesons has been measured by many experimenters, with essentially the same result as ours, $I_\theta = I_v \cos^n\theta$, with $n=2$ or 2.1.

Rossi has recently published a curve showing the differential range spectrum in the vertical direction of mesons at sea level, as deduced from the results of many different experimenters.[16] The solid curve of Fig. 10 marked "0°" is essentially a reproduction of Rossi's curve. The results of our present experiments (II, III, and VIII) on the absolute differential vertical intensity of mesons are in perfect agreement with this curve at range 105 g cm^{-2}, and are not shown on the graph. We have plotted the results of our delayed coincidence measurements, the results of the anti-coincidence zenith angle experiment, and the delayed coincidence measurements of two other experimenters on the graph.[7,18] Since none of these were measurements of absolute intensities, it has been necessary to normalize them. The procedure was as follows: we had three delayed coincidence measurements of the relative differential vertical intensity at three different ranges. The largest range among these corresponded to 86 g cm^{-2} of air, whereas our absolute (anti-coincidence) measurement of the differential vertical intensity was at 105 g cm^{-2} of air. Because our measurements and the data of Sands[7] both indicate that the differential vertical intensity is a very insensitive function of the range, it was considered legitimate to extrapolate over this 19 g cm^{-2} of air so as to fit the delayed coincidence measurements to the anti-coincidence measurements on an absolute scale. Sands' data, on the other hand, have been normalized to the curve at 200 g cm^{-2} of air, while those of Shamos and Levy have been adjusted to show that they are not inconsistent with the shape of the curve. The anti-coincidence zenith angle measurement, experiment V, has been normalized at the vertical intensity, and the standard errors indicated on the 30 and 60 degree measurements are those of the ratio i_θ/i_v.

It is clear that the 0° curve is consistent with the available slow meson data at sea level. We have not included any of the meson intensity measurements made underground or with cloud chambers in Fig. 10. Rossi has shown that these data are in agreement with the curve.

The other curves in Fig. 10 labeled 30° and 60° were deduced as follows. For the small ranges, our zenith angle measurements have been used. For the larger ranges (>1000 g cm^{-2}) we know of no differential measurements, and have calculated the curves. Sands[7] has found a meson production spectrum which predicts accurately many features of the meson component. This production spectrum is $N(x,R)=(R+210)^{-2.9}\times\exp(-x/125)$ where $N(x,R)dxdR$ is proportional to the number of mesons created at atmospheric depth x in dx g cm^{-2} of air with residual range R in dR g cm^{-2} of air. By taking proper account of the meson decay, and integrating over the atmosphere, vertical meson intensities may be predicted. The 0° curve is in fact a curve calculated in this way.

We have extended this production spectrum to include other zenith angles by assuming it to be of the form $(R+210)^{-2.9}\exp(-x/125\cos\theta)/\cos\theta$, keeping the same normalization as used for 0°. The spectra so calculated have been used in the 30° and 60° curves for ranges greater than 1000 g cm^{-2}. The calculated spectra for smaller ranges do not agree with our observations, the observations indicating higher intensities than those calculated. This is not surprising since we have assumed that mesons when produced follow the direction of the producing component, whose intensity we have assumed in turn to fall off as $\exp(-x/125\cos\theta)$. Further, we have neglected atmospheric Coulomb scattering. These assumptions are clearly correct only in the limit of high energies.

It should be pointed out that an integration of the curves of Fig. 10 results in a zenith angle dependence for the *integrated* meson intensity which is in excellent agreement with observations. Figure 10 then, we regard as representing reasonably well the sea level meson intensity for 0, 30, and 60 degrees.

B. Measurements at Echo Lake

Some of the results of the Echo Lake experiments have been discussed briefly in earlier sections. It will be noticed that the vertical intensity of slow mesons at Echo Lake, as deduced from the delayed coincidence experiments IV and VI, is not in good agreement with the similar determinations from experiments VII and VIII. From experiments IV and VI we have 2.0±0.2 for

[17] L. Janossy, *Cosmic Rays* (Oxford University Press, London, 1948).

[18] M. H. Shamos and M. G. Levy, Phys. Rev. **73**, 1396 (1948).

ratio Echo Lake/Ithaca, where as from experiments VII and VIII we have 2.6 ± 0.2 and 2.5 ± 0.3. The probability for a deviation this large is about 5 percent. The weighted mean of the three ratios, assuming the deviations to be purely statistical, is 2.37 ± 0.12. Sands[7] and Rossi, Sands, and Sard[19] have measured the variation of the number of slow mesons with altitude by using a delayed coincidence apparatus in an airplane. The points nearest to ours were taken at 600 and 1030 g cm^{-2} of air. If these results are interpolated to 707 and 1007 g cm^{-2} for Echo Lake and Ithaca respectively, the corresponding ratio is 3.3. It is not possible to say whether this large difference in supposedly comparable measurements represents a real effect, an unfortunate statistical fluctuation, or instrumental difficulties.

Calculations similar to those made for the sea level meson spectrum were carried out for the altitude of Echo Lake (707 g cm^{-2}). Contrary to what might first be supposed, the predicted zenith angle dependence for slow mesons is stronger than that predicted for sea level. This comes about because even at sea level, there is predicted appreciable local production of slow mesons near the zenith, and almost none at large angles. As the atmospheric depth decreases, this local production near the zenith increases very rapidly, but because of the exponential nature of the absorption of the producing radiation, there is still only an insignificant number of slow mesons locally produced by primaries traveling at large zenith angles. Now our *measured* zenith angle dependence of slow mesons was the same at Echo Lake as it was at Ithaca. It is likely that there are particles capable of producing low energy mesons that have not traversed the amount of atmosphere implied by the zenith angle of the produced meson. This could result either from large angular spread in the producing event, or from angular spreads in a series of nuclear interactions from which the producing particle descended. It is of interest to note that the maximum transverse momentum that a μ-meson may receive from the decay of a π-meson is about 30 Mev/c, so that practically speaking, the μ-mesons with which we are concerned have taken on the direction of their parent π.

It has been pointed out that the ratio of anti-coincidences to delayed coincidences did not remain constant in going from Ithaca to Echo Lake. Similarly, at Echo Lake this ratio was not constant under different absorbers. Both of these observations are consistent with the assumption that non-decaying particles were contributing appreciably to our anti-coincidence measurement under the 8-inch lead absorber at Echo Lake. Let us assume that none of these particles contributes to the anti-coincidence rates at Ithaca, or at Echo Lake under 20.5 in. of lead. Then our anti-coincidence and delayed coincidence data are compatible if the intensity of these non-decaying particles under 8 in. of lead at Echo Lake is about 4×10^{-6} g^{-1} sterad^{-1} sec.$^{-1}$, or some 20 percent of the differential slow meson intensity. We believe the most likely particles to be identified with this intensity are slow protons either incident upon the apparatus or produced in our absorbers. Rossi[13] has estimated from some data of Leprince-Ringuet[20] that the differential vertical intensity of protons having a range of 100 g cm^{-2} of air should be 4×10^{-7} g^{-1} sterad^{-1} sec.$^{-1}$ at an altitude of 1000 meters. Assuming that the number of protons varies with atmospheric depth, x, as $\exp(-x/125)$, the intensity at Echo Lake should be $\sim2.5\times10^{-6}$ g^{-1} sterad^{-1} sec.$^{-1}$, in reasonable agreement with the estimate given above.

IV. THE SEA LEVEL ELECTRON COMPONENT

We have used the total integrated intensity measurements of Greisen[2] and our meson intensity measurements to deduce electron intensities. An attempt has been made to include the effect of scattering on the energy limits set for electrons by Greisen's apparatus, and we find for the integrated intensity of electrons with energy greater than 10 Mev, 0.60×10^{-2} cm^{-2} sec.$^{-1}$.

The intensity of the meson-produced electrons can be calculated (given the decay products), since their origin and behavior may be described by well-founded general principles. Thus Rossi and Greisen[21] have described a method of calculating the electrons arising from the decay of fast mesons ($p/\mu>2.5$) using the conservation laws in a manner which avoids sensitive dependence on the meson spectrum or detailed cascade shower theory. Rossi and Klapman[22] have calculated accurately the track length for shower electrons above 10 Mev as a function of the primary electron energy, and have applied these results to a calculation of the electron intensity arising from the collision processes of mesons. Greisen,[2] making use of conservation laws, has calculated the electrons arising from the decay of slow mesons ($p/\mu<2.5$). We have applied these methods to a calculation of the intensity of electrons of energy greater than 10 Mev, and under two likely hypotheses of the meson decay scheme, find:

	Intensity, cm^{-2} sec.$^{-1}$ Average Energy of Decay Electron	
Source	$\frac{1}{3}\mu c^2$	$\frac{1}{2}\mu c^2$
Decay of fast mesons	0.303×10^{-2}	0.455×10^{-2}
Decay of slow mesons	0.010	0.015
Collision processes	0.114	0.114
Decay of mesons at rest	0.003	0.005
Total (from mesons)	0.430	0.589

The measured electron intensity of 0.60×10^{-2} cm^{-2} sec.$^{-1}$ is in good agreement with the calculated total electron intensity obtained by assuming that half of the meson rest energy is given to the electron.[23] However,

[19] Rossi, Sands, and Sard, Phys. Rev. 72, 120 (1947).

[20] L. Leprince-Ringuet, Comptes Rendus 221, 406 (1945).

[21] B. Rossi and K. Greisen, Phys. Rev. 61, 121 (1942).

[22] B. Rossi and S. Klapman, Phys. Rev. 61, 414 (1942).

[23] We have used 2.15×10^{-6} sec. for themean life and 109 Mev/c^2 for the mass of the meson. Bernardini *et al.*[1] have used 2.3×10^{-6} sec. and 90 Mev/c^2, respectively. Their calculated electron intensities agree with ours if this is taken into account.

it has been pointed out repeatedly that the zenith angle and altitude dependence of the electron component near sea level are such that a source of electrons other than mesons is indicated. The zenith angle dependence of the total meson component is $\cos^2\theta$, and the electrons from this source should have a zenith angle dependence no stronger than this, while the observed electron zenith angle dependence is more nearly $\cos^3\theta$. Similarly, the electron component appears to increase with altitude faster than can be explained by meson processes alone. It therefore seems likely that on the average, only $\frac{1}{3}$ of the meson rest energy is given to the electron, and that there is an additional intensity of about 0.17×10^{-2} cm^{-2} sec.$^{-1}$ probably arising from nuclear interactions. Such an additional source would be expected to have a very steep zenith angle and altitude dependence because of the exponential character of the absorption of high energy nucleons in the atmosphere, and would therefore account for the observed zenith angle and altitude dependence of the total electron component. This is likewise in agreement with the recent cloud-chamber experiments of Anderson, Leighton, and Seriff,[24] which suggest that the decay products of the μ-meson are an electron and two neutrinos.

V. SUMMARY

The present investigation has been concerned mostly with the meson component. We have made a careful measurement of the absolute intensity of the number of mesons in a given range interval, and believe that these measurements have succeeded in eliminating most of the errors associated with the serious discrepancies among similar measurements reported in the literature. The differential intensity as a function of zenith angle has been measured for mesons having two different residual ranges, and it has been found that the zenith angle dependence is considerably stronger than that for the integral intensity, but approximately the same for the two low energy groups. Using the method of delayed coincidences, we have investigated the shape of the low energy end of the meson spectrum in the vertical direction, and found that the differential range spectrum is essentially flat in this low energy region. Since it is flat in the vertical direction, and the zenith angle dependence is independent of range up to $\sim$100 g cm^{-2}, the differential range spectrum is also rather flat for ranges up to $\sim$100 g cm^{-2} at large zenith angles.

Measurements similar to those made at Ithaca have been made at Echo Lake, Colorado (altitude 3240 m), and it has been found that the differential range spectrum is still moderately flat up to ranges corresponding to $\sim$100 g cm^{-2} of air. The differential intensity as a function of zenith angle was found to be similar to that at Ithaca, as is the zenith angle dependence of the integrated intensity. By comparing anti-coincidence and delayed coincidence data under 230 g cm^{-2} of lead, we have suggested that the differential intensity of protons under this thickness of lead may be $\sim4\times10^{-6}$ g^{-1} sec.$^{-1}$, or $\sim$20 percent of the differential slow meson intensity. The slow meson intensity was found to increase by a factor 2.4 ± 0.1 between Ithaca and Echo Lake, while the integrated intensity of all penetrating particles increased by 1.74.

We have applied our meson intensity measurements to a re-evaluation of the sea-level electron intensity using the total cosmic-ray intensity as measured by Greisen. These considerations are consistent with the electron-2 neutrino decay scheme for the μ-meson, provided there are some electrons at sea level not descended from mesons.

In conclusion, the author wishes to express his gratitude to Professor K. I. Greisen who directed this investigation. Drs. G. Cocconi and V. Cocconi-Tongiorgi contributed much helpful advice. Part of the data included is a by-product of an experiment performed by Dr. V. Cocconi-Tongiorgi and the author in collaboration. A portion of the work was supported by the Office of Naval Research and a portion by the Research Corporation. Further acknowledgment is due Drs. Iona and Cohn of Denver University and the Inter-University High Altitude Laboratory.

[24] Anderson, Leighton, and Seriff, Phys. Rev. **75**, 1466A (1949).

Transient Nutations in Nuclear Magnetic Resonance*

H. C. TORREY
Physics Department, Rutgers University, New Brunswick, New Jersey
(Received June 23, 1949)

Transient nutations of the resultant nuclear magnetic moment vector are set up by applying radiofrequency power in the form of pulses in the neighborhood of resonance ($\omega=\gamma H_0$). The nutations have an initial amplitude depending on the state of magnetization at the start of a pulse and on the proximity to resonance, and are damped by spin-spin and spin-lattice interaction. The thermal relaxation time can be directly found by observing the dependence of initial amplitude on the time between pulses. The spin-spin time constant T_2 can be found from the rate of decay even in the presence of normally disturbing inhomogeneity in magnetic field. Sensitivity is in many cases comparable to that obtained in the modulation method with narrow band amplifiers. The fast response due to the relatively wide band widths used can be applied to a rapid search for unknown resonances. The effects observed are in qualitative accord with predictions based on the Bloch theory.

I. INTRODUCTION

SINCE the original work on the detection of nuclear magnetic resonance in bulk matter[1,2] many improvements in technique and method have been introduced by various workers.[3–6] In most of the methods currently in use a steady state is set up which may be described as an equilibrium resulting from the competition between the applied radiofrequency magnetic field on the one hand which tends to equalize the populations of the Zeeman levels and thus to demagnetize the system and on the other hand the effect of the interactions between the spins and the thermal motions of the nuclei which tends always to restore the system to thermal equilibrium as governed by the Boltzmann distribution.

In case absorption is being detected an optimum radiofrequency power exists which gives maximum signal strength; in the case of dispersion a maximum signal results for large radiofrequency power. As Bloch[7] has shown the two maxima are the same being given in his notation by [8,9]

$$-v_{\max}=u_{\max}=\tfrac{1}{2}(T_2/T_1)^{\frac{1}{2}}M_0. \qquad (1)$$

In many cases $T_2/T_1\ll 1$ and the maximum values of u and v are much less than M_0.

The steady state may be attained either by a very slow approach to resonance in which case the steady state conditions may be assumed to hold at each instant of time, or by a relatively rapid approach to the resonant conditions in which case transient motions of the magnetic moment vector will be set up eventually decaying to a steady state motion in a time determined by the relaxation constants T_1 and T_2. During these transients u and v may attain values much larger than the steady state maximum (1), approaching in fact the value M_0. It appears therefore that considerably larger signal strengths are in many cases available through such transients. This does not of course imply that more sensitivity may be expected to result from utilization of the transients, since the fact that they last for only finite times limits the minimum band widths that may be used in the amplifying and detecting circuits and thus limits the minimum noise power which determines the ultimate sensitivity. Nevertheless, as we shall show (Section VII), the sensitivity to be expected from detection of the transients is often comparable and in some cases superior to that obtainable from the steady state even with the use of band widths in the latter case as small as 10^{-1} cycle/sec.

Quite aside from the question of sensitivity the study of the transients appears capable of yielding, in a straightforward manner, data on the relaxation constants T_1 and T_2 which allows their separate evaluation. Furthermore, it appears to be possible by study of the transients in certain circumstances to measure T_2 even if this quantity cannot be determined from the steady state because its effect on the resonance width is obscured by inhomogeneities in the magnetic field. Finally the high sensitivity obtainable from the transients even with band widths of 10^3 cycles/sec. or more seem to offer some promise in their utilization in the search for unknown resonances, since the search can be conducted in far shorter times than is possible in the steady state case. We have made theoretical and experimental investigations of these transients and although our results so far are preliminary they seem to have sufficient interest to merit publication in advance of a more exhaustive study.

Before analyzing the effects that have been expected and observed from the transients under review it would

* Presented in part at the meeting of the American Physical Society, New York, January 29, 1949 (Phys. Rev. 75, 1326 (1949)). This work has been supported by the joint program of the ONR and the AEC, by the Research Corporation, by the Rutgers University Research Council, and by the Radio Corporation of America.

[1] Purcell, Torrey, and Pound, Phys. Rev. 59, 37 (1946).
[2] Bloch, Hansen, and Packard, Phys. Rev. 69, 127 (1946).
[3] Bloembergen, Purcell, and Pound, Phys. Rev. 73, 679 (1947).
[4] R. V. Pound, Phys. Rev. 72, 527 (1947).
[5] A. Roberts, Rev. Sci. Inst. 18, 845 (1947).
[6] J. R. Zimmerman, and D. Williams, Phys. Rev. 73, 94 (1948).
[7] F. Bloch, Phys. Rev. 70, 460 (1946).
[8] In Bloch's paper the factor $\frac{1}{2}$ is missing evidently due to a computational error.
[9] This notation is explained in Section II of this paper.

be well to distinguish them from certain transient effects which have already been discussed and in some cases observed by other writers.

(a) In the introduction to his paper Bloch[7] suggests the possibility of observing nuclear induction in the absence of a r-f field by first disorienting the resultant nuclear moment with a strong field pulse. When this driving pulse has disappeared a signal resulting from the free precession of the nuclear moment should be observable. This effect to the best of our knowledge has not yet been observed. It differs from the transient effects treated here in that the latter occur before rather than after the driving pulse is extinguished; thus the motion of the nuclear moment vector is in the present case forced rather than free.

(b) In the same paper Bloch discusses in some detail the effects to be expected from an approach to resonance which is fast in comparison to the relaxation times T_1 and T_2 but slow in comparison to the nutation time $(\gamma H_1)^{-1}$ of the magnetic moment vector. This case gives rise to a nuclear induction which attains a maximum value near M_0 at resonance. The signal strength is thus large, but its duration is necessarily short compared with T_2. The theory of this effect is based on an approximate solution of Bloch's differential equations which is of such complexity as to make a detailed interpretation of experimental results in terms of the relaxation constants somewhat difficult. Bloch, Hansen, and Packard[10] have, however, obtained experimental results which show at least a qualitative similarity to the effects expected. In contrast, the effects considered here result from a sudden approach to the resonant condition taking place in a time short compared both to $(\gamma H_1)^{-1}$ and to T_2 and T_1. Once the resonant condition is thus established, the effective external parameters of the theory H_1, ω and H_0 are kept constant. The Bloch equations take in this case the form of linear equations with constant coefficients and are thus susceptible to exact solution in terms of exponential and sinusoidal functions of time, making the interpretation of the data relatively simple.

(c) Another transient effect was observed by Bloembergen, Purcell, and Pound[3] and called by them "the wiggles." It has been analyzed theoretically by Jacobsohn and Wangness.[11] It bears no relation to the effects considered here.

II. THEORY

The theory of the transients will be based on the general macroscopic theory of Bloch.[7] This theory (as pointed out by Bloch) is only semi-quantitative, but it has virtue of simplicity. It does not seem feasible at this time to undertake a more rigorous treatment. Not the least interest, perhaps, in an experimental investigation of the transients will be found in an elucidation of the limitations of the Bloch theory.

It is supposed that a sample of material with nonvanishing nuclear moments is placed in an applied magnetic field consisting of two components: a steady component of magnitude H_0 oriented in the z-direction and an oscillating component $2H_1\cos\omega t$ in the x-direction. As is well known the oscillating component can be further decomposed into two circularly polarized components in the x–y plane rotating in opposite directions about the z-axis. Only one of these, namely that one rotating in the same sense as the free Larmor precession of the nuclear moment, is effective in disorienting the nuclear moment; the other can and in fact will be completely ignored. The resultant nuclear moment M of the sample may be resolved into three components: M_z in the z-direction, u parallel to the effective rotating component of the magnetic field and v orthogonal to M_z and leading the effective rotating field component by 90°.

The time dependence of these components of magnetic moment is governed in the Bloch theory by the differential equations:

$$du/d\tau+\beta u+\delta v=0, \tag{2a}$$

$$dv/d\tau+\beta v-\delta u+M_z=0, \tag{2b}$$

$$dM_z/d\tau+\alpha M_z-v=M_0, \tag{2c}$$

where

$$\begin{aligned} &\tau=\gamma H_1 t, && \delta=(\omega_0-\omega)/\gamma H, \\ &\beta=1/\gamma H_1 T_2, && \omega_0=\gamma H_0, \\ &\alpha=1/\gamma H_1 T_1, && M_0=\chi_0 H_0, \end{aligned} \tag{3}$$

t is the time, γ the absolute value of the nuclear gyromagnetic ratio, and χ_0 the static susceptibility. The above notation is the same as that of Bloch, except that we use γ in place of his $|\gamma|$.

It is shown in the appendix that if w stands for any one of u/M_0, v/M_0, or M_z/M_0 the general solution of these equations may be written in the form

$$w=Ae^{-a\tau}+Be^{-b\tau}\cos s\tau+\frac{C}{s}e^{-b\tau}\sin s\tau+D. \tag{4}$$

The first three terms in (4) give the transient effects and the last term the steady state. The values obtained for D must of course agree as in fact they do with the Bloch steady state solution.[12] The constants a, b, s, A, B, C, and D of Eq. (2) are functions of α, β, and δ. Of these constants a, b, and s are independent of the initial conditions and are the same for all components of M; A, B, C, and D depend on which component w stands for, and all except D depend on the initial values u_0, v_0, and $(M_z)_0$ of u, v, and M_z. The factors a, b, and s and the coefficients A, B, C, and D are evaluated in the appendix, implicitly in the general case and explicitly in the special cases (a) $\delta=0$, i.e., the case of exact

[10] Bloch, Hansen, and Packard, Phys. Rev. **70**, 474 (1946).

[11] B. A. Jacobsohn and R. K. Wangness, Phys. Rev. **73**, 1509 (1948).

[12] See Eq. (56) in reference 7.

resonance; (b) $\alpha=\beta$ or $T_1=T_2$; and (c) in case the radiofrequency magnetic field H_1 is sufficiently large so that $\alpha\ll 1$ and $\beta\ll 1$.

In the following section the method now being used for experimental observation of the transients is outlined. As explained there the quantity directly observed is v as a function of time. The Bloch theory developed in the appendix gives for v in the three cases (m_0 is the initial value of M_z/M_0; it is assumed that $u_0=v_0=0$):

(a) $(\delta=0)$

$$-v/M_0=\frac{\alpha}{1+\alpha\beta}\left[1-e^{-(\alpha+\beta)\tau/2}\cos\left(1-\left(\frac{\alpha-\beta}{2}\right)^2\right)^{\frac{1}{2}}\tau\right]+\left[m_0-\frac{\alpha(\alpha+\beta)}{2(1+\alpha\beta)}\Big/\left(1-\left(\frac{\alpha-\beta}{2}\right)^2\right)^{\frac{1}{2}}\right]\times e^{-(\alpha+\beta)\tau/2}\sin\left(1-\left(\frac{\alpha-\beta}{2}\right)^2\right)^{\frac{1}{2}}\tau, \quad (5)$$

(b) $(\alpha=\beta)$

$$-v/M_0=\frac{\beta}{1+\beta^2+\delta^2}[1-e^{-\beta\tau}\cos(1+\delta^2)^{\frac{1}{2}}\tau]+\frac{1}{(1+\delta^2)^{\frac{1}{2}}}\left(m_0-\frac{\beta^2}{1+\beta^2+\delta^2}\right)e^{-\beta\tau}\sin(1+\delta^2)^{\frac{1}{2}}\tau, \quad (6)$$

(c) $(\beta\ll 1)$

$$-v/M_0=\frac{-\beta}{\delta^2+\beta/\alpha}-\frac{\delta(\beta-\alpha)^2}{1+\delta^2}\left(\frac{m_0}{1+\delta^2}-\frac{1}{\delta^2+\beta/\alpha}\right)e^{-a\tau}+\frac{1}{1+\delta^2}\left[\frac{(\beta-\alpha)\delta^2 m_0}{1+\delta^2}+\alpha\right]e^{-b\tau}\cos(1+\delta^2)^{\frac{1}{2}}\tau-\frac{m_0}{(1+\delta^2)^{\frac{1}{2}}}e^{-b\tau}\sin(1+\delta^2)^{\frac{1}{2}}\tau+O(\beta^2), \quad (7)$$

where

$$b=\beta-\frac{1}{2}\frac{\beta-\alpha}{1+\delta^2}+O[(\beta-\alpha)^3], \quad (8)$$

$$a=\frac{\beta+\alpha\delta^2}{1+\delta^2}+O[(\beta-\alpha)^3]. \quad (9)$$

If $m_0\sim 1$ the last term in the above expression for v is dominant and

$$v/M_0\cong-\frac{m_0}{(1+\delta^2)^{\frac{1}{2}}}e^{-b\tau}\sin(1+\delta^2)^{\frac{1}{2}}\tau, \quad (10)$$

or

$$v/M_0\cong-\frac{m_0\gamma H_1}{\Omega}\exp-\left[\frac{1}{T_2}-\frac{1}{2}\left(\frac{1}{T_2}-\frac{1}{T_1}\right)\left(\frac{\gamma H_1}{\Omega}\right)^2\right]t\times\sin\Omega t, \quad (11)$$

where

$$\Omega=(\gamma^2H_1^2+(\omega_0-\omega)^2)^{\frac{1}{2}}. \quad (12)$$

In cases (b) and (c) it will be seen that s is always real and thus the transients consist of damped oscillations superposed on an exponential decay; the latter (the term in A) vanishing at resonance. The oscillations can be interpreted as arising from a periodic nutational motion of the magnetic moment vector, damped by the relaxation processes.

It is obvious in fact that the transients must have this general form quite independent of any special predictions of the Bloch theory. In the absence of relaxation effects the motion of the magnetic moment vector is exactly determined by the second law of motion.[13]

$$d\mathbf{M}/dt=\gamma(\mathbf{M}\times\mathbf{H}). \quad (14)$$

Here $\mathbf{H}$ is the resultant magnetic field composed of H_0 (in the z-direction) and the effective rotating a.c. component H_1. Let us now transform to a system of axes rotating about the z-axis in the same sense as H_1 and with the same angular velocity ω. Let $D\mathbf{M}/dt$ be the velocity of $\mathbf{M}$ as viewed in the rotating system. Then by a familiar kinematical transformation we have

$$D\mathbf{M}/dt=d\mathbf{M}/dt+\mathbf{M}\times\boldsymbol{\omega},$$

or by (14)

$$D\mathbf{M}/dt=\gamma(\mathbf{M}\times\overline{\mathbf{H}}), \quad (15)$$

where

$$\overline{\mathbf{H}}=\mathbf{H}+\boldsymbol{\omega}/\gamma. \quad (16)$$

In the rotating system $\overline{\mathbf{H}}$ is constant in time and thus the solution of (15) can be stated at once: it consists in a uniform precession of $\mathbf{M}$ about $\overline{\mathbf{H}}$; the angle of the cone of precession being determined by the initial conditions. At the same time $\overline{\mathbf{H}}$ of course precesses about the z-axis with angular velocity ω. The motion of $\mathbf{M}$ about $\overline{\mathbf{H}}$ has the angular velocity

$$\Omega=\gamma|\overline{\mathbf{H}}|$$

or

$$\Omega=(\gamma^2H_1^2+(\omega_0-\omega)^2)^{\frac{1}{2}}. \quad (17)$$

The projection of this motion on the x–y plane will obviously result in oscillations in u and v with the angular frequency Ω. Near resonance $\Omega\ll\omega$ and the motion as viewed from the laboratory system appears as a slow nutation superposed on a rapid precession about the z-direction.

The effect of relaxation processes may be expected to take the form of a damping of these oscillations. The Bloch theory makes explicit predictions as to the form of this damping and also predicts (see Eqs. (5)–(12)) that the frequency of the oscillations is unaffected by relaxation in the case $T_1=T_2$ or in any case if $\beta\ll 1$. In

[13] Reference 7, Eq. (11).

some cases, however, e.g., if $\delta=0$ and $[(\beta-\alpha)/2]^2\ll 1$ the damping may be sufficiently large so as to suppress the oscillations.

III. EXPERIMENTAL OBSERVATION OF THE TRANSIENT EFFECTS

It is clear that the transient situation may be set up by any approach to the resonant condition which is rapid compared to the nutation time $1/\gamma H_1$. To accomplish this any one of the three external parameters H_0, H_1, or ω may be varied with the time in the form of a pulse starting at say time $t=0$. In case H_0 or ω is varied: for time $t<0$ we must have $\delta=(\gamma H_0-\omega)/\gamma H_1 \gg 1$ and for $t>0$, δ should be of order unity or less. In case H_1 is pulsed, δ need not be large for $t<0$, but H_1 (for $t<0$) must be sufficiently small so that $\mathbf{M}$ is initially in the z-direction; at $t=0$, H_1 is increased to a relatively large value. There are experimental difficulties associated with the pulsing of any one of these parameters. In the case H_0 or ω is pulsed a very flat-topped rectangular pulse must be produced. It is especially difficult to get the required flatness with a sufficiently fast rise time in the case of H_0. On the other hand if H_1 or ω is pulsed there are difficulties associated with the response time of the radiofrequency circuits. In particular the inherent frequency sensitivity of radiofrequency bridge circuits is troublesome. However, in case H_1 is pulsed, the requirement of flatness of the pulse is considerably less severe than for H_0 or ω. For this reason we have chosen H_1 as the most suitable parameter for pulsing.

There is shown in Fig. 1 a block diagram of the apparatus now in use. In the interests of frequency stability we have chosen to pulse H_1 by gating a continuously operating oscillator. The oscillator is a R.C.A. 19427 which, although electron coupled, has excellent frequency stability. The gating modulator is shown in Fig. 2. It consists of a twin-T null network which is normally balanced to a null. Part of the effective conductance in the lower arm is provided by the output impedance of the 6J6 cathode follower. A negative gating pulse on the grid cuts the tube off and the impedance changes rapidly from 200 ohms to 500 ohms thus unbalancing the bridge.

The resulting radiofrequency pulse is amplified and fed into a conventional bridge circuit shown in Fig. 3. The primary of the transformer is adjustable in position relative to the two secondaries, by means of a micrometer head. A second balancing adjustment is provided by a small trimming condenser across one of the tuned circuits. These adjustments are nearly orthogonal. By symmetrizing the two arms of this bridge especially with regard to the Q's of the two parallel tuned circuits, the bridge can be made sufficiently broad band to pass the pulse without appreciable distortion. The bridge is ordinarily balanced in the range between 40 db to 60 db. Because of absorption and dispersion by nuclear moments in the coil containing the sample under investigation, the radiofrequency pulse put out by the bridge is amplitude modulated; the modulation voltage being proportional to u or to v or to some mixture of the two depending on the character of the bridge balance.[14] In all work to date the bridge has been balanced in phase so that the output modulation is proportional to v.

The modulated radiofrequency pulse put out by the bridge is amplified and detected by a IN34 germanium crystal rectifier. This rectifier is biased negatively so that it removes the small modulation from the relatively large pedestal due to the unbalance of the bridge. The detected signal is amplified and displayed on the vertical plates of a cathode-ray tube. The horizontal linear sweep of this tube is triggered by the leading edge of the d.c. pulse which gates the modulator. The vertical deflection gives directly the quantity v as a function of time. Typical results are shown in Figs. 4 and 5. Figure 4 shows $-v$ as a function of time for $\delta=0$ due to proton resonance in 1.5 cc of glycerine at room temperature, and Fig. 5 shows a corresponding result for the same volume of distilled water at room temperature. In these examples the sweep duration is 0.01 second, the radiofrequency is 9 mc/sec., $H_0=2100$ gauss, and the radiofrequency magnetic field H_1 is 0.17 and 0.15 gauss, respectively. We will return to a discussion of these curves in Section VI.

The pulse durations required depend of course on the particular application being made. If measurements of the decay time of the transient is desired and if inhomogeneity effects are unimportant the pulse length must be of the order of T_2 or longer. If measurements are to be made of the relaxation time T_1 the pulse should last until the transients have ceased i.e., for a time long compared with T_2 (the effect of inhomogeneity on these considerations is discussed in Section VI).

IV. MEASUREMENT OF THERMAL RELAXATION TIME

The pulse technique in connection with the transients lends itself readily to a direct and straight forward measurement of the thermal relaxation time T_1, i.e., the time required to bring the spin system into thermal equilibrium with the lattice. For example suppose that the radiofrequency field H_1 is large enough to satisfy the inequality

$$\gamma H_1 \gg 1/T_2, \text{ i.e., } \beta\ll 1,\ \alpha\ll 1.$$

The solution of the Bloch equations which holds in this case is given in the appendix. At resonance ($\delta=0$) we have for M_z

$$M_z/M_0=m_0\exp\left[-\frac{1}{2}\left(\frac{1}{T_1}+\frac{1}{T_2}\right)t\right]\times\left(\cos\tau+\frac{\beta-\alpha}{2}\sin\tau\right)+O(\alpha\beta). \quad (18)$$

[14] For a discussion of this effect of bridge balance see reference 3.

If the pulse duration is sufficiently long compared with the damping time $2T_1T_2/(T_1+T_2)$, the ultimate value of M_z will be very small compared with M_0. That is to say, the sample will have become nearly completely demagnetized. During the interval between the end of one pulse and the start of the next the sample will regain some magnetization because of the relaxation process. If, then, m_0M_0 is the value of M_z at the start of a pulse we shall have

$$m_0=1-e^{-T/T_1}, \tag{19}$$

where T is the time between pulses.

If m_0 has a substantial value, i.e., if $m_0\sim 1$, then from (10) it is evident that the initial amplitude of v will be closely proportional to m_0. Thus by observing the dependence of the initial amplitude of v on the time T between pulses and making use of (19) the quantity T_1 can be directly measured.

V. MEASUREMENT OF T_2

The quantity T_2 is a measure of the time required for a nuclear spin to become disoriented as a result of interactions with neighboring nuclei or with paramagnetic ions. This quantity can be measured by its effect on the damping of the oscillations in v. From Eq. (5) we see that this damping time T_0 is given by

$$1/T_0=\tfrac{1}{2}(1/T_1+1/T_2) \tag{20}$$

at resonance.

Inhomogeneities in H_1 or H_0 can also give rise to a damping of the oscillations in v. If these effects are unimportant, T_2 can be directly found from (20) once T_1 is known. In many cases $T_1\gg T_2$ and a knowledge of T_1 is unnecessary. The effect of inhomogenities is considered in the next section.

VI. EFFECT OF INHOMOGENEITIES IN H_1 AND H_0

The most important effect of inhomogeneities in H_1 or H_0 is the resultant distribution of nutational frequency (see Eq. (17)) over the sample. The signal from the whole sample can be regarded as due to a superposition of signals from the several parts of the sample, each part being in an essentially homogeneous field. Signals from the several parts will differ somewhat in frequency because of the variation of $\omega_0=\gamma H_0$ over the sample. Since they start out all in phase the initial integrated amplitude is large, but after a few oscillations phase differences develop which damp the resultant signal.

Consider first the effect of an inhomogeneity in H_1. The frequency of oscillation of v (nutational frequency) at resonance is $\gamma H_1/2\pi$. Consequently an inhomogeneity in H_1 of order ΔH_1 may be expected to result in appreciable damping in a time of order $1/\gamma\Delta H_1$.

The effect of inhomogeneity in H_0 is somewhat different, however, since the frequency of oscillation does not depend on H_0 at resonance. In fact from (17) the angular frequency is

$$\Omega=(\gamma^2H_1^2+(\gamma H_0-\omega)^2)^{\frac{1}{2}}.$$

Thus if H_1 is large compared with the inhomogeneity of H_0 there will be relatively little variation in Ω over the sample. Investigation in fact shows that if a gaussian distribution in H_0 is assumed with full width at half maximum of ΔH_0 the signal resulting at resonance after integration over H_0 will be: (it is assumed that $\beta\ll 1$ and that $(H_1/\Delta H_0)^2\gg 1$)

$$v/M_0\cong\frac{-m_0}{[1+(t/T_H)^2]^{\frac{1}{2}}}\cdot e^{-t/T_0}\sin(\gamma H_1t+\varphi), \tag{21}$$

where T_0 is the natural damping time (Eq. (20)),

$$T_H=\frac{5.6H_1}{\gamma(\Delta H_0)^2}, \tag{22}$$

and φ is a slowly varying phase factor.

It is apparent from this expression that if (as assumed) $H_1\gg\Delta H_0$ we shall have $T_H\gg 1/\gamma\Delta H_0$. Consequently the damping due to H_0 can be made negligibly small for H_1 sufficiently large. Furthermore, it does not appear that this general qualitative result depends on any special assumptions of the Bloch theory.

Of course it does not pay to increase H_1 indefinitely, but only until the effect of inhomogeneity in H_1 is about that of H_0. By concentrating the sample near the center of the r-f coil the inhomogeneity in H_1 can be considerably reduced at the expense of signal strength. It

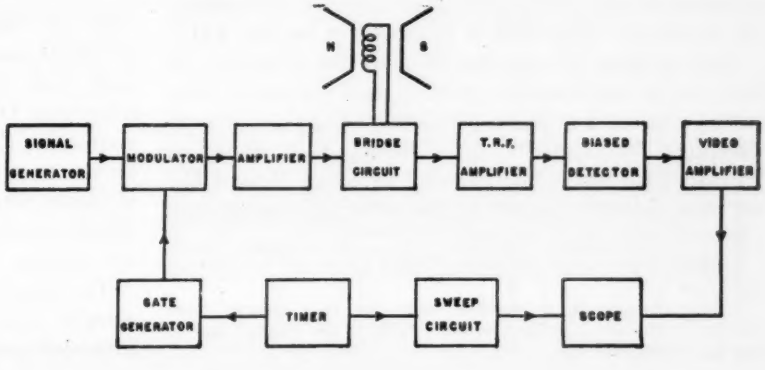

FIG. 1. Block diagram of circuitry used in observation of the transients.

would seem in fact that the effects of inhomogeneities can be reduced to the point where very much larger values of T_2 can be measured than can be found by line-width determinations.

This possibility has not been completely explored as yet. However, if we consider the observed damping in the case of distilled water (Fig. 5) it appears that the signal has been attenuated by about 25 percent in a time of 10^{-2} second. In this case since T_1 and T_2 are known[15] to be long compared with 10^{-2} sec. all the observed damping must be attributed to inhomogeneities. The actual inhomogeneity in H_0 in this case was found by a measurement of line width in the conventional manner to be 0.03 gauss. This gives for $1/\gamma\Delta H_0$ a value of 1.2×10^{-3} sec., a time very much shorter than the observed damping time. On the other hand the value of T_H (Eq. (22)) is 5×10^{-2} sec. A value of T_H as large as this would not produce appreciable damping in a time of 10^{-2} sec. according to Eq. (21). Thus, it would appear that most of the observed damping in this case must be attributed to inhomogeneity in H_1. This conclusion is strengthened by the observed fact that an increase in H_1 resulted in a shorter damping time contrary to the expected result if inhomogeneity in H_0 were responsible for the damping. Further evidence is provided by the marked increase in damping off resonance. This effect is discussed in Section VIII.

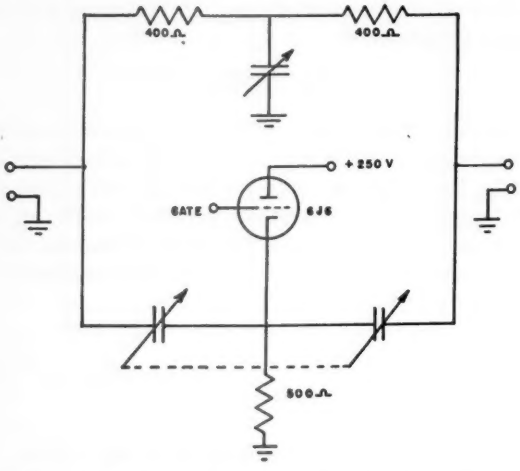

FIG. 2. Twin-T network used to pulse-modulate the radiofrequency power.

The damping in the case of glycerine (Fig. (4)) is seen to be considerably greater than for water, the extra attenuation being evidently due to natural damping. By comparing[16] the damping for glycerine with that for water for the same values of H_1 and H_0, we have obtained a value for the natural damping time for glycerine at room temperature of

$$T_0=2\left(\frac{1}{T_1}+\frac{1}{T_2}\right)^{-1}=1.1\times10^{-2}\text{ sec.}$$

The theory of Bloembergen *et al.*[3] leads to the conclusion that $T_1\sim T_2$ in this case. This assumption together with their experimental value of T_1 at room temperature is in reasonable accord with the observed value of T_0. We cite this datum not for any particular intrinsic interest but rather as an illustration of the potentialities of the pulse method in the measurement of abnormally large values of T_2.

The conventional method for the measurement of T_2 by line width observations, assuming our inhomogeneity of 0.03 gauss, would be limited to values of T_2 less than about 10^{-3} sec.

It is interesting to note that the effects of inhomogeneities can in a sense be suppressed in certain cases even if H_1 is smaller than the inhomogeneity in H_0. If for example $T_1\sim T_2$ and both T_1 and T_2 are sufficiently long (e.g., as in distilled water) so that $\beta\ll1$ and $\alpha\ll1$ even for $H_1\ll\Delta H_0$, the resultant signal to be expected can be obtained by integrating (see Eq. (5))

$$-v/m_0=\frac{m_0}{(1+\delta^2)^{\frac{1}{2}}}e^{-\beta\tau}\sin(1+\delta^2)^{\frac{1}{2}}\tau$$

over δ. The resultant signal will be

$$v_r=\int_{-\infty}^{+\infty}v(\delta)f(\delta)d\delta,$$

where $f(\delta)d\delta$ gives the distribution of δ over the sample due to inhomogeneity. In this case $f(\delta)$ varies slowly compared with v and

$$-v_r/M_0\simeq\pi f(0)m_0e^{-\beta\tau}J_0(\tau),$$

where $J_0(\tau)$ is the Bessel function of order zero.

The fact that the natural decay ($e^{-\beta\tau}$) is exponential while the decay due to the inhomogeneity given by the Bessel function $J_0(\tau)$ is slow ($\tau^{-\frac{1}{2}}$) permits their separation and the evaluation of β and hence of T_2.

VII. SENSITIVITY

It was mentioned in the introduction that considerably greater signal strengths are available in many cases from the transient than from the steady state resonance. On the other hand, the band width of the amplifying and detecting circuits are necessarily larger for the transients because of their finite durations. The ultimate sensitivity is determined by the ratio of signal-to-noise power at the indicator. We first estimate the amount of signal power available.

The tuned circuit of which the coil containing the sample forms a part will be assumed to have an unloaded quality factor Q_0 and an unloaded shunt con-

[15] Bloembergen *et al.* (reference 3) find $T_1\sim2$ sec. and predict that $T_2\sim T_1$.

[16] This comparison is possible since the two samples were located in the same position relative both to the magnet and to the radiofrequency coil.

ductance g. A change ΔV in the voltage across this circuit gives rise to an available power of

$$(P_s)_p=(\Delta V)^2/16g. \tag{23}$$

On the other hand if ΔV is caused by nuclear spin resonance

$$\Delta V=4\pi\chi''\zeta Q_0 V=2\pi Q_0 v\zeta(V/H_1), \tag{24}$$

where V is the undisturbed pulse r-f voltage, $\chi''=v/2H_1$ is the imaginary part of the nuclear magnetic susceptibility, ζ is the "filling factor" of the r-f coil (see appendix to reference 3) and v and H_1 have the meanings assigned to them in Section II. In case H_1 is sufficiently large so that $\gamma H_1 \gg 1/T_2$ and if the time between pulses $\gg T_1$, v (see Eq. (10)) consists of a damped sinusoid with initial amplitude of

$$|v_m|=M_0=\chi_0 H_0, \tag{25}$$

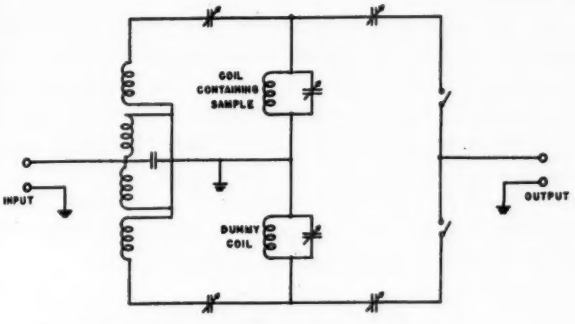

FIG. 3. Radiofrequency bridge circuit.

where χ_0 is the static susceptibility given by

$$\chi_0=N\gamma^2 I(I+1)\hbar^2/3kT, \tag{26}$$

where N is the number of spins per unit volume, I the nuclear spin, and T the absolute temperature.

The factor V/H_1 occurring in (24) may be found from the definition of Q_0:

$$Q_0=\omega W/P_0, \tag{27}$$

where

$$W=(1/2\pi)H_1^2 V_c \tag{28}$$

is the energy stored in the tuned circuit, V_c is the effective volume of the coil and

$$P_0=V^2/2g \tag{29}$$

is the power dissipated in the unloaded circuit. From (27) (28) and (29) we find

$$V^2/H_1^2=\omega V_c g/\pi Q_0. \tag{30}$$

From (23), (24), (25), (26), and (30) we obtain

$$(P_s)_p=\frac{1}{72}\zeta^2 Q_0 V_c N^2\gamma^2 I^2(I+1)^2\hbar^4\nu_0^3/k^2T^2. \tag{31}$$

Here $\nu_0=\omega/2\pi=\gamma H_0/2\pi$. Comparing (31) with the expression derived by Bloembergen *et al.*[17] for the

[17] Appendix to reference 3. We have put their factor $A=1$.

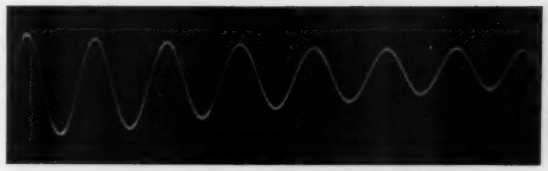

FIG. 4. Proton resonance in glycerine (exact resonance). Sweep time=0.01 sec., $H_1=0.17$ gauss, $\nu_0=9.0$ mc/sec.

available signal power $(P_s)_m$, in the modulation method we find

$$(P_s)_p=16(T_1/T_2^*)(P_s)_m. \tag{32}$$

Here T_2^* is the line width parameter which is equal to T_2 if the inhomogeneity in H_0 does not contribute to the line width and is of order $1/\gamma\Delta H_0$ if the inhomogeneity ΔH_0 is the major factor.

The factor $16T_1/T_2^*$ in (32) can be interpreted as arising in part from the fact that in the transient $v_m=M_0$ while in the steady state $v_m=\frac{1}{2}(T_2^*/T_1)^{\frac{1}{2}}M_0$ (Eq. (1)). This contributes a factor $4T_1/T_2^*$. The remaining factor of 4 is accounted for by the fact that in the modulation method the maximum signal occurs half-way down the resonance curve and thus has an amplitude of $v/2$.

The ratio of available noise power in the two methods, assuming equal noise figures, will be simply given by the ratios of the noise-band-widths, B_p for the pulse method and B_m for the modulation method:

$$N_p/N_m=B_p/B_m. \tag{33}$$

In the pulse method B_p has an optimum value which depends on the conditions of measurement. If for example we are dealing with the case $\beta\ll 1$ and if the band width is limited by a RC filter in the video amplifier the optimum band width is about $\gamma H_1/4$. With this band width the available signal power is reduced to half the value it would have for a wide band and thus if ρ is the ratio of signal-to-noise in the pulse method to that in the modulation method we obtain in this case

$$\rho=(32T_1B_m/\gamma H_1 T_2^*). \tag{34}$$

In this case it would be possible to adjust H_1 so that if $T_1\sim 1$ sec., $\rho\sim 1$ for $B_m=\frac{1}{10}$ sec.$^{-1}$. Thus for $T_1\sim 1$ sec. the sensitivity available is comparable to that of the modulation method with a narrow band width amplifier.

Of course the comparison of signal-to-noise ratios for

FIG. 5. Proton resonance in distilled water (exact resonance). Sweep time 0.01 sec., $H_1=0.15$ gauss, $\nu_0=9.0$ mc/sec.

the two methods is only qualitative at best because of the different methods of presentation. The actual comparison of sensitivities in the two cases is controlled to a considerable extent by psychological factors which are difficult to assess.

For example: according to (31) the signal strength in the pulse method does not improve if T_1 is decreased by the addition of a paramagnetic catalyst. Actually, however, the sensitivity does improve somewhat with short T_1 since the larger pulse repetition frequencies which become possible in this case permit visual integration of noise.

A further improvement in sensitivity at the expense of some distortion can be obtained by using after the detector a tuned amplifier tuned to the frequency $\gamma H_1/2\pi$ in place of the low pass video amplifier.

VIII. OTHER FEATURES AND LIMITATIONS

In Figs. 6 and 7 the appearance of the oscillations in v in glycerin is shown somewhat off resonance. Otherwise the conditions are the same as for Fig. 4. The steady magnetic field is displaced off resonance by 0.21 gauss in Fig. 6 and by 0.51 gauss in Fig. 7. As expected from the theory the frequency of the oscillations has increased following the theoretical formula (17).

The attenuation has markedly increased from resonance to 0.2 gauss off resonance. This effect which is also observed in the case of distilled water cannot be explained by the theoretical variation of the attenuation constant as given by Eq. (8). In the present case $T_1 \sim T_2$ so $\beta \sim \alpha$ and b should be nearly independent of δ. Even in the extreme case of $\alpha=0$, there would be at most a factor of two between the attenuation time on and off resonance. The observed increase can be accounted for on the basis of the inhomogeneity effect discussed above. Off resonance the dominant term in the expression for the nutational frequency is $\gamma H_0-\omega$ rather than γH_1 and the inhomogeneity in H_0, therefore, exerts a relatively strong effect on the damping. On this basis it would be expected that once $\gamma H_0-\omega > \gamma H_1$ a further increase in $(\gamma H_0-\omega)$ would not greatly affect the damping time. This expectation is confirmed by comparison of the damping in Figs. 6 and 7.

The proximity to resonance may be estimated by observation of any one of three quantities (*a*) initial amplitude, (*b*) nutational frequency, (*c*) attenuation time. In the case of glycerin or water the attenuation time is the most sensitive criterion. In the case of a substance for which $T_2 < 1/\gamma\Delta H$ this will probably not be true, however. According to Eq. (10) the initial amplitude should decrease in going off resonance in the same proportion that the nutational frequency increases. The nutational frequency can, however, be observed with much greater sensitivity than the amplitude and will probably be the most sensitive criterion for proximity to resonance in case $T_2 < 1/\gamma\Delta H$. In Figs. 6 and 7 the initial amplitude decreases faster than the nutational frequency increases because of the action of a RC filter in the video amplifier.

According to Eq. (5) the angular nutational frequency at resonance is

$$\Omega_{res}=[\gamma^2 H_1^2-\tfrac{1}{4}(1/T_2-1/T_1)^2]^{\frac{1}{2}}. \tag{35}$$

If $T_1=T_2$ or, in any case, if $\gamma H_1 \gg \frac{1}{2}(1/T_2-1/T_1)$ we should expect that $\Omega_{res}=\gamma H_1$. This prediction has been tested and verified in the case of the water resonance. There is a possibility that $1/T_2-1/T_1$ could be measured by means of Eq. (35). This could be done, however, only for small H_1 and in this case the nutational period becomes large compared with the damping time leading to a suppression of the oscillations.

It does not appear that the pulse method will be useful in ascertaining the structure of resonance lines, since the resolving power is in general somewhat less than that of conventional methods.

In the search for unknown resonance the pulse method should be useful because of its very fast response. Its utility in this application is not vitiated by the fact that ordinarily a time $>T_1$ must elapse between pulses, since (*a*) in this case relatively short pulses which do not saturate the sample are permissible and (*b*) in the act of searching no power is absorbed by the sample until one is close to resonance. We have not as yet attempted to exploit this application.

ACKNOWLEDGMENTS

We wish to acknowledge our gratitude to Professor F. G. Dunnington and the other members of the Rutgers physics research staff for much helpful assistance and encouragement, and especially to Professors H. S. Sommers, and P. R. Weiss for their stabilization of the electromagnet. We have benefited from the technical assistance of Messrs. Monroe Sheppard, Jay Thomas, Sidney Gray, and Ralph Campbell.

APPENDIX

The Bloch equations (Eqs. (2) of the text) with constant coefficients are most conveniently handled by operational methods making use of the Laplace transform:

$$\bar{f}(p)=\int_0^\infty f(\tau)e^{-p\tau}d\tau.$$

The Laplace transforms of the Bloch equations are

$$\left.\begin{aligned}(p+\beta)\bar{u}+\delta\bar{v}&=u_0M_0,\\ -\delta\bar{u}+(p+\beta)\bar{v}+\bar{M}_z&=v_0M_0,\\ -\bar{v}+(p+\alpha)\bar{M}_z&=\alpha M_0/p+m_0M_0,\end{aligned}\right\} \tag{36}$$

where $\bar{u}$, $\bar{v}$, and $\bar{M}_z$ are the transforms, and u_0M_0, v_0M_0, and m_0M_0, the initial values of u, v and M_z, respectively.

The solutions of (16) are

$$\left.\begin{aligned}p\Delta(p)\bar{u}/M_0&=u_0p[1+(p+\alpha)(p+\beta)]+\delta\alpha+pm_0+v_0,\\ p\Delta(p)\bar{v}/M_0&=u_0\delta p(p+\alpha)+v_0p(p+\alpha)(p+\beta)\\ &\qquad -(\alpha+m_0p)(p+\beta),\\ p\Delta(p)\bar{M}_z/M_0&=u_0\delta p+v_0p(p+\beta)+(\alpha+m_0p)[(p+\beta)^2+\delta^2],\end{aligned}\right\} \tag{37}$$

where

$$\Delta(p)=(p+\alpha)(p+\beta)^2+p+\beta+\delta^2(p+\alpha) \tag{38}$$

is the determinant of the coefficients in (36).

FIG. 6. Proton resonance in glycerine. Conditions same as in Fig. 4 except that H_0 is displaced off resonance by 0.21 gauss.

FIG. 7. Proton resonance in glycerine. Conditions same as in Fig. 4 except that H_0 is displaced off resonance by 0.51 gauss.

If now we let w stand for anyone of the components u/M_0, v/M_0 or M_z/M_0 it is clear that

$$\bar{w}(p)=g(p)/p\Delta(p), \tag{39}$$

where $g(p)$ is a cubic form in p, different for the three components $\bar{u}$, $\bar{v}$, and $\bar{M}_z$. Now the equation $\Delta(x)=0$ will have at least one real negative root. Let this root be $-a$, then $\Delta(p)$ can be factored into

$$\Delta(p)=(p+a)[(p+b)^2+s^2], \tag{40}$$

where it is not implied that s is necessarily real. The expression (39) for $\bar{w}(p)$ can now be expanded in partial fractions:

$$\bar{w}(p)=\frac{A}{p+a}+\frac{B(p+b)+C}{(p+b)^2+s^2}+\frac{D}{P}. \tag{41}$$

The inverse transform of this expression is

$$w=Ae^{-a\tau}+Be^{-b\tau}\cos s\tau+(C/s)e^{-b\tau}\sin s\tau+D. \tag{42}$$

The first three terms give the transient effects and the last term the steady state. The coefficients A and D are given by

$$D=\lim_{p\to 0}[p\bar{w}(p)],$$
$$A=\lim_{p\to -a}[(p+a)\bar{w}(p)].$$

The other coefficients are most conveniently found by applying the initial conditions directly to (42). We find

$$D=g(0)/a(b^2+s^2), \tag{43}$$
$$A=-g(-a)/a[(b-a)^2+s^2]. \tag{44}$$

(a) for $w=u/M_0$

$$B=-A+D+u_0,\quad C=aA+bB-\beta u_0-\delta v_0, \tag{45}$$

(b) for $w=v/M_0$

$$B=-(A+D)+v_0,\quad C=aA+bB-m_0+\delta u_0-\beta v_0. \tag{46}$$

(c) for $w=M_z/M_0$

$$B=-(A+D)+m_0,\quad C=aA+bB+\alpha(1-m_0)+v_0. \tag{47}$$

The time constants b and s are most conveniently calculated by expanding (38) and (40) in powers of P and equating coefficients. We find

$$\begin{aligned} 2b+a&=2\beta+\alpha,\\ b^2+s^2+2ab&=2\alpha\beta+\beta^2+\delta^2+1,\\ a(b^2+s^2)&=\alpha(\beta^2+\delta^2)+\beta. \end{aligned} \tag{48}$$

With the aid of the last equation the expression for D becomes

$$D=g(0)/[\alpha(\beta^2+\delta^2)+\beta]. \tag{49}$$

Substituting $g(0)$ as obtained from (37) we find for the steady state solutions

(a) $w=u/M_0$ $\qquad D=\alpha\delta/[\alpha(\beta^2+\delta^2)+\beta]$, (50a)

(b) $w=v/M_0$ $\qquad D=-\alpha\beta/[\alpha(\beta^2+\delta^2)+\beta]$, (50b)

(c) $w=M_z/M_0$ $\qquad D=\alpha(\beta^2+\delta^2)/[\alpha(\beta^2+\delta^2)+\beta]$. (50c)

These agree with steady state solutions given by Bloch. The other coefficients are more difficult to find in the general case since they depend on the solutions of the cubic $\Delta(x)=0$. However, there are certain special cases in which this cubic has simple roots and these cases are adequate to cover most conditions of physical interest.

(a) If $\delta=0$ (the condition for exact resonance) a real root of $\Delta(x)=0$ is $x=-\beta$. Then

$$a=\beta \tag{51a}$$

and from (48)

$$b=\tfrac{1}{2}(\alpha+\beta), \tag{51b}$$
$$s^2=1-\tfrac{1}{4}(\beta-\alpha)^2. \tag{51c}$$

The coefficients A, B, and C for the various components of magnetic moment are in this case (assuming $u_0=v_0=0$)

(1) $w=u/M_0$

$$A=B=C=0, \tag{52}$$

(2) $w=v/M_0$

$$A=0,\quad B=\alpha/(1+\alpha\beta),\quad C=\alpha(\alpha+\beta)/2(1+\alpha\beta)-m_0, \tag{53}$$

(3) $w=M_z/M_0$

$$A=0,\quad B=m_0-\alpha\beta/(1+\alpha\beta), \tag{54}$$
$$C=(\beta-\alpha)m_0/2+\alpha\left[1-\frac{\beta(\alpha+\beta)}{2(1+\alpha\beta)}\right].$$

(b) If $\alpha=\beta$ (i.e., $T_1=T_2$) we again find as a root of $\Delta(x)=0$, $x=-\beta$. Thence

$$a=\beta, \tag{55a}$$

and from (48)

$$b=\beta, \tag{55b}$$
$$s^2=1+\delta^2. \tag{55c}$$

We find for the coefficients A, B, and C in this case (taking $u_0=v_0=0$).

(a) $w=u/M_0$

$$\left.\begin{aligned} A&=-\delta(1-m_0)/(1+\delta^2),\\ B&=\frac{\delta}{1+\delta^2}\left(\frac{\beta^2}{1+\beta^2+\delta^2}-m_0\right),\\ C&=-\delta\beta/(1+\beta^2+\delta^2), \end{aligned}\right\} \tag{56}$$

(b) $w=v/M_0$

$$\left.\begin{aligned} A&=0,\\ B&=\beta/(1+\beta^2+\delta^2),\\ C&=-m_0+\beta^2/(1+\beta^2+\delta^2), \end{aligned}\right\} \tag{57}$$

(c) $w=M_z/M_0$

$$\left.\begin{aligned} A&=(\beta^2+\delta^2)/(1+\beta^2+\delta^2),\\ B&=(m_0-\beta^2/(1+\beta^2+\delta^2))/(1+\delta^2),\\ C&=\beta/(1+\beta^2+\delta^2). \end{aligned}\right\} \tag{58}$$

(c) A third special case of interest occurs when the radio-frequency magnetic field H_1 is sufficiently large so that $\alpha\ll 1$ and $\beta\ll 1$. Since $\alpha<\beta$ the second of these conditions implies the first. It is possible to evaluate the time factors a, b, and s under the less restrictive condition $\beta-\alpha\ll 1$.

A real root of $\Delta(x)=0$ can be extracted in this case as follows: Putting

$$z=x+\beta=\beta-a.$$

We find that $\Delta(x)=0$ reduced to

$$z=(\beta-\alpha)[1-1/(1+\delta^2+z^2)].$$

It is evident that $z<(\beta-\alpha)$ and so if $\beta-\alpha\ll 1$, $z\ll 1$ and by iteration we find

$$z=(\beta-\alpha)\frac{\delta^2}{1+\delta^2}\left\{1+\frac{\delta^2(\beta-\alpha)^2}{(1+\delta^2)^3}+\frac{\delta^4(2-\delta^2)(\beta-\alpha)^4}{(1+\delta^2)^6}+O[(\beta-\alpha)^6]\right\}.$$

For most purposes it suffices to include only the leading term.

This gives

$$a=(\beta+\alpha\delta^2)/(1+\delta^2)+O[(\beta-\alpha)^3], \tag{59a}$$
$$b=\beta-\tfrac{1}{2}(\beta-\alpha)/(1+\delta^2)+O[(\beta-\alpha)^3], \tag{59b}$$
$$s^2=1+\delta^2+O[(\beta-\alpha)^2]. \tag{59c}$$

For the coefficients A, B, and C we find in this case (again taking $u_0=v_0=0$).

(1) $w=u/M_0$

$$\left.\begin{aligned} A&=\frac{\delta}{1+\delta^2}\left(m_0-\frac{1+\delta^2}{\delta^2+\beta/\alpha}\right)+O(\beta^2),\\ B&=-\frac{m_0\delta}{1+\delta^2}+O(\beta^2),\\ C&=\frac{\delta}{1+\delta^2}\left[\frac{m_0(\beta-\alpha)(\frac{1}{2}-\delta^2)}{1+\delta^2}-\alpha\right]+O(\beta^3),\end{aligned}\right\} \tag{60}$$

(2) $w=v/M_0$

$$\left.\begin{aligned} A&=-\frac{\beta-\alpha}{(1+\delta^2)^2}\cdot\delta^2\left(m_0-\frac{1+\delta^2}{\delta^2+\beta/\alpha}\right)+O(\beta^3),\\ B&=\frac{1}{1+\delta^2}\left[\frac{(\beta-\alpha)\delta^2 m_0}{1+\delta^2}+\alpha\right]+O(\beta^3),\\ C&=-m_0+O(\beta^2).\end{aligned}\right\} \tag{61}$$

(3) $w=M_z/M_0$

$$\left.\begin{aligned} A&=\frac{\delta^2}{1+\delta^2}\left(m_0-\frac{1+\delta^2}{\delta^2+\beta/\alpha}\right)+O(\beta^2),\\ B&=m_0/(1+\delta^2)+O(\beta^2),\\ C&=\alpha+m_0(\beta-\alpha)(\tfrac{1}{2}+2\delta^2)/(1+\delta^2)+O(\beta^3).\end{aligned}\right\} \tag{62}$$

PHYSICAL REVIEW VOLUME 76, NUMBER 8 OCTOBER 15, 1949

Atomic Beam Magnetic Resonance Experiments with Radioactive Elements Na^{22}, K^{40}, Cs^{135}, and Cs^{137}*

LUTHER DAVIS, JR., DARRAGH E. NAGLE, AND JERROLD R. ZACHARIAS
*Department of Physics and Research Laboratory of Electronics,** Massachusetts Institute of Technology, Cambridge, Massachusetts*

(Received July 12, 1949)

Modifications of the atomic beam magnetic resonance method for the determination of nuclear spins and moments by observation of the hyperfine structure of atomic ground states are described which make it possible to work with very small quantities in samples with low concentrations. These modifications include the analysis of the beam by means of a mass spectrometer while performing the resonance experiment. A new source of beams of atomic alkali metals is described. The results are shown in the following tabulation:

	Spin	h.f.s. $\Delta\nu$ mgc/sec.	Nuclear magnetic moment nuclear magnetons
Na^{22}	3	1220.64 ±0.04	1.746 ±0.003
K^{40}	4	1285.73 ±0.05	−1.290 ±0.005
Cs^{135}	7/2	9724 ±8	2.724 ±0.010
Cs^{137}	7/2	10,126 ±7	2.837 ±0.010

ATTEMPTS to compare the various forms of the Fermi theory of beta-ray disintegration with experiments usually meet with the difficulty that those characteristics of the decay which make it possible to observe the nuclear angular momentum directly are just those characteristics which make the observation of the energetics of the decay more difficult and less precise. In particular, the long half-lives of C^{14}, K^{40}, and Rb^{87} permit the use of large amounts of material in observation of nuclear spin,[1,2] but the determination of the shapes[3,4] of their beta-ray spectra, especially in the low energy regions, is less reliable than could be obtained with more active materials because of the effect of scattering in the source. For tritium, on the other hand, one can work with extremely active sources because the radiation (beta-rays of less than 18 kev) is all absorbed by the containing vessel, but only recently has the spectrum shape been observed.[5] It is therefore desirable to develop a method for the observation of nuclear moments which can be applied to more energetic substances with shorter half-lives, since it is for such materials that decay schemes and spectra can be well studied. Preliminary calculations and experience with K^{40} indicated that the molecular beam magnetic resonance method might well be applicable to radio isotopes of the alkali metals because of the excellent existing method of detection. The techniques described in the present paper, devoted to Na^{22}, K^{40}, Cs^{135}, and Cs^{137}, can be extended to other nuclear species with some additional development. From the point of view of radioactive decay, Na^{22} has been most carefully studied by Good, Peaslee, and Deutsch[6] and Cs^{137} is being extensively examined by a number of workers including Townsend, Cleland, and Hughes[7] and Mitchell and Peacock.[8]

* Preliminary reports of some of these results are given by Luther Davis, Jr., Phys. Rev. **74**, 1193 (1948), Phys. Rev. **76**, 435 (1949), and D. E. Nagle, Phys. Rev. **76**, 847 (1949).

** This work was supported in part by the Signal Corps, the Air Materiel Command, and the ONR.

[1] F. A. Jenkins, Phys. Rev. **74**, 355 (1948).
[2] J. R. Zacharias, Phys. Rev. **61**, 270 (1942).
[3] D. E. Alburger, Phys. Rev. **75**, 1442 (1949).
[4] C. S. Wu and R. D. Albert, Phys. Rev. **75**, 315 (1949).
[5] G. C. Hanna and B. Pontecorvo, Phys. Rev. **75**, 983 (1949); Curran, Angus, and Cockcroft, Phil. Mag. **40**, 53 (1949).
[6] Good, Peaslee, and Deutsch, Phys. Rev. **69**, 313 (1946).
[7] Townsend, Cleland, and Hughes, Phys. Rev. **74**, 499 (1948).
[8] A. C. G. Mitchell and G. L. Peacock, Phys. Rev. **75**, 197 (1949).

In considering various possible methods for the observation of nuclear moments one is struck by the requirement imposed by chemical manipulation of minute quantities of radioactive material. One is usually forced to considerable dilution and most of the possible methods are not at their best when working with great dilutions, especially with isotopes of the element under investigation. In the method of microwave spectroscopy, collision broadening by foreign atoms reduces the line intensity in proportion to the dilution. Band spectroscopic determination of nuclear spin requires a molecule with two similar atoms and this always sets a requirement of high concentration. Hyperfine structure measurement in the visible or near visible region of atomic spectra is likely to suffer only from overlapping due to strong lines and seems to be very promising for atoms with large isotope shift. In principle, the method to be described here can be used with such small amounts of material and with such great dilution that extension of it to rare isotopes with half-lives only long enough to permit manipulation in the apparatus seems possible.

THEORY OF THE METHOD

The experimental method is a modification of the well-known molecular beam magnetic resonance method which follows in many details the experiment described by Kusch, Millman, and Rabi[9] and that described by Zacharias[2] in a determination of the nuclear spin and magnetic moment of K^{40}. The power of the method depends on the ability to observe the Zeeman effect of the atomic ground state of the isotope in question in an externally applied magnetic field which is sufficiently weak to preserve strong coupling between the nuclear spin and the resultant angular momentum of the atomic electrons. In the case of the alkali atoms discussed in the present paper, the atomic ground state is $^2S_{\frac{1}{2}}$ and in weak field this combines with a nuclear angular momentum, I, to give resultants of $F=I+\frac{1}{2}$ and $F=I-\frac{1}{2}$. The preservation of this coupling can most easily be described by saying that the nucleus finds itself in a large magnetic field (of the order of 10^6 gauss) produced by the atomic electrons which are precessing about the direction of the applied field. The combined system then has the total angular momentum $F=I+J$ where J is the angular momentum of the atomic electron configuration. The magnetic moment, however, associated with this total angular momentum F is overwhelmingly that of the electrons. Thus the magnitude of the Zeeman splitting of the atomic ground state in weak field is very closely $eH/4\pi mcF$ or 1.400 H/F Mc/sec. Observation of the frequency of transition between two adjacent levels separated only by the Zeeman splitting in weak field yields a value of F and correspondingly a value of I. To determine I for a nucleus of unknown spin, one can successively assume integral values 0, 1, 2, 3, 4, 5, 6, 7, as possible spin values for nuclei with even mass number or 1/2, 3/2, 5/2, 7/2, 9/2, 11/2, or 13/2 for nuclei with odd mass number. In a known small magnetic field the search for radiofrequency transitions is extremely simple since it is only necessary to try to observe transitions at the frequencies 1.400 H/F Mc/sec. for the eight or nine assumed I values. It should be pointed out that no prior knowledge of the nuclear magnetic moment or gyromagnetic ratio is necessary or even useful in this search. The value of the small applied magnetic field can be easily determined beforehand by observing the same type of transition with an atom of known nuclear and atomic properties. This method can be applied to any atom with a known value of the electronic angular momentum provided it is not zero. It is unfortunately not applicable to such important elements as helium, beryllium, carbon, magnesium, etc. There is an additional complication present in samples containing the radio-isotope under investigation mixed with a large amount of other isotopes. If, for instance, both isotopes have the same spin then the Zeeman effect in weak field will occur at the same frequency. Obviously this is not possible with Na^{22} and Na^{23} because the former must have integral spin and the latter has a spin of 3/2. With the cesium isotopes of odd mass number, we find that the spins are all equal. There are two methods for avoiding this trouble, and fortunately they can be used simultaneously. The first of these depends on the fact that as the applied magnetic field is increased from weak values to strong

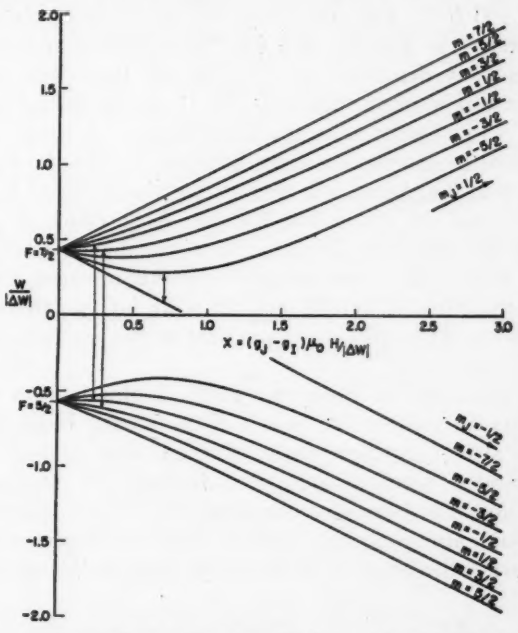

FIG. 1. Diagram to show the variation with magnetic field of the ground state energy levels for an atom with electronic angular momentum $J=\frac{1}{2}$ and nuclear angular momentum $I=3$. The nuclear magnetic moment is taken as positive. If the nuclear magnetic moment is negative the diagram is inverted and all m values change sign. The transitions marked by arrows are those observed in the present experiment with Na^{22}. The spin value is determined from observation of the transitions marked by the shortest of the three arrows.

[9] Kusch, Millman, and Rabi, Phys. Rev. 57, 765 (1940).

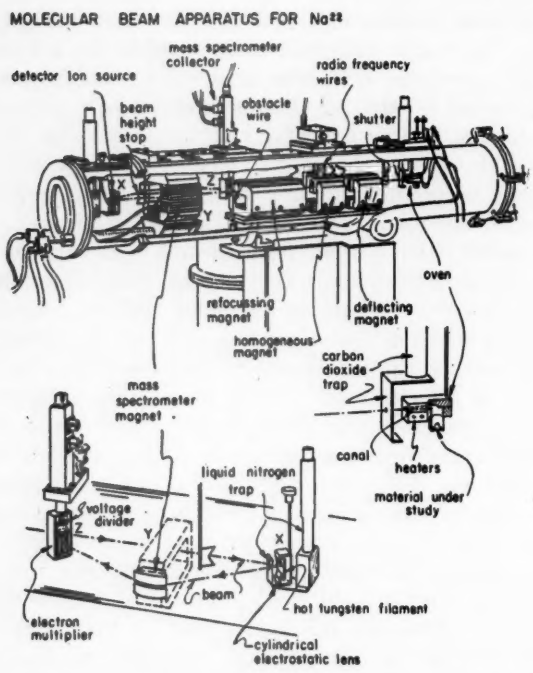

FIG. 2. Cut-away sketch of atomic beam apparatus indicating its important components. To avoid confusion, many details such as differential pumping chamber, pumping system, defining slots, and some magnet coils have been omitted.

values the coupling between I and J begins to break and the Zeeman splitting begins to depart from the value of 1.400 H/F. The behavior in the region intermediate between the Zeeman and the Paschen-Back region is completely described for $J=\frac{1}{2}$ by the Breit-Rabi formula and is shown plotted in Fig. 1 for the special case of $I=3$ and positive magnetic moment. It is most convenient to observe the transitions marked by the short arrow in Fig. 1 and it is obvious that the value of magnetic field at which the Paschen-Back effect of the hyperfine structure begins to be noticeable depends on the magnitude of the nuclear magnetic moment, since the hyperfine structure separation $\Delta\nu$ for two isotopes with the same spin is proportional to the nuclear magnetic moments.

The second of these two methods depends on the ability to convert the atoms of the atomic beam into ions after they have passed through that part of the apparatus required for the radiofrequency magnetic method. For beams of alkali metals, indium, gallium, barium, aluminum, etc., this is easily accomplished by allowing the beam to strike a hot tungsten filament of

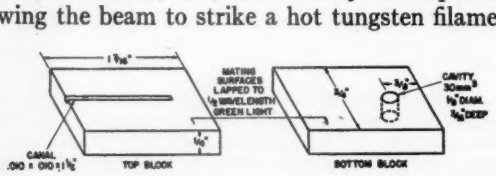

FIG. 3. Main parts of oven for beams of atomic alkali metals. Alkali azide solution is placed in bottom of cavity in bottom block. Top block is pressed against bottom one with the canal overlapping the cavity.

sufficiently high work function. The ions are then accelerated by an adjustable electric field and allowed to pass through a mass spectrometer magnet. With sufficient resolution the various isotopes can be separated and it is possible to determine whether a particular radiofrequency transition belongs to one isotope or another. Although in principle it is possible, it is certainly not practical to separate two nuclei which differ only because one of them is in an excited state. The isomeric levels of In^{113} and In^{115} are case in point. In these, however, the nuclear spins of the two states will certainly be different.

Once the nuclear spin has been determined as indicated above, it is possible to determine the hyperfine structure $\Delta\nu$, and, incidentally, the nuclear magnetic moment, by observing the Zeeman splitting in successively larger fields until the Paschen-Back effect is strong. The h.f.s. $\Delta\nu$ is then calculated from the observed frequency values and the Breit-Rabi[10] formula. It is frequently possible to make a direct observation of the h.f.s. $\Delta\nu$ by making $\Delta F=\pm 1$ transitions in weak field. Although at the present time it might not seem extremely valuable to the advancement of nuclear physics to know the h.f.s. $\Delta\nu$ of the ground state of a heavy atom like Na^{22} to the precision achievable by the radiospectroscopy method, unless the nuclear magnetic moments are similarly known, a precise value of the h.f.s. $\Delta\nu$ is nonetheless necessary in the determination of the sign of the nuclear magnetic moment by the method employed in the present paper. This method for determination of the sign of the moment depends on being able to measure the very small contribution to the magnitude of the Zeeman splitting that arises directly from the interaction of the nuclear magnetic moment with the applied field. Since this effect is of the order of one thousand times smaller than the Zeeman splitting and, since to such precision the Paschen-Back effect sets in at very small values of magnetic field, it is important not to confuse these two effects of the nuclear moment.

As will be seen later in the discussion of the apparatus, low frequency transitions in the present experiment are restricted to those for which m_F goes from $-F$ to $-(F-1)$. Although the Breit-Rabi formula expresses this transition in closed form, it is perhaps instructive to express it as an expansion about $H=0$ in order to identify the terms referred to above.

Neglecting terms in powers of H higher than two and other small terms, and letting $g_J J\mu_0/h$ equal to 1.400 Mc/sec./gauss, we can write

$$\nu=1.400H/F+1.400\mu_I H/\mu_J F +(1.400)^2(H^2/F^2)(2I/\Delta\nu). \quad (1)$$

The first term is the weak field Zeeman splitting and so predominates over the second term, which is the nuclear magnetic interaction with the applied field, that it can be used directly for the spin evaluation

[10] G. Breit and I. I. Rabi, Phys. Rev. 38, 2080 (1931).

without knowing the second term. The third term indicates the beginning of the hyperfine Paschen-Back effect. In practice, the complete Breit-Rabi formula is used, but one has to evaluate the nuclear magnetic moment and the h.f.s. $\Delta\nu$ by a series of successive approximations, obtaining first a rough value of the h.f.s. $\Delta\nu$ from which a sufficiently good value of the nuclear magnetic moment is obtained by comparison with a known stable isotope. This moment value is first assumed positive, and calculations are made with several observed frequency values to find a consistent value of the h.f.s. $\Delta\nu$. Finally, a check can be made of the h.f.s. $\Delta\nu$ directly, since by then the range of high frequency over which one is required to search is sufficiently narrowed to make the process possible. This requirement becomes more evident if it is pointed out that the range of h.f.s. $\Delta\nu$ values for the alkali metals varies from a few hundred megacycles for Li^6 to over ten thousand megacycles for Cs^{137}.

APPARATUS

Figure 2 is an artist's cut-away sketch of the apparatus. Much of the apparatus is similar to that described by Zacharias,[2] in that it was designed for use with rare isotopes in great dilution. The deflecting and refocusing magnets have relatively small ratio of gradient to field in order that a large beam height might be used. Since the beam spreads in height as it leaves the source, the ratio of gradient to field in the refocusing magnet is about half that in the deflecting magnet. Increasing its length to make up for this, offsets to only a small extent the gain from the increased beam height. The slit system is correspondingly wide by comparison with early molecular beam experiments. The widths of the source, the collimator slit, and the detector are all about 0.010 in. The obstacle wire is only a few mils wider than is necessary to shield the hot tungsten filament detector from the undeflected molecules in the beam. Those features which are novel to molecular beam technique are: (1) the oven which is designed to conserve material, (2) the mass spectrometer system which is used to separate the feeble beam of radioactive material from any other ions evaporating from the detector filament, and (3) the Allen type electron multiplier which provides an increase in sensitivity over the best conventional FP54 electrometer by a factor of about 100. The electron multiplier and associated circuits are described in a companion paper by Dr. Hin Lew.

As shown in Fig. 3 the source assembly consists of two simply constructed blocks which are held together by means of a holder containing all heaters, thermocouples, and positioning adjustments. The two lapped surfaces of the blocks when placed in contact must fit well enough so that the main leak out of the oven is through the exit canal which faces the beam detector. The narrow exit canal shown in Fig. 3 is used to diminish the number of atoms diffusing from the slit for a given

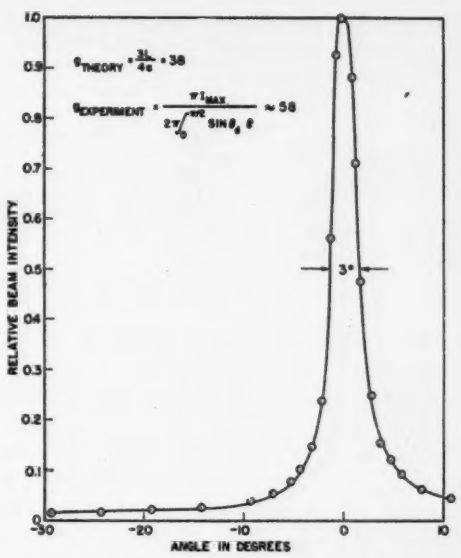

FIG. 4. Relative beam intensity as a function of angle of beam with respect to axis of the canal of the source. For this case, the dimensions of the canal were $0.12\times0.12\times6.3$ mm.

intensity toward the detector. If we define G as the ratio of atoms diffusing through a hole in an ideal thin wall to the number effusing through the canal for the same forward intensity we have following Smoluchowski[11] and Knudsen,[12] $G=3L/4A$ which is dependent only on the ratio of the length L to the width A. Measurements as shown in Fig. 4 have shown this to be roughly correct provided, of course, that the pressure in the oven is less than 3×10^{-3} mm, in order that the mean free path be larger than the length of the canal.

Trials with different kinds of materials for the oven blocks show that many materials are unsuited for minute quantities of alkali metals. One unsuccessful run using stainless steel blocks in which the free sodium was prepared by distillation from a mixture of NaCl and calcium chips displayed two sources of difficulty. The

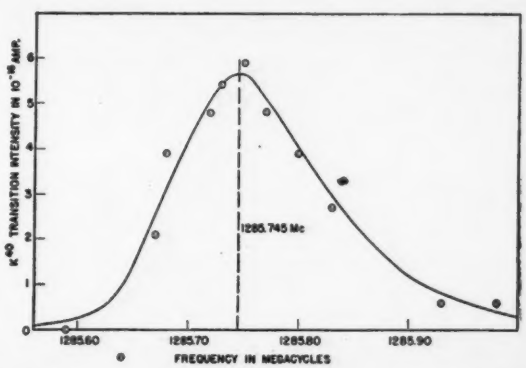

FIG. 5. Resonance curve for the unresolved transitions for the two lines in the K^{40} spectrum given by $F=9/2$, $m_F=\mp1/2\leftrightarrow F=7/2$, $m_F=\pm1/2$ for a steady magnetic field of 5.65 gauss.

[11] M. V. Smoluchowski, Ann. d. Physik **33**, 1559 (1910).
[12] M. Knudsen, Ann. d. Physik **31**, 633 (1910).

TABLE I. Observed low frequency transitions for Na^{22}. Corresponding values for the observed frequencies for Na^{23} are included so that by comparison the spin of Na^{22} can be determined.

Na^{23} freq. Mc/sec.	Na^{22} freq.	Ratio	Theoretical ratios
1.10	0.62	0.564	$I=3$ 0.572
1.40	0.80	0.572	$I=4$ 0.444
1.36	0.80	0.588	$I=2$ 0.800
10.37	5.97	0.576	
22.524	13.193	0.586	

calcium chips introduced a large quantity of Na^{23} contamination so that the beam was deficient in Na^{22} for an oven pressure that fulfilled the Knudsen condition. At the end of the run, the Na^{22}, which is an ideal tracer substance for itself, showed that even after washing the oven carefully, a large quantity remained on or in the oven walls, which could be removed only by etching away a considerable thickness of steel.

Trials with other materials such as quartz, nickel, and boron carbide showed either physical absorption or chemical reaction with the oven walls. Of the materials tried, only monel metal seemed satisfactory, and even in this case a small surface area was presented to the metal vapor to minimize such effects.

The surface ionization wire used to ionize the atoms of the beam consists of a flat tungsten ribbon, 0.007 in. wide, mounted flush with the surface of a plane metal guard electrode. These elements are held at an adjustable accelerating voltage with respect to an appropriately slotted plate 0.5 cm away which is held at ground potential. This combination provides excellent ion optics for the mass spectrometer since the field configuration is simple and the initial velocity of the ions is only that due to evaporation from the filament.

The mass spectrometer magnet as indicated in Fig. 2 is a conventional 60° wedge produced by ingot iron pole pieces. It provides an ion path radius of 8 cm in the curved portion. It is to be expected that a mass spectrograph of this sort should have an intensity efficiency of nearly unity, since there are no causes for loss of ions and because the hot tungsten filament converts all incident alkali atoms into ions.

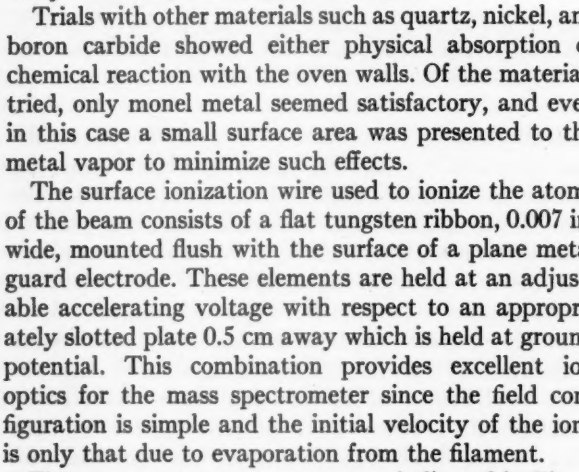

FIG. 6. Transition intensity *vs.* frequency of oscillating field for the two Na^{22} lines $F=7/2$, $m_f=\pm 1/2 \leftrightarrow F=5/2$, $m_f=\mp 1/2$ at a field of 6.17 gauss. One count/sec. is equivalent to about 7 atoms/sec.

The Research Laboratory of Electronics provides a number of signal generators for supplying the radio-frequency current in the homogeneous field "flopping" region, permitting continuous frequency coverage from 0.05 to 2500 Mc/sec. Similarly, there is a variety of frequency meters which includes a laboratory standard, frequently compared with the Bureau of Standards *WWV* 5-Mc/sec. signal.

PROCEDURE AND RESULTS

K^{40}

The first isotope to be tried by the present method was K^{40}, which because of its availability and extremely long radioactive half-life did not require the use of either the long canal oven nor the electron multiplier. A gram of potassium was loaded into a conventional molecular beam oven and heated to give a total beam at the hot wire of 10^9 atoms per second. Of this, about 10^5 atoms per second are of K^{40} and the transition intensities should be a few percent of this. An FP54 electrometer with a sensitivity of 400 ions/sec./mm makes it possible to obtain curves like that of Fig. 5. Without the mass spectrometer, these curves would be superposed on a background which requires some discussion. First, with a common element like potassium, any tungsten filament has bad contamination, which, to be sure, can be largely eliminated, by flashing momentarily to a high temperature and catching the exudate on a liquid air trap surrounding the hot wire. Second, although an obstacle wire provides an almost perfect shadow for protecting the hot wire from direct radiation from the oven, when the deflecting and refocusing fields are energized, there is a background of the order of several tenths of one percent of the beam, the origin of which is discussed more fully in the paper by Dr. Lew. Thus, even though the spin of K^{40} is even and the spins of K^{39} and K^{41} are odd, this large background would make observation of the K^{40} transitions very difficult without the introduction of the mass analysis. It is indeed the product of two discrimination factors, mass analysis and h.f.s. analysis, which permits the experiment to be performed with such small relative abundances.

The $\Delta F=0$ transitions at mass number settings 39 and 40 of the mass spectrometer were observed for various values of the homogeneous magnetic field and, in each case, the only resonance which could be found at the mass 40 position corresponded to $I=4$ for K^{40}, and the transitions for $I=3/2$, which could be clearly identified as being due to K^{39} or K^{41} which the mass spectrometer allowed to fall into the K^{40} position.

With the homogeneous field so low that it was impossible to resolve the various $\Delta F=\pm 1$ lines, search revealed transitions centered at 1285.8 Mc/sec. Sufficient field was then applied to resolve these lines and

the observations made which are shown in Fig. 5. These transitions yield a value of $\Delta\nu = 1285.73 \pm 0.050$ which confirms the previous measurement of Zacharias.[2]

Na^{22}

A sample of radiosodium was prepared in the M.I.T. cyclotron by Dr. Eric Clarke in connection with other work, using the $Mg^{24}(d,\alpha)Na^{22}$ reaction. This Na^{22} was then separated from the magnesium by Professor J. W. Irvine, Jr., who exercised the greatest precautions to avoid Na^{23} contamination during the chemical transformations. These procedures can be found in a paper by Irvine and Clarke,[13] who show that the abundance of Na^{22} in the sodium of the sample is about one part in 10^4, and who believe that most of the contamination was contained in the original magnesium target. For the purposes of the present experiment, this abundance provides a reasonable compromise between what is needed for the chemical reactions which must take place in the beam oven and the desire to reduce background as much as possible. Some of the sodium discussed above was converted to NaN_3 by Professor Irvine. A total of 3×10^{-9} mole of $Na^{22}N_3$ along with its carrier was placed in a monel metal oven and the temperature raised to 300°C so that the azide decomposed to give free nitrogen and free sodium. The decomposition of the azide is immediately obvious because of the emission of gas into the chamber surrounding the oven. After the nitrogen is pumped away, the temperature of the oven is lowered to maintain the vapor pressure of the sodium at a proper value.

With the mass spectrometer set for mass number 23, and the homogeneous field set at a value of a few gauss, the $\Delta F=0$ transition for Na^{23} was observed and the spectrometer reset for mass number 22. A search was conducted at frequencies which correspond to I of 0, 1, 2, 3, 4, 5, 6, and 7. At no frequency other than that for $I=3$ was any resonance observed. The efficiency of the electron multiplier is such that this peak corresponds to about 40 counts per second. This is just the intensity that was to be expected for the number of states for an atom with $I=3$, with the known abundance of radiosodium in the sample, and the intensity of the Na^{22} transitions mentioned above. The homogeneous field was then reset to several different values and in each case the transitions at mass 22 were observed at a frequency corresponding to $I=3$. At each value of the field it was observed that no such transition occurred at mass number 21.7 nor at mass number 22.3. Since the atomic beam apparatus, the detection system, etc., preclude the possibility of this series of transitions being due to any other type of atom or molecule, it is inescapably concluded that the spin of Na^{22} is 3. The appropriate data are shown in Table I.

Observations of this sort were continued up to a field of 170 gauss as shown in Table II. This table also

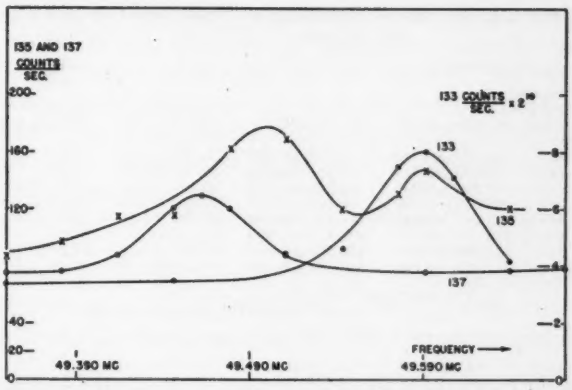

FIG. 7. Resonance curves taken for three different values of mass spectrograph setting. Open circles are for mass 137, dots for 133, and crosses for 135.

includes values of the h.f.s. $\Delta\nu$ calculated from the data on the assumption, first, that the sign of the magnetic moment is positive and, second, that the sign is negative. From these data either assumption gives reasonably self-consistent results but the results are nonetheless quite different. The magnetic field was then lowered to such a value that the $\Delta F=\pm1$ lines would be unresolved and a search was made for $\Delta F=\pm1$ transitions. Only in the neighborhood of 1220.7 Mc/sec. was any resonance observable. In order to obtain an accurate value of the h.f.s. $\Delta\nu$, the field was raised to separate the lines and the data shown in Fig. 6 were taken. The observed line at 1220.694 Mc/sec., when corrected for the small effect due to magnetic field, gives a value of the h.f.s. $\Delta\nu$ of 1220.64 Mc/sec. Thus the sign of the magnetic moment is unambiguously positive. Consideration of the possible sources of error in the high frequency measurements has led us to assign an error of 0.040 Mc/sec. By comparison with the h.f.s. $\Delta\nu$ and magnetic moment μ_I [14] of Na^{23}, we obtain a value of the nuclear magnetic moment for Na^{22} of $+1.746 \pm 0.003$ nuclear magnetons.

It is of interest to consider the amount of radioactive material used in this experiment. For Na^{22} with a 3-year half-life, the 3×10^{-9} mole loaded into the oven was determined by observing the strength of the radioactivity to be 350 microcuries. The total running time

TABLE II. Observed low frequency transitions for Na^{22}. Corresponding values for Na^{23} are included. The values of h.f.s. $\Delta\nu$ given are calculated for the two possible signs of the nuclear moment of Na^{22}.

Av. freq. Na^{22}	Av. freq. Na^{23}	h.f.s. $\Delta\nu$ of Na^{22} μ_I pos.	h.f.s. $\Delta\nu$ of Na^{22} μ_I neg.
27.719±0.020	46.038±0.020	1219.2±7.6	1234.2±7.6
30.256±0.010	50.024±0.010	1218.9±3.2	1232.6±3.2
43.126±0.020	69.694±0.020	1216.0±3.4	1225.2±3.4
95.095±0.100	141.900±0.100	1221.9±5.0	1225.4±5.0
	Weighted average of	1218.7±2.2	1229.0±2.2

[13] J. W. Irvine, Jr., and E. T. Clarke, J. Chem. Phys. **16**, 686 (1948).

[14] H. Taub and P. Kusch, Phys. Rev. **75**, 1481 (1949).

TABLE III. Transition frequencies observed with Cs^{133} and Cs^{137} and calculated h.f.s. $\Delta\nu$'s.

Magnetic field in gauss	Av. freq. Cs^{137}	Av. freq. Cs^{133}	h.f.s. $\Delta\nu$ of Cs^{137} μ_I pos.	h.f.s. $\Delta\nu$ of Cs^{137} μ_I neg.
125	44.934±0.020	45.092±0.020	10,198±250	11,301±250
136	49.162±0.015	49.338±0.010	10,130±130	11,093±130
217	79.842±0.026	80.289±0.013	10,107±80	10,673±80
257	95.531±0.030	96.198±0.030	10,160.9±69	10,627.4±69
448	175.025±0.030	177.105±0.030	10,105.9±21	10,341.3±21
693	289.280±0.070	294.873±0.090	10,115.1±21	10,247.3±21
815	352.300±0.04	360.560±0.04	10,123.5±12	10,229.5±12
1096	512.125±0.050	529.275±0.160	10,141.0±11	10,207.8±11

Weighted average $\Delta\nu=10,126.5\pm7$ Mc/sec.
$\mu_I=2.837\pm0.010$ nuclear magnetons

of the experiment was 16 hours and it was found to have required about 40 microcuries or 4×10^{-10} mole of Na^{22} evaporated from the oven, by observing that the remainder was still in the oven. It is felt that if the running time were reduced by making use of the rapid response of the electron multiplier and photographic recording of data, that it should be possible to perform such an experiment with not much more than 10^{13} atoms. It should thus be possible to work with samples with half-lives as short as are chemically feasible. For instance, 10^{13} atoms with a mean life of 10^3 sec. would amount to $\frac{1}{3}$ curie, which even if lost would not contaminate an apparatus after a few days.

Cs^{137}

A one-millicurie unit of $Cs^{137}Cl$ was obtained from the Isotopes Division of the Atomic Energy Commission. It was found to contain approximately one part Cs^{135} to one part Cs^{137}, as both are fission products and descend from unstable Xe isotopes. A total of 2×10^{-5} mole of $Cs^{133}Cl$ was mixed with 2×10^{-8} mole of $Cs^{137}Cl$ and about 3×10^{-5} mole of NaN_3 and placed in the oven. When in the vacuum the temperature was raised so that the azide decomposed to give free sodium. Because of the higher vapor pressure of Cs, it was displaced from the chloride by the sodium, yielding free cesium.

The $\Delta F=0$ transition of Cs^{133} was then observed, the mass spectrometer tuned for mass number 137, and a search conducted at each frequency corresponding to $I=1/2$ to $I=2\,3/2$. At no frequency other than that corresponding to $I=7/2$ was any transition observed, but for $I=7/2$ about 60 counts per second were observed.

TABLE IV. Transition frequencies observed with Cs^{133} and Cs^{135} and calculated h.f.s. $\Delta\nu$'s.

Av. freq. Cs^{133}	Av. freq. Cs^{135}	h.f.s. $\Delta\nu$ of Cs^{135} μ_I pos.	h.f.s. $\Delta\nu$ of Cs^{135} μ_I neg.
45.092±0.020	44.996±0.020	9777±240	10,800±240
49.338±0.010	49.235±0.010	9717±100	10,600±100
80.289±0.013	79.998±0.026	9769±80	10,290±80
360.560±0.040	355.155±0.040	9732.1±9	9825±9
408.360±0.040	402.190±0.040	9717.0±7	9795±7

Weighted average $\Delta\nu=9724.0\pm7$ Mc/sec.
$\mu_I=2.724\pm0.010$ nuclear magnetons

This is just the intensity to be expected from the known abundance ratio and the Cs^{133} intensity observed. It was shown that this transition was not associated with any other odd mass number definitely assigning it to 137. Since the atomic beam apparatus excludes the possibility of observing anything but an alkali atom, the spin of $I=7/2$ may be definitely associated with Cs^{137}.

The $\Delta F=0$ transition of both Cs^{133} and Cs^{137} were then observed for various magnetic fields up to about 1100 gauss. These data are shown in Table III, also shown are the calculated values of $\Delta\nu$ assuming μ_I first positive and then negative. Consistent results are obtained only for a positive nuclear magnetic dipole moment. As no oscillators were readily available for the frequencies associated with $\Delta F=\pm1$ transitions, the value of $\Delta\nu=10,126.5\pm7$ Mc/sec. is obtained from the $\Delta F=0$ data. By comparison with the $\Delta\nu$ and moment μ_I *** of Cs^{133} we get a nuclear magnetic dipole moment $\mu_I=+2.837\pm0.010$ nuclear magnetons.

Cs^{135}

In order to observe Cs^{135} in the sample of radioisotope obtained from the Isotopes Branch of the Atomic Energy Commission, our experimental procedure was varied slightly from that used for Cs^{137}, since there was considerable residual Cs^{133} at the 135 position of the mass spectrometer. The mass spectrometer was improved somewhat by narrowing the ionizing hot tungsten wire and the receiving slit of the electron multiplier, until the abundance resolution of the spectrometer was better than 1/100 for two mass numbers at 133. The concentration of radio isotope was increased over that for 137 to a concentration of 1/100 so that the Cs^{135} peaks might be clear of background. Figure 7 shows resonance curves taken for three different settings of the mass spectrometer. Without any question there are present three isotopes of the masses 133, 135, and 137 all with spins of 7/2, but with slightly different hyperfine structure and corresponding nuclear magnetic moments. The data of Table IV represent the experimental results and show that, in order to make them self-consistent, it is necessary to assume that the nuclear moment of Cs^{135} is likewise positive. The value of the h.f.s. $\Delta\nu$ can be taken to be 9724.0±8 Mc/sec. and the magnetic moment calculated by comparison

TABLE V. Summary of results.

	Spin	h.f.s. $\Delta\nu$ Mc/sec.	Nuclear magnetic moment μ_I in nuclear magnetons
Na^{22}	3	1220.64±0.04	1.746±0.003
K^{40}	4	1285.73±0.05	−1.290±0.005
Cs^{133}	7/2	9192.76±0.10	2.575±0.007
Cs^{135}	7/2	9724.00±8	2.724±0.010
Cs^{137}	7/2	10,126.50±7	2.837±0.010

*** The value of the nuclear moment of Cs^{133} given by Taub and Kusch (see reference 14) has been recomputed using $I_{133}=7/2$.

with the $\Delta\nu$ and the nuclear moment of Cs^{133} yields 2.724 ± 0.010 nuclear magnetons.

The result, including values for Cs^{133} given by Kusch and Taub,[15] and Bitter[16] are summarized in Table V.

DISCUSSION AND RESULTS

K^{40}

The results previously reported by Zacharias[2] have all been confirmed. In addition, it is of interest to note that the mass assignment to mass 40 is, due to the mass spectrometer, completely unambiguous. In the previous observations this assignment depended on the principle of exclusion applied to all other known alkali metals, and this type of reasoning is never quite as satisfactory as a positive identification.

The value of the h.f.s. $\Delta\nu$ determined in the present experiment completely confirms the negative sign for the magnetic moment of K^{40}. Various writers, chiefly Inglis,[17] have pointed out that with the large spin of 4, one has to invoke nuclear states with outlandishly large values of orbital angular momentum in order to concoct a negative moment. In a private communication, Dr. E. Feenberg has pointed out that, if one assumes *JJ* coupling for the coupling between the proton angular momentum and the neutron angular momentum, it is possible to devise a reasonable level scheme that will give a satisfactorily large value of the negative moment. This may add weight to the type of level scheme recently proposed by Mayer and Teller to account for the so-called magic numbers.

Na^{22}

Na^{22} is the heaviest of the nuclei with equal odd numbers of neutrons and protons for which the spin has been determined. Until the present observation it was thought that these nuclei all had a spin of 1 like the deuteron. Now it is known that B^{10} and Na^{22} depart from this rule. On the other hand, the magnetic moments of B^{10} and of Na^{22} would indicate that these nuclei can be described by the sum of an orbital angular momentum of 2 with an associated nuclear magnetic moment of 1 nuclear magneton and a spin angular momentum of 1 with a magnetic moment of that of the deuteron. We thus have to compare a theoretical value of 1.85 for both with the experimental values of 1.80 for B^{10} and 1.76 for Na^{22}.

The beta-ray spectrum and energy level scheme has been investigated by many observers, the most reliable of which seem to us to be that of Good, Peaslee, and Deutsch[6] who say that the positron emission to an excited state of Na^{22} is allowed but unfavored and is followed by a prompt gamma-ray to the ground state of Na^{22}. Direct transition by positron emission to the ground state of Na^{22} they say has not been observed. In a private communication, Professor Deutsch has said that this latter transition is less than 1 part in 5000 of the observed transition. An angular momentum change of three is sufficient to account for this result. Furthermore, if Gamow-Teller selection rules hold, then it can be concluded that the angular momentum of the excited state of Na^{22} is 2, 3, or 4. Since the positron emission and the gamma-ray are in prompt coincidence it should be possible to observe the spin of this intermediate state of Na^{22} by angular correlation experiments. Professor Deutsch and his co-workers are endeavoring to perform this experiment, which may indeed throw some light on the question of the selection rules in beta-ray theory.

Cs

The most striking feature of the present set of experimental results is a new confirmation of the observation that the addition of two neutrons to a nucleus has very little effect. In the case of these Cs isotopes this effect occurs twice with no change in spin and only a gradual change in the nuclear magnetic moment. It is not expected, however, that the ratios of the h.f.s separations will not be equal to the ratios of the nuclear magnetic moments as found by Bitter[18] in the case of rubidium, since the spins of the cesium isotopes are the same, the magnetic moments are roughly equal so that whatever nuclear volume effects give rise to the small discrepancy in rubidium would not likely be present here. We feel justified in computing the nuclear magnetic moments by the ratio method.

There has recently been considerable discussion of the spin assignment to be made to Cs^{137}, which at present is best summarized by Mitchell and Peacock[8] and by Shull and Feenberg.[19] Since the spin of Cs^{137} is unambiguously 7/2, it is now possible to conclude that the angular momentum of the 153-sec. metastable level of Ba^{137} cannot be as large as 13/2 and still maintain a probability of transition to the ground state which is small compared to the probability of transition to the metastable state. Also it is difficult to see how the spectroscopic determination of the spin of the ground state of Ba^{137} by Benson and Sawyer[20] could be interpreted to give a value of 1/2 instead of 3/2. There remains only the possibility that the theoretical interpretation of the lifetime of the metastable state and of the internal conversion ratio measurements are not adequate to differentiate between angular momentum changes of 4 and 5.

[15] P. Kusch and H. Taub, Phys. Rev. **75**, 1477 (1949).
[16] F. Bitter, Phys. Rev. **75**, 1326 (1949).
[17] D. R. Inglis, Phys. Rev. **60**, 837 (1941).
[18] F. Bitter, Phys. Rev. **76**, 150 (1949).
[19] F. B. Shull and E. Feenberg, Phys. Rev. **75**, 1768 (1949).
[20] A. N. Benson and R. A. Sawyer, Phys. Rev. **52**, 1127 (1937).

The Hyperfine Structure and Nuclear Moments of the Stable Chlorine Isotopes*

LUTHER DAVIS, JR., BERNARD T. FELD, CARROL W. ZABEL,** AND JERROLD R. ZACHARIAS
*Department of Physics and Research Laboratory of Electronics, Massachusetts Institute of Technology,*** Cambridge, Massachusetts*

(Received July 12, 1949)

The hyperfine structure of the $^2P_{3/2}$ ground states of Cl^{35} and Cl^{37} is investigated by the atomic beam magnetic resonance method. Values of the magnetic dipole interaction constant, a, and the electric quadrupole interaction constant, b, are found to be

$$a_{35}=205.288\pm0.010 \text{ Mc/sec.}, \quad a_{37}=170.686\pm0.010 \text{ Mc/sec.},$$
$$b_{35}=55.347\pm0.020 \text{ Mc/sec.}, \quad b_{37}=43.256\pm0.020 \text{ Mc/sec.}$$

No octupole interaction is required to account for the experimental results. A simple method is introduced for calculating accurate values of the electric quadrupole moments Q from these data and the corresponding values are

$$Q_{35}=-(0.0795\pm0.0005)\times10^{-24} \text{ cm}^2 \quad \text{and} \quad Q_{37}=-(0.0621\pm0.0005)\times10^{-24} \text{ cm}^2.$$

This method can be extended to many other cases for which the interaction constants a and b and the nuclear gyromagnetic ratio are known. Experimental details are given for the production and detection of beams of atomic chlorine.

I. INTRODUCTION

IN the preceding paper, henceforth referred to as DNZ, an atomic beam detecting system, capable of the separate identification of individual isotopes, has been described. In the course of those experiments it was found that a beam of chlorine could be detected. Chlorine atoms, when allowed to fall on a hot tungsten ribbon, evaporate as negative ions. These are separated, by the mass spectrometer, from the electrons which are emitted by the tungsten, and are measured as a negative ion current by an electrometer.

Chlorine contains two stable isotopes of mass numbers 35 and 37 and abundances of 75 percent and 25 percent, respectively. The nuclei of both isotopes are known[1] to have spins of 3/2. The nuclear moments were measured by Kusch and Millman[2] and by Bitter.[3] Taub and Kusch[4] have recently re-evaluated the moments; they give for the magnetic moments in nuclear magneton units:

$$\mu^{35}=+0.8222\pm0.032 \text{ percent};$$
$$\mu^{37}=+0.683\pm0.44 \text{ percent}.$$

Hyperfine structure has been observed, by the technique of microwave spectroscopy, in transitions between rotational levels in a variety of molecules containing chlorine.[1,5] The structure has been attributed to an electrostatic interaction between the nuclear electric quadrupole moment and the gradient of the molecular electric field at the chlorine nucleus. The "quadrupole coupling," eQd^2V/dz^2, has been observed for the chlorine nuclei in the simple polyatomic molecules, ClCN, ICl, and CH_3Cl.

Townes[6] has outlined a procedure for estimating d^2V/dz^2 in some molecules, based on arguments which indicate that for molecules in which Cl is covalently bonded, the gradient of the electric field at the Cl nucleus is only slightly different from the gradient in the Cl atom in the ground state. On this basis, Townes estimated the nuclear electric quadrupole moments of the Cl isotopes to be

$$Q^{35}=-6.7\times10^{-26} \text{ cm}^2;$$
$$Q^{37}=-5.1\times10^{-26} \text{ cm}^2.$$

The possibility of detecting a beam of atomic chlorine makes it feasible to measure the hyperfine structure splitting in the ground state of atomic chlorine, by the atomic beam magnetic resonance method.[7] Since the ground state of Cl is a $^2P_{3/2}$ configuration, a measurement of the hyperfine structure splitting allows a direct evaluation of the nuclear electric quadrupole moment, as described in the following section.

II. THEORY

In the present paper we are presenting the theory of atomic hyperfine structure and its Zeeman effect in greater detail than has been done by other investigators.[8,9] In applying the radiofrequency methods to atomic spectra it is frequently difficult to find some of the spectral lines necessary for the evaluation of the constants. It is also a complicated process to make a positive identification of the lines, when found. The experimental procedures lean heavily on theory because, if the interaction constants are not known in advance,

* Preliminary results have been reported in Phys. Rev. 73, 525 (1948).

** Now at Los Alamos Scientific Laboratory, Los Alamos, New Mexico.

*** This work has been supported in part by the Signal Corps, the Air Materiel Command, and the ONR.

[1] Townes, Holden, Bardeen, and Merritt, Phys. Rev. 71, 644 (1947).
[2] P. Kusch and S. Millman, Phys. Rev. 56, 527 (1939).
[3] F. Bitter, Phys. Rev. 75, 1326 (1949).
[4] H. Taub and P. Kusch, Phys. Rev. 75, 1481 (1949).
[5] Gordy, Simmons, and Smith, Phys. Rev. 72, 344 (1947).
[6] C. H. Townes, Phys. Rev. 71, 909 (1947).
[7] Kusch, Millman, and Rabi, Phys. Rev. 57, 765 (1940).
[8] D. R. Hamilton, Phys. Rev. 56, 30 (1939).
[9] N. A. Renzetti, Phys. Rev. 57, 753 (1940); G. E. Becker and P. Kusch, Phys. Rev. 73, 584 (1948).

it is necessary to use methods of successive approximation, which are alternatively theoretical and experimental, in order to determine where in the radiofrequency spectrum to search. Since a new method is presented for making accurate evaluations of nuclear quadrupole moments, it seems profitable to clarify the nature of the assumptions on which it is based.

A. The Hyperfine Structure Pattern in a Magnetic Field

The hyperfine structure of the ground state of chlorine arises out of two effects. The first is the magnetic dipole-dipole interaction, resulting from the interaction between the nuclear magnetic dipole moment with the magnetic field, at the position of the nucleus, due to the electronic configuration; the hyperfine splitting resulting from this interaction obeys the "interval rule." The second interaction is due to the nuclear electric quadrupole moment; it gives rise to deviations from the interval rule.

Characterizing the atomic electron configuration by the total angular momentum quantum number, J, and the nucleus by the spin I, the terms in the Hamiltonian for the atom which lead to the hyperfine splitting are conveniently[a] written:[10]

$$(1/h)\mathcal{H}(\text{h.f.s.})=a\mathbf{I}\cdot\mathbf{J}+bQ_{\text{op}}, \tag{1}$$

where

$$Q_{\text{op}}=\frac{3(\mathbf{I}\cdot\mathbf{J})^2+(3/2)(\mathbf{I}\cdot\mathbf{J})-I(I+1)J(J+1)}{2I(2I-1)J(2J-1)}, \tag{2}$$

and a and b are constants, of dimensions sec.$^{-1}$, characterizing the atomic and nuclear magnetic and electric properties. $Q_{\text{op}}=0$ for $J=0$ or $\frac{1}{2}$. Both terms are diagonal in the representation in which $\mathbf{F}=\mathbf{I}+\mathbf{J}$ and $m=F_z$ are good quantum numbers. For the ground state of chlorine, $I=J=\frac{3}{2}$, the relative positions of the h.f.s. levels, with respect to their center of gravity, are

$$\begin{aligned}(E/ha)_{F=0}&=-15/4+5\gamma/4,\\ (E/ha)_{F=1}&=-11/4+\gamma/4,\\ (E/ha)_{F=2}&=-\tfrac{3}{4}-\tfrac{3}{4}\gamma,\\ (E/ha)_{F=3}&=9/4+\gamma/4,\end{aligned} \tag{3}$$

where $\gamma=b/a$.

The application of an external (constant) magnetic field H, along the z axis, will remove the degeneracy. If the magnetic field is of such strength that the magnetic interaction energy is *small* compared to the *fine* structure splitting, but not necessarily small compared to the hyperfine structure splitting, the Hamiltonian becomes

$$\mathcal{H}=\mathcal{H}(\text{h.f.s.})+\mathcal{H}(\text{mag}), \tag{4}$$

$$\mathcal{H}(\text{mag})=\mu_0(g_J\mathbf{J}\cdot\mathbf{H}+g_I\mathbf{I}\cdot\mathbf{H}). \tag{5}$$

In the above $\mu_0=e\hbar/2mc$, the Bohr magneton; g_J is the Landé g-factor for the electronic configuration, and g_I is the nuclear g-factor. It is convenient to express $\mathcal{H}(\text{mag})$ in the following form:

$$\mathcal{H}'(\text{mag})=\mathcal{H}(\text{mag})/ha=xJ_z+(g_I/g_J)xI_z, \tag{6}$$

where[b] $x=\mu_0 g_J H/ha$.

The matrix for $\mathcal{H}(\text{mag})$, in the F, m representation, contains off-diagonal elements connecting terms of the same m but with F differing by ±1. The required matrix elements are given by Condon and Shortley,[11] they are

$$(F,m|J_z|F+1,m)=-\left\{\frac{[(F+1)^2-(J-I)^2](I+J+2+F)(I+J-F)[(F+1)^2-m^2]}{4(F+1)^2(2F+1)(2F+3)}\right\}^{\frac{1}{2}}, \tag{7}$$

$$(F,m|J_z|F,m)=\left\{\frac{F(F+1)+J(J+1)-I(I+1)}{2F(F+1)}\right\}\text{or,} \tag{8}$$

$$(F,m|J_z|F-1,m)=-\left\{\frac{[F^2-(J-I)^2][(I+J+1)^2-F^2][F^2-m^2]}{4F^2(4F^2-1)}\right\}^{\frac{1}{2}}. \tag{9}$$

The matrix elements for I_z are obtained by interchanging I and J when $\Delta F=0$, and by multiplying by -1 when $\Delta F=\pm1$, in the above relations.

The energy values of the system in an external magnetic field can now be obtained by solving the secular equation derived from the matrix $\mathcal{H}$. The secular equation factors into one fourth-order determinant and pairs of first-order, second-order and third-order determinants. The determinantal equations have been evaluated numerically for various values of x and γ, assuming $g_I=0$ (i.e., neglecting the term in (g_I/g_J)). The results are being collected, to be issued in a technical report of the M.I.T. Research Laboratory of Electronics. The results, for $\gamma=0$, are plotted in Fig. 1, where E/ha is plotted against x (proportional to the external magnetic field).

[a] Our definition of b differs from the one frequently used in spectroscopy, according to which the quadrupole term is taken to be $bC(C+1)$.

[10] H. Kopferman, *Kernmomente* (Edwards Brothers, Inc., Ann Arbor, Michigan, 1945).

[b] This definition of x is slightly different from the one conventionally used in cases when $J=1/2$. Becker and Kusch (see reference 9) use the same definition in their interpretation of the $^2P_{3/2}$ state of Ga.

[11] E. U. Condon and G. H. Shortley, *Theory of Atomic Spectra*, (Cambridge University Press, London, 1935), pp. 63, 64, and 67.

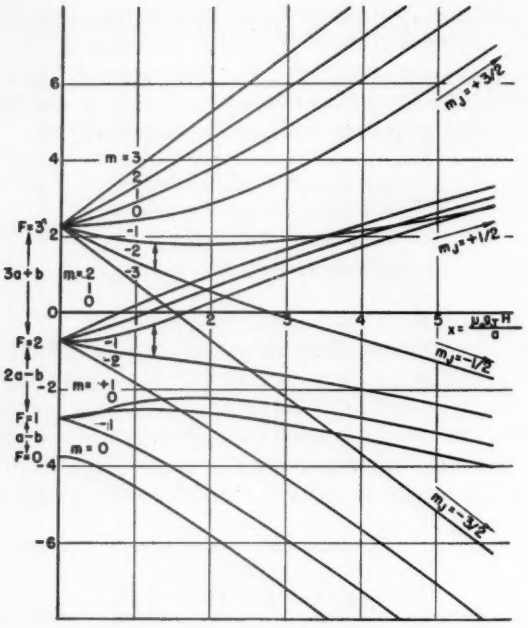

FIG. 1. Diagram to show dependence on magnetic field of the energy levels of an atom with nuclear angular momentum $I=3/2$ and electronic angular momentum $J=3/2$ on the assumption that the electron nuclear interaction arises only from magnetic dipole coupling.

B. Selection Rules and Transition Probabilities

In the magnetic resonance method, as employed in these experiments, transitions between the h.f.s. energy levels are induced by the application of a relatively weak, oscillating magnetic field. The effect of the oscillating field can be described by adding to the Hamiltonian of the system a perturbation of the form

$$\mathcal{H}'=\mu_0(g_J\mathbf{J}+g_I\mathbf{I})\cdot\mathbf{H}', \tag{10}$$

where

$$H'=(H_x'\mathbf{i}+H_y'\mathbf{j}+H_z'\mathbf{k})\sin\omega t. \tag{11}$$

In the Zeeman region of the h.f.s. the possible transitions are those for which there exist non-vanishing matrix elements of $\mathcal{H}'$ in the F, m representation.[11] These are easily seen to obey the conditions $\Delta F=0$, ±1, $\Delta m=0$, ±1. The matrix elements for $m=0$ are proportional to H_z', while those of $\Delta m=\pm1$ are proportional to $(H_x'+iH_y')$. In the experiments herein reported, the oscillating field has components in all three directions, thereby permitting the observation of both types of transitions.

Of particular interest is the value of the transition probability at resonance. It can be shown[12] that, provided the transition probability, $P_{Fm;F'm'}$, is small compared to one,

$$h^2P_{Fm;F'm'}\cong\pi^2t^2\mu_0^2g_J^2 \times|(F,m|J_xH_x'+J_yH_y'+J_zH_z'|F',m')|^2, \tag{12a}$$

where t is the time spent by the atom in the oscillating magnetic field. Because of the different values of the transition matrix element for different transitions, as seen in Table I, the optimum oscillating fields may differ by an order of magnitude from transition to transition.

C. Nuclear Moments from the Hyperfine Structure

In the absence of externally applied fields, the hyperfine structure interaction Hamiltonian is diagonal in the F, m representation; the positions of the h.f.s. levels (in units of sec.$^{-1}$) are

$$(E/h)_F=\frac{aC}{2}+b\left\{\frac{\frac{3}{4}C(C+1)-I(I+1)J(J+1)}{2I(2I-1)J(2J-1)}\right\}, \tag{12b}$$

where $C=F(F+1)-I(I+1)-J(J+1)$. Thus, measurement of the frequency difference between the h.f.s.

TABLE I. $|(F,m|\mathbf{J}|F';m')|^2\times40$ for $I=J=3/2$. The bold numbers correspond to $\Delta m=0$; these must be multiplied by $H_z'^2$ to obtain the required matrix element factor in the transition probability. The others must be multiplied by $(H_x'^2+H_y'^2)$.

F', m' \ F,m	3, 3	3, 2	2, 2	3, 1	2, 1	1, 1	3, 0	2, 0	1, 0	0, 0	1, −1	2, −1	3, −1	2, −2	3, −2	3, −3
3, 3	—	15	15													
3, 2	15	—	**10**	25	10											
2, 2	15	**10**	—	1	10	24*										
3, 1		25	1	—	**16**		30	6								
2, 1		10	10	**16**	—	24*	3	15	12*							
1, 1			24*		24*	—		4*	5	25						
3, 0				30	3		—	**18**				3†	30			
2, 0				6	15	4*	**18**	—	**32***		4	15*	6			
1, 0					12*	5		**32***	—	**50**	5	12				
0, 0						25			**50‡**	—	25					
1, −1								4†	5	25	—	24		24		
2, −1							3	15*	12		24	—	**16***	10	10	
3, −1							30	6				**16***	—	1	25*	
2, −2											24	10	1†	—	**10**	15
3, −2												10	25*	**10**	—	15
3, −3														15	15	—

* Observable in our experiment by the ordinary refocusing condition.
† Observable in our experiment by the special refocusing condition.
‡ Transition used to obtain the $F=1$, $F=0$ energy difference.

[12] I. I. Rabi, Phys. Rev. 51, 652 (1937).

lines, in zero magnetic field, leads directly to the determination of a and b.

The evaluation of the nuclear moments from the constants a and b has been discussed in complete detail by Casimir.[13] In the following, we abstract those of his results which are applicable to the experiments discussed in this and the following paper.

For an atom in which there is a single valence electron, in addition to any number of completed shells, the wave function for the valence electron can usually be written as a product of a spacial term, a term involving the orbital angular momentum (spherical harmonic), and a spin term. The magnetic h.f.s. constant, a, arises from the interaction between the nuclear magnetic dipole moment and the magnetic field, at the position of the nucleus, due to the electronic configuration

$$E_{\text{mag}} = -\boldsymbol{\mu}_{\text{nucl}} \cdot \mathbf{H}_{\text{elect}}.$$

The magnetic field at the nucleus is

$$\mathbf{H}_{\text{elect}} = -\mu_0 \langle r^{-3} \rangle_{Av} f(L, J) \mathbf{J},$$

which, when combined with

$$\boldsymbol{\mu}_{\text{nucl}} = -\mu_0 g_I \mathbf{I},$$

yields

$$ha = E_{\text{mag}}/(\mathbf{I} \cdot \mathbf{J}) = -\mu_0^2 g_I \langle r^{-3} \rangle_{Av} f(L, J). \quad (13)$$

In the above $\langle r^{-3} \rangle_{Av}$ is obtained by averaging over the spacial part of the electron wave function, and

$$f(L, J) = \frac{2L(L+1)}{J(J+1)} \mathfrak{F}, \text{ for } J = L \pm 1/2;$$

$\mathfrak{F}$ is a small relativistic correction, given by Casimir.[13]

The electric quadrupole interaction energy is given the expression

$$hb = E_{\text{quad}} = -e^2 Q \left\langle \left\{ \frac{3\cos^2\theta - 1}{r^3} \right\}_{J,J} \right\rangle_{Av}, \quad (14)$$

where the subscripts indicate that the average is to be taken over the electronic configuration in the state $m_J = J$. The nuclear electric quadrupole moment is conventionally defined as

$$Q = Z\langle (3z^2 - r^2)_{I,I} \rangle_{Av}, \text{ averaged over the nucleus.}$$

On the assumption of the separability of the electron wave function,

$$\left\langle \left\{ \frac{3\cos^2\theta - 1}{r^3} \right\}_{J,J} \right\rangle_{Av} = \langle (r^{-3}) \rangle_{Av} R \langle (3\cos^2\theta - 1)_{J,J} \rangle_{Av}, \quad (15)$$

[13] H. B. G. Casimir, *On the Interaction between Atomic Nuclei and Electrons* (Teyler's Tweede Genootschap, Haarlem, 1936), pp. 57, 58.

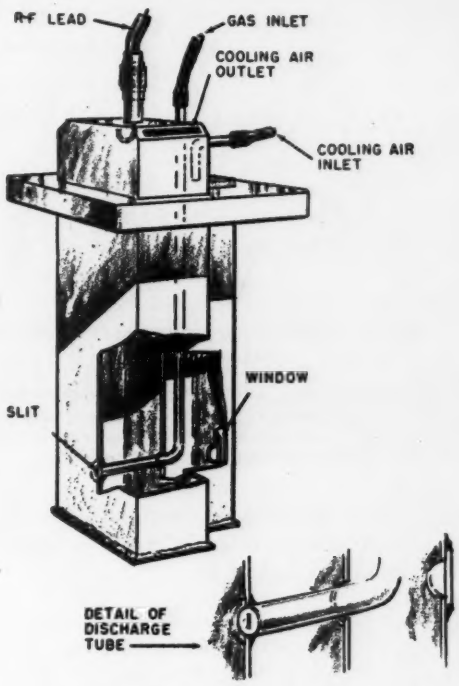

FIG. 2. Cut-away sketch of resonant cavity and gas system for producing atomic chlorine from Cl_2.

with

$$\langle (3\cos^2\theta - 1)_{J,J} \rangle_{Av} = \frac{-2L}{2L+3} \text{ for } J = L + 1/2. \quad (16)$$

R is still another small relativistic correction. For other values of $J \neq L + \frac{1}{2}$ the evaluation of $\langle (3\cos^2\theta - 1)_{J,J} \rangle_{Av}$ is somewhat more complicated, but we need only point out that

$$\langle (3\cos^2\theta - 1)_{J,J} \rangle_{Av} = 0 \text{ for } J = \tfrac{1}{2}.$$

In the particular case of interest in our experiments, the electronic configuration is $^2P_{3/2}$. It is, however, important to note that for chlorine, we are dealing not with a single valence electron, but with an electron shell which lacks a single electron of being closed. As

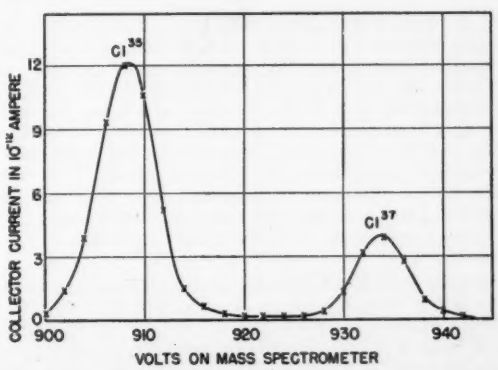

FIG. 3. Mass spectrometer curve presented to show ease with which it is possible to work with the separate chlorine isotopes. Care must be taken to avoid searching for Cl^{37} spectrum lines with the mass spectrograph set for mass 35.

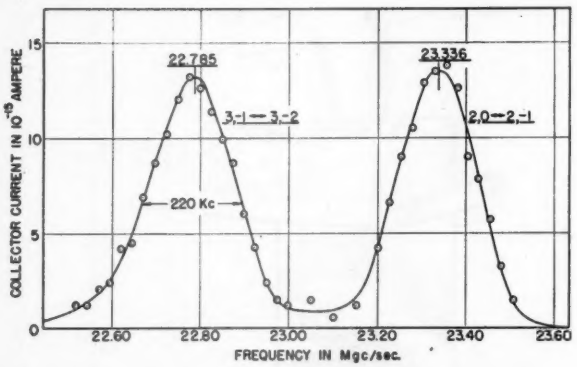

FIG. 4. Resonance curves for the two low frequency resonances, which fulfill the refocusing condition of the present experiment. The widths of the lines are due to inhomogeneity of the steady magnetic field. Similar curves are obtained for Cl^{37}.

far as the above relations are concerned, this is equivalent to a single valence electron in a $^2P_{3/2}$ state, except for a change in the sign of b.[c]

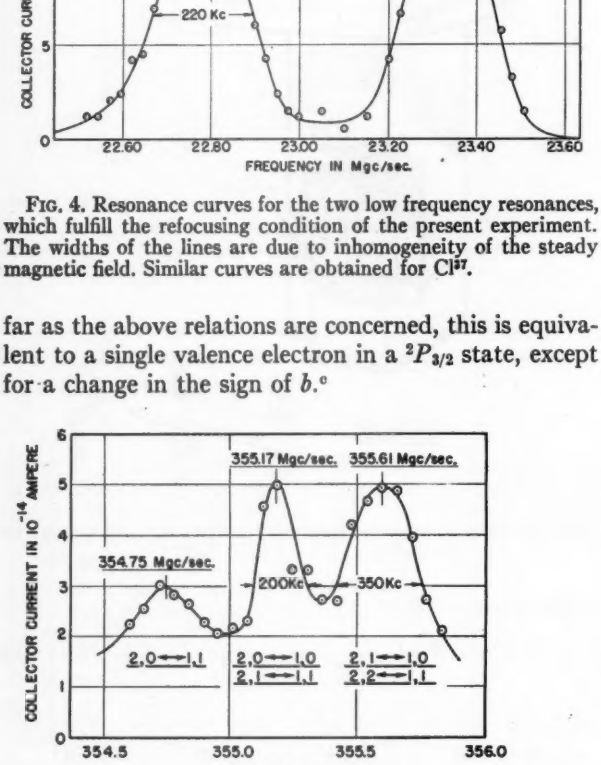

FIG. 5. Upper curve shows resonance curve for Cl^{35} for the transitions between $F=1$ and $F=2$. The five possible transitions are coalesced into three. The intensities can be qualitatively accounted for by considering the transition probabilities of Table I and remembering that in the present experiment the radiofrequency field is predominantly perpendicular to the steady field. The line widths are due to inhomogeneity of the steady field, and to incomplete superposition of adjacent peaks. Lower part of diagram shows positions, frequencies, and quantum number assignments for five of the high frequency transitions of Cl^{35}, in a field strong enough so that all five lines are resolved.

[c] The case of a closed shell minus one electron can be treated by subtracting, from the energy of the closed shell (no h.f.s.), the interaction due to a single electron in a $^2P'_{3/2}$ state, with $\mathbf{S}'=-\mathbf{S}$, $\mathbf{L}'=-\mathbf{L}$, and $\mathbf{J}'=-\mathbf{J}$. Since both magnetic terms in the h.f.s. formula are linear in J', and must be subtracted, there results no change in sign. The quadrupole term, however, is quadratic in J'; hence, subtraction leads to a change of sign.

Alternatively, it is possible to replace the hole in the shell by an electron and a positron both having quantum numbers $\mathbf{S}'$, $\mathbf{L}'$, $\mathbf{J}'$, but with the positron having a *negative* mass. This treatment yields the same results.

Both methods lead to an inversion in the order of the fine structure doublet, as compared to the single electron case.

Combining all factors, we have, for the h.f.s. interaction constants of Cl,

$$ha=-\mu_0^2 g_I \mathfrak{F}\frac{2L(L+1)}{J(J+1)}\langle r^{-3}\rangle_{Av}, \tag{17}$$

$$hb=-e^2QR\frac{2L}{(2L+3)}\langle r^{-3}\rangle_{Av}, \tag{18}$$

$$\gamma=(b/a)=\frac{e^2Q}{\mu_0^2 g_I}\frac{R}{\mathfrak{F}}\frac{J(J+1)}{(L+1)(2L+3)}=\frac{3}{8}\frac{e^2Q}{\mu_0^2 g_I}\frac{R}{\mathfrak{F}}. \tag{19}$$

From the definition of the nuclear g-factor,

$$g_I=-(m/M_P)\mu/I,$$

where μ is the nuclear magnetic moment in nuclear magnetons, we have, alternatively,

$$\gamma=-\tfrac{3}{8}(e^2/\mu_0^2)(M_P/m)(I/\mu)(R/\mathfrak{F})Q. \tag{20}$$

In the approximation used above, in which it is valid to separate the radial and angular electron wave functions, the dependence of a and b on r is, in both cases, through the same factor, $\langle r^{-3}\rangle_{Av}$. Hence, the ratio γ does not involve the radial factor, and the value of Q can be obtained directly from γ and a knowledge of μ. However, if μ is not known, or if it is desired to compute either a or b, it is necessary to be able to obtain $\langle r^{-3}\rangle_{Av}$ by an independent means. The separation between the two members of the fine structure doublet provides an estimate of $\langle r^{-3}\rangle_{Av}$. Casimir gives for the doublet separation, δ,

$$h\delta=\mu_0^2 Z_i(2L+1)H\langle r^{-3}\rangle_{Av}. \tag{21}$$

Here H is still another relativistic correction, and Z_i is slightly (≈ 4 units) less than the nuclear charge. The main difficulty, in using this relationship to estimate $\langle r^{-3}\rangle_{Av}$, arises from the uncertainty in Z_i.

III. APPARATUS

The apparatus used in this experiment is the same as that described by DNZ with minor modifications. A source of atomic chlorine is needed in place of the oven for alkali beams and it was found possible to use chlorine with the discharge tube previously used by Nagle, Julian, and Zacharias for atomic hydrogen.[14] Their source has not been described elsewhere and a diagram of it is shown in Fig. 2. A glass tube with a narrow slit in one end is placed at a voltage antinode in a microwave resonant cavity so that a glow discharge occurs in the chlorine gas for a centimeter or so directly behind the slit. To maintain the discharge, it was necessary to feed into the resonant cavity about 50 watts of cw radiation at 3000 Mc/sec. Cooling of the outer wall

[14] Nagle, Julian, and Zacharias, Phys. Rev. 72, 971 (1947).

of the glass tube was adequately provided by an air blast. In this device no metal is in contact with the atomic gases and a good ratio of atoms to molecules is found in the resulting beam, as shown by simple magnetic deflection analysis. The flow of chlorine at a rate of 1 cm³ at N.T.P. per minute was controlled by a Bourdon-type variable leak.

Beam detection was accomplished by the use of the same tungsten hot wire surface ionization detector used by DNZ. In the present experiment, the accelerating potential was reversed so that negative ions produced at the surface of the wire would pass through the mass spectrometer. The efficiency of the detection of chlorine in this manner was found to be about 10^{-4}, but varied from this and in some cases was less by a factor of 10. In the first attempt to detect a beam of chlorine, the efficiency of formation of negative ions correlated well with the existing data on the work function of tungsten and the electron affinity of atomic chlorine, which gives 10^{-4} as the Boltzmann factor. The experiments reported were done at this efficiency. Subsequent attempts with different tungsten wire gave efficiencies from 100 to 1000 times smaller. Figure 3 shows a curve of intensity *versus* accelerating voltage for chlorine. In the experiments the isotope was selected by adjusting the accelerating voltages.

IV. EXPERIMENTS

A. The Determination of the h.f.s. Constants

The experiments were of the "flop-in" type, used first by Zacharias[15] and described in DNZ. In this type of experiment there is a selection rule in addition to the usual $\Delta F=0, \pm1$, $\Delta m=0, \pm1$. For detection of the transition, the effective atomic magnetic moment must have reversed directions in the field of the deflecting and refocusing magnets. Assuming that the spins of the Cl nuclei are $\frac{3}{2}$, it may be seen from Fig. 1 that eleven transitions satisfy all these conditions, when the fields in the deflecting and refocusing magnets are sufficiently large so that x is ten or more. Two of these transitions as shown in Fig. 4 have $\Delta F=0$, $\Delta m=\pm1$ and for them the corresponding frequencies approach zero as the field approaches zero. The remaining transitions are of the $\Delta F=\pm1$, $\Delta m=0, \pm1$ type. With the fields of the magnets adjusted to refocus atoms which make a transition involving a change in m_J at high fields ($x>10$) of $\pm\frac{1}{2}\leftrightarrow\mp\frac{1}{2}$, the two observable low frequency transitions $(3,-1\leftrightarrow3,-2)$ and $(2,0\leftrightarrow2,-1)$ were easily found for both isotopes. To first-order in H the two transitions have the same frequency.

$$\nu(3,-1\leftrightarrow3,-2)=\frac{g_J\mu_0H}{2h}+\frac{1}{20}\frac{(g_J^2\mu_0^2H^2)}{ha(1+\gamma/3)}, \quad (22)$$

$$\nu(2,0\leftrightarrow2,-1)=\frac{g_J\mu_0H}{2h}+\frac{1}{20}\frac{g_J^2\mu_0^2H^2}{ha}\times\left\{\frac{2}{(1-\gamma/2)}-\frac{1}{3(1+\gamma/3)}\right\}. \quad (23)$$

The second-order terms indicate that the $(2,0\leftrightarrow2,-1)$ transition will have the higher frequency, provided γ is sufficiently small.

Most of the high frequency transitions, observable with the above refocusing condition, occur between the states $F=2$ and $F=1$. The corresponding transition frequencies will be found near the value $2a-b$ for small x. An estimate of the $F=2\leftrightarrow F=1$ transition

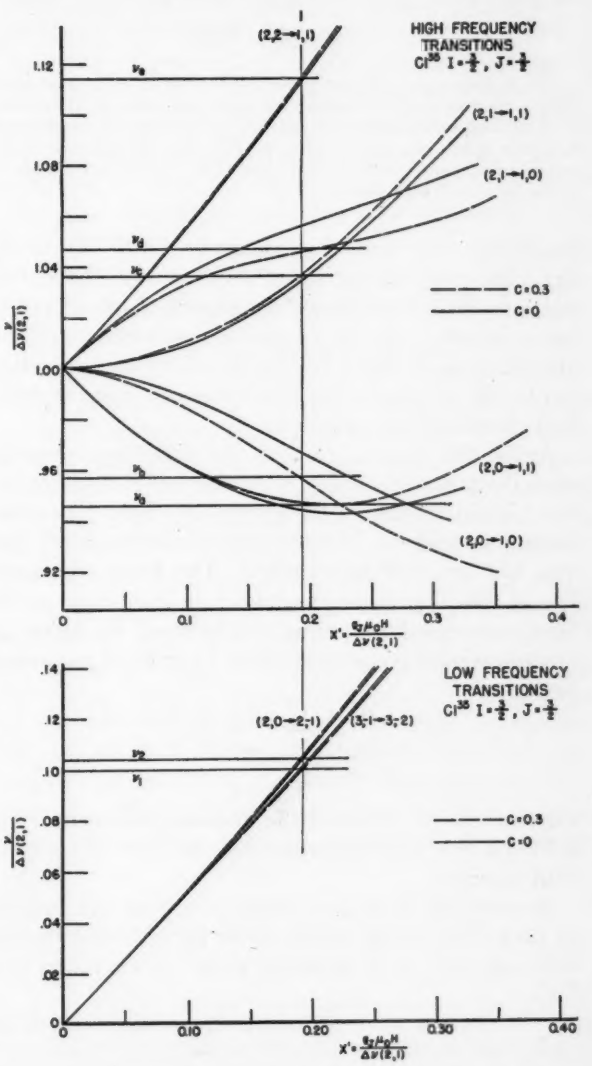

FIG. 6. Plot of the transition frequencies in terms of $\Delta\nu(2,1)=2a-b$ for the seven transitions between states $F=1$ and $F=2$ subject to the refocusing condition that m_J change from $\pm\frac{1}{2}$ to $\mp\frac{1}{2}$. The solid curves are plotted for b/a assumed zero and the dashed curves for $b/a=0.3$. The horizontal lines are drawn in at ordinate values corresponding to observed transitions. They should intersect the theoretical curves for one pair of values of x' and b/a.

[15] J. R. Zacharias, Phys. Rev. 71, 909 (1947).

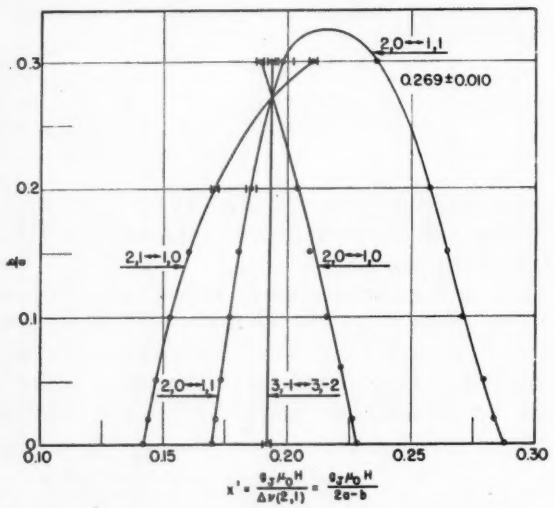

FIG. 7. Plot of b/a against x' for four of the experimental data. Each experimentally observed frequency is used to determine pairs of values of b/a and x', in the neighborhood of values expected to give a consistent set for all four. The common point of intersection of all four curves yields a value of b/a, which is substituted in the secular determinant.

frequency was made by assuming $b/(2a-b)$ to be negligible and solving for $(2a-b)$ in the above two relations for low frequency transitions observed at the same (small) x. In this manner a first estimate of 340 Mc/sec. was obtained for the frequency corresponding to $(2a-b)$. A search near this frequency value in weak fields revealed five resonances.

Again the identification of the transitions depends upon the assumed value of γ. As the field is reduced, the two highest frequency lines which are field dependent become unresolved. The next two lines also merge into one, but are field independent. The lower frequency line is field dependent, increasing in frequency as the field is decreased. Assuming γ to be small, the following identification is tentatively made. In order of increasing frequency,

$$a=(2,\,0\leftrightarrow1,\,1),\quad d=(2,\,1\leftrightarrow1,\,0),$$
$$b=(2,\,0\leftrightarrow1,\,0),\quad e=(2,\,2\leftrightarrow1,\,1).$$
$$c=(2,\,1\leftrightarrow1,\,1),$$

Figure 5 shows curves of the unresolved lines at a low field and the relative positions of the lines at a greater field strength.

Attempting to obtain a value of γ from the analysis of these data, using second-order perturbation theory, does not result in a consistent value. It was found that when the value of the homogeneous field was sufficiently low, so as to make second-order theory applicable, the large line width made the accuracy of the measurements insufficient to determine γ. A numerical solution of the secular determinant for the energy levels was then made for several values of x and γ. With these, a graphical analysis was made on a set of data taken at a field high enough to permit accurate frequency measurements. Figure 6 is a plot of the theoretical transition frequency *vs.* $x'=g_i\mu_0H/(2a-b)$ for two assumed values of γ for the five transitions of interest. The observed transition frequencies, in the same magnetic field, are shown as horizontal lines, from which it is easily seen that the value $\gamma=0$ does not correlate with the observed frequencies for any given value of x', while $\gamma=0.3$, $x'\cong0.19$ would be consistent with the data. When the same data, and curves for several values of γ are plotted with expanded scales, the appropriate values of x' and γ can easily be determined. Figure 7 is a plot of the values of γ which yield the observed frequencies, against the field parameter x'. The only consistent values are $\gamma=0.269\pm0.010$ and $x'=0.196$.

From this preliminary determination of γ and the value of $2a-b$, the other two zero field h.f.s. separations may be calculated and search for them can be undertaken. With the same refocusing condition, $m_J=\pm\frac{1}{2}\leftrightarrow\mp\frac{1}{2}$, the only observable transition between $F=3$ and $F=2$ is $(3,\,-1\leftrightarrow2,\,-1)$. A resonance was found at 671.208 Mc/sec. which was field independent and could be ascribed to the $(3,\,-1\leftrightarrow2,\,-1)$ transition.

There are no transitions between the states $F=1$ and $F=0$ involving a change in the sign of the effective atomic magnetic moment at high fields. However, the effect of a non-refocusing transition was observed by establishing a competition which involved atoms in one of the states for which a transition can be observed. The apparatus was adjusted so that a transition was being observed between the states $F=1$ and $F=2$, say $(2,\,1\leftrightarrow1,\,0)$. If now a second r-f field is superposed at a frequency which corresponds to the transition $(1,\,0\leftrightarrow0,\,0)$, there will exist a competition for atoms which are in the state, $F,\,m=1,\,0$. Those atoms which make the transition $(1,\,0\rightarrow0,\,0)$ will be, in the high field of the second deflecting magnet, in a state of $m_J=-\frac{3}{2}$ and thus will be deflected past the detector ribbon. The observed $(2,\,1\leftrightarrow1,\,0)$ transition intensity will therefore decrease. Such an effect was observed; with a $(2,\,1\leftrightarrow1,\,0)$ intensity corresponding to a 300-mm

TABLE II. Frequencies of various transitions observed in weak magnetic field.

	Cl^{35}			Cl^{37}		
Transition used	$(1,\,0\rightarrow0,\,0)$	$(2,\,0\leftrightarrow1,\,0)$	$(3,\,-1\leftrightarrow2,\,-1)$	$(1,\,0\rightarrow0,\,0)$	$(2,\,0\leftrightarrow1,\,0)$	$(3,\,-1\leftrightarrow2,\,-1)$
Observed frequency	150.020 mc	355.229	671.208	127.477 mc	298.116	555.310
$\Delta F=0$ transition frequency $(3,\,-1\leftrightarrow3,\,-2)$	0.510 mc	0.500	1.500 mc	0.499	0.516	1.500
Corrected frequency $(x=0)$	149.996 mc	355.230 mc	671.212	127.428	298.117	555.317 mc
Theoretical splitting $(x=0)$	$a-b$	$2a-b$	$3a+b$	$a-b$	$2a-b$	$3a+b$

TABLE III. Values of nuclear electric quadrupole moments.

Nucleus	γ	μ	I	$\mathcal{F}/R$	$Q\times10^{24}$ cm^2
$_{13}Al^{27}$	0.198	3.6419	5/2	0.99640	0.156
$_{17}Cl^{35}$	0.26961	0.8222	3/2	0.99385	−0.0795
$_{17}Cl^{37}$	0.25342	0.683	3/2	0.99385	−0.0621
$_{31}Ga^{69}$	0.32768	2.001	3/2	0.97960	0.2318
$_{31}Ga^{71}$	0.16252	2.543	3/2	0.97960	0.1461
$_{49}In^{115}$	1.85599	5.502	9/2	0.94930	1.166

galvanometer deflection, a decrease of 30 mm was observed when the frequency corresponding to the (1, 0→0, 0) transition was applied.

Precise values of the h.f.s. separation frequencies were obtained by observing a high frequency transition, for which $F=\pm1$, and a low frequency transition for which $F=0$, both in the same very small field. The $F=0$ transition frequency and the approximate values of a and b were used to obtain the value of the field parameter, x, which was then used in the expressions obtained by second-order perturbation theory to correct the measured frequency of the $F=\pm1$ transition to its value at zero field. Table II contains the results for both isotopes.

B. Sign of the Magnetic Moment

As described in the previous paper, a change in the sign of the nuclear magnetic moment alters the energy level diagram, shown in Fig. 1, in three ways: (1) The diagram will invert; for a positive moment, which corresponds to positive a, the largest F value has the highest energy, while for a negative moment, the lowest F value has the highest energy. (2) The inversion of the diagram, with change of sign of the nuclear moment, is accompanied by a change of the signs of the low field quantum number m and the high field quantum numbers m_I and m_J. Thus the curve in Fig. 1 which corresponds to $F=1$, $m=-1$, and $m_I=\frac{1}{2}$, $m_J=-\frac{3}{2}$ for positive a, becomes $F=1$, $m=1$, $m_I=-\frac{1}{2}$, $m_J=\frac{3}{2}$ for a negative moment. (3) Change of sign produces a slight change in the energy level values, as described in DNZ.

A particular observable transition frequency will, therefore, involve states whose quantum numbers depend upon the sign of the nuclear magnetic moment. Since the direction of the forces on the atoms in an inhomogeneous magnetic field depends upon the sign of m_J, the trajectory for a given transition will depend upon the sign of the nuclear moment.

A transition frequency was chosen which corresponds to a change in m_J from $+\frac{1}{2}$ to $-\frac{3}{2}$, if μ_n is positive, and from $-\frac{1}{2}$ to $+\frac{3}{2}$ if μ_n is negative. To observe this transition, the field in the refocusing magnet must be lowered by a factor of three, to refocus the $m_J=\pm\frac{3}{2}$ states. A determination of which of the two possible trajectories is the one involved in the transition is made by observing the transition intensity as the obstacle wire is moved to obstruct one of the possible paths.

The experiment was done with Cl^{35} by observing the transition characterized by $(2, 0, -\frac{1}{2}, \frac{1}{2}\rightarrow1, -1, \frac{1}{2}, -\frac{1}{2})$ for nuclear moment assumed positive or characterized by $(2, 0, \frac{1}{2}, -\frac{1}{2}\rightarrow1, 1, -\frac{1}{2}, \frac{1}{2})$ for nuclear moment assumed negative. The intensity corresponding to this transition was found to disappear when the wire was moved in the direction of decreasing field. Therefore, it can be concluded that the sign of the Cl^{35} nuclear moment is positive. The experiment was not repeated for Cl^{37}, but it is assumed that the signs of the magnetic moments are alike for the two isotopes, since the magnitudes of the spin, magnetic, and quadrupole moments are so similar.

V. RESULTS AND DISCUSSION

A. The Nuclear Spin

One result of the experiments described above is to confirm the assignment of the spin value $\frac{3}{2}$ for both chlorine isotopes. The spin value is arrived at by two independent sets of observations: (1) The observed h.f.s. pattern is consistent with no other value of the nuclear spin than $I=\frac{3}{2}$ and no other value of the electronic angular momentum than $J=\frac{3}{2}$. Any other values would lead to a completely different set of observable transitions, and a completely different dependence of the frequencies of these transitions on the strength of the applied magnetic field. (2) Observations of the slope of the curve of frequency *vs.* applied field, for the low frequency transitions in weak magnetic field, are consistent only with $I=\frac{3}{2}$, assuming a $^2P_{3/2}$ electronic configuration. The use of this method for nuclear spin determination has been described in the preceding paper.

TABLE IV. Effective nuclear charge, Z_i, as computed from the magnetic h.f.s. splitting and the fine structure.

Isotope	Z	I	State	a(Mc/sec.)	$\delta(10^4$ Mc/sec.)	$\mathcal{F}/H$	Z_i	$Z-Z_i$
Al^{27}	13	5/2	$^2P_{1/2}$	488.0	335.78	1.0127	9.85	3.15
			$^2P_{3/2}$	94.27		0.9996	10.04	2.96
Cl^{35}	17	3/2	$^2P_{3/2}$	205.288	2641.0	0.9993	13.64	3.36
Cl^{37}	17	3/2	$^2P_{3/2}$	170.686		0.9993	13.63	3.37
Ga^{69}	31	3/2	$^2P_{1/2}$	1338.78	2476.1	1.0770	25.72	5.28
			$^2P_{3/2}$	190.790		0.9974	33.43	−2.43
Ga^{71}	31	3/2	$^2P_{1/2}$	1701.05	2476.1	1.0770	25.73	5.27
			$^2P_{3/2}$	242.424		0.9974	33.44	−2.44
In^{115}	49	9/2	$^2P_{1/2}$	5706.5	6632.8	1.2175	41.87	7.13
			$^2P_{3/2}$	242.156		0.9925	64.35	−15.35

TABLE V. Ratio of magnetic h.f.s. interactions.

Isotope	$a(1/2)/a(3/2)$ uncorrected	$\mathfrak{F}(1/2)$	$\mathfrak{F}(3/2)$	$a(1/2)/a(3/2)$ corrected
Al^{27}	5.17	1.017	1.004	5.10
$Ga^{69,71}$	7.02	1.102	1.020	6.50
In^{115}	9.43	1.291	1.052	7.68

B. The h.f.s. Interaction Constants

The data of Table II lead to the following values of the interaction constants

$$a_{35}=205.288\pm0.010 \text{ Mc/sec.},$$
$$b_{35}=55.347\pm0.020 \text{ Mc/sec.},$$
$$\gamma_{35}=(b/a)_{35}=0.26961\pm0.00010,$$
$$a_{37}=170.686\pm0.010 \text{ Mc/sec.},$$
$$b_{37}=43.256\pm0.020 \text{ Mc/sec.},$$
$$\gamma_{37}=(b/a)_{37}=0.25342\pm0.00010.$$

The measurements yield three independent frequencies between the 4 h.f.s. levels, but there are only two independent constants involved. The fact that all the data are consistent with the above constants, to within the experimental accuracy, provides an excellent check for the theory of the atomic hyperfine structure and its Zeeman effect, and indicates that we have not left out of consideration any significant interactions.

In addition, this consistency enables us to set an upper limit for the nuclear magnetic octupole interaction. An expression for the nuclear magnetic octupole term in the atomic h.f.s.[d] has been derived by Kramers and by Casimir and Karreman,[16]

$$E_{\text{oct}}=hc\{C^3+4C^2+\tfrac{1}{2}C[-3J(J+1)I(I+1)+J(J+1)+I(I+1)+3]+4I(I+1)J(J+1)\}. \quad (24)$$

For $I=J=\frac{3}{2}$, this becomes

$$E_{\text{oct}}=hc\left[C^3+4C^2-\frac{507}{20}C+\frac{225}{4}\right]. \quad (25)$$

TABLE VI. Comparison of atomic and molecular nuclear electric quadrupole interaction constants.*

Nucleus	Molecule	$-eQ[(\partial^2V)/\partial Z^2]$ in Mc/sec.
Cl^{35}	atom	110.694
	ClCN	83.2
	ICl	82.5
	CH_3Cl	75.13
	SiH_3Cl	40.0
Cl^{37}	atom	86.512
	ClCN	65.9
	CH_3Cl	59.03
	SiH_3Cl	30.8

* These values are taken from B. T. Feld, Preliminary Report No. 2, Nuclear Science Series, Nat. Res. Council (1948). The references to the original work may be found in that report.

[d] We are indebted to Dr. W. A. Nierenberg for helpful discussions concerning the correct form of the octupole term.

[16] H. A. Kramers, Proc. Roy. Acad. Amsterdam **34**, 965 (1931); H. B. G. Casimir and G. Karreman, Physica **9**, 494 (1942).

If this term is added to the expression for the interaction energy, the three measured frequencies can then be solved for the three unknowns, a, b, and c. Within the accuracy of the experimental results, $c=0\pm1$ kc/sec.

C. The Nuclear Electric Quadrupole Moments

From the expressions given in Section B, the nuclear electric quadrupole moment of Cl is

$$Q=-(8/3)(\mu_0^2/e^2)(m/M_P)(\mu/I)(\mathfrak{F}/R)(b/a), \quad (26)$$

$$Q=-0.54137(\mu/I)(\mathfrak{F}/R)(b/a)\times10^{-24} \text{ cm}^2. \quad (27)$$

For chlorine, $\mathfrak{F}/R=0.99385$; together with our values for a and b and the values of Taub and Kusch[4] for μ_{35}, we get

$$Q_{35}=(-0.0795\pm0.0005)\times10^{-24} \text{ cm}^2,$$
$$Q_{37}=(-0.0621\pm0.0005)\times10^{-24} \text{ cm}^2.$$

The negative sign follows from the observation that (b/a) is positive and that μ is positive, in agreement with the independent determination of the sign of μ by Kusch and Millman.[2] The accuracy of the above values of Q is limited only by the accuracy in the knowledge of μ, and in the calculation of the relativistic corrections.

The method used by us to evaluate Q is much more accurate than the one involving the fine structure splitting. As far as we know, it has not been previously used, even in the cases where a, b, and μ were known with sufficient accuracy. We have therefore re-evaluated the results of the previous measurements, and obtained more accurate values of the nuclear electric quadrupole moments as shown in Table III. The Ga data are from the paper of Becker and Kusch.[9] The values for In^{115} were given by Mann and Kusch.[17] The nuclear moments are taken from the Table III of Taub and Kusch.[4]

D. Atomic Properties from the h.f.s.

As previously noted, the usual procedure for evaluating the nuclear electric quadrupole moment, from the observed h.f.s. interaction, involves the use of the atomic fine structure splitting, δ, in order to eliminate the factor $\langle r^{-3}\rangle_{Av}$. This method requires estimating the factor Z_i the effective nuclear charge, which is usually taken to be $Z-4$. We have eliminated this uncertainty, by the method discussed in the preceding sections.

However, it should be possible to reverse the usual procedure, and to obtain an estimate of Z_i from the observed h.f.s. and fine structure splitting, by comparing the magnetic dipole interactions in the two cases. Application of the formulas yields

$$Z_i=(\mu/I)(m/M)(\mathfrak{F}/H)\frac{2L(L+1)}{(2L+1)J(J+1)}\left(\frac{\delta}{a}\right). \quad (28)$$

The values of Z_i, computed from this formula on the

[17] A. K. Mann and P. Kusch, Phys. Rev. **76**, 163 (1949).

basis of the constants previously discussed, are given in Table IV. Whenever available, the h.f.s. interactions in the $^2P_{1/2}$ state have been used as well as those for the $^2P_{3/2}$ state.

The most striking aspect of Table IV is the serious failure to obtain agreement, for the heavy elements, between the two values of Z_i calculated, from the constants for the two atomic states. Indeed, for Ga and In the values of Z_i, derived from the $^2P_{3/2}$ data, are actually larger than the nuclear charge, Z. This discrepancy is very serious, and casts considerable doubt on the adequacy of the theory, in the case of heavy elements.

The failure of the theory for heavy elements is probably associated with its breakdown at distances close to the nucleus. The value of $\langle r^{-3}\rangle_{Av}$ is strongly dependent on the shape of the wave function close to the nucleus, as is the quantity $\langle(1/r)(\partial V/\partial r)\rangle_{Av}$, which appears in the expression for δ, and which is approximated by $Z_i\langle r^{-3}\rangle_{Av}$.

The departures of the theory from the simple form, applicable for light elements, is presumably taken into account by the relativistic corrections. For Ga and In the individual corrections become quite large, although the ratios which appear in some of our expressions, may be fortuitously small. Thus, for instance, the correction, $\mathfrak{F}$, for the nuclear magnetic dipole interaction constant, is 1.102 for Ga and 1.291 for In, in the $^2P_{1/2}$ states. The large size of these corrections is another manifestation of difficulties with the simple theory at distances close to heavy nuclei.

The conclusion to be drawn from the failure of the theory is that the radial dependence of the wave function, in the vicinity of the nucleus, is different for the $J=\frac{3}{2}$ and the $J=\frac{1}{2}$ states. This is illustrated by a comparison of the magnetic dipole h.f.s. terms, for the same nucleus, corresponding to these states. The simple theory gives

$$[(a/\mathfrak{F})^2P_{1/2}/(a/\mathfrak{F})^2P_{3/2}]=5.$$

Table V gives the experimental values of the above ratio, uncorrected for relativistic effects (column 2), and corrected (last column). For the heavy nuclei, the ratio deviates considerably from the value 5.

It should be pointed out that, despite the discrepancies discussed above, the values of the nuclear electric quadrupole moments, computed by our method and given in Table III, do not suffer from these difficulties. Our method takes advantage of the fact that, whatever the shape of the electronic wave function, the dependence on the wave function is the same for both the magnetic dipole and electric quadrupole terms, and can therefore be eliminated, provided only that the radial and angular dependence are separable.

While there seems no reason to believe that the failure of the theory is associated with any inadequacy of the Russel-Saunders coupling approximation, these results indicate that L-S coupling requires more careful investigation, in the case of heavy nuclei.

E. Molecular Properties from the h.f.s.

As mentioned in the introduction to this paper, C. H. Townes has proposed a method for computing the nuclear electric quadrupole interaction in certain molecules. The nuclear electric quadrupole moments of the chlorine isotopes, as estimated by Townes, are in reasonable agreement with the values obtained by us.

However, once the nuclear electric quadrupole moment is known, the molecular h.f.s. constant can be used to obtain information concerning the molecular properties. In particular, for a molecule in which the Cl atom is predominantly covalently bonded, the deviation of the observed quadrupole interaction constant, $eQ(\partial^2V/\partial Z^2)$, from that predicted from the atomic case can be used to draw conclusions regarding the amount of non-covalent bonding, the $s-p$ hybridization, and other important molecular properties.

Table VI compares the quadrupole interaction constants of atomic Cl and a number of symmetric rotor molecules. The atomic constant, which corresponds to the molecular $eQ(\partial^2V/\partial Z^2)$ is, in this case, $-2b$; the factor, -2, arises from the fact that the molecular quadrupole interaction constant is defined as the average about the axis of molecular symmetry.

The Hyperfine Structure of the $^2P_{3/2}$ State of Al^{27}. The Nuclear Electric Quadrupole Moment

HIN LEW
Department of Physics and Research Laboratory of Electronics, Massachusetts Institute of Technology, Cambridge, Massachusetts*
(Received July 12, 1949)

The hyperfine structure of the $3p\ ^2P_{3/2}$ state of Al^{27} has been measured by the atomic beam magnetic resonance method. The magnetic dipole and electric quadrupole interaction constants a and b have been found to be

$$a=94.25\pm0.04 \text{ Mc/sec.}, \quad b=18.76\pm0.25 \text{ Mc/sec.}$$

From these, the electric quadrupole moment of the nucleus has been calculated to be

$$Q=(0.156\pm0.003)10^{-24} \text{ cm}^2.$$

INTRODUCTION

THE experiment on Al^{27}, which is the subject of this paper, was undertaken as part of the program of this laboratory to measure the nuclear spins and quadrupole moments of light nuclei by the atomic beam magnetic resonance method. Among the nuclei in which there is theoretical interest are the boron nuclei. The high boiling point and the high ionization potential make the problems of generation and detection of an atomic beam of boron rather formidable. As a step towards boron, it was decided to try aluminum, which has a lower boiling point than boron, but a higher boiling point than any that had previously been done by the atomic beam magnetic resonance method. Its ionization potential is lower than that of boron but is sufficiently high so that it was not certain whether it could be detected by the familiar surface ionization method. It is related to boron in belonging to the same chemical family. Both have a $^2P_{1/2}$ atomic ground state and a $^2P_{3/2}$ atomic metastable state. The interaction between the atomic electrons in these two states and the respective nuclei is thus similar in the two elements. The theory of this interaction is exactly the same as that for chlorine described in the preceding paper,[1] hereafter referred to as DFZZ.

The nuclear spin and magnetic moment of Al^{27} were known prior to the present experiment. Further, the hyperfine splitting in the atomic ground state had been measured. A spin of $(5/2)\hbar$ for Al was first found by Heyden and Ritschl[2] using optical spectroscopic methods. This has been confirmed by the present experiment. The first accurate determination of the g-value of the nucleus was made by Millman and Kusch[3] by the magnetic resonance method using a beam of molecules. They obtained a nuclear g-factor of $-1.451\pm0.004\ \mu_n/\hbar$. With $I=5/2$, the nuclear magnetic moment of Al^{27} is 3.628 ± 0.010 nuclear magnetons and positive. The hyperfine separation of the $3p\ ^2P_{1/2}$ ground state of Al was measured by Jackson and Kuhn,[4] who found

$$\Delta\nu(F=3\rightarrow F=2)=0.048\pm0.001 \text{ cm}^{-1}$$
$$=1440\pm30 \text{ Mc per sec.}$$

It is the purpose of this paper to report the measurement of the hyperfine separations of the atomic $^2P_{3/2}$ metastable state and to calculate from them the nuclear electric quadrupole moment.

THEORY

The interaction between the atomic electrons in the $^2P_{3/2}$ state and the nucleus with $I=5/2$ gives rise to four hyperfine levels corresponding to total quantum numbers $F=1$, 2, 3, and 4. When the atom is placed in an external magnetic field H, each hyperfine level is split up into $2F+1$ magnetic levels. There are therefore $(2I+1)(2J+1)=24$ magnetic levels belonging to the $^2P_{3/2}$ term. These levels are the eigenvalues of the Hamiltonian

$$\mathcal{H}/h=aI\cdot J+bQ_{0p}+g_J\mu_0 J\cdot H+g_I\mu_0 I\cdot H,$$

where the meanings of the symbols are as explained in DFZZ. This assumes that perturbations due to states near the $^2P_{3/2}$ are negligible, an assumption which will subsequently be examined. The calculation of the eigenvalues is exactly similar to that for chlorine described in DFZZ, except that I is 5/2 instead of 3/2. The results for $b=0$ are shown in Fig. 1. It is noted that the h.f. separations are given in terms of the constants a and b by

$$\begin{aligned}\Delta\nu(F=4\rightarrow F=3)&=4a+4b/5,\\ \Delta\nu(F=3\rightarrow F=2)&=3a-9b/20,\\ \Delta\nu(F=2\rightarrow F=1)&=2a-4b/5.\end{aligned} \tag{1}$$

Thus, when any two separations are known, the constants may be calculated.

The interval factor a may be estimated from the fine structure separation $3\ ^2P_{3/2}-3\ ^2P_{1/2}=112.01 \text{ cm}^{-1}$. This is done through the use of the relations for a and δ in Section IIC of DFZZ. Using $g_I=-1.451\ m/M$ and $Z_i=Z-3.5$, we get for the $^2P_{1/2}$ state $a\cong500$ Mc/sec. and for the $^2P_{3/2}$ state $a\cong100$ Mc/sec.

Once a and b have been determined from the h.f.

* This work has been supported in part by the Signal Corps, the Air Materiel Command, and the ONR.
[1] Davis, Feld, Zabel, and Zacharias, Phys. Rev., this issue.
[2] M. Heyden and R. Ritschl, Zeits. f. Physik **108**, 739 (1938).
[3] S. Millman and P. Kusch, Phys. Rev. **56**, 303 (1939).
[4] D. A. Jackson and H. Kuhn, Proc. Roy. Soc. **A164**, 48 (1938).

separations, the quadrupole moment of the nucleus is calculated by the method described in DFZZ.

THE METHOD OF THE EXPERIMENT

The method used in the present experiment is the atomic beam magnetic resonance method. The particular variation used is that described in detail by Davis, Nagle, and Zacharias in a preceding paper.[5] Of the transitions between levels of the hyperfine multiplet which are allowed by the selection rules, only those are observable in which m_J at high magnetic fields changes sign between the initial and final states. In the present experiment, the gradients in the deflecting fields are such that only transitions between levels with equal and opposite m_J are observable. Hence, the observable transitions are governed by the selection rules:

$$\left.\begin{aligned}\Delta F&=0,\pm1\\ \Delta m_F&=0,\pm1\end{aligned}\right\}\text{in the } C \text{ field},$$
$$m_J=\tfrac{1}{2}\rightleftarrows m_J=-\tfrac{1}{2} \text{ in the deflecting fields.}$$

APPARATUS

The apparatus in which the present experiment was performed is the one described in the paper of DNZ. Except for the source of atoms, all of the components used in the radioactive nuclei experiments are also used in the aluminum experiment. There are some differences in the operating conditions, however, and these differences are discussed below.

In a high magnetic field the effective magnetic moment of Al atoms in the $^2P_{3/2}$ metastable state with $m_J=\pm\frac{1}{2}$ is $\mp\frac{2}{3}$ Bohr magneton as compared to one Bohr magneton for the alkalis. The temperature of the Al atoms is about 1650°K as compared to, for example, 540°K for Na. Hence, greater deflecting power or narrower slit widths are required for Al. The deflecting power used is the maximum that the apparatus is capable of, *viz.*, about 7000 gauss/cm in the *B* magnet and about 16,000 gauss/cm in the *A* magnet. The widths of the various slits used are as follows: source slit 0.01 cm, collimator slit 0.01 cm, detector slit 0.015 cm. Calculations indicate that with this geometry, about 90 percent of the atoms should be deflected completely away from the detector. Actually about 50 percent of the beam was never deflected, possibly because of a high percentage of aluminum molecules in the beam.

To stop the insufficiently deflected atoms or molecules from reaching the detector, an obstacle wire of 0.013 cm in diameter is placed in the direct path of the beam at the end of the *B* magnet. Atoms which undergo the proper transitions are caused to go around the obstacle wire to reach the detector.

The detector used for aluminum is the one described in DNZ. The wire used for ionization is commercial tungsten. Its operating temperature is about 1780°K. At this temperature, the surface of the wire is probably free from tungsten oxide. Hence, the work function of the surface is that of pure tungsten, i.e., 4.5 volts. The efficiency of this surface in the ionization of aluminum atoms, which have an ionization potential of 5.98 volts, is experimentally estimated to be about 10^{-6}. The efficiency goes up with an increase in temperature of the tungsten. However, it has been found that tungsten of commercial purity, when heated to temperatures of 1700°K and above, gives off ions of elements which are present in the tungsten as impurities. In a mass spectrographic analysis of the ions, the atoms Na^{23}, Al^{27}, K^{39}, K^{41}, and Cs^{133} are identified. These Al ions always constitute an undesirable background. The intensity of ions from impurities in the filament increases with its temperature. Although this intensity decreases with age and with flashing, it was not possible to reduce it to zero. The temperature of 1780°K used in the present experiment seemed to be the best compromise between background and detection efficiency under the conditions of the experiment.

The ions from the detector, after having been analyzed by a mass spectrograph, are allowed to strike the first plate of an electron multiplier. Electrons liberated from this plate are multiplied by a succession of surfaces of high secondary-emission ratio and finally cause a pulse of voltage to appear at the last stage. This voltage pulse is amplified by a vacuum-tube amplifier and counted in a pulse counting system.

Prior to the experiments described in the present series of papers, the ions from the surface ionization detector have always been measured as an ion current by means of a d.c. amplifier and galvanometer. The practical limit of sensitivity of which this method is capable is set by the maximum time constant that can be tolerated. In atomic beam work, the maximum tolerable time constant is about ten seconds, for otherwise, the search for transitions would be very tedious and severe requirements would be imposed on the constancy of the atomic beam. Under these restrictions, a usable sensitivity of about 3×10^{-17} amp./mm is about the best that has been attained. By counting individual ions, however, it is possible to do better than this. An electron multiplier can be constructed which has a background counting rate of less than one a second. The time constant of the instrument is less than a microsecond. The time required for an individual reading, however, is dictated by statistical considerations. When the transition intensities are appreciably above the background, the short time constant permits a rapid search for transitions.

The construction of the multiplier used in this experiment and in the experiments of Davis, Nagle, and Zacharias is shown in Fig. 2. The geometry of the plates is copied from that of the RCA 931-A.** The material of the electrodes is commercial beryllium

[5] Davis, Nagle, and Zacharias, Phys. Rev., this issue.

** The author wishes to thank Dr. A. M. Glover of RCA for providing him with several sets of nickel dynodes of the 931-A with which some preliminary experiments were done.

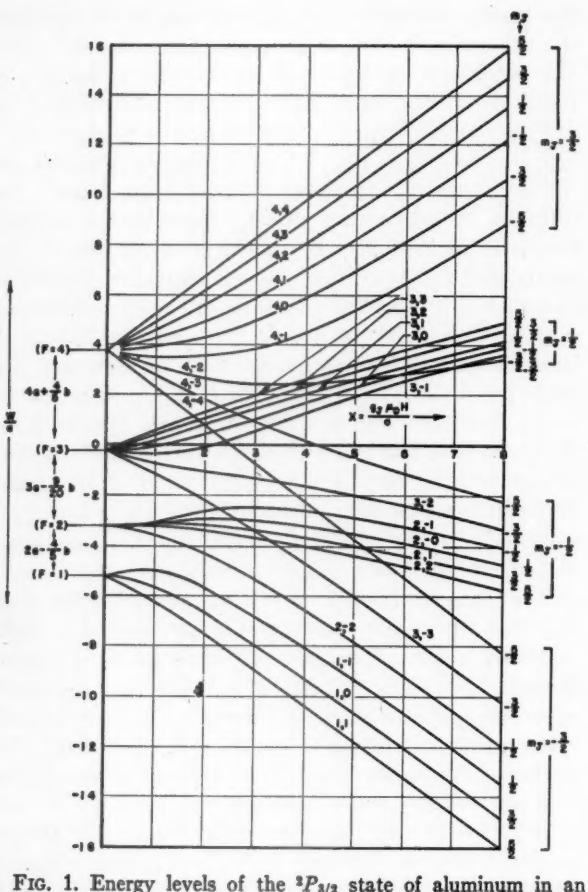

FIG. 1. Energy levels of the $^2P_{3/2}$ state of aluminum in an external magnetic field with the nuclear quadrupole moment assumed zero.

copper alloy (4 percent Be, 96 percent Cu), 0.012 cm thick. The two end pieces between which the dynodes are mounted are of Lavite. Just before the dynodes are mounted in position between the Lavite pieces, they are scrubbed with fine emery cloth and washed in acetone. The assembly is then placed in a vacuum and heated for about fifteen minutes at 900–1100°K, as recommended by Allen.[6] The vacuum should be about 10^{-5} mm Hg. The heating may be by induction or by radiation. When this temperature range is greatly exceeded, it is found that the Be—Cu deposits metal on the Lavite, resulting in leakage between the dynodes. All matter which has a higher vapor pressure than Be—Cu, such as cadmium and solder, should be excluded from the vicinity of the multiplier during the heat treatment. After the firing, the multiplier is immediately mounted in its housing. The housing is a rectangular iron box lined with thin mica. It holds, in addition to the multiplier, a bank of eleven resistors mounted on a piece of Lavite. Ten of these resistors constitute a voltage divider whereby the proper operating voltages for the multiplier are obtained; the eleventh resistor is the output load resistor. The resistors are of ½-watt, 10-megohm rating and are of the commercial type with composition bodies. Although they probably have a high vapor pressure, the gas they give off is insufficient to affect the vacuum of the apparatus in which they are used. Connection between the dynodes and the proper terminals on the resistor bank is made by 0.06 cm nickel wire insulated with glass tubing. A total of 3000 volts is applied to the voltage divider, thus providing 300 volts between successive stages of the multiplier. For positive ion detection, the first dynode is at −3000 volts with respect to the box or ground. Thus, ions entering the front slit of the box acquire an additional 3000 electron-volts of energy before striking the multiplier.

A multiplier constructed in the above manner has been found to have an efficiency of 15 percent in the detection of Na and K ions of 3600 ev total energy. That is, 15 percent of the incident ions give measurable pulses.

In the apparatus of DNZ, the multiplier is located near the inlet port of an oil diffusion pump of 600 liters/sec. capacity. It has been observed that, with the multiplier in this position, the background counting rate is of the order of 30 a second. This is ten or twenty times as high as it is when the multiplier is situated several feet from the mouth of a well-baffled pump. It may therefore be that there are ions in the oil vapor. At any rate, when a copper baffle cooled with liquid air is placed immediately in front of the multiplier, the background counting rate goes down to less than one a second. The baffle has a slit which is in line with the entrance slit of the multiplier.

When the ion intensity incident on the multiplier is so great that the counting rate exceeds 10,000 per second, it is not convenient to count the individual pulses from the multiplier with the counting circuits we have on hand. However, the ion current is then large enough to be measured with a d.c. amplifier and galvanometer. The ions are collected on a probe mounted just beside and parallel to the slit of the multiplier. The ion beam is deflected onto the probe by changing the accelerating voltage in the ion source. It is obvious that one can measure the counting efficiency of the multiplier with this arrangement.

The oven which is the source of aluminum atoms is shown in Fig. 3. It consists essentially of an aluminum oxide crucible placed within a thin-walled graphite jacket. Tantalum foil is wrapped around the crucible to prevent it from being in contact with the graphite. The aluminum to be evaporated is placed in the crucible in the form of wire. This design of the oven was arrived at through trial and error. Our first attempt was to use a molybdenum tube of the same shape as the graphite jacket and to put the aluminum to be evaporated in direct contact with the molybdenum. It was found that the aluminum crept up the walls of the tube and clogged the slit. Then we tried replacing the molybdenum with graphite. We found then that the molten aluminum

[6] J. S. Allen, Rev. Sci. Inst. 18, 739 (1947).

went into the pores of the graphite and cracked it. Containing the aluminum in a tantalum cup placed within the graphite jacket did not overcome the trouble because the aluminum crept over the sides of the cup and down into the graphite again. An aluminum oxide crucible was then tried and found to contain the aluminum satisfactorily. It was necessary, however, to isolate the crucible with tantalum foil from direct contact with the graphite in order to prevent its reduction by the carbon.

The heating of the oven is accomplished by passing alternating current directly through the graphite jacket. With water-cooled radiation shielding surrounding the oven, 800 watts of power is necessary to raise the temperature of the oven in the region of the slit to 1670°K, the operating temperature. The maximum usable temperature of this oven is about 1700°K for, beyond this, the aluminum oxide seems to decompose and liberate enough oxygen to cause the pressure in the oven chamber to exceed 5×10^{-5} mm Hg. The intensity of the aluminum beam then drops because of scattering.

Although the temperature of the central region of the oven is about 1670°K, that of the coolest part is probably somewhat below this. This temperature has not been measured but it may be estimated by the amount of time a given charge of aluminum lasts in the oven. A charge of 0.17 gram lasts about six hours. The effusion rate through the slit is then about 3×10^{-7} mole/sec. Using a well-known formula for the rate of effusion of atoms through a hole in a thin wall,[7] the vapor pressure in the oven is calculated to be 0.17 mm Hg. This vapor pressure corresponds to a temperature of 1650°K[8] and therefore the coolest part of the oven is at this temperature. This estimate is rough because some of the aluminum combines with the graphite to form yellow Al_4C_3 and is therefore lost from the beam. On the other hand, the decomposition of the Al_2O_3 of the crucible yields Al atoms which contribute to the beam.

At 1650°K, about 65 percent of the atoms are in the $^2P_{3/2}$ metastable state which is 112 cm^{-1} above the $^2P_{1/2}$ ground state. The mean life of an atom in the metastable state is long compared to the transit time in the apparatus.

For the alignment of the apparatus and the calibration of the homogeneous C field during measurements on aluminum, a beam of sodium atoms is used. An oven for the generation of a sodium beam is mounted beside the aluminum oven. It is of iron and is heated by radiation from a tungsten coil. It may be moved in front of the aluminum oven through an external control to the proper oven position.

The sources of radiofrequency power are a General Radio Type 805C signal generator which covers the range from 16 kc to 50 mc and a F-4800 Lighthouse Tube Airborne Transmitter which covers the range from 270 mc to 2500 mc. Frequency is measured in their respective ranges on a General Radio Type 620A heterodyne frequency meter and calibrator and a U. S. Army Signal Corps Type TS-175/U frequency meter.

EXPERIMENTAL PROCEDURE

When all the components of the apparatus except the Al oven are lined up by means of a sodium beam, the aluminum oven is brought up to a temperature of about 1670°K, as observed by an optical pyrometer. The obstacle wire is swung out of the line of the beam and the Al oven is moved into a position which gives the maximum detected beam intensity. With the tungsten ribbon detector at about 1780°K, the detected beam intensity as measured by the galvanometer should correspond to a counting rate of the order of 300,000 a second. This figure may vary by as much as 50 percent, for it depends strongly on the temperature of the tungsten ribbon. In any run, the latter is adjusted to give the maximum ratio of transition signal to background.

After the positioning of the Al oven, the obstacle wire is swung back into position. This cuts off the beam entirely and the counts registered by the multiplier on mass number 27 are due mostly to Al ions given off by the tungsten detector itself. Under our conditions of operation, the counting rate is about 500 a second. When the A and B deflecting fields are turned on, however, but without any r-f power in the C region, the counting rate goes up to from 2000 to 5000 a second. The reason for this is that high velocity atoms in the penumbra of the beam are deflected so little that the joint effect of the two deflecting fields working in the

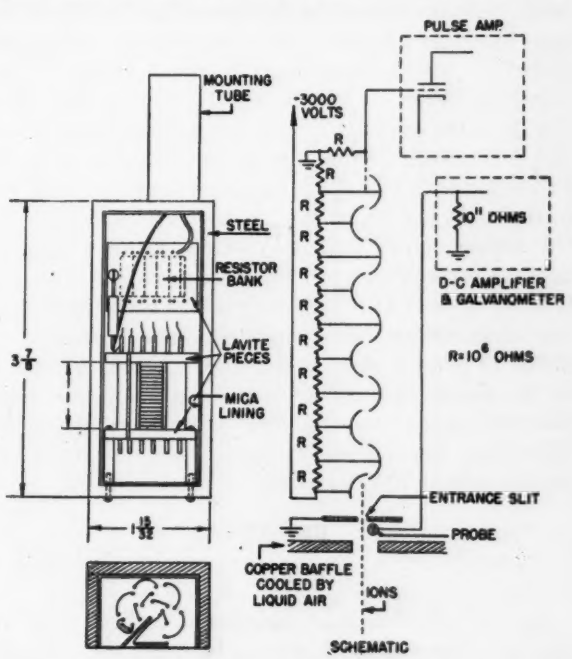

FIG. 2. Electron multiplier and circuit.

[7] I. Esterman, Rev. Mod. Phys. 18, 300 (1946).
[8] R. W. Ditchburn and J. C. Gilmour, Rev. Mod. Phys. 13, 310 (1941).

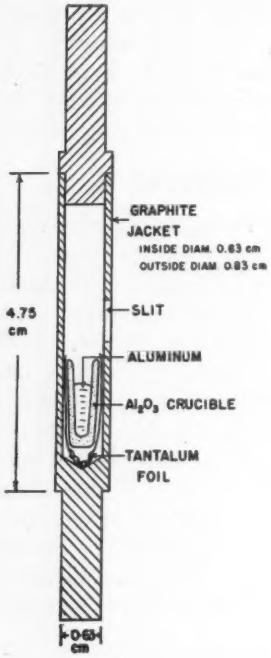

FIG. 3. Oven for generating a beam of aluminum atoms.

same direction is to throw these atoms around the obstacle wire into the detector. The trajectory of such atoms is shown by the solid lines in Fig. 4 while the dotted lines show what the trajectory would be if there were greater deflecting power in proportion to the width of the slits used. Although narrowing the slits would remove this source of background, it would reduce the beam intensity and consequently the intensity of the induced transitions. The weak transitions might then be buried in the background from the tungsten ribbon itself. A transition, to be observed, must show up above the background. The latter has been found to fluctuate about 10 percent in intensity, probably due to fluctuations in the intensity of the aluminum beam. When, in a search for transitions, a change in the counting rate of the multiplier is observed and it is suspected that this is due to transitions, the r-f oscillator is tuned through the suspected peak repeatedly. If the occurrence of the peak coincides with the tuning of the oscillator over a certain frequency range, it is considered probable that a genuine transition is being observed. This technique has been used on all the observations. The strongest lines observed are about 75 percent above background. No detailed plots of the shapes of the lines have been made but it has been estimated that the line widths are about 200 kilocycles. The accuracy of each observation is approximately ± 100 kilocycles.

RESULTS

$^2P_{3/2}$

By the selection rules mentioned earlier, there are fourteen observable transitions between the magnetic levels of the hyperfine multiplet of the $^2P_{3/2}$ state. These are listed in Table I. The transition probabilities are also shown. Two of the lines involve no change in the quantum number F; twelve involve a change of ± 1. At very low magnetic fields, the frequencies of the $\Delta F=0$ lines are given by

$$\nu = g_F \mu_0 H/h,$$

where

$$g_F = g_J \frac{F(F+1)+J(J+1)-I(I+1)}{2F(F+1)} + g_I \frac{F(F+1)-J(J+1)+I(I+1)}{2F(F+1)}.$$

Neglecting the second term in g_F, the frequencies of the two $\Delta F=0$ lines are

$$\nu(4, -2 \rightarrow 4, -3) = \tfrac{1}{2}\mu_0 H/h,$$
$$\nu(3, -1 \rightarrow 3, -2) = (7/18)\mu_0 H/h.$$

Agreement has been found between these theoretical expressions and the observed frequencies, using the ($F=2$, $m_F=-1 \rightarrow F=2$, $m_F=-2$) line of Na as the calibration of the field H. This agreement is interpreted as confirming a spin of 5/2 for Al.

Of the lines involving $\Delta F=\pm 1$, five are π-lines ($\Delta m_F=0$) and seven are σ-lines ($\Delta m_f=\pm 1$). The former are induced by components of the oscillating magnetic field parallel to the constant homogeneous field and the latter are induced by components perpendicular to the constant field. The ribbon which carries the radiofrequency power is such that the oscillating field is mainly perpendicular to the constant field. Thus σ-lines are expected to be stronger than π-lines. The points in Figs. 5 and 6 show the observed transitions plotted against the intensity of the C field. Figure 6 shows the $(4, -2) \rightarrow (3, -2)$ line, the only line which is observable between the $F=4$ and $F=3$ levels. Figure 5 shows transitions between $F=3$ and $F=2$ levels. The association of the experimental points with various lines is done by trial and error. In the figures, the curves shown are calculated for $\Delta\nu(F=4 \rightarrow F-3)=392.0$

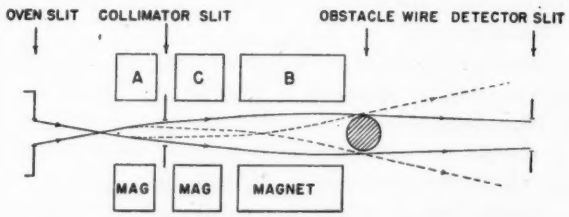

FIG. 4. Diagram of the essentials of an atomic beam system illustrating the effect of insufficient deflecting power.

Mc/sec. and $\Delta\nu(F=3 \rightarrow F=2)=274.3$ Mc/sec. The fit between the curves and the experimental points is fairly good in spite of the fact that not all the points fall on some curve. Further evidence of the correctness of the identification is seen in the fact that, in Fig. 5, the

σ-lines (solid curves) contain more experimental points than the π-lines (dashed curves). In fact, except for the line $(3,0)\rightarrow(2,0)$, the π-lines are not definitely observed, indicating that the parallel component of the oscillating field is too weak. Perhaps the reason that the $(3,0)\rightarrow(2,0)$ line is observed is that its transition probability is slightly higher than that of the other π-lines, as seen in Table I. As to the reason why the π-line $(4,-2)\rightarrow(3,-2)$ is so strong, it may be that the r-f oscillator delivers more power to the r-f hairpin ribbon at 392 Mc than around 274 Mc. From the data

TABLE I. Observable transitions and transition probabilities. For absolute values, the above probabilities should be multiplied by $(\pi t\mu_0 g_I/\hbar)^2$ where t is the time the atom spends in the transition field $H'=H_x i+H_z k$. See DFZZ.

$^2P_{3/2}$ state		$^2P_{1/2}$ state	
Transition	Probability	Transition	Probability
$3,3\rightarrow2,2$	$0.53\ H_x^2$	$3,3\rightarrow2,2$	$0.035\ H_x^2$
$3,2\rightarrow2,2$	$0.9\ H_x^2$	$3,2\rightarrow2,2$	$0.09\ H_x^2$
$3,2\rightarrow2,1$	$0.9\ H_x^2$	$3,2\rightarrow2,1$	$0.09\ H_x^2$
$3,1\rightarrow2,2$	$0.09\ H_x^2$	$3,1\rightarrow2,2$	$0.009\ H_x^2$
$3,1\rightarrow2,1$	$1.4\ H_x^2$	$3,1\rightarrow2,1$	$0.1\ H_x^2$
$3,1\rightarrow2,0$	$0.53\ H_x^2$	$3,1\rightarrow2,0$	$0.035\ H_x^2$
$3,0\rightarrow2,1$	$0.26\ H_x^2$	$3,0\rightarrow2,1$	$0.017\ H_x^2$
$3,0\rightarrow2,0$	$1.6\ H_x^2$	$3,0\rightarrow2,0$	$0.11\ H_x^2$
$3,0\rightarrow2,-1$	$0.26\ H_x^2$	$3,0\rightarrow2,-1$	$0.017\ H_x^2$
$3,-1\rightarrow2,0$	$0.53\ H_x^2$	$3,-1\rightarrow2,0$	$0.035\ H_x^2$
$3,-1\rightarrow2,-1$	$1.4\ H_x^2$	$3,-1\rightarrow2,-1$	$0.11\ H_x^2$
$3,-1\rightarrow3,-2$	$0.38\ H_x^2$	$3,-2\rightarrow3,-3$	$0.017\ H_x^2$
$4,-2\rightarrow4,-3$	$0.87\ H_x^2$		
$4,-2\rightarrow3,-2$	$0.7\ H_x^2$		

available, the most probable values of the hyperfine separations are, with estimated errors,

$$\Delta\nu(F=4\rightarrow F=3)=392.0\pm0.2\text{ Mc},$$
$$\Delta\nu(F=3\rightarrow F=2)=274.3\pm0.1\text{ Mc}.$$

Using Eq. (1) the constants a and b are

$$a=94.25\pm0.04\text{ Mc},\quad b=18.76\pm0.25\text{ Mc},$$
$$b/a=0.199\pm0.003.$$

The nuclear electric quadrupole moment is calculated by the technique described in Section IIC of DFZZ. For a $^2P_{3/2}$ state arising from a single p electron, we have for the interaction constant a,

$$a=-16g_I\mu_0^2\langle r^{-3}\rangle_{Av}/15h,$$

and for the interaction constant b,

$$b=2e^2Q\langle r^{-3}\rangle_{Av}/5h,$$

where in both relations we have neglected small relativistic corrections. Eliminating $\langle(r^{-3})\rangle_{Av}$ from these relations and using previously quoted values of g_I and b/a, we obtain for the value of the nuclear electric quadrupole moment

$$Q=(0.156\pm0.003)10^{-24}\text{ cm}^2.$$

$^2P_{1/2}$

Of the possible transitions between magnetic levels of the $3p\ ^2P_{1/2}$ state, only one is observable for which

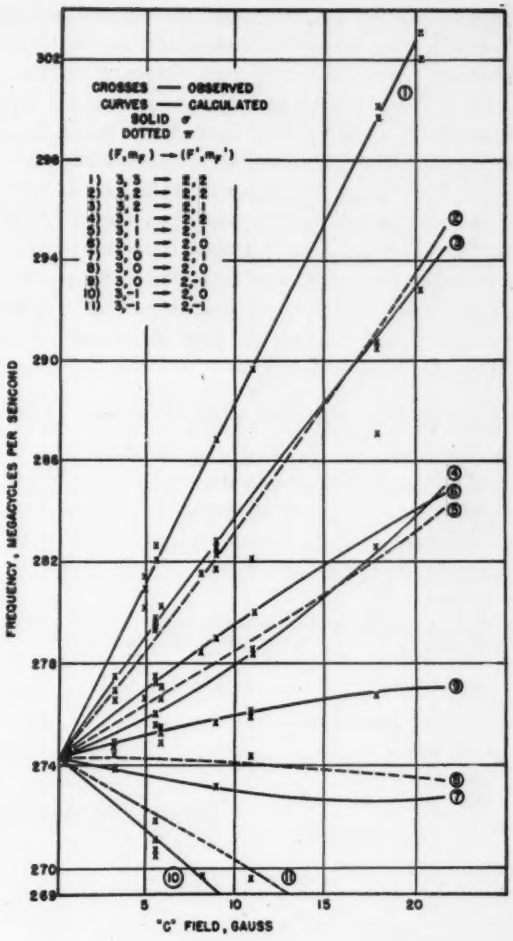

FIG. 5. Observed transitions between $F=3$ levels and $F=2$ levels of the $^2P_{3/2}$ state of Al plotted as a function of the external magnetic field.

$\Delta F=0$, *viz.*, $(3,-2)\rightarrow(3,-3)$. The frequency of this line has been measured as a function of the magnetic field up to a field of 250 gauss. The transition intensities were very weak. When the magnetic field was increased beyond the above value, it was necessary to change from the General Radio Type 805C oscillator to one of lower power and the line was not picked up again. From

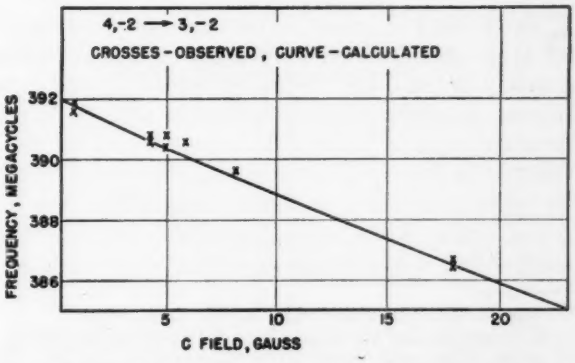

FIG. 6. Observed line $(F=4,\ m_F=-2)\rightarrow(F=3,\ m_F=-2)$ of the $^2P_{3/2}$ state of Al plotted as a function of external magnetic field.

the measurements at 250 gauss, the hyperfine separation of the $^2P_{1/2}$ state was calculated to be 1500±50 megacycles per second. Several attempts were then made to find transitions between $F=3$ and $F=2$. Both because of the lower power output of the Lighthouse Tube oscillator in the region around 1500 Mc and because of the lower transition probabilities of the lines relative to those of the $^2P_{3/2}$ state, as seen in Table I, no transition with $\Delta F=\pm 1$ was detected. The inaccurate value of $\Delta\nu$ obtained, however, serves as further indication that the element that has been studied is aluminum, since it overlaps the spectroscopic value found by Jackson and Kuhn.

Perturbations between Fine Structure Levels

We have so far ascribed the deviation from the interval rule of the hyperfine structure of the $^2P_{3/2}$ state to the effect of a nuclear quadrupole moment. The same effect, however, may be caused by perturbations due to neighboring fine structure levels. Casimir[9] has shown that levels with the same F and differing in J by 0 or 1 repel each other with an interaction energy of the order of (hyperfine splitting)^2/(fine structure separation). Thus the $F=3$ and $F=2$ levels of the $^2P_{3/2}$ state interact with the corresponding levels of the $^2P_{1/2}$ state. The total width of the hyperfine structure of the former state is about 900 Mc/sec. and the $^2P_{3/2}-^2P_{1/2}$ separation is about 3.36×10^{12} cycles. The magnitude of the repulsion is therefore 0.25 Mc or about one percent of the observed deviation from the interval rule.Thus we are justified in ascribing the latter to the effect of a nuclear electric quadrupole moment.

[9] H. B. G. Casimir, *On the Interaction between Atomic Nuclei and Electrons* (Teyler Tweede Genootschap, Haarlem, 1936).

ACKNOWLEDGMENT

The author wishes to thank Professor Jerrold R. Zacharias for his guidance and suggestions in the course of the problem. Thanks are due to Dr. Carrol W. Zabel for his generous help in the theoretical phases of the problem. To Drs. Darragh E. Nagle and Luther Davis, Jr., the author is indebted for general assistance in the use of the atomic beam apparatus for which they have been largely responsible.

PHYSICAL REVIEW VOLUME 76, NUMBER 8 OCTOBER 15, 1949

Extensive Air Showers at High Altitudes

HENRY L. KRAYBILL*
Department of Physics, University of Chicago, Chicago, Illinois
(Received June 22, 1949)

The latitude dependence, density properties, and lateral extension of extensive cosmic-ray air showers have been studied at 9200 m elevation, with coincidence counters in a B-29 airplane. On a flight between 0° and 63°N geomagnetic latitude, no significant variation of shower frequency with latitude has been detected.

Relations between the counting rates of coincidence counter sets of different orders from threefold to ninefold are in agreement with a power law density spectrum for the showers, with constant negative exponent. The measured value of this exponent is 1.73±0.04 at 9200 m, 1.82±0.07 at 11,000–12,000 m, and 1.53±0.07 at 720 m. The counting rate of a threefold coincidence counter set was found to decrease 33 percent as the total spread of the counters was increased from 2.8 m to 13 m at 9200 m altitude. The corresponding decrease at 720 m is 21 percent. The altitude dependence of the extensive showers was measured up to 12,300 m, and a definite maximum shower rate has been found near an altitude of 8000 m.

I. INTRODUCTION

SINCE their discovery more than ten years ago,[1–3] large cosmic-ray air showers have been studied intensively in the lower atmosphere. However, the rapid increase in number of showers with altitude in the lower atmosphere indicates that most of them are being absorbed in this region, and that their source is high in the upper atmosphere. Investigations conducted nearer to the origin of the showers should provide a more sensitive test of hypotheses concerning their production and growth than similar studies at lower altitudes. Therefore, coincidence counter measurements of the properties of extensive air showers have been undertaken in a B-29 airplane flying between 6000 and 12,000 m above sea level. The altitude dependence has been measured up to 12,300 m. The density structure of the air showers was studied at 9200 m and higher altitudes, by determining the counting rate as a function of the number of counters in coincidence. Observations were also made of the variation of shower frequency with latitude and with total spread of the coincidence counters. Preliminary reports of the altitude dependence have been published previously.[4,5]

* Now at Yale University, New Haven, Connecticut.
[1] K. Schmeiser and W. Bothe, Ann. d. Physik **32**, 161 (1938).
[2] Auger, Maze, and Grivet-Meyer, Comptes Rendus **206**, 1721 (1938).
[3] Kohlhörster, Matthes, and Weber, Naturwiss. **26**, 576 (1938).
[4] H. L. Kraybill and P. Ovrebo, Phys. Rev. **72**, 351 (1947).
[5] H. L. Kraybill, Phys. Rev. **73**, 632 (1948).

This paper contains a more complete account of the results of these experiments.

II. METHOD AND APPARATUS

Nine Geiger counters were mounted just beneath the roof of a B-29 airplane, as shown in Fig. 1. The counters were connected to five threefold coincidence circuits, as indicated in Fig. 2. Details of the counter geometry are given in Fig. 2a (arrangement A). Circuits numbered 2 and 4 measured the counting rate of three uniformly spaced counters with a total spread of 2.8 m. Circuits numbered 1 and 3 measured the counting rate of three counters with a total spread of 4.2 m. The spacings were chosen so as to afford the widest possible separation of the counters in the rear pressurized cabin of the airplane. Since circuits 1 and 3, and circuits 2 and 4, were connected to counter arrangements with identical geometry, a check of the functioning of each of these circuits was available. The circuit numbered 5 was connected to two counters in the rear cabin and to one counter in the front cabin, having a total spread of 13 m.

The circuits were of the usual Rossi type. All counters were shielded with metal boxes. A cathode follower mounted at each counter fed the pulses through shielded coaxial cable to the coincidence circuits.

In mounting the counters in the airplane, it was necessary to displace some of them by slight horizontal distances (up to 5 cm) from the positions shown in Fig. 2a. From the rather slight dependence of counting rate upon counter spread which was observed at all altitudes (see Fig. 7), it is considered that these small displacements had negligible influence upon the counting rates. Counters numbered 5 and 6 were displaced vertically a few centimeters in order that no set of three counters connected to one circuit should lie on a straight line. Thus there was a minimum possibility for a single particle to trip any of the circuits.

The counters were of all-metal construction with brass walls. The wall thickness was 0.8 mm. The active length was 32 cm and the inside diameter was 2.34 cm, so that the active area was 75 cm^2. They were filled with the usual nine to one mixture of argon and ethyl alcohol.

Coincidences from each threefold circuit were recorded as lines flashed by neon lamps on a moving photographic film. The channels for each coincidence ran side by side on the film, so that the simultaneous occurrence of any combination of coincidences could be detected. In this manner various orders of coincidence from threefolds to ninefolds were observed. For example, the simultaneous discharge of circuits 1 and 2 indicated a fourfold coincidence, and the simultaneous discharge of circuits 1, 2, 3, and 4 indicated an eightfold coincidence. A typical record is shown in Fig. 3. The error of resolution of the recorder was less than one percent for the threefold coincidences and was two to three percent for the higher order coincidences.

The errors due to counter deadtime and accidental coincidence counts were determined as follows: The counters were tested and found to have an efficiency of at least 99 percent for ionizing cosmic rays at Chicago, with a background of about 200 counts/min. The resolving times of the coincidence circuits were determined to be between 1.5 and 2.0 μsec., by measuring accidental counting rates when radium was placed near the counters. The effective total deadtime of counters and circuits was determined by measuring the inefficiency with high single counting rates in each counter. A value of 240 ± 20 μsec. was obtained for the deadtime.

Counting rates of individual counters were measured during the airplane flights with a portable pulse rate meter. The average rate of a single counter ranged from 50 to 35 counts/sec. at 9200 m elevation, between 63 degrees north geomagnetic latitude and the equator. At 12,300 m (41°N), the highest altitude which was reached, the average rate per counter was 85 counts/sec. Under these conditions, the threefold accidental counting rate, given by $3N^3T^2$, where N is the single counting rate and T is the resolving time, is 0.03 count/hr. Since the slowest threefold counting rate was 11/hr., accidental counts were always negligible. The deadtime inefficiency at the fastest single counting rate was 2.0 percent per counter. For most of the data, which were taken at an altitude of 9200 m, the deadtime correction was approximately 1.2 percent per counter.

III. LATITUDE DEPENDENCE OF AIR SHOWERS

The counting rate of the arrangement in Fig. 2a was measured as a function of latitude on a flight between

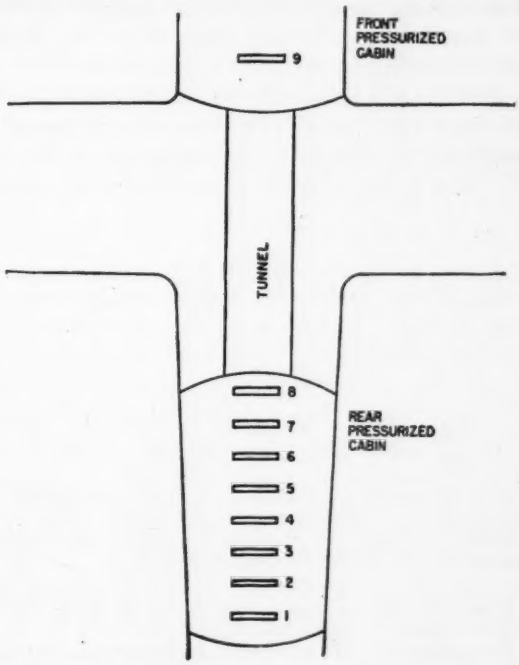

FIG. 1. Top view of B-29 airplane showing positions of shower counters (arrangement A).

northern Canada (63°N geomagnetic latitude) and Lima, Peru, on the magnetic equator. The airplane flew at a constant pressure altitude of 30,000 feet (9200±50 m), corresponding to a pressure of 22.6 cm of mercury. Since a barometric altimeter was used on the airplane, the flight was made at constant pressure rather than constant elevation above sea level. All altitudes stated in this article will refer to the reading of the altimeter, and will therefore denote a pressure which can be obtained from the standard pressure-altitude curve in terms of which the altimeter was calibrated.[6]

Table I compares the counting rates between 0° and 30°N with the rates between 30° and 63°N geomagnetic latitude, for different coincidence combinations. In all cases the counting rates are slightly higher in southern latitudes than in northern latitudes. The differences, however, are within the limits of statistical fluctuations. It is concluded that if a latitude effect of the usual type is present, with higher shower frequency in northern latitudes, it can hardly be as great as 10 percent. If a 10 percent latitude variation should actually exist, the probability of obtaining a deviation equal to or greater than that of the observed results would be one in 370. Further evidence of the lack of a geomagnetic latitude effect is provided by a single flight at 11,000 m altitude at Lima, Peru. The counting rate on this flight was slightly higher than the value given by the altitude curve of Fig. 8, which was based upon observations at 41°N.

The absence of a large latitude effect at these high altitudes confirms less accurate observations of Kraybill and Ovrebo,[4] and it indicates that if the primary particles producing the showers are charged, nearly all must have energies greater than 60 billion electron volts. This result is predicted by the hypothesis[7] that the showers arise principally by cascade multiplication from single high energy electrons near the top of the atmosphere, having an energy spectrum of the form $E^{-1.8}$. It has been shown[8] that showers detected by

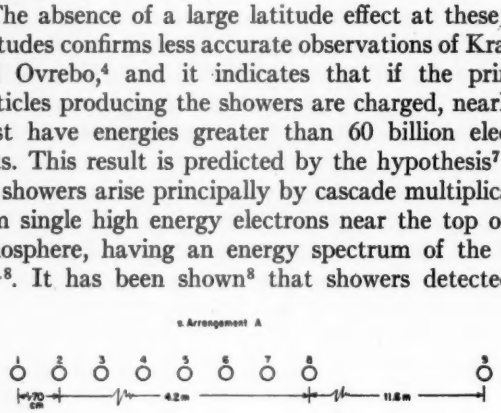

FIG. 2. Side view of coincidence counter arrangement. The following circuit connections were used: Circuit 1—counters 1, 5, 7; circuit 2—counters 3, 5, 7; circuit 3—counters 2, 6, 8; circuit 4—counters 4, 6, 8; circuit 5—counters 6, 8, 9.

[6] These data are contained in Report No. 538 of the National Advisory Committee for Aeronautics.

[7] This assumption will be referred to hereafter as the "single electron hypothesis."

[8] Mark M. Mills, thesis (California Institute of Technology, 1948—to be published).

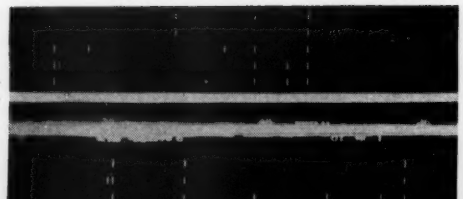

FIG. 3. Typical record of coincidences.

counters of the area used in these experiments would be produced by single electrons of energy greater than 10^{12} ev.

Although the earth's magnetic field should not produce an observable latitude effect upon the large showers, a small variation in counting rate might be expected on the basis of cascade theory, because of differences in air temperature at the same pressure at different latitudes. An increase of temperature at constant pressure reduces the air density and increases the lateral spread of the shower electrons. It can be shown from the single electron hypothesis that the counting rate of a coincidence counter arrangement measuring air showers should be roughly proportional to $\rho^{2(\delta-1)-\alpha}$, where δ is the exponent in the integral density spectrum of the showers falling at a given position, ρ is the air density, and $\alpha=(-d\ \ln C/d\ \ln L)$, where C is the counting rate and L is the separation of the counters. From Fig. 7, it is estimated that α has a value of the order of 0.2 for counters of about 2.8 m spread at 9200 m altitude. At the same elevation, δ was found to be 1.73 (see Table III), so that the counting rate should vary roughly as $\rho^{1.3}$ or as $T^{-1.3}$, where T is the absolute temperature of the air. Thus, for a temperature variation of 15°C at 9200 m, the counting rate might vary by approximately 8 percent.

The above latitude flight was made in early June, when the sun was overhead at a geomagnetic latitude near 30° north. The outside air temperature, which was indicated by the airplane thermometer, is plotted as a function of latitude in Fig. 4. Also plotted are the average counting rates for each latitude zone of twenty degrees. A curve is drawn showing the expected variation of counting rate due to temperature changes. It is clear that considerably more data are needed to establish the presence or absence of a correlation with temperature.

IV. DENSITY OF AIR SHOWERS

Table II shows the number of counts of the various combinations of circuits, obtained at 9200 m with the arrangement of Fig. 2a. The listed values have been

corrected for deadtime errors. The combinations of coincidences which do not include circuit 5 all consist of counters having a spread between 2.8 and 4.9 m. Comparison of the counting rates of circuits 1 and 3 with those of circuits 2 and 4 shows that the counting rate of threefold coincidences is not highly sensitive to variations in counter spread within this range. Comparison of the counting rates for sixfold coincidences of somewhat different geometry (circuit combinations 13, 24, 14, and 23, in Table II) shows a similarly slight dependence upon total spread of the counters. It is therefore believed that at these high altitudes a large proportion of the recorded showers do not have strong variation of particle density over distances of the order of 3 to 5 m. If the integral density spectrum of the showers falling at a given point has the form $K(\Delta)^{-\delta}$, where K is a constant and Δ is the particle density, it is possible to compute the ratios of higher-fold coincidence counts to threefold coincidence counts, assuming that the separations between the counters may be neglected, so that the same density occurs at each counter. The counting rate of an n-fold coincidence set is given[9] by:

$$C_n=\delta\int_0^\infty(1-e^{-\Delta A})^n K\Delta^{-\delta-1}d\Delta, \quad (1)$$

where A is the counter area. An integration of this expression by parts,[10] and expansion of the binomial under the integral sign yields the formula:

$$C_n=nA^\delta[\Gamma(1-\delta)]\sum_{i=1}^{n}\frac{\lfloor n-1}{\lfloor i-1\,\lfloor n-i}(-1)^{i-1}(i)^{\delta-1}, \quad (2)$$

where Γ is the well-known gamma-function. The same method may be applied to calculate the counting rate of independent showers which discharged any one of the circuits 1, 2, 3, and 4, of Fig. 2a or any combination of these circuits. The formula is:

$$C_{1,2,3,4}=4A^\delta[\Gamma(1-\delta)][2\cdot 2^{\delta-1}-8\cdot 4^{\delta-1}+5\cdot 5^{\delta-1}+6\cdot 6^{\delta-1}-7\cdot 7^{\delta-1}+2\cdot 8^{\delta-1}]. \quad (3)$$

Curves of C_n/C_3 plotted against n, for different values of δ, are shown in Fig. 5. Plotted on the same figure are the experimental ratios taken from the data in Table II. A curve representing a constant δ-value can be drawn in agreement with the experimental points. Now, although Lewis[11] has shown that the separation of coincidence counters measuring showers cannot be neglected entirely at high altitudes, Mills[8] has computed an "effective" density spectrum in the form of a power law for counters with a separation of 2.8 m, up to an altitude of about 12,000 m. The experimental data plotted on Fig. 5 are considered to determine an effective δ-value for counters with a total spread of about four meters. At an elevation of 9200 m this value is 1.73.

Measurements were also taken using the arrangement shown in Fig. 2b, in which counters 1, 3, 5, and 7 were moved very close to counters 2, 4, 6, and 8, respectively. The distance between axes of the counters in a pair was then only 2 inches. This arrangement does not change the geometry of the threefold and fourfold coincidences, but it might increase the counting rate of sixfold and higher order coincidences, if marked spatial correlation, or clustering, were present in the showers. The points plotted on Fig. 5 show close agreement of the data from the two different arrangements, for all orders of coincidence. Hence there is no evidence of marked clustering in the spatial distribution of particles at these altitudes. Also, not many shower particles appear to enter the counters at angles greater than 60 degrees with the zenith, since such particles could pass through two counters at once in the closely spaced arrangement of Fig. 2b, and should have increased the number of higher order coincidences.

TABLE I. Latitude dependence of coincidence counting rates.

Latitude range	0–30 deg. N	30–63 deg. N
Total time in minutes	1063	1015
Threefold counts with average counter spread of 3.5 m (average of circuits 1, 2, 3, and 4)	24.6±0.8 per hr.	23.3±0.7 per hr.
Eightfold coincidences with counter spread of 4.9 m (simultaneous counts of circuits 1, 2, 3, and 4)	5.4±0.5	5.2±0.5
Threefold coincidences with counter spread of 13 m (circuit 5)	17.2±1.0	15.8±0.9
All independent counts or combinations of counts of circuits 1, 2, 3, and 4	59.0±1.8	55.4±1.8

Note: Errors listed are standard deviations due to statistical fluctuations.

Data taken at altitudes of 720 m and of 11,000–12,000 m are also shown in Fig. 5. Figure 6 shows coincidence ratios for counter combinations including counter nine, having a total spread of 13 to 16 m.

Table III summarizes the experimental values of δ obtained at different altitudes, compared with theoretical values deduced by Mills from the single electron hypothesis. The values of δ increase with altitude, as predicted by theory. However, the experimental values are lower than the theoretical values at high altitudes. Some of this difference may be due to the material above the counters, which averaged 1.8 g per cm^2 of duralumin and glass. Another factor is the approximation involved in assuming uniform density over all counters. Because of this approximation, it does not

[9] See, for example, Cocconi, Loverdo, and Tongiorgi, Phys. Rev. **70**, 841 (1946).

[10] Several authors have published calculations of this type. Compare A. Migdal, J. Phys. U.S.S.R. **9**, 183 (1945); J. Daudin, J. de phys. et rad. **8**, 301 (1947); Mark M. Mills, reference 8; J. E. Treat and K. I. Greisen, Phys. Rev. **74**, 414 (1948).

[11] H. W. Lewis, Phys. Rev. **73**, 1341 (1948).

appear that the differences between the theoretical and experimental δ-values at high altitudes are significant.

V. LATERAL SPREAD OF AIR SHOWERS

A brief measurement was made of the threefold coincidence counting rate at 9200 m, with counter spreads shorter than 2.8 m. The principal purpose of these measurements was to determine whether any local showers were affecting the threefold rate of the counters with a spread of 2.8 m. The arrangement is shown in Fig. 7. Two counters were placed at a fixed separation of 1.4 m, and a third counter was placed at varying distances (D) from a point midway between the fixed counters. The counting rate is plotted in Fig. 7 as a function of the distance D. The increase in counting rate, as D is changed from 2.1 m to zero, is 12 percent. The small size of this increase indicates that at 9200 m altitude no appreciable fraction of the counts recorded when D equals 2.1 m are caused by local showers generated in the airplane.

The variation of coincidence counting rate with D at an altitude of 720 m is also plotted on Fig. 7, after multiplication of the counting rates at the lower altitude by a constant factor to facilitate comparison with the data at 9200 m. The counting rate decreases as D is increased from 2.1 m to 12.3 m, by 33 percent at 9200 m, and by 21 percent at 720 m. It appears that the decrease of shower frequency with increasing counter separation is somewhat more rapid at high elevations than near sea level, although the observed difference is subject to considerable statistical error.

This result has been predicted qualitatively by Lewis from the single electron hypothesis. He showed that the axes of the recorded showers will fall nearer to the counter arrangement at high altitudes, and therefore the counters should be in a region of more rapidly varying particle density. As a result, the counting rate should decrease more rapidly with increased counter separation at high altitude.

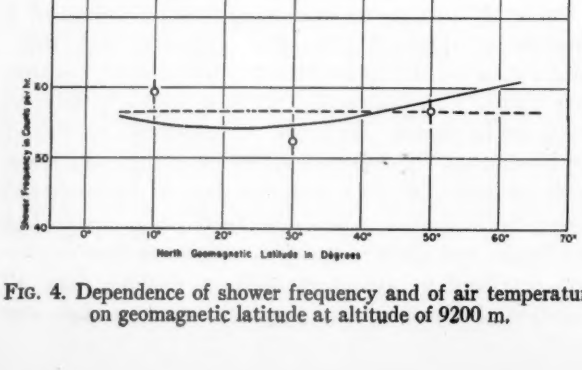

FIG. 4. Dependence of shower frequency and of air temperature on geomagnetic latitude at altitude of 9200 m.

TABLE II. Counting rates of the combinations of circuits in arrangement A at 9200 meters, for all latitudes between 0°N and 63°N geomagnetic latitude.

Circuit combination	Counts[a]	Order of coincidence	Average counting rate per hour[b]	Standard deviation
1	779			
2	855	3	24.0	±0.7
3	777			
4	806			
5	555	3[c]	16.5	±0.7
12	455			
34	433	4	13.4	±0.5
35	308			
45	291	4[c]	9.8	±0.5
345	213	5[c]	6.5	±0.4
13	249			
23	269	6	7.9	±0.4
14	252			
24	262			
15	169	6[c]	5.4	±0.4
25	179			
123	212			
124	209	7	6.5	±0.4
134	201			
234	213			
135	142			
235	152	7[c]	4.4	±0.35
145	134			
245	138			
1234	177	8	5.6	±0.4
1235	123			
1245	116	8[c]	3.8	±0.3
1345	120			
2345	126			
12345	107	9[c]	3.4	±0.3
Independent combinations of 1, 2, 3, and 4	1955	—	56.5	±0.3

[a] For a total time of 2078 minutes.
[b] Corrected for deadtime errors.
[c] Total counter spread is 13–16 m.

VI. ALTITUDE DEPENDENCE OF AIR SHOWERS

The altitude variation of the counting rate of the counter arrangement of Fig. 2b was measured between 4600 m and 12,300 m (15,000 to 40,000 feet) at 41°N. The counting rate in the lower atmosphere was measured at 720 m pressure-altitude, at China Lake, California. Table IV gives the rates observed for a threefold arrangement with total spread of 2.8 m (circuits 2 and 4). The values are plotted on Fig. 8, together with theoretical altitude curves calculated by Mills and by Lewis. The theoretical curves were normalized to fit the experimental point at 720 m. Also plotted are measurements previously obtained by Kraybill and

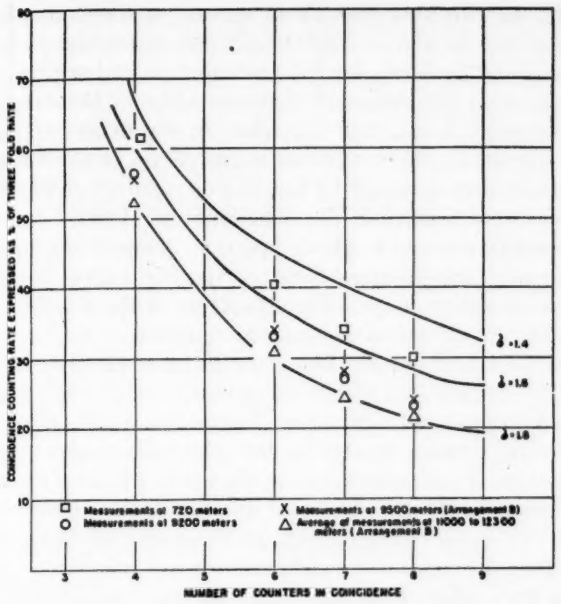
COINCIDENCE COUNTING RATE EXPRESSED AS % OF THREE FOLD RATE
NUMBER OF COUNTERS IN COINCIDENCE
δ=1.4
δ=1.6
δ=1.8
Measurements at 720 meters
Measurements at 9200 meters
Measurements at 9500 meters (Arrangement B)
Average of measurements at 11000 to 12300 meters (Arrangement B)

FIG. 5. Dependence of coincidence counting rate upon the number of counters in coincidence, for counter spreads of 2.8 to 4.9 m.

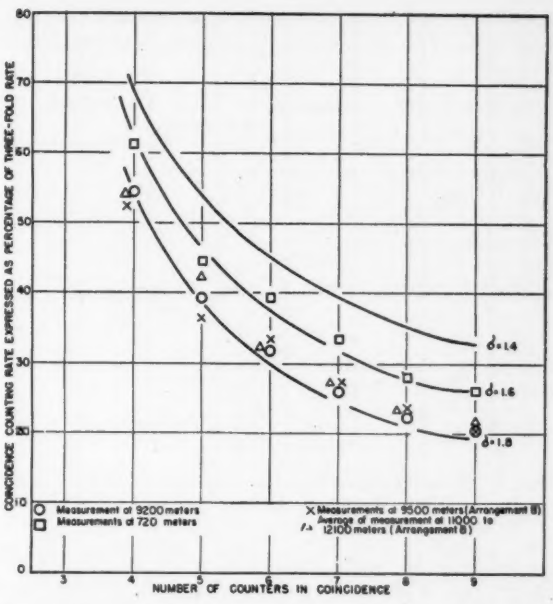
COINCIDENCE COUNTING RATE EXPRESSED AS PERCENTAGE OF THREE-FOLD RATE
NUMBER OF COUNTERS IN COINCIDENCE
δ=1.4
δ=1.6
δ=1.8
Measurement at 9200 meters
Measurements at 720 meters
Measurements at 9500 meters (Arrangement B)
Average of measurement at 11000 to 12100 meters (Arrangement B)

FIG 6. Dependence of coincidence counting rate upon the number of counters in coincidence, for counters with total spread of 13.0 to 16.5 m.

Ovrebo at Wright Field, Ohio (51°N), using a different threefold geometry, with total spread of 3.5 m. The data at Wright Field were multiplied by a constant factor of 0.82, in order to correct the ground counting rate for the different geometry and slightly larger counter area (80 cm²). The rates at high altitudes are then in reasonable agreement with the more recent observations. The later measurements are considered more reliable, since they represent the average of two separate sets of counters with identical geometry, which gave consistent counting rates.

The altitude data for threefold coincidence counters with a total spread of 13 m (Fig. 2, circuit 5) are also plotted in Fig. 8. The counting rate at 9200 m for the 13 m counter spread is 24 times the rate at 720 m. The counting rate at 9200 m for counters with 2.8 m spread is 28 times the rate at 720 m. There is no indication that the shape of the curve for the counters with large extension differs at high altitudes from the curve for counters of shorter extension.

The theoretical curves in Fig. 8 represent independent calculations by Lewis and by Mills for threefold counter arrangements, assuming electrons incident at the top of the atmosphere with a power law energy spectrum of the form $E^{-1.8}$. Lewis used an analytical method to calculate the counting rate of three isotropically sensitive counters separated by a negligibly small distance. His assumptions appear to be applicable to the author's experimental arrangement in the lower half of the atmosphere. In regions less than 11 radiation units below the top of the atmosphere, he considers his values to be higher than actual counter measurements would indicate, because of his neglect of the finite separation of the counters.

Mills has made a careful numerical computation specifically designed for the threefold counter arrangement used by this author, at atmospheric depths between 5 radiation units and 30 radiation units. He used the following expression for the total number (N) of electrons in a shower of energy E_0, at a depth of t radiation units:[12]

$$N(E_0,t)=\left[\frac{1}{(2\pi)^{\frac{1}{2}}}\right]\left(\frac{1}{s}\right)\frac{H_1(s)K_1(s,-s)}{[\lambda_1''(s)t+1/s^2]^{\frac{1}{2}}}\times\left(\frac{E_0}{\epsilon}\right)^{s}\exp[\lambda_1(s)t]. \quad (4)$$

TABLE III. Theoretical and experimental values of the exponent in the air shower density spectrum.

Altitude	720 m	9200 m	9500 m	11,000–12,000 m
Theoretical value of δ computed by Mills for counters of 2.8 m spread	1.41	1.94	1.95	2.01
Experimental values of δ obtained from Fig. 5 for counters of about 3.5 m spread	1.53±0.07	1.73±0.04	1.72±0.04	1.82±0.07
Experimental value of δ computed from the ratio $\frac{C_{1234}}{C_3}$	1.51±0.05	1.73±0.03	1.70±0.03	1.76±0.06
Experimental values of δ obtained from Fig. 6 for counters of 13 to 16 m spread	1.58±0.08	1.75±0.05	1.75±0.05	1.74±0.09

Note: The indicated errors are standard deviations due to statistical fluctuations of a single point on the graph. The values were actually obtained from consideration of several partially interdependent points. Therefore, actual statistical errors should be somewhat less than those listed above.

[12] The symbols of Eq. (4) are those used in reference 14. The letter s denotes the well-known parameter of cascade theory. It is expressed implicitly in terms of E_0 and t by the equation

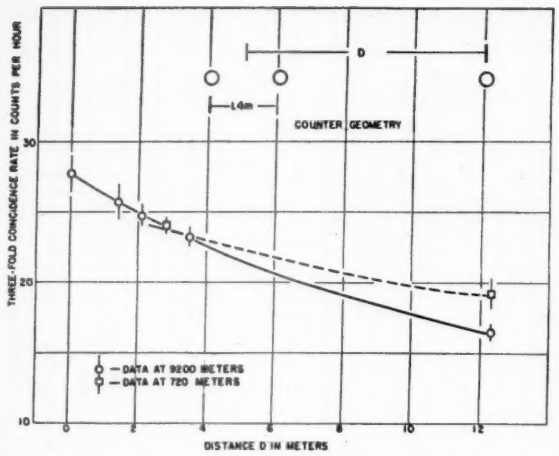

FIG. 7. Threefold coincidence counting rate at 9200 m as a function of separation of counters.

This formula is based upon the work of Snyder and Serber[13] and is given in a review article by Rossi and Greisen.[14] For the lateral distribution of the shower electrons at the maximum of the shower, he made an empirical approximation to the curve computed by Moliere.[15] This lateral distribution, for showers not at their maximum, was modified[16] by the factor $1/r^{1-s}$. The density spectrum produced by showers striking a single point at a given depth in the atmosphere was then calculated, for particles incident from the zenith direction. Mills modified this vertical density spectrum by an approximate method to take account of the counter separation. The result was an "effective" density spectrum for showers incident from one single direction, in which the same density was considered to exist at each of the three counters. This effective density spectrum for showers from a single direction was then integrated over all directions in the hemisphere about the zenith direction, taking into account the increase in effective thickness of the atmosphere with zenith angle, and the change in counter separation and effective area of the counters with incident direction of the shower. The result of this integration could be represented as a power law integral density spectrum for showers striking a point in the atmosphere from all directions. From this spectrum the counting rate of three counters was calculated, according to the formula (1).

The theoretical curve of Mills, calculated for counters with 83 cm² area and 2.8 m spread, is shown as the solid line in Fig. 8. The dotted line shows the curve computed by Lewis for 100 cm² counters and negligible separation. The theoretical curves agree rather closely in general shape. The difference in the height of the maximum in the two curves is due partly to the larger counter area assumed by Lewis. For counters of 80 cm² area, the height of the maximum of Lewis' curve should be reduced by about 8 percent. A more important factor in the difference between the two curves lies in Lewis' neglect of the finite separation of the counters.

The experimental increase in counting rate at high altitudes is about 2.6 times the increase predicted by Mills' calculation. Mills has estimated that neglect of fluctuations and his approximate treatment of the effect of counter separation may cause his results to be too low at the maximum of his curve by a factor of approximately 1.5. There is another factor, however, which causes the maximum in the curve of Mills, as well as the curve of Lewis, to be too low relative to the sea level value. Formula (4), which was used by Mills, expresses the number of electrons in a shower as a function of the thickness of matter in terms of radiation units, where one radiation unit (X_0) is defined by the expression:[17]

$$1/X_0 = 4\alpha(N/A)Z^2r_0^2 \ln(183Z^{-\frac{1}{3}}). \qquad (5)$$

This formula is based upon the original calculations of Bethe and Heitler[18] for bremsstrahlung and pair pro-

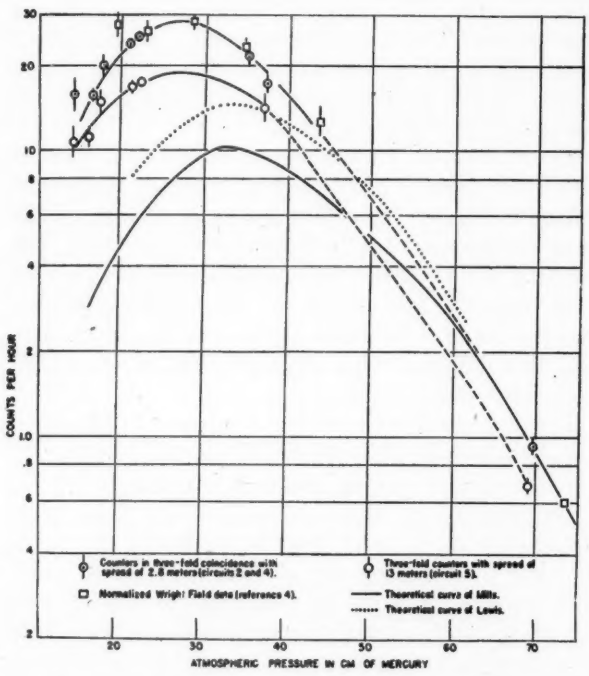

FIG. 8. Altitude dependence of extensive air showers.

$t=(-1/\lambda_1'(s))[\ln(E_0/\epsilon)-(1/s)]$. ϵ is the critical energy of electrons in air, and $\lambda_1(s)$, $H_1(s)$, and $K_1(s,-s)$ are functions tabulated in reference 14.

[13] H. Snyder, Phys. Rev. **53**, 960 (1938); R. Serber, Phys. Rev. **54**, 317 (1938).

[14] B. Rossi and K. Greisen, Rev. Mod. Phys. **13**, 240 (1941).

[15] G. Molière, Naturwiss. **30**, 87 (1942); W. Heisenberg, *et al.*, *Vorträge über Kosmische Strahlung* (Verlag, Julius Springer, Berlin, 1943; Dover Publications, New York, 1946).

[16] Here r denotes the lateral distance from the axis of the shower, in terms of "lateral units," as defined in *Cosmic Radiation* (Dover Publications, New York, 1946). Compare Pomeranchuk, J. Phys. U.S.S.R. **8**, 17 (1944); A. Migdal, reference 12.

[17] Here α denotes the fine structure constant, $r_0=e^2/mc^2$, Z is the atomic number, A is the atomic weight, and N is Avogadro's number. X_0 is expressed in grams per cm².

[18] H. Bethe and W. Heitler, Proc. Roy. Soc. **146**, 83 (1934).

duction processes in the Coulomb fields of nuclei. It fails to take account of the contribution of the fields of the atomic electrons to these processes. It has been suggested[19] that the effect of the atomic electrons may be approximately accounted for by re-defining the radiation unit in terms of the following formula:

$$1/X_0 = 4\alpha(N/A)Z(Z+1)r_0^2 \ln(183Z^{-\frac{1}{3}}). \quad (6)$$

The form of expression (4), giving the total number of electrons in a shower in terms of radiation units, is then left unchanged. But the number of radiation units in the atmosphere is increased from 24 to 27.5. The effect of this change upon the theoretical curves plotted in Fig. 8 will be to place the maxima of the curves at slightly higher altitudes, and to increase the value of the calculated counting rate at the maximum, compared with the value at sea level. Both of these effects tend to counteract the discrepancies between the theoretical and experimental curves in Fig. 8.

VII. DISCUSSION

The experimental results indicate that the extensive air showers at altitudes of 9200 m have lower average density than the showers near sea level. The density of showers detected by counter spreads of 13 to 16 m at 9200 m altitude does not differ greatly from that of showers detected by counter spread of 3 to 5 m. The decrease in the number of recorded showers with increasing counter separation is slightly more rapid at 9200 m than at sea level. The large showers do not exhibit an observable latitude effect at 9200 m altitude. These effects are predicted qualitatively by the hypothesis that the air showers arise from single electrons near the top of the atmosphere with an energy spectrum of the form $E^{-1.8}$.

[19] J. A. Wheeler and W. E. Lamb, Phys. Rev. **55**, 858 (1939); E. Clemental and G. Puppi, Nuovo Cimento **4**, 277 (1947). Compare also J. A. Richards and L. W. Nordheim, Phys. Rev. **74**, 1106 (1948); R. W. Williams, Phys. Rev. **74**, 1689 (1948).

The frequency of large air showers as recorded by coincidence counters has been shown to have a maximum value near an altitude of 8000 m, for threefold counters with a total spread of 2.8 m. The altitude curve for counters of 13 m extension is similar to the curve for counters with shorter spread, except for a slightly lower ratio of the counting rate at high altitudes to the rate at sea level. Theoretical calculations based upon the single electron hypothesis also lead to an altitude curve having a maximum in the upper atmosphere. The above experimental results do not indicate a mechanism for the large air showers essentially different from that of an electron cascade arising from one or a few particles starting near the top of the atmosphere.

TABLE IV. Altitude dependence of threefold coincidence counters with spreads of 2.8 m and of 13 m (circuits 2 and 4, and circuit 5, respectively).

Altitude	Pressure	Geomagnetic latitude	Time	Counting rates of spread of 2.8 m	Threefold coincidences spread of 13 m
720 m	69.9 cm	41 N	20820 min.	0.88 ± 0.04 hr.$^{-1}$	0.70 ± 0.05 hr.$^{-1}$
5650	37.3	41 N	158	17.5 ± 1.8	13.5 ± 2.3
6130	34.9	41 N	203	22.0 ± 2.0	data missing
9200	22.6	9–63 N	2078	24.8 ± 0.7	16.6 ± 0.7
9500	21.5	35–50 N	1474	24.2 ± 0.8	16.1 ± 0.9
11000	17.1	0	266	20.0 ± 1.8	14.7 ± 1.9
11400	16.2	41 N	556	16.0 ± 1.0	11.0 ± 1.1
12300	14.5	41 N	97	16.1 ± 2.3	10.6 ± 2.6

It is a pleasure to acknowledge the advice and encouragement of Professor Marcel Schein, who suggested this work. I am also indebted to Dr. Mark M. Mills, of California Institute of Technology, for sending me his thesis before publication, and for valuable discussions of his work. The Office of Naval Research and the U. S. Army Air Force furnished the B-29 airplane for these experiments. Ivar Kahlberg and George Manning assisted in constructing the equipment and installing it in the airplane. David Haskin constructed the counters which were used in the experiments.

Star Production by Negative μ-Mesons in a Silver Chloride Crystal*

H. G. VOORHIES** AND J. C. STREET
Department of Physics, Harvard University, Cambridge, Massachusetts
(Received June 16, 1949)

A silver chloride crystal has been used to detect μ-mesons which stop in the crystal or in some brass immediately below it. It is found that such mesons and their decay electrons produce pulses well above noise and with rise times of 0.2 to 0.35 μ-sec. On the basis of 79 decay events, the meson mean life is found to be 1.9±0.3 μ-sec. By comparing the pulse height distribution for stopped mesons with the distribution for the hard cosmic-ray component, it is shown that the crystal response is proportional to energy loss for slow, heavily ionizing particles. During an experimental run 263 mesons stop. Forty are observed to decay, and it is calculated that 78 are negative mesons which stop in the crystal. It is first shown that, in general, nuclear capture of negative μ-mesons does not result in the production of stars in which the charged particles carry on the average half the meson rest energy. Further analysis shows that, if stars are produced, the average energy of the charged particles is but a very few Mev, probably less than 3 Mev. Five large pulses associated with stopped particles might be interpreted as star pulses, but some of these may be due to stopped protons.

I. INTRODUCTION

IT has been shown by van Heerden that single, fast particles can produce detectable pulses in a silver chloride crystal and that the pulse amplitudes due to β-rays are a measure of the energy which the particles expend in the crystal.[1] We describe here the use of AgCl crystals in investigating star production by negative μ-mesons.[2] A nucleus, when it captures a meson, is excited and may give rise to a star. Our experimental arrangement permits a measurement of the energy of the charged particles in the star, if such particles exist.

When the present experiment was begun, not much was known about the fate of negative mesons. Later, O. Piccioni cited evidence indicating that it is unlikely that captured negative mesons result in stars containing charged particles of appreciable energy.[3] Recent results, obtained using thin foils in a cloud chamber, also indicate little or no such star production.[4] Lattes and Gardner,[5] using photo-plates, first reported some evidence for weak stars from μ-mesons, but recent reports from Berkeley based on more extensive observations reverse this conclusion. On the assumption that the negative μ-meson results in a charge exchange reaction with the nucleus with the emission of a neutral particle (neutrino), J. Tiomno and J. A. Wheeler[6] have calculated for various models the resultant distribution of nuclear excitation energy and conclude that for most reactions the excitation is too low for the emission of even one proton. For heavy elements neutrons would be expected and have been observed by Sard *et al.*[7]

Two other problems concerning the crystal itself will be discussed. The first is the investigation of the use of the crystal in making relative time measurements in the microsecond region. The second is the investigation of the relation which exists between pulse amplitude and the energy expended in the crystal by a particle. The investigation has been restricted to slow, heavy particles near the end of their range and ionizing well above the minimum ionization.[8]

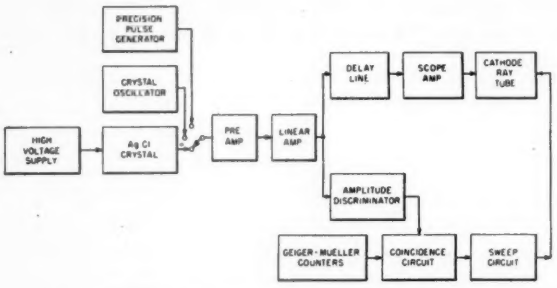

FIG. 1. Block diagram of meson detection system.

II. EXPERIMENTAL ARRANGEMENT

The events of interest to us are those in which a meson of the natural cosmic radiation stops in the crystal or immediately below it, arriving from above within a prescribed solid angle. The meson as it moves through the crystal releases conduction electrons which, under the influence of an applied electric field, move toward the anode, giving rise to a transient current and producing a pulse. The discharge of Geiger-Mueller counters above the crystal simultaneously with the appearance of a crystal pulse indicates the arrival of a particle, and the absence of a discharge in the G-M counters below the crystal indicates the stopping of the particle. The block diagram of Fig. 1 shows the method of correlating the counter and crystal pulses. The crystal signal is amplified, using an amplifier with a

* This work was supported by the Joint Program of the ONR and the AEC; it is based in part on the Doctoral Thesis of one of the authors (H.G.V.).
** Present address: The General Electric Research Laboratories, Schenectady, New York.
[1] P. J. van Heerden, Dissertation (Utrecht 1945).
[2] Unless stated otherwise, a meson is understood to be a μ-meson.
[3] O. Piccioni, Phys. Rev. 73, 411 (1948).
[4] W. Y. Chang, Rev. Mod. Phys. 21, 166 (1949). R. L. Cool *et al.*, Phys. Rev. 75, 1275 (1949).
[5] C. Lattes and E. Gardner, Phys. Rev. 74, 1236A (1948).
[6] J. Tiomno and J. A. Wheeler, Rev. Mod. Phys. 21, 153 (1949).
[7] Sard, Ittner, Conforto, and Crouch, Phys. Rev. 74, 97 (1948).
[8] W. L. Whittemore, Phys. Rev. 76, 170A (1949) and Thesis (Harvard Univ. 1949), has investigated crystal response to fast mesons ionizing at or near the minimum rate.

pulse rise time of 0.15 μsec., and is fed to an amplitude discriminator and, simultaneously, to a delay line. If the pulse is large enough, the discriminator operates and transmits a signal to the coincidence circuit. This circuit in turn generates a trigger which starts the cathode ray tube (*CRT*) sweep, provided the proper G-M counter discharges have occurred. Meanwhile, the crystal signal has been delayed by 36 inches of delay line;[9] it appears on the *CRT*, delayed with respect to the beginning of the sweep, and is photographed. A precision pulse generator provides a pulse height calibration, and a 1.6 Mc/sec. quartz crystal oscillator provides a time calibration of the sweep. A pulse shaping line in the linear amplifier makes the crystal pulses 0.7 μsec. wide.[10]

The AgCl crystal, obtained from the Harshaw Chemical Company, has dimensions 3.0×1.3×0.25 inches and is used with an applied field of 2400 volts/cm.[11] Thin layers of silver, developed on the two large surfaces (over an area 1.88×1.13 square inches), form electrodes. The upper (signal) electrode is made negative with respect to the lower (ground) electrode. During experimental observations the crystal's temperature is maintained at 77°K by placing the crystal on a horizontal, silver plated brass cooling plate in an evacuated light-tight box; the plate is in contact with

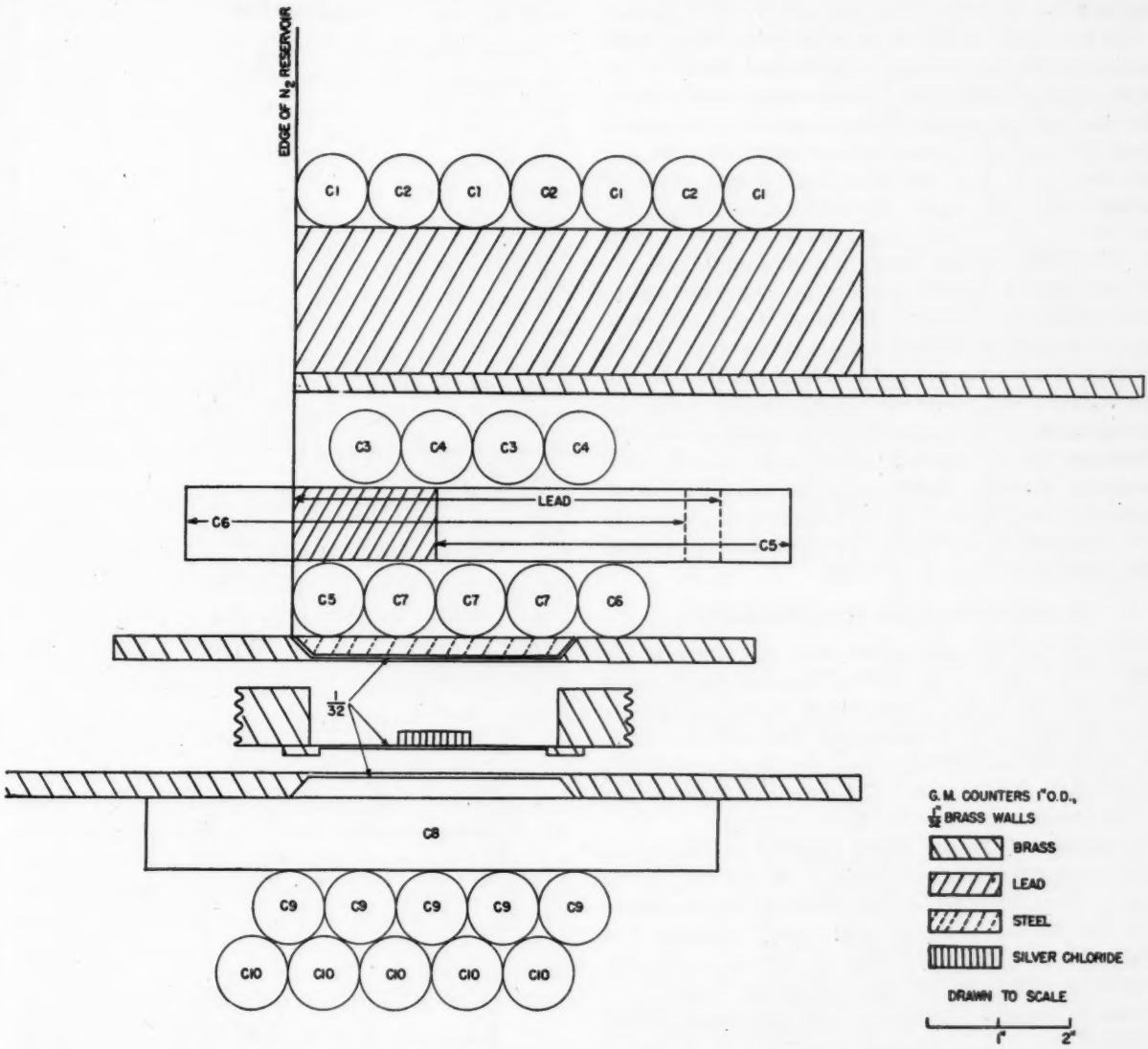

FIG. 2. Counter geometry in the second run.

[9] Continuous wound, 1100 ohm, delay approximately 1 μsec. per ft., J. Millen Company, Malden, Massachusetts.

[10] For the most part the equipment was based on Los Alamos designs, the amplifier due to W. C. Elmore, the precision pulser and coincidence circuit due to M. Sands, and the sweep and discriminator circuits as reported by Fitch and Titterton in Rev. Sci. Inst. 18, 821 (1947).

[11] Few of the purchased crystals were useful. The crystal used was selected by trial from a large group to have good time and fair amplitude response.

FIG. 3. Meson decay events.

a liquid nitrogen reservoir. The low crystal temperature is required because the crystal is an ionic conductor at room temperature but at 77°K is nearly a perfect insulator.[12]

The data were taken at sea level (Cambridge, Massachusetts) during two runs characterized chiefly by the use of different G-M counters and counter geometry. In the first run two counter trays, A and B, were placed above the crystal, X, and anti-coincidence trays, D, were below X. Four inches of lead above A and B covered the solid angle. The events examined were $(A+B+X-D)$ events, designated as anti-coincidence or AC events. It was found that the number of AC events observed, G(obs), exceeded by a factor of nearly 2 the number of calculated AC events, G(calc),[13] and it was also found that the difference was due chiefly to the presence of side showers. In the second run the effect of side showers was essentially eliminated by using the arrangement of Fig. 2; agreement was obtained between G(obs) and G(calc). In this case in order that the CRT sweep be started, signals must be obtained simultaneously from either $C1$ or $C2$ but not both, either $C3$ or $C4$ but not both, $C7$, and the crystal, but no signal must appear in $C5$, 6, 8, 9, or 10.

III. RELATIVE TIME MEASUREMENTS

The crystal produced pulses with rise times at the CRT of 0.2 to 0.35 μ sec. A few pulses had either longer or shorter rise times. Examples of crystal pulses are given in Fig. 3. It is estimated that relative times, i.e., times between crystal pulses, can be measured with an accuracy of 0.03 μsec. (s.d.), provided the pulses do not overlap.

A number of mesons which stopped in the crystal were observed to decay. Figure 3 shows two of the events. The initial pulse was produced by the meson and the second pulse by the decay electron. We can make a statistical check on the crystal's time measuring properties by determining the mean life τ of positive mesons,[14] using the individual measured life times. During an operating period of 950 hours (the first and second runs combined), 79 mesons with life times in the range 1.00 to 5.50 μsec., inclusive, were observed to decay. (The CRT sweep length was about 6.0 μsec.) Using a method developed by Peierls,[15] τ is calculated to be 1.9 ± 0.3 (s.d.) μsec. The presently accepted value is 2.15 ± 0.07 μsec. The only important error in τ is the statistical one, and it is large because only a relatively few (79) decays are measured.

Figure 4 shows the integral decay time curve. It has been corrected for eight decay events which, it is calculated, were missed because of the short sweep length.

IV. STAR PRODUCTION AND AMPLITUDE RESPONSE

As the initial step in the first run, a flux curve, Fig. 5, was measured. We define the flux as the number of particles per min. traversing the crystal and lying within the solid angle defined by the counters. (For a flux measurement the AC counters are disconnected.) The measured flux F is a function of the amplitude discriminator setting D; the flux curve, which is actually an integral pulse height curve, gives the relation between the two. Most of the particles which contribute to F are high energy mesons which ionize at or near the minimum rate. Even if all mesons ionized at the same average rate, all pulses would not have the same amplitude because of statistical fluctuations in ionization.[16] This fact together with the distribution of the meson zenith angles can be shown to explain the shape of the flux curve.

From the flux curve we estimate that the total flux, F(obs), is 4.5 ± 0.4 particles/min., corresponding to $D=20$. (The curve is probably influenced appreciably by noise for smaller D values.) We calculate that 4.7 ± 0.5 particles/min.$=F$(calc) and conclude that the crystal detected most of the fast particles which passed through it.[13]

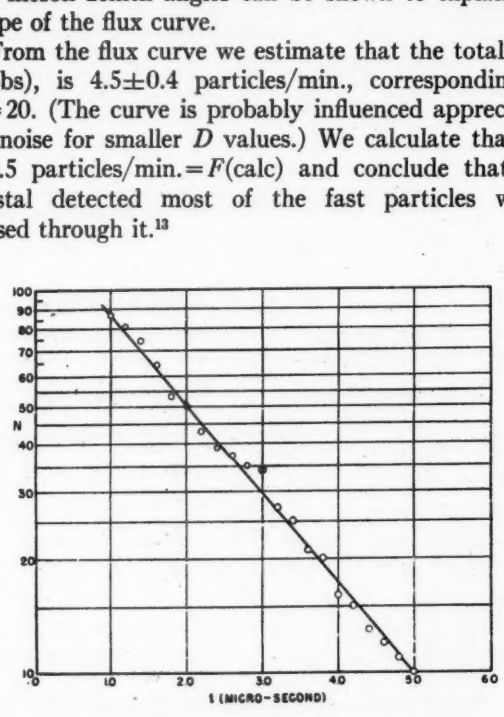

FIG. 4. Integral decay time curve.

[12] Mott and Gurney, *Electronic Processes in Ionic Crystals* (Oxford University Press, London, 1941).

[13] F and G are calculated using data given by B. Rossi, Rev. Mod. Phys. 20, 537 (1948). The authors are indebted to W. L. Kraushaar for information concerning the angular distribution of slow mesons at sea level.

[14] That practically none of the negative mesons decay in AgCl is inferred from the results of Conversi, Pancini, and Piccioni and others, Phys. Rev. 68, 232 (1945) and 71, 209 (1947).

[15] R. Peierls, Proc. Royal Soc. 149, 467 (1935).

[16] K. Symon, thesis, Harvard University, 1948.

From K. Symon's theory of energy loss fluctuations[16] and the analysis of the shape of the flux curve, we find that the knee of the flux curve, which is at 210 μvolts, corresponds to a particle energy loss in the crystal of 3.7 Mev, or that the signal-energy loss conversion ratio C_E is 56 μvolts/Mev. We use this value of C_E together with a value of 7.0 ev per conduction electron (the average energy required to liberate one conduction electron[1,8]) to calculate the mean path, w, of conduction electrons in the crystal. The calculation is made according to a simple procedure described by Mott and Gurney (page 117),[12] and we obtain $w=0.064$ cm, or one-tenth the crystal thickness. Due to the small value of w the pulse height is almost exactly proportional to particle energy loss in the crystal. Thus, the pulse height is relatively independent of the point in the crystal at which conduction electrons are released.

With the AC counters connected, $4.6\pm0.4=G$(obs) particles/hr were observed to stop for a typical set of operating conditions in the first run. It was calculated that $1.7\pm0.2=G$(calc) mesons/hr should stop. As explained previously the discrepancy is chiefly due to side showers. A detailed analysis of the pulse heights for stopped particles is very difficult in the first run because of the effect of side showers and because the first run was really a preliminary run, and consequently changes were made from time to time in the operating conditions. However, a rough check on the crystal's amplitude response is obtained using the largest pulses only. Fifteen percent (or 9) of the mesons which stopped and were observed to decay produced pulses larger than 900 μvolts, the average pulse height being 1100 μvolts and the maximum 1400 μvolts. These large pulses must have been produced by mesons which stopped at or near the bottom of the crystal, i.e., by mesons which lost a maximum amount of energy in the crystal. Using the angular distribution of slow mesons[13] and a calculated range *versus* energy ($R-E$) curve for mesons in AgCl,[17] we calculate that the "average" maximum energy loss of a meson which stops in the crystal is 17.5 Mev. The "average" is taken over the 15 percent of particles with angles and ranges chosen to give the largest pulses. The corresponding pulse height is, therefore, $56\times17.4=1000$ μvolts, to be compared with the observed value of 1100 μvolts.

A second rough qualitative check on amplitude response exists because find that the slow mesons which stopped (the ones observed to decay) produced a set of pulses significantly larger in amplitude than the pulses in the set produced by fast mesons, i.e., the pulses of the flux curve.

The second run was started one month after the end of the first run. The flux curve given in Fig. 5 indicates that the crystal properties were different in the second run; a plateau is barely in evidence, and a knee is perhaps discernible at 120 μvolts ($D=20$), which would make $C_E=32$ μvolts/Mev, but the existence and position of the knee are too indefinite to permit a good calculation of C_E. However, using $C_E=56$ μvolts/Mev from the first run and considering the whole of the flux curves for both runs, we can establish that C_E for the second run is about 44 μvolts/Mev. The reason for the crystal change is uncertain.[18] It was possible, however, in the second run to obtain useful information about the crystal properties and about star production.

A value for the total flux F(obs) is not obvious from examination of the flux curve. F(obs)=4.6 particles/min. is probably the lower limit. F(calc) is found to be 5.4 ± 0.5 particles/min., i.e., F(obs) is smaller than F(calc) by 15 percent. We can conclude that also in the second run the crystal detected most of the fast particles which passed through it.

In the second run with the discriminator set to accept pulses larger than approximately 180 μvolts, 301 particles stopped in 320.5 hours. An additional number (18) of positive mesons which stopped were not observed because they decayed with life times less than 0.7 μsec., and the decay electrons discharged the AC

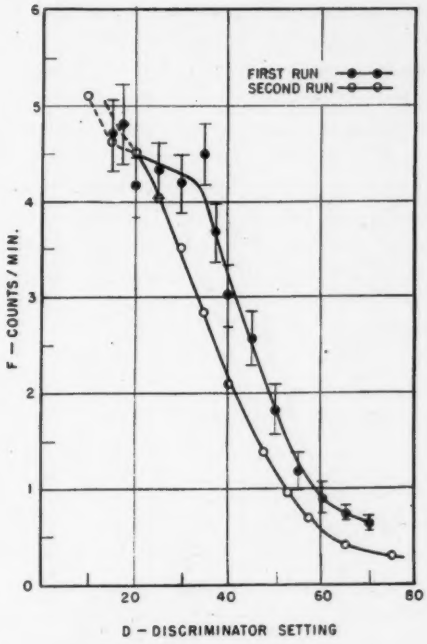

FIG. 5. Flux curves.

counters. (In order to allow for spontaneous lags in the discharge of the AC counters, the circuits excluded events in which the AC counters discharged within 0.7 μsec. following a complete set of coincidence pulses.) Thus, G(obs)$=1.00\pm0.06$ particles/hr whereas G(calc)$=1.1\pm0.2$ stopped mesons/hr. The observed integral pulse height distribution is given in Fig. 6. Five pulses have amplitudes greater than 1200 μvolts;

[17] H. G. Voorhies, Thesis (Harvard University, 1949).

[18] Checks on the crystal flux rate indicated that the crystal properties remained essentially constant during each run.

three at about 1500, one at 2000, and one at 3000. Forty of the pulses can be identified as positive meson pulses because they are accompanied by a delayed pulse. The integral distribution for the 40 is given also in Fig. 6. The 40 pulse heights lie between 200 and 1200 μ-volts.

For purposes of analysis consider two groups of pulses. Let all pulses larger than 200 μvolts (produced by stopped particles) constitute group A; let the 40 pulses produced by stopped positive mesons observed to decay constitute group B. Thus, group B, which forms part of group A, contains only positive meson pulses; group A contains pulses produced by both positive and negative mesons as well as other possible particles. The 12 percent of the pulses with amplitudes less than 200 μvolts are excluded from group A because these small pulses are probably not meson pulses in view of the group B distribution. (The exclusion of these makes $G(\text{obs})=0.9\pm0.07$ stopped mesons/hr.) Probably AC counter inefficiency accounts for most of the small pulses. An inefficiency of only 0.05 percent is necessary to account for all of the 12 percent.

The particles we are considering stopped either in the crystal or the brass which separates the bottom of the crystal from the active volume of the AC counters. The crystal represents 0.635 cm of AgCl stopping material and the brass 0.508 cm of AgCl equivalent stopping material. We now calculate the expected numerical distribution of mesons in the stopping material. Relative stopping powers of the AgCl and brass chiefly determine the distribution for group A. For group B the distribution is determined both by the relative stopping powers and by the detection efficiency for decay elec-

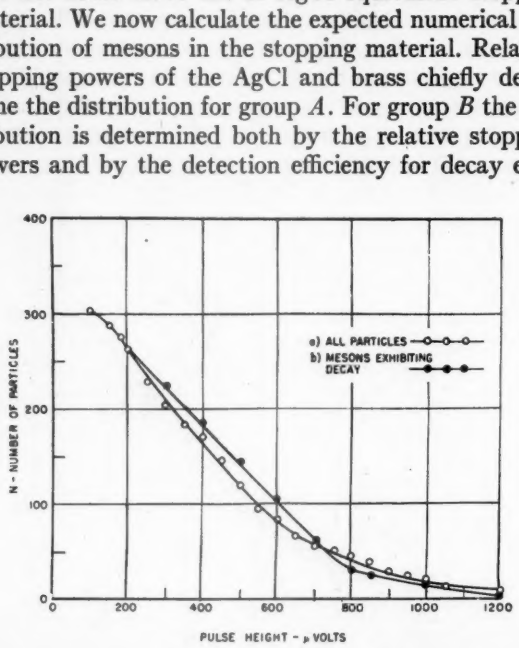

FIG. 6. Integral pulse height curves for stopped particles in the second run. Curve b is normalized to curve a at 200 μvolts.

trons originating in the crystal and brass.[19] A summary of the expected numerical distribution[20] is given in Table I. The important thing to notice is that 78 of the pulses of group A have the possibility of modification by star particles because the pulses are due to negative mesons which stopped in the crystal, whereas none of the pulses of group B can be affected by star particles. We assume that stars are detected only if they originate in the crystal. If for the moment we exclude from group A the five pulses exceeding 1200 μvolts, then for group A only 10 percent (or 26) of the pulses exceed 1000 μvolts, and only 3 percent (7) are 1200 μvolts; in group B, 7 percent (3) exceed 1000 μvolts, and 3 percent (1) are 1200 μvolts. Thus, except for five pulses in group A larger than 1200 μvolts, the relative numbers of large pulses in the two groups are about the same. If a negative meson stopped in the crystal and produced a star in which the charged particles carried on the average approximately half the meson rest energy, a pulse exceeding 2000 μvolts would result. It is evident from our data that this star process occurs rarely or not at all. The five pulses of group A with amplitudes exceeding 1200 μvolts could be produced by protons since the average pulse of a stopped proton would be about 1400 μvolts and the maximum pulse about 2500 or 3000 μvolts.[21] We cannot, however, exclude the possibility that these 5 pulses are star pulses.

TABLE I. Expected distribution of mesons in stopping material for the second run.

Material	Group A	Group B
Crystal	147 (±) 78 (−), 56% 69 (+)	28 (+), 70%
Brass	116 (±) , 44%	12 (+), 30%

We now examine our data for the presence of weak stars. Let V_A and V_B be the average pulse sizes for groups A and B, respectively. $V_A=527$ μvolts, and $V_B=546$ μvolts, where a small (2 percent) correction has been made to V_A for possible meson-decay electron overlap. In order to determine the reliability of V_A and V_B we assume that the pulse height distributions of Fig. 6 are Gaussian. This is only approximately true but will give us a first order estimate of errors. We find that $V_A=527\pm15$ (s.d.) μ-volts, and $V_B=546\pm35$ μvolts. Let V_T be the average pulse height for mesons which stop uniformly in depth in the crystal and brass and which produce no stars. Thus, V_T is essentially the average pulse height obtained for group A when the effects of stars are subtracted. V_T would equal V_A if no star production occurred. Let V_S be the average contribution to pulses due to stars originating in the crystal. Then,

$$V_T=(263V_A-78V_S)/263. \quad (1)$$

[19] The detection efficiency ϵ cannot be calculated accurately. For example, ϵ(obs) is 0.29 ± 0.08 and ϵ(calc) is 0.40 ± 0.10.

[20] We assume that equal numbers of positive and negative mesons stop. The excess of negatives expected to stop in the crystal exists because decay electrons from positive mesons with short life times can discharge the AC counters and, thus, exclude the mesons from observation, as explained previously.

[21] As is shown later, the average pulse height for stopped mesons is about 525 μvolts. From the R-E curves we find that, approximately, the average pulse height for stopped protons is 2.6 times the average meson pulse height.

In our experiment the ratio V_T/V_B, designated as k, has a particular value determined by the distribution of stopping material and the detection efficiencies for decay electrons originating at various points in the stopping material. We write,

$$V_T = kV_B. \tag{2}$$

Substituting in Eq. (1) for V_T, using Eq. (2), we find

$$V_S = 3.37(V_A - kV_B),$$

or

$$V_S = 3.37(527 - k546) \pm 128 \ \mu\text{volts}. \tag{3}$$

The ratio k of the average pulse height for mesons stopping uniformly in depth in the crystal and brass with no star production to the average pulse height for mesons observed to decay is determined in the following manner. Using the $R-E$ curve for AgCl, we calculate a set of relative pulse height curves for mesons which stop in the crystal and brass. Relative pulse height Y is plotted *versus* range R in the stopping material with zenith angle as a parameter. For a meson with range R in the stopping material,

$$Y(R) = \text{const.}\ \Delta E, \tag{4}$$

where ΔE is the energy loss of the meson in the crystal. Equation (4) is a consequence of the fact that the mean path of conduction electrons is short relative to the crystal thickness. Using the relative pulse height curves and estimates of the detection efficiency for decay electrons from mesons with various ranges in the stopping material, we calculate relative pulse heights for V_T and V_B and find that $k=1.07$. Consequently, $V_S = -193 \pm 128$ μvolts.

In order to express V_S in units of energy we must know C_E, the signal-energy loss conversion ratio. We can check the value $C_E = 44$ μvolts, obtained previously, by determining C_E by another method. We calculate the average energy $\langle \Delta E \rangle$ lost in the crystal by mesons which stop uniformly in the crystal and brass, i.e., the mesons of group A (with no star production). $\langle \Delta E \rangle = 12.2$ Mev. The average pulse height for such mesons is given approximately by $V_T = 1.07 \times 546 = 584$ μvolts. Thus, $C_E = 48$ μvolts/Mev. Using an average value, $C_E = 46$ μvolts/Mev, we obtain for the average size of star pulses

$$V_S = -4 \pm 3 \text{ Mev}.$$

It is difficult to estimate the error introduced in the calculation of k. We might best consider two extreme cases. For case (a), we assume that mesons of group B stopped uniformly in the crystal and the brass, i.e., that the detection efficiency ϵ of decay electrons is unity for mesons stopping both in the crystal and in the brass, We then find that $k=1.0$ and $V_S = -1.4 \pm 2.8$ Mev. For case (b), we assume that mesons of group B stopped uniformly in the crystal and none stopped in the brass, i.e., $\epsilon=1$ in the crystal and $\epsilon=0$ in the brass. We find that $k=1.25$ and $V_S = -12 \pm 2.8$ Mev.

From our results we conclude that probably no stars are produced by nuclear capture of negative μ-mesons and that if stars are produced, the average energy of the charged particles is but a very few Mev, probably less than 3 Mev.

If no star production occurs, then V_T is given very closely by V_A, or 527 ± 15 μvolts; therefore,

$$C_E = 527/12.2 = 43 \ \mu\text{volts/Mev}.$$

This value is somewhat high in comparison with 32 μvolts/Mev from the knee of the flux curve but in good agreement with the value 44 μvolts/Mev obtained from comparison of the first and second flux curves as a whole. We observe that the value 43 μvolts/Mev for C_E has been obtained using experimental data for slow, heavily ionizing mesons and agrees with the value 44 μvolts/Mev obtained using data of the flux curves for fast, lightly ionizing mesons.

V. ACKNOWLEDGMENTS

One of the authors (H.G.V.) would like to express his appreciation to the Shell Oil Company for a fellowship given to him during the course of the work described in this paper. Both of us would like to thank Professor Matthew L. Sands for his helpful assistance on several occasions.

UNIVERSITY OF MICHIGAN LIBRARIES

High Frequency Surface Resistivity of Tin in the Normal and Superconducting States*

WILLIAM M. FAIRBANK**
*Sloane Physics Laboratory, Yale University, New Haven, Connecticut****
(Received June 29, 1949)

Measurements have been made at a frequency of 9400 megacycles per second of the unloaded Q of a tin cavity from 74.9°K down to 1.26°K. From the value of the unloaded Q and a knowledge of the geometry of the cavity, the high frequency surface resistivity of white tin has been calculated as a function of temperature in both the normal and the superconducting states. In the normal state at low temperatures, the surface resistivity becomes independent of the d.c. resistivity in agreement with workers at other frequencies. In this region the experimental data are compared with the theoretical curves of Sondheimer and Reuter and a value obtained for the number of conduction electrons per atom. Below the superconducting transition temperature the resistivity drops rapidly with temperature, approaching asymptotically a value of 1.9 percent of the value of the resistance at the transition temperature. The results are compared with the data of Pippard and the probable dependence of residual resistance on the method of preparing the tin samples is discussed.

I. INTRODUCTION

THE London model of superconductivity assumes that in the superconducting state the conduction electrons simultaneously exhibit two modes of behavior. A certain superconducting fraction behaves according to the phenomenological equations of F. London and H. London.[1] The rest exhibit the normal resistive behavior. The presence of a steady applied e.m.f. results in the flow of only superconducting electrons with the resulting zero resistance observed experimentally.

In 1934 H. London[2] predicted that high frequency alternating electromagnetic fields would cause the simultaneous flow of normal and superconducting electrons in the surface of the superconductor, the flow of the normal electrons giving rise to a small but finite resistance. This high frequency resistance should reach zero only when all the conduction electrons are in the superconducting state, a condition thought to exist only at absolute zero.

In 1940 H. London[3] experimentally verified the existence of this resistance in superconducting tin at a frequency of 1500 megacycles per second. He measured the Joule heating produced in a tin ellipsoid placed in a high frequency electromagnetic field. The resistance dropped suddenly at the superconducting transition temperature to a small but finite value, decreasing with further decrease in temperature, probably to zero at the absolute zero.

In the same experiment London observed an anomalous behavior in the high frequency surface resistance of non-superconducting tin in the region just above the superconducting transition temperature. The experimental value was much higher than that predicted from direct current conductivity measurements and the classical theory of the skin effect. He concluded that this value of resistance might be due to the long mean free path of the electrons which exceeds the high frequency skin depth at these temperatures.

The present experiment was begun in an effort to extend the work of London to a higher frequency, making use of the improvements in microwave techniques brought about as a result of the war. Measurements have been completed[4] at a frequency of 9400 megacycles per second on the unloaded Q of a Hilger tin cavity from 75°K down to 1.26°K. From the value of the unloaded Q and a knowledge of the geometry of the cavity, the high frequency surface resistance of white tin has been calculated as a function of temperature in both the normal and the superconducting states.

Other postwar investigators[5–9] have extended London's work both experimentally and theoretically. The results of their work will be compared with the results of this experiment in the section on results.

II. METHOD

The measurements at each temperature consisted in determining as a function of frequency near resonance the standing wave ratio looking into a very pure tin cavity. As will be discussed below, these data yield for each temperature three different Q's: Q_u, the unloaded Q of the cavity; Q_L, the loaded Q of the cavity; Q_R, the radiation Q, where

$$Q_u = 2\pi \frac{\text{Energy stored in cavity}}{\text{Energy dissipated in cavity walls per cycle}},$$

* This is part of a dissertation presented in May, 1948, to the faculty of the Graduate School of Yale University in partial fulfillment of the degree of Doctor of Philosophy.
** Now at Amherst College, Amherst, Massachusetts.
*** Assisted by the ONR.
[1] F. London and H. London, Physica **2**, 341 (1935).
[2] H. London, Nature **133**, 497 (1934).
[3] H. London, Proc. Roy. Soc. **A176**, 522 (1940).
[4] W. M. Fairbank, Phys. Rev. **76**, 167 (1949).
[5] A. B. Pippard, Proc. Roy. Soc. **A191**, 371 (1947).
[6] Bitter, Garrison, Halpern, Maxwell, Slater, and Squire, Phys. Rev. **70**, 97 (1947).
[7] Maxwell, Marcus, and Slater, Phys. Rev. **74**, 1234 (1948).
[8] A. B. Pippard, Nature **162**, 68 (1948).
[9] G. E. H. Reuter and E. H. Sondheimer, Proc. Roy. Soc. **A195**, 336 (1948).

$$Q_L = 2\pi \frac{\text{Energy stored in cavity}}{\text{Energy dissipated in cavity walls} + \text{energy radiated back to line per cycle}},$$

$$Q_R = 2\pi \frac{\text{Energy stored in cavity}}{\text{Energy radiated back to line per cycle}}.$$

The surface resistance is calculated from the unloaded Q, and the consistency of the radiation Q serves as a check on the accuracy of the unloaded Q.

The use of a magic T bridge and a recorder make possible a very rapid measurement of standing wave ratios. The unloaded Q can be measured in a single run on the same cavity throughout the entire range of temperature, even though the Q changes from a value of 6,000 at 75°K to 1,180,000 at the lowest temperature reached.

III. EXPERIMENTAL DETAILS

A block diagram of the apparatus is shown in Fig. 1. Oscillator 1 is a Pound IF stabilized oscillator,[10] stabilized by a wave meter whose frequency can be varied by very small increments. This is accomplished by inserting a fine micrometer controlled probe of diameter 0.045 inches axially into one end of a standard TE_{011} wave meter. A change of 0.0001 inches in the probe depth represents a change in frequency of about 1.5 kc/sec. The change in frequency of oscillator 1 caused by a given change in setting of the reference wave meter can be determined by two methods: (1) The shift in the beat frequency between oscillators 1 and 2 can be measured accurately on the BC-221 frequency meter when oscillator 2 is held at a constant frequency while the frequency of oscillator 1 is varied. (2) Side band signals caused by the superposition of the outputs of the BC-221 frequency meter and oscillator 1 can be observed on the spectrum analyzer. As the frequency of oscillator 1 is varied, the frequency shift can be measured by observing the shift of the side band pattern on the analyzer.

The output of oscillator 1 is fed past a monitor and magic T[11] to one arm of the magic T shown at the lower right hand side of the diagram. This magic T bridge contains the tin cavity on one side arm and a matched load on the other. The output arm contains a detecting crystal C, the output of which is fed to a photo-cell amplifier and then to recorder 1, a Brown recording potentiometer. It is assumed that the energy received by crystal C is proportional to the energy reflected from the cavity.[11] In order to insure that this is true, the magic T bridge containing the cavity has been carefully matched, and three very well matched 3 db attenuator pads have been inserted in the arms of the bridge as shown. Recorder 2 serves to continually monitor the signal incident on the tin cavity. It is connected to a 20 db two-hole directional coupler.

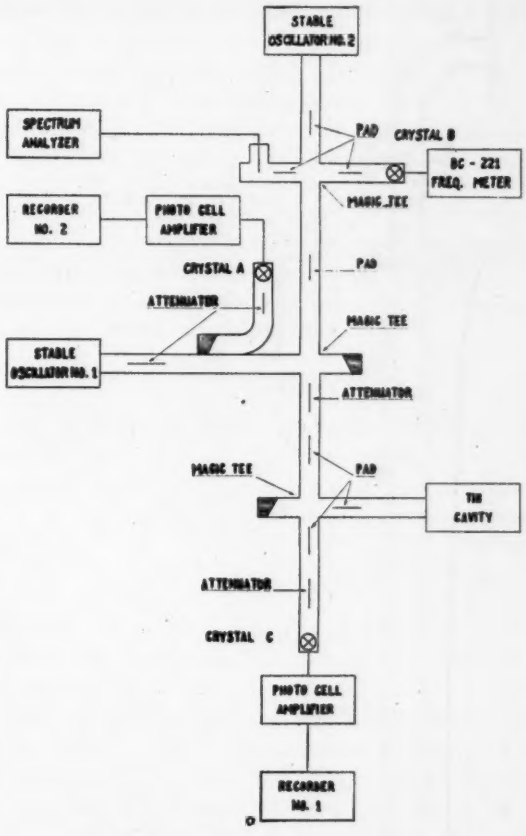

FIG. 1. Block diagram of the apparatus.

Oscillator 2 is also IF stabilized and serves as a monitor on the frequency of oscillator 1. The beat frequency between the two oscillators can be monitored on the BC-221 frequency meter. The spectrum analyzer serves as a convenient check on the two stabilized oscillators.

A Q measurement is made in the following way. The frequency of the stabilized oscillator is varied in small discontinuous jumps by means of the fine frequency control on the reference wave meter. A signal is recorded on the recorder, the amplitude of which is proportional to the power reflected from the tin cavity. The ratio of this amplitude to the amplitude of the signal reflected far from resonance gives the fraction of power reflected from the cavity at the given frequency. This assumes that the cavity acts as a perfect reflector far from resonance. Account must be taken of the variation in output of the oscillator with frequency. This is done by use of the recorder 2 which serves as a monitor, or by extrapolation from the signal received far from resonance on each side of the Q curve. Subject to this correction, one thus obtains on the recorder the percent power reflected from the cavity as a function of frequency. This yields directly the standing wave ratio, and hence Q_R, Q_u, and Q_L.

[10] R. V. Pound, Rev. Sci. Inst. 17, 490 (1946).
[11] C. G. Montgomery, *Technique of Microwave Measurements*, (McGraw-Hill Book Company, Inc., New York, 1948), Radiation Laboratory Series, Vol. 11.

UNIVERSITY OF MICHIGAN LIBRARIES

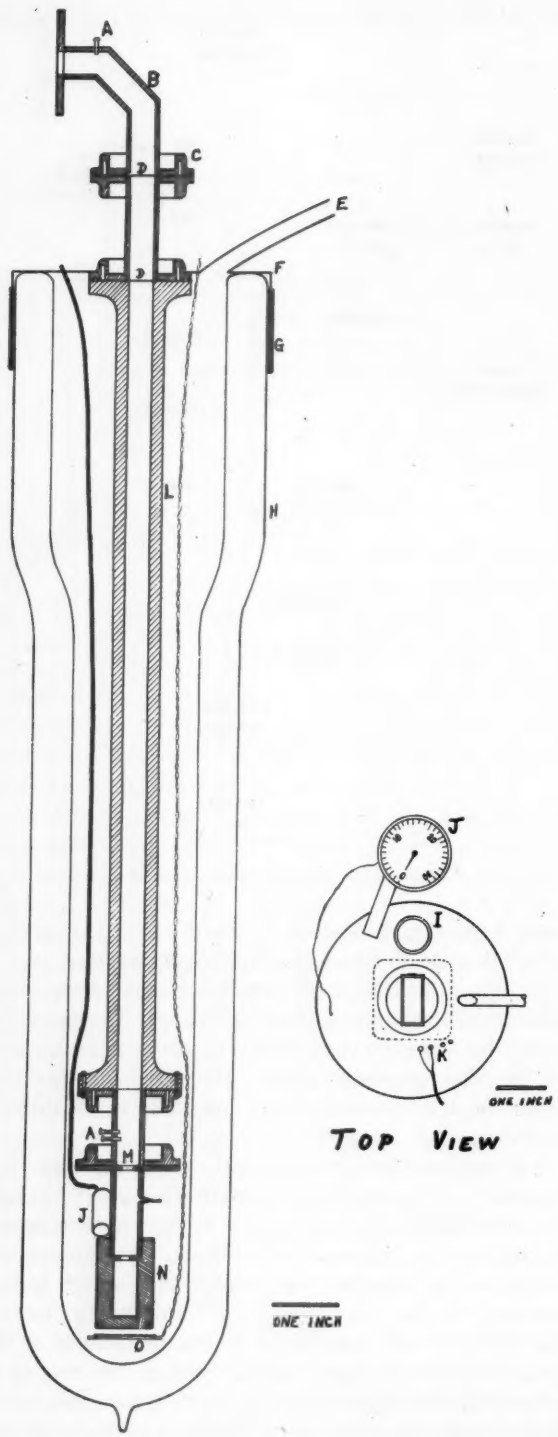

FIG. 2. Section view of the helium Dewar assembly. *A*—matching screw, *B*—brass wave guide, *C*—choke flange coupling, *D*—mica seal, *E*—exit tube (also used for manometer line), *F*—metal top, *G*—rubber gasket, *H*—helium dewar, *I*—inlet tube (also used for pumping line), *J*—constant volume helium thermometer, *K*—metal to glass connectors, *L*—silvered glass wave guide, *M*—resonant glass window, *N*—tin cavity, *O*—heater.

The tin sample measured consisted of a rectangular cavity 0.400 inches high by 0.898 inches wide by 0.882 inches long, coupled to the wave guide by a hole approximately 0.170 inches in diameter. The cavity was the same cross section as the coupling wave guide and was electrically one-half wave-length long. This type of cavity was used since the radiation Q of such a cavity is independent of the unloaded Q. It also offers advantages in ease of assembly. The cavity was made from spectroscopically pure tin supplied by Johnson, Matthey and Company of London, the purity being 99.992 percent.

In an attempt to obtain a very smooth uncontaminated surface, the cavity was pressed out with a die. The die was formed from tool steel, hardened, and polished to a mirror finish with a rouge lapping wheel. The cavity was cut along the center line in the wide side of the guide, the die completely forming each half. No currents flow across this particular plane, hence no loss should be caused by poor contact at this point. The two halves of the cavity were sealed with eutectic solder in a hydrogen oven and coupled to the external wave guide through a resonant glass window of the type used in making TB boxes for radar sets.[12] The final cavity was evacuated and sealed tight.

Figure 2 shows a section view of the helium Dewar and assembled apparatus. The cavity was connected to the top of the Dewar by means of a rectangular glass wave guide to minimize heat leak. With the glass wave guide it was possible to keep helium for as long as eight hours, and to make measurements at temperatures above 4.2°K as will be described below. The guide was formed from thick round glass tube by a series of tapered graphite dies inserted when the glass was molten. Flange ends had been welded on to the glass tube before the die was inserted. The inside of the glass wave guide was made slightly undersize and then ground and polished to size. The wave guide was silvered on the inside by chemical deposition. The other microwave plumbing shown in Fig. 2 was made from the standard rectangular wave guide, coupled by the usual choke flange coupling.

In order to avoid any possibility of the formation of grey tin on the surface of the cavity, the cavity was cooled down very rapidly to nitrogen temperature and warmed up rapidly from this point when a run had been completed. The temperature in the helium region was determined by vapor pressure measurements making use of the 1937 Leiden temperature scale. Heat was supplied by heater 0 at the bottom of the flask when raising the temperature in the helium I region. This insured temperature equilibrium during the process.

To obtain Q measurements in the region above 4.2°K, the following technique was used. When the liquid helium had completely evaporated from the flask, the flask was evacuated and allowed to warm up very slowly toward the temperature of the surrounding nitrogen jacketing flask. The cavity, insulated by the

[12] M. D. Fiske, Rev. Sci. Inst. 17, 478 (1946).

vacuum and glass wave guide, took several hours to warm up, and it was possible to measure Q curves at several intermediate points between liquid helium and liquid nitrogen temperatures. The temperature of the cavity was determined by the constant volume helium thermometer shown as J in Fig. 2.

IV. CALCULATION OF Q

As can be seen from the definitions given previously,

$$1/Q_L=1/Q_R+1/Q_u.$$

If we define r_0 as the voltage standing wave ratio looking into the cavity at resonance, then it can be shown[11,13] that

$Q_u=(1+r_0)\times Q_L$ and $Q_R=Q_u/r_0$ for overcoupled cavity,

and

$Q_u=(1+1/r_0)\times Q_L$ and $Q_R=Q_u\times r_0$ for undercoupled cavity. The width of the resonance curve determines Q_L. Q_u and Q_R can also be determined if r_0 is known.

As has been pointed out above, one can calculate from the data on the recorder the standing wave ratio r looking into the tin cavity as a function of frequency near resonance. The equation for the resonance curve can be put in a very convenient form to make maximum use of the data.[13] This form of the equation for the resonance curve is:

$$(2\Delta Q_u G/Y_0)^2(Y_0/G)+Y_0/G+G/Y_0=(1+r^2)/r$$

where ω_0=frequency at resonance, r=voltage standing wave ratio at frequency ω, Y=line admittance, $\Delta=(\omega-\omega_0)/\omega_0$, and G=input conductance to the cavity.

If the cavity is undercoupled, $Y_0/G=1/r_0$, and if overcoupled, $Y_0/G=r_0$. Thus, the equation of the resonance curve is, for the undercoupled case,

$$4Q_u^2r_0\Delta^2+(1+r_0^2)/r_0=(1+r^2)/r,$$

and for the overcoupled case

$$(4Q_u^2/r_0)\Delta^2+(1+r_0^2)/r_0=(1+r^2)/r.$$

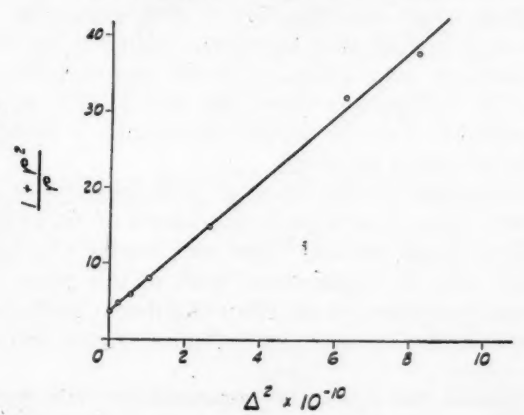

FIG. 3. Sample of straight line graph used to determine Q_u and Q_R.

[13] E. Maxwell, J. App. Phys. 18, 629 (1947).

These two equations are equations of straight lines with intercepts at $(1+r_0^2)/r_0$, and with slopes $4Q_u^2r_0$ for the undercoupled case and $(4Q_u^2/r_0)$ for the overcoupled case. Thus, if Δ^2 is plotted against $(1+r^2)/r$, both Q_u and r_0 can be calculated from the slope and intercept of the curve. Q_R can be calculated from r_0 and Q_u by the formulas given above.

Figure 3 is a sample of a graph of $(1+r^2)/r$ plotted as ordinate against Δ^2 as abscissa. The self-consistency of the data can be checked by observing whether or not the above curve is a straight line, and whether or not Q_R is constant for all values of Q_u.

V. RESULTS

The unloaded Q of the tin cavity described above increased from 6060 at 74.9°K to an almost constant value of 23,000 as the temperature was lowered to 3.722°K. Below this temperature Q_u increased rapidly, reaching a value of 1,180,000 at 1.26°K, the lowest temperature reached. The 1937 temperature scale was used in evaluating the data. For all values of Q_u, Q_R remained constant at 190,000 to within an average deviation of 3 percent. This serves as a check on the accuracy of Q_u.

The experimental data can be divided into two parts, that obtained above the superconducting transition temperature of 3.722°K, and that obtained below this temperature. The former will be considered first.

In order to compare the data with those of other workers in the field, the surface resistivity, R, has been calculated from the unloaded Q and a knowledge of the geometry of the cavity.[5,11,14] For the cavity used, $R=1/0.00505Q_u$. A plot of $1/R$ against the $\sigma^{\frac{1}{2}}$, where σ is the d.c. conductivity, should result in a straight line as long as the classical expression for the skin depth holds. The data obtained above 4.2° are plotted in this fashion in Fig. 4.

The d.c. conductivity was calculated using the data of Onnes and Tuyn,[15] assuming the conductivity at

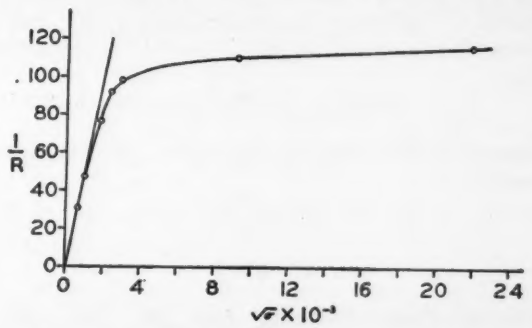

FIG. 4. A plot of the data above the superconducting transition temperature. $1/R$ is calculated from Q_u and σ is the d.c. conductivity. The straight line is the theoretical curve under the assumption that the classical expression for the skin depth holds.

[14] S. A. Schelkunoff, *Electromagnetic Waves* (D. van Nostrand Company, Inc., New York, 1943).

[15] H. Kammerlingh Onnes and Tuyn, Int. Crit. Tab. 6, 124 (1929).

UNIVERSITY OF MICHIGAN LIBRARIES

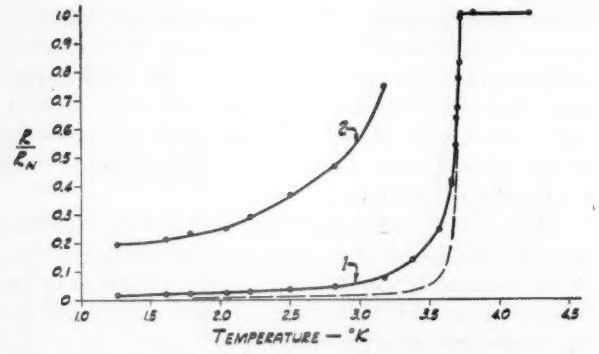

FIG. 5. Graph of the data below the superconducting transition temperature of 3.722°K. R_n is the surface resistivity at the transition temperature. The dotted line indicates the results of Pippard taken at the lower frequency of 1200 megacycles per second. For clarity, R/R_N has been multiplied by 10 and plotted in curve 2.

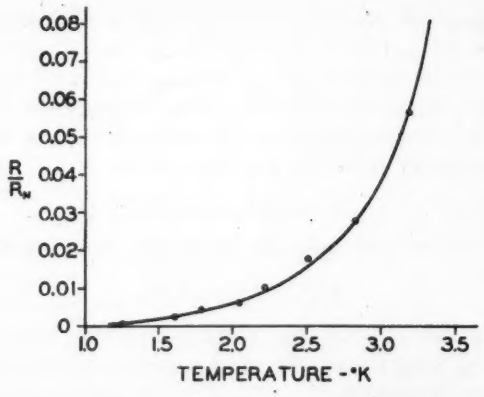

FIG. 6. The solid curve is a graph of the equation $r=0.0865\times[t^4(1-t^2)/(1-t^4)^2]$, where $t\equiv T/T_c$, given by Pippard as an empirical equation representing below 3.3°K his data on tin at 9200 megacycles per second. The circles represent the data of the present experiment after the residual resistivity, $R=0.019R_n$, has been subtracted from the original data.

4.2°K to be 4.8×10^8 ohm^{-1} cm^{-1} as obtained by Pippard[4] for a sample of Johnson Matthey tin of similar purity. The validity of Matthiessen's rule was assumed.

An inspection of Fig. 4 reveals that $1/R$ becomes almost independent of the d.c. conductivity for low temperatures (high σ). At a lower frequency of 1200 megacycles per second, Pippard[5] has observed the same effect for several metals including tin. He has proposed a theoretical explanation based on the long mean free path of the electrons which at low temperatures exceeds the penetration depth of the high frequency electromagnetic fields. Maxwell, Marcus, and Slater[7] and Nowak and Slater[16] have studied the same effect in tin at 24,000 megacycles per second.

Reuter and Sondheimer,[9] using the modern theory of metals, have given a rigorous extension of Pippard's theory. For the microwave region they have plotted two theoretical curves, one assuming perfectly specular reflection of electrons from the surface of the metal ($p=1$), the other assuming completely diffuse reflection ($p=0$). Instead of plotting $1/R$ against $\sigma^{\frac{1}{2}}$ as done in Fig. 4 for the experimental data, they have plotted A/R against $\alpha^{1/6}$ where A is a normalizing factor and $\alpha^{1/6}$ where A is a normalizing factor and $\alpha^{1/6}$ is proportional to $\sigma^{\frac{1}{2}}$.

$$A=6^{\frac{1}{2}}(\pi\omega/\epsilon c^2)^{\frac{1}{2}}(h^3/72\pi n^2)^{1/9}$$

(obtained from combining Eqs. (20) and (51) in reference 9),

$$\alpha=\frac{3^{5/3}\pi^{1/3}\omega\sigma^3h^2}{8^{2/3}c^2\epsilon^4n^{4/3}}$$

(obtained from combining Eqs. (8), (19), (20) of reference 9), where ω=angular frequency of the electromagnetic waves, h=Planck's constant, c=velocity of light, ϵ=electronic charge, n=number of conduction electrons per cubic centimeter of tin. Electrical quantities are expressed in Gaussian units.

[16] W. B. Nowak and J. C. Slater, Phys. Rev. **76**, 469 (1949).

Since both A and $\alpha^{1/6}$ are proportional to $n^{-2/9}$, a value for n can be obtained by adjusting A to give an approximate fit between experimental and theoretical curves. The exact value obtained for n depends upon the type of reflection assumed at the surface of the tin. If diffuse reflection is assumed and the experimental data of this experiment are fitted to the lower theoretical curve ($p=0$), a value of 7.3×10^{21} conduction electrons per cc or 0.20 conduction electrons per atom is obtained. If specular reflection is assumed and the data are fitted to the upper theoretical curve ($p=1$), a value of $n=4.3\times10^{21}$ conduction electrons per cc or 0.12 conduction electrons per atom is obtained. Pippard's data yield a median value of 0.87 conduction electrons per tin atom,[9] while Maxwell, Marcus and Slater[17] have obtained values of 0.12 and 0.20 assuming, respectively $p=1$, and $p=0$.

The second part of the experiment involves the resistivity R in the superconducting region below $T_c=3.722$°K. R_N is the resistivity at T_c. Figure 5 is a plot of $r\equiv R/R_N$ against temperature. Also plotted on the same graph is a dotted line representing the data of Pippard taken at a frequency of 1200 megacycles per second. Pippard's data have been shifted to the 1937 temperature scale. The transition temperatures are 3.725°K in Pippard's experiment and 3.722°K in this experiment. For any given temperature, r increases with increase in frequency.

Subsequent to his work at 1200 megacycles per second, Pippard performed experiments on tin at 9200 megacycles per second.[8] These were conducted concurrently with the experimental work of this paper and permit comparison of the effect of different methods of preparing the tin specimen.[18] Pippard states that his

[17] Maxwell, Marcus, and Slater, paper submitted to the Physical Review.

[18] In a private communication, Pippard has discussed the two experiments and states that his specimens are ¼ wave resonant wires prepared by drawing molten tin into thin-walled glass tubes

results in these experiments can be represented for $T_c<3.3°K$ by the empirical equation

$$r=A'[t^4(1-t^2)/(1-t^4)^2],$$

where $t\equiv T/T_c$ and $A'=0.0865$. The curve in Fig 6. is a graph of this empirical equation with r plotted against T.

Extrapolation of the experimental data of this paper (Fig. 5) to absolute zero gives a residual value of $r=0.019$. The circles in Fig. 6 represent the data of the present experiment after the residual value of R has been subtracted from the original data. It is seen that, after this subtraction is made, the data of the present experiment at 9400 megacycles per second agree with Pippard's data at 9200 megacycles per second.

London has assumed that all of the electrons become superconducting at the absolute zero, and that therefore the limiting value of $r=R/R_N$ at this temperature should be zero. The tin specimens used by Pippard were cast into wires which were mounted by means of low loss dielectric supports. In order to determine r for very low temperatures it was necessary to subtract out the loss due to the dielectric supports. After subtracting out this dielectric loss, Pippard found at 1200 megacycles per second that r apparently does extrapolate to zero for mercury but not for tin, although the dielectric loss is difficult to calculate with certainty. At 9200 megacycles per second, Pippard's results for tin apparently do extrapolate to zero after accounting for the dielectric loss.[18] In the present experiments and in the experiments by Maxwell, Marcus, and Slater,[7] the tin was pressed into a rectangular cavity requiring no dielectric material in the cavity. As mentioned above, an apparently constant residual resistance of $r=0.019$ was found in the present experiment. A residual resistance of 0.09 was found by Maxwell, Marcus, and Slater at 24,000 megacycles per second.[17]

In any experiment of this kind, one of the most difficult experimental problems is to prepare surfaces which behave exactly as the bulk metal. Electrically the cavity used in this experiment operates in a single mode, and the resistivity R can be calculated from the Q_u and the dimensions of the cavity. Q_R remains constant for all values of Q_u and serves as a check on the validity of each measurement of Q_u. Great care was taken in making the die and pressing out the cavity. The cavity was soldered under vacuum and carefully annealed. The presence of a residual resistivity of 1.9 percent of R_N found in this type of cavity and apparently lacking in the cast specimens used by Pippard at 9200 megacycles per second, seems to indicate that a pressed surface acts less like the bulk metal than a cast surface. Unless some new frequency effect is appearing at 24,000 megacycles per second, the residual resistance found in the pressed cavities of Maxwell, Marcus, and Slater indicates the same effect.

The data in the normal state also seem to indicate a more ideal surface for the cast specimens than for the pressed specimens. According to the theory of Sondheimer and Reuter,[9] R_N should vary with frequency as $\omega^{\frac{1}{3}}$. A frequency variation of $\omega^{0.86}$ is found when R_N in this experiment is compared with R_N found by Pippard at 1200 megacycles per second, while Pippard has quoted a variation of $\omega^{\frac{1}{2}}$ in comparing his two experiments with cast specimens.[18] It was observed above that n, the number of superconducting electrons per tin atom, was larger when calculated from Pippard's data at 1200 megacycles per second than when calculated from the data of this experiment or the experiment of Maxwell, Marcus, and Slater. This may give further indication of the same effect.

It has been shown that, when the superconducting residual resistance found in this experiment is subtracted from the experimental values of R and R_N, the value of $r\equiv R/R_N$ is in close agreement with the data of Pippard at 9200 megacycles per second. It appears probable either that some constant loss which has not been accounted for exists in the cavity used in this experiment or that part of the surface penetrated by the electromagnetic field, of the order of 1.9 percent, remained non-superconducting after being subjected to the pressing process. The formation of grey tin would give this effect, but as has been pointed out above, great care was taken to avoid this transformation.

The author is particularly indebted to Professor C. T. Lane for his frequent advice and encouragement. He is also indebted to Professor Henry A. Fairbank, Dr. Robert T. Webber, and other members of the low temperature group at Yale, for assistance in collecting the data. He wishes to express his appreciation to Professors C. G. Montgomery and E. R. Beringer for their helpful suggestions on microwave techniques, and to M. D. Fiske of General Electric for the glass window used to seal the cavity.

under vacuum, the glass being later removed. The method of preparing the sample constitutes the main difference in the two experiments.

UNIVERSITY OF MICHIGAN LIBRARIES

Kinetic Energy Release in Fission of U^{238}, U^{235}, Th^{232}, and Bi^{209} by High Energy Neutrons

J. JUNGERMAN AND S. C. WRIGHT
Radiation Laboratory, Department of Physics, University of California, Berkeley, California
(Received June 6, 1949)

The ionization produced by single fission fragments was observed in an ionization chamber using electron collection. If fission is induced by 90-Mev neutrons, the distribution of kinetic energy of the fission fragment *versus* the number of fragments is found to have a single peak in contrast to the double-peaked curve corresponding to the fission made by thermal neutrons. Fission induced by 45-Mev neutrons gives a distribution in which two peaks appear. The dip between the two peaks is about twenty percent of the height of the peaks. The mean kinetic energy is found to be 80±2 Mev for U^{238}, 83±1.5 Mev for U^{235}, 82±2 Mev for Th^{232}, and 71±2 Mev for Bi^{209} in the case of fission produced by 90-Mev neutrons. The mean kinetic energy is 79±3 Mev for U^{238} and 84±3 Mev for Th^{232} if 45-Mev neutrons are used. The most probable kinetic energy of the fragment is 83 Mev for U^{238}, 80 Mev for U^{235}, 83 Mev for Th^{232}, and 75 Mev for Bi^{209} in the case of fission produced by 90-Mev neutrons. The bearing of these observations on the mechanism of fission is discussed.

INTRODUCTION

THE kinetic energy release occurring in fission induced by low energy neutrons has been studied by Jentschke,[1] Flammersfeld *et al.*,[2] Brolley,[3] Deutsch and Ramsey,[4] and Fowler and Rosen.[5] The results of these experiments show that the distribution of the kinetic energy of single fragments *versus* the number of fragments consists of two peaks. The energy distribution is consistent with the mass distribution of the fragments known from chemical evidence and the assumption that the kinetic energy observed is derived only from the coulomb repulsion of two charged fragments.[4] The object of the experiment reported here was to investigate the kinetic energy distribution of single fragments produced in fission caused by 90-Mev and 45-Mev neutrons and the influence of the increased excitation on the mean fragment energy. To this aim the kinetic energy of single fragments was measured by the use of an ionization chamber, a linear amplifier, and a camera for photographically recording pulse heights on an oscilloscope.

EXPERIMENTAL

Figure 1 shows a diagram of the ionization chamber employed. Each target plate had a foil spot welded to its surface. This foil was covered with the element under investigation. The foils in the cases of uranium and thorium were prepared by painting solutions of the nitrates on 1-mil aluminum and baking at 500°C until the oxides were formed.[6] The amount of material never exceeded 3×10^{-5} g/cm². Foils surfaced with 5×10^{-5} gm/cm² of bismuth were prepared by evaporation of the metal on 1-mil aluminum.

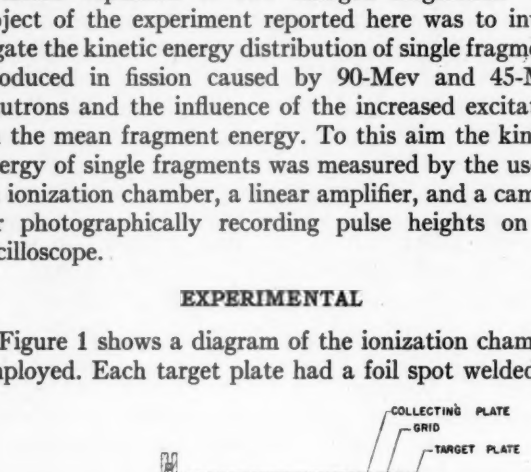

FIG. 1. Fission chamber.

The grids G consisted of 3-mil nichrome wire 50 mils apart. The chamber was filled with pure argon at a pressure of 160 cm of Hg. The electrodes were so arranged that at this gas pressure the distance between the target plate T and the grid G was greater than the range of the fragments. The voltages were such that a stronger electric field existed between the grid and collecting plate than between the grid and the target plate. This tended to funnel the lines of force through the spaces in the grid and to prevent electrons from being collected at the grid.

Charged particles produced by the neutron beam in the chamber electrodes and gas caused spurious ionization pulses to be superimposed on the pulses from the fission fragments. In order to reduce this background ionization as much as possible, the chamber walls and electrodes were made as thin as practicable. The neutron beam entered through a 2-mil stainless steel window, traversed a 1-mil aluminum foil with the sample on it, the grid, and finally a 0.5-mil aluminum foil collecting plate. It then passed on through a similar unit of two plates and a grid. There were four such units in all. The last usually contained a sample of U^{235} for calibration purposes.

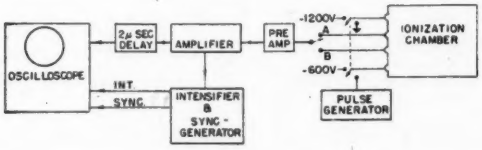

FIG. 2. Electronic circuit.

[1] W. Jentschke, Zeits. f. Physik **120**, 165 (1943).
[2] A. Flammersfeld, Zeits. f. Physik **120**, 450 (1943).
[3] J. E. Brolley, CN 1840.
[4] M. Deutsch and Ramsey, LADC 257.
[5] J. L. Fowler and L. Rosen, Phys. Rev. **72**, 926 (1947).
[6] T. Jorgensen, MDDC 467.

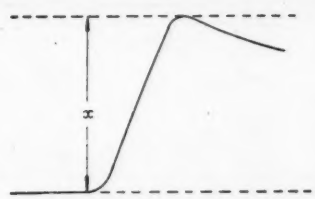

FIG. 3. Fission pulse.

FIG. 4. Rejected fission pulse.

The electronic circuit is shown schematically in Fig. 2. This arrangement was employed in order to discriminate both electronically during the experiment and visually during the film analysis, against pulses caused by high energy neutron reactions in the argon and chamber plates along the path of the beam. A pulse from the ionization chamber was amplified and then fed directly onto the oscilloscope deflection plates via a 2-μsec. delay line. Another amplifier output fed the pulse to the discriminator housed in the intensifier and sync-generator chassis. If the pulse was high enough to be accepted by the discriminator, an intensifying pulse traveled to the oscilloscope grid. At the same time the pulse initiated a 5-μsec. sweep on the oscilloscope. In this way it was possible to see the start of the trace, the pulse rise, and the first part of the decay. Figure 3 shows the form of a typical pulse. The distance x in the figure was taken to be the pulse height. Any pulse in which the initial base line and the pulse rise form differed from that in Fig. 3 was rejected. Figure 4 is an exaggerated example of such a rejected pulse. These unsatisfactory pulses were assumed to be due to a combination of fission fragment ionization and ionization produced by neutron reactions in the electrodes and gas. Their number never amounted to more than 5 percent of the total. The discriminator on the intensifier circuit prevented a large number of low energy pulses from being recorded. This considerably simplified the photographic analysis and made the readings more accurate. The amplifier was of the fast rise time variety stabilized by inverse feed back. The fission pulses had a rise time of 1.5-μsec. and decayed to $1/e$ in 10-μsec. A fast rise time pulse generator connected when required to the grid of the chamber, checked the linearity and amplification of the equipment on the different bombardments. Calibration pulses from the pulse generator were used before and after each run.

The pulses on the Dumont 248 oscilloscope were photographed with a camera using continuously moving 35-mm Super XX film. All pulse heights were measured on the same microfilm viewer.

In order to check the resolution of the apparatus and to calibrate the energy scale, the usual experimental arrangement in the ionization chamber was to have a sample of U^{235} on plate A and samples of the element under investigation on plate B (see Fig. 1). Immediately before or after a cyclotron run, a fission fragment energy distribution was made with slow neutrons on U^{235} using the same chamber gas and the same setting of the amplifier and oscilloscope. The resolution of the chamber was considered satisfactory if the U^{235} (slow n, fission) fragment energy distribution agreed with the curves of Deutsch and Ramsey[4] within statistics. The absolute energy scale was determined by comparison of the Deutsch and Ramsey U^{235} distribution (assumed correct) to the U^{235} (slow n, fission) curves obtained in this experiment. The latter were in turn used to obtain the energy scale for the high energy neutron fission fragment distributions. This energy scale was checked within experimental error by measuring the pulses produced in our apparatus by the α-particles of U^{234}. Since the cyclotron magnetic field was different at the bombardment and calibration positions, a check of the effect of position on the amplification of the apparatus was made by making slow neutron runs at both locations. The pulse height average was found to be 3 percent higher at the bombardment position. This factor has been included in the energy scale calculation.

The high energy neutrons used in these experiments were formed by bombardment of a $\frac{3}{8}$-in. Be target with 190-Mev or 95-Mev deuterons. Serber[7] gives the theoretical energy distribution of the neutrons. According to him if the incident deuteron has 190 Mev, then the width at $\frac{1}{2}$ maximum is 26 Mev. In the case of incident deuterons of 95 Mev, the width at $\frac{1}{2}$ maximum is 19 Mev. The possibility of near thermal neutrons being present in the neutron beam was investigated by taking a cadmium difference with the U^{235} target. No effect was observed. This distribution has been checked experimentally in the course of n-p scattering experiments.[8] The most probable neutron energies in the two cases are 90 Mev and 45 Mev, respectively. This is the meaning of the terms 90-Mev and 45-Mev neutrons as used in this paper. Ra-Be enclosed in paraffin provided a thermal neutron source.

RESULTS

Figures 5, 6, 7, 8, 9, and 10 show the actual histograms of the fragment energy distributions of U^{238}, U^{235}, Th^{232}, and Bi^{209}, obtained in the experiment. Figure 11 shows a typical slow neutron calibration histogram. Figures 12 and 13 show the probable distributions corresponding to these histograms. Each curve is normalized to 1000 pulses. In order to check that all pulses corresponding to 40 Mev or more were due to the active material, cyclotron runs were made with an aluminum blank of the same thickness, 1 mil, as that supporting the sample. These blank runs

[7] R. Serber, Phys. Rev. **72**, 1008 (1947).
[8] R. Serber, Phys. Rev. **75**, 326 (1949).

UNIVERSITY OF MICHIGAN LIBRARIES

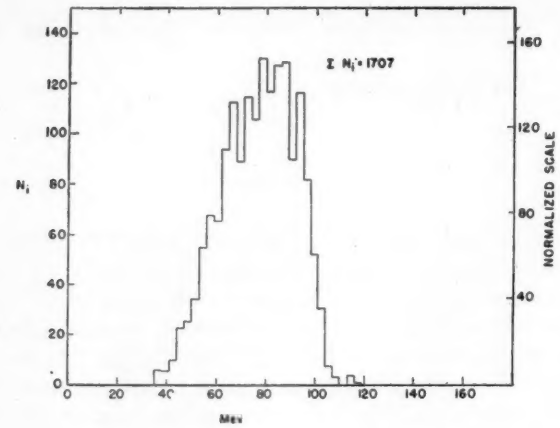

FIG. 5. Single fragment energy distribution 90-Mev neutrons on U^{238}.

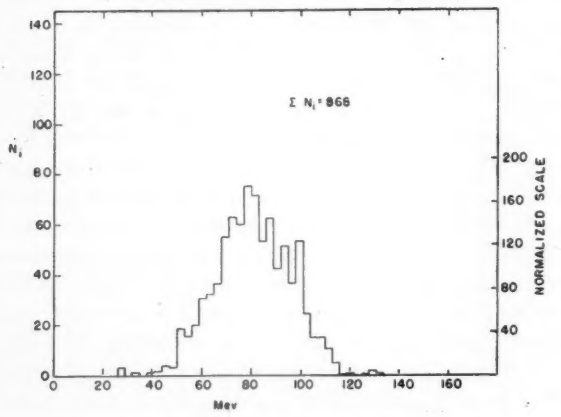

FIG. 6. Single fragment energy distribution 90-Mev neutrons on U^{235}.

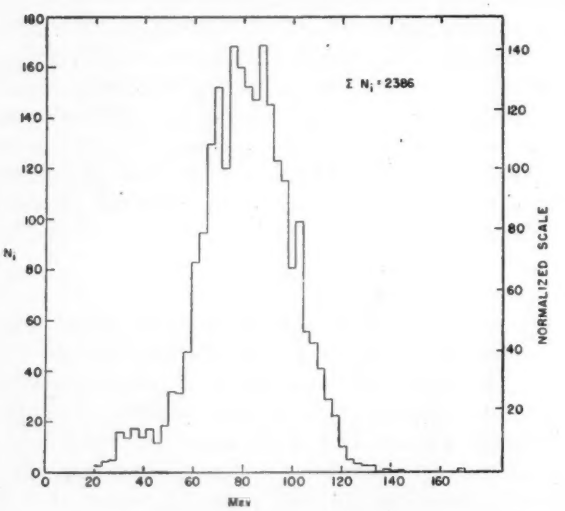

FIG. 7. Single fragment energy distribution 90-Mev neutrons on Th.

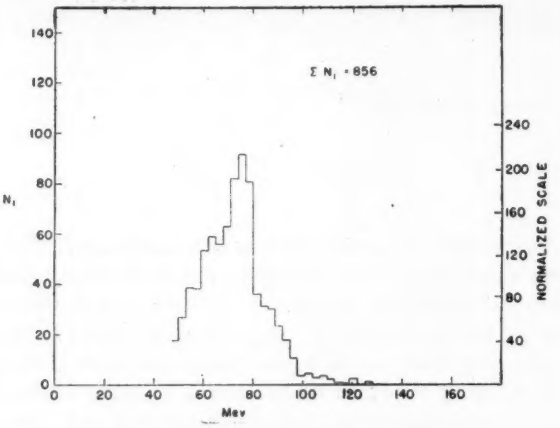

FIG. 8. Single fragment energy distribution 90-Mev neutrons on Bi.

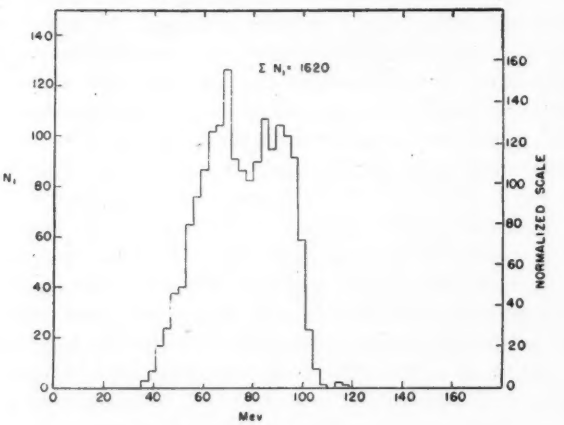

FIG. 9. Single fragment energy distribution 45-Mev neutrons on U^{238}.

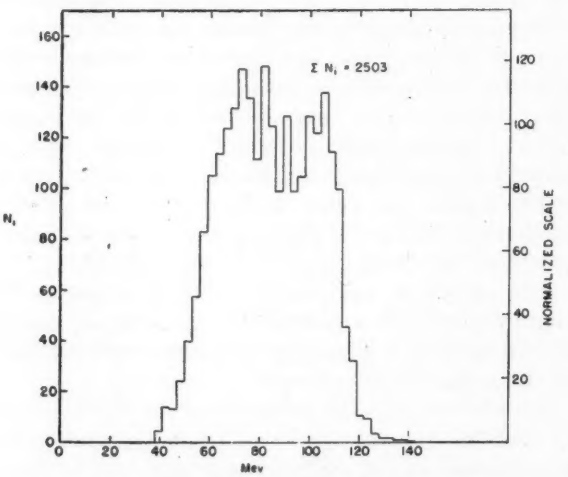

FIG. 10. Single fragment energy distribution 45-Mev neutrons on Th^{232}.

showed that the number of pulses corresponding to fission fragments of 40 Mev or higher were negligible. For fission induced by 90-Mev neutrons it is found that the mean fragment energy is 80±2 Mev for U^{238}, 83±1.5 Mev for U^{235}, 82±2 Mev for Th^{232}, and 71±2 Mev for Bi^{209}. The energy spread at one-half maximum

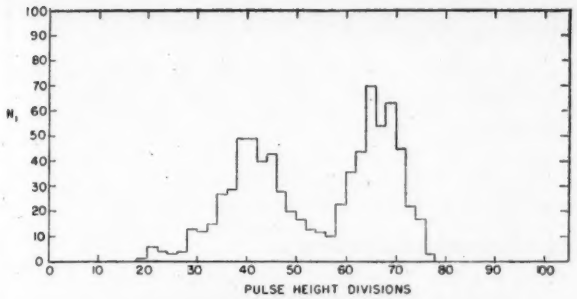

FIG. 11. Single fragment energy distribution slow neutrons on U^{235}.

is 40 Mev for U^{238}, 38 Mev for U^{235}, 44 Mev for Th^{232}, and 24 Mev for Bi^{209}. For fission induced by 45 Mev neutrons two peaks appeared in the energy distributions. For Th^{232} the maxima are at 73 Mev and 104 Mev, for U^{238} at 68 Mev and 89 Mev. The mean fragment energy is 84±3 Mev for Th^{232} and 79±3 Mev for U^{238}. The form of the distributions should be accurate within statistics.

DISCUSSION

The foregoing assumes that the number of ion pairs is proportional to the energy of the fission fragments producing them.

If the fission is assumed to be binary, as is most probable, this experiment shows that the mode of fission induced by 90-Mev neutrons that gives equal kinetic energies to the fragments is the most probable one in contrast to the results of thermal neutron fission. The mean kinetic energy of the fragments is, in the case of U^{235}, only 5-Mev higher than that from fission induced by slow neutrons. The kinetic energy of the incident neutron must therefore be accounted for by some other mechanism than appearance in the kinetic energy of the fission fragments.[9]

Goeckermann and Perlman[10] have investigated fission products formed from bismuth by 200-Mev deuterons. They find that the mass-number distribution has a maximum at about 100-mass units. This indicates a loss of approximately 10 neutrons during the fission process.

The following mechanism is tentatively suggested for the fission process caused by high energy neutrons. The mechanism is shown schematically in Fig. 14. The compound nucleus Z^{A+1*} is formed from the nucleus Z^{A} by capture of a high energy neutron. This compound nucleus evaporates neutrons until fission can effectively compete with the neutron emission. The competition occurs until the energy A of the compound nucleus is less than the binding energy C of a neutron to the nucleus Z^{A+1-J}, where J is the number of neutrons

[9] According to M. L. Goldberger, Phys. Rev. **74**, 1269 (1948), the average excitation a nucleus receives from a collision with a 90-Mev neutron is appreciably less than 90 Mev.

[10] R. H. Goeckermann and I. Perlman, Phys. Rev. **73**, 1127 (1948).

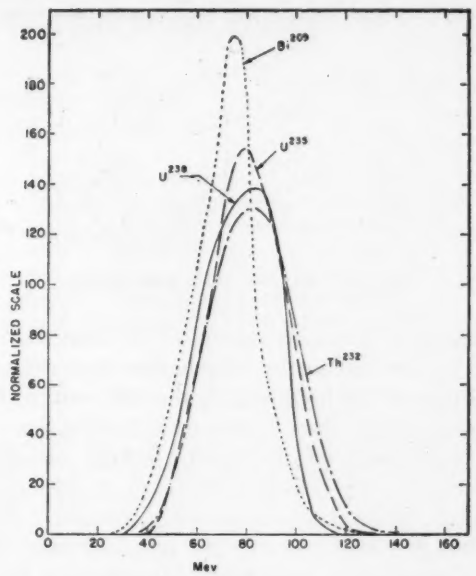

FIG. 12. Probable fragment energy distributions 90-Mev neutrons on U^{238}, U^{235}, Th^{232}, and Bi^{209}.

previously evaporated. Fission may be expected to have a threshold at some energy B above the ground level.

According to this picture the excess nuclear excitation is largely removed by neutron emission. It also predicts that the cross section for fission should be less than the total cross section with fluctuations from element to element. This is in agreement with the following. Recent measurements by Jungerman, Kelly, Wiegand, and Wright give the absolute fission cross section for 90-Mev neutrons on uranium and thorium to be 1.4 barns and 1.0 barns respectively. In each case the cross section is less than one half the geometric cross section and the two values differ considerably. There is no evidence at present concerning the time of neutron emission relative to the fission process.

In the high energy neutron fission of U^{235} the mean kinetic energy of the fragments is only slightly higher than that of the thermal neutron fission fragments. For

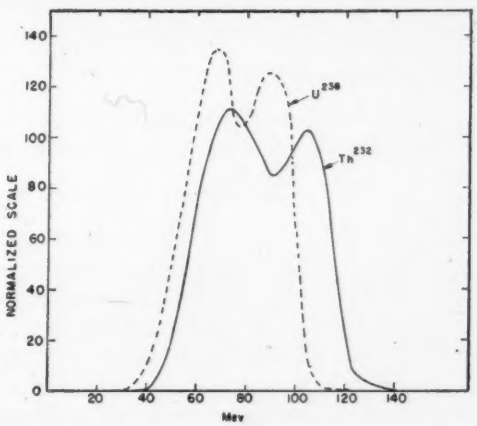

FIG. 13. Probable fragment energy distribution 45-Mev neutrons on U^{238} and Th^{232}.

UNIVERSITY OF MICHIGAN LIBRARIES

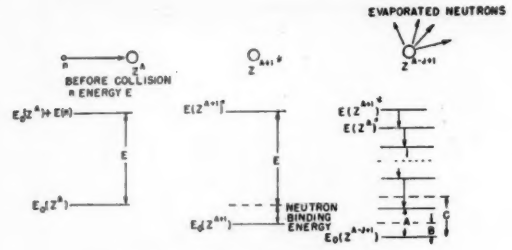

FIG. 14. Tentative fission mechanism.

Bi^{209} the mean fragment energy is 0.91 times the latter. It was pointed out in the introduction that the energy distribution of the fragments in thermal neutron fission is consistent with their known mass distribution under the assumption that the kinetic energy observed is derived from the coulomb repulsion of two charged fragments. Since it has been suggested above that in high energy neutron fission the actual division of the nucleus only occurs in a relatively unexcited state, in fact of the same order of excitation as in the thermal neutron case, the high energy case should agree with a similar treatment. This can be easily checked for symmetrical fission with the crude model of Fig. 15. At the moment of sparation the two fragments are assumed spherical in shape with a uniform distribution of charge and radii $R=r_0\times A^{\frac{1}{3}}$ where A is the mass number of the fragment and r_0 is a constant. Also the charge of the fragments is assumed proportional to their mass. Under these conditions the coulomb potential energy E_c at the moment of separation will be

$$E_c=\frac{(Z_1Z_2)e^2}{r_0(A_1^{\frac{1}{3}}+A_2^{\frac{1}{3}})},$$

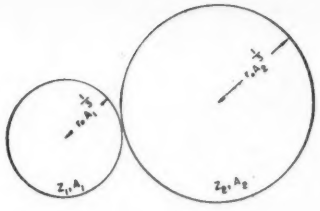

FIG. 15. Fission fragments at the moment of separation.

and for symmetrical fission

$$E_{c,s}=\frac{(Z_1e)^2}{2r_0(A_1)^{\frac{1}{3}}}=\frac{(Ze/2)^2}{2r_0((A+J-1)/2)^{\frac{1}{3}}}.$$

Comparison of $E_{c,s}$ for 90-Mev neutrons on Bi^{209} and on U^{235} and placing J equal to 10 gives the ratio 0.88 which agrees moderately well with the experimental value 0.94 ± 0.04 considering the model used.

The fragment energy distributions obtained by the use of 45-Mev neutrons are interesting in that they exhibit the transition region between single and double peaked distributions characteristic of fission with 90 Mev and slow neutrons respectively. However, the actual energy distribution of the neutrons incident upon the fissionable material in this case has a width at half maximum of approximately 19 Mev so that it is impossible at present to say in what energy region the transition occurs.

ACKNOWLEDGMENTS

We wish to thank C. Wiegand for some electronic equipment and for many valuable suggestions during the course of this work. We are deeply indebted to Professor E. Segrè for suggesting this problem and for many stimulating discussions throughout the course of the investigation. Thanks are also due the 184-inch cyclotron crew for valuable cooperation.

Small Angle Diffraction of Neutrons and Similar Wave Phenomena*

OTTO HALPERN AND EDWARD GERJUOY
University of Southern California, Los Angeles, California
(Received March 4, 1949)

A study of the diffraction of waves under very small angles is presented; the diffraction objects are ideal microcrystals, crystallites, assemblies of polycrystals and amorphous bodies. The diffraction cross section was found to depend in a very sensitive way on the angle of scattering and on the nature and orientation of the scattering object. The most significant result found consisted in the observation that the integral cross section of the diffraction object is in general proportional not to the number Z of atoms contained in the scatterer but to a higher power ($Z^{4/3}$ or $Z^{7/6}$). The results are applied to the interpretation of a number of experiments on the small angle scattering of neutrons and of light waves; possible effects on the polarization of neutrons are also discussed.

1. INTRODUCTION AND TERMINOLOGY

THE present paper contains a discussion of diffraction phenomena occurring under small angles. While all fine points of the theory of Laue spots have been discussed in the literature in great detail the subject of small angle diffraction has not received equal attention.** We intend in this paper to present the theory for several cases of general importance and to apply the mathematical results obtained to the interpretation of a number of experiments. Some of these experiments[1] have been carried out since the publication of our first note;[2] others may perhaps be undertaken on the basis of the theoretical results.

The essential points of interest are exemplified by simple cubic crystals. The discussion will be limited to crystals of this type to minimize the mathematical difficulties. The following terminology is used in this report. A microcrystal shall be understood to be an assembly of perfectly ordered unit cells. A crystallite or crystal grain shall be considered to consist of an assembly of microcrystals, the centers of which may show deviations from their ideal positions; assumptions about the deviations will be introduced in the discussion. It shall, on the other hand, be assumed that the microcrystals within a crystallite are not appreciably rotated with respect to each other.

A macroscopic crystal in our definition is nothing but a large crystallite. A polycrystalline body is an assembly of crystallites which are arbitrarily oriented with respect to each other. In any particular experiment the centers of these crystallites may be regarded as having a more or less orderly arrangement; the amount of disorder which can be ascribed, as explained below, depends on the nature of the material and the scattering angle.

Unless stated to the contrary, it is assumed that microcrystals and crystallites show no extinction, i.e., that the primary wave excites all parts of the microcrystal (crystallite) with approximately equal strength.

2. SMALL ANGLE DIFFRACTION BY A MICROCRYSTAL OF FIXED ORIENTATION

A. Scattering into Angles of the Order of $\lambda/\pi Na$

We consider the simplest possible case, a microcrystal in the shape of a rectangular parallelopiped, whose edges of lengths $(N_x-1)a$, $(N_y-1)a$, $(N_z-1)a$ are parallel to the crystallographic axes. The crystallographic axes lie along the mutually perpendicular unit vectors $\mathbf{i}_1$, $\mathbf{i}_2$, $\mathbf{i}_3$ and the distance between nearest neighbors is a. If a plane wave of wave-length λ is incident upon the microcrystal, then the amplitude of the diffracted wave is given by Laue's fundamental expression

$$A'=A\frac{\sin(\pi a/\lambda)N_x(\mathbf{q}\cdot\mathbf{i}_1)}{\sin(\pi a/\lambda)(\mathbf{q}\cdot\mathbf{i}_1)}\frac{\sin(\pi a/\lambda)N_y(\mathbf{q}\cdot\mathbf{i}_2)}{\sin(\pi a/\lambda)(\mathbf{q}\cdot\mathbf{i}_2)}\times\frac{\sin(\pi a/\lambda)N_z(\mathbf{q}\cdot\mathbf{i}_3)}{\sin(\pi a/\lambda)(\mathbf{q}\cdot\mathbf{i}_3)}. \quad (1)$$

In (1), A stands for the amplitude of the wave scattered by a single atom, while the vector $\mathbf{q}$ is defined by

$$\mathbf{q}=\mathbf{k}_0-\mathbf{k}_s. \quad (2)$$

Here, $\mathbf{k}_0$ and $\mathbf{k}_s$ denote the unit vectors in the direction of the incident and diffracted waves, respectively.

Limiting now the discussion to the case of very small scattering angles θ, for which $\theta=\sin\theta=|q|$, one notices that the scattering amplitude of the microcrystal remains of the order of $N_xN_yN_z=N^3$ if N_x, N_y, N_z all $\sim N$, provided the scattering angle is of the order of $\lambda/\pi Na$ or smaller. This obvious remark can be immediately demonstrated by expanding the sine functions in

* We wish to thank the Office of Naval Research for financial assistance in performing some of the numerical calculations.

** There is a considerable body of literature on small angle X-ray scattering and its use to measure the size of colloidal particles. See J. H. Donnay and C. G. Shull, "X-Ray Small-Angle Scattering Annotated Bibliography," Am. Soc. X-Ray and Electron Diffraction (March 1, 1946) and the review by O. Kratky and G. Porod, J. Colloid Sci. 4, 35 (1949). Although many of the basic problems in this field are similar to the problems discussed by us, the various points of view summarized by Kratky and Porod appear to be different from ours, possibly because we have been thinking primarily of applications to neutron scattering. Our principal results do not seem to have been stated previously.

[1] Hughes, Burgy, Heller, and Wallace, Phys. Rev. 75, 344 (1949).

[2] Otto Halpern, Phys. Rev. 73, 653 (1948).

UNIVERSITY OF MICHIGAN LIBRARIES

the numerators and denominators of (1). The differential scattering cross section becomes, therefore, proportional to N^6; all atoms contained in the microcrystal scatter practically in phase. The integral cross section, on the other hand, is obtained by integrating the differential cross section essentially over that range of angles in which the amplitude is proportional to N^3. Now this angular range subtends a solid angle of about $\pi\theta^2=\pi(\lambda/\pi Na)^2$. So the integral cross section becomes proportional to $N^4=Z^{4/3}$.

This simple result, though stemming from the Laue formula (1), is merely a reformulation of the fact that the microcrystal as a whole, while it is large compared to the wave-length, necessarily produces a narrow diffraction pattern in the forward direction. It is clear that the width and intensity of this diffraction pattern, irrespective of the precise shape of the microcrystal, will be of the order of magnitude just determined. One should remember that the intensity of reflection at a Bragg angle is also proportional to N^6; but since this is true only for a very narrow range of angles of incidence, of solid angle $\sim\lambda/Na$, the integrated intensity becomes, as is well known, again proportional to the total number of atoms in the microcrystal. In the present case, which constitutes diffraction into the zero order, every direction of incidence may be called incidence under a Bragg angle; this increases the integral cross section by a factor of the order N.

Particular care is necessary in discussing the problem of primary extinction if one takes into account the cross section for small angle scattering. In the customary treatments, only the scattering into Laue spots of order higher than zero is considered; a microcrystal of linear dimensions 10^{-4} cm, an atomic cross section of the order 10^{-24} cm^2 and wave-length and lattice distance both of the order of 10^{-8} cm has under these assumptions an integral cross section into a single Laue spot of approximately 10^{-12} cm^2. To this cross section must now be added the expression which has been derived, which, as we saw, is about 10^4 times larger. This means that the microcrystals will, in general, scatter the incident wave into angles of the order of 3×10^{-5} radians after traversing a thickness of only 10^{-4} cm. If the thickness is much larger than this, say 10^{-3} cm, the primary beam must, strictly speaking, be regarded as almost completely extinguished. The angular spread of the diffracted beam under these conditions results from a succession of repeated scatterings. The width cannot, however, be estimated by the usual multiple scattering formula which in this case would make the angular spread $(3\times10^{-5})(10)^{\frac{1}{2}}$ radians. The reason is that at these small angles the phases of the successive scatterings are to a considerable degree coherent. As the usual multiple scattering formula assumes the phases of the successive scatterings are incoherent, $(3\times10^{-5})(10)^{\frac{1}{2}}$ radians is probably an upper limit to the spread. Certainly it is difficult to see how a succession of coherent scatterings can generally result in a wider spread than a succession of wholly incoherent scatterings.

Under ordinary experimental conditions these scattering angles are small in comparison to the width of the original beam. The scattered beams are in effect reabsorbed in the main beam, and the small angle scattering may, therefore, be ignored. With very well defined beams, however, the considerations of this section become significant.

B. Scattering into Angles of the Order of $(\lambda/\pi Na)^{\frac{1}{2}}$

In addition to the always-present scattering into angles of the order of $\lambda/\pi Na$ with an intensity proportional to N^6, there exists a diffraction effect at angles of the order of $(\lambda/\pi Na)^{\frac{1}{2}}$ with an intensity proportional to N^5, provided that one of the crystal axes is approximately perpendicular to the direction of the incident beam. To demonstrate this, define two systems of rectangular coordinates, primed and unprimed. The unprimed system coincides with the unit vectors $\mathbf{i}_1$, $\mathbf{i}_2$, $\mathbf{i}_3$ along the crystallographic axes. Let the incident wave be parallel to the $\mathbf{i}_3'=z'$ axis and assume that, e.g., the x and x' axes shall coincide. In other words, we assume for the present that the incident wave is exactly perpendicular to one of the crystallographic axes. Then $\mathbf{i}_2$ and $\mathbf{i}_3$ have obviously no x or x' components. We consider the wave scattered in the x', z' plane into a small angle $|q|$ relative to the z' axis. The intensity of this wave is of course proportional to

$$A'^2=A^2\frac{\sin^2(\pi aN_x/\lambda)(\mathbf{q}\cdot\mathbf{i}_1)}{\sin^2(\pi a/\lambda)(\mathbf{q}\cdot\mathbf{i}_1)}\frac{\sin^2(\pi aN_y/\lambda)(\mathbf{q}\cdot\mathbf{i}_2)}{\sin^2(\pi a/\lambda)(\mathbf{q}\cdot\mathbf{i}_2)}\times\frac{\sin^2(\pi aN_z/\lambda)(\mathbf{q}\cdot\mathbf{i}_3)}{\sin^2(\pi a/\lambda)(\mathbf{q}\cdot\mathbf{i}_3)}. \quad (3)$$

We allow the scattering angle $|q|$ to assume values of the order of $(\lambda/\pi Na)^{\frac{1}{2}}$, where as before N_x, N_y, N_z all $\sim N$. With our assumptions the vector $\mathbf{q}$ is very nearly parallel to $\mathbf{i}_1$. Consequently, the first factor in (3) is of order $(\lambda/\pi a|q|)^2=N\lambda/\pi a$, because the numerator equals $\frac{1}{2}$ on the average $(N\pi a|q|/\lambda\sim(N\pi a/\lambda)^{\frac{1}{2}}\gg1)$, whereas the sines in the denominator of (3) may be replaced by their arguments $(\pi a|q|/\lambda\sim(\pi a/N\lambda)^{\frac{1}{2}}\ll1)$. The second and third factors are each of order N^2. This can be seen immediately by expressing the scalar products $(\mathbf{q}\cdot\mathbf{i}_2)$ and $(\mathbf{q}\cdot\mathbf{i}_3)$ in terms of their components in the primed system. These scalar products are proportional to $(\mathbf{q}\cdot\mathbf{i}_3')$ which for small $|q|$ is of order $|q|^2$. Thus the sines in the numerator of the second and third factors of (3) may also be replaced by their arguments, for $|q|\sim(\lambda/\pi Na)^{\frac{1}{2}}$, which is sufficient to prove the intensity is $\sim N^5\lambda/\pi a$.

To obtain from the differential cross section proportional to N^5 the integral cross section of scattering, we have to integrate keeping $\mathbf{k}_0$ constant over an angular domain of $\mathbf{k}_s$, so chosen that in this domain the assumptions made remain valid. The directions of the crystal

axes remain fixed. We leave out of consideration the much larger intensities occurring at angles of the order $\lambda/\pi Na$ as well as possible much smaller intensities at angles considerably larger than $(\lambda/\pi Na)^{\frac{1}{2}}$.

Let the direction of $\mathbf{k}_s$ be defined by spherical coordinates (θ, φ) with $\mathbf{k}_0$ as the polar axis. As we have seen, in the x', z' plane, θ extends over a range of the order $(\lambda/\pi Na)^{\frac{1}{2}}$. The angular domain $\sin\theta d\theta d\varphi$ therefore becomes $(\lambda/\pi Na)d\varphi$. To determine the permissible range of φ, we observe that as long as $\mathbf{k}_s$ has only a small component perpendicular to the x', z' plane the value of $(\mathbf{q}\cdot\mathbf{i}_2')$ will be of the order of $\theta\varphi$. The scalar products $(\mathbf{q}\cdot\mathbf{i}_2)$ and $(\mathbf{q}\cdot\mathbf{i}_3)$ will, therefore, continue to be of the order of magnitude θ^2 as long as $(\mathbf{q}\cdot\mathbf{i}_2')$ remains of the order of θ^2. This means that φ may occupy a range of the order of θ. The integral cross section, therefore, becomes proportional to $N^{7/2}(\lambda/\pi a)^{5/2}$, or to $Z^{7/6}$.

As pointed out above, these diffraction effects at angles $|q|\sim(\lambda/\pi Na)^{\frac{1}{2}}$ arise only if one of the crystal axes is perpendicular to $\mathbf{k}_0$. How accurately this condition of perpendicularity must be satisfied can be easily seen, as follows: Obviously, all factors in (3) retain their values determined under the assumption that the x and x' axes coincide, provided only that the angle between the x and x' axes remains of the order of $(\lambda/\pi Na)^{\frac{1}{2}}$. The probability of such an occurrence is, therefore, apart from a permutation factor proportional to $(\lambda/\pi Na)^{\frac{1}{2}}$. More precisely, $\mathbf{k}_0$ may lie in a range of solid angles $2\pi\sin\theta d\theta$, with the x axis now the polar axis. Hence $\sin\theta\sim 1$ and $d\theta\sim(\lambda/\pi Na)^{\frac{1}{2}}$, which shows the probability, equal to $1/4\pi$ the allowed range of solid angles, is $\sim(\lambda/\pi Na)^{\frac{1}{2}}$. If we deal with a solid microcrystal of *random* orientation, we can, therefore, anticipate the following effects: (A) scattering into angles of the order $\lambda/\pi Na$ with an integral cross section of the order $Z^{4/3}$ (normal forward diffraction pattern); (B) scattering into angles of the order $(\lambda/\pi Na)^{\frac{1}{2}}$ with an integral cross section proportional to Z; (C) scattering into the various Debye rings with an integral cross section proportional to Z.

3. SMALL ANGLE DIFFRACTION BY AN ASSEMBLY OF INDEPENDENT MICROCRYSTALS

The results for scattering under small angles obtained in Section 2 can now be extended for the treatment of an assembly of independently scattering microcrystals. Such an assembly is approximately realized in a powder consisting of microcrystals of various sizes. If the space between the microcrystals is comparable to the volume occupied by them, i.e., in the case of a loose powder, the microcrystals can be considered to scatter independently of each other. This remark is not entirely obvious; its justification stems from the formulas in Section 4 for the scattering from a non-ideal single crystal. It follows from those formulas that incoherent scattering becomes appreciable at angles $\sim\lambda/Na$ or greater when the distances between successive microcrystals differ by amounts $\sim Na$.

When the microcrystals scatter incoherently, the total scattered intensity can be assumed to be additive. To determine the intensity scattered by an assembly of independently scattering microcrystals, we have to average the previously obtained results over all possible orientations of the microcrystals. This procedure differs again for the two angular domains of interest, $\sim\lambda/\pi Na$ and $\sim(\lambda/\pi Na)^{\frac{1}{2}}$.

One can see easily that for $|q|\lesssim\lambda/\pi Na$ the integral cross section from an individual microcrystal becomes independent of the orientation of the microcrystal and is proportional to N^4. The integral cross section from an assembly of M^3 independently scattering microcrystals therefore $=\sim M^3A^2N^6\pi(\lambda/\pi Na)^2$. A more exact calculation, using the integral whose evaluation is described below, shows that the integral cross section is actually more nearly $3\pi M^3A^2N^6(\lambda/\pi Na)^2$. In other words, the effective angle of scattering, within which all atoms scatter very nearly in phase, is about $\sqrt{3}\lambda/\pi Na$ instead of the crudely estimated $\lambda/\pi Na$.

The problem of calculating the average intensity scattered into the angular domain $|q|\sim(\lambda/\pi Na)^{\frac{1}{2}}$, though easy in principle, offers very considerable analytical difficulties. Keeping the directions of the incident and scattered beam constant, we have to average over all possible orientations of the microcrystal. This involves a three-dimensional integration since the microcrystal is a rigid body and has three degrees of freedom of rotation. In preference to this procedure we keep the three crystal axes fixed as our axes of coordinates, allow the direction of incidence $\mathbf{k}_0$ to take on all values, and then, for each $\mathbf{k}_0$, integrate over $\mathbf{k}_s$ keeping the angle between the incident and the scattered beam constant. This three-dimensional integration may now be replaced by an integration over all directions of $\mathbf{q}$ and over all incident directions consistent with the conditions that the magnitude of $\mathbf{q}$ is fixed and that $\mathbf{q}$ must be the vector difference between two unit vectors. However, since the scattered intensity (3) depends only on $\mathbf{q}$, the last integration does not affect the average.

Analytically, this procedure leads to the following expression: The intensity of scattering for an arbitrary value of $|q|$ is given by $N^6A^2G(w)$ where

$$G(w)=\frac{1}{4\pi}\int_0^{\pi}d\theta\int_0^{2\pi}d\varphi\,\sin\theta\frac{\sin^2(w\sin\theta\cos\varphi)}{N^2\sin^2\left(\frac{w}{N}\sin\theta\cos\varphi\right)}$$
$$\times\frac{\sin^2(w\sin\theta\sin\varphi)}{N^2\sin^2\left(\frac{w}{N}\sin\theta\sin\varphi\right)}\frac{\sin^2(w\cos\theta)}{N^2\sin^2\left(\frac{w}{N}\cos\theta\right)},\quad(4)$$

and

$$w=(N\pi a|q|/\lambda).\quad(5)$$

Obviously (4) is obtained from (3) by simply writing $N_x=N_y=N_z=N$ and introducing spherical coordinates

UNIVERSITY OF MICHIGAN LIBRARIES

with the polar axis along $\mathbf{i}_3$. The integrand in (4) is large for very small values of w. It decreases rapidly when w becomes comparable with unity and takes on large values again only in the neighborhood of the first Laue maximum where w is comparable with N. We are here concerned only with its evaluation for very small values of w/N, i.e. $|q| \lesssim \sim(\lambda/\pi Na)^{\frac{1}{2}}$. This allows us to replace all the sines in the denominator by their arguments. We have, therefore,

$$G(w)=\frac{1}{4\pi}\int_0^{\pi} d\theta \int_0^{2\pi} d\varphi \sin\theta \frac{\sin^2(w\sin\theta\cos\varphi)}{w^2\sin^2\theta\cos^2\varphi} \times\frac{\sin^2(w\sin\theta\sin\varphi)}{w^2\sin^2\theta\sin^2\varphi}\frac{\sin^2(w\cos\theta)}{w^2\cos^2\theta}. \quad (6)$$

$G(w)$, as defined by (6), constitutes an involved transcendental function of w. One of the authors (E.G.), using a rather lengthy analytical method, has succeeded in reducing the double integral to a transcendental function and a single integral; the single integral permits numerical evaluation as a function of the parameter w. In the appendix a verification of the results found is given with the aid of a comparatively simple method. It seems unlikely, however, that the results could have been originally derived by the method of the appendix.

It was found in this way that, without further approximation,

$$G(w)=\frac{3}{4w^4}\left\{\frac{\sqrt{3}\sin 2w\sqrt{3}}{w}-\frac{\sin^2 w\sqrt{3}}{w^2} -\frac{3\sqrt{2}\sin 2w\sqrt{2}}{w}+\frac{3\sin^2 w\sqrt{2}}{w^2}+\frac{\sin 2w}{w}-\frac{3\sin^2 w}{w^2}\right\} +\frac{3}{w^4}\left\{\frac{\pi}{2}\sin^2 w+\int_0^1 dx\frac{(1+2x^2)}{1+x^2}\cos[2w(1+x^2)^{\frac{1}{2}}] -\int_0^1 dx\frac{x^2}{1+x^2}\cos[2w(2+x^2)^{\frac{1}{2}}]\right\}. \quad (7)$$

Asymptotically $G(w)$ behaves for large w as

$$G(w)\sim(3\pi/2)(\sin^2 w/w^4). \quad (8)$$

This can be learned by inspection of (7). This asymptotic behavior can also be demonstrated directly from (6) if one replaces the integration over all solid angles by an integration over the very small range of angles for which $\mathbf{q}$ is very nearly parallel to one of the crystal axes. This result provides a rigorous justification of the more qualitative arguments by which, in Section 2B, we estimated the average intensity from a randomly oriented microcrystal. At angles $|q|\sim(\lambda/\pi Na)^{\frac{1}{2}}$ the scattering from a collection of microcrystals results from scattering by that small fraction of microcrystals which are so oriented that the incident vector $\mathbf{k}_0$ is very nearly perpendicular to one of the crystal axes.

In the calculations so far carried out, the microcrystal (crystallite) was assumed to be bounded by planes perpendicular to the principal directions of the unit cell. When calculations are carried out for microcrystals which are bounded by other lattice planes, it turns out that large intensities occur at angles of the order of $(\lambda/\pi Na)^{\frac{1}{2}}$ only if the incident wave vector $\mathbf{k}_0$ is approximately parallel to one of the plane faces of the microcrystal. The significant factor in the scattering at these small angles is therefore the shape of the scatterer and not the orientation of the crystallographic axes. This result receives support from a consideration of the diffraction by an amorphous parallelopiped. As shown in Section 8 below, for a material the index of refraction of which differs from unity only by infinitesimal amounts, the diffracted amplitude is proportional to

$$\rho=\frac{\sin(\pi L_1/\lambda)(\mathbf{q}\cdot\mathbf{i}_1)}{(\pi/\lambda)(\mathbf{q}\cdot\mathbf{i}_1)}\frac{\sin(\pi L_2/\lambda)(\mathbf{q}\cdot\mathbf{i}_2)}{(\pi/\lambda)(\mathbf{q}\cdot\mathbf{i}_2)} \times\frac{\sin(\pi L_3/\lambda)(\mathbf{q}\cdot\mathbf{i}_3)}{(\pi/\lambda)(\mathbf{q}\cdot\mathbf{i}_3)}. \quad (9)$$

Here L_1, L_2, L_3 denote, respectively, the lengths of the sides of the parallelopiped along the directions $\mathbf{i}_1$, $\mathbf{i}_2$, $\mathbf{i}_3$. Comparison of (9) with (1) shows the identical structure of the two expressions. One can therefore deduce, just as done in Section 2B, the appearance of large diffraction effects at angles of the order of $(\lambda/\pi L)^{\frac{1}{2}}$ for $\mathbf{k}_0$ very nearly parallel to one of the parallelopiped faces, even though the scattering material is perfectly homogeneous.

By examining the general expression for the scattering from a homogeneous material of arbitrary shape (see Section 8 below), it is possible to show that for arbitrary directions of incidence the scattering intensity I is, for angles $|q|\sim(\lambda/\pi L)^{\frac{1}{2}}$

$$I=[C(1-\mu^2)^2/\lambda^4]L^2(\lambda/\pi|q|)^4, \quad (10)$$

provided only the surface does not have too many irregularities and the radius of curvature is nowhere very large. In (10) C is a numerical factor depending on the shape, μ is the index of refraction, and L is some average dimension. Comparison of (10) with (5) and (8), remembering the average intensity for the microcrystals is $N^6A^2G(w)$, shows that the form of (8), in particular its dependence on $|q|$ and on the number of scatterers, does not depend on the cubic shapes used to obtain (8).*** In addition, we have calculated the average scattered intensities, using the appropriate accurate Laue formulas, for a rectangular parallelopiped whose dimensions are $2Na$, Na, $Na/2$, and for a 45° wedge whose volume is N^3a^3. In the asymptotic region $|q|\sim(\lambda/N\pi a)^{\frac{1}{2}}$ the average scattered intensity from each of these shapes differs from the average for a cube of length Na by not more than about ten percent. It

*** The average intensity scattered by homogeneous spheroidal particles has been calculated by L. C. Roess and C. G. Shull, J. App. Phys. 18, 308 (1947).

appears therefore that our computations for cubic microcrystals will not be far off for the actual shapes which will occur in practice.

4. THE SCATTERING BY A CRYSTALLITE (NON-IDEAL SINGLE CRYSTAL)

The crystallite is assumed to be made up of microcrystals; the letters M_x, M_y, M_z refer respectively to the number of microcrystals along different coordinate axes which we here take parallel to the axes of the microcrystals. The microcrystals themselves consist of $N_xN_yN_z$ identical scattering centers. The microcrystals are assumed to be more or less parallel to each other, but their centers shall be located respectively at the points $\mathbf{R}$, coordinates $(R_xN_xa+\delta_x,\ R_yN_ya+\delta_y,\ R_zN_za+\delta_z)$. The quantities R_x, R_y, R_z are integers $0\leqslant R_x\leqslant M_x-1$, $0\leqslant R_y\leqslant M_y-1$, $0\leqslant R_z\leqslant M_z-1$. The vector $\boldsymbol{\delta}$ may vary, microcrystal to microcrystal; its components determine collectively the deviation of the crystallite from the ideal case in which all $\boldsymbol{\delta}$ would be zero.

The wave scattered by the crystallite is, in simple extension of the results of Section 2, given by the following expression

$$A''=A'\sum_{R_x,\,R_y,\,R_z}\exp\left(\frac{2\pi i}{\lambda}\mathbf{R}\cdot\mathbf{q}\right). \tag{11}$$

Here the amplitude A' is again given by the expression (1), with A being the amplitude produced by the single scatterer.

One can convince oneself easily that in the case of an ideal crystallite (all $\boldsymbol{\delta}$ zero) the expression (11) can be immediately summed to give an analogous expression to (1) in which every N_x is replaced by M_xN_x, etc.

If, on the other hand, the deviation from the ideal structure has to be considered, then no summation of (11) is feasible, and we have to be satisfied with statements concerning the average value of the square of (11). This average value requires for its determination a knowledge of the statistical distribution of the components of $\boldsymbol{\delta}$. We want to treat here in detail a particularly simple assumption according to which the values of $\boldsymbol{\delta}$ for every microcrystal are independent of those of the other microcrystals. This assumption is obviously unrealistic for a crystallite since the positions of the neighboring microcrystals affect each other. Still it seems that a calculation based on this admittedly arbitrary assumption is not without value, particularly because it gives us a qualitative and semiquantitative insight into a number of special cases of physical significance. The assumption becomes a better approximation to actual facts if we are dealing with a loose powder rather than a solid crystallite or single crystal. (The microcrystals in a powder are not parallel but this merely requires an average over orientation in the argument below.)

The calculation of the average value of $|A''|^2$ can now be carried out in a straightforward manner. We write first

$$|A''|^2=A'^2\left[\sum_{R_x,\,R_y,\,R_z}\exp\left(\frac{2\pi i}{\lambda}\mathbf{R}\cdot\mathbf{q}\right)\right]\times\left[\sum_{R_x',\,R_y',\,R_z'}\exp\left(\frac{-2\pi i}{\lambda}\mathbf{R}'\cdot\mathbf{q}\right)\right], \tag{12}$$

and introducting the abbreviation $\nu=2\pi/\lambda$ and

$$\tau(R_x,R_y,R_z)=a\mathbf{q}\cdot[R_xN_x\mathbf{i}_1+R_yN_y\mathbf{i}_2+R_zN_z\mathbf{i}_3], \tag{13}$$

we can also write (12) in the form

$$|A''|^2=A'^2\sum_{R_x,\,R_y,\,R_z,\,R_x',\,R_y',\,R_z'}\exp i\nu\{\tau(R_x,R_y,R_z)-\tau(R_x',R_y',R_z')+\mathbf{q}\cdot\boldsymbol{\delta}(R_x,R_y,R_z)-\mathbf{q}\cdot\boldsymbol{\delta}(R_x',R_y',R_z')\}. \tag{14}$$

The average value of $|A''|^2$ is now simply obtained by multiplying the expression (14), which is, among other things, a function of the $3M_xM_yM_z$ components of $\boldsymbol{\delta}(R_x,R_y,R_z)$ by a function determining the probability of a definite set of values of $\boldsymbol{\delta}(R_x,R_y,R_z)$ and integrating over all possible values of $\boldsymbol{\delta}(R_x,R_y,R_z)$. According to our assumption of uncorrelated displacements, this probability function is a product of identical functions of the displacements of each microcrystal. That is, if $g[\boldsymbol{\delta}(R_x,R_y,R_z)]d\delta_xd\delta_yd\delta_z$ is the probability that the components of the displacement $\boldsymbol{\delta}$ of the microcrystal specified by the triad (R_x,R_y,R_z) lie between δ_x and $\delta_x+d\delta_x$, etc., the total probability function is given by

$$P=\prod_{R_x,\,R_y,\,R_z}g[\boldsymbol{\delta}(R_x,R_y,R_z)]d\delta_x(R_x,R_y,R_z)d\delta_yd\delta_z. \tag{15}$$

When $|A''|^2$ in (14) is multiplied by P in (15) and integrated over all values of $\boldsymbol{\delta}(R_x,R_y,R_z)$ there appear terms in the resultant $3M_xM_yM_z$ dimensional integral which refer to one microcrystal only, and which are of the form

$$A'^2\int\prod_{R_x,\,R_y,\,R_z}g[\boldsymbol{\delta}(R_x,R_y,R_z)]\times d\delta_x(R_x,R_y,R_z)d\delta_yd\delta_z=A'^2, \tag{16}$$

and other terms which refer to two microcrystals, and which are of the form

$$QA'^2\int d\boldsymbol{\delta}d\boldsymbol{\delta}'g(\boldsymbol{\delta})g(\boldsymbol{\delta}')\exp[i\nu\mathbf{q}\cdot(\boldsymbol{\delta}-\boldsymbol{\delta}')]. \tag{17}$$

The factor Q appearing in (17) is angle-dependent through the functions $\tau(R_x,R_y,R_z)$ and $\tau(R_x',R_y',R_z')$ but is *independent* of the special choice of the probability functions $g(\boldsymbol{\delta})$. The expression (17) can now be simply evaluated in a symbolic form. It equals

$$QA'^2\left|\int d\boldsymbol{\delta}g(\boldsymbol{\delta})\exp i\nu(\mathbf{q}\cdot\boldsymbol{\delta})\right|^2=QA'^2|T|^2. \tag{18}$$

UNIVERSITY OF MICHIGAN LIBRARIES

The actual values of $|T|^2$ will be given below for various choices of $g(\delta)$. The average value of $|A''|^2$ therefore takes on the final form

$$\langle|A''|^2\rangle = S_1A'^2 + S_2A'^2|T|^2. \quad (19)$$

In (19), the factors S_1 and S_2 are functions of angle (between $\mathbf{q}$ and the coordinate axes) and of the number of microcrystals, but are not dependent on the actual choice of the distribution function.

To determine S_1 and S_2 we evaluate (19) for two limiting cases in which $\langle|A''|^2\rangle$ can be assumed to be known without further calculation.

A. In the case of a perfect crystallite, the function $g(\delta)$ reduces to Dirac's delta function, T becomes equal to 1 and the crystallite becomes equal to a microcrystal consisting of M_xN_x, M_yN_y, M_zN_z scatterers along the various coordinate axes. But in this case we have obviously, as in (3),

$$\langle|A''|^2\rangle = A^2\frac{\sin^2(\pi a/\lambda)M_xN_x(\mathbf{q}\cdot\mathbf{i}_1)}{\sin^2(\pi a/\lambda)(\mathbf{q}\cdot\mathbf{i}_1)}\cdots$$

$$= A'^2\frac{\sin^2(\pi a/\lambda)M_xN_x(\mathbf{q}\cdot\mathbf{i}_1)}{\sin^2(\pi a/\lambda)N_x(\mathbf{q}\cdot\mathbf{i}_1)}\cdots = A'^2W^2. \quad (20)$$

B. We assume that the displacements of the various microcrystals become so large that the scattering by them can be assumed to be independent. In that case, obviously, $|T|^2$ approaches zero, as is always the case for a form factor in which the displacements are very large compared to the wave-length, and $\langle|A''|^2\rangle$ equals the sum of the intensities coming from the independently scattering microcrystals, i.e.,

$$\langle|A''|^2\rangle = M_xM_yM_zA'^2. \quad (21)$$

We have thus obtained the following two equations for S_1 and S_2:

$$S_1A'^2 + S_2A'^2 = A'^2W^2, \quad S_1A'^2 = M_xM_yM_zA'^2. \quad (22)$$

Combining (19) and (22) we obtain for intermediate values of T the general expression

$$\langle|A''|^2\rangle = M_xM_yM_z[1-|T|^2]A'^2 + |T|^2W^2A'^2. \quad (23)$$

Some typical values of $|T|^2$ follow. If the center of each microcrystal may with equal probability lie anywhere within a parallelopiped of dimensions $2\epsilon_x$, $2\epsilon_y$, $2\epsilon_z$ along $\mathbf{i}_1$, $\mathbf{i}_2$, $\mathbf{i}_3$ respectively, then we have

$$T = \frac{\sin\nu\epsilon_x(\mathbf{q}\cdot\mathbf{i}_1)}{\nu\epsilon_x(\mathbf{q}\cdot\mathbf{i}_1)}\frac{\sin\nu\epsilon_y(\mathbf{q}\cdot\mathbf{i}_2)}{\nu\epsilon_y(\mathbf{q}\cdot\mathbf{i}_2)}\frac{\sin\nu\epsilon_z(\mathbf{q}\cdot\mathbf{i}_3)}{\nu\epsilon_z(\mathbf{q}\cdot\mathbf{i}_3)}. \quad (24)$$

A Gaussian distribution of displacements along the crystal axes gives

$$T = \exp\left[\frac{-\nu^2}{4}(q_x^2\epsilon_x^2 + q_y^2\epsilon_y^2 + q_z^2\epsilon_z^2)\right]. \quad (25)$$

Obviously, the angle dependence of the scattered intensity is not very different for different forms of "g." For very small angles $|T|^2$ approaches 1 so that the scattering is nearly that of a perfect large microcrystal. $|T|^2$ decreases rapidly with increasing angle, and the scattered intensity then becomes $M_xM_yM_zA'^2$. Assuming for the moment that $\epsilon_x = \epsilon_y = \epsilon_z = \epsilon$, we obtain as an estimate of the angle θ at which the scattering begins to be appreciably incoherent, i.e., the angle at which $|T|^2$ begins to deviate markedly from 1, $\nu^2|q|^2\epsilon^2/4 \sim 1$, or

$$(\pi\epsilon/\lambda)\sin\theta \sim 1. \quad (26)$$

According to (23) the scattered intensity divides into a coherent part $|T|^2W^2A'^2$ and an incoherent part $M_xM_yM_zA'^2(1-|T|^2)$. The dependence of $W^2A'^2$ on angle is the same as that discussed in Section 2 for perfect crystals, if one only remembers that the number of scatterers in these perfect crystals are now $M_xM_yM_zN_xN_yN_z$. Consequently the coherent part has an angular width of the order $\lambda/\pi aMN$. The width of the incoherent part is of the order $\lambda/\pi aN$. The latter estimate is valid for random orientation of the crystallite, provided $|T|^2$ does not remain too near unity for angles $\sim\lambda/\pi aN$. Substituting in (26), this requires that ϵ be $\sim aN$. This justifies our assertions in the first paragraph of Section 3, especially since with a collection of randomly oriented microcrystals the probability function (15) must be supplemented by a distribution function in orientation; it can be seen that this results in a reduction of the amount of coherent scattering and therefore effectively in a further diminution of $|T|^2$.

If, on the other hand. the crystallite and therefore the microcrystals have the exceptional orientation that $\mathbf{q}$ vector becomes parallel to a crystal axis, then, as shown in Section 2, the respective scattering widths are $(\lambda/\pi aMN)^{\frac{1}{3}}$ and $(\lambda/\pi aN)^{\frac{1}{3}}$. It is necessary to note that the precise form of W^2 depends on our assumption that the crystallite is a parallelopiped. It can, however, be shown that our results are not changed by assuming any other shape for the entire scattering region.

Some remarks should be added in this connection concerning the case of an assembly of randomly oriented crystallites. The only new feature arising in this case comes from possible large distributions of favorably oriented crystal grains (crystallites). The calculation proceeds very analogously to that given above so that we refrain from reproducing it to save space. It can easily be seen that if the crystallites are not too tightly packed, then for large lattice errors the scattered intensity results from adding incoherently the waves scattered by all the microcrystals, averaged over orientation as in the preceding section. If the crystallites are very nearly perfect the scattering can be obtained by considering the crystallites to be giant microcrystals of dimensions $\sim MNa$.

If, on the other hand, we are dealing with closely packed crystallites, the preceding calculations, which

neglect correlations in position and orientation become unrealistic; one can then obtain simple information by using for example the amorphous picture. If the whole scatterer is represented by an amorphous large block of material, then the only angles under which large diffraction can occur are of the order of $\lambda/\pi L$ or, under certain favorable conditions, $(\lambda/\pi L)^{\frac{1}{2}}$ (L=length of one side of the scatterer). A hole in this amorphous block of the form of a parallelopiped will, therefore, in first (Born) approximation give rise to a diffraction pattern which is equal to that of an equivalent isolated small parallelopiped.

5. MAGNETIC SCATTERING UNDER VERY SMALL ANGLES

As a first illustration of the theoretical principles developed, we discuss a phenomenon of scattering under very small angles, which has lately been reported by Hughes and his collaborators.[1] It was observed that a primary beam of neutrons passing through a sheet of iron was broadened if the iron was unmagnetized but remained unchanged in angular distribution if the iron was magnetized. It was found experimentally that for neutrons of a wave-length of approximately 1.8A° the broadening was proportional to the square root of the thickness of the iron plate and had a value of 0.4 minutes for one centimeter of unmagnetized iron.[3]

The fact that the phenomenon disappears for magnetized iron suggests immediately a general line of explanation. According to well-established concepts, unmagnetized iron consists of fully magnetized domains of random orientation; in the state of magnetization the directions of the magnetic moment of the elementary domains become nearly parallel. The scattering center in each domain affects neutrons for two reasons. There is a nuclear scattering amplitude A_N as well as a magnetic scattering amplitude A_m. The nuclear scattering amplitude is the same throughout the whole iron sheet; the diffraction pattern due to it is, therefore, limited to an angle of the order of $\lambda/\pi L$ or $(\lambda/\pi L)^{\frac{1}{2}}$, depending on the shape and orientation of the sheet. L is of the order of the linear dimensions of the entire sheet. Consequently, these angles are in most cases unobservably small. The same is true for the magnetic scattering amplitude in the case of magnetized iron sheets. For unmagnetized iron, on the other hand, the amplitude varies in sign almost at random from domain to domain; the resultant diffraction pattern, therefore, consists in a superposition of the intensity produced by the individual domains. If the broadening of the beam per domain is of the order of $\lambda/\pi D$, where D indicates a linear dimension of the domain, then the broadening produced by the iron sheet is proportional to the square root of the number of domains traversed, using the usual multiple scattering formula. Thus we have obtained the simple dependence of the effect on the thickness of the iron plate.

[3] Private communication.

To derive theoretically the value for the absolute broadening φ by one centimeter of iron, we have to use the formula

$$\varphi=\varphi_0(1/D)^{\frac{1}{2}} \tag{27}$$

in which φ_0 is the average broadening per domain. We use (27) in preference to the more customary $\varphi=\varphi_0(n\sigma)^{\frac{1}{2}}$, where n is the number of scatterers per unit volume and σ the cross section, because as we shall see below the cross section σ is so large that the beam is almost certain to be scattered by each domain it encounters. The number of domains encountered in 1 cm of path is about $1/D$. Leaving extinction effects out of consideration, we have previously obtained for φ_0 the value $\varphi_0\sim\lambda/\pi D$ or perhaps $\sqrt{3}\lambda/\pi D$ (Section 3). Agreement with the experimental value of 0.4 minute is reached by putting D equal to $\sim 10^{-3}$ cm.

This procedure is not quite correct. We have emphasized in Section 2A that our estimate of φ_0 holds only in the absence of extinction. This means that not too large a fraction of the primary beam must be scattered in one domain. If we, on the other hand, insert the numerical value[4] $A_m=\sim 5\times 10^{-13}$ for the average scattering amplitude due to the magnetic moment of the iron atoms and calculate the total intensity scattered by a block of linear dimension 10^{-3}, we obtain $\sigma=3\pi A_m^2N^4(\lambda/\pi a)^2=\sim 7.5\times 10^{-5}$. With $n=10^9$, $n\sigma x>1$ for $x=10^{-3}$. This result clearly indicates that within one domain extinction and multiple scattering occur.

Hughes and his collaborators have given a somewhat different theory for the effect observed by them. They make use of the concept of magnetic double refraction[5] as it has been developed previously and consider the spreading of the primary beam as being caused by *refraction* of the neutrons at the boundaries of successive domains. Since in the unmagnetized state these domains are magnetized at random, the various polarization states of the neutrons will be deflected, according to this picture, by varying amounts at each boundary; the effect obviously will be proportional to the square root of the thickness traversed.

A closer study of the quantitative conditions makes it clear that this theoretical picture is over idealized. The magnetic index of refraction is, of course, only another aspect of the effect of scattering; but for the domain sizes involved one can easily see that the process does not yet fall into the range of geometrical neutron optics but rather into the field of neutron diffraction as described above. In fact, the angular deflection produced by the assumed refraction is smaller than the diffraction angle $\lambda\sqrt{3}/\pi D$.

6. SMALL ANGLE SCATTERING OF NEUTRONS BY POWDERS

On the basis of the discussions which have been given, we may expect to find powders producing observable small angle scattering of neutrons, although

[4] O. Halpern and M. H. Johnson, Phys. Rev. 55, 898 (1939).
[5] Halpern, Hamermesh, and Johnson, Phys. Rev. 59, 981 (1941).

UNIVERSITY OF MICHIGAN LIBRARIES

the same scattering substance produces no observable scattering as a solid. If the powder is sufficiently loose that the scattering under small angles from the various crystallites or grains become more or less independent, then the formula (7) applies directly, remembering that we are now regarding the crystallite as a gigantic microcrystal. Whether we are in the limit in which w is large, Eq. (8), or w small, $G(w)\sim 1$, depends of course on the statistical distribution of grain size and on the angles under which observation is made.

An angular definition of about 1° can be obtained without much effort. It follows that the very intense small angle scattering, w small, can only be important for grain sizes $Na<\sim 20\lambda$, or perhaps more accurately (Section 3) $Na<\sim 20\lambda\sqrt{3}$. In any actual experiment information about the statistics of the grain sizes is necessary before the expected scattering can be theoretically estimated. The total cross section is obviously given by the formula

$$\sigma=\int dD\, n(D)\sigma(D), \tag{28}$$

where $n(D)$ is the number of grains of dimension D and $\sigma(D)$ is the cross section for grains of this size. In this range of angles $\sigma(D)\sim 3\pi A^2(D/a)^4(\lambda/\pi a)^2$, as shown in Section 3.

It is most noteworthy to point out that already a small percentage of material present in form of very fine grains may give rise to a cross section which is very large in proportion to the amount of material producing it. This is, of course, caused by the $N^4=(D/a)^4$ law for the cross section. To give a numerical illustration, if 1 percent of the material is present in grains of the average size of 100 lattice distances, then the cross section due to these grains will equal the total cross section of scattering into large angles, for $\lambda/\pi a\sim 1$.

Discussing now the scattering into angles of the order of $(\lambda/\pi D)^{\frac{1}{2}}$, we notice again that only a limited range of grain sizes can contribute. For $\theta>1°$ they must lie below $10^3\lambda$ approximately and are, of course, much larger than the grain size previously discussed. The exact dependence of the cross section on the incident wave-length can only be given if grain size statistics are available. For the larger grains, we use (28) still, with however $\sigma(D)$ now given by

$$\sigma(D)=(3\pi/4)A^2(D/a)^2(\lambda/\pi a)^4(2\pi)\int_\theta^\infty d\theta/\theta^3$$
$$=(3\pi^2/4)A^2(D/a)^2(\lambda/\pi a)^4 1/\theta^2. \tag{29}$$

Equation (29) is obtained from (8) letting $\sin^2 w=\frac{1}{2}$ and assuming the first Bragg angle is very large compared to the scattering angle θ so that the integral of $G(w)$ over angle can be extended to ∞. For any given grain size D the total cross section for scattering into angles greater than $(\lambda/\pi D)^{\frac{1}{2}}$ equals $(3\pi^2/4)A^2(D/a)^3\times(\lambda/\pi a)^3$. In general, however, the cross section for scattering into angles greater than any given angle for a given grain size can only be found from the exact expression (7) for $G(w)$.

It is our understanding that experiments of the type discussed in this section have already been carried out.[6] Detailed comparison with the experiments will, of course, have to await a full publication of the results. According to the preceding paragraph the small angle scattering into angles greater than $(\lambda/\pi D)^{\frac{1}{2}}$ would, when $\lambda=\pi a$, equal

$$\sigma'=(3\pi^2/4)A^2=(3\pi/16)\sigma_0, \tag{30}$$

per atom, where we have let the cross section for the isolated atom σ_0, equal $4\pi A^2$. It follows from (30) that to account theoretically for cross sections per atom exceeding strongly σ_0, very small grains must be present, as discussed in the first part of this section.

It is emphasized that the remarks of this section have referred to the scattering by individual grains. Multiple scattering by the grains increases the likelihood of observing these effects. Thus if $\lambda/\pi D$ is only 10^{-4}, the very small angle scattering, $G(w)\sim 1$, can make a sizable contribution at angles of 1°, if 25,000 grains are traversed.

7. NEUTRON SCATTERING AND POLARIZATION UNDER SMALL ANGLES IN SOLID FERRO MAGNETS

The influence of very small grains on the total scattering cross section may reveal itself also in some experiments in solid materials which would well deserve to be carried out.

As previously discussed, a compact solid would diffract only under angles of the order of $(\lambda/\pi L)$ and $(\lambda/\pi L)^{\frac{1}{2}}$, which are usually too small for observation. If, on the other hand, the solid contains "holes" of very small size, then diffraction patterns will arise under angles of the order of $\lambda/\pi D'$, wherein D' denotes a linear dimension of a hole. These diffraction patterns will for random holes simply add in intensity; it is clearly seen that the holes within a solid body will play the part previously played by the fine grains in vacuum.

Since the density of solids is usually constant to better than one part in 100 or perhaps even one part in 1000, the total volume of these holes must be very small compared to the volume of the compact material. Still, as shown before, these holes may contribute to the total scattering cross section much in excess of their volume because their cross section is again proportional to D'^4. If, for example, the volume of the holes would amount to 1 percent and each hole be of the order of magnitude of 100 lattice distances, then, with $\lambda=\pi a$, the forward scattering cross section due to these holes would extend over an angle of $\sim 1°$, and be approximately σ_0, per atom.

Since it may not be easy to detect these neutrons scattered under very small angles, a method based on more sensitive polarization effects is perhaps indicated.

[6] Private communication to O. Halpern.

If we use as scattering material a ferromagnetic body, then there will be a polarization effect of the neutrons scattered by the holes. This polarization effect will again be due to the interference of nuclear and magnetic scattering; the characteristic feature of the present arrangement lies in the fact that for the scattering under very small angles the form factor of the magnetically scattered wave is equal to 1. According to the well-known treatment of such cases, the polarization effect of the scattering by holes will, therefore, be proportionally very much larger than that produced by scattering into the various Debye-Scherrer rings.[4] Therefore, even if the hole-scattering cross section should be small, its contribution to the polarization may still be sizable and permit detection.

The interesting feature of this phenomenon lies in the fact that it will occur even for wave-lengths which are larger than the "cut-off" wave-length[4] in iron. It could be detected, for example, by studying the single transmission effect of neutrons through iron with counters subtending different angles with the scattering material.

8. SCATTERING FROM A PARALLELOPIPED

Our results, that at small angles $(\lambda/\pi L)^{\frac{1}{2}}$ the scattering from a parallelopiped is large for special angles of incidence in which the incident wave vector $\mathbf{k}_0$ is perpendicular to one of the edges of the parallelopiped, appears to be experimentally verifiable for the case of visible light and bodies of ordinary macroscopic size. This experiment is particularly interesting since it should occur for wholly amorphous and homogeneous materials, as well as for crystals.

To fix our ideas, for $\lambda=5000\text{A}^\circ$ and $L=1$ cm, $(\lambda/\pi L)^{\frac{1}{2}}=0.25$ degree, which should be an observable angle. For smaller L, the angle is of course larger. The cross section can be obtained as follows. The (scalar) potential satisfies everywhere the equation

$$\Delta\varphi+\kappa_0^2\varphi=(\kappa_0^2-\kappa^2)\varphi. \tag{31}$$

In (31) $\kappa=2\pi/\lambda$. $\boldsymbol{\kappa}=\kappa\mathbf{k}$ is the propagation vector of the wave anywhere in space. κ differs from κ_0, the magnitude of the propagation vector at infinity, only within a parallelopiped of dimensions L_1, L_2, L_3. In the customary way, using the Green's function, the solution which is an outgoing spherical wave at infinity is

$$\varphi(\mathbf{r})=-\frac{1}{4\pi}(\kappa_0^2-\kappa^2)\int d\mathbf{r}'\frac{\exp(i\kappa_0|\mathbf{r}-\mathbf{r}'|)}{|\mathbf{r}-\mathbf{r}'|}\varphi(\mathbf{r}') \tag{32}$$

where, when $(\kappa_0^2-\kappa^2)$ is sufficiently small, we may replace $\varphi(\mathbf{r}')$ by $\exp(i\kappa_0\mathbf{k}_0\cdot\mathbf{r}')$, with $\mathbf{k}_0$ defined as in (2). Then, at infinity,

$$\varphi(\mathbf{r})=-\frac{1}{4\pi}(\kappa_0^2-\kappa^2)\frac{\exp(i\kappa_0 r)}{r}\times\int d\mathbf{r}'\exp[i\kappa_0\mathbf{r}'\cdot(\mathbf{k}_0-\mathbf{k}_s)] \tag{33}$$

with $\mathbf{k}_s$ also as in (2).

When integrated over the volume of the parallelopiped the integral in (33) yields precisely the expression (9), except for a phase factor. The differential cross section is therefore

$$\sigma'(\theta,\varphi)=\frac{1}{16\pi^2}(\kappa_0^2-\kappa^2)^2\frac{\sin^2(\pi L_1/\lambda)(\mathbf{q}\cdot\mathbf{i}_1)}{(\pi^2/\lambda^2)(\mathbf{q}\cdot\mathbf{i}_1)^2}\times\frac{\sin^2(\pi L_2/\lambda)(\mathbf{q}\cdot\mathbf{i}_2)}{(\pi^2/\lambda^2)(\mathbf{q}\cdot\mathbf{i}_2)^2}\frac{\sin^2(\pi L_3/\lambda)(\mathbf{q}\cdot\mathbf{i}_3)}{(\pi^2/\lambda^2)(\mathbf{q}\cdot\mathbf{i}_3)^2}. \tag{34}$$

Assuming $\mathbf{k}_0$ perpendicular to $\mathbf{i}_1$, one finds, in strict analogy to the results derived in Section 2B, that the integral cross section, with $L_1=L_2=L_3=L$, is

$$\sigma\sim(\pi/2)(1-\mu^2)^2(L/\pi\lambda)^{\frac{1}{2}}L^2, \tag{35}$$

where μ is the index of refraction. For $\lambda=5000\text{A}^\circ$ and $L=1$ cm (31) is ~1 if $(1-\mu^2)$ is as small as $\sim10^{-3}$.

It is evident therefore that under most experimental circumstances multiple scattering and extinction of the main beam will occur, although $(1-\mu^2)$ might be made small enough by immersing the scatterer in a liquid of very nearly equal index of refraction. Experimentally, in the limit that $(1-\mu^2)$ is sufficiently small, the scattered beam will be fan-like, being much wider in the plane of incidence (on the plane to which $\mathbf{k}_0$ is nearly parallel) than in the plane perpendicular to the plane of incidence. The fan-like effect should disappear as soon as the angle between $\mathbf{k}_0$ and one of the edges deviates from 90° by more than 0.2°. We stress that this high scattering when $\mathbf{k}_0$ lies in one of the faces is a volume effect, as is apparent from the mode of derivation of (35), and is not physically of the same character as the large coherent reflection ordinarily observed at angles of incidence near 90°.

Since angles of ~1 minute have been measured with neutron beams,[3] it may be possible to observe this effect also for neutrons, using $\lambda/\pi\sim10^{-3}$, $L\sim0.1$ cm. Estimating[5] the index of refraction for neutrons of this wave-length as 5×10^{-6}, it is readily determined that with $L=0.1$ cm the cross section (35) is $\sim10^{-3}$. Consequently $n\sigma L\sim0.1$ so that the effect is certainly observable, but multiple scattering and extinction should not be too important (at these relatively wide angles $\sim(\lambda/\pi L)^{\frac{1}{2}}$).

With either visible light or neutrons it is necessary that the surfaces of the scatterer not deviate too much from accurate planes; otherwise the effect may be greatly diminished. To investigate the effect of surface irregularities we write the integral in (33) as

$$\int_\tau d\mathbf{r}'\exp(i\kappa_0\mathbf{r}'\cdot\mathbf{q})=\int_p d\mathbf{r}'\exp(i\kappa_0\mathbf{r}'\cdot\mathbf{q})+\int_{\Delta\tau}d\mathbf{r}'\exp(i\kappa_0\mathbf{r}'\cdot\mathbf{q}) \tag{36}$$

where the volume $\Delta\tau$ is the small difference between

UNIVERSITY OF MICHIGAN LIBRARIES

the actual volume τ and the perfect parallelopiped p. It follows that the effect of surface irregularities will be small if the integral over $\Delta\tau$ in (36) is small compared to (9). Assuming $\mathbf{q}$ nearly parallel to $\mathbf{i}_1$

$$\int_{\Delta\tau} d\mathbf{r}' \exp(i\kappa_0\mathbf{r}'\cdot\mathbf{q}) = \int_{-L/2}^{L/2} dx\, s(x) \exp(i\kappa_0|q|x) = \Delta\rho \quad (37)$$

where $s(x)$ is the area of the section of $\Delta\tau$ by the plane perpendicular to i_1, at depth x. The effect of irregularities in the surface depends therefore on the Fourier component of the incremental area $s(x)$ at wave-length $\lambda' = \lambda/|q| = \sim(\pi\lambda L)^{\frac{1}{2}}$. If $s(x)$ varies but little in a distance $\sim L$, it follows by comparing with (9) that the change in intensity due to $\Delta\tau$ is $\sim\delta/L^2$ (with δ some average $s(x)$), and is negligible. Since even in the neutron case $\lambda' \sim 10^{-4} = \sim 10^4$ atomic diameters, it is more likely that $s(x)$ varies randomly and rapidly in a distance $\sim\lambda'$. In this event $\Delta\rho$ in (37) can be estimated from the well-known connection between the Fourier analysis of a random function and the correlation function.[7] In fact, we have from (37)

$$\langle|\Delta\rho|^2\rangle = \int_{-L/2}^{L/2} dx \int_{-L/2}^{L/1} dx' \langle s(x)s(x')\rangle \times \exp[i\kappa_0|q|(x-x')] = \langle s^2\rangle \int_{-L/2}^{L/2} dx \int_{-L/2}^{L/2} dx' \times \exp[i\kappa_0|q|(x-x') - |x-x'|/\beta]. \quad (38)$$

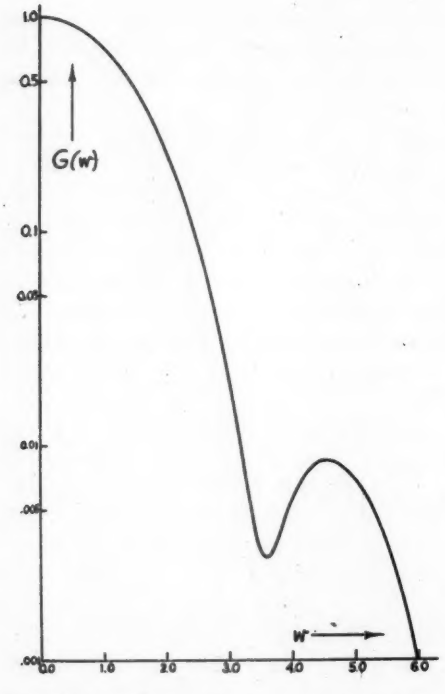

FIG. 1. Plot of $G(w)$ against w using series expansion Eqs. 13 to 15 of Appendix.

[7] S. O. Rice, Bell Sys. Tech. J. 23, 282 (1944); 24, 46 (1945).

In (38) the $\langle\ \rangle$ indicate an average and the quantity β is the distance within which there is appreciable correlation between $s(x)$ and $s(x')$. Since β is $\ll L$ we can approximate (38) by

$$\langle|\Delta\rho|^2\rangle = \langle s^2\rangle \int_{-L/2}^{L/2} dx \int_{-\infty}^{\infty} dx' \times \exp[i\kappa_0|q|(x-x') - |x-x'|/\beta] = \frac{2L\langle s^2\rangle(1/\beta)}{\kappa_0^2|q|^2 + 1/\beta^2}. \quad (39)$$

The correlation distance β can hardly be much greater than 100 atomic diameters. Hence $\kappa_0^2|q|^2 \ll 1/\beta^2$ and we obtain, as an estimate of the effect of surface irregularities, using (9)

$$\left|\frac{\Delta\rho}{\rho}\right| \sim \frac{(2L\beta\langle s^2\rangle)^{\frac{1}{2}}}{\lambda L^2/\pi|q|} = \sim 2(2\pi)^{\frac{1}{2}}\left(\frac{\beta}{\lambda}\right)^{\frac{1}{2}}\left(\frac{\Delta L}{L}\right). \quad (40)$$

In (40) $\langle s^2\rangle$ has been replaced by $(2L\Delta L)^2$. With $\Delta L \sim 10^{-4}$ cm, $|\Delta\rho/\rho|$ from (40) is $\ll 1$ for either visible light or neutrons, if $\beta \sim 10^{-6}$ cm. Obviously (40) would remain $\ll 1$ for values of β considerably larger than 10^{-6} cm. Scattering from parallelopipeds into angles $\sim(\lambda/\pi L)^{\frac{1}{2}}$, as described in this section, should therefore be observable with either visible light or neutrons. The possibility of a large Fourier amplitude of $s(x)$ at wavelength $\sim\lambda'$ cannot be entirely ruled out, but such large regular variations in $s(x)$ seem unlikely.

We wish to thank Mr. Norman Perry for his assistance in performing the numerical calculations.

Mathematical Appendix

E. GERJUOY

We shall prove that the integrals

$$F(w) = \frac{1}{4\pi}\int_0^{\pi} d\theta \int_0^{2\pi} d\varphi \sin\theta \frac{\sin(w\sin\theta\cos\varphi)}{w\sin\theta\cos\varphi} \times \frac{\sin(w\sin\theta\sin\varphi)}{w\sin\theta\sin\varphi} \frac{\sin(w\cos\theta)}{w\cos\theta}$$

$$G(w) = \frac{1}{4\pi}\int_0^{\pi} d\theta \int_0^{2\pi} d\varphi \sin\theta \frac{\sin^2(w\sin\theta\cos\varphi)}{w^2\sin^2\theta\cos^2\varphi} \times \frac{\sin^2(w\sin\theta\sin\varphi)}{w^2\sin^2\theta\sin^2\varphi} \frac{\sin^2(w\cos\theta)}{w^2\cos^2\theta}$$

equal respectively the functions

$$F_1(w)=\frac{3\pi}{2}\frac{\sin w}{w^3}-\frac{6}{w^3}\int_0^1 dx\frac{\sin[w(2+x^2)^{\frac{1}{2}}]}{(1+x^2)(2+x^2)^{\frac{1}{2}}}$$

$$G_1(w)=\frac{3}{4w^4}\left\{\frac{\sqrt{3}\sin 2w\sqrt{3}}{w}-\frac{\sin^2 w\sqrt{3}}{w^2}-\frac{3\sqrt{2}\sin 2w\sqrt{2}}{w}\right.$$

$$\left.+\frac{3\sin^2 w\sqrt{2}}{w^2}+\frac{\sin 2w}{w}-\frac{3\sin^2 w}{w^2}\right\}$$

$$+\frac{3}{w^4}\left\{\frac{\pi}{2}\sin^2 w+\int_0^1 dx\frac{(1+2x^2)}{1+x^2}\cos[2w(1+x^2)^{\frac{1}{2}}]\right.$$

$$\left.-\int_0^1 dx\frac{x^2}{1+x^2}\cos[2w(2+x^2)^{\frac{1}{2}}]\right\}. \quad \text{(A)}$$

The integral $F(w)$ is related to the average amplitude scattered from a randomly oriented microcrystal. Its evaluation is appended since knowledge of its value may prove useful in some calculations. The evaluation of the integrals is based on the theorem[a] that if $f(x)$ is a continuous function and $\int_0^\infty dx f(x)\exp(-x^2t)=0$ for all sufficiently large positive values of t, then $f(x)$ is identically zero.

Evaluation of $F(w)$

As is well known[b]

$$\int_0^\infty dx\exp(-x^2t)\cos bx=\frac{1}{2}\left(\frac{\pi}{t}\right)^{\frac{1}{2}}\exp(-b^2/4t). \quad (1)$$

Thus

$$\int_0^b db\int_0^\infty dx\exp(-x^2t)\cos bx$$

$$=\int_0^\infty dx\int_0^b db\exp(-x^2t)\cos bx$$

$$=\int_0^\infty dx\exp(-x^2t)\frac{\sin bx}{x}$$

$$=\frac{1}{2}\left(\frac{\pi}{t}\right)^{\frac{1}{2}}\int_0^b db\exp(-b^2/4t)$$

$$=\frac{b}{2}\left(\frac{\pi}{t}\right)^{\frac{1}{2}}\int_0^1 dy\exp(-b^2y^2/4t). \quad (2)$$

Consequently, transforming from polar to rectangular coordinates

$$\int_0^\infty dw\exp(-w^2t)w^2F(w)$$

$$=\frac{1}{4\pi}\int_{-\infty}^\infty dx\int_{-\infty}^\infty dy\int_{-\infty}^\infty dz\frac{\sin x}{x}\frac{\sin y}{y}\frac{\sin z}{z}$$

$$\times\exp[-(x^2+y^2+z^2)t]$$

$$=\frac{1}{4\pi}\left(\frac{\pi}{t}\right)^{\frac{3}{2}}\int_0^1 dx\int_0^1 dy\int_0^1 dz$$

$$\times\exp[-(x^2+y^2+z^2)/4t]. \quad (3)$$

Since the integrands are all continuous and the integrals uniformly convergent, these changes of variable and inversions of the order of integration are valid. The same is true of all integrals considered below.

Considering now $F_1(w)$

$$\int_0^\infty dw\exp(-w^2t)\int_0^1 dx\frac{\sin[w(2+x^2)^{\frac{1}{2}}]}{w(1+x^2)(2+x^2)^{\frac{1}{2}}}$$

$$=\int_0^1 dx\frac{1}{(1+x^2)(2+x^2)^{\frac{1}{2}}}\int_0^\infty dw\exp(-w^2t)\frac{\sin[w(2+x^2)^{\frac{1}{2}}]}{w}$$

so that, using (2)

$$\int_0^\infty dww^2\exp(-w^2t)F_1(w)$$

$$=\frac{3\pi}{4}\left(\frac{\pi}{t}\right)^{\frac{1}{2}}\int_0^1 dz\exp(-z^2/4t)$$

$$-3\left(\frac{\pi}{t}\right)^{\frac{1}{2}}\int_0^1 dx\int_0^1 dz\frac{\exp[-(2+x^2)z^2/4t]}{1+x^2}$$

$$=3\left(\frac{\pi}{t}\right)^{\frac{1}{2}}\int_0^{\pi/4} d\varphi\int_0^1 dz\exp(-z^2/4t)$$

$$\times\left[1-\exp\left(\frac{-z^2\sec^2\varphi}{4t}\right)\right]$$

$$=3\left(\frac{\pi}{t}\right)^{\frac{1}{2}}\int_0^{\pi/4} d\varphi\int_0^1 dz\exp(-z^2/4t)$$

$$\times\int_0^{z\sec\varphi} d\rho\frac{\rho\exp(-\rho^2/4t)}{2t}. \quad (4)$$

In cylindrical coordinates $\rho=x\sec\varphi$. Therefore the triple integral (4) equals

$$\frac{3}{2}\left(\frac{\pi}{t^3}\right)^{\frac{1}{2}}\int dxdydz\exp[-(x^2+y^2+z^2)/4t] \quad (5)$$

integrated over the volume bounded by the planes $\varphi=0$, $\varphi=\pi/4$, $z=x$, and $z=1$. This volume is that portion of the unit cube $0<x<1$, $0<y<1$, $0<z<1$ for which $y<x$ and $x<z$. To any given triad of numbers $0<a<b<c<1$ there corresponds a set of six points in

[a] G. N. Watson, *A Treatise on the Theory of Bessel Functions* (The Macmillan Company, New York, 1944), p. 382.

[b] B. O. Peirce, *A Short Table of Integrals* (Ginn and Company, New York, 1929), p. 64.

UNIVERSITY OF MICHIGAN LIBRARIES

the unit cube: (a, b, c), (a, c, b), (b, a, c), (b, c, a), (c, b, a), (c, a, b). For each of these points $x^2+y^2+z^2=a^2+b^2+c^2$, and furthermore one and only one of these points lies in the volume $y<x<z$. Consequently, the volume of integration in (5) is exactly one sixth the volume of the unit cube and

$$\int_0^\infty dw \exp(-w^2t)w^2F_1(w)=\frac{1}{4\pi}\left(\frac{\pi}{t}\right)^{\frac{3}{2}} \times\int_0^1 dx\int_0^1 dy\int_0^1 dz \exp[-(x^2+y^2+z^2)/4t]. \quad (6)$$

Comparing Eqs. (3) and (6)

$$\int_0^\infty dw \exp(-w^2t)w^2[F(w)-F_1(w)]=0$$

so that, by the theorem quoted, $F(w)=F_1(w)$.

Evaluation of $G(w)$

From the definition of $G(w)$, after transforming from polar to rectangular coordinates,

$$\int_0^\infty dw \exp(-w^2t)w^4G(w) =\frac{1}{4\pi}\int_{-\infty}^\infty dx\int_{-\infty}^\infty dy\int_{-\infty}^\infty dz(x^2+y^2+z^2) \times\frac{\sin^2x}{x^2}\frac{\sin^2y}{y^2}\frac{\sin^2z}{z^2}\exp[-(x^2+y^2+z^2)t] =\frac{3}{4\pi}\int_{-\infty}^\infty dx\int_{-\infty}^\infty dy\int_{-\infty}^\infty dz\exp(-x^2t)\sin^2x \times\left(\exp(-y^2t)\frac{\sin^2y}{y^2}\right)\left(\exp(-z^2t)\frac{\sin^2z}{z^2}\right). \quad (7)$$

Using Eq. (2)

$$\int_0^b dm\int_0^\infty dx \exp(-x^2t)\frac{\sin mx}{x} =\int_0^\infty dx\int_0^b dm \exp(-x^2t)\frac{\sin mx}{x} =2\int_0^\infty dx \exp(-x^2t)\frac{\sin^2(bx/2)}{x^2} =\frac{1}{2}\left(\frac{\pi}{t}\right)^{\frac{1}{2}}\int_0^b dmm\int_0^1 dy \exp(-m^2y^2/4t) =\frac{1}{2}\left(\frac{\pi}{t}\right)^{\frac{1}{2}}\int_0^1 dy\int_0^b dmm \exp(-m^2y^2/4t) =(\pi t)^{\frac{1}{2}}\int_0^1 dy\frac{[1-\exp(-b^2y^2/4t)]}{y^2}.$$

Integrating the last integral by parts, it follows that

$$\int_0^\infty dx \exp(-x^2t)\frac{\sin^2bx}{x^2}=b^2\left(\frac{\pi}{t}\right)^{\frac{1}{2}}\int_0^1 dy \exp(-b^2y^2/t) -\frac{(\pi t)^{\frac{1}{2}}}{2}[1-\exp(-b^2/t)]. \quad (8)$$

Moreover, by Eq. (1)

$$\int_0^\infty dx \exp(-x^2t)\sin^2bx=\int_0^\infty dx \exp(-x^2t)\frac{(1-\cos 2bx)}{2} =\frac{1}{4}\left(\frac{\pi}{t}\right)^{\frac{1}{2}}[1-\exp(-b^2/t)]. \quad (9)$$

Using Eqs. (8) and (9) in (7) yields

$$\int_0^\infty dw \exp(-w^2t)w^4G(w) =\frac{3}{4\pi}\frac{8}{4}\left(\frac{\pi}{t}\right)^{\frac{1}{2}}[1-\exp(-1/t)] \times\left\{\left(\frac{\pi}{t}\right)^{\frac{1}{2}}\int_0^1 dy \exp(-y^2/t) -\frac{(\pi t)^{\frac{1}{2}}}{2}[1-\exp(-1/t)]\right\}^2 =\frac{3}{2}\left(\frac{\pi}{t}\right)^{\frac{1}{2}}[1-\exp(-1/t)] \times\left\{\frac{1}{t}\int_0^1 dx\int_0^1 dy \exp[-(x^2+y^2)/t] -[1-\exp(-1/t)]\int_0^1 dy \exp(-y^2/t) +\frac{t}{4}[1-\exp(-1/t)]^2\right\}. \quad (10)$$

Furthermore

$$\int_0^1 dx\int_0^1 dy \exp[-(x^2+y^2)/t] =2\int_0^{\pi/4} d\varphi\int_0^{\sec\varphi} d\rho\rho \exp(-\rho^2/t) =t\int_0^{\pi/4} d\varphi\left[1-\exp\left(-\frac{\sec^2\varphi}{t}\right)\right] =\frac{\pi t}{4}-t\int_0^1 dx\frac{\exp[-(1+x^2)/t]}{1+x^2}. \quad (11)$$

Substituting (11) in (10)

$$\int_0^\infty dw\exp(-w^2t)w^4G(w)=\tfrac{3}{8}(\pi t)^{\frac{1}{2}}[1-\exp(-1/t)]^3$$
$$-\frac{3}{2}\left(\frac{\pi}{t}\right)^{\frac{1}{2}}[1-\exp(-1/t)]^2\int_0^1 dy\exp(-y^2/t)$$
$$+\frac{3}{8}\left(\frac{\pi^3}{t}\right)^{\frac{1}{2}}[1-\exp(-1/t)]$$
$$-\frac{3}{2}\left(\frac{\pi}{t}\right)^{\frac{1}{2}}[1-\exp(-1/t)]\exp(-1/t)$$
$$\times\int_0^1 dy\frac{\exp(-y^2/t)}{1+y^2}. \quad (12)$$

A straightforward application of Eqs. (1), (2), (8), and (9), and collection of terms shows that $\int_0^\infty dw\exp(-w^2t)w^4G_1(w)$ equals precisely the expression on the right side of Eq. (12). Thus again by the theorem quoted, $G(w)=G_1(w)$.

A graph of the function $G(w)$ is given in Fig. 1. For small values of w, $G(w)$ can be calculated from the series

$$G(w)=24\sum_{n=0}^{\infty}\frac{(2w)^{2n}(-)^nD_n}{(2n+4)!} \quad (13)$$

where

$$D_n=\frac{3}{2n+6}(3^{n+2}-2^{n+3}+1)+\frac{1}{n+2}[2^{n+2}+(2n+3)E_{n+2}]$$
$$-\frac{2}{2n+5}+2B_{n+1}-2C_{n+2}, \quad (14)$$

and the other quantities are defined by recursion relations

$$B_n=B_{n-1}+C_n$$
$$C_n=\frac{4nC_{n-1}+3^n}{2n+1} \quad (15)$$
$$E_n=\frac{2nE_{n-1}+2^n}{2n+1}$$

and $B_0=C_0=E_0=1$.

Equations (13)–(15) result from expansion of $G_1(w)$ in a power series in w. It is possible, by appropriate manipulation of the integrals in (A) to obtain the asymptotic expansion

$$G(w)\sim\frac{48}{(2w)^4}\left\{-\frac{\pi}{4}-\frac{\pi}{4}\cos2w\right.$$
$$+\pi wJ_0(2w)+\frac{\pi^2w}{2}\mathbf{H}_0(2w)J_1(2w)$$
$$-\frac{\pi^2w}{2}\mathbf{H}_1(2w)J_0(2w)+\frac{\pi}{\sqrt{2}}J_1(2w\sqrt{2})-\pi J_1(2w)$$
$$-\left(\frac{\pi}{2}\right)^{\frac{1}{2}}\frac{\sin2w\sqrt{2}}{(2w\sqrt{2})^{\frac{1}{2}}}+\left(\frac{\pi}{2}\right)^{\frac{1}{2}}\frac{\cos2w\sqrt{2}}{(2w\sqrt{2})^{\frac{1}{2}}}+\frac{\sin2w}{4w}$$
$$+\frac{13}{8\sqrt{2}}\frac{\cos2w\sqrt{2}}{(2w\sqrt{2})^{\frac{1}{2}}}+\frac{13}{8\sqrt{2}}\frac{\sin2w\sqrt{2}}{(2w\sqrt{2})^{\frac{1}{2}}}-\frac{\cos2w\sqrt{2}}{2w^2}$$
$$\left.+\frac{3}{8w^2}\cos2w-\frac{1}{8w^2}\right\}. \quad (16)$$

The expansion (16) differs from the accurate series (13) by no more than 2 percent in the range $4.2\leqslant w\leqslant 6$. It should therefore be sufficiently accurate for $w\geqslant 4$. For very large w the functions proportional to w inside the brackets approach $\pi/2$ and $G(w)\sim(3\pi/2)\sin^2w/w^4$. The functions $\mathbf{H}_0$ and $\mathbf{H}_1$ are the *bold faced* functions tabulated by Watson.[a]

UNIVERSITY OF MICHIGAN LIBRARIES

On Magneto Optics of Neutrons and Some Related Phenomena

OTTO HALPERN
University of Southern California, Los Angeles, California
(Received February 17, 1949)

Formulas are derived describing the phenomenon of total reflection of neutrons by a ferromagnet in dependence on the state of magnetization. It is shown how experiments of this kind can give information concerning the magnetic interaction between neutrons and atomic magnetic moments. A method to obtain well-polarized neutron beams with an intensity loss of only 50 percent of the primary beam is outlined. The effect of pure magnetic scattering and its influence on the transmission effect is discussed; an experimental arrangement for its observation is described. The significance of the approach to saturation in the single transmission effect is discussed in connection with the saturation theory of ferromagnets. Remarks are made concerning the possibility of detecting wall effects of magnetic domains through depolarization of neutron beams.

1. INTRODUCTION

THE present paper contains the discussion of a number of effects which are produced by the passage of neutrons through a ferromagnetic material. They are otherwise only indirectly connected with each other; some of them are more concerned with neutron properties, while others refer to information concerning the solid state which can be gained using neutrons as tools of exploration. Frequently in this paper we shall have occasion to refer to formulae derived and results obtained in three earlier papers[1] which shall be referred to in the following as I, II, and III.

2. REFRACTION, TOTAL REFLECTION AND POLARIZATION OF NEUTRONS BY FERROMAGNETS[2]

In paragraph 5 of III, we have derived expressions for the indices of refraction of neutrons passing through a (ferromagnetic) medium. This refraction is due to the scattering of the neutrons by the nuclei (and by the magnetic moments of the ferromagnetic atoms). Only the coherent scattering by the nucleus contributes to the index of refraction; the scattering due to the interaction of the neutrons of the atoms' magnetic moments is coherent in the case of ferromagnets but shows the added complication that it depends upon the relative orientations of the atomic magnetic moment and the neutron spin. If we resolve the spin of the incident neutron along the axis of magnetization, then a neutron of spin i has in general $2i+1$ indices of refraction which for $i=\frac{1}{2}$ are given by

$$n_{\pm}-1=\frac{2\pi N}{k^2}\left(C\pm\frac{e^2\gamma S}{mc^2}\right). \tag{1}$$

In (1) the following abbreviations have been used: $k=2\pi/\lambda$, $N=$number of atoms/cm^3, $C=$coherent scattering amplitude of nucleus, $\gamma=$neutron moment in nuclear Bohr magnetons, and $S=$spin of iron atom in units.

In the experiments of Fermi and Marshall,[3] use has been made of the index of refraction of neutrons to obtain for a number of elements total reflection of neutrons incident under a small glancing angle. It is clear that such experiments can be extended to cover the more involved case of total reflection by magnetized ferromagnets.

To sketch the arrangement in its simplest form, we allow neutrons to impinge upon a plate of iron which we assume to be magnetized. If, e.g., the direction of magnetization should lie in the plane of the plate, then neutrons with spins parallel or anti-parallel to the direction of magnetization will exhibit respectively indices of refraction given by

$$n_{\pm}-1=n_0\pm\frac{2\pi N}{k^2}\frac{e^2\gamma S}{mc^2}-1. \tag{2}$$

Here, n_0 stands for the index of refraction determined in Fermi's experiments. The critical glancing angles φ for neutrons with the two different spin orientations will, therefore, be given by

$$\varphi_{\pm}=2(1-n_{\pm})^{\frac{1}{2}}. \tag{3}$$

They will lie on both sides of the critical angle found by Fermi and Marshall. It is also obvious that for the *larger* of the two critical glancing angles the reflected beam will be *almost completely polarized*, while for the smaller critical angle both polarization states will occur in the reflected beam.

A numerical evaluation leads to the following data for iron as a reflector: $\varphi_+\sim 13$ minutes, $\varphi_-\sim 6$ minutes, $\varphi_0\sim 10$ minutes (unmagnetized state).

It seems from the estimate given that there should be no essential difficulty in carrying out the experiments in the way sketched. It will, of course, be necessary to avoid magnetic stray fields which would lead to a depolarization of the reflected neutrons. Techniques

[1] O. Halpern and M. H. Johnson, Phys. Rev. **55**, 898 (1939); O. Halpern and T. Holstein, Phys. Rev. **59**, 960 (1941); Halpern, Hamermesh, and Johnson, Phys. Rev. **59**, 981 (1941).
[2] O. Halpern, Phys. Rev. **75**, 343 (1949).
[3] E. Fermi and L. Marshall, Phys. Rev. **71**, 666 (1947).

similar to those employed by D. J. Hughes[4] and his collaborators in measuring the double transmission effect of neutrons in ferromagnets should prove successful in the present case.

The experiments sketched may also be useful for the purpose of testing the assumed interaction between the magnetic moments of the neutrons of the iron atom. Theory leads to the following expression for the amplitude of magnetic scattering C_m as function of the angle ϑ and the direction of magnetization κ relative to the directions $\mathbf{k}_0$, $\mathbf{k}$ of incident and scattered beam:

$$C_m=\frac{e^2\gamma S}{mc^2}2(\mathbf{s}\cdot\mathbf{q})$$
$$\mathbf{q}=\mathbf{e}(\mathbf{e}\cdot\kappa)-\kappa \qquad (4)$$
$$\mathbf{e}=\frac{\mathbf{k}_0-\mathbf{k}}{|\mathbf{k}_0+\mathbf{k}|}.$$

If, as assumed before, the direction of magnetization is lying in the plane of the mirror, the magnetic scattering amplitude becomes a maximum. It drops to its minimum value if $\kappa\|\mathbf{e}_0$

$$C_m=0. \qquad (5)$$

A study of the variation of the splitting of the two critical angles with changing orientation of the magnetic field would, therefore, allow a test of the theoretical expression (4) and of the assumptions made concerning the magnetic interaction function.

3. PURE MAGNETIC SCATTERING

In the arrangement originally proposed by Bloch,[5] the change in transmission of a neutron beam due to magnetization of the iron plate was ascribed to the interference of the scattering from the iron nucleus and from the magnetically active electrons of the ion shell. The fact that this phenomenon has two causes offered considerable difficulties to attempts aimed at obtaining quantitative theoretical expressions for this single transmission effect.

The pure magnetic scattering which is proportional to the square of the iron's magnetic moment did not enter into these calculations because it was assumed to be independent of the over-all state of magnetization of the material.

We shall show that due to the peculiar angle dependence of the magnetic scattering discussed in I §6 this simplification is not generally permissible; this will lead to a comparatively weak (negative) transmission effect linear in the thickness of the transversed material, in addition to the usually observed (positive) transmission effect which for complete saturation is quadratic in the thickness of the transmitted material.

This linear transmission effect comes about as follows: The amplitude of the scattered wave containing nuclear as well as magnetic scattering is given by

$$C_s=C+C_m=C+(e^2\gamma S/mc^2)2\mathbf{s}\cdot\mathbf{q}.$$

Assuming as it is experimentally convenient that the direction of magnetization κ is perpendicular to the direction of the incident beam $\mathbf{k}_0$, we obtain for the scattered intensity

$$J\sim C^2+4C\frac{e^2\gamma S}{mc^2}\mathbf{s}\cdot\mathbf{g}+\left(\frac{e^2\gamma S}{mc^2}\right)^2 4(\mathbf{s}\cdot\mathbf{q})^2. \qquad (6)$$

If the material is originally *unmagnetized*, then the directions of magnetization in the various domains make random angles with $\mathbf{k}_0$ and we obtain, therefore, for a *fixed* scattering angle an intensity given by

$$J\sim C^2+(e^2\gamma S/mc^2)^2\mathbf{q}^2. \qquad (7)$$

The second part in (6) refers to the well-known positive transmission effect; we here want to note the actual value of the third term in the *unmagnetized* state which, after averaging, becomes

$$J\sim C^2+(e^2\gamma S/mc^2)^2\tfrac{2}{3}. \qquad (7a)$$

If, on the other hand, the material is near magnetic saturation, then we are only allowed to average over the azimuth of the scattering angle, and obtain from (6) the following expression for the intensity

$$J\sim C^2+\left(\frac{e^2\gamma S}{mc^2}\right)^2\frac{1+\sin^2\vartheta/2}{2}. \qquad (8)$$

The difference between the third terms in (7a) and (8) gives the previously discussed linear transmission effect. We find that even the sign of this difference varies with the scattering angle; it is positive for small and negative for large angles.

To demonstrate the influence of pure magnetic scattering most clearly, it is advisable to make this term as large as possible, while, at the same time, reducing the amount of the positive transmission effect. We remember for this purpose that the positive transmission effect is extremely sensitive to deviations from saturation; theory[1] and experiment[6,7] show in full agreement that for some materials a deviation from saturation of several percent is sufficient to reduce the transmission effect by one or two orders of magnitude.

The following experimental arrangement is, therefore, proposed to test the theory: A wave-length close to 4A is chosen; in that case the scattering occurs only under about 180°, i.e., only the first Debye ring is formed. We learn from III that the amplitude of scattering in this case amounts to 1.14C. The form factor of the

[4] Unpublished results.
[5] F. Bloch, Phys. Rev. **50**, 259 (1936).
[6] Bloch, Nicodemus, and Staub, Phys. Rev. **74**, 1025 (1948). There also earlier literature.
[7] Hughes, Wallace, and Holtsmann, Phys. Rev. **73**, 1277 (1948).

UNIVERSITY OF MICHIGAN LIBRARIES

magnetic scattering is in this case as shown in III or in the paper by M. Hamermesh[8] given by $\sim\frac{1}{4}$. The total purely magnetic scattering cross section, under these assumptions, takes on the value 8.10^{-25} unmagnetized and 12.10^{-25} cm^2 magnetized. This compares with a total nuclear scattering cross section of $\sim 12.10^{-24}$ cm^2. Deferring discussion of the interference term, we would, therefore, predict a negative transmission effect of $\sim$3.2 percent/cm.

The interference term is theoretically, as well as experimentally, of course, of higher order of magnitude if saturation is approached; but for incomplete saturation, e.g., of 90 percent, the depolarization of the neutrons inside of the iron is so strong as to almost annihilate the influence of the interference term. Theory and experiment show that the positive transmission Δ effect for incomplete saturation is given by (see II)

$$\Delta=\Delta_\infty(2/pd)=(w^2d/p).$$

Here w is the cross section due to the middle term in (6) and p is the coefficient of depolarization which is proportional to the deviation from saturation. For $\lambda\sim 4$A and 90 percent saturation $w\sim 0.9$, $p\sim 200$ and Δ therefore $\sim$0.4 percent/cm which constitutes only a correction to the previously calculated negative transmission effect.

A determination of the transmission effect as function of magnetization should, therefore, lead to an isolation of the pure magnetic scattering and permit a direct experimental determination of the form factor of scattering for the first Debye ring. The experiment could, of course, be extended to smaller wave-lengths, but since very soon other Debye rings will appear, which, according to (8), would diminish the effect, it would soon become impracticable.

The effect here discussed is also of some significance in the evaluation of experiments near saturation. It is true that then the well-known positive transmission effect will greatly outweigh the negative transmission effect here discussed, but, since this negative transmission effect is *always* present, the true theoretical value of the positive transmission effect is larger than the observed experimental value by the amount of the previously neglected negative transmission effect. The structure of (8) indicates that this correction will only be of real numerical significance if sufficiently long wave-lengths are used.

4. REMARKS ON THE LAW OF MAGNETIZATION NEAR SATURATION

It is well known that the simple picture of rotation of the vector of the magnetic moment of the individual crystallites into the direction of the external field leads to a saturation law of the form

$$M=M_\infty[1-(a/H^2)], \tag{9}$$

for high field strengths this theoretical law is not confirmed by experiment, which instead gives a behavior of the type

$$M=M_\infty[1-(b/H)]. \tag{10}$$

Attempts to derive the $1/H$ term have been unsuccessful.

The experiments of Hughes[7] and his collaborators have thrown new light on the situation and, at least in a negative sense, have eliminated a number of theoretical possibilities. They indicate that any successful theory will have to derive the empirically observed saturation law on the basis of crystallites of the same order of magnitude as the microscopically measured grain sizes. Special assumptions ascribing slow saturation to smaller splinters which are exposed to additional crystal forces are ruled out by the observations. This conclusion can be established, as follows: The experiments indicate that the positive transmission effect approaches its asymptotic value according to the law $1-b/H$. The transmission effect, on the other hand, depends only on the depolarization due to deviation from ideal saturation. As predicted in II and verified in reference 7 the depolarization follows different laws, depending upon the size of the individual domain. If the domain, i.e., in our case the individual crystal grain, satisfies the relation

$$\delta/v\sim T, \tag{11}$$

δ=domain length, T=Larmor period, v=velocity, then the law of depolarization is given by e^{-px}; if, on the other hand, the domain size satisfies the inequality

$$\delta/v\ll T, \tag{12}$$

then the law of depolarization takes on the form $\exp[-px(\delta/vT)^2]$. In this second case, the depolarization is obviously much smaller than in the first one; the saturation value of the transmission effect would, therefore, be approached much earlier than in the first case.

The fact now that, as shown in reference 7, the *depolarization effect* follows a law of the type (11) in which δ is of the order 10^{-3} cm indicates that the investigated materials have domain sizes satisfying (11). It is, therefore, not possible to assume a certain percentage of the material to be present in the forms of microscopic grains which only very slowly take on the saturation value of magnetization; these small grains could perhaps account for a slow saturation as determined by measurements of the magnetic flux, but would be quite unobservable in the transmission effect. The fact that the saturation of magnetization follows the same law as the saturation of the transmission effect constitutes a cogent argument for the identity of the domains that are responsible for both phenomena.

5. THE INFLUENCE OF WALLS SEPARATING DOMAINS

In II theoretical formulas and experimental methods have been described to determine the sizes and orienta-

[8] M. Hamermesh, Phys. Rev. 61, 17 (1942).

tions of individually magnetized domains in various parts of the magnetization curve and their dependence upon external parameters. Experiments carried out along these lines have partially been published;[6,7] additional observations on similar effects, although presented at meetings of the American Physical Society, have not yet appeared in print.

In a recent note, Newton and Kittel[9] attempt to extend the method of II for the purpose of measuring the wall thickness between individual domains present for very small external fields. We should like to comment on some aspects of this question.

In II the influence of the domain walls was neglected for all parts of the magnetization curve; this is rigorously justified for *sizable* external magnetic fields when the domains are practically wiped out and only crystallite boundaries remain, and it seemed justified for most cases of practical interest because the time of passage through a domain wall (at very low magnetic fields) was assumed to be so small that the processes could be considered practically instantaneous. On the basis of estimates given by Becker and Doering[10] we assumed the domain walls to have a thickness of 30 to 100 lattice distances. For average neutron velocities of the order of 10^5 cm/sec. the time spent in traversing a domain wall is of the order of 2.10^{-11} sec. which is very small compared to a Larmor period which is about 2.10^{-8} sec. in iron and still larger in other ferromagnets. In addition to it, the depolarization by the domains themselves, which we assumed to be large compared to the domain walls, made it only consistent to neglect the wall effect.

Newton and Kittel do not specify the type of experiment which they have in mind; we shall, therefore, try to discuss their suggestions on a basis which seems to us most favorable for their attempt. It is obviously necessary that the domains themselves shall not contribute to depolarization if one wants to isolate the wall effects. This makes it necessary to have the magnetization of the domains lined up in directions parallel and anti-parallel to each other, a case which we discussed in II, paragraph 5. Unless such an orientation of domains is obtained, the wall effect will always be small compared to the domain effects, and the experiment of Newton and Kittel will, therefore, become impractical.

Treating, on the other hand, the just-mentioned case of parallel and antiparallel domains, we derived the result that, apart from wall effects, the component of the spin of the incident neutrons parallel to the direction of magnetization should pass through unchanged, while the components perpendicular are depolarized. If the experiment of Newton and Kittel should, therefore, be carried out, it would be necessary to transmit a beam of neutrons polarized, e.g., parallel to the hexagonal axis of a cobalt crystal; the beam then would show depolarization which could be ascribed to the wall effect, provided that the domains are really lined up in the way described. The difficulty encountered in these experiments has been partly already discussed by Newton and Kittel; namely, the smallness of the passage time through a domain wall compared to the Larmor period. Newton and Kittel estimate the passage time on the basis of values for the wall thickness which are considerably larger than those suggested by Becker and Doering; we have no personal opinion as to which values are preferable. The large values claimed for permalloy do not seem to us to be very helpful because we do not know whether it will be possible to achieve a perfect orientation of the domains parallel and antiparallel to each other in the case of the cubic crystal permalloy.

The extension of our method to the measurement of wall thicknesses would, of course, be highly welcome; the remarks here made are intended to serve the purpose of pointing out several requirements that are necessary prerequisites for such experiments.

[9] R. Newton and C. Kittel, Phys. Rev. **74**, 1604 (1948).
[10] Becker and Doering, *Ferromagnetismus* (Edward Brothers, Ann Arbor, Michigan, 1943), p. 189.

UNIVERSITY OF MICHIGAN LIBRARIES

Further Results on Neutron Production by Cosmic-Ray Particles at Sea Level*

R. D. Sard, A. M. Conforto,** and M. F. Crouch
Washington University, St. Louis, Missouri

(Received June 22, 1949)

Further measurements at sea level on neutrons coincident with charged cosmic-ray particles are reported. It is shown that the coincident neutrons are neither incident from the air nor produced in the neutron detector; they are produced in the Pb in our experimental arrangement. The earlier evidence for neutrons associated with the stopping in Pb of charged particles filtered by 12.7 cm Pb is confirmed. Evidence is presented for a second effect-neutron production in Pb in some kind of penetrating ionizing event. These neutron-penetrating particle coincidences may well be related to those discovered by Tongiorgi in penetrating showers; their bearing on the interpretation of neutron-stopped particle coincidences is discussed. With increasing thickness of the Pb filter above the G-M tube telescope, the frequency of the latter is essentially constant, while the frequency of the "neutron showers" increases steadily. Intensity considerations indicate that the bulk of the neutron-stopped particle coincidences are due to μ-mesons stopped in the Pb; the neutron penetrating particle coincidences may well be due to incident nucleons. A very crude estimate of the average number of neutrons per stopped negative meson gives 2 or 3; the systematic errors are so uncertain that we can only conclude that the multiplicity is with high probability less than about 5.

IN a previous communication,[1] we reported the observation of neutrons coincident with the stopping in a Pb absorber of charged particles filtered by 12.7 cm Pb. In a control experiment, in which the anti-coincidence counters under the absorber were disconnected, we found a doubling of the neutron coincidence rate, and we suggested that this increase was due to neutrons produced by or contained in penetrating ionizing events. Our investigation of these two kinds of neutron coincidences, coincidences with stoppings and coincidences with penetrations, has been continued[2] with the modified arrangement shown in Fig. 1. The filter is now above the double-coincidence telescope made up of the two G-M tube groups A and B, and the number of boron-ten slow neutron counters[3] in the paraffin thermalizer has been increased to seven. In addition, we now measure concurrently the neutron coincidences $(AB{:}N)$ and $(AB{-}C{:}N)$. Coincidences (AB) and anticoincidences $(AB{-}C)$ each produce equal "gate" pulses, delayed about 5μsec. and 170μsec. long, through which any neutron counter pulse, N, can pass. If an N pulse occurs while the (AB) gate is on, an $(AB{:}N)$ coincidence is recorded; sometimes, the $(AB{-}C)$ gate is also on, and an $(AB{-}C{:}N)$ coincidence is then also recorded. Thus we have, in effect, direct observations of $(AB{-}C{:}N)$ events—neutrons associated with stoppings—and $(ABC{:}N)$ events—neutrons associated with penetrations. The counts (AB), $(AB{-}C)$, N, $(AB{:}N)$ and $(AB{-}C{:}N)$ are not only totalized on electromechanical counters but are individually recorded on the moving chart of an Esterline-Angus Company "Operation Recorder." This gives a valuable check on the operation of the equipment.

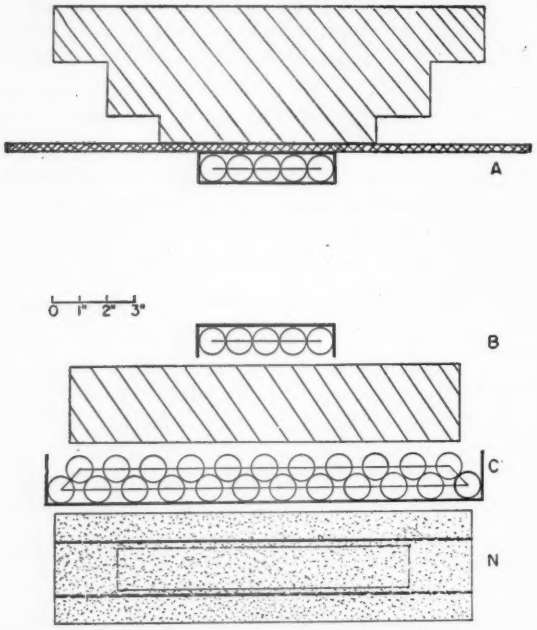

FIG. 1. Arrangement of apparatus.

Measurements have been made (under a thin wooden roof) with and without the 78.9 g/cm² Pb absorber for three filter thicknesses—0, 28.8 g/cm² Pb, and 158 g/cm² Pb (the Pb equivalent of 143 g/cm² Pb plus 10 g/cm² Fe). For each configuration data were taken with and without 1 mm Cd sheaths on the neutron counters.

The results for neutrons coincident with stoppings, $(AB{-}C{:}N)$, are given in Table I. Each box of this table refers to a particular configuration; and in each box we have the data obtained without Cd (top line) and with Cd (third line). The second and fourth lines give the expected numbers of chance coincidences (casuals) in the two cases, taken as the product of the $(AB{-}C)$ rate, the N rate, the gate length, and the duration. The sans-Cd rate corrected for casuals is given by the observed

* Research assisted by the Joint Program of the ONR and the AEC.

** International Study Fellow of the American Association of University Women.

[1] Sard, Ittner, Conforto, and Crouch, Phys. Rev. **74**, 97 (1948).

[2] The results in the present paper have been reported in part at the Chicago Meeting of the American Physical Society, November 26, 1948, Phys. Rev. **75**, 327 (1949) and in full at the St. Louis meeting of the Mid-West Cosmic-Ray Colloquium, April 9, 1949.

[3] Proportional counters lined with metallic boron enriched in the isotope of mass ten. We are grateful to the Argonne National Laboratory for the continued loan of these counters.

TABLE I. Neutrons associated with stoppings (AB–C:N).

Absorber	Filter: None	Filter: 28.8 g/cm² Pb	Filter: 158 g/cm² Pb equivalent
None (0.69 g/cm² brass in G-M tube walls)	sans Cd: 0 in 107.0h expected casuals: 0.846 with Cd: 0 in 40.22h expected casuals: 0.198 corrected rate: 0	sans Cd: 2 in 111.07h expected casuals: 0.531 with Cd: 0 in 88.67h expected casuals: 0.360 corrected rate: 0.01±0.01/h	sans Cd: 6 in 76.18h expected casuals: 0.257 with Cd: 1 in 58.43h expected casuals: 0.119 corrected rate: 0.08±0.03/h
78.9 g/cm² Pb (plus 0.69 g/cm² brass in G-M tube walls)	sans Cd: 52 in 117.02h expected casuals: 4.30 with Cd: 0 in 25.75h expected casuals: 0.231 corrected rate: 0.41±0.06/h	sans Cd: 129 in 146.32h* expected casuals: 4.19 with Cd: 1 in 38.00h expected casuals: 0.762 corrected rate: 0.85±0.08/h	sans Cd: 157 in 248.85h expected casuals: 2.43 with Cd: 4 in 142.6h expected casuals: 0.790 corrected rate: 0.60±0.05/h

* Actually, only 122 counts in this time, but 38 of them were obtained during a period when the (AB) and (AB–C) rates were low in the same proportion because of a faulty G-M tube and the 38 have, therefore, been scaled up to 45. The estimated statistical standard error of the corrected rate is $(122)^{\frac{1}{2}}$ divided by 146.32h.

counts less the expected casuals, divided by the duration, with a standard error estimated as the square root of the observed counts, divided by the duration. The with-Cd rate corrected for casuals is computed in the same way. If it exceeds its estimated standard error, it is subtracted from the corrected sans-Cd rate to give the "corrected rate" in the fifth line of the box, the two estimated standard errors being compounded quadratically. Otherwise, the "corrected rate" is simply the corrected sans-Cd rate. It is seen that the observed numbers with Cd are always of the order of magnitude of the expected numbers of casuals. This is also the case sans-Cd when the absorber is absent, but when the absorber is in place, the observed coincidences far exceed the expected casuals.

One sees from Table I that the (AB–C:N) rate for all filter thicknesses is essentially zero in the absence of the absorber, and is essentially constant when the absorber is in place. Its vanishing in the absence of absorber is significant, as the (AB–C) rate is then not negligible (2.28/min., 1.68/min., 0.98/min. for the three filter thicknesses) compared with its value when the absorber is in place (11.02/min., 7.85/min., and 2.41/min. for the three filter thicknesses). This shows that the Pb absorber is essential to the production of the neutrons detected. The approximate constancy of (AB–C:N) when the absorber is in place and the filter thickness is changed shows that a large fraction of the coincident neutrons are produced in the absorber by particles present in the air, and that these particles are not electrons. We feel that no quantitative significance need be attached to the changes in (AB–C:N) with filter thickness, because of the poor statistics and because there were sizeable fluctuations in the N rate for each geometry which may possibly have been associated with fluctuations in neutron detecting efficiency.[4]

[4] Correction for an observed steady increase with time in the (AB) rate for a given geometry (about 5 percent between the middle of October and end of December, 1948) and for an observed increase of neutron detecting efficiency with filter thickness (for Po-Be neutrons originating in the absorber the efficiencies are in the ratio 0.92:0.96:1.00) leaves the (AB–C:N) rates in the ratio 0.45±0.7:0.84±0.08:0.60±0.05.

Table II presents the results for (ABC:N)—neutrons coincident with penetrations; it is made up in exactly the same way as Table I except that (ABC) replaces (AB–C) in the calculation of the casuals. One sees, first of all, that there are essentially no neutron-charged particle coincidences in the absence of filter and absorber. This means that the effect of any neutron showers incident on the apparatus is negligible, as well as neutron production in the paraffin or neutron counters. We conclude that the non-vanishing neutron coincidence rates in Tables I and II represent the effect of neutron production in the absorber or filter. The rates in the first row of Table II are points of the transition curve for "neutron showers" produced in the lead filter by ionizing or non-ionizing radiation from any direction; these "showers" are characterized by having one or more charged particle passing through A, B, and C, and one or more detectable neutron. The steady increase with filter thickness shows that these showers are not associated with the electronic-photonic component. The rates in the second row are harder to interpret, as production and absorption in both filter and absorber are involved.

It is likely that an appreciable fraction of these neutron showers from the filter give (AB–C:N) coincidences when the 80 g/cm² Pb absorber is inserted. Comparison of the rates in the corresponding columns (especially the first!) of the first row of Table II and the second row of Table I shows that this effect does not suffice to explain the major part of the (AB–C:N) coincidences, which must be due either to μ-meson stoppings in the absorber or to proton stoppings there.

UNIVERSITY OF MICHIGAN LIBRARIES

TABLE II. Neutrons associated with penetrations ($ABC:N$).

Absorber	Filter: None	Filter: 28.8 g/cm² Pb	Filter: 158 g/cm² Pb equivalent
None (0.69 g/cm² brass in G-M tube walls)	sans Cd: 25 in 107.0h expected casuals: 14.7 with Cd: 3 in 40.22h expected casuals: 3.60 corrected rate: 0.10±0.05/h	sans Cd: 50 in 111.1h* expected casuals: 11.9 with Cd: 11 in 88.67h expected casuals: 8.04 corrected rate: 0.34±0.06/h	sans Cd: 49 in 76.18h expected casuals: 7.63 with Cd: 3 in 58.43h expected casuals: 3.46 corrected rate: 0.54±0.09/h
78.9 g/cm² Pb (plus 0.69 g/cm² brass in G-M tube walls)	sans Cd: 92 in 117.0h expected casuals: 11.5 with Cd: 1 in 25.75h expected casuals: 0.608 corrected rate: 0.69±0.08/h	sans Cd: 225 in 146.3h** expected casuals: 16.9 with Cd: 4 in 38.00h expected casuals: 3.08 corrected rate: 1.42±0.11/h	sans Cd: 383 in 248.9h expected casuals: 28.2 with Cd: 14 in 142.6h expected casuals: 9.29 corrected rate: 1.43±0.08/h

* Actually, only 46 counts in this time, but 18 of them were obtained during a period when the (AB) and (AB–C) rates were low in the same proportion because of a faulty G-M tube, and the 18 have, therefore, been scaled up to 22.

** Actually, only 212 counts in this time, but 68 of them were obtained during a period when the (AB) and (AB–C) rates were low in the same proportion because of a faulty G-M tube, and the 68 have, therefore, been scaled up to 81.

Intensity considerations argue against the latter.[5] Consider the no-filter case (first column); here any π-mesons stopped in the absorber would have first to be produced there by stopped protons, and, therefore, an argument against a protonic origin of the (AB–C:N) events applies to π-mesons as well. The (AB–C:N) rate is 0.4/hr. The meson stopping rate is approximately equal to the difference of the (AB–C) rates with and without the absorber when the 158 g/cm² Pb filter is in place: 2.41−0.98=1.43/min., which is 210 times greater. As explained below, this ratio corresponds to an average number of neutrons per stopped negative meson of the order of two or three, a plausible result. Little is known, on the other hand, of the frequency with which protons get stopped by nuclear collisions at sea level, other than that it is extremely small. An experiment now under way on the behavior of the neutron coincidence rates with increasing depth should settle the question; in the meanwhile, we proceed on the assumption that the bulk of the (AB–C:N) events are due to μ-mesons.

It is not excluded, on the other hand, that the neutron showers are produced by nucleons. Consider again the no-filter case. The (ABC:N) rate is 0.7/hr, while the (ABC) rate is 29.1/min., 2500 times greater. Protons compose from 0.5 to 5 percent of these particles.[6,7]

A determination of the average number of neutrons produced per stopped negative meson would indicate the extent of nuclear excitation by μ-meson capture. Our arrangement is not suited for such a measurement; one is tempted, nevertheless, to draw some inferences as to order of magnitude. We have measured the efficiency of the neutron-detecting system for Po−Be neutrons originating in the Pb absorber; this was done by measuring the N rate with a calibrated source placed at various positions inside the Pb. The result is 5×10^{-3}, for incoherent neutron counting. For neutron coincidences, the efficiency is reduced by the factor $1-\exp(l/\tau)$, where l is the gate length, and τ the mean life of a thermal neutron in the detector. τ was measured by observing (AB:N) coincidences simultaneously with two different gate lengths, one extending from 5 to 78μsec. after (AB), the other from 5 to 178μsec. The corrected numbers of (AB:N) coincidences were 120 and 179, respectively, giving $\tau=80\mu$sec. The coherent neutron efficiency, therefore, is 4.5×10^{-3}. Assuming that the meson-stopping rate is 1.4/min., that 45 percent of these mesons are negative, that the neutrons resulting from this capture are detected with an efficiency of 4.5×10^{-3}, and that the true (AB–C:N) rate from the absorber is 0.4/hr., one obtains 2.4 for the multiplicity. The systematic errors in this estimate are so uncertain that we dare only infer that the average multiplicity is less than about 5.

Some indication that the coincident neutrons detected have an energy spectrum like that of Po−Be neutrons is given by measurements we carried out with the boron counters vertical instead of horizontal ("long counter geometry"). The counting rate for Po−Be neutrons was reduced by the factor 0.57±0.13, the corrected (AB–C:N) rate by the factor 0.52±10, and the corrected (ABC:N) rate by the factor 0.58±0.05. The uncertainties indicated are estimated statistical standard errors.

[5] Statistically significant data obtained at sea-level with a magnetized iron analyzer would settle the question, as protons are not focussed by these devices. The newer data of G. W. McClure and G. Groetzinger, Phys. Rev. 75, 340 (1949), obtained at 4300 m elevation speak in favor of μ-mesons, though in our ignorance of the geometrical arrangement we must leave room for the slight possibility that the 16 neutron coincidences reported could be ascribed to π^--mesons incident on the analyzer at this altitude.

[6] B. Rossi, Rev. Mod. Phys. 20, 537 (1948), Table II.

[7] Todd, Henderson, Miller, and Potter, Phys. Rev. 76, 591, 1949.

Scattering of Protons by Tritons*

A. HEMMENDINGER, G. A. JARVIS, AND R. F. TASCHEK
Los Alamos Scientific Laboratory, Los Alamos, New Mexico
(Received July 7, 1949)

The proton-triton differential scattering cross section has been measured for laboratory angles between 45° and 135° and proton energies between 0.7 and 2.5 Mev. In this angular range the scattering is predominantly nuclear and shows a rapid increase in intensity for angles greater than 90° in the center of mass system. Some indications of anomalous behavior near the threshold for $T^3(p,n)He^3$ are reported.

I. INTRODUCTION

THE systematic study of the scattering of the lightest nuclei may, one hopes, lead to a better theoretical knowledge of the nature of nuclear forces. Such studies have been made, with sufficient accuracy for detailed theoretical treatment, of the scattering of neutrons by protons[1] and deuterons;[2] of protons by protons,[3] deuterons[4] and alpha-particles;[5] and of deuterons by deuterons.[6] The recent advent of the nuclei of T^3 and He^3 in the laboratory increases greatly the number of light scattering pairs available for experimental investigation.

The possibility of obtaining, at low energies, experimental information of use in calculations involving specific nuclear force theories may arise from the large size of the nuclei immediately above hydrogen, with the result that waves with angular momentum quantum number $l \geq 1$ become effective (as pointed out by Buckingham and Massey[7] for the scattering of neutrons by deuterons). Extension of their theory has allowed Critchfield[8] to explain the main features of p-d scattering for proton energies below the $D^2(p,n)$ threshold. The work described below adds experimental information on the scattering of hydrogen of mass one by mass three hydrogen nuclei.

Measurements of proton-triton scattering were first made during a preliminary investigation of the proton-triton interaction using the Los Alamos 2.5-Mev electrostatic accelerator to project protons into a target of tritium gas. During this early work the comparison of scattering of protons by tritium and hydrogen targets proved to be a practical means of ascertaining the relative abundance of the hydrogen contaminant in a tritium sample.[9] It was soon apparent that the small volume scattering chamber, already described elsewhere,[10] was quite suitable for the observation of charged particle scattering and detailed measurements were made.

II. EXPERIMENTAL

The tritium target pressure was set at approximately 5 cm of mercury and was read with a traveling microscope on a mercury manometer. The target temperature was indicated by a thermometer waxed to the body of the target. These two measurements, together with the concentration of tritium in the target as determined by p-p scattering give the volume density of tritons. The scattered particles were detected by an argon-filled proportional counter with a slit system to define a small solid angle at the center of the target. The counter could be set at any angle between 45° and 135° with respect to the direction of the incident protons. The differential scattering cross section at scattering angle θ is

$$\sigma(\theta) = Y \sin\theta/(Nng),$$

where Y is the number of scattered particles counted at angle θ per microcoulomb of beam current integral, $N(=6.25\times10^{12})$ is the number of protons per microcoulomb of beam current integral, n is the number of tritons per unit volume, and g is a geometry factor for the counter slit system.[10]

A few minor changes in the target as described originally have been made. A background count, inde-

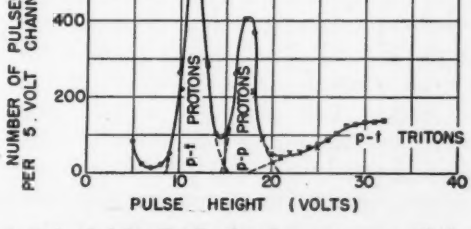

FIG. 1. Pulse height distribution from an argon-filled proportional counter at a laboratory scattering angle of 45° and a proton beam energy of 2.335 Mev.

* This document is based on work performed under U. S. Government Contract Number W-7405-Eng-36 at the Los Alamos Scientific Laboratory of the University of California.

[1] H. H. Barschall and R. F. Taschek, Phys. Rev. **75**, 1819 (1949). Lampi, Freier, and Williams, Phys. Rev. **76**, 188 (1949).

[2] J. H. Coon and R. F. Taschek, Phys. Rev. **76**, 710 (1949).

[3] Blair, Freier, Lampi, Sleator, and Williams, Phys. Rev. **74**, 553 (1948).

[4] Sherr, Blair, Kratz, Bailey, and Taschek, Phys. Rev. **72**, 662 (1947).

[5] Freier, Lampi, Sleator, and Williams, Phys. Rev. **75**, 342A (1949).

[6] Blair, Lampi, Freier, Sleator, and Williams, Phys. Rev. **74**, 1594 (1948).

[7] R. A. Buckingham and H. S. W. Massey, Proc. Roy. Soc. **A179**, 123 (1941).

[8] C. L. Critchfield, Phys. Rev. **73**, 1 (1948).

[9] Taschek, Jarvis, Hemmendinger, Everhart, and Gittings, Phys. Rev. **75**, 1361 (1949).

[10] R. F. Taschek, Rev. Sci. Inst. **19**, 591 (1948).

UNIVERSITY OF MICHIGAN LIBRARIES

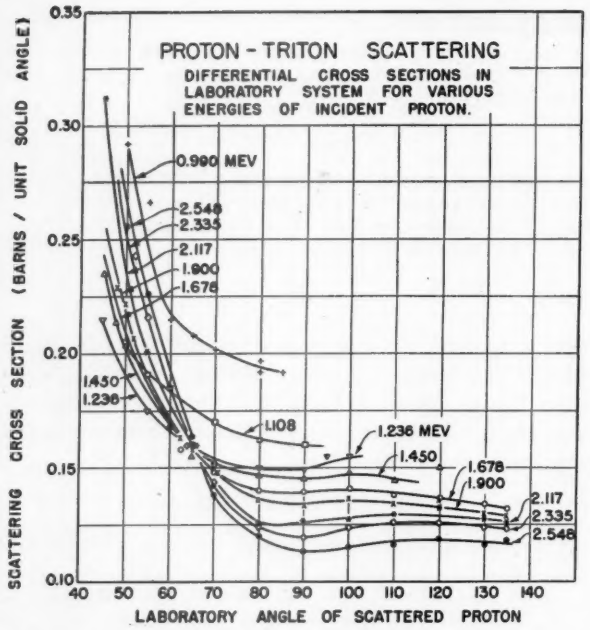

FIG. 2. Proton-triton scattering, differential cross sections in the laboratory system for various energies of protons incident on a gaseous tritium target. Additional points at 750 kev not conveniently plotted are 45°, 0.571; 50°, 0.475; 60°, 0.338.

pendent of gas pressure, due to scattering at the edge of the entrance aperture to the target was eliminated by the use of a second slightly larger aperture inside the target. An insulated ring, placed just ahead of the Faraday cage used for current measurement and held at a potential of −200 volts, served as an effective electron barrier to prevent the escape of secondary electrons formed in the cage. Scattering measurements with and without a transverse magnetic field in this region gave identical results.

The beam current integrator circuit built by H. T. Gittings[11] was checked frequently and was stable and accurate to ±0.2 percent.

The pulses from the several groups of scattered particles were resolved, as was done by Sherr *et al.*[4] in the *p-d* scattering experiment, by means of the Sands 10-channel pulse height selector.[12] In the present experiment there are, in addition to the protons scattered by tritons, the recoil tritons and the protons from contamination proton-proton scattering if the angle is less than 90°. At the lower incident proton energies the recoil tritons were stopped in the 0.1-mil thick aluminum counter window that separated counter and target fillings. As the beam energy was increased, the tritons showed up at small pulse height and the peak in their pulse height distribution moved gradually across the more nearly stationary peaks of scattered protons. In Fig. 1 is shown a pulse height distribution at a high energy where the triton peak is at the extreme right. Systematic observations were necessary to avoid the possibility at some angles of two of the peaks coinciding in pulse height. A small shift in the beam energy or scattering angle, or even the target pressure, shifts the relative position of the scattered particle peaks considerably and this expedient was used to improve resolution or to identify the various peaks when there was any question about them. All of the *p-T* scattering measurements were made on the proton peak.

The proton energy scale for the accelerator was established by the measurement by Herb, Snowden, and Sala[13] of the $Li^7(p,n)$ threshold. The threshold for $T^3(p,n)He^3$ was measured recently in this laboratory,[14] so the effective thickness for the entrance window to the target was determined by measuring the beam energy at which neutrons were observed from the target. The energy loss in the window was then determined for other beam energies from the range-energy relation for protons.

In the early phases of this work frequent measurements were made of proton-proton scattering in order to establish the reproducibility of measurements and to check all parameters of the measurement. An error of 5 percent (results were too high), which persisted in *p-p* scattering measurements, referring to those of Herb, Kerst, Parkinson, and Plain[3] as standard, is ascribed to an error in the determination of *g*. Since it has not been possible so far to re-measure the distances involved (because the target has been in use), all measurements have been normalized to agree with those of HKPP.

For this type of experiment the 0.1-mil aluminum counter window must be perfectly tight. The decay rate of tritium is so great that the slightest leak in this window, even though the counter pressure was greater than target pressure, let enough tritium diffuse into the counter to produce excessive counter background noise. The selection and trial of a suitable aluminum foil for this window was so tedious that the use of a nylon window was attempted, but it proved to be much too transparent to tritium, even though it was quite tight for argon. When a good aluminum window was finally selected it served for all measurements and the argon counter filling was not disturbed over a period of five months.

There was a small but continuous change in concentration of tritium in the target, possibly due to exchange of tritium in the stopcock grease of the conical seals, which suggests that chemically stable packings should be used instead of ground cones for further work of this kind. The proton-triton scattering at 50° was measured frequently during a run at any energy and these data were used to correct for small changes in the tritium concentration. As a further check, above the

[11] H. T. Gittings, AECD-1984 (1948) and Rev. Sci. Inst. **20**, 325L (1949).
[12] E. W. Dexter and M. Sands, AECD-2255 (1948).
[13] R. G. Herb, S. C. Snowden, and O. Sala, Phys. Rev. **75**, 246 (1949).
[14] Taschek, Argo, Jarvis, and Hemmendinger, Phys. Rev. **75**, 1268 (1949).

threshold for the reaction $T^3(p,n)$, the concentration was monitored and corrected by counting neutrons with a long counter.[15]

The measurements reported below were made with a front target window of 0.2-mil aluminum (0.9 cm air equivalent) and an exit window of the same thickness. The lowest beam energy used was 750 kev after passage through the front foil, and this was reduced to 380 kev by the exit window. This residual range appears to be great enough to permit accurate measurements of beam current since the calculated energy straggling[16] in each of the 0.2-mil foils is approximately 15 kev at 10 Mev incident proton energy.

III. RESULTS

The laboratory system differential cross sections measured are shown in Fig. 2. The proton energies shown are calculated for a point at the center of the scattering volume. The cross sections are good to about ±5 percent for $E_p \geq 1.1$ Mev on the basis of estimated systematic and statistical errors, including the error of the tritium concentration measurement. For proton energies below about 1.2 Mev additional factors which become important in the measurement are the large energy loss in entrance and exit foils to the scattering volume and the rapidly increasing small angle Rutherford scattering in the entrance foil. The energy straggling, which is about 15 kev in the entrance foil at 1 Mev, contributes primarily to spreading the proton energies and is therefore most serious where the change in cross section is most rapid, i.e., at low energy. The Rutherford scattering by the foil into small angles is presumably of second order importance because a proton leaving the entrance foil with such an angle as to miss the gas volume which can be seen by the counter would also miss entering the Faraday cage and therefore no false contribution to the measurement can be made for single scattering. The energy *spread*, however, can falsify a cross-section measurement when some of the protons fail to have enough energy to enter the Faraday cage through its entrance foil; this would lead to an apparently high cross section at the very lowest proton energies, and for this reason there may be some doubt about the 700 and 800 kev values shown in Fig. 4, although only 550 kev are necessary for the *average* proton to penetrate the foil into the cage.

The center of mass system differential cross sections are shown in Fig. 3. These are calculated from the observed laboratory cross sections of the scattered protons from

$$\sigma(\phi) = \cos(\phi - \theta)(\sin^2\theta/\sin^2\phi)\sigma(\theta),$$

where $\sigma(\theta)$ and $\sigma(\phi)$ are respectively the laboratory and

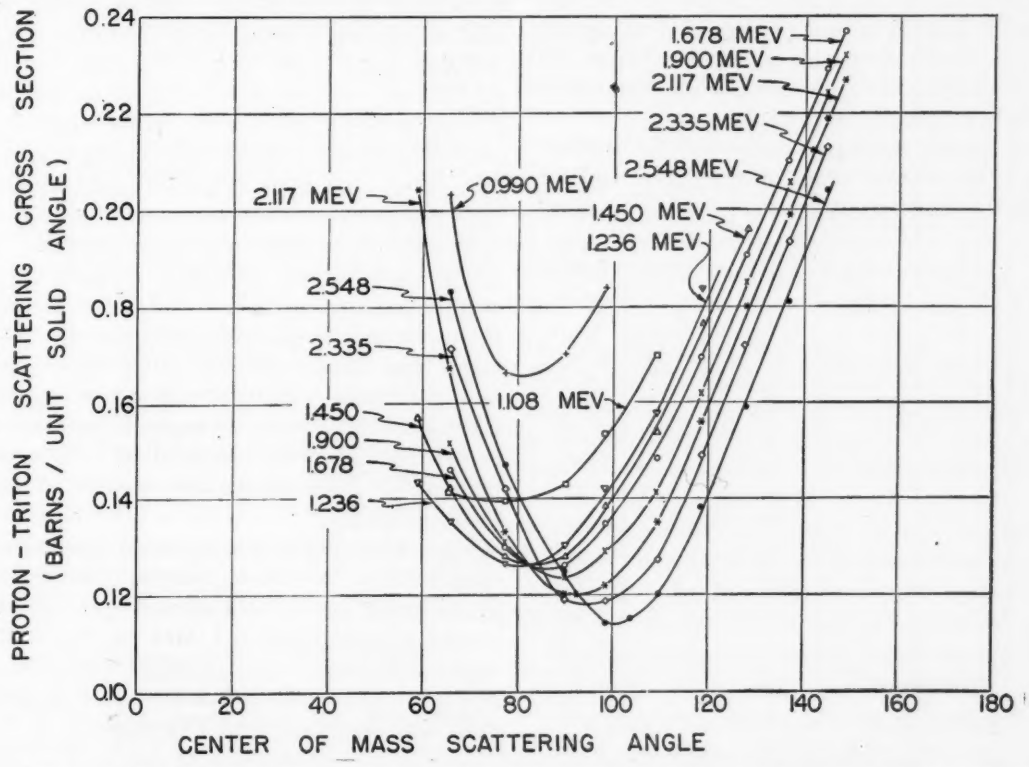

FIG. 3. Proton-triton scattering, differential cross sections in the center of mass system for various energies of incident protons. Additional points at 750 kev are 58.8°, 0.381; 65.7°, 0.330; 77.5°, 0.256.

[15] A. O. Hanson and J. L. McKibben, Phys. Rev. **72**, 673 (1947).
[16] M. S. Livingston and H. A. Bethe, Rev. Mod. Phys. **9**, 283 (1937).

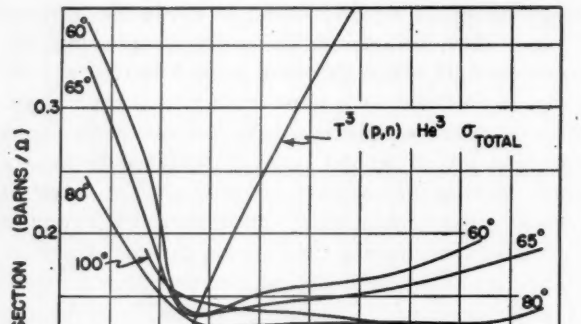

FIG. 4. Proton-triton scattering, data from Fig. 3 plotted as a function of energy to show the minimum near the threshold for $T^3(p,n)$.

center of mass differential cross sections at the corresponding angles θ and ϕ.

Figure 3 shows the rapid increase in intensity at angles beyond about 90° which is indicative of strong nuclear scattering. At the smallest angles and energies a considerable portion of the differential cross section arises from coulomb scattering as calculated from the Rutherford formula, but even here the observed values are at least five times Rutherford.

A rather striking similarity exists between the p-T scattering in the angular range observed here and the same range in p-d scattering.[4] This is especially apparent

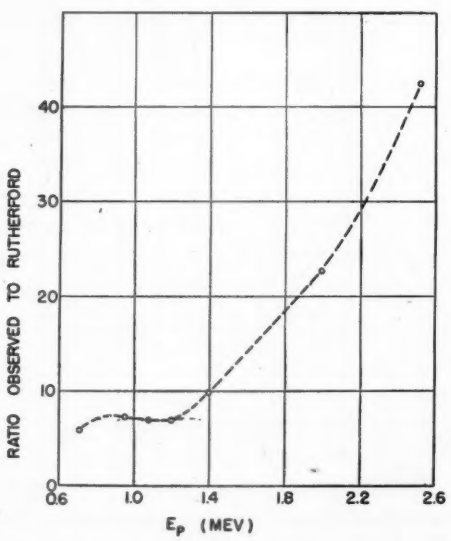

FIG. 5. Ratio of differential scattering cross section to Rutherford scattering cross section for center-of-mass scattering angle of 65°.

if one plots $k^2\sigma(\phi)$ against $\cos\phi$, where $k=2\pi/\lambda$ for the proton, as done by Critchfield,[8] and comparing curves corresponding to the same center of mass energy.

In Fig. 4 are shown some curves for differential cross section at several fixed angles as a function of proton energy, together with a plot of the total cross section[17] for the $T^3(p,n)He^3$ reaction, the threshold of which is at 1019 kev.[14] It will be observed that all the differential cross sections appear to increase suddenly near this threshold as the proton energy is decreased. Although the lowest energy cross-section values and trend with energy are subject to the straggling and scattering difficulties mentioned above it would seem that the phenomenon observed is too large to be accounted for entirely by such processes. As the proton energy is reduced, the contribution to the cross section from coulomb scattering increases rapidly but one finds that between 1.2 Mev and 0.8 Mev the ratio of observed to Rutherford scattering at 65° is approximately constant, while above 1.2 Mev it increases rapidly, as is shown in Fig. 5.

Tentatively, it would appear that the sudden increase in scattering at energies below 1.1 Mev is associated with the threshold for the $T^3(p,n)He^3$ reaction. From the viewpoint of the older theories on pure potential scattering far from a resonance the phenomenon apparently observed should not occur, but a recent theory of Wigner[18] points out that even an elastic scattering cross section may show a cusp of the form $a+b|E-E_n|^{\frac{1}{2}}$ +higher order terms in $|E-E_n|$ near the threshold E_n for a new nuclear process, which in this case is the p,n reaction. The phenomena to be expected are thus somewhat similar to those in resonance scattering. The constants a and b are not determined by the theory and in any case would be complicated by the large Rutherford scattering at these low energies.

The experimental difficulties inherent in the low energy measurements which lead to the above interpretation are understood by the writers, as discussed above, and several check experiments, together with reductions in the entrance foil thicknesses are being pursued to investigate this low energy region in particular. Similar experiments near the threshold of $Li^7(p,n)Be^7$ would perhaps be more satisfactory because of the higher incident energy.

Since resonance scattering could produce somewhat similar effects, we wish to point out that we have found no evidence for a sharp excited state in He^4 at an energy corresponding to 1 Mev for this collision, but there does appear to exist a broad excited state of the alpha-particle at about 2.5 Mev as observed[19] in the yield of gamma-rays from $T^3(p,\gamma)He^4$.

[17] Jarvis, Hemmendinger, Argo, and Taschek, Phys. Rev. **76**, 168 (1949).
[18] E. P. Wigner, Phys. Rev. **73**, 1002 (1948).
[19] Argo, Gittings, Hemmendinger, Jarvis, Mayer, and Taschek, Phys. Rev. **76**, 182 (1949).

The writers are indebted to E. S. Robinson and his colleagues in the Radiochemistry Group at Los Alamos for their collaboration in the preparation and handling of the tritium samples, and they gratefully acknowledge the assistance of G. G. Everhart in the operation of the electrostatic accelerator.

APPENDIX

TABLE I. Proton-triton scattering; experimental results for differential cross sections in both laboratory and center-of-mass systems as a function of angle in barns per unit solid angle.

		E_p=0.708 Mev		E_p=0.990 Mev		E_p=1.108 Mev		E_p=1.236 Mev		E_p=1.45 Mev		E_p=1.678 Mev		E_p=1.90 Mev		E_p=2.117 Mev		E_p=2.335 Mev		E_p=2.548 Mev	
θ_{lab}	ϕ_{CM}	σ_{lab}	σ_{CM}	σ_{lab}	σ_{CM}	σ_{lab}	σ_{CM}	σ_{lab}	σ_{CM}	σ_{lab}	σ_{CM}	σ_{lab}	σ_{CM}	σ_{lab}	σ_{CM}	σ_{lab}	σ_{CM}	σ_{lab}	σ_{CM}	σ_{lab}	σ_{CM}
45	58.8	0.571	0.381					0.215	0.144	0.235	0.157					0.306	0.204				
50	65.7	0.475	0.330	0.292	0.203	0.204	0.142	0.195	0.135	0.204	0.142	0.210	0.146	0.218	0.152	0.240	0.167	0.256	0.171	0.264	0.183
60	77.5	0.338	0.256	0.219	0.166	0.184	0.140	0.167	0.127	0.169	0.128	0.171	0.130	0.173	0.131	0.176	0.133	0.185	0.140	0.193	0.147
70	90.0			0.202	0.170	0.170	0.143	0.155	0.130	0.152	0.128	0.150	0.126	0.147	0.124	0.143	0.120	0.142	0.119	0.148	0.125
80	98.5			0.194	0.184	0.162	0.154	0.150	0.142	0.146	0.138	0.142	0.135	0.136	0.129	0.129	0.122	0.124	0.118	0.120	0.114
90	109.4					0.160	0.170	0.149	0.158	0.145	0.154	0.140	0.148	0.134	0.142	0.127	0.135	0.120	0.127	0.113	0.120
100	118.8							0.153	0.184	0.147	0.176	0.141	0.169	0.135	0.162	0.130	0.156	0.124	0.149	0.115	0.138
110	128.									0.144	0.196	0.140	0.191	0.136	0.185	0.132	0.180	0.126	0.171	0.117	0.159
120	136.8											0.137	0.210	0.134	0.206	0.131	0.199	0.126	0.193	0.118	0.181
130	144.8											0.134	0.229	0.131	0.225	0.128	0.219	0.124	0.213	0.116	0.199
135	148.5											0.132	0.237	0.129	0.232	0.126	0.227	0.121	0.218		
55	71.1			0.251	0.182																
65	83.7			0.208	0.166	0.176	0.140			0.160	0.127										
75																0.135	0.120				
85										0.149	0.149									0.115	0.115
95										0.152	0.171										

PHYSICAL REVIEW VOLUME 76, NUMBER 8 OCTOBER 15, 1949

Cross Section as a Function of Angle for the D(d,n)He^3 Reaction for 10-Mev Bombarding Deuterons*

K. W. ERICKSON, J. L. FOWLER, AND E. J. STOVALL, JR.
Los Alamos Scientific Laboratory, Los Alamos, New Mexico

(Received February 23, 1949)

By counting He^3 particles with a proportional counter, the differential cross sections for the reaction D(d,n)He^3 have been measured at laboratory angles from 16.5 degrees to 38.2 degrees (39.3 degrees to 95.0 degrees in center of mass system), for an incident deuteron energy of 10.3 Mev. In the center of mass system, the differential cross section is 4.5×10^{-27} cm^2 at 90 degrees, decreasing to a minimum of 2.2×10^{-27} cm^2 at about 45 degrees, and rising steeply at lower angles. By determining the neutron yield with $Cu^{63}(n,2n)Cu^{62}$ detectors, the differential cross section at zero degrees is found to be about five times that at 90 degrees (center of mass).

I. INTRODUCTION

SINCE the discovery of the D+D→He^3+n reaction by Oliphant, Harteck, and Rutherford,[1] a number of investigations[2–11] of the yield and the angular distribution of the products have been made for bombarding energies below five Mev. The earlier measurements on the angular distribution were made at zero and 90 degrees to the beam direction and the differential cross section in the center of mass system was fitted to a $(1+A(E)\cos^2\theta)$ law. This law has been found to hold[12–17] at a number of angles for the competing reaction, D+D→H^3+H^1.

For the D(d,n)He^3 branch of the reaction in the bombarding energy region above one Mev, more recent work[18–19] shows that terms up to $\cos^6\theta$ must be included in the Fourier expansion of the differential cross section

* This document is based on work performed at Los Alamos Scientific Laboratory of the University of California under Government Contract W-7405-eng-36.

[1] Oliphant, Harteck, and Rutherford, Proc. Roy. Soc. (London) A144, 692 (1934).
[2] Manley, Coon, and Graves, Phys. Rev. 70, 101 (1946).
[3] Bennett, Mandeville, and Richards, Phys. Rev. 69, 418 (1946).
[4] H. T. Richards, Phys. Rev. 60, 167 (1941).
[5] R. Ladenburg and M. H. Kanner, Phys. Rev. 52, 911 (1937).
[6] Amaldi, Hafstad, and Tuve, Phys. Rev. 51, 896 (1937).
[7] R. B. Roberts, Phys. Rev. 51, 810 (1937).
[8] R. Ladenburg and R. B. Roberts, Phys. Rev. 50, 1190 (1936).
[9] T. W. Bonner and W. M. Brubaker, Phys. Rev. 49, 19 (1936).
[10] Kempton, Browne, and Maasdorp, Proc. Roy. Soc. (London) A157, 386 (1936).
[11] K. D. Alexopoulos, Helv. Phys. Acta 8, 601 (1935).
[12] Bretscher, French, and Seidl, Phys. Rev. 73, 815 (1948).
[13] Manning, Huntoon, Myers, and Young, Phys. Rev. 61, 371 (1942).
[14] Huntoon, Ellett, Bayley, and Van Allen, Phys. Rev. 58, 97 (1940).
[15] H. Neuert, Physik. Zeits. 39, 890 (1938).
[16] H. Neuert, Physik. Zeits. 38, 122 (1937).
[17] K. D. Alexopoulos, Helv. Phys. Acta 8, 513 (1935).
[18] Blair, Freier, Lampi, Sleator, and Williams, Phys. Rev. 74, 1599 (1948).
[19] G. T. Hunter and H. T. Richards, Phys. Rev. 75, 335 (1949).

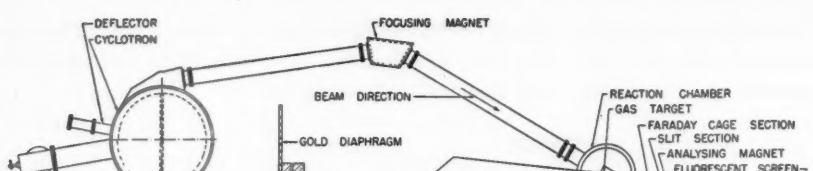

FIG. 1. Apparatus assembly.

as a function of angle. Konopinski and Teller[20] have formed a qualitative theory of the angular variation of this reaction showing how $A(E)$ (the coefficient of the first term of the Fourier expansion) should change with the energy of the bombarding deuterons.

For bombarding energies above five Mev, very little experimental or theoretical research has been done on this reaction. Preliminary work in this laboratory at 10 Mev over limited angular range has been previously reported.[21] The thick target yield of neutrons from this reaction has been obtained with 10-Mev deuterons.[22]

The present experiment consists of bombarding a thin deuterium gas target with 10-Mev deuterons from the Los Alamos 42-inch cyclotron and counting the number of reaction particles which come off at various angles per coulomb of beam current. From these values and the geometry of the system, the differential cross section is calculated. Since the cyclotron does not hold the energy of the deuterons constant (see Table II), this energy is measured at frequent intervals and all data corrected to 10.3 Mev. For center of mass angles larger than 39 degrees the He^3 particles were counted by means of a proportional counter. For zero degrees the neutrons from the reaction were counted indirectly by measuring the 10-minute activity produced in copper foils by a $Cu^{63}(n,2n)Cu^{62}$ reaction. The essential results of this research have been reported in a Letter to the Editor in the *Physical Review*.[23]

TABLE I. Summary of the results of analysis for possible excited states of the He^3 nucleus.

Lab angle between He^3 and beam	Energy of main He^3 peak Mev	Energy region examined for He^3 group Mev	Limit of required He^3 excitation levels to fall in column 3 Mev
31.4°	7.4	4.8–6.8	3.1–0.9
26.7°	8.6	4.8–7.7	4.5–1.0
22.4°	9.1	7.2–8.7	3.2–0.9
19.5°	9.6	7.7–9.2	3.2–0.9
16.5°	10.2	7.8–8.7	3.8–2.6

[20] E. J. Konopinski and E. Teller, Phys. Rev. **73**, 822 (1948).
[21] Curtis, Rosen, and Fowler, Phys. Rev. **73**, 648 (1948).
[22] L. W. Smith and P. G. Kruger, Phys. Rev. **74**, 1258 (1948).
[23] Erickson, Fowler, and Stovall, Phys. Rev. **75**, 894 (1949).

II. APPARATUS

The equipment used in this experiment was, in general, the same as that described by Curtis, Fowler, and Rosen.[24] The general outline of the apparatus is shown in Fig. 1. The 10-Mev deuteron beam passes from the focusing magnet and thence into a six-foot length of six-inch diameter tubing. Gold defining slits, together with an antiscattering slit in this tubing, collimate the beam to ± 0.6 degree as it enters the $\frac{1}{4}$-inch diameter mica window of the gas target. In order to cut down on background due to neutrons, and also to confine the source of neutrons (Section IV) the gas targets were designed as short as possible consistent with the condition that the volume defined by the slit of the counter not include any material being bombarded by the deuteron beam except the deuterium gas. Rutherford scattering in the front mica window of the target was small for 10-Mev deuterons; the measured effective spread of the beam after passing through the window was increased from ± 0.6 degree to ± 0.8 degree; less than one deuteron in 10^5 in the beam was scattered at such an angle as to strike the target wall in front of the proportional counter slit system. After passing through the gas target, the beam entered the Faraday cage which was used with a current integrator to monitor the beam. The cage could be moved to allow the beam to continue to the analyzing magnet for energy measurements.

The slit system defining the He^3 particles consisted of a $\frac{1}{8}$-inch vertical slit attached to the target immediately in front of the target window and a $\frac{1}{8}$-inch hole in the proportional counter. Since there was nothing between the target and an absorber foil immediately in front of the counter to produce scattering of particles into the counter (Fig. 1), an antiscattering slit between the target and the counter was unnecessary. Reaction volume and solid angle calculations were made in essentially the same manner as suggested by Herb, Kerst, Parkinson and Plain.[25] Pulses from the proportional counter were fed to a linear amplifier and thence to a ten-channel pulse amplitude analyzer from which the data were recorded.

[24] Curtis, Fowler, and Rosen, Rev. Sci. Inst. **20**, 388 (1949).
[25] Herb, Kerst, Parkinson, and Plain, Phys. Rev. **55**, 998 (1939).

In an effort to improve the effective resolution of the proportional counter, several additions and improvements were made to the equipment described by Curtis, Fowler, and Rosen.[24] The most important of these was the addition of a selsyn controlled foil system mounted on the reaction chamber lid so that one hundred combinations of foil thicknesses were available for slowing down the reaction particles to make the ends of their paths lie in the counter. The proportional counter was redesigned with a 0.005-inch collecting wire offset $\frac{1}{4}$ inch from the center of the counter. A palladium leak was added to the target filling system in order to improve the purity of the deuterium in the target.

The beam spread and position was measured by using the proportional counter, with a $\frac{1}{8}$-inch diameter entrance window, as an ionization chamber (with about one atmosphere of argon pressure and minus 135 volts on the center wire). This counter was set at various positions near zero degrees and the amount of ionization (and hence the beam strength) was obtained as a function of angle. Since the beam was defined by a $\frac{1}{4}$-inch diameter diaphragm at the position of the target entrance window (Fig. 1), and since the distances involved were known, it was possible to calculate the angular spread of the beam from this measurement. The measurement was repeated after the target was in place in order to determine the scattering effect of the two mica windows.

The current integrator and Faraday cage were checked by measuring, by thermocouple, the temperature rise of an 83-gram piece of copper faced with 15 grams of gold which was placed in the beam just in front of the Faraday cage. The beam was monitored by the He^3 particles from the $D(d,n)He^3$ reaction which had in turn been calibrated against the current integrator. From the temperature rise of the block while it was in the beam, the specific heat of the block, and from the beam energy, the total charge striking the block was computed and compared with the charge indicated by the He^3 particles passing through the counter. Results of this test indicate agreement between these two measurements within three percent.

III. DISTRIBUTION OF He^3 PARTICLES

The procedure used in taking the primary data was quite similar for all these points. At the beginning of each day of operation the ten-channel amplitude analyzer was calibrated against an automatically variable pulse generator; the current integrator was calibrated against known constant leakage currents; and the target and counter were flushed and refilled with fresh gas. The counter voltage was adjusted to give a gas multiplication of ten. When a usable cyclotron beam was obtained, the absorber foils in front of the counter were adjusted to give the best He^3 peak on the ten channel analyzer and the amplifier gain was set to cause this peak to occur at a convenient position on the analyzer. When these adjustments had been completed, a data run was made, usually consisting of about 128 current integrator counts (i.e., about 14 microcoulombs). The raw data consisted of the number of pulses recorded in each channel of the ten-channel pulse amplitude analyzer and the number of current integrator counts obtained. The cyclotron beam was such that a normal run usually required about two minutes. On the completion of a data run, the absorber foil wheels were adjusted so that they would completely stop the He^3 particles and a background run was made. Immediately after such a set of runs (and without turning off the cyclotron), the Faraday cage was moved and the

TABLE II. Summary of results for the differential cross section of the $D(d,n)He^3$ reaction.

Lab. angle degrees	Energy of deuterons Mev	Differential cross section in lab. system $cm^2 \times 10^{-26}$
16.5	10.0	1.55
16.5	10.2	1.54
19.5	9.9	1.12
19.5	10.3	1.13
22.4	10.0	1.33
22.4	10.3	1.37
26.7	10.5	1.90
26.7	10.6	1.91
29.2	10.4	2.11
29.2		2.14
31.4	10.5	2.17
31.8	10.1	2.21
35.9	9.7	2.22
35.9	9.8	2.16
35.9	10.2	2.13
38.2	9.7	1.98
38.2	10.2	2.04
38.3	10.3	2.18

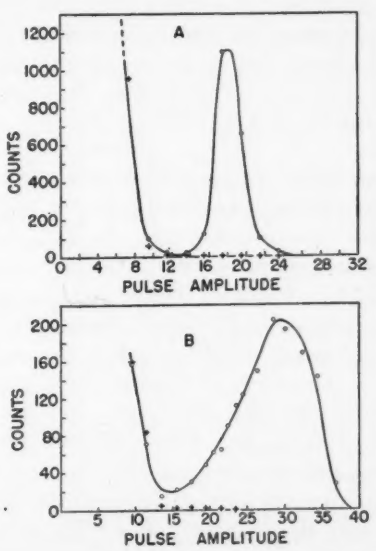

FIG. 2. Distribution of pulses from proportional counter due to He^3 particles. Curve A is for He^3 particles which make an angle of 16.5 degrees with the deuteron beam. Curve B is for He^3 particles which make an angle of 38.2 degrees with the deuteron beam. The crosses represent the background obtained by stopping the He^3 particles before they reach the counter.

FIG. 3. Differential cross section of D(d,n)He³ reaction in center of mass system.

energy of the beam was measured by means of magnetic deflection.

Figures 2A and 2B give typical distribution of pulses from the proportional counter as obtained during data runs. By comparison of the pulse amplitudes with pulses from plutonium alphas, one determines that the peaks are due to doubly charged particles. That the peaks are due to He³ particles from the reaction D+D→He³+n +3.3 Mev[26] is demonstrated by the amount of absorber, between the counter and the target, required to obtain maximum peak height and best resolution from background. The air equivalent of the absorbers plus the mica windows and gas in the target and counter corresponded to the expected range of the He³ particles.

For laboratory angles from 16.5 degrees to 32.0 degrees, the low energy tail of the distribution is of the order of one percent of the maximum peak as in Fig. 2A. Near 40 degrees to the beam, where the range of the He³ particles approaches the air equivalent of the mica windows, the resolution of the peak is not as complete (Fig. 2B). For all the curves used to obtain the data in this report the low energy tail was less than 12 percent of the peak.

The curves similar to Fig. 2A provide information on the possibility of excited states of the He³ nucleus. The width of the minimum between the peak and background sets a limit to the energy region in which no secondary He³ peak exists (at least to one part in forty compared to the main He³ peak). From the energy of the main He³ group which is lost in the counter, one can calculate the energy of a group which would fall in the minimum between the peak and background. Table I gives a summary of the results of this analysis. Columns one and two give, respectively, the laboratory angle and the energy of the He³ particles in the main peak. Column three gives the energy region corresponding to the minimum in which peaks could be detected if they were present. Column four gives the limits of the excitation levels of the He³ nucleus which would be required to give groups in the energy region tabulated in column three. Since these groups were not found, the interpretation of Table I is: at the angles listed there are not energy levels, detectable by this method, above the ground state of the He³ nucleus between the limits listed in column four.

The total number of counts in the He³ peak per coulomb of beam current (corrected for background as mentioned above), together with geometrical factors, and the pressure and temperature of the gas in the target, allows one to calculate the differential cross section of the D(d,n)He³ reaction at the various angles at which data were taken. Table II gives a summary of the results. Column one gives the angle defined by the slit system between the He³ particles and the deuteron beam. The maximum angular spread defined by the slits and counter window is ±1.1 degrees for angles near 40 degrees and is ±1.3 degrees for angles near 20 degrees. The effective angular spread of the deuteron beam including Rutherford scattering of the deuterons in the front window of the target is ±0.8 degree. Rutherford scattering of the He³ particles by the mica windows in the side port adds to the angular spread. This scattering was calculated for the foils and energies involved. Near 20 degrees only about three percent of the He³ particles were scattered between one and two degrees by the mica. Because the energy of the He³ particles is less near 40 degrees, about nine percent are scattered between one and two degrees in this angular region. Such scattering introduces a negligible error in the differential cross section, providing the cross section does not vary rapidly over angular intervals of about two degrees. This follows from the fact that, under the above conditions, as many particles are scattered into the counter as are scattered out of it.

Column two of Table II records the deuteron beam energy as measured directly after data and background runs as described above. While the accuracy of this measurement is about two percent, relative measurements are good to about one percent so that an appreciable part of the variation of the energy (given in column two) is real. This variation has been correlated with changes in the cyclotron such as oscillator frequency, etc.

The measured differential cross section for production of He³ by the D(d,n)He³ reaction is given in column three. This is the cross section per unit solid angle, in units of 10^{-26} cm². Since no two measurements at the same angle were taken on the same day, the data appear to be very reproducible under different conditions. The statistical error expected from the number of counts in each run is about one percent or less. For most of the runs the error involved in estimating the background is less than one percent, although for the runs near 38 degrees the error may be as large as three percent. The error in the geometrical factor (including the error in measurement of the angle to the beam) is about two percent. The Faraday cage measurement of the deuteron current is possibly in error by two percent. The

[26] H. V. Argo, Phys. Rev. 74, 1293 (1948).

check of the beam current discussed in Section II agrees to about this accuracy when the error of the energy measurement is taken into consideration. Treating the errors as random, the estimated accumulated standard error in the figures in column three is about four percent over most of the range. Near 40 degrees these errors may be about six percent. The differential cross section as measured is the average value over an angular region of about ± two degrees in the laboratory system. Thus, if this differential cross section varies rapidly over an angular region of this size the variation will not be resolved.

IV. NEUTRONS AT ZERO DEGREES

The differential cross section of the $D(d,n)He^3$ reaction, for the case in which the neutron emerges at zero degrees to the direction of the deuteron beam, was measured by allowing the neutrons to irradiate copper foils, and by means of Geiger counters, determining the number of copper atoms so activated. The deuteron beam was monitored by counting He^3 particles with the proportional counter. The copper activity has a half-life of ten minutes and is produced by the reaction $Cu^{63}(n,2n)Cu^{62}$. Two separate runs were made with deuterium in the target and one run with hydrogen. The latter run was made to correct for background neutron flux which was found to be about 14 percent at zero degrees.

The Cu^{62} activity has been produced elsewhere in this laboratory by a known flux of 14-Mev neutrons[27] and with the cyclotron by a known flux of neutrons from the threshold to 12.6 Mev.[28] Combining this information it is possible to estimate the activation cross section for 13.3-Mev neutrons (obtained with the present set-up) and hence arrive at an estimate of the flux of the D−D neutrons at zero degrees. This involved an intercalibration of the various Geiger counters used in the different measurements. This calibration was carried out by using a standard thermal neutron flux to produce five-minute Cu^{66} by the $Cu^{65}(n,\gamma)Cu^{66}$ reaction, with activity was counted on the various Geiger counters. The beta-ray from the Cu^{66} has about the same energy as the beta-ray from Cu^{62} (2.6 Mev).[29]

Using this method of detecting neutron flux, one obtains an estimate for the $D(d,n)He^3$ cross section at zero degrees. This value is not very accurate, mainly because of the unreliability of the estimate of the activation cross section of the Cu^{63} at 13.3 Mev, which may be in error by 30 percent. The result, translated into differential cross section, is plotted in Fig. 3.

[27] R. W. Davis and D. D. Phillips (private communication).
[28] J. L. Fowler and J. M. Slye, Phys. Rev. **76**, 169 (1949).
[29] J. Mattauch, *Nuclear Physics Tables* (Interscience Publishers, Inc., New York).

V. CONCLUSIONS

The data given in Table II have been plotted as a function of beam energy and from this family of curves the cross sections for 10.3-Mev beam energy obtained. These values of the differential cross section (corrected for the intensity per unit solid angle in the laboratory system compared to the intensity per unit solid angle in the center of mass system) have been plotted in Fig. 3 as a function of angle in the center of mass system. The measurements, when translated to the center of mass angles, extend from 39.3 degrees to 95.0 degrees. Below 39.3 degrees the dotted curve indicates a rough extrapolation on the basis of neutron measurements using the $Cu^{63}(n,2n)Cu^{62}$ threshold detector as explained in Section IV. The symmetry of the reaction in the center of mass system makes the curve in Fig. 3 symmetrical about 90 degrees. The data in Fig. 3, the differential cross section as a function of angle in the center of mass system, has been analyzed, by least squares, in terms of normalized Legendre polynomials of even order. The result is:

$$\sigma = 7.13P_0 + 3.29P_2 + 4.22P_4 + 1.83P_6 + 0.18P_8$$

in millibarns. The last term is about equal to the estimated uncertainty in the data.

Preliminary measurements made over a somewhat limited angular region and with much less precision[21] gave values of the differential cross section of 3.5×10^{-27} cm^2 in rough agreement with the results of Fig. 3 for angles near 90 degrees in the center of mass system. These measurements, however, did not extend over a large enough angular region nor were they precise enough to detect the minimum which shows up in Fig. 3 nor the maximum at zero degrees (center of mass system). This minimum in the differential cross-section curve begins to appear at bombarding energies of 2.5 Mev and is very pronounced at 3.5 Mev.[18] The total cross section obtained by integrating the curve of Fig. 3 over the entire solid angle is 0.07×10^{-24} cm^2. The steep rise in the cross section below 40 degrees makes the total cross section somewhat higher than the value reported earlier (0.04×10^{-24} cm^2)[21] which was obtained from differential cross section measured in the more or less flat region of the curve near 90 degrees. The value of 0.07×10^{-24} cm^2 fits the cross section *versus* energy curve extrapolated from measurements which extend to 3.5 Mev.[18]

We wish to acknowledge the assistance of members of the cyclotron group at Los Alamos who helped run the cyclotron while the data for this experiment were being taken. We wish to thank Dr. J. H. Williams for his aid in installing the palladium leak, and for several helpful suggestions relative to this problem.

Investigation of Nuclear Energy Levels in Lead

H. H. BARSCHALL, C. K. BOCKELMAN, R. E. PETERSON, AND R. K. ADAIR
University of Wisconsin, Madison, Wisconsin

(Received July 12, 1949)

The total neutron cross section of lead was measured from 20 kev to 750 kev with an energy spread of 10 kev. Maxima were observed at 350, 525, and 720 kev, each maximum being preceded by a minimum. In the region surrounding these anomalies, measurements were carried out with a resolution of about 5 kev. An attempt was made to interpret the maxima as due to resonances corresponding to isolated levels in the compound nucleus Pb^{209}. No energy levels were resolved when similar measurements were carried out for bismuth.

INTRODUCTION

A PREVIOUS investigation[1] indicated that the total cross section of lead for fast neutrons did not vary smoothly with energy when measured with neutrons of about 70-kev energy spread. For an element as heavy as lead this observation was unexpected, and it appeared desirable to obtain more detailed information about this anomaly. In the present study the experiment was repeated with better energy resolution.

There is experimental evidence that the density of nuclear energy levels is smaller in lead than in other heavy elements. Lead does not show resonances for slow neutrons,[2] and furthermore it has a very small absorption cross section[3] and a relatively small cross section for inelastic scattering at intermediate energies.[4] The only other heavy element for which similar neutron properties have been observed is bismuth. For this reason bismuth was investigated in the same manner as lead.

EXPERIMENTAL

Total neutron cross sections were measured by simple transmission experiments as described previously.[5] A counter filled with enriched BF_3 and surrounded by paraffin served as neutron detector. As in the earlier work, monoenergetic neutrons of variable energy were produced by the Li(p,n) reaction. The spread in energy of these neutrons depends on three factors; the spread in energy of the incident protons, the thickness of the Li target, and the angle subtended by the detector at the target. The maximum energy spread introduced by this last effect can be calculated from the conservation laws, although the details of the effective energy distribution depend on the variation of the sensitivity of the detector over the detector surface, which was not known. In the geometry used, the maximum energy spread because of angle amounts to ± 1.5 kev at 120 kev and increases to ± 3 kev at 1 Mev for measurements in the forward direction with respect to the incident protons.

Previously, the whole proton beam emerging from the electrostatic generator had been used to bombard the Li target. The energy of these protons was measured and regulated by passing the diatomic hydrogen beam through a small electrostatic analyzer and using a signal from the exit slit of the analyzer to adjust the generator voltage. This method had the disadvantage that the energy spread of the protons could only be estimated and that, for a given voltage on the analyzer, variations in energy occurred which were presumably produced by changes in the geometry of the analyzer because of temperature changes caused by the beam.

In order to obtain higher resolution and more reproducible energy settings, the large electrostatic analyzer described by Warren, Powell, and Herb[6] was used in the present experiments. By appropriate settings of the slit system of this analyzer, a portion of the proton beam of well-defined energy spread could be selected, and the energy of the protons could be accurately determined. For controlling the energy of the generator, the following procedure was used. A signal produced by the magnetically analyzed proton beam was taken off the entrance slit of the analyzer. This signal served to adjust and stabilize the voltage of the generator. The magnetic field was varied until the proton beam passed through the electrostatic analyzer, the generator voltage following the changes of the magnetic field automatically. This method requires short time stability of the magnetic field, but the energy of the proton beam emerging from the electrostatic analyzer is determined solely by the voltage across the analyzer.

For measuring the thickness of the Li target, the method described by Taschek and Hemmendinger[7] was used. The rise of the forward yield of neutrons near threshold is observed as a function of proton energy. The width of the rise depends on the target thickness and the proton energy spread. For the purpose of estimating the neutron energy spread, only the resulting

[1] Bockelman, Peterson, Adair, and Barschall, Phys. Rev. **76**, 277 (1949).
[2] Havens, Rabi, and Rainwater, Phys. Rev. **72**, 634 (1947).
[3] Hughes, Spatz, and Goldstein, Phys. Rev. **75**, 1781 (1949). See also reference 2.
[4] Barschall, Battat, Bright, Graves, Jorgensen, and Manley, Phys. Rev. **72**, 881 (1947).
[5] Adair, Barschall, Bockelman, and Sala, Phys. Rev. **75**, 1124 (1949).
[6] Warren, Powell, and Herb, Rev. Sci. Inst. **18**, 559 (1947).
[7] R. F. Taschek and A. Hemmendinger, Phys. Rev. **74**, 373 (1948).

effect of both these factors needs to be known. By reducing the slit widths of the analyzer and thereby reducing the energy spread of the protons to less than the stopping power of the target, it was possible, however, to measure the energy spread introduced by the target thickness alone.

In the present work, experiments with two different neutron energy spreads were carried out. They will be referred to as being performed with 5-kev and 10-kev resolution, respectively. For the measurements with 5-kev resolution, the slits of the electrostatic analyzer were set to give a proton energy spread of 0.1 percent, while for 10-kev resolution a proton energy spread of 0.2 percent was used. With these slit settings, maximum proton beam currents of 1 and 2.5 microamperes, respectively, were obtained on the target.

A typical measurement of the variation of forward neutron yield with proton energy near threshold is shown in Fig. 1. The difference in proton energy between the threshold for neutron production and the first peak in the yield curve is 4 kev, which may be taken as a measure of the neutron energy spread introduced by the proton beam and the target, since the neutron and proton energy spreads are approximately the same. The actual energy spread may be slightly larger than 4 kev because the sensitivity of the counter used for the detection of the neutrons increased with decreasing neutron energy. Measurements taken with this target will be referred to as having an energy resolution of 5 kev. It was found that, after a day's bombardment, the yield curve rose to the maximum in the same energy interval, but the yield fell off more slowly beyond the maximum. This effect may be caused by non-uniformity of target thickness produced by the beam. Rise curves were taken about twice a day. Whenever a flattening of the maximum was observed, the beam was shifted to another portion of the target.

In principle, it is possible to improve the energy resolution considerably over that used in the present experiments, the only limitation being the Doppler spread which amounts to about ± 200 ev. In practice, the neutron intensity decreases so rapidly as the resolution is improved that measurements with less than 5 kev neutron energy spread appeared to be too time-consuming at present. Furthermore, background difficulties would have decreased the accuracy of the results if the detector were moved farther from the target in order to reduce the neutron energy variation with angle.

MEASUREMENTS ON LEAD

Figure 2 shows the total cross section of lead as a function of neutron energy, taken with a neutron energy spread of about 10 kev. The points represent averages of several runs; their vertical height is a measure of the statistical uncertainty. Sample thicknesses were chosen to give a transmission of about 60 percent at all energies. Corrections for background and scattering into the detector were applied to the cross section. The latter correction amounts to 3 percent assuming isotropic scattering of the neutrons by lead.

In Fig. 2 maxima appear at neutron energies of 350 kev, 525 kev, and 720 kev. The first two maxima are preceded by strong minima; a weak minimum is indicated in front of the third peak. Below 200 kev the cross section shows a rapid rise with decreasing neutron energy, possibly caused by the presence of some unresolved peaks at lower energy.

Using a resolution of 5 kev the three observed peaks were investigated in more detail. The results are shown in Figs. 3–5. In all cases the maxima become higher and the minima lower as the neutron energy spread is decreased.

As mentioned before, the correction for scattering into the detector was applied under the assumption of elastic and isotropic scattering. This assumption is undoubtedly not valid and will introduce some error into the measurements. The cross section for inelastic scattering of neutrons in the energy range under investigation by lead is presumably small.[4] An attempt was made to study this effect by placing some boron carbide in front of the detector at the energy of the minimum at 500 kev. No change of the measured transmission was observed. The effect of anisotropic scattering, however, may be appreciable. Anisotropic scattering will be caused by diffraction scattering and by resonance scattering of neutrons of more than zero units of angular momentum. According to calculations by Professor S. Fluegge, diffraction scattering will increase the correction for scattering into the detector

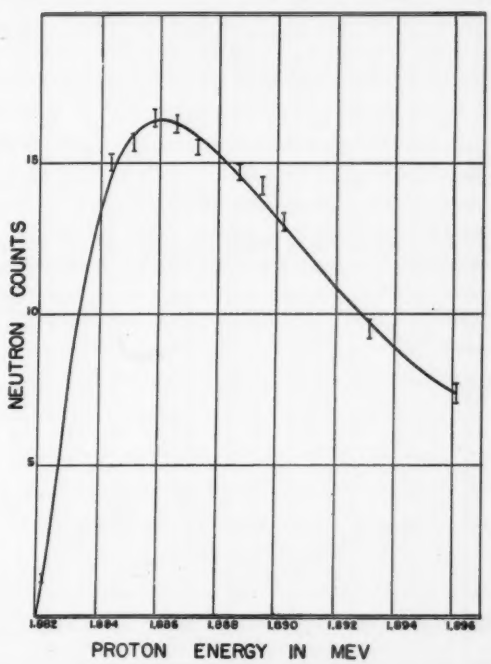

FIG. 1. Forward neutron yield near threshold of Li(p,n) reaction. The energy interval between the threshold for neutron production and the peak is a measure of the neutron energy spread caused by target thickness and energy spread of the incident protons.

by a factor of 3.5 at 500 kev. This means that the cross section should be raised by 7 percent.

Another uncertainty is caused by the hardening of the neutrons in the case of measurements near a sharp peak.

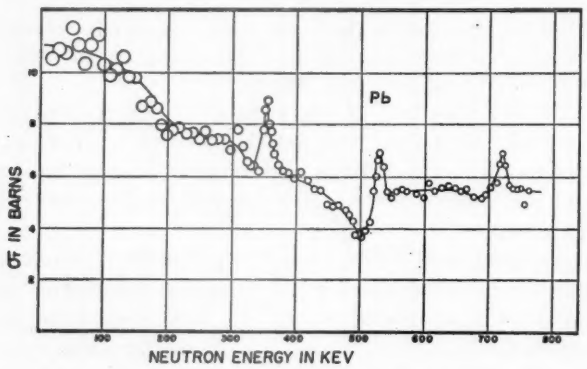

FIG. 2. Total cross section of lead as a function of neutron energy measured with a resolution of 10 kev.

MEASUREMENTS ON BISMUTH

Measurements of the total cross section of bismuth have previously been carried out with a resolution of 20 kev.[8] In view of the results found for lead, the measurements on bismuth were repeated with better resolution and better statistical accuracy. The results obtained with a neutron energy spread of 10 kev are shown in Fig. 6. No evidence for maxima was obtained, indicating that in the energy range up to 500 kev there are no levels wider than 3 kev.

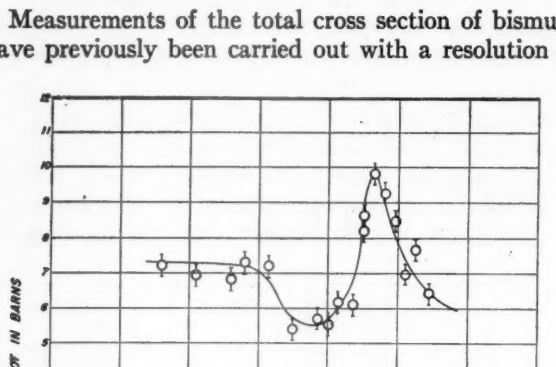

FIG. 3. Total cross section of lead in the neighborhood of the 350-kev resonance investigated with a resolution of about 5 kev.

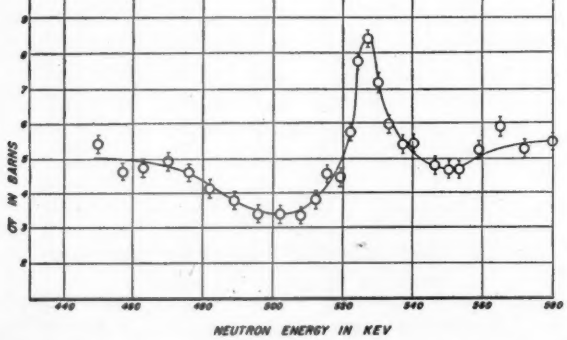

FIG. 4. Total cross section of lead in the neighborhood of the 525-kev resonance investigated with a resolution of about 5 kev.

DISCUSSION

Common lead consists of four isotopes which have approximately the following abundances: Pb^{204} 1 percent, Pb^{206} 24 percent, Pb^{207} 23 percent, and Pb^{208} 52 percent. In the present experiments, only the three more abundant isotopes could produce measurable effects. Relatively wide separations of nuclear energy levels are most likely to be found in observations of the interaction of neutrons with Pb^{208}. According to Wapstra,[9] the binding energy of an additional neutron to Pb^{208} is only 3.7 Mev compared to about twice this number for the other lead isotopes and for most other heavy nuclei. A low binding energy for Pb^{208} may be expected on the basis of the idea of the existence of closed shells in nuclei,[10] since 82 protons and 126 neutrons are believed to form closed shells. According to most theories, the level density in heavy nuclei will increase rapidly with increasing excitation energy. Consequently, the low excitation energy of the compound nucleus Pb^{209} should result in a relatively wide spacing of levels.

Assuming that the observed maxima are due to isolated resonances in the compound nucleus Pb^{209}, it is possible to make statements regarding the angular momenta involved. For the 350-kev resonance the measured difference in cross section between the maximum and the minimum is somewhat greater than 4 barns. A difference of this magnitude would be expected if the compound nucleus has an angular momentum of

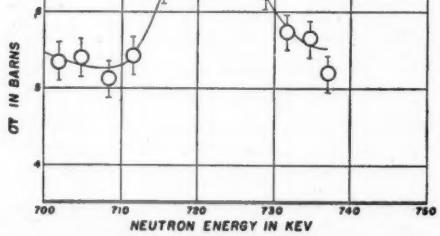

FIG. 5. Total cross section of lead in the neighborhood of the 720-kev resonance investigated with a resolution of about 5 kev.

[8] Barschall, Bockelman, and Seagondollar, Phys. Rev. **73**, 659 (1948).

[9] A. H. Wapstra, Nature **161**, 529 (1948). L. Rosenfeld, *Nuclear Forces* (Interscience Publishers, New York, 1949), p. 525.

[10] M. G. Mayer, Phys. Rev. **74**, 235 (1948).

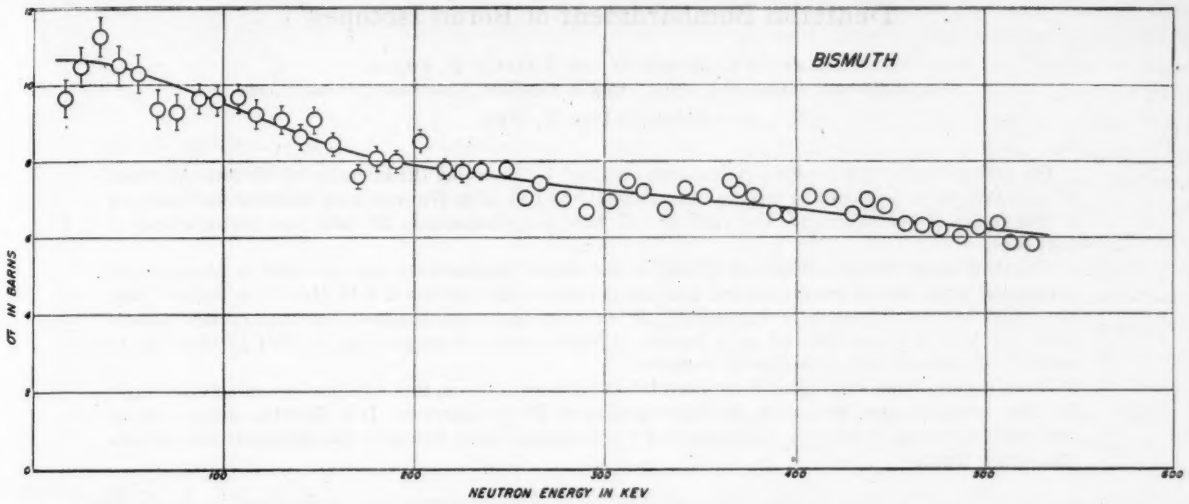

FIG. 6. Total cross section of bismuth as a function of neutron energy measured with a neutron energy spread of 10 kev.

$\frac{1}{2}\hbar$, provided that Pb^{208} has zero spin.[11] Such a compound nucleus may be formed by neutrons of either 0 or 1 unit of angular momentum. Since at this energy about 80 percent of the potential scattering should be *s*-scattering, the presence of the strong minimum, which is presumably due to destructive interference between resonance and potential scattering, indicates that the resonance is caused by *s*-neutrons.

At the 525-kev resonance the difference between maximum and minimum is 5 barns. To account for this it is necessary to assume that the compound nucleus has $\frac{3}{2}$ units of angular momentum, and must therefore be formed by either *p*- or *d*-neutrons. The magnitude of the minimum again points toward neutrons of small angular momentum. Even if one attributes the resonance to *p*-neutrons, it seems, however, difficult to understand that the cross section could reach as low a value as it does at 500 kev.

The resonance at 720 kev has an amplitude corresponding to the formation of a compound nucleus of half a unit of angular momentum and should therefore be produced by *s*- or *p*-neutrons. For *s*-neutrons of this energy one should expect a pronounced minimum and a small maximum. Since the observations indicate the opposite behavior, it is believed that the resonance is most likely caused by *p*-neutrons.

The assignment of the observed maxima to the most abundant lead isotope appears reasonable also from the preceding discussion. If either Pb^{206} or Pb^{207} were the target nuclei involved, it would be necessary to assign the resonances to neutrons of higher angular momenta, which, however, is incompatible with the observed interference effects.

All these arguments presupposed that all the lead isotopes have roughly the same neutron cross section. It is further assumed that the resonances are completely resolved. While all the peaks appear to be wider than the expected neutron energy spread of 5 kev, there is no direct evidence that this was the actual effective resolution. For the first two resonances which appear experimentally sharpest, an increase of the height of the peaks would make it more difficult to fit the measurements to the theoretically predicted behavior.

The authors wish to thank Mr. R. L. Henkel for his assistance in these experiments.

The work was supported in part by the Wisconsin Alumni Research Foundation and in part by the AEC.

[11] H. Kopfermann, Zeits. f. Physik 75, 363 (1932).

Deuteron Bombardment of Boron Isotopes*†

EMMETT L. HUDSPETH AND CHARLES P. SWANN
Bartol Research Foundation of the Franklin Institute, Swarthmore, Pennsylvania

(Received June 27, 1949)

The excitation of curve for $B^{11}(d,p)$ has been obtained by observing the intensity of the beta-rays from B^{12} as a function of bombarding voltage from about 0.3 to 1.85 Mev. No resonance structure was observed in this region of bombardment. The yield at 1.47 Mev is approximately 10^7 beta-rays/microcoulomb of deuterons.

The short-range protons which are formed in the above reaction were also observed in photographic plates, and range measurements showed that the Q-value of the reaction is 0.15 Mev. It is believed that this value does not represent the formation of B^{12} in its ground state, however, but in an excited state at about 1.1 Mev. A group believed to be protons of higher energy (corresponding to $Q=1.25$ Mev) but of much lower intensity was subsequently observed.

It was shown, by bombardment of enriched B^{10} and of normal boron, that a gamma-ray of approximately 1.1 Mev energy is associated with the disintegration of B^{11} by deuterons. It is therefore almost certain that this gamma-ray arises from the decay of B^{12} to its ground state. Intensity measurements also indicate that this is the case.

I. INTRODUCTION

THE bombardment of boron by deuterons leads to the following reactions:

$$B^{10}+H^2\rightarrow B^{11}+H^1+Q_1, \quad (1)$$

$$B^{10}+H^2\rightarrow C^{11}+n^1+Q_2, \quad (2)$$

$$B^{11}+H^2\rightarrow B^{12}+H^1+Q_3, \quad (3)$$

$$B^{11}+H^2\rightarrow C^{12}+n^1+Q_4, \quad (4)$$

$$\text{or}\rightarrow 3He^4+n^1+Q_5. \quad (5)$$

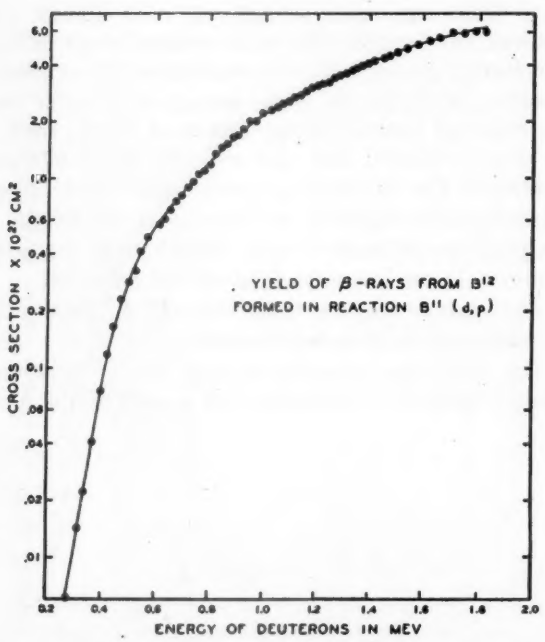

FIG. 1. Yield of beta-rays from boron target under deuteron bombardment. Coincidence counters recorded all beta-rays of energy greater than approximately 2.5 Mev.

The $B(d,\alpha)$ reactions also occur and have been previously studied. Several proton groups have been observed[1,2] from reaction (1). The neutrons emitted in reactions (2), (4), and (5) have been observed[3,4] by both cloud chamber and photographic plates. It has not been possible to correlate all of the observed neutron groups with the disintegration of a specific isotope, although some assignments can be made from calculated limits of the Q-values. The protons from reaction (3) have not heretofore been observed; the reaction has been inferred through observation of beta-rays emitted in the disintegration of B^{12}. The precise mode of decay of B^{12} has not been established in detail, although the end-point of the beta-spectrum has been the subject of numerous investigations.[5–7] Finally, the energies of the gamma-rays which are produced by deuteron bombardment of normal boron have been measured,[8,9] and the origin of all but the gamma-ray of lowest energy (~1.5 Mev) can be deduced.

The reactions which lead to the production of charged particles have been observed[10] by bombarding separated isotopes of boron and the assignment of reactions, except for $B^{11}(d,p)$, has been definitely confirmed.

The purpose of the present investigation was to study the excitation function for reaction (3), and to establish the value of Q_3 by direct observation of the protons; to determine whether the reported ~1.5 Mev gamma-ray is associated with this reaction; and to obtain more information about the decay scheme of B^{12}.

* Assisted by the Joint Program of the ONR and AEC.

† A preliminary account of some of this work has already appeared: E. L. Hudspeth and C. P. Swann, Phys. Rev. 74, 1722 (1948).

[1] J. D. Cockcroft and W. B. Lewis, Proc. Roy. Soc. 154, 246 (1936).
[2] Pollard, Davidson, and Schultz, Phys. Rev. 57, 1117 (1939).
[3] T. W. Bonner and W. M. Brubaker, Phys. Rev. 50, 308 (1936).
[4] C. F. Powell, Proc. Roy. Soc. 181, 344 (1942).
[5] D. S. Bayley and H. R. Crane, Phys. Rev. 52, 604 (1937).
[6] Frank L. Hereford, Phys. Rev. 74, 574 (1948).
[7] Hornyak, Dougherty, and Lauritsen, Phys. Rev. 74, 1727 (1948).
[8] Gaerttner, Fowler, and Lauritsen, Phys. Rev. 55, 27 (1939).
[9] J. Halpern and H. R. Crane, Phys. Rev. 55, 415 (1939).
[10] C. L. Smith and E. B. M. Murrell, Proc. Camb. Phil. Soc. 35, 298 (1939).

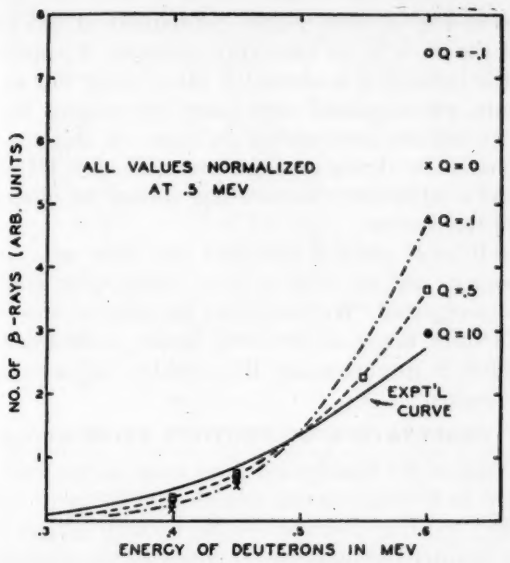

FIG. 2. Family of curves showing attempt to fit the theoretical formula to the observed excitation curve for $B^{11}(d,p)$ up to 0.6-Mev bombarding energy.

II. THE EXCITATION CURVE FOR $B^{11}(d,p)$

The bombardment of boron with deuterons leads to the formation of a radioactive isotope which decays with the emission of beta-rays of maximum energy 13.43 Mev[7] and with a half-life of 0.02 seconds. The endpoint of the beta-ray spectrum has been examined carefully by several investigators, one of whom[6] worked with the apparatus in this laboratory. The excitation function has already been observed[5] in the region up to about 0.6 Mev, and it was our purpose to carry this to higher voltage.

Thin targets of elemental boron and of boron trioxide were used in most of this work; these were made by evaporation of the compound in a vacuum. Thickness of the targets was determined by weighing them on a microbalance; a typical thickness was about 25 kev. The beta-rays were detected by coincidence counters. Before producing coincidences, the beta-rays penetrated the target backing, the first counter, and the wall and cylinder of the second counter. This added to a total of 1.3 g/cm^2, which is sufficient to stop all beta-rays whose energy is below about 2.5 Mev.

The excitation curve which we obtained is shown as Fig. 1. The cross section which is plotted is the cross section for the production of beta-rays of energy greater than 2.5 Mev; beta-rays of lesser energy were absorbed before reaching the second counter. Rough checks with a single counter showed that only a relatively small fraction of the beta-rays had energy less than this amount, as one would expect from the shape of the beta-ray spectrum. The excitation curve displays no resonance characteristics, but only a rather rapid rise in yield with increase in bombarding voltage. This is in contrast to $Li^7(d,p)$ which leads to the radioactive nucleus Li^8; three resonances in this reaction have been observed[11] up to a bombarding voltage of 1.4 Mev. (These resonances were also observed in the course of the present work; this was done simply as a check on our operation.) The excitation energy of the intermediate C^{13} nucleus as formed by $B^{11}(d,-)$ is, over the range of bombardment which we employed, between 18.7 and about 20.5 Mev. The excitation level of Be^9 as formed by $Li^7(d,-)$ is, for zero bombarding energy, at 16.66 Mev, and the three resonance levels found just above this value are only about 0.3 Mev apart. Since C^{13} is a heavier nucleus and since it is formed in a higher state of excitation, it seems likely that any resonance structure would not be resolved in our experiments. Indeed, the states are apparently so close together that we observe only a smooth increase in yield of B^{12} with bombarding voltage, although we believe that maxima separated by as little as about 15 kev could have been located. The work of Fünfer[12] has indicated 22 excitation levels in the region between 12.7 and 16.7 Mev, the higher ones being only about 120 kev apart, so that our failure to observe any resonance structure is not surprising. The excitation curve is flattening rather rapidly in the vicinity of our maximum bombarding voltage.

It was thought that we could, by following the procedure of Rumbaugh, Roberts, and Hafstad[13] for

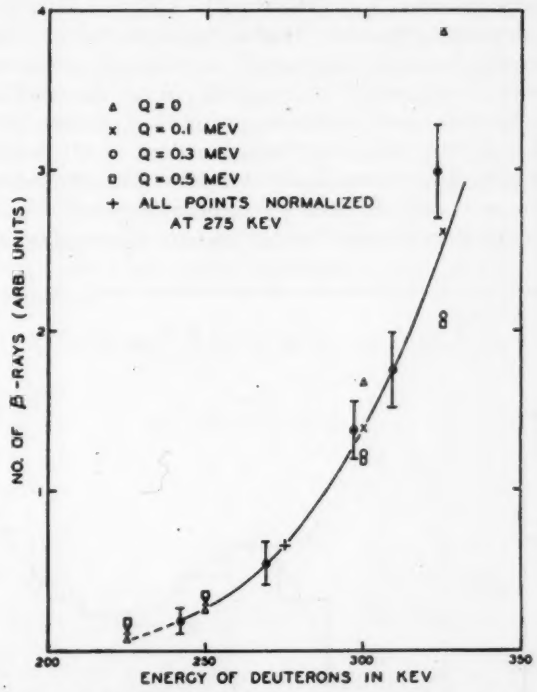

FIG. 3. The $B^{11}(d,p)$ excitation curve in the very low energy region. Over this restricted interval, the formula gives the best fit for Q=0.1 Mev, although no "good fit" is obtained.

[11] Bennett, Bonner, Richards, and Watt, Phys. Rev. **71**, 11 (1947).
[12] E. Fünfer, Ann. d. Physik **35**, 147 (1939).
[13] Rumbaugh, Roberts, and Hafstad, Phys. Rev. **54**, 657 (1938).

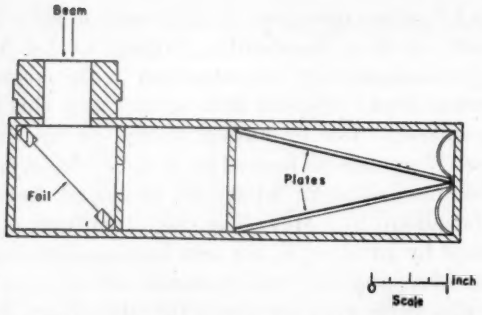

FIG. 4. Diagram of the camera employed for the detection of scattered particles and particles of transmutation. This was used for detection of the short-range protons from the reaction $B^{11}(d,p)$.

the case of Li^8 formation, deduce a Q-value for the $B^{11}(d,p)$ reaction by the shape of the excitation curve. In our case, we have

$$E_p=(13/12)Q+(11/12)E_d,$$

where E_p is the energy of the emitted proton and E_d is the energy of the bombarding deuteron; energies are computed in the center of mass system. We assume also[13] that the cross section may be expressed[13,14] as

$$\sigma=Kv_d^{-1}\exp(-2\pi zZ\alpha cv_d^{-1})\exp(-2\pi zZ\alpha cv_p^{-1}), \quad (6)$$

where K is a constant, v_d and v_p are relative velocities for the deuteron and proton, z and Z are the nuclear charges involved, c is the velocity of light and α the fine-structure constant. Over a region of many close levels this formula might apply with enough precision to yield the value of Q (or, explicitly, of v_p). An attempt was therefore made, as shown in Fig. 2, to fit our data to Eq. (6) by assuming various values of Q; points were arbitrarily normalized at 0.5 Mev. This procedure led to no "good fit," and we accordingly sought to fit the data over a more limited region. The results are shown in Fig. 3, with points normalized at 275 kev. While the fit is in no case very accurate, it appeared that the value of Q is about 0.1 Mev. Using this as an estimate, we calculated what range the protons would have at various bombarding voltages; in this way it was possible to devise an experiment (Section III) and to select a satisfactory bombarding voltage for observation of the protons.

The $B^{11}(d,p)$ reaction has often been used as a beta-ray source, and the yield at low bombarding voltage has been reported.[5] We found that the yield of beta-rays from a thick target of elemental boron, bombarded at 1.47 Mev, is approximately 10^7 particles/microcoulomb of deuterons.

III. OBSERVATION OF PROTONS FROM $B^{11}(d,p)$

In view of the anticipated short range of the protons emitted in $B^{11}(d,p)$, it was thought advisable to avoid an effort to bring them out of the vacuum system and into a counter through foils. It appeared that detection would be most straightforward by the use of photographic plates, and a small and simple "camera" was built. This is illustrated in Fig. 4.

The deuteron beam struck a thin target of elemental boron which was evaporated onto a very thin (150 $\mu g/cm^2$) aluminum leaf. The leaf was supported on a brass frame and was placed at 45° to the bombarding beam. Two Eastman NTB photographic plates, with emulsions 50μ thick, were placed at 90° to the bombarding beam and were set so that particles struck them at a grazing angle of about 10°.

Only a very brief exposure (a few microcoulombs of bombardment) was sufficient to get a satisfactory number of tracks on the plates. With a bombarding voltage of 1.67 Mev, two groups of particles, with mean range of 14.3 and 18.9 microns, were observed; the first group corresponds to the scattered deuterons and the

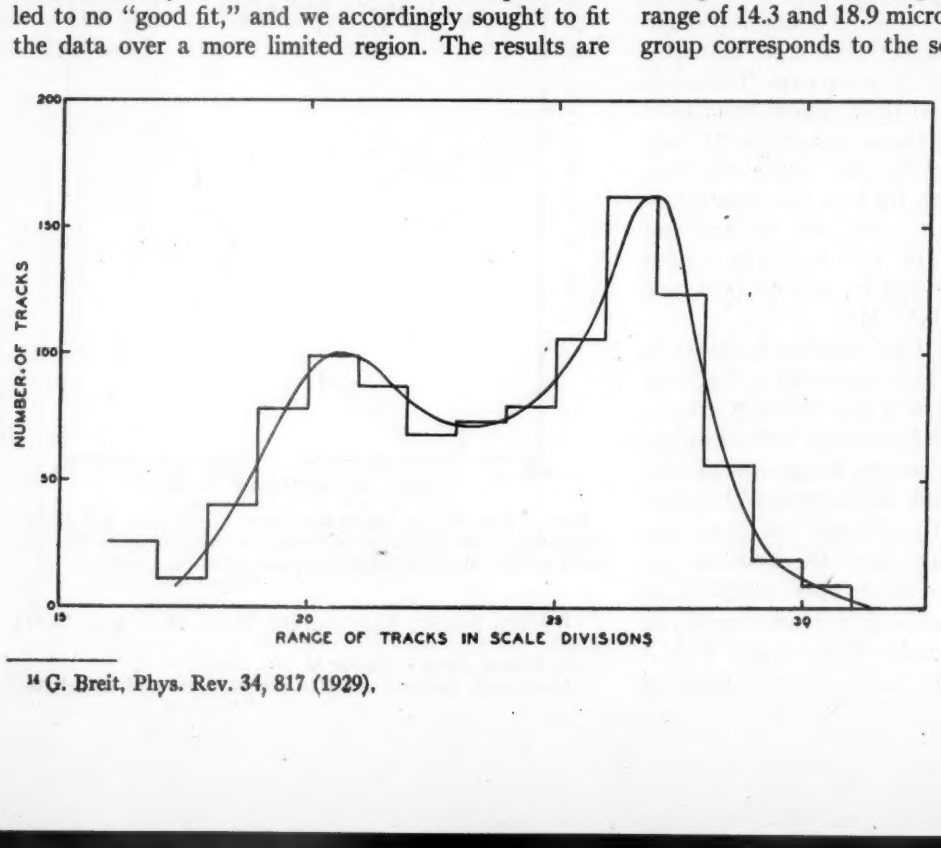

FIG. 5a. Spectrum of particles observed in photographic plate. Peaks at approximately 21 and 27 scale divisions (14.7 and 18.9 microns) represent scattered deuterons and protons from the reaction $B^{11}(d,p)$, respectively.

[14] G. Breit, Phys. Rev. 34, 817 (1929).

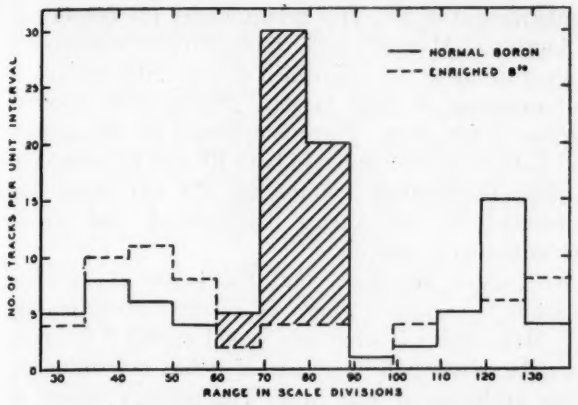

FIG. 5b. Spectrum of particles observed in the region between 30 and 130 scale divisions (21 to 91 microns). The shaded area represents a group which apparently arises from the bombardment of B^{11}; it is interpreted as a proton group associated with the formation of B^{12} in its ground state. This group is about 1/60 as intense as the group of range 27 scale divisions (Fig. 5a). (The range scale is distorted in this plot of equal energy intervals.)

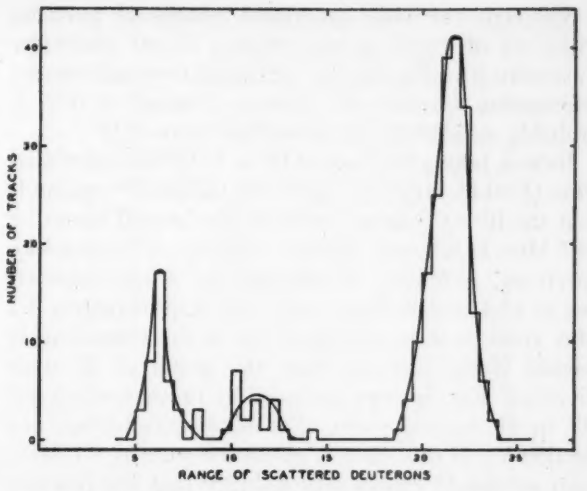

FIG. 6. Spectrum of the 1.68-Mev deuterons scattered from a thin aluminum foil. Secondary peaks are due to diatomic and triatomic beams which appeared when generator built up voltage after a spark.

second is ascribed to the protons from the reaction $B^{11}(d,p)$. The results of these observations are shown in Fig. 5a, where number of tracks per unit interval is plotted as a function of length of tracks in scale divisions of the eyepiece used in our microscope. The eyepiece was calibrated by use of a substage micrometer and it was found that 1 scale division is equal to 0.70 microns. The plot in Fig. 5a represents the results of three observers; each observer found two well-defined maxima, and most of the high-energy tail appeared in only one set of observations.

A control run was made by bombarding a plain aluminum foil, and the spectrum shown in Fig. 6 was obtained. The main peak at about 21.5 scale divisions (15.1 microns) represents the deuterons which have been elastically scattered through approximately 90° before falling on the photographic plate. The groups at 6.25 and 11.0 scale divisions represent the tracks produced by protons from diatomic and triatomic ions which were scattered in like manner; these ions were brought onto the aluminum target as the generator built up voltage after a spark. All of the groups may be used to determine something of the range-energy relation for particles of these low energies in the photographic emulsion. The maxima in Figs. 5a and 6 representing scattered deuterons do not correspond precisely in energy, but this is of course due to the fact that deuterons scattered by boron have, on the average, only about 78 percent as much energy as those scattered from aluminum. The slightly greater width of the groups in Fig. 5a is ascribed to the thickness of the boron film.

Following the bombardments of normal boron and of the aluminum foil, we obtained some enriched B^{10} (96 percent) from Oak Ridge. As a further check (to exclude the possibility that the protons we observed represented a strong group which might be produced by $B^{10}(d,p)$), we bombarded a target of the enriched B^{10}. The proton group observed in the bombardment of normal boron was not present.

It is known[10] that the reaction $B^{11}(d,\alpha)Be^{9}$ yields particles of 4.5 cm range, and these would lie close to the group which we observed at 27.0 scale divisions. That the latter group could not consist of α-particles, however, was proved by performing our observations at lower bombarding voltage. The resultant change in position of the group at 27.0 scale divisions showed that it could not be associated with $B^{11}(d,\alpha)$.

From the position of the longer range group in Fig. 5a, one may calculate the mass of B^{12} as it is produced in this reaction. A range of 27.0 scale divisions (18.9 microns) corresponds to a range in air of 3.76 cm, indicating a proton of energy 1.37 Mev. The mean energy of the impinging deuterons is taken as 1.6 Mev. Then, since

$$Q=(M/M_{B^{12}})E_{p^{90°}}-[(M_{B^{12}}-M_d)/M_{B^{12}}]E_d,$$

one has

$$Q=0.15 \text{ Mev}.$$

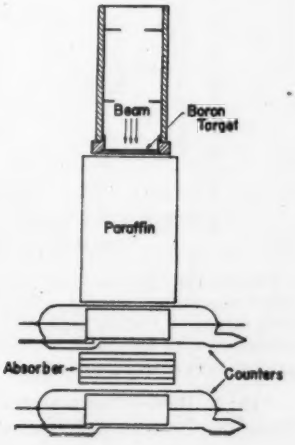

FIG. 7. Diagram of the arrangement used for coincidence absorption measurements. The paraffin was of sufficient thickness to absorb the beta-rays emitted in B^{12} decay.

Although the only prominent groups of particles which we observed on examination of our plates are those shown in Fig. 5a, we concluded from subsequent information (Section IV) that a Q-value of 0.15 is probably associated with an excited state of B^{12}.

Indeed, taking the mass of B^{12} as 12.01927 (calculated from $Q=0.15$ Mev) and of C^{12} as 12.00382,[15] one finds that the $B^{12}-C^{12}$ decay should evolve a total energy of 14.5 Mev. It is known that the end point of the beta-ray spectrum, accurately determined[7] by a spectrometer, lies at 13.43±0.06 Mev, and hence approximately 1.1 Mev remains to be accounted for in the transition. It seemed likely therefore that the group at 27 scale divisions (Fig. 5a) was produced by protons which left B^{12} in an excited state. (For other possibilities, see Section V.) If this state of excitation were at 1.1 Mev, then we should expect a probability that the reaction $B^{11}(d,p)$ may yield longer range protons than those at 27 scale divisions; the Q-value for this case should be 0.15 Mev+1.1 Mev, or 1.25 Mev.

With this possibility in mind, we re-examined our previously exposed plates in search of such a group. The results of this search are shown in Fig. 5b, where tracks of range between approximately 30 and 130 scale divisions are plotted. It is known that the production of alpha-particles from $B^{10}(d,\alpha)2\alpha$ gives rise to a continuous distribution of particles which tend to obscure any peaks produced by particles from the bombardment of normal boron, but it has been previously shown[10] that no particles of range greater than approximately 4.5 cm are formed in bombardment of B^{11} by deuterons of 0.55 Mev energy. It is apparent from Fig. 5b that a group of particles at approximately 77 scale divisions in range may be attributed to the bombardment of B^{11}. This group, under the conditions of Smith and Murrell's experiments,[10] could correspond to their group at 2.8 cm, which they ascribe to carbon contamination of their targets, although the specific reaction is not given. There is evidence for its appearance in their bombardment of both B^{10} and B^{11}, although at their bombarding voltage the 2.8 cm peaks are superposed on an intense background and hence interpretation is difficult.

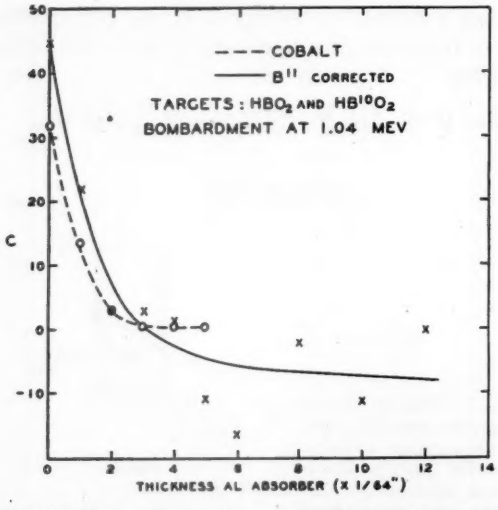

FIG. 8. The "B^{11} corrected" curve was obtained by subtracting (after normalization) the coincidence absorption curves obtained with targets of normal B_2O_3 and of $B_2{}^{10}O_3$. The resultant curve is compared with a coincidence absorption curve obtained from the gamma-rays emitted by Co^{60}.

[15] H. A. Bethe, *Elementary Nuclear Theory* (John Wiley and Sons, Inc., New York, 1947).

We believe, therefore, that the group at 77 scale divisions is a proton group of energy approximately 2.35 Mev, which is what one would expect if it arises from the reaction $B^{11}(d,p)$ and if it has a Q-value, as seems probable, of 1.25 Mev. The primary source of error in the 2.35 Mev measurement lies in our lack of an accurate range-energy relationship for these emulsions; this is probably not in error by more than 8 percent at this energy. The number of tracks in the group shown at 2.35 Mev is 50; in an equal area of the photographic plate, approximately 3000 tracks were found in the proton group of Fig. 5a. It therefore appears that the excited state of B^{12} at 1.1 Mev is formed approximately 60 times as often as the ground state (observation at 90°, bombarding voltage 1.67 Mev). More accurate data, preferably with highly enriched B^{11}, should be obtained to confirm these results.

We have made an attempt to estimate the total yield of short-range protons and to correlate this number with the emission of the beta-rays from B^{12}. The number of protons recorded on the photographic plate is considerably more than would be expected from the yield data previously obtained by the observation of the beta-rays with coincidence counters. This could be due to the fact that the protons observed at 90° do not represent the "average yield" as a function of angle, while the beta-rays are of course emitted isotropically. We hope to investigate this point in more detail.

IV. GAMMA-RAYS PRODUCED BY DEUTERON BOMBARDMENT

The gamma-rays which are emitted when boron is under bombardment by deuterons have been observed by Gaerttner, Fowler, and Lauritsen[8] and by Halpern and Crane.[9] The first group reports gamma-rays of 1.5, 2.2, 4.4, 6.9, and 9.1 Mev, while Halpern and Crane report 1.4, 2.4, 4.2, 6.0, and 9.1 Mev, in generally satisfactory confirmation. These gamma-rays may be accounted for directly by correlating them with known excited states of product nuclei, except in the case of the gamma-ray at about 1.5 Mev. It has been speculated[2, 8] that this gamma-ray is associated with the reaction $B^{11}(d,p)$, and that it is involved in the decay-scheme of B^{12}; it may be associated[2] also with transitions between two excited levels (5.8 to 4.4 Mev) in the B^{11} formed in $B^{10}(d,p)$. We thought it worth while to determine definitely whether it was associated in any case with the bombardment of the B^{11} rather than the

B^{10} isotope. Rough examinations were made of the "average absorption coefficient" in several absorbers of the radiation produced by bombardment of normal boron and of enriched (96 percent) B^{10}. Indications were that the low energy radiation was from the normal target. Interpretation of such data is always difficult, however, and we therefore shifted our attention to coincidence-absorption experiments.

The technique of measuring the range of the secondary electrons produced by gamma-radiation has been frequently used[16] and will not be described here. The arrangement of apparatus is shown in Fig. 7. About 3 in. of paraffin was placed between the target and the coincidence counters; this is sufficient to stop all of the beta-rays which are emitted by B^{12}. Observations of number of coincidences as a function of absorber thickness were made with targets of normal boron and of enriched (96 percent) B^{10}. Before we had obtained boron in elemental form, we also made observations with HBO_2 and oxides of titanium and zinc, data from the oxide targets being used to correct for effects from oxygen.

The range of secondaries produced by the gamma-rays of highest energy (9.1 Mev) would be a maximum of 1.9 cm (48/64 in.) in aluminum, and of course the other radiation would yield numerous secondaries of shorter range. By comparing the shapes of the curves obtained with normal and with enriched boron, however, we hoped that the source of the ~1.5 Mev radiation might be determined.

Figure 8 shows the result of a comparison of the coincidence absorption curves for the gamma-radiation emitted by normal and by enriched B^{10} under deuteron bombardment. The boron in each case was in the form of a thick target of HBO_2. A target of TiO_2 was bombarded also, and the "oxygen correction" was thus ascertained; the number of coincidences from oxygen was only about 10 percent (at 1.05 Mev deuteron energy) of the total number from $HB^{10}O_2$ at the smallest absorber values. After making the oxygen correction, it was found that, in the case of normal boron, the number of coincidences observed beyond about 10/64 in. Al absorber could be ascribed almost entirely to the B^{10}-content of normal boron. (This could not be strictly true, since part of the high energy-radiation is known to come from the bombardment of B^{11}. The number of coincidences produced by this radiation is negligible, however, compared with the total number of coincidences observed with small thicknesses of absorber.) Hence the data were "normalized" at 10/64 in. Al absorber. It was then possible to determine the value of "B^{11} corrected," which is plotted in Fig. 8. This rather indirect approach would have been unnecessary if we could have obtained highly enriched B^{11}, but only B^{10} was available in concentrated form. This particular method of obtaining the net effect of B^{11} explains why the ordinates associated with solid line of Fig. 8 could drop to negative values.

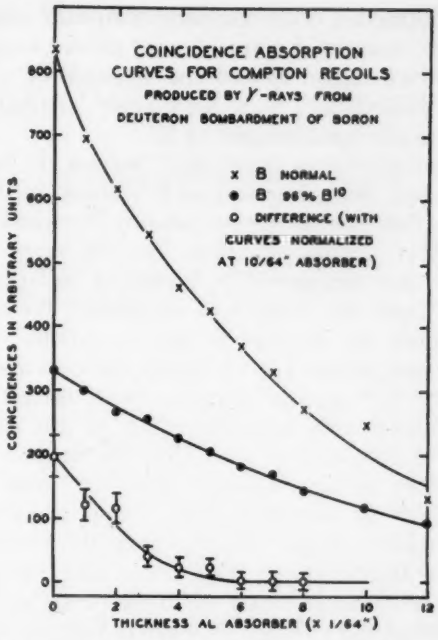

FIG. 9. Coincidence absorption curves obtained from gamma-rays produced by deuteron bombardment of normal boron and of enriched B^{10}, both in elemental form. The difference curve is also plotted, and again shows that a gamma-ray of energy ~1.3 Mev is associated with the bombardment of B^{11}.

It was concluded that a gamma-ray of ~1.5 Mev energy was emitted when B^{11} is bombarded by deuterons. In order to get a closer check on this value, we replaced our target by a source of Co^{60}; this isotope emits two gamma-rays of energies slightly over 1.1 and 1.3 Mev. The end point of the absorption curve for the secondary electrons produced by the 1.3 Mev radiation should lie between 4/64 in. and 5/64 in. Al absorber. It appears that the radiation attributed to B^{11} under deuteron bombardment is very close to this value. The relative position of the two curves, as shown in Fig. 8, is strongly dependent on the accuracy of the corrections applied in obtaining the "B^{11}-corrected" curve. The shapes of the two curves are very similar for the smallest values of absorber thickness, and the γ-rays from Co^{60} and from "B^{11}-corrected" are obviously of approximately the same energy. It is thought (see Section IV) that the energy of the γ-ray represented by the "B^{11}-corrected" curve should be 1.1 Mev.

After the completion of the work with HBO_2, we were supplied with enriched B^{10} (96 percent) in elemental form; this was prepared from the $CaF_2 \cdot BF_3$ complex by Dr. W. B. Keighton, who had previously prepared the HBO_2. This made it possible to repeat our observations without the background effect produced by the presence of oxygen. The results are shown graphically in Fig. 9. Complete absorption curves for the secondaries produced by deuteron bombardment of B^{10} and of normal boron are plotted, and a point-by-

[16] A general discussion may be found by Fowler, Lauritsen, and Lauritsen, Rev. Mod. Phys. 20, 236 (1948).

point subtraction (after normalization, with correction for the B^{10} content of normal boron) yielded a resultant curve which again showed the presence of the low energy gamma-ray; it is accordingly attributed, as before, to the bombardment of B^{11}.

We had previously determined (Section II) the yield of beta-rays from the decay of B^{12} formed in $B^{11}(d,p)$, and we therefore sought to measure the yield of the $\sim$1.5 Mev gamma-radiation. The efficiency of the counters was determined by observing radiation from the Co^{60}, and was found to be 0.9 percent. We had also determined the coincidence rate, at various absorber thicknesses, produced by secondary electrons associated with the Co^{60} gamma-radiation (with correction for the gamma-gamma coincidence rate of this element). It was thus possible to show that the intensity of the $\sim$1.5 Mev gamma-radiation produced when B^{11} is bombarded by deuterons was of approximately the same intensity as the beta-rays from B^{12}, produced in the same bombardment. This means that this gamma-ray is quite intense compared to the others emitted at our bombarding voltage. This agrees roughly with the results previously observed by Gaerttner, Fowler, and Lauritsen[8] at a bombarding voltage of 550 to 850 kev peak; Halpern and Crane,[9] using a bombarding voltage of 700 kev maximum found that the most intense line was at 4.2 Mev. We sought therefore to get information of the type shown in Fig. 9 at different bombarding voltages. No quantitative conclusion can be drawn from our data except to state that the ratio of intensities of the $\sim$1.5 Mev gamma-ray and the 4.2 Mev gamma-ray does not seem to change so markedly with bombarding voltage as the reported results would indicate. We were able to show that the excitation curve for the production of low energy radiation was of the same shape as the yield function for B^{12} (see Fig. 1) up to 1.05 Mev bombarding voltage; the fact that the intensities were found to be approximately the same, however (see preceding paragraph), is of more significance, since the excitation curves for most of the products of boron disintegration are probably quite similar in this region.

V. DECAY SCHEME OF B^{12}

It appears that the gamma-ray of $\sim$1.5 Mev discussed in the preceding section could very well be of 1.1 Mev energy and that it comes from the decay of B^{12} (usually formed in an excited state) to its ground state. The nucleus B^{12} may then decay by beta-emission either to the ground state of C^{12} or to one of the known excited levels of C^{12}. (It does not seem likely that it ever decays to an excited level in C^{12} at 1.1 Mev, since no level is known or expected in this region.)

In order to get more information on these points, we have made a search for β-γ-coincidences in B^{12} decay.

The beta-rays were detected by two counters and the gamma-rays with a third counter; all three of the counters fed into a triple coincidence circuit. The experiment is complicated by the fact that effects of gamma-rays associated with the disintegration of B^{10} are several times as intense as those associated with the disintegration of B^{11}; furthermore, gamma-gamma-coincidences which can occur in the former case must be taken into consideration. After increasing resolving time to a limit of less than 10^{-7} second, we could detect no β-γ-coincidence rate which was more than about one-third as great as that which would be expected from our previous measurements of the intensity of the beta-rays, assuming that these are in coincidence with gamma-emission. The small coincidence rate can probably be accounted for, within experimental error, by uncertainties in the gamma-gamma-coincidence rates, efficiency of counters, measurement of resolving time, and chance coincidences; part of it may also be due to true β-γ-coincidences which sometimes occur when B^{12} decays from its ground state to an excited state of C^{12}.

Generally satisfactory conclusions appear to be the following: The B^{12} formed in the $B^{11}(d,p)$ reaction is usually in an excited state at 1.1 Mev, but may be (in approximately 1/60 of the cases) in its ground state. The low energy gamma-ray observed in the bombardment of B^{11} by deuterons has a measured energy which is consistent with 1.1 Mev. It further appears that B^{12} subsequently decays primarily to the ground state of C^{12}, although our observations do not preclude the possibility that decay also takes place to excited levels of C^{12}; indeed, a small net β-γ-coincidence rate indicates that this may sometimes be the case.

These conclusions agree with cloud-chamber experiments,[5] which have indicated that no appreciable number of γ-rays is emitted following the decay of B^{12}. Additional evidence for the postulated transitions could be furnished by utilizing counters in a search for delayed gamma-emission (by stopping bombardment periodically and searching for gamma-rays), as has been pointed out[8] previously, and by a new search for beta-gamma coincidences with highly enriched targets of B^{11}.

VI. ACKNOWLEDGMENTS

The separated isotopes used in this experiment were obtained from Oak Ridge. The isotopes were then reduced to elemental form by Dr. W. B. Keighton; we are greatly indebted to him for his contribution to this work. Information regarding the procedure for making HBO_2 from $CaF_2 \cdot BF_3$ was kindly supplied by Dr. D. M. Yost of the California Institute of Technology. We wish also to thank Dr. Leonard Eisenbud for several interesting discussions concerning our results.

The technical assistance of Mr. Joseph T. Peoples has been of particular value and is gratefully acknowledged.

PHYSICAL REVIEW VOLUME 76, NUMBER 8 OCTOBER 15, 1949

Radiative Corrections to Nuclear Forces in the Pseudoscalar Meson Theory*

K. M. WATSON AND J. V. LEPORE
The Institute for Advanced Study, Princeton, New Jersey
(Received June 13, 1949)

The fourth-order corrections to nuclear forces in the charged and symmetrical pseudoscalar meson theories are obtained by the Feynman-Dyson method. All infinite parts are reconciled in terms of renormalization of mesonic and nucleonic mass and charge. The potentials obtained by a non-relativistic approximation yield ordinary spin independent forces which behave as $1/r^3$ in the non-relativistic region. This singularity is reduced to $1/r$ by relativistic effects. The potentials are in disagreement with experiment but the neutron-proton scattering problem is treated in order to obtain insight into the nature of relativistic corrections at 90 Mev, and it is shown that they are not small.

INTRODUCTION

THE success of the renormalization program[1] of quantum electrodynamics has given impetus to a re-examination of the difficulties of meson theories of nuclear forces. In particular, there are three questions to be asked in this connection: (1) Can the renormalization program of electrodynamics be successfully applied to any of the current meson theories? (2) In view of the largeness of the coupling constants describing the interaction of meson and nucleon fields, can one obtain valid solutions to problems concerned with these interactions? (3) Will conclusions drawn from these theories agree with experiment?

Case's[2] treatment of the anomalous magnetic moments of the neutron and proton indicates that there are examples for which an affirmative answer can be given to the first question; however, his results are not in agreement with experiment—in the pseudoscalar theory, for instance, the meson field seems to be too closely bound to the nucleon. It also appears that the renormalization of mass and mesonic charge will not always make all measurable quantities finite. Case[3] has found that one cannot obtain finite nucleon magnetic moments with a vector meson theory and tensor coupling to the nucleon field. Indeed, Dyson[4] has remarked that renormalization of mass and mesonic charge does not seem to be sufficient to remove all divergences in any theory for which a gradient coupling is used. Furthermore, Dyson[4] has shown that the scattering cross section of mesons by mesons is probably infinite for all present meson theories. It seems quite doubtful, then, that present treatments of field interactions will be successful when applied to meson fields.

The second question above poses formidable analytical difficulties, since one is accustomed to obtain solutions which are in the form of power series in the not-small coupling constants. In the hope of minimizing the uncertainty arising from the terms of higher order in the coupling constant it has appeared worth while to investigate the scattering of neutrons by protons to the fourth order in the coupling constant—previous treatments have considered only the second-order interaction between nucleons. That the deuteron problem can be expected to be quite sensitive to higher order radiative corrections follows from the fact that the least unsatisfactory nuclear potentials calculated in meson theory are too highly singular in regions of space outside the nucleon Compton wave-length to predict a reasonable model for the deuteron. Any possible tendency of higher order corrections to smooth out such singularities will thus be of critical importance. However, in the scattering problem the effective impact parameters tend to be greater than the de Broglie wave-length of the colliding particles, and so the scattering cross section can be expected to be somewhat less sensitive to corrections arising at very small distances of approach.

The pseudoscalar meson theory with pseudoscalar coupling was chosen because of its relative simplicity and because the fourth-order terms should be large compared to the second-order terms, since the Dirac matrix $\gamma_5(=0(v/c))$ occurs in the second order but not in the important fourth-order terms.

I. THE SCATTERING MATRIX

We assume the nucleon field to interact with a pseudoscalar meson field. The term in the Hamiltonian density representing the interaction of the fields is (we use units in which $\hbar=c=1$)

$$H(x)=if_\mu\bar{\psi}(x)\tau_\mu\gamma_5\psi(x)\phi_\mu(x). \tag{1}$$

τ_i $(i=1, 2, 3)$ are the isotopic spin matrices. $\gamma_5=\gamma_1\gamma_2\gamma_3\gamma_4$ where the γ_μ's are the Dirac matrices. $\psi, \bar{\psi}$ are the spinor operators of the nucleon field given by Schwinger,[5] and the ϕ_μ are the mesonic field variables. ϕ_1 and ϕ_2 are the field variables for the charged field; and ϕ_3 is that for the neutral field. The coupling constants f_μ are restricted by charge conservation to values for which $f_1=f_2$, but are otherwise arbitrary real quantities. The Schwinger-Tomonaga equation for the state function Ψ of the system is, in the interaction representation,

$$i[\delta\Psi/\delta\sigma(x)]=H(x)\Psi. \tag{2}$$

* This work was reported at the Washington Meeting of the American Physical Society (Phys. Rev. 76, 193 (1949)).
[1] See, for instance, F. J. Dyson, Phys. Rev. 75, 486 (1949).
[2] K. M. Case, Phys. Rev. 76, 1 (1949).
[3] K. M. Case, Phys. Rev. 75, 1440 (1949).
[4] F. J. Dyson, unpublished.

In this representation the commutation relations for the field variables are those for free fields, and have been given by Case,[2] Schwinger,[5] and others.

Since we are interested in a scattering problem, we shall use the scattering matrix of Dyson,[1] which is the operator transforming the state vector Ψ of the system from its initial value in the infinite past to its final value in the infinite future, according to Eq. (2). The

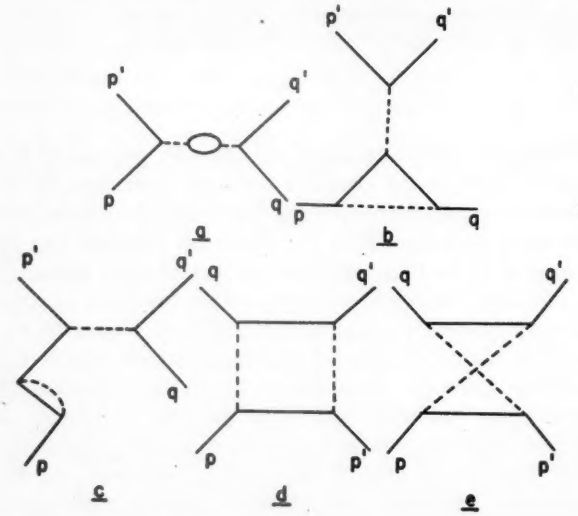

FIG. 1. Graph (a) gives the analog of the vacuum polarization of electrodynamics. A meson self-energy term is included in the contribution from this graph. (b) is the analog of the graph that accounts for most of the Lamb shift in electrodynamics. (c) contains the effects of the nucleon self-energy. (d) and (e) correspond to simple scattering processes in which two mesons are exchanged by the nucleons. (e) can be obtained from (d) by reversing the direction of the arrow on one of the nucleon lines, or analytically by taking the charge conjugate of one of the nucleon current operators in (d).

formal expression for the scattering matrix is

$$S=\sum_{n=0}^{\infty}(-i)^n\frac{1}{n!}\int_{-\infty}^{+\infty}dx_1\cdots\times\int_{-\infty}^{+\infty}dx_nP[H(x_1)\cdots H(x_n)], \quad (3)$$

where the P-bracket orders the product of the H's in such a way that those whose arguments lie on earlier time-like surfaces precede those on later surfaces. We restrict ourselves to the terms S_2 and S_4, which contain the coupling constant to the second and the fourth power, respectively.

We assume that the incoming nucleons have four-momenta p_μ, q_μ, while the outgoing nucleons have four-momenta p_μ', q_μ'. Then the second-order scattering matrix can be written immediately:

$$S_2=-i\tfrac{1}{2}(2\pi)^4(\bar\psi_{p'}\tau_\lambda\gamma_5\psi_p)(\bar\psi_{q'}\tau_\lambda\gamma_5\psi_q)(f_\lambda^2/\Delta p_\mu^2+\mu^2), \quad (4)$$

where μ is the meson rest-mass and $\Delta p_\mu=p_\mu'-p_\mu=q_\mu-q_\mu'$, since the four-momenta are restricted by energy-momentum conservation. ψ_p is the Fourier component of $\psi(x)$ referring to an electron with momentum p. It is implicitly defined by

$$\psi(x)=\int d^3p\psi_p\exp(ip_\mu x_\mu).$$

$\bar\psi_{p'}$ is defined similarly.

To find S_4 we must consider the Feynman-Dyson graphs shown in Fig. 1. (Heavy lines are nucleon lines, broken ones are meson lines.)

II. THE EVALUATION OF S_4

A: Graph (a)

One obtains[1]

$$S_a=-(\tfrac{1}{2})^5\int dx_1\cdots\int dx_4f_\lambda f_\sigma f_\nu f_\rho\delta_{\lambda\sigma}\delta_{\nu\rho}\Delta_F(x_1-x_2)\times\Delta_F(x_3-x_4)(\bar\psi(x_1)\tau_\lambda\gamma_5\psi(x_1))(\bar\psi(x_4)\tau_\rho\gamma_5\psi(x_4))\times Sp\{S_F(x_3-x_2)\tau_\nu\gamma_5S_F(x_2-x_3)\tau_\sigma\gamma_5\}, \quad (5)$$

where $Sp\{\cdots\}$ means that one must take the spur of the isotopic spin and Dirac matrices occurring in the parenthesis. S_F and Δ_F are the functions given by Dyson,[1] and are

$$S_F(x)=2\left[\frac{i}{(2\pi)^4}\right]\int d^4k\exp(ik_\sigma x_\sigma)\frac{[i\gamma_\lambda k_\lambda+\kappa_0]}{k_\lambda^2+\kappa_0^2-i\epsilon},$$
$$\Delta_F(x)=-2\left[\frac{i}{(2\pi)^4}\right]\int d^4k\exp(ik_\sigma x_\sigma)\frac{1}{k_\lambda^2+\mu^2-i\epsilon}, \quad (6)$$

where, as before, μ is the mesonic rest-mass, κ_0 is the nucleonic rest-mass, and ϵ is a positive, real parameter which tends to zero after the integrations are performed. The function of ϵ is to determine the manner by which one passes poles in the integrand. It can be shown that this choice of the sign of ϵ is equivalent to choosing outgoing waves for the scattered system and is a consequence of having fixed the initial state of the system in the solution (3) of Eq. (2).

Using Eq. (6) and performing the spatial integrations in Eq. (5), we have:

$$S_a=-4f_\lambda^2(\bar\psi_{p'}\tau_\lambda\gamma_5\psi_p)(\bar\psi_{q'}\tau_\rho\gamma_5\psi_q)\frac{\delta_{\lambda\rho}}{[\Delta p_\mu^2+\mu^2]^2}f_\rho^2I, \quad (7)$$

where

$$I=\int d^4l\frac{l_\alpha^2+\kappa_0^2-l_\alpha\Delta p_\alpha}{(l_\mu^2+\kappa_0^2)[(l_\mu-\Delta p_\mu)^2+\kappa_0^2]} \quad (8)$$

where the $-i\epsilon$ term of Eq. (6) is considered as being included in μ^2 and κ_0^2 when needed. I diverges quadratically, but Eq. (7) includes a correction to S_2 in Eq. (4) arising from the meson self-energy. Interpreting

[5] J. S. Schwinger, Phys. Rev. 74, 1439 (1948).

this mass correction as being included in the "experimental" value of the mass, one can remove the quadratic divergence from Eq. (8) as follows. We consider the change in S_2 resulting from varying μ:[6]

$$\delta S_2=(dS_2/d\mu_\rho)\delta\mu_\rho. \tag{9}$$

We insert for $\delta\mu_\rho$ in Eq. (9) the meson self-energy[7] to order f^2,

$$\delta\mu_\rho=(i/\mu)f_\rho{}^2[4/(2\pi)^4]I_0, \tag{10}$$

(the index ρ not summed) where I_0 is obtained from I (Eq. (8)) by replacing Δp_α by k_α, the energy-momentum vector for a free meson, obeying the relation $k_\mu{}^2=-\mu^2$. Considering the $\delta\mu_\rho$ as being included in μ, we subtract δS_2 from S_a. On doing this I is replaced by I', where

$$I'=I-I_0=I-I(\Delta p_\mu{}^2=-\mu^2). \tag{11}$$

I' diverges logarithmically, but it still contains a term which is to be interpreted as a coupling constant renormalization. Replacing f_λ in Eq. (4) by $f_\lambda+\delta f_\lambda$, and keeping only the linear term in δf_λ, we again obtain an expression $\delta' S_2$ of the form of S_a if

$$\delta f_\lambda=-i\frac{4}{(2\pi)^4}f_\lambda{}^3\left[\lim_{\Delta p^2\to-\mu^2}\left(\frac{I'}{\Delta p_\mu{}^2+\mu^2}\right)\right].$$

Again subtracting $\delta' S_2$ from $S_a-\delta S_2$ we have an expression with I' replaced by I'', where

$$I''=I'-(\Delta p_\mu{}^2+\mu^2)\lim_{\Delta p_\mu{}^2\to-\mu^2}\left(\frac{I'}{\Delta p_\mu{}^2+\mu^2}\right). \tag{12}$$

Using the Feynman representation for product denominators,

$$\frac{1}{ab}=\int_0{}^1\frac{dx}{[ax+b(1-x)]^2}, \tag{13}$$

$$I''=\tfrac{1}{2}i\pi^2[\Delta p_\mu{}^2+\mu^2]\int_0{}^1\ln\left[1+\frac{\Delta p_\mu{}^2}{\kappa_0{}^2}x(1-x)\right]dx$$
$$+\text{terms of } 0\left(\left(\frac{\mu}{\kappa_0}\right)^2\right). \tag{14}$$

The final expression for S_a is obtained by replacing I by I'' in Eq. (7).[8]

B: Graphs (b) and (c)

Writing the term in the S-matrix arising from graph (b) and performing the integration over coordinates, we obtain

$$S_b=-\frac{f_\lambda{}^2f_\sigma{}^2}{\Delta p_\mu{}^2+\mu^2}[\bar\psi_{p'}\tau_\lambda\tau_\sigma\tau_\lambda\gamma_5\psi_p][\bar\psi_{q'}\tau_\sigma\gamma_5\psi_q]U, \tag{15}$$

where

$$U=\int d^4k\frac{k_\alpha{}^2}{[(k_\mu+p_\mu')^2+\kappa_0{}^2][(k_\mu+p_\mu)^2+\kappa_0{}^2][k_\mu{}^2+\mu^2]} \tag{16}$$

is a logarithmically divergent integral.

From graph (c), we have

$$S_c=\frac{f_\rho{}^2f_\sigma{}^2}{\Delta p_\nu{}^2+\mu^2}[\bar\psi_{q'}\tau_\sigma\gamma_5\psi_q]\{\bar\psi_{p'}\tau_\sigma\gamma_5\frac{[-i\gamma_\lambda p_\lambda+\kappa_0]}{p_\mu{}^2+\kappa_0{}^2}$$
$$\times[I_1(i\gamma_\alpha p_\alpha+\kappa_0)+I_2\kappa_0]\psi_p\}, \tag{17}$$

where

$$I_1=\int_0 dx(1-x)\int\frac{d^4k}{[k_\mu{}^2+A]^2},$$
$$I_2=\int_0{}^1 dxx\int\frac{d^4k}{[k_\mu{}^2+A]^2}, \tag{18}$$

and $A=\kappa_0{}^2x^2+\mu^2(1-x)$. The Feynman relation (13) has been used in obtaining Eq. (18). It appears most reasonable to evaluate the indeterminate form in Eq. (17) as

$$\frac{[-i\gamma_\lambda p_\lambda+\kappa_0][i\gamma_\sigma p_\sigma+\kappa_0]}{p_\mu{}^2+\kappa_0{}^2}\to 1. \tag{19}$$

The term in Eq. (17) that contains I_2 is due to the nucleon self-energy. This may be seen if we replace "the self-energy part"[1] of graph (c) by a term arising from an additional term in the interaction Eq. (2),

$$\delta H=\delta\kappa_0\bar\psi\psi,$$

where[9]

$$\delta\kappa_0=if_\sigma{}^2[I_2\kappa_0/(2\pi)^4]. \tag{20}$$

Substracting the contribution to Eq. (17) arising from $\delta\kappa_0$ removes the I_2-term from Eq. (17). The remainder, containing I_1, diverges logarithmically.

In electrodynamics the I_1 term in S_c cancels the diverging term in U, leaving a finite result.[10] Here, were we dealing only with neutral mesons ($f_1=f_2=0$), this would happen also. However, when a nucleon emits a charged meson, it changes its isotopic spin state. Reference to graph (b) indicates that this will modify its ability to interact with another nucleon. In physical terms, this represents a change in the probability that either of the original nucleons will remain in its initial isotopic spin state to interact with the other nucleon. This manifests itself in a change in the effective value of the coupling constants. Indeed, we

[6] Compare S. T. Epstein, Phys. Rev. **73**, 177 (1948).

[7] This can be easily obtained by adding a term $\mu_\rho\delta\mu_\rho\phi_\rho{}^2$ to $H(x)$ in Eq. (1) and equating to zero the resulting expression in S for the scattering of a single meson in interaction with its virtual nucleon field. This equation can be solved for $\delta\mu_\rho$.

[8] Essentially this result, as a correction to the f^2 nuclear potential, has been given previously by F. J. Dyson in a lecture at the Institute for Advanced Study.

[9] This can be obtained in the same manner as $\delta\mu_\rho$. See reference 7.

[10] J. S. Schwinger, Phys. Rev. **75**, 651 (1949).

replace the coupling constants f_λ in S_2 (Eq. (4)) by $f_\lambda+\delta' f_\lambda$, where

$$\delta' f_k = i\frac{f_k}{(2\pi)^4}\left\{\sum_{\rho=1}^{3} f_\rho{}^2 2I_1+\left[\sum_{j=1}^{3} f_j{}^2-2f_k{}^2\right]U(\Delta p_\mu{}^2=-\mu^2)\right\},$$

$$(k=1,\ 2,\ 3). \quad (21)$$

The $\delta' f_\lambda$ terms are subtracted from Eqs. (15) and (17) and considered as included in the measurable values of the coupling constants. The remaining part of the scattering matrix is equivalent to Eq. (15) with U replaced by U^1, where

$$U^1 = U-U(\Delta p_\mu{}^2=-\mu^2)$$

$$=-i\pi^2\int_0^1 \ln\left[1+\frac{(\Delta p_\mu)^2}{\kappa_0{}^2}x(1-x)\right]dx$$

$$+\text{terms of order } (\mu/\kappa_0)^2. \quad (22)$$

The validity of the interpretation of expressions (21) as coupling constant renormalization is less clear than for the case of graph (a). In particular, it does not seem at all certain that when one goes to higher orders in the coupling constant that the combinations (21) will always re-occur correctly.

C: Graphs (d) and (e)

Graphs (d) and (e) correspond to scattering processes in which two mesons are exchanged by the interacting nucleons. Included in graph (d) is the second Born approximation of the f^2 potential. It can be expected, however, that for non-relativistic energies that vacuum fluctuation phenomena will give the largest contribution, since the matrix γ_6 is of the order v/c (v is the nucleon velocity) when it couples positive energy states (simple scattering of nucleon) and of order unity when it couples a positive to a negative energy state (pair creation). For this reason graphs (d) and (e) will give the major contribution to the total scattering matrix for non-relativistic energies. These graphs do not contain renormalization effects and lead to a finite scattering matrix.

Performing the integrations over coordinate space, using (Eqs. (6)), we obtain for S_d:

$$S_d=[\bar\psi_{p'}\tau_\sigma\tau_\lambda\gamma_\alpha\psi_p][\bar\psi_{q'}\tau_\rho\tau_\nu\gamma_\beta\psi_q]f_\lambda{}^2 f_\sigma{}^2\delta_{\lambda\nu}\delta_{\sigma\rho}V_{\alpha\beta}, \quad (23)$$

where

$$V_{\alpha\beta}=\int d^4k\frac{k_\alpha k_\beta}{[(k_\mu+p_\mu)^2+\kappa_0{}^2][(k_\sigma-q_\sigma)^2+\kappa_0{}^2]\times[(k_\lambda+\Delta p_\lambda)^2+\mu^2][k_\rho{}^2+\mu^2]}. \quad (24)$$

Again the $-i\epsilon$ term (Eqs. (6)) is considered as included in $\kappa_0{}^2$ and μ^2. It will be necessary here to make explicit use of $-i\epsilon$, since graph (d) contains intermediate states for which energy is conserved (i.e., it is possible to conserve energy for each of two successive scatterings).

To evaluate $V_{\alpha\beta}$ we use the following generalization of Eq. (13).

$$\frac{1}{abcd}=6\int_0^1 dx\int_0^x dy\int_0^y dz[az+b(y-z)+c(x-y)+d(1-x)]^{-4}. \quad (25)$$

Using Eq. (25) and performing the k-integration, we obtain

$$S_d=\pi^2\frac{i}{2}\frac{f_\lambda{}^2 f_\rho{}^2}{\kappa_0{}^2}\{L_1(\bar\psi_{p'}\tau_\rho\tau_\lambda\gamma_\alpha\psi_p)(\bar\psi_{q'}\tau_\rho\tau_\lambda\gamma_\alpha\psi_q)+L_2\kappa_0(\bar\psi_{p'}\tau_\rho\tau_\lambda\psi_p)(\bar\psi_{q'}\tau_\rho\tau_\lambda i\gamma_\beta p_\beta\psi_q)+L_3(\bar\psi_{p'}\tau_\rho\tau_\lambda\gamma_\alpha(p_\alpha-q_\alpha)\psi_q)\times(\bar\psi_{q'}\tau_\rho\tau_\lambda\gamma_\beta(p_\beta-q_\beta)\psi_q)\}, \quad (26)$$

where

$$L_1=\frac{1}{2}\int_0^1 dx\int_0^x dy\int_0^y dz\frac{1}{\Lambda},$$

$$L_2=-2\frac{dL_1}{d\kappa_0{}^2}, \quad (27)$$

$$L_3=\frac{2}{\kappa_0{}^2}\frac{dL_1}{d\theta'},$$

and

$$\Lambda=\{(x-y-z)^2+(1-x)(y-z)\theta+z(y-x)\theta'+\rho(1-x+y-z)-i\epsilon\}$$

$$\theta=\frac{(p_\mu'-p_\mu)^2}{\kappa_0{}^2},\quad \theta'=\frac{(p_\mu-q_\mu)^2}{\kappa_0{}^2},\quad \rho=\left(\frac{\mu}{\kappa_0}\right)^2. \quad (28)$$

Similarly, from graph (e) we obtain

$$S_e=-\pi^2\frac{i}{2}\frac{f_\lambda{}^2 f_\rho{}^2}{\kappa_0{}^2}\{N_1(\bar\psi_{p'}\tau_\rho\tau_\lambda\gamma_\alpha\psi_p)(\bar\psi_{q'}\tau_\lambda\tau_\rho\gamma_\alpha\psi_q)+N_2\kappa_0(\bar\psi_{p'}\tau_\rho\tau_\lambda\psi_p)(\bar\psi_{q'}\tau_\lambda\tau_\rho i\gamma_\beta p_\beta\psi_q)+N_3(\bar\psi_{p'}\tau_\rho\tau_\lambda\gamma_\alpha(p_\alpha-q_\alpha)\psi_q)\times(\bar\psi_{q'}\tau_\lambda\tau_\rho\gamma_\beta(p_\beta-q_\beta)\psi_q)\}, \quad (29)$$

where

$$N_1=\frac{1}{2}\int_0^1 dx\int_0^x dy\int_0^y dz(1/\Gamma),$$

$$N_2=-2(dN_1/d\kappa_0{}^2), \quad (30)$$

$$N_3=+(2/\kappa_0{}^2)(dN_1/d\theta'),$$

and

$$\Gamma=\{(x-y+z)^2+(1-x)(y-z)\theta+(\theta'-\theta)z(x-y)+\mu^2(1-x+y-z)\}. \quad (31)$$

It should be noted that $i\epsilon$ has been set equal to zero in Eq. (31) since Γ is positive definite ($\theta'\geqslant\theta$). This corresponds to the fact that graph (e) has no intermediate states for which energy can be conserved, since it corresponds to processes in which two mesons are successively emitted.

In a non-relativistic approximation we can drop L_3 and N_3 terms and the γ_i's ($i=1, 2, 3$) in S_d and S_e. This gives

$$S_d=\pi^2\frac{i}{2}\frac{f_\lambda^2 f_\rho^2}{\kappa_0^2}[L_1-\kappa_0^2L_2](\bar\psi_{p'}\tau_\rho\tau_\lambda\psi_p)(\bar\psi_{q'}\tau_\rho\tau_\lambda\psi_q),$$
$$S_e=-\pi^2\frac{i}{2}\frac{f_\lambda^2 f_\rho^2}{\kappa_0^2}[N_1-\kappa_0^2N_2](\bar\psi_{p'}\tau_\rho\tau_\lambda\psi_p)(\bar\psi_{q'}\tau_\lambda\tau_\rho\psi_q). \quad (32)$$

Since these expressions do not contain spin operators, we conclude that there will be no tensor force between nucleons in a non-relativistic approximation for this theory.

The exact integration of Eqs. (27) and (30) would present severe analytical difficulties. However, it is possible to obtain terms of order $(v/c)^2$ and higher. The leading term in L_1 is of order (c/v). It arises from the region of z-integration for which Λ is small. This term can be integrated explicitly. The next order terms in L_1 have the form

$$\ln[(\Delta p_\mu^2/\kappa_0^2)+\text{const.}],$$

and a term that is essentially a constant. The leading term of order (c/v) comes from the second Born approximation of the f^2 potential and is complex even in the limit $\epsilon\to 0$, because of the pole in the integrand.

Since Γ (Eq. (31)) is non-vanishing, N_1 does not contain the (c/v) term, but is otherwise similar to L_1.

In a non-relativistic approximation the leading terms in L_1 and N_1 are canceled by corresponding terms in $\kappa_0^2L_2$ and $\kappa_0^2N_2$ respectively (see Eqs. (32)). In lowest order approximation one obtains

$$L_1-\kappa_0^2L_2=-(N_1-\kappa_0^2N_2)\equiv\Delta(\theta)=-\frac{1}{4}\left\{\ln\rho+\left(\frac{\theta+4\rho}{\theta}\right)^{\frac{1}{2}}\times\ln\left[\frac{1+[\theta/(\theta+4\rho)]^{\frac{1}{2}}}{1-[\theta/(\theta+4\rho)]^{\frac{1}{2}}}\right]\right\}, \quad (33)$$

where ρ and θ are defined in Eq. (28).

We can obtain a non-relativistic expression for the momentum space representation of the potential energy of two nucleons (using Eq. (33)) as that expression which leads to Eqs. (32) in a Born approximation.[11]

$$\begin{aligned}(p'q'|V^4|pq)&=-\frac{1}{4}\frac{1}{(2\pi)^3}\left[\frac{f_\lambda^2 f_\mu^2}{(2\pi)^2}\right]\frac{\Delta(\theta)}{\kappa_0^2}\times\tau_\lambda^{(1)}\tau_\mu^{(1)}(\tau_\lambda^{(2)}\tau_\mu^{(2)}+\tau_\mu^{(2)}\tau_\lambda^{(2)})\\&=-1/(2\pi)^3(f^2/2\pi)^2\Delta(\theta)/\kappa^2\\&\quad\text{(charged theory; } f_1=f_2=f,\ f_3=0)\\&=-\tfrac{3}{2}[1/(2\pi)^3](f^2/2\pi)^2\Delta(\theta)/\kappa_0^2\\&\quad\text{(symmetric theory; } f_1=f_2=f_3=f), \quad (34)\end{aligned}$$

where the superscripts (1) and (2) on the τ-operators imply that they refer to particles (1) and (2), respectively. The f^2 potential is non-relativistically:

$$(p'q'|V^2|pq)=-\frac{1}{8\kappa_0^2}\left(\frac{f_\lambda^2}{2\pi}\right)\frac{1}{2\pi^2}\frac{\sigma^{(1)}\cdot\Delta p\,\sigma^{(2)}\cdot\Delta p}{(\Delta p)^2+\mu^2}\tau_\lambda^{(1)}\tau_\lambda^{(2)}. \quad (35)$$

From Eq. (35) it is seen that in a non-relativistic approximation V^4 does not contain tensor forces, nor does it contain exchange forces. It is further seen from Eq. (33) that V^4 in coordinate space has a $1/r^3$ singularity at the origin (for $r\sim 1/\kappa_0$, relativistic corrections reduce this to a $1/r$ singularity). Each of these conclu-

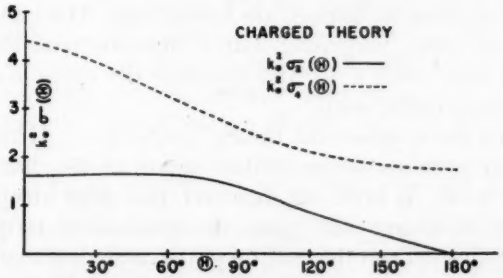

FIG. 2. Partial differential cross sections for the charged theory at 90 Mev contributed by the terms S_2 and S_4 in the scattering matrix taken individually.

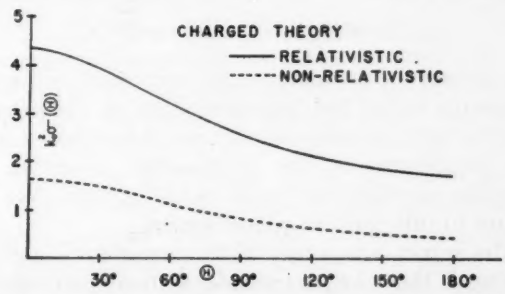

FIG. 3. Effect of relativistic corrections, as herein defined (page 17) on the partial cross section contributed by the S_4 term in the scattering matrix.

[11] That the potential can be obtained in this manner was first noted by Professor H. A. Bethe, Phys. Rev. 76, 191 (A) (1949).

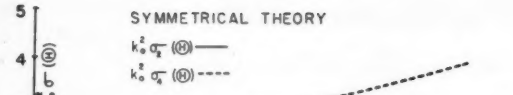

FIG. 4. Partial differential cross sections for the symmetrical theory at 90 Mev contributed by the terms S_2 and S_4 in the scattering matrix taken individually.

FIG. 5. Estimate of differential cross sections for the charged theory computed by using the eighth-order S-matrix (Eq. (A. 1)).

sions is in contradiction to experiment; however, it is not impossible that higher order radiative corrections might modify this result.

To see the importance of relativistic corrections, we investigate the differential scattering cross section.

III. SCATTERING CROSS SECTIONS

For the case of the charged theory the constant $f_3=0$ and $f_1=f_2=f$. As a consequence of the fact that only charged mesons are present the matrix element corresponding to diagram (b) vanishes identically since it is incompatible with electric charge conservation. For the problem of neutron-proton scattering (e) vanishes on the same grounds and (d) contributes. Similarly for the scattering of identical particles (d) vanishes and (e) contributes. The contributions of the two diagrams are, however, identical in a non-relativistic approximation (see Eq. (32)). After the infinite part of diagram (a) has been interpreted in terms of charge and mass renormalization it gives a very small effect on the cross section of the order of a percent.

The neutron-proton scattering cross section has been treated in the approximation of retaining consistently all relativistic effects of order $(v/c)^2$ in those terms of the scattering matrix up to the fourth power of the coupling constant. Figure 2 shows the partial cross sections at 90 Mev contributed by the second- and fourth-order terms taken separately. Thus in the center of gravity system

$$\sigma_2(\theta)=\pi^2E^2|S_2|^2, \quad \sigma_4(\theta)=\pi^2E^2|S_4|^2. \tag{36}$$

The flatness of the fourth-order curve and the forward maximum reflect the high singularity of the potential and the fact that only ordinary and not exchange forces are contributed by the fourth-order potential. The coupling constant was chosen as $(f^2/2\pi)=6.4$. We shall return to this point in a later section.

The importance of relativistic corrections is indicated in Fig. 3. Here the partial cross section contributed by the fourth-order term in the scattering matrix alone has been plotted with and without inclusion of relativistic terms. Since there is some ambiguity as to what one might mean by a relativistic correction, it seems worth while to discuss this point in some detail. As we have pointed out before (Eqs. (26) and (29)), the scattering matrix can be written in terms of the two invariant collision parameters θ, θ' which represent the square of the momentum transfer divided by κ_0^2 and the maximum value of this quantity respectively. In terms of the angle of scattering Θ there exists the following relation:

$$\theta=\theta' \sin^2(\Theta/2). \tag{37}$$

In terms of these parameters $\sigma_4(\Theta)$ may be written

$$\sigma_4(\theta,\theta')=\sigma_{40}(\theta)+(\theta')^{\frac{1}{2}}\sigma_{41}(\theta,\theta')+\theta'\sigma_{42}(\theta,\theta')+\cdots.$$

The terms in $(\theta')^{\frac{1}{2}}$ and θ', etc., can be said to represent relativistic corrections since in the center of gravity system

$$\theta'=4p^2/\kappa_0^2\sim(v/c)^2, \tag{38}$$

where $\mathbf{p}$ is the momentum of one of the colliding particles.

If we now let θ' tend toward zero the terms involving σ_{41} and σ_{42}, etc., tend to zero whereas σ_{40} remains finite and is identical with the partial cross section which would have been contributed by the non-relativistic potential (Eq. (34)). The meaning of the non-relativistic cross section σ_{40} seems rather unique when the limiting process is characterized in terms of the invariant quantity θ'. The condition for the validity of our non-relativistic cross section is simply

$$\theta'\ll 1 \quad \text{or} \quad (2p)^2\ll\kappa_0^2. \tag{39}$$

Inspection of the curves in Fig. 3 shows that relativistic effects, when so defined, are rather large. The result is, at first sight, surprising, but it must be remembered that at 90 Mev $\theta'\sim\frac{1}{5}$ and therefore the terms σ_{41} and σ_{42} need not be small.

For the symmetrical theory $f_1=f_2=f_3=f$. Here due to the presence of the neutral meson all the diagrams play a role. It turns out, however, that after identifications of charge and mass renormalization terms in diagrams (a) and (b) that they contribute less than one percent to the cross sections. Barring the inconsequential effect of the Lamb shift and vacuum polarization terms there are, in the non-relativistic limit, no

exchange forces contributed by the fourth-order potential in the symmetrical theory (Eq. (34)).

The partial cross sections $\sigma_2(\Theta)$, $\sigma_4(\Theta)$ obtained in the case of the symmetrical theory are shown in Fig. 4. They have been computed in the same approximation as the corresponding terms in the charged theory. Again the flatness of the fourth-order curve reflects the high singularity of the potential. The fact that the forward-backward cross-section ratio for this curve is about one must be attributed to exchange forces introduced by relativistic corrections. The coupling constant $(f^2/2\pi)\sim 4.8$ was determined roughly by the requirement that the fourth-order partial cross section agrees with the corresponding quantity in the case of the charged theory.

We are indebted to Professor Bethe for sending his results to us in advance of publication and to Professor J. R. Oppenheimer for helpful criticism.

This work was carried out while one of us (K.W.) was supported by a grant-in-aid through the Institute for Advanced Study supported by the Atomic Energy Commission and the other (J.V.L.) was the holder of an Atomic Energy Commission Postdoctoral Fellowship.

APPENDIX

The S-matrix which has so far been obtained may be used to compute the cross section up to terms proportional to f^8. There are, of course, other terms involving f^8 due to higher order terms in the S-matrix. An attempt was made to improve the present approximation by taking the potential which we have obtained (Eqs. (34) and (35)) and solving the equation of motion again.

$$i(\partial\Psi/\partial t)=V\Psi.$$

This equation may be solved in the same manner as Eq. (2) and the S-matrix can be found. We may now identify those terms in S corresponding to the terms S_2 and S_4 which have been correctly dealt with. Thus an S-matrix of the form,

$$S=S_2+S_4+S_6'+S_8', \tag{A.1}$$

can be found. Of course, the terms in S_6' and S_8' depend on the singular potential (Eq. (34)) so that it is necessary to cut off the integrations. This cut-off was arbitrarily chosen as the nucleon Compton wave-length. The results are not sensitive to this choice since the relativistic effects would introduce a cut-off in this region anyway.

A coupling constant $f^2/2\pi=6.4$ was estimated in this way by fitting the total cross section at 90 Mev reported by Segrè and his collaborators.[12] The results are given in Fig. 5. The total cross sections are nearly energy independent in the range considered.

[12] Hadley, Kelly, Leith, Segrè, Wiegand, and York, Phys. Rev. 75, 351 (1949).

PHYSICAL REVIEW VOLUME 76, NUMBER 8 OCTOBER 15, 1949

The Photo-Disintegration of the Deuteron

INGVAR F. E. HANSSON,
Institute of Mechanics and Mathematical Physics, Lund, Sweden

AND

LAMEK HULTHÉN,
Royal Institute of Technology, Stockholm, Sweden

(Received May 9, 1949)

The photo-magnetic and photoelectric cross sections have been calculated for γ-energies 2.62, 2.76 and 6.2 Mev, using different values of the deuteron binding energy (2.19 and 2.24 Mev). The calculations were carried out for a symmetrical theory with meson potential (Møller-Rosenfeld theory), the corresponding neutral theory (ordinary force) and a third version with no ^3P-interaction. Non-central forces were neglected. Results are given for two ranges, equivalent to meson masses 200 and 300. The influence of the γ-ray momentum on the angular distribution of the photo-nucleons should be noted.

FROM the point of view of nuclear force theory the photo-disintegration of the deuteron is one of the fundamental experiments. Measurements of the total cross section and the angular distribution of the photo-neutrons (or -protons) for moderate energies are now in progress in several laboratories,[1–5,*] and we hope that the theoretical results presented in this note will be of some use for the interpretation of the experiments.

We have calculated the photo-magnetic and photo-electric cross sections, σ_m and σ_e,[**] for the γ-energies mainly used in experiments so far: 2.62, 2.76 and 6.2 Mev. As a theoretical basis we have employed the Møller-Rosenfeld (MR) theory and, for comparison, the corresponding neutral theory (N) and a third version (O) where the interaction in the ^3P-state is assumed to be zero. The three cases can be characterized

[1] Wilson, Collie, and Halban, Nature 163, 245 (1949).
[2] N. O. Lassen, Phys. Rev. 74, 1533 (1948); Phys. Rev. 75, 1099 (1949).
[3] B. Hamermesh and A. Wattenberg, Phys. Rev. 75, 1290 (1949).
[4] Meiners, Smith, and Slack, Phys. Rev. 75, 1632 (1949).
[5] Snell, Barker, and Sternberg, Phys. Rev. 75, 1290 (1949).
[*] We are indebted to Dr. Hans Halban, Oxford, and Dr. N. O. Lassen, Copenhagen, for kindly informing us of experimental results before publication.

[**] For a survey of the theory of the photo-disintegration, see e.g., L. Rosenfeld, *Nuclear Forces* (North-Holland Publishing Company, Amsterdam, 1948), pp. 132–135, 175–179, 452–453.

TABLE I.

Theory	Interaction in state ^1S	^3S	^3P	
MR	$-A$	$-B$	$+B/3$	$\times e^{-\kappa r}/r$, $\kappa = M_m c/\hbar$, (M_m meson mass).
O	$-A$	$-B$	0	
N	$-A$	$-B$	$-B$	

by the static interactions in the states concerned, as shown in Table I.

Non-central forces have been neglected and hence all kinds of quadrupole effects must be left out of consideration. This restricts the validity of the calculations to the region of small and moderate excess energies ($h\nu - |E_0|$ of the order of $|E_0|$ or smaller). On the other hand, the contribution to σ_m from the charge exchange according to the MR-theory[6] has been taken into account but turned out to be very small (see Tables II and III).

The calculations were carried out for two different meson masses. The constants A and B were chosen so as to give the "right" cross section for scattering of epithermal neutrons by protons (21×10^{-24} cm^2) and binding energy of the deuteron.[7] Originally the work was based on the value 2.187 Mev but the paper of Bell and Elliott[8] induced us to repeat the calculations,

TABLE II. Theoretical results based on deuteron binding energy 2.187 Mev.

$h\nu$ (Mev)	Theory	Meson mass	σ_m	σ_e	σ ($=\sigma_m+\sigma_e$)	$\left[\frac{\sigma(0)}{\sigma(\pi/2)}\right]_{MC}$	$\left[\frac{\sigma(0)}{\sigma(\pi/2)}\right]_{Lab}$
2.62	N	200	3.07	13.50	16.6	0.132	0.150
2.62	O	200	3.07	12.20	15.3	0.144	0.164
2.62	MR	200	3.06	11.89	15.0	0.147	0.167
2.62	N	300	3.19	10.27	13.5	0.172	0.196
2.62	O	300	3.19	9.95	13.1	0.176	0.201
2.62	MR	300	3.23	9.86	13.1	0.179	0.204
2.76	N	200	2.66	17.73	20.4	0.091	0.102
2.76	O	200	2.66	15.87	18.5	0.100	0.113
2.76	MR	200	2.65	15.42	18.1	0.103	0.116
2.76	N	300	2.74	13.41	16.1	0.120	0.135
2.76	O	300	2.74	12.95	15.7	0.124	0.139
2.76	MR	300	2.78	12.82	15.6	0.126	0.142
6.20	N	200	0.60	27.42	28.0	0.014	0.016
6.20	O	200	0.60	25.05	25.6	0.016	0.017
6.20	MR	200	0.56	24.41	25.0	0.015	0.017
6.20	N	300	0.55	22.33	22.9	0.016	0.018
6.20	O	300	0.55	20.98	21.5	0.017	0.019
6.20	MR	300	0.55	20.64	21.2	0.017	0.019

TABLE III. Theoretical results based on deuteron binding energy 2.237 Mev.

$h\nu$ (Mev)	Theory	Meson mass	σ_m	σ_e	σ	$\left[\frac{\sigma(0)}{\sigma(\pi/2)}\right]_{MC}$	$\left[\frac{\sigma(0)}{\sigma(\pi/2)}\right]_{Lab}$
2.62	N	200	3.27	11.37	14.6	0.161	0.185
2.62	O	200	3.27	10.31	13.6	0.174	0.200
2.62	MR	200	3.26	10.05	13.3	0.178	0.204
2.62	N	300	3.42	8.71	12.1	0.207	0.238
2.62	O	300	3.42	8.44	11.9	0.213	0.245
2.62	MR	300	3.46	8.36	11.8	0.216	0.249
2.76	N	200	2.83	15.65	18.5	0.108	0.122
2.76	O	200	2.83	14.05	16.9	0.118	0.134
2.76	MR	200	2.82	13.66	16.5	0.121	0.137
2.76	N	300	2.92	11.92	14.8	0.140	0.159
2.76	O	300	2.92	11.50	14.4	0.145	0.164
2.76	MR	300	2.96	11.38	14.3	0.148	0.168
6.20	..... values practically the same as in Table II.						

[6] A. Pais, Copenhagen Acad. Mat.-fys. Medd. **XX**, No. 17 (1943), p. 17, formula (24).
[7] L. Hulthén, Arkiv. f. Mat., Astr. o. Fys. **29B**, No. 1 (1942). See also L. Hulthén and A. Pais, Phys. Soc. Cambridge Conference Report 177–180 (London, 1947).
[8] R. E. Bell and L. G. Elliott, Phys. Rev. **74**, 1552 (1948).

TABLE IV. Some experimental results concerning angular distributions.

Authors	γ-energy (Mev)	$\left[\frac{\sigma(0)}{\sigma(\pi/2)}\right]_{MC}$	$\left[\frac{\sigma(0)}{\sigma(\pi/2)}\right]_{Lab}$
Graham, Halban[a]	2.62		0.21±0.06[f]
Lassen[b]	2.76	0.15±0.03	
Hamermesh, Wattenberg[c]	2.76		0.19[f]
Meiners, Smith, Slack[d]	2.76		0.16±0.02[f]
Gibson, Green, Livesey[e]	6.0±0.2		small (nearly $\sin^2$-distribution)

[a] G. A. R. Graham and H. Halban, Jr., Rev. Mod. Phys. 17, 297 (1945).
[b] See reference 2.
[c] See reference 3.
[d] See reference 4.
[e] Gibson, Green, and Livesey, Nature 160, 534 (1947).
[f] These authors give a value for σ_m/σ_e, a quantity which must be calculated from $(\sigma(0)/\sigma(\pi/2))_{Lab}$. In reversing this calculation we have assumed that no correction for the γ-ray momentum has been applied and have therefore used the simple formula

$$(\sigma(0)/\sigma(\pi/2))_{Lab}=(\sigma_m/\sigma_e)/(1.5+(\sigma_m/\sigma_e)).$$

using their value for the binding energy: 2.237 Mev. As will be clear from the following tables, the corresponding change in the cross sections can be appreciable. This is natural because the cross sections (especially σ_e) depend sensitively on the excess energy.

It is, of course, essential for calculations of this kind to have accurate approximations for the eigenfunctions and much time has been devoted to this aspect of the problem. This part of the work has been, or will be, reported elsewhere. The eigenfunctions connected with the ground state have been computed by Hulthén and Laurikainen, using a variational method;[9] the eigenfunctions of the continuous ^3P-spectrum have been calculated by Hansson[10] and those of the ^1S-spectrum by Hulthén.[11]

In previous work it has usually been assumed that the influence of the γ-ray momentum can be neglected for small and moderate excess energies. This is not justified, however, as far as the angular distribution of the photo-nucleons is concerned, although the corresponding Doppler effect is negligible, only about 1 kev.[12] If $(\sigma(0)/\sigma(\pi/2))_{MC}=\sigma_m/(\sigma_m+1.5\sigma_e)$ is the intensity ratio in the mass center system (angles referred to the direction of the γ-ray) simple geometrical considerations show that the corresponding ratio in the laboratory system (deuteron initially at rest), $(\sigma(0)/\sigma(\pi/2))_{Lab}$, is obtained from

$$[\sigma(0)/\sigma(\pi/2)]_{Lab}=[\sigma(0)/\sigma(\pi/2)]_{MC}\times\{1+2\bar{v}/v+(2.5-[\sigma(0)/\sigma(\pi/2)]_{MC})\bar{v}^2/v^2\},$$

$\bar{v}$ being the velocity of the mass center of neutron and proton in the laboratory system and v the velocity of

[9] L. Hulthén, Kgl. Fysiograf. Sällsk. Lund Förhandl. 15, No. 22 (1945), pp. 6–9; L. Hulthén and K. V. Laurikainen, unpublished calculations.
[10] I. F. E. Hansson, Kgl. Fysiograf. Sällsk. Lund Förhandl. 18, No. 12 (1948).
[11] L. Hulthén, Arkiv f. Mat., Astr. o. Fys. 35A, No. 25 (1948).
[12] As far as we know, this was first pointed out by the late Professor J. Blaton, Cracow. See J. Blaton, Copenhagen Acad. Mat.-fys. Medd. XXIV, No. 20 (1949).

TABLE V. Some experimental results on total cross sections.

Authors	γ-energy (Mev)	$\sigma\times10^{28}$
Wilson, Collie, Halban[a]	2.62	14.8±1.0
Wilson, Collie, Halban	2.76	15.6±1.0
Russell, Sachs, Wattenberg, Fields[b]	2.76	16.4(±27%?)
Snell, Barker, Sternberg[c]	2.76	14.5(±10%)
van Allen, Smith[d]	6.2	11.6±1.5

[a] See reference 1.
[b] Russell, Sachs, Wattenberg, and Fields, Phys. Rev. 73, 545 (1948).
[c] See reference 5.
[d] J. A. van Allen and N. M. Smith, Jr., Phys. Rev. 59, 618 (1941).

neutron (or proton) relative to the mass center; thus

$$\frac{\bar{v}}{v}=\frac{h\nu}{2(Mc^2(h\nu-|E_0|))^{\frac{1}{2}}},$$

(M mass of neutron or proton; $|E_0|$ binding energy of deuteron). Higher order terms in $\bar{v}/v$ have been neglected. The corresponding formula for $(\sigma(\pi)/\sigma(\pi/2))_{Lab}$ is obtained by changing the sign of $\bar{v}/v$. Hence, if the average ratio $[(\sigma(0)+\sigma(\pi))/2\sigma(\pi/2)]$ is considered (see the experiment of Lassen[2]), the correction factor is very close to 1,*** $\bar{v}/v$ being small ($\approx$0.05–0.07) for the energies in question.

The results are summed up in Tables II and III, where the cross sections are expressed in 10^{-28} cm^2 as a unit.

For comparison some experimental results concerning the angular distribution are given in Table IV.

Evidently there is no discrepancy between theory and experiment, as far as the angular distribution is concerned. Regarding the most accurate experiments, those at 2.76 Mev, one might say that the best fit is obtained with a meson mass $\approx$300 and the new value of the deuteron binding energy (Table III). However, turning to the total cross sections, we realize that any theoretical conclusion would be premature. Some experimental results are listed in Table V.

The disagreement between theory and experiment at 6.2 Mev is obvious. On the other hand, the absolute cross sections for 2.62 and 2.76 Mev do not constitute any discrepancy, though the ratio $\sigma_{2.76}/\sigma_{2.62}$ does, as already pointed out by Wilson, Collie, and Halban.[1] Thus Tables II and III give values between 1.19 and 1.26 whereas the ratio given by the authors quoted is 1.05±0.08.

A more detailed account will be published by one of us (I. F. E. H.).

The present work was done at the Institute of Mechanics and Mathematical Physics, University of Lund, and we extend our thanks to Professor Torsten Gustafson for his courtesy and hospitality. One of us (I.F.E.H.) is much indebted to the Swedish Atomic Committee for a scholarship.

*** = 1.009 for $h\nu\approx$2.7 Mev.

Effects of Scattering and Absorption of Mesons on Coincidence-Anticoincidence Measurements

ROGERS D. RUSK AND ALMA ROSENBAUM*
Mount Holyoke College, South Hadley, Massachusetts

(Received June 27, 1949)

Effects due to absorption and scattering of cosmic-ray mesons with respect to position and nature of various materials were studied with a coincidence-anticoincidence counter. Lead, iron, and paraffin and combinations of them were used. The position of the material was found to account for large variations in the counting rate which could be greater or less than that with no absorber. Effects which had sometimes been previously reported by others to indicate the presence of neutral particles are shown to be largely due to the geometry and other incidental causes. There was, however, a small residual effect due to paraffin, greater than the statistical error, always in the direction which could be interpreted in terms of exchange of charge or the production of neutral rays.

IN a number of earlier experiments by other investigators[1] using coincidence circuits a difference in counting rate was observed upon changing the position of a layer of lead from above to below the upper tube of an array. In 1940 Rossi[1] and others showed that the results of these experiments which had been sometimes interpreted to indicate the presence of incident neutral particles could be explained by such effects as knock-on showers, scattering, and side showers. In a further attempt to detect incoming neutral rays they placed anticoincidence tubes above an array of coincidence tubes. Again the change in counting rate when lead was used as the absorber was given a similar explanation in terms of showers and incidental effects. A more recent report by de Vos and du Toit[2] states that an effect believed to be due to incoming neutral particles in the cosmic rays was obtained by interchanging a thin layer of paraffin from above to below the upper tube of a coincidence counter arrangement. In such a thin layer of paraffin the above effects due to showers, etc., would be expected to be small.

In the present experiments measurements were made with a coincidence-anticoincidence array, the second tube from the top being in anticoincidence.[3] It is shown that considerable variations in counting rate are obtained, due chiefly to absorption and scattering not only when a heavy absorbing layer was moved from below to above a tube but also when it was moved to a different position between two tubes. The effect of paraffin alone was found to be slight. Such absorption and scattering due to heavier materials could easily obscure other lesser effects as, for instance, those possibly due to neutral rays if they were present. Comparison was made of the effects of iron, lead, and paraffin singly and in combination in various positions with respect to the counter tubes. The lead was used because of its high scattering power. Iron was used in order to compare effects of scattering and absorption with lead. Paraffin was used to test the existence of any effect in the heavier materials sensitive to the presence of a light material.

The Geiger-Müller tubes were placed, as indicated in Fig. 1, in a horizontal position, one above the other in a vertical array, and were connected in a conventional Rossi-type circuit with constant voltage regulation. They were 18 in. long, $2\frac{1}{4}$ in. in diameter, and were separated 14 in., 12 in., and 12 in. between centers, starting from the top. The thicknesses of absorbing layers used in all cases were 10, 7, and 3.7 cm of iron, lead, and paraffin, respectively. The positions of the absorbing layers are indicated by the letters A, B, C, and B'. In positions A, B, and C the layers were placed directly above the tubes and were so supported at the ends that no other material intervened between the tubes except in the case of lead which rested upon a comparatively thin iron plate. In position B' the material was raised $5\frac{1}{2}$ in. above tube 3 and was then close to the anticoincidence tube above it. The width of the absorbing layers was such as to just cover the tubes without projecting appreciably at the sides in order to reduce side effects of scattering and absorption to a minimum. The absorbing layer above the array due to the building in which the measurements were made was equivalent to 18 cm of lead. Due to the slow counting rates, observations were carried out over a period of many months. Frequent checks were made of the operation of the counter, and frequent tests were made of the ability to repeat measurements in different positions.

In practice, the counts actually recorded by such a coincidence-anticoincidence counter may be due chiefly to two types of effects: (1) Approximately vertical effects such as a single ray (or its secondaries) passing through all counter tubes but failing to discharge the anti-tube because of faulty alignment; (2) side effects as shower rays, or accidental coincidences (or their secondaries produced in the apparatus) which discharge the coincidence tubes within a period of time less than the resolving time of the circuit.

Various preliminary control measurements made with two, three, and four tubes, both in line and out of line, gave information as to relative counting rates due to

* Now at General Electric Company, Schenectady, New York.
[1] Rossi, Janossy, Rochester, and Bound, Phys. Rev. **58**, 761 (1940). (See this for list of previous work.)
[2] P. J. G. de Vos and S. J. du Toit, Phys. Rev. **70**, 229 (1946).
[3] The measurements were concluded by Rogers D. Rusk.

vertical and side effects and also of the efficiency of the tubes and circuit. The over-all efficiency was believed to be greater than 99 percent. That the counting rates obtained with the tubes in line as shown in Fig. 1 was approximately the same as when the tubes were moved out of line indicated that most of the counts with no absorbing materials were due to side effects. Any variation in rate in the presence of absorbing layers must hence be interpreted in terms of the geometry of the system. Measurements of the resolving times made by using a radioactive source gave 10^{-3} sec. which indicated that a considerable part of the counts obtained could be accounted for by accidental coincidences directly or indirectly due to side particles.

Measurements were made with various absorbers in different combinations and in different positions. The results are given in Table I. With lead in position C, the effects due to lead, iron, and paraffin were tried in positions A and B. With iron in position A, and lead in position C, the effects of paraffin in positions B and B' were tried. Measurements were made without lead at C in order to detect effects due to soft secondaries as distinguished from penetrating rays. The results are indicated in the table.

When no other absorbers were in position, the presence of the lead layer above the lowest tube (position C) decreased the counting rate a considerable amount from what it was with no absorbers at all. When the lead was moved from position C to position B, a further decrease in the counting rate was obtained. With the absorbing layer of lead in position C and a similar layer of lead added in position B the counting rate was still lower. If most counts were due to side effects, it would appear that the lead in position B or C served in large part to shield either by absorption or scattering the tube below it from soft rays coming from the side. Any increase in counting rate due to showers in the lead was hence either negligible or obscured by the larger effects.

When the lead was placed in position A above the anti-tube instead of below, with no absorber at C, a considerable increase in counting rate was obtained over the rate when no lead was present. This increase could hardly have been due to shower particles from the lead hitting tubes 3 and 4 without passing through the anti-tube because of the size of the lead screen. If many shower particles were produced in the lead above the anti-tube which then traversed the anti-tube, there should have been a diminution in counting rate due to increased deadtime of the anti-tube. However, the lead was of such a thickness as to cut off most of such shower particles due to rays coming in from above. It might be expected that shielding the anti-tube with lead just above it would produce an opposite effect from lead placed just above a coincidence tube if it is true that the material shields the counters from soft side-shower particles and accidentals by absorption. However, the effect was considerably greater than would be expected from a consideration of the resolving time alone.

Rossi, *et al.*,[1] found that the presence of lead directly under the anti-tube increased the counting rate observed in their arrangement. This is in contradiction to the present results obtained with lead at B, however; the geometry of their experimental arrangements was quite different from the above. A further test of the effect of position in the present experiment was made by raising the lead from position B to B'. The counting rate was then observed to increase and be above the value with

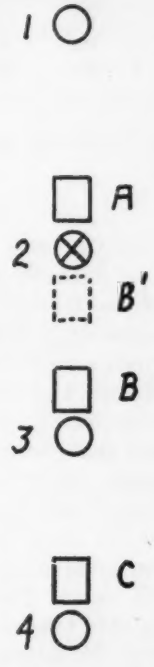

FIG. 1. Arrangement of tubes and absorbers. Tube 2 is in anticoincidence.

no lead and in agreement with results observed by Rossi. The increase as observed by Rossi was attributed largely to showers produced in the lead. In the present experiment the difference in counting rate between B and B' seems chiefly due to the fact that in position B the lead acts as a more complete shield of the tube below it, while in position B' the lead shields the lower tube to a much less degree and is itself shielded by the anti-tube above it. Obviously if the difference were due to effects of the first type as mentioned above, the change in position of the lead from B to B' would have little effect. The increase in counts in position B' could hardly be due to showers as suggested, as these should be even more effective when the absorber was in the lower position B. The geometry of the system indicates that, in general, small angle scattering inward would approximately balance small angle scattering outward. A considerable number of additional rays incident at a small angle to the vertical, however, could be scattered out if the angle of scattering were large. If such scattering be taken as the explanation of the decrease in counting rate with lead at B, it would seem necessary to assume a nucleon scattering cross section larger than

TABLE I. Variations in the counting rate for different absorbers in different positions are given in terms of counts per hour and the probable statistical error is indicated. (P=paraffin.)

Positions				Total	Total	Count	Statistical
A	*B*	*B'*	*C*	counts	hours	per hr.	error
—	—	—	—	913	141.7	6.42	±0.21
Pb	—	—	—	1060	114.6	9.25	±0.28
—	Pb	—	—	866	189.9	4.56	±0.16
—	—	Pb	—	594	67.4	8.80	±0.35
—	—	—	Pb	285	53.6	5.31	±0.31
Pb	—	—	Pb	916	173.7	5.27	±0.17
Pb	P	—	Pb	922	161.5	5.70	±0.18
Pb	P	—	—	1374	145.6	9.44	±0.25
—	Pb	—	Pb	583	169.5	3.44	±0.14
Fe	—	—	Pb	1223	288.5	4.23	±0.12
Fe	P	—	Pb	1449	307.5	4.70	±0.12
Fe	—	P	Pb	2039	453.0	4.51	±0.10

10^{-26} cm^2; this may be estimated by application of the formula[4]

$$J=F/tN,$$

where J is the cross section for scattering, N is the number of nucleons per cc, t is the thickness of the absorber, and F is the fraction of rays undergoing large-angle scattering presumably due to other than Coulomb forces. Such a large cross section is not in accord with previous work, which leads to a cross section more nearly of the order of 10^{-28} cm^2 for mesons of spin $\frac{1}{2}$. Hence, it is concluded that the observed diminution in counting rate is chiefly due to screening by absorption. With lead in positions B and C, a rate of 3.44 counts per hour was obtained. An equal weight of iron at B instead of the lead gave a variation of less than the statistical error from this value. The major part of the decrease in counting rate can hence be attributed to absorption. Since the absorptions of the two substances for the thickness used should be approximately the same, any difference between the counting rates could be attributed to scattering but was evidently small.

If a neutral ray were produced in an absorber above the anti-tube by exchange of charge or any other process involving an ionizing ray passing through the first tube, this neutral might pass through the anti-tube and produce an ionizing ray in any material between the counters (or in the material of the counter) and discharge the lower tubes resulting in a count. To test for such an effect, paraffin was placed below the anti-tube while iron was placed above it. Any vertical ray producing ionization in tubes 1, 3, and 4 but not in tube 2 would result in a count. If such counts were due to inefficiency of the tube or circuit they would not be influenced by the presence of an absorbing medium above the anti-tube. Some other process such as exchange of charge resulting in a neutral ray, or production of a photon passing through the next counter, would be influenced by the absorbing material. Such an effect if resulting from a double transition would of course have a low probability. However, when paraffin was used below the anti-tube in position B, the count obtained was always increased more than could be explained by the statistical fluctuations and it was always in the same direction. In order to make a further test of this effect, some evidence of which had been previously reported,[5] a lengthy set of runs was made with paraffin at B, B', and without paraffin. The reduction of the effect when the paraffin was moved up to position B' was too small to warrant the conclusion that the main difference was not due to vertical rays. Since the measurements extended over a considerable period of time, it was believed that any minor fluctuations due to local atmospheric variations would cancel off.

From these experiments, in addition to the effect due to paraffin, it is concluded that the larger part of the observed differences in counting rates is due to absorption of rays coming from the side together with some scattering. These effects vary greatly with the position of the absorber. When such is between an anticoincidence tube it is worth noting that it may produce either an increase or decrease depending on the geometry of the system.

[4] R. P. Shutt, Phys. Rev. 61, 61 (1942).

[5] R. D. Rusk and A. Rosenbaum, Phys. Rev. 74, 110 (1948).

PHYSICAL REVIEW VOLUME 76, NUMBER 8 OCTOBER 15, 1949

Interstitial Atomic Diffusion Coefficients*

C. WERT AND C. ZENER
Institute for the Study of Metals, University of Chicago, Chicago, Illinois
(Received April 19, 1949)

An attempt is made to interpret the temperature independent factor D_0 of the previously determined diffusion coefficients of interstitial solute atoms in metals. The primary uncertainty in the value of D_0 given by the standard reaction rate theory resides in an entropy factor $\exp(\Delta S/R)$. When cognizance is taken of an additional strain in the lattice surrounding a solute atom as it passes over a potential energy divide, and of the increase in entropy associated with an increase in lattice strain energy, one can estimate a "theoretical" range within which these entropy factors should lie. All past observations except for C and N in α—Fe are consistent with this theoretical range. The D_0's for these two systems were, therefore, redetermined by more precise measurements, and are found to be an order of magnitude higher than the original values. The associated entropy factors are consistent with the theoretical range.

I. INTRODUCTION AND RESULTS

THE mechanism of diffusion of interstitial solute atoms in solid solution is well understood. The solute atoms diffuse by simply jumping between interstitial positions, the direction of each particular jump being random. The purpose of the present paper is to see how well the theoretical diffusion rate based upon this simple model and the observed diffusion rates can be brought into quantitative agreement.

The observed atomic diffusion coefficients are usually expressed in terms of two constants, D_0 and $\mathbf{E}$, as follows:

$$D=D_0e^{-\mathbf{E}/RT}. \tag{1}$$

The theoretical diffusion coefficient for interstitial atoms in a cubic lattice has the form

$$D=\alpha a^2/\tau. \tag{2}$$

Here a is the lattice constant, τ is the mean time-of-stay in one interstitial position between jumps, and α is a numerical coefficient whose value depends upon the location of the interstitial positions. The values of α for face centered cubic (f.c.c.) and for body centered cubic (b.c.c.) lattices are computed in Section II and are listed in Table I. While our knowledge of the cohesive forces is not sufficient to permit an evaluation of the heat of activation $\mathbf{E}$, the constant D_0 may be estimated fairly accurately. Towards this end one observes that, at least over a limited temperature range, the mean time-of-stay τ has a heat of activation, i.e.,

$$\tau^{-1}=\tau_0^{-1}e^{-\mathbf{E}/RT}. \tag{3}$$

TABLE I. Diffusion constants.

Lattice type	B.C.C.	F.C.C.
α	1/24	1/12
n	4	12

The "constant" τ_0^{-1} is found in Section II to be given by

$$\tau_0^{-1}=n\nu e^{\Delta S/R}. \tag{4}$$

In this equation n is the number of nearest neighbor interstitial positions, ν is the frequency of vibration of a solute atom in an interstitial position, and ΔS is an entropy of excitation whose precise definition must be delayed until Section II. Corresponding to the interstitial positions being at the center of the unit cell and at the centers of the cube edges in a f.c.c. lattice, and at the center of the faces and edges of the unit cells in b.c.c. lattices,[1] the number of nearest neighbors is 12 and 4 for these two lattices, respectively. Upon comparing Eqs. (1)–(4), we obtain for D_0 the following theoretical equation

$$D_0=n\alpha e^{\Delta S/R}a^2\nu. \tag{5}$$

The only solution in which the constant D_0 has been measured accurately is that of carbon in γ-iron.[2] In the case of b.c.c. metals an alternative method is available for a test of the theoretical Eq. (4). In this method one studies the internal friction associated with the interstitial solute atoms, a type of internal friction which was first observed and correctly interpreted by Snoek.[1] From these internal friction measurements one finds directly the relaxation time τ_r for the establishment of an equilibrium distribution between the three types of interstitial positions, corresponding to the three principal axes along which the tetragonal axis of an interstitial position may lie. This relaxation time is equal to $1/\omega_m$, where ω_m is the angular frequency at which the internal friction is a maximum. It has been shown by Polder[3] that the time of relaxation τ_r is related to the mean time-of-stay τ by the relation

$$\tau=(\tfrac{3}{2})\tau_r. \tag{6}$$

From such internal friction measurements one may thus determine directly the mean time-of-stay τ, and may

*This research has been supported partially by the ONR, U.S.N. (Contract No. N-6ori-20-IV, Contract NR 015 018).

[1] J. Snoek, Physica 8, 711 (1941).
[2] C. Wells and R. Mehl, Trans. A.I.M.E. 140, 294 (1940).
[3] D. Polder, Philips Research Reports 1, 1 (1945).

TABLE II. Data relevant to diffusion.

System	C in γ−Fe	C in α−Fe			N in α−Fe		C in Ta	N in Ta	O in Ta
		Snoek[a,b]	Polder[c]	Present work	Snoek[a,b]	Present work			
D_0 (in cm /sec.)	0.07[d]	0.0005		0.008		0.0014	0.0018	0.29	0.030
τ_0^{-1} (in 10^{13} sec.$^{-1}$)	—	1.5		23[e]	0.29	3.7[e]	4.2[f]	640[g]	66[f]
E (in cal./mole)	32,000[d]	18,000		19,800	16,400	17,700	25,000	44,000	29,000
ν (in 10^{13} sec.$^{-1}$)	0.94	1.3		1.3	1.1	1.1	1.3	1.6	1.1
$\exp(\Delta S/R)$									
"empirical"	6	0.3		4	0.07	0.8	0.8	100	15
Theor. range	1–60	1–13		1–13	1–13	1–10	1–10	1–64	1–16

[a] See reference 1.
[b] See reference 5.
[c] See reference 3.
[d] See reference 2.
[e] This paper.
[f] See reference 10.
[g] See reference 8.

thereby effect a comparison with theory through use of Eq. (4).

The theoretical expressions (4) and (5) for τ_0 and for D_0 contain the factors ν and $\exp(\Delta S/R)$, the numerical values of which are rather uncertain. An estimate of the vibration frequency ν will be obtained through the assumption that as a solute atom moves from one interstitial position to an adjacent interstitial position, its potential energy varies in a simple sinusoidal manner. Thus if x is the coordinate along this path, we shall assume that

$$V(x)=(\tfrac{1}{2})E(1-\cos 2\pi x/\lambda), \tag{7}$$

where E is the height of the potential barrier, which may be taken as approximately equal to the heat of activation, and λ is the distance between the interstitial positions. The vibration frequency ν is then, according to this approximation, given by

$$\nu=(E/2m\lambda^2)^{\frac{1}{2}}. \tag{8}$$

The values so calculated are given in Table II. As mentioned above, the interstitial positions in b.c.c. lattices have tetragonal rather than cubic symmetry, and hence the vibrations of solute atoms are not isotropic within these positions. Since the paths leading from any given interstitial position to each of its four nearest neighboring interstitial positions lie in a plane normal to the tetragonal axis, the frequency ν defined by Eq. (8) refers to the frequency of that component of vibration resolved upon this plane.

From a consideration of the fact that the lattice has more strain energy when a solute atom is midway between two interstitial positions than when it is at an interstitial position, and of the fact that strain energy reduces the local elastic moduli of the lattice,[4] we anticipate that ΔS will be positive, and hence the entropy factor to be greater than unity. Comparison between theory and experiment can, therefore, best be obtained by inserting the empirical values of τ_0^{-1} or of D_0 into Eqs. (4) or (5), respectively, and then, using the above estimated value of ν, compute the entropy factor. The "empirical" entropy factor so obtained should be greater than unity but should be less than that value which would correspond to all the heat of activation E being in the form of lattice strain energy. This upper limit to the entropy factor is estimated in Section II.

The empirical values of the entropy factor, together with the theoretical range, are given in Table II. Only in the case of C in γ−Fe was D_0 determined directly from diffusion experiments. The value recorded refers to the limiting case of infinite dilution. The values of D_0 for C and N in α−Fe were deduced from magnetic measurements.[5] The values of D_0 for C, N and O in tantalum were obtained from internal friction measurements. When cognizance is taken of the fact that only a 2 percent error in the determination of E changes the empirical value of the entropy factor by a factor of 2, it is seen that only in the case of C in α−Fe is there a serious discrepancy between the empirical entropy factor and its theoretical range. The attempt to resolve this discrepancy instigated the experimental work reported upon in Section III. As therein described, these experiments demonstrate that at the carbon concentrations ($\sim$0.1 atomic percent) used, the jumping of the carbon atoms between adjacent interstitial positions cannot be described by a single time of relaxation, as was assumed in the original work. They further suggest that this anomalous behavior is due to the interaction of the solute atoms.

II. ANALYSIS

We shall first evaluate for f.c.c. and for b.c.c. lattices the numerical coefficient α in Eq. (2). Since the diffusion coefficient is a scalar in cubic systems, it suffices to consider that the concentration gradient is parallel to a principal axis, which will be denoted as the z axis. The plane $z=0$ will be chosen as lying in a (001) plane of atoms. We then denote by $n(r,t)$ the number of interstitial atoms per unit area of the r'th (001) plane above $z=0$. We shall further denote by 2β the probability that, when a solute atom jumps into a new interstitial

[4] C. Zener, Acta Cryst. 2, 163 (1949).

[5] J. L. Snoek, Physica 6, 591 (1939).

position, the jump will be into a new (001) plane. Then

$$n(r,t+\tau)=(1-2\beta)n(r,t)+\beta\{n(r+1,t)+n(r-1,t)\}.$$

If we now subtract $n(r,t)$ from both sides, and consider n to vary only very slightly during a time interval τ or from one (001) plane to an adjacent (001) plane, we obtain

$$\partial n/\partial t=(\beta/\tau)\partial^2 n/\partial r^2.$$

In both f.c.c. and in b.c.c. lattices the (001) planes are spaced $\frac{1}{2}a$ apart, and hence the atomic diffusion coefficient is given by

$$D=\beta a^2/4\tau.$$

From a consideration of the spacing of the interstitial positions we readily see that β is $\frac{1}{3}$ and $\frac{1}{6}$ for f.c.c. and b.c.c. lattices, respectively. We are thereby led to the values of α listed in Table I.

Since the jumping of a solute atom from one interstitial position to another may be regarded as one of the simplest examples of a rate process, it is natural to deduce the mean rate of jumping, $1/\tau$, from the standard rate theory developed by Eyring.[6] This theory gives

$$1/\tau=(nkT/h)P^*/P. \tag{9}$$

Here P^* is the partition function of the system of solute atom plus lattice, the solute atom being confined to move in a plane passing through the divide separating two interstitial positions, and oriented normal to the line joining the two interstitial positions. In the second partition function P no restraint is placed upon the solute atom. The dominant part of P will, therefore, arise from the region in the immediate vicinity of an interstitial position, where the forces may be regarded as harmonic. It is to be noted that P refers to one more degree of freedom than does P^*.

In order to obtain a ratio of partition functions having the same number of degrees of freedom, we make the approximation of separating P into two factors

$$P=P_v\cdot P_1^*,$$

where P_v is the partition function for a single linear oscillator, and where P_1^* is the partition function of the complete system with the solute atom constrained to move in a plane passing through an interstitial position. With this factoring of P Eq. (9) becomes

$$1/\tau=(nkT/hP_v)e^{-\Delta F/RT}, \tag{10}$$

where ΔF is the work required to transfer one gram

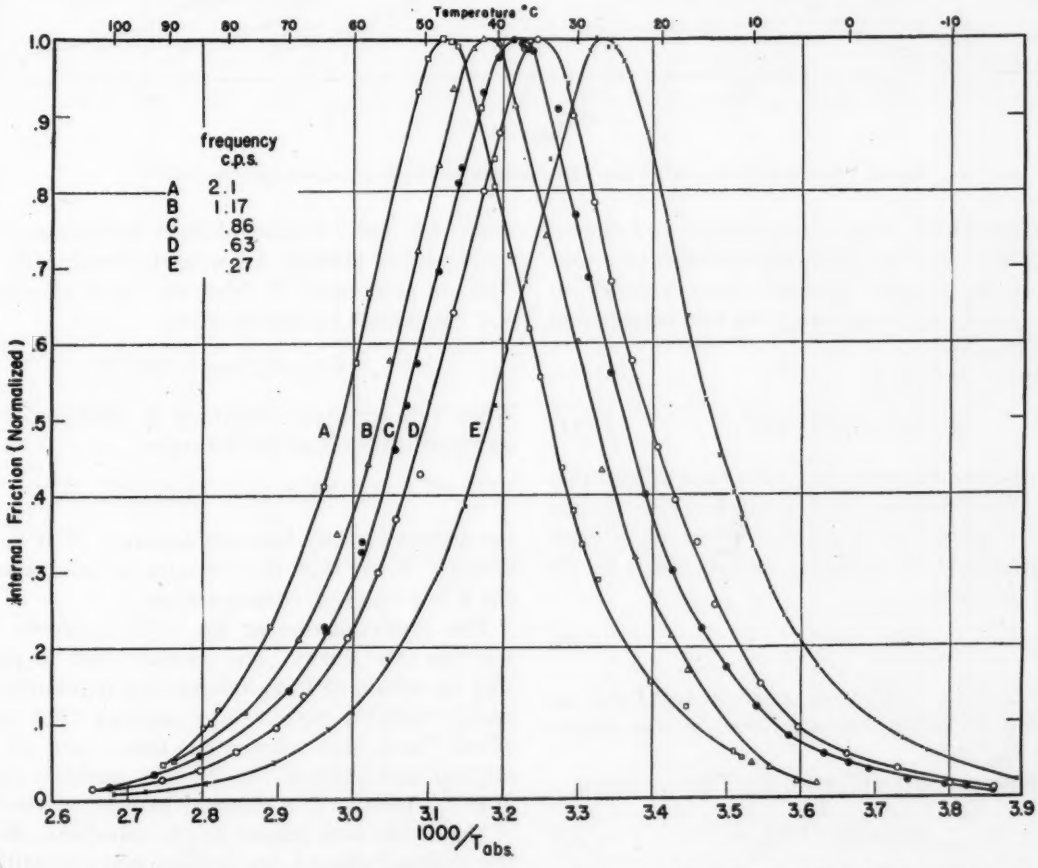

FIG. 1. Variation with temperature of internal friction of an iron specimen containing dissolved C at five frequencies of vibration.

[6] H. Eyring, J. Chem. Phys. 3, 107 (1932); Glasstone, Laidler, and Eyring, *The Theory of Rate Processes* (McGraw-Hill Book Company, Inc., New York, 1941), pp. 184–191.

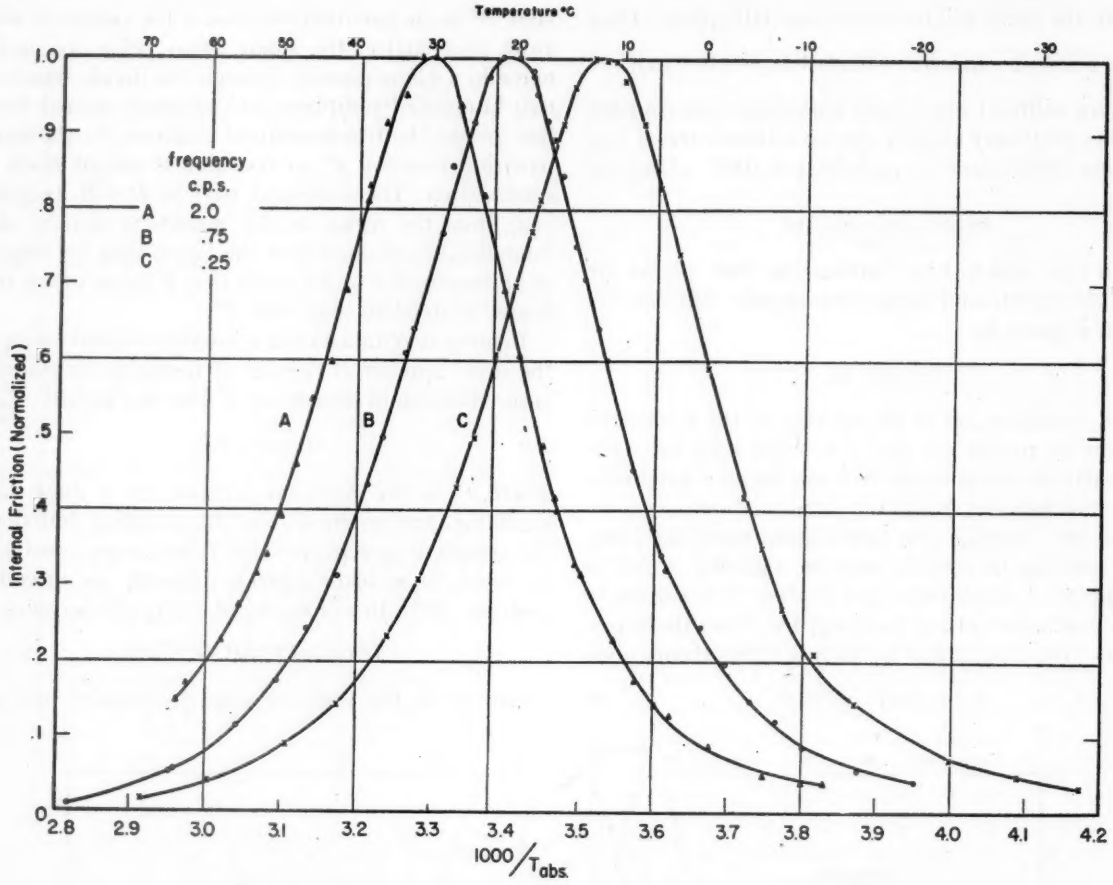

FIG. 2. Variation of internal friction with temperature for iron containing dissolved N.

mole of solute atoms from a constrained two-dimensional vibration about an interstitial position to a constrained two-dimensional vibration about a divide in a plane normal to the line joining the two neighboring interstitial positions.

Upon observing that

$$P_\nu^{-1}=2\sinh(h\nu/2kT), \tag{11}$$

where ν is the frequency of vibration of the solute atom in an interstitial position, and upon observing that in the cases of interest in this paper only a slight error will be introduced by replacing $\sinh(h\nu/2kT)$ by its argument, we obtain

$$kT/hP_\nu=\nu. \tag{12}$$

Even in the high degeneracy case of $h\nu/kT=2$, an error of only 18 percent is introduced by the simplification of Eq. (12).

Upon combining Eq. (12) with Eq. (10) we obtain

$$1/\tau=n\nu e^{-\Delta F/RT}. \tag{13}$$

This equation now reduces to Eqs. (3)–(4) when we write

$$\Delta F=\Delta E-T\Delta S,$$

where ΔE and ΔS have obvious interpretations, provided we can identify ΔE with the empirically defined "heat of activation" $\mathbf{E}$. Now the "heat of activation" of τ^{-1} is defined by the equation

$$\mathbf{E}=-Rd(\ln\tau^{-1})/d(1/T).$$

When this empirical definition is combined with the standard thermodynamic formula

$$\Delta E=d(\Delta F/T)/d(1/T),$$

the desired identity becomes apparent. It is to be particularly noted that this identity is valid whether or not $\mathbf{E}$ is a function of temperature.

The approximation of Eq. (12) is seldom used in reaction rate theory. The authors wish to point out that by refraining from making this approximation one merely deludes oneself into thinking that quantum effects have been adequately taken care of. In the original derivation of Eq. (9) one considers the solute atom to behave in a classical manner in the vicinity of the divide with respect to the coordinate describing the position along a line joining two interstitial positions. Quantum effects are, therefore, not adequately taken account of by merely retaining the quantum expression for the partition function corresponding to a

vibration near a minimum in the potential energy. While the first-order quantum effects at the divide may be estimated by the method introduced by Wigner,[7] such a refinement would not be justified at the present time in view of the other uncertainties in the theory.

Our final task in this section is an estimation of the entropy factor $e^{\Delta S/R}$ in Eq. (4). Towards this end we set

$$\Delta S = -\partial \Delta F/\partial T.$$

If all the work ΔF went into straining the lattice, then ΔF would have essentially the same temperature coefficient as the elastic moduli. An upper limit to ΔS is thus obtained by setting

$$\Delta S \simeq -\mathbf{E}(d \ln \mu/dT),$$

where μ is the shear modulus. Upon taking the values -0.00026[8] and -0.00020[9] for the temperature coefficients $d \ln \mu/dT$ of iron and tantalum, respectively, one obtains the upper limits to the entropy factors given in Table II.

III. EXPERIMENTS

The experimental work described in this section had as its aim the accurate determination of τ_0 and E. Once this was done, all the remaining empirical factors in Table II could be computed. For these measurements use was made of the internal friction peak arising from the stress induced redistribution in the three types of lattice sites of the interstitially dissolved atoms of C and N. It is well known that for an internal friction process involving a single relaxation time, the magnitude of the internal friction, Δ, is given by

$$\Delta = 2\Delta_0/[(1/\tau_r\omega)+\tau_r\omega], \tag{14}$$

where Δ_0 is the maximum magnitude of the internal friction. This maximum clearly occurs when the angular frequency, ω, of the impressed stress is equal to the reciprocal of the relaxation time, τ_r. While Δ_0 is but a slowly varying function of temperature, τ_r in this instance is expected to vary rapidly with temperature according to the equation

$$\tau_r = \tau_{r0} \cdot \exp(\mathbf{E}/RT). \tag{15}$$

The experimental work involved in the measurement of τ_{r0} and of $\mathbf{E}$ in Eq. (15) was the measurement of Δ *vs.* temperature at a number of frequencies with C or N in solid solution in the iron specimen. The method of measuring Δ was the same as that used previously in this laboratory for such determinations.[8,10] The speci-

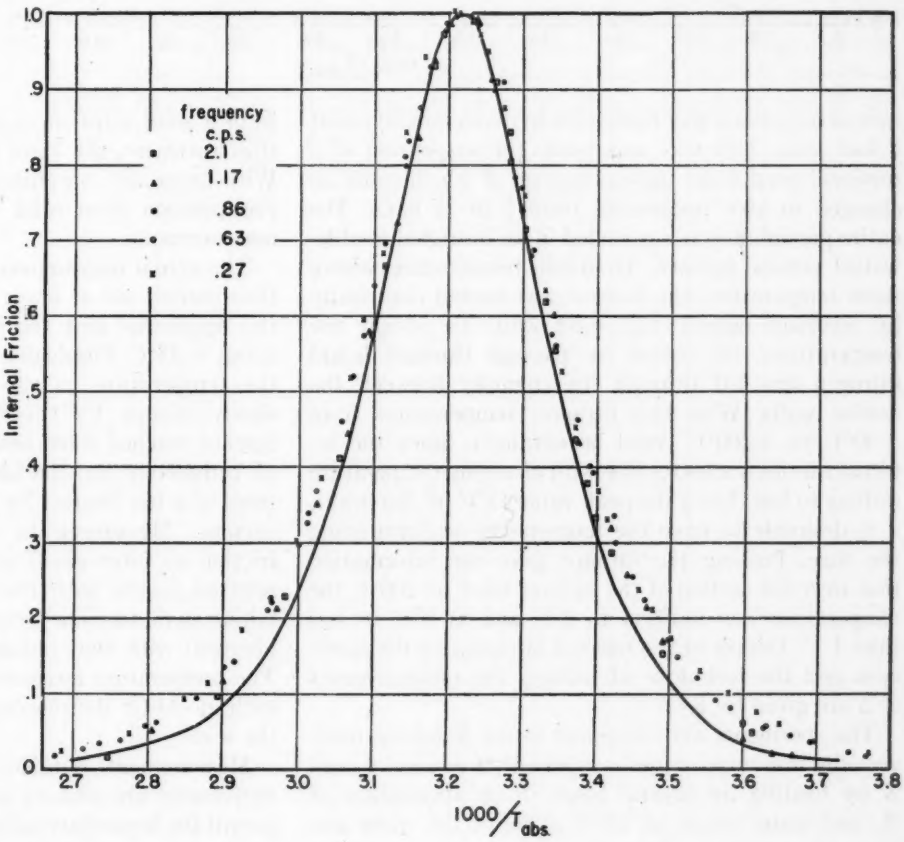

FIG. 3. Superposition of the internal friction peaks for C shown in Fig. 1. To avoid confusion about one-half of the points at the maxima of the curves shown in Fig. 1 have been omitted in this plot. The drawn curve is computed from Eqs. (14) and (15) with $\mathbf{E}_C$ = 19,800 cal./mol.

[7] E. Wigner, Phys. Rev. **40**, 749 (1932).
[8] T. S. Kê, Metals Tech. June, 1948, T.P. No. 2370.
[9] T. S. Kê, Phys. Rev. **74**, 914 (1948).
[10] T. S. Kê, Phys. Rev. **74**, 9 (1948).

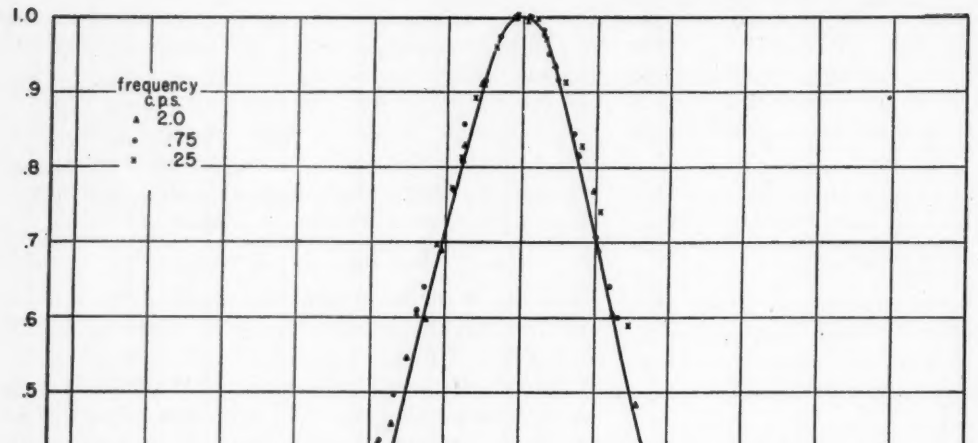

FIG. 4. Superposition of the internal friction peaks for N shown in Fig. 2. The drawn curve is computed from Eqs. (14) and (15) with $E_N = 1{,}7700$ cal./mol.

men of iron was a wire 0.026 inch in diameter and about 1 foot long. This wire was made the suspension of a torsional pendulum; the inertia arm of which could be changed to give frequencies from $\frac{1}{4}$ to $2\frac{1}{4}$ c.p.s. The entire pendulum was suspended in an insulated double-walled vertical furnace. To obtain temperatures above room temperature, the furnace was heated electrically by windings outside the outer wall. To obtain low temperatures, air cooled by passage through liquid nitrogen was led through the chamber between the double walls. With this furnace, temperatures from -30°C to $+200$°C could be obtained. Since the internal friction varies rapidly with changing temperature (falling to less than $\frac{1}{2}$ the peak value 15°C off the peak), it is desirable to have the temperature uniform along the wire. Probing the furnace gave the information that over the section of the furnace used, at 200°C the temperature was uniform to 2°C and at 0°C to less than 1°C. Details of the method of clamping the specimen and the technique of making the measurements of Δ are given by Kê.[8,10]

The specimens were prepared in the following manner: the iron wires were first cleaned of residual C and N by heating for several hours in an atmosphere of H_2 and water vapor at 720°C. One of the wires was heated in a mixture of dry H_2 and n-heptane at 720°C for two hours to form a solid solution of about .015 percent C in α-iron. The other wire was heated for three hours in a mixture of H_2 and NH_3 at 590°C to form a solid solution of about 0.015 percent N. After this treatment, the wires were quenched in cold water. With these low concentrations of solute, no observable precipitation from solid solution occurred during the measurements.

The actual measurement of the internal friction was then carried out at once. A specimen was mounted in the apparatus and the temperature was lowered to about -35°C. Gradually reducing the air flow allowed the temperature to rise to room temperature very slowly (about 1°C every five minutes). When the furnace reached room temperature, the air was turned off completely and the furnace was heated to 100°C in steps of a few degrees by gradually raising the furnace current. Measurements were made of the internal friction at intervals. Further measurements made at selected points with the temperature of the furnace falling again to room temperature gave data practically identical with that obtained with rising temperature. The temperature measurements themselves were made with an Al-Cr thermocouple placed near the center of the wire.

Measurements obtained for C and N at a number of frequencies are plotted in Figs. 1 and 2. These plots permit the immediate calculation of E using an equation amply discussed elsewhere.[9]

$$E = -R \cdot \left. \frac{d(\ln\omega)}{d(1/T)} \right|_{\Delta=\text{const.}} \tag{16}$$

To determine $\mathbf{E}$ from Figs. 1 and 2, plots were made of $\ln\nu$ *vs.* $1/T$ at $\Delta/\Delta_{max}=0.1$, $\Delta/\Delta_{max}=0.2$ etc., for both sides of the internal friction peak. While each set of points lay on a straight line, the slopes of these lines showed a consistent variation, increasing slightly in passing from the extreme left to the extreme right side of the internal friction curve. The average of these slopes was substituted into Eq. (16), yielding for the effective heats of activation $\mathbf{E}_C$ the value 19,800±400 and for $\mathbf{E}_N$ the value 17,700±400 cal/mole. From these values of E and from an observation of τ_{r0}, the position of the maximum at a given frequency, the value of τ_0 was computed. For nitrogen τ_{r0} is determined to be 1.8×10^{-14} sec., hence τ_0^{-1} in Table II is 4×10^{13} sec.$^{-1}$. For carbon τ_{r0} is 2.92×10^{-15} sec., hence τ_0^{-1} is 2.3×10^{14} sec.$^{-1}$. It is to be observed that the estimated errors in the determination of E lead to large errors in the determination of τ_0^{-1} and hence in the calculation of D_0 and $e^{\Delta S/R}$. Thus D_0 and $e^{\Delta S/R}$ are possibly in error by a factor of 2.

The values of $\mathbf{E}_C$ and of $\mathbf{E}_N$ previously determined by Snoek[1] were significantly smaller, being 18,000 and 16,200, respectively, and hence led to estimated values of D_0 about 10 times smaller than those estimated from our experiments. Snoek determined these values originally by magnetic relaxation measurements, and later found these values to be in fair agreement with his internal friction measurements, but stated that slightly higher values would have been in better agreement.

If the internal friction were accurately described by Eqs. (14) and (15), then on a plot of Δ *vs.* $1/T$ it should be possible to superpose all the curves by shifting them on the $1/T$ axis. Further, all the curves should fit a curve computed using Eq. (15) with a value for E as determined above. Such plots are shown in Figs. 3 and 4. It is seen that for both C and N the experimental points lie significantly outside the computed curves. This slight excess in the breadth of the experimental curves over that of the theoretical curve finds a ready interpretation in a possible slight dispersion of relaxation times. Such a dispersion would indicate that all the interstitial positions were not quite energetically equivalent, and hence either that the lattice contains imperfections, or that the solute atoms interact with one another. This interpretation is strengthened by the observation that the experimental curves lie closer to the theoretical curve the higher the frequency of vibration, and hence the higher the average temperature during a run. A higher temperature will reduce any tendency of the solute atoms to cluster about lattice imperfections or about one another. The same type of discrepancy between the experimental and ideal single relaxation-time internal friction curves were found by Kê[8,10] in his study of C, N and O in tantalum. It is interesting to observe that the order C, N and O is both the order for an increasing discrepancy and for an increase in concentration, as measured by the peak in the internal friction curve. This coincidence indicates that, at least in tantalum, interaction between solute atoms is responsible for the discrepancy, rather than lattice imperfections. Such an interaction is consistent with the strong attraction between interstitial solute atoms in b.c.c. lattices found by one of the authors.[11]

[11] C. Zener, Phys. Rev. **74**, 634 (1948).

Interaction between Elementary Particles. Part I

ALFRED LANDÉ
Mendenhall Laboratory, Ohio State University, Columbus, Ohio

(Received June 13, 1949)

An elementary particle is considered as a mathematical point which under an invariant law of communication involving a universal length a establishes a primary potential in space-time. Due to the peculiar communication law, $r^2-c^2t^2+a^2=0$ or $S^2=0$, in contrast to the light signal law $R^2=0$, the primary potential is without singularity at $r=0$. It becomes the background of a regular electrodynamic or mesonic field and automatically yields a finite radius a to the charge distribution, with a density falling off as $(a/r)^5$ at larger distances. The potentials of different particles are additive so that all quantities obey the superposition law. The total force on the Nth particle is produced under the same invariant communication law $S=0$ by integration of the force density k_N over the volume elements of the instantaneous rest system. K_N is the resultant of mutual and self-forces, $K_N=S_MK_{MN}$. Only retarded field interaction is admitted between different particles. The original production of the self-charge by the center and its force reaction on the center is derived from a heuristic scheme involving half-retarded, half-advanced potentials, as a substitute for the instantaneous reaction between the "parts" of a charge. In the dynamics of the particle a variable "acceleration mass" of field origin is added to the mechanical mass. An experimental determination of mass differences under various very high accelerations could reveal the unknown ratio between the field mass and the mechanical mass of a charged particle.

1. POINT PARTICLE *VERSUS* FINITE RADIUS

THERE are two ways of approaching the problem of elementary particles and their fields. When it became obvious that the primitive model of a charged ball was incompatible with relativistic dynamics, one turned to point particles as primary sources in spite of the field singularity at $r=0$. The last twenty years have seen heroic efforts of removing the divergencies inherent in the fields of point charges, first by arbitrarily cutting off undesirable terms, and lately by systematic elimination methods. Nevertheless, to many it seemed appropriate to construct a theory which would never introduce a cause for divergencies at least in the classical domain rather than to rely on laborious elimination methods at a later stage.

Dirac[1] tried to remove the point singularity from the very outset by assuming an effective potential equal to half the difference between retarded and advanced potential as responsible for the self-force of the electron. Dirac's theory led to an ever increasing self-acceleration of an isolated electron, and to a premonitory acceleration under an incoming light impulse due to signal communication *faster* than the velocity of light. Wheeler and Feynman in their absorber theory of radiation[2] assume half the sum of the retarded and advanced potential to be effective between *different* particles, maintaining that an accelerated isolated electron would not suffer a self-force at all.

The second approach, through unitary field theories, strives to replace the arbitrary construction of finite balls of charge by modified field equations which automatically produce stable charge concentrations of finite radius. The most famous of these attempts, the Born-Infeld theory[3] (1934) replaces the linear Maxwell scheme by non-linear field equations involving a basic length a. The same a then becomes the width of the resulting field maximum. However, non-linear theories in which resonance depends not only on frequency but also on amplitude, are unwieldy to quantization. Furthermore, the lack of superposition makes it impossible to define the individual fields of various particles at close distance from one another.

The following attempt of establishing an invariant theory of interaction between particles including self-reaction is related in various respects to the aforementioned theories, but tries to avoid some of the difficulties of the latter. Similar to Born-Infeld, we obtain a particle of finite electric radius a in an invariant fashion without introducing a special structural hypothesis; yet the linearity and superposition of the ordinary Maxwell field equations is not abandoned. Second, similar to Dirac, we admit advanced as well as retarded potentials for the communication "inside" of the particle, and retarded potentials for the interaction between different particles; but instead of half the difference we use half the sum of the two self-potentials, and yet we obtain a finite self-energy as well as a finite mutual energy between particles even at distances $r \ll a$ and $r=0$. It was Dirac's half-difference which seemed objectionable to Wheeler and Feynman until they were able to show that Dirac's results are derivable from their assumption of half the sum of the two potentials. In contrast to W. and F., however, we use only *retarded* potentials for the interaction between different particles and admit a self-force also for an isolated particle.

2. THE SIGNAL EQUATION OF A POINT PARTICLE

Let us start with an analogy. When a particle is tested as to the simultaneous values of its energy and

[1] P. A. M. Dirac, Proc. Roy. Soc. **167**, 148 (1938).
[2] J. A. Wheeler and R. P. Feynman, Rev. Mod. Phys. **17**, 157 (1945).
[3] M. Born and L. Infeld, Proc. Roy. Soc. **142**, 410 (1934); **144**, 425 (1934); **147**, 522 (1934); **150**, 141 (1935).

momentum, e.g., by its Compton reaction to photons, then various E and p values are found to satisfy the relation

$$p^2-(E/c)^2+b^2=0, \quad (b=m_0c), \tag{1}$$

and the particle is said to have rest mass $m_0=b/c$. We know that particles exist which satisfy this relation, although with different values of the constant b. Figure 1 shows the two hyperbolic surfaces in E/c, p space with the gap $2b$ between positive and negative E/c-values. The 3-dimensional p-space is continuous.

We now propose an analogous definition of a point particle in space-time:

When effects or "potentials" are received in a variety of world points r, t related by the equation

$$r^2-(ct)^2+a^2=0, \quad \text{or} \quad S^2=0 \quad (a=\text{signal radius}), \tag{2}$$

when these effects have their common source in a point particle located in the world point 0 ($r=t=0$). Figure 2 shows the two hyperbolic signal surfaces of the past and future characterizing a particle of signal radius a. Of course we do not know whether elementary particles actually possess signal surfaces $S=0$ rather than light cones $R=0$; yet Eq. (2) would be the simplest invariant way of introducing a finite radius a and eliminating divergencies without resorting to a structural hypothesis or to non-linear field equations. Equation (2) was first proposed by the author[4] in 1939 under the impression of Born's *Principle of Reciprocity*.

As seen from Fig. 2 there is an initial time lag, $t=a/c$, for signals or "potentials" emerging from the point particle even to reach the immediately surrounding points $r=0$. The communication time to distances r in general is $t=1/c[r^2+a^2]^{\frac{1}{2}}>r/c$ with asymptotic value $t=r/c$ for $r\gg a$. The "phase velocity" with which points along a radius are passed is $dr/dt=c[1+(a/r)^2]^{\frac{1}{2}}$, faster than c. Yet since this sudden spurt of communication over a range of order a (which is responsible for the lack of infinities at $r=0$) starts only after the initial time lag, the total time for a signal to reach a point r is always longer than r/c so that *the signal velocity is less than c.*

3. THE MAXWELL FIELD

Before applying the signal Eq. (2) to the theory of electric particles we comment on the Maxwell-Lorentz theory in general. An electromagnetic field F containing a continuous charge-current density J can be derived from a 4-potential ϕ, satisfying the Lorentz condition $\mathrm{Div}\phi=0$, in the following fashion. The 6-vector F is obtained as

$$F=\mathrm{curl}\phi, \tag{3}$$

from which the first Maxwell couple follows as an *identity*. The 4-vector J is *defined* as

$$4\pi J=\Delta ivF, \tag{4}$$

which is the same as the second Maxwell couple; the latter thus is but a *definition* of J in terms of F, in accordance with the experimental procedure. From (4) follows the continuity equation of J as an identity. Equation (4) may also be written as

$$4\pi J=-\Box^2\phi. \tag{5}$$

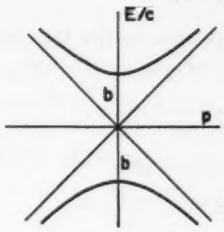

FIG. 1.

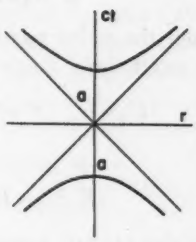

FIG. 2.

At last, the 4-vector Lorentz force density and work rate density of the field is defined as

$$k=[J, F], \tag{6}$$

from which follows the identity $k=-\Delta ivT$ where T is the symmetric stress-energy-momentum tensor of the field. These equations, or rather *definitions* in terms of the original 4-vector ϕ, hold for any divergenceless function $\phi(x_1\cdots x_4)$. One also may reverse the potential Eq. (5) to

$$\phi=-\frac{1}{\pi}\int(Jd\Sigma/R^2), \tag{7}$$

where $d\Sigma=dx_1\cdots dx_4$ and R is the world distance between $d\Sigma$ and the field point. Whenever a J-distribution is given which satisfies the Maxwell theory, i.e., which is derived from any function ϕ with $\mathrm{Div}\phi=0$, then this J may conversely be considered as a source "producing" a potential ϕ according to (7) with light velocity retardation ($R=0$).

We now introduce a special choice for the field potential ϕ surrounding an elementary *point particle* moving with any variable velocity $U_k=dx_k/d\tau$ ($\tau=$proper time) on any world line. If the point particle were a point charge $+\epsilon$ one would choose the Liénard-Wiechert potential

$$\phi=\mp\epsilon\left[\frac{U}{(R\cdot U)}\right]_{R=0}, \tag{8}$$

whose Div vanishes, but which is singular at the point charge. We replace (8) by

$$\phi=\mp\epsilon\left[\frac{U}{(R\cdot U)}\right]_{S=0}, \tag{9}$$

whose Div also vanishes. The subscript $S=0$ indicates that the primary potential ϕ in various world points is established by the point particle with a time retardation

[4] A. Landé, Phys. Rev. **56**, 482 (1939). J. Frank. Inst. **231**, 63 (1941).

(or advancement in case of the lower sign) according to Eq. (2).

Once this potential is established it produces, or defines, a perfectly normal Maxwellian field sustaining a certain charge distribution J. In this Maxwell field (7) is still the inversion of (5).

4. STATIC SOLUTION

When the point particle is at rest in the 0-point of space at all times t' one has $U_1=U_2=U_3=0$, and

$$\left.\begin{aligned} U_4=ic,\quad S^2=0=r^2-c^2(t-t')^2+a^2,\\ \text{hence}\\ R_4=ic(t-t')=\pm i(r^2+a^2)^{\frac{1}{2}},\\ (R\cdot U)=R_4U_4=\pm c(r^2+a^2)^{\frac{1}{2}}. \end{aligned}\right\} \tag{10}$$

The scalar electric potential $\varphi=\phi_4/i$ and the density ρ become

$$\varphi=\frac{\epsilon}{(r^2+a^2)^{\frac{1}{2}}},\quad \rho=\frac{\epsilon}{4\pi}\frac{3a^2}{(r^2+a^2)^{5/2}} \tag{11}$$

regular at $r=0$. At a large distance from the point particle (which is not a point charge) the condition $S=0$ is identical with $R=0$ so that our results coincide with those of point charges in the limit of $r\gg a$. The result (11) is the first test passed by the theory. It holds for retarded as well as advanced effects, and also for half their sum. (Half the difference would yield $\varphi=0$ and $\rho=0$ everywhere; we therefore reject this possibility.)

A nucleon of "charge" g may become the source of a *meson field* derivable from the primary potential

$$\phi=g\mp[U/(R\cdot U)\exp\{(R\cdot U)\kappa/c\}]_{S=0}. \tag{12}$$

In the static example (10) it yields

$$\varphi=g/(r^2+a^2)^{\frac{1}{2}}\exp\{-(r^2+a^2)^{\frac{1}{2}}\kappa/c\}. \tag{12'}$$

5. THE FORCE DENSITY ON THE SELF-CHARGE

If we assume that the charge-current density J_N which the Nth particle surrounds itself is obtained from half the sum of retarded and advanced potentials (9), as a substitute for the instantaneity within a point charge, we obtain in various space-time points:

$$\phi_N{}^{\text{self}}=\tfrac{1}{2}(\phi_{N,\text{ret}}{}^{\text{self}}+\phi_{N,\text{adv}}{}^{\text{self}})=\text{self-potential} \tag{13}$$

$$F_N{}^{\text{self}}=\tfrac{1}{2}(F_{N,\text{ret}}{}^{\text{self}}+F_{N,\text{adv}}{}^{\text{self}})=\text{self-field} \tag{13'}$$

$$J_N=\tfrac{1}{2}(J_{N,\text{ret}}+J_{N,\text{adv}})=\text{current density}. \tag{13''}$$

Only the resulting J_N is used further on, namely, as a source of an ordinary *retarded* potential ϕ_N and field $F_N=\text{Curl}\phi_N$. The same J_N is the source of ϕ_N but half a source, half a sink of $\phi_N{}^{\text{self}}$. ϕ_N, and F_N are "physical," i.e., derived from J_N, $\phi_N{}^{\text{self}}$ and $F_N{}^{\text{self}}$ "virtual," i.e., constructed as a heuristic scheme for deriving J_N.

Force and work rate density are defined in the Maxwell-Lorentz theory as $k=[J,F]$. Correspondingly when F is the total physical field $=S_MF_{MN}+F^{\text{ext}}$ we define the force density k_N which ultimately contributes to the total force K_N on the Nth particle

$$k_N=\tfrac{1}{2}k_{N,\text{ret}}+\tfrac{1}{2}k_{N,\text{adv}} \tag{14}$$

according to the division of J_N in two parts in (13''). Here we have

$$k_{N,\text{ret}}=[J_{N,\text{ret}},F] \tag{15}$$

and similarly $k_{N,\text{adv}}$. Another possibility would be to assume that the total force is the charge multiplied by the field at the point particle itself.

So far, this theory may be summarized as follows. In order to surround a point particle with a finite charge-current density J_N dependent on the world line of the center, we introduce a heuristic Maxwellian scheme involving retarded and advanced potentials and leading to $\phi_N{}^{\text{self}}$ and $F_N{}^{\text{self}}$ and then to J of (13''). The latter, irrespective of its mode of calculation,* becomes the source of an ordinary *retarded* potential ϕ_N and a corresponding field F_N, differing from the "virtual" $F_N{}^{\text{self}}$. The physical F_N alone produces, when acting on the J_M of another particle, a contribution K_{NM} to the force on the latter.

5. THE SELF-FORCE ON A PARTICLE

When asking for the self-force and work rate K_N on the Nth particle, it is logical that the k_N-contributions in the surrounding volume elements should react on the center according to the same communication law, $S=0$, which the center originally employed in establishing J_N. We tentatively define the four components of $K_N{}^0$ in the instantaneous rest system of the center by an integral of $k_N{}^0$ over the volume elements dV^0 of the same rest system:

$$K_N{}^0=\int[k_N{}^0]_{S=0}dV^0. \tag{16}$$

More specifically we assume that $k^0{}_{N,\text{ret}}$ is reported to the center in an advanced fashion, and $k^0{}_{N,\text{adv}}$ in a retarded way:

$$K_N{}^0=\frac{1}{2}\int\{[k^0{}_{N,\text{ret}}]_{\text{adv}}+[k^0{}_{N,\text{adv}}]_{\text{ret}}\}dV^0, \tag{17}$$

with the integrand given in (15) or (15') or (15''). This definition provides a maximum of simultaneity in spite of the finite communication velocity to and from the center. K_N is clearly divided into self-, mutual, and pure field contributions:

$$K_N=K_{1N}+K_{2N}+\cdots K_{NN}+\cdots+K_N{}^{\text{ext}}. \tag{18}$$

K_{MN} depends only on the world lines of the particles M and N.

The (apparent) trouble with the above definition (17) is that the fourth component of $K_N{}^0$ which repre-

* $\phi_N{}^{\text{self}}$ is defined by means of the rule $S=0$. Yet the relation between $\phi_N{}^{\text{self}}$ and J, as well as between J and ϕ is that of a communication law $R=0$.

sents i times the work rate of the field on the particle, may have a finite value even in the instantaneous rest system of the center, which is not the rest system of the surrounding J_N distribution. Of course, $K_4{}^0$ vanishes in static examples and in case of a constant acceleration. However, during times of a varying acceleration (in general, when there are non-vanishing odd order time derivatives of the acceleration), the field works on the particle even in the instantaneous rest system of the center. The particle then accumulates the well-known "acceleration energy" (G. E. Schott[5]) which is carried along by the particle and contributes to its inertia. During times of decreasing acceleration

The equations of motion of a particle with τ=proper time are

7. DYNAMICS

The equations of motion of a particle with τ=proper time are

$$dP/d\tau=K, \tag{19}$$

where K now is the 4-vector of force work rate resulting from both mechanical and field forces, and P is the momentum-energy vector of the particle satisfying the invariant relation $P^2+(m_0c)^2=0$. Since the work rate may possess a finite value even in the instantaneous rest system of the particle, the scalar m_0 is not a constant but rather a function of the proper time τ along the world line, representing mechanical plus variable "acceleration mass." When splitting P in two factors, namely, a scalar m_0 and a 4-vector acceleration $dU/d\tau$, (19) becomes

$$m_0(dU/d\tau)+U(dm_0/d\tau)=K. \tag{20}$$

In the instantaneous rest system where $(U_4)^0=ic$ and $(dU_4/d\tau)^0=0$ the four components of (20) read

$$[m_0(dU_1/dt)]^0=(K_1)^0,\ \cdots,\ [ic(dm_0/dt)]^0=(K_4)^0. \tag{21}$$

The four right-hand sides are sums of external mechanical plus self- and mutual field forces (the field forces depend only on the world lines. On the left of (21) one has the "unknowns" m_0, $U_1U_2U_3$ and their derivatives with respect to the time. Finding solutions in a system of several particles, each subjected to four equations of the form (21) is a matter of great complexity. Our aim was only that of deriving the field forces consisting of self- and mutual parts in a system of charged particles led along *prescribed* world lines.

8. CONCLUDING REMARKS

We have attempted to consider particles as mass points which react on each other at a distance through forces calculated by means of an intermediate kinematic scheme representing a superposition of self and mutual fields. Essentially this is a *unitary theory* of interaction between particles in which the fields are subordinate entities with no degrees of freedom of their own (unless one admits also pure fields in superposition).

Radiation theory rests on the dualistic view of particles and field representing separate entities, with a mutual perturbation energy being responsible for acts of emission and absorption. This view can be applied also to our theory as an approximation, when regarding the combined field of other particles as an "external pure field." In this approximation the potential energy-momentum of the particle, instead of being the product $(\epsilon\phi\cdot U)$ at the place of the center, will be an integral over the distribution of $(J\cdot\phi)$ in space. In case of an external field of wave-length $\lambda\ll a$ the resulting perturbation energy will be much smaller than in case of a point charge, and the integration over the whole radiation spectrum will behave as though it were cut off at wave-lengths $\lambda\sim a$.

[5] G. E. Schott (Cambridge University Press, London, 1912). Refer also to the remarks of Dirac, reference 1, p. 155.

On the Use of Subtraction Fields and the Lifetimes of Some Types of Meson Decay

J. STEINBERGER*
The Institute for Advanced Study, Princeton, New Jersey
(Received June 13, 1949)

The method of subtraction fields in current meson perturbation theory is described, and it is shown that it leads to finite results in all processes. The method is, however, not without ambiguities, and these are stated. It is then applied to the following problems in meson decay: Decay of a neutral meson into two and three γ-rays, into a positron-electron pair, and into another neutral meson and photon; decay of a charged meson into another charged meson and a photon, and into an electron (or μ-meson) and neutrino. The lifetimes are tabulated in Tables I, II and III. The results are quite different from those of previous calculations, in all those cases in which divergent and conditionally convergent integrals occur before subtraction, but identical whenever divergences are absent. The results are discussed in the light of recent experimental evidence.

I. INTRODUCTION

RECENTLY Pauli and Villars[1] have shown that it is possible in electrodynamics to make the self energy of the light-quantum zero, by the use of some formal subtraction methods. One of these may most easily be understood as consisting in the introduction of several fictitious subtraction fields in addition to the electron-positron field. The idea, which is due to Rivier and Stücklberg,[2] is the following: The matrix element contains an infinite integral over the momenta of the intermediate virtual electron-positron pairs which are responsible for the self energy. To this matrix element are added and from it subtracted several others for the same process, in which however the virtual pairs have different masses. Since the infinities have the same structure, it is possible to choose the number and masses of the additional fields so as to make the expression converge. In the case of the photon self-energy, the conditions which are necessary to bring convergence are also sufficient to make it vanish. One may regard this procedure as a subtraction method; no real processes involving these additional fictitious fields, such as their self energy, or scattering are considered, and one requires the masses of the extra fields to be very large. It is also possible to treat the other infinite quantities[3] in electrodynamics, the electron self-energy, and the charge renormalizations in the same way. However, this is academic, since one may disregard them, finite or infinite. In meson theories this is not so. Divergencies of a sort that cannot be removed by name-calling occur,[4] especially the decay of mesons into other particles via an intermediate Fermi-Dirac (nucleon) field. We discuss these processes in this paper.

* Present address: University of California, Berkeley, California.
[1] W. Pauli and F. Villars, Rev. Mod. Phys. **21**, 433 (1949).
[2] D. Rivier and E. C. G. Stücklberg, Phys. Rev. **74**, 218, 986 (1948).
[3] It has been shown by F. J. Dyson, Phys. Rev. **75**, 486 (1949), that all the infinite quantities in the perturbation theory of quantum electrodynamics are either of the form of a correction to the mass of the electron or to its charge.
[4] Divergences of this sort have been exhibited by K. M. Case, Phys. Rev. **75**, 1440 (1949), in the calculation of the magnetic moment of nucleons due to their tensor coupling to a vector meson field.

II. SUBTRACTION FIELDS

Since it is very convenient in these and other field theoretical problems to use the Feynman diagrams,[5] the reader is assumed to be familiar with this mode of computation. It is equivalent to the older methods. For purposes of illustration, consider the disintegration of a scalar meson into two lighter scalar mesons, via an intermediate neutron field, and the scalar interaction. The Feynman diagrams are as follows:

The initial meson, of four-momentum k makes a neutron-anti-neutron pair; then either the neutron or the anti-neutron can radiate the meson k_1, before the particles annihilate with the production of the other meson k_2. The two matrix elements are

$$\frac{gg'^2}{(8E_kE_{k_1}E_{k_2})^{\frac{1}{2}}}\int\frac{d^4p}{(2\pi)^4}Sp \times\frac{[(p_\mu+k_{1\mu})\gamma_\mu+im][p_\nu\gamma_\nu+im][(p_\omega-k_{2\omega})\gamma_\omega+im]}{(p^2+m^2)[(p+k_1)^2+m^2][(p-k_2)^2+m^2]}$$

$$+\text{same term with } k_1,\ k_2 \text{ interchanged}$$

$$=\frac{gg'^2}{(2E_kE_{k_1}E_{k_2})^{\frac{1}{2}}}\int\frac{d^4p}{(2\pi)^4}(im) \times\frac{[3p^2+2p(k_1-k_2)-m^2-k_1\cdot k_2]}{(p^2+m^2)[(p+k_1)^2+m^2][(p-k_2)^2+m^2]}.$$

The integral is logarithmically divergent. However, if it is now regarded as a function of m, the virtual nucleon mass, and we subtract and add other nucleon fields of much larger mass, m_i (m_0 is the mass of the neutron), the sum will be finite provided $\sum_i m_iC_i=0$. $C_i=\pm1$ and indicates whether the ith field is to be added or subtracted. However, there will be a term left of the form $\sum_i C_im_i\ln m_i$, which becomes infinite as the m_i ($i\neq0$) are made large, unless it is required that $\sum C_im_i\ln m_i=\text{const}$. This constant seems to be arbitrary, and as long as it is so, the subtraction is not

[5] F. J. Dyson, Phys. Rev. **75**, 486 (1949).

FIG. 1.

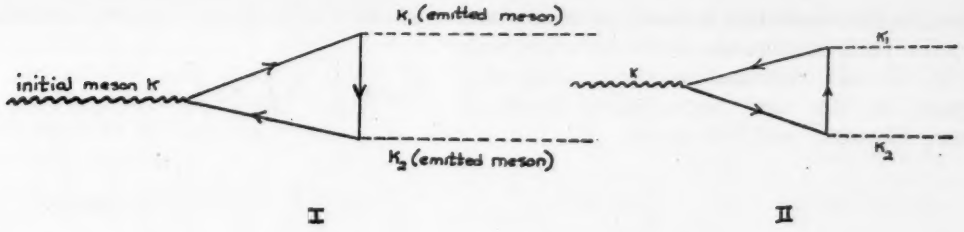

unique. In the following, it has been taken to be zero. This has the intuitively correct result that the final convergent matrix element will be small, if the intermediate mass m is large.

All infinities in field theory are similar to that of this example. Somewhere in the Feynman diagram there is a closed loop which gives rise to the infinite integral. Furthermore this loop contains a world line which begins and ends in the loop. In the above example this was the neutron line, in the case of the neutron self energy this is the meson line. The infinite integrals are either logarithmically, linearly, or quadradically divergent. They are always made finite by requiring a sufficient number of the following conditions for the masses of the additional fields of the type whose line begins and ends in the loop.

1. $\sum C_i=0$,
2. $\sum C_i m_i=0$,
3. $\sum C_i m_i^2=0$,
4. $\sum C_i \ln m_i=0$,
5. $\sum C_i m_i \ln m_i=0$,
6. $\sum C_i m_i^2 \ln m_i=0$.

Condition 1 has been used by Feynman. Pauli has required conditions 1 and 3 in the treatment of the photon self energy, and conditions 1 and 4 in the calculation of the electron self energy. Different problems require different conditions, but conditions 1–6 may be simultaneously fulfilled and always suffice.

As already pointed out in the example, the constant (zero in 4, 5, and 6) in the logarithmic condition is arbitrary although the choice which is made here is the simplest and leads to intuitively correct results.

If one applies this procedure to all virtual fields, then all Feynman diagrams give independently finite results. This is illustrated on a more complicated diagram:

It represents the scattering of a nucleon by another, through the intervention of two types of mesons, of mass κ and μ. There are two loops I_1 and I_2, giving rise to a divergent double integral. The only lines which begin and end in the same loop are those of the meson μ. The subtraction method described here requires that this matrix element be supplemented by $(n+1)^2-1$ others, in which the masses of the two intermediate μ-mesons range independently from 0 to n. One really should increase the number of diagrams still more, by also allowing the mass of the κ-meson to range over its values. However in the limit of large mass κ all such diagrams give the result zero, and one is left just with those diagrams in which the mass of the κ-meson is κ_0. Now all those diagrams are considered separately in which one of the μ-mesons, say the bottom one, has fixed mass μ_i and the top μ-meson mass runs from 0 to n. The integral I_1 is then finite, and if now μ_i is allowed to assume all its values, the double integral becomes finite. One then permits the extra masses μ_i, $i\neq 0$ to become very large and the matrix element becomes independent of them.

It does not seem possible, however, to put the method into Hamiltonian form, and this is so because some of the extra fields must be subtracted rather than added. It is rather an algorithm, defined only in terms of perturbation theory. There are no equations of motion, and therefore no rigorous solution with which the perturbation approximation can be compared. This has as its consequence that some results which follow immediately in the Hamiltonian formalism have to be reexamined. One of these, the unitarity of the "S" matrix, still holds true, and so do gauge and Lorentz invariance. Furthermore, because the formalism is convergent throughout, these properties cannot be lost during the calculation. How they may otherwise be lost in processes in which infinities occur is shown by Wentzel[6] in a calculation of the photon self-energy.

Although gauge invariance, Lorentz invariance and probability conservation are maintained in this subtraction procedure, at least one theorem, that of the equivalence of pseudoscalar and pseudovector coupling of the pseudoscalar meson to the nucleon, is not. It is lost for those processes which are convergent with pseudoscalar coupling, but divergent with pseudovector coupling before subtraction. For these cases the ordinary proof of equivalence is not rigorous, since divergent expressions occur. It is perhaps a serious difficulty, and does not seem to be connected with the lack of uniqueness of the logarithmic conditions. Of course, the equivalence is maintained for all those processes in which both couplings give convergent results before subtraction.

In this paper the word divergent is applied indiscriminately to all integrals which do not have a unique value regardless of whether or not it is possible to obtain finite values by choosing special integration

FIG. 2.

[6] Gregor Wentzel, Phys. Rev. 74, 1070 (1948).

procedures. In this connection it should be pointed out that *all* infinities or ambiguities of this sort which are present in the old perturbation theory find their counterparts in the new perturbation theory of Tomonaga,[7] Feynman[8] and Schwinger.[9]

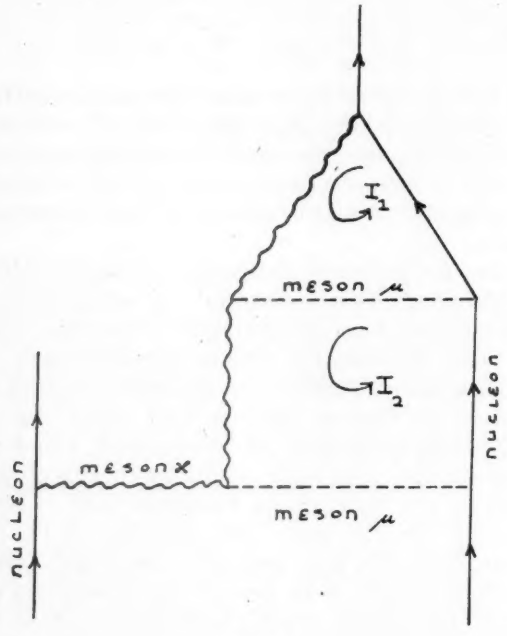

FIG. 3.

III. SOME MESON DECAYS NOT INVOLVING THE FERMI COUPLING OF THE NUCLEONS

The notation and the equations of motion are given in an appendix. Here it may suffice to point out that natural units are used, and that heavyside units are used throughout except for the electromagnetic field. There $e^2=1/(137)^{\frac{1}{2}}$. The nucleon-meson coupling constants have been left explicitly in the results; their values are not known because of the well-known failure of meson theory in the quantitative analysis of the nuclear force problem. However, they are believed to be of order of magnitude 1.

(A) Decay of a Neutral Scalar Meson into 2 Photons[10]

(1) Scalar meson with scalar coupling.

$$M=\frac{ge^2}{(2\kappa)^{\frac{1}{2}}\pi^4}A_\mu(k_1)A_\nu(k_2)[I_{\mu\nu}+J_{\mu\nu}],$$

where

$$I_{\mu\nu}=m\int_0^1 dx\int_0^x dy\int d^4p \times\frac{\{[m^2+p^2-\kappa^2y(1-x)]\delta_{\mu\nu}-4p_\mu p_\nu\}}{[p^2+m^2-\kappa^2y(1-x)]^3},$$

$$J_{\mu\nu}=\frac{-\kappa^2m}{2}\left(\delta_{\mu\nu}+\frac{2k_{1\nu}k_{2\mu}}{\kappa^2}\right)\int_0^1 dx\int_0^x dy\int d^4p \times\frac{1-4y(1-x)}{[p^2+m^2-\kappa^2y(1-x)]^3}.$$

The quantities k_1 and k_2 are the photons which appear as decay products; $k=k_1+k_2$ is the momentum of the decaying meson. $J_{\mu\nu}$ is convergent but $I_{\mu\nu}$ converges only conditionally. We therefore use the subtraction field technique. Regard M as a function of m and add and subtract auxiliary matrix elements such that condition (2) $\sum C_im_i=0$ is fulfilled. This suffices to determine M uniquely. $J_{\mu\nu}$ is unchanged in the limit of large masses. The formerly divergent part of $I_{\mu\nu}$, which is now finite, is

$$\int_0^1 dx\int d^4p\sum m_iC_i\frac{(p^2\delta_{\mu\nu}-4p_\mu p_\nu)}{[(p^2+m_i^2)-\kappa^2y(1-x)]^3}=0$$

the remaining part of I

$$\sum C_im_i\int_0^1 dx\int_0^x dy\int d^4p\frac{[m_i^2-\kappa^2y(1-x)]}{[p^2+m_i^2-\kappa^2y(1-x)]^3} =\frac{\pi^2}{2}\sum m_iC_i\int_0^1 dx\int_0^x dy=\frac{\pi^2}{4}\sum m_iC_i=0.$$

So that $I_{\mu\nu}=0$.

As was pointed out by Fukuda and Miyamoto,[11] the same result may be obtained by an application of the principle of gauge invariance as a help in evaluating the integral. If $A_\mu(k_1)$ and $A_\nu(k_2)$ are permitted to undergo gauge transformations:

$$A_\mu(k_1)\rightarrow A_\mu'(k_1)+k_{1\mu}\Lambda(k_1),$$
$$A_\nu(k_2)\rightarrow A_\nu'(k_2)+k_{2\nu}\Lambda(k_2),$$

the principle of invariance requires

$$k_{1\mu}(I_{\mu\nu}+J_{\mu\nu})=k_{2\nu}[I_{\mu\nu}+J_{\mu\nu}]=0,$$

now $k_{1\mu}J_{\mu\nu}=k_{2\nu}J_{\mu\nu}=0$ already, since

$$k_{1\mu}\left(\delta_{\mu\nu}+\frac{2k_{1\nu}k_{2\mu}}{\kappa^2}\right)=0=k_{2\nu}\left(\delta_{\mu\nu}+\frac{2k_{1\nu}k_{2\mu}}{\kappa^2}\right)$$

[7] S. Tomonaga, Prog. Theor. Phys. **1**, 27 (1946). Koba, Tati, and Tomonaga, Prog. Theor. Phys. **2**, 101 (1947); **2**, 198 (1947). S. Kanesawa and S. Tomonaga, Prog. Theor. Phys. **3**, 1 (1948).

[8] R. P. Feynman, Phys. Rev. **76**, 748 (1949).

[9] J. Schwinger, Phys. Rev. **74**, 1439 (1948); **75**, 651 (1949).

[10] J. R. Oppenheimer was the first to point out that present theory requires the γ-instability of neutral mesons coupled to nucleons. The calculations were first made by R. Finkelstein, Phys. Rev. **72**, 415 (1949).

[11] Fukuda and Miyamoto, Prog. Theor. Phys. (in press), were the first to notice that the old results were not gauge invariant. Their work formed the starting point of this research. I wish to thank H. Yukawa for making their results available to me before publication.

if one just remembers that $k^2=-\kappa^2=(k_1+k_2)^2=2k_1\cdot k_2$. So we must demand $k_{1\mu}I_{\mu\nu}=k_{2\nu}I_{\mu\nu}=0$. Now $I_{\mu\nu}$ is a function of m and κ only, and therefore must be $I_{\mu\nu}=f(\kappa,m)\delta_{\mu\nu}$ and $k_{1\nu}f(\kappa,m)=0$ requires $f(\kappa,m)=0$; $I_{\mu\nu}=0$. With both methods we have the result:

$$M=\frac{ge^2}{4\pi^2}\left(\frac{\kappa}{2}\right)^{\frac{1}{2}} mA_\mu(k_1)A_\nu(k_2)\left(\delta_{\mu\nu}+\frac{2k_{1\nu}k_{2\mu}}{\kappa^2}\right)$$
$$\times\int_0^1 dx\int_0^x dy\frac{1-4y(1-x)}{m^2-\kappa^2y(1-x)}$$

and from this the lifetime

$$\tau^{-1}\approx g^2e^4/\pi_3(\kappa/12m)^2\kappa=8\times10^{13}g^2\text{ sec.}^{-1}.$$

Here, as in all the following calculations, this is the first non zero term in an expansion in κ/m. κ is taken to be $300m_e$.

(2) Decay of pseudoscalar meson into two photons via pseudoscalar coupling.

$$M=\frac{mge^2}{\pi^4}\left(\frac{\kappa}{2}\right)^{\frac{1}{2}}\mathbf{k}_1\cdot\mathbf{A}_1\times\mathbf{A}_2\int_0^1 dx\int_0^x dy\int d^4p$$
$$\times\frac{1}{[p^2+m^2-\kappa^2y(1-x)]^3}.$$

This is uniformly convergent, gauge invariant and unchanged by the subtraction fields.

$$\tau^{-1}\cong\frac{g^2e^4}{\pi^3}\left(\frac{\kappa}{8m}\right)^2\kappa=1.8\times10^{14}g^2\text{ sec.}^{-2}$$

(3) Decay of pseudoscalar meson into two photons via pseuodovector coupling.

$$M=\frac{fe^2}{2\pi^4(2\kappa)^{\frac{1}{2}}}A_\mu(k_1)A_\nu(k_2)\int d^4p$$
$$\times\frac{\frac{1}{4}\,\mathrm{Tr}\gamma_5\gamma_\alpha\gamma_\beta\gamma_\mu\gamma_\nu p_\beta k_{2\alpha}}{[(p+k_2/2)^2+m^2][(p-k_2/2)^2+m^2]}$$
$$+\frac{\frac{1}{4}\,\mathrm{Tr}\gamma_5\gamma_\alpha\gamma_\beta\gamma_\mu\gamma_\nu k_{1\alpha}p_\beta}{[(p+k_1/2)^2+m^2][(p-k_1/2)^2+m^2]}$$
$$-\frac{m^2\,\mathrm{Tr}\gamma_5\gamma_\alpha\gamma_\beta\gamma_\mu\gamma_\nu k_{1\alpha}k_{2\beta}}{(p^2+m^2)[(p+k_1)^2+m^2][(p-k_2)^2+m^2]}.$$

Of the three terms in the integral, the first two are only conditionally convergent, and the convergent last term is the term required by the theorem of equivalence of pseudoscalar and pseudovector coupling.[12] However, if subtraction fields are used, not only do the first two terms converge (to zero), but the last term is changed, so as to destroy the equivalence between the two types of coupling. The condition needed for convergence is (1) $\sum C_i=0$. Then

$$M=\sum C_i\frac{2fe^2}{(2\kappa)^{\frac{1}{2}}\pi^2}\int_0^1 dx\int_0^x dy\frac{\kappa\mathbf{k}_1\cdot\mathbf{A}_1\times\mathbf{A}_2}{[1-\kappa^2/m_i^2y(1-x)]}$$
$$\cong\frac{2fe^2}{(2\kappa)^{\frac{1}{2}}\pi^2}\frac{\kappa^2\kappa}{m^2}\frac{\mathbf{k}_1\cdot\mathbf{A}_1\times\mathbf{A}_2}{24},$$

$$\tau^{-1}=\frac{f^2e^4}{\pi^3}\left(\frac{\kappa}{m}\right)^4\frac{\kappa^3}{(24)^2}=(\kappa f)^2\times5.5\times10^{10}\text{ sec.}^{-1}$$

from the third term alone, without subtraction fields, we would get

$$\tau^{-1}\cong(2mf)^2\frac{e^4}{\pi^3}\left(\frac{\kappa}{8m}\right)^2\kappa=(2mf)^2\times1.8\times10^{14}\text{ sec.}^{-1}$$

in agreement with the equivalence theorem.

In this case it is, therefore, possible to derive two plausible results. The equivalence theorem is of course not rigorously valid here, since, because of the divergence of the pseudovector case, the arguments can be carried through only formally. However, it is a strong argument against this subtraction procedure that it does not maintain such general theorems. On the other hand, the result obtained on the basis of equivalence is also questionable, since it is independent of the mass of the intermediate nucleons, whereas intuitively we require longer lifetimes with heavier nucleons.

(4) Scalar meson with vector coupling, vector meson with both types of coupling.

These transitions are forbidden by the charge conjugation theorem of Furry.[13]

(5) Pseudovector meson with pseudovector coupling.

The matrix element of this process is infinite, but becomes finite and gauge invariant by the subtraction of fields obeying (1) $\sum C_i=0$; the result is zero for both longitudinal and transverse modes of the photon. It is not difficult to prove that the transition is forbidden in all orders of the mass ratio and coupling constants.**

(B) Decay of the Vector Meson into Three Photons

The matrix element is conditionally convergent. The integral is made convergent on the introduction of the subtraction fields. It can then be seen from gauge invariance arguments that the first non-vanishing term in the matrix element occurs in 4th order of the mass ratio. The matrix element for this process resembles very

[12] The equivalence of pseudoscalar and pseudovector coupling has been discussed by E. Nelson, Phys. Rev. **60**, 830 (1941); F. J. Dyson, Phys. Rev. **73**, 929 (1948) and K. M. Case, Phys. Rev. **76**, (1949).

[13] W. H. Furry, Phys. Rev. **51**, 125 (1937).

** *Note added in proof.*—It has been proven by E. Wigner that the two photon decay of the vector meson of either parity is forbidden by angular momentum conservation arguments. I am indebted to Professor Wigner for a private communication.

much that for the scattering of light on light; there also, for small momenta of the light quanta, the first non-vanishing term is of the fourth-order in the ratio of energy of light quantum to electron mass. Because of the difficulty of the problem we content ourselves with an order of magnitude estimate.

$$M\approx\frac{ge^3}{(\kappa)^{\frac{1}{2}}\pi^2}\frac{\kappa}{m^4}[\mathbf{k}_1\cdot\mathbf{k}_2\mathbf{A}_2\cdot\mathbf{A}_1\mathbf{A}_3\cdot\mathbf{k}_1-\mathbf{k}_1\cdot\mathbf{A}_2\mathbf{k}_2\cdot\mathbf{A}_1\mathbf{k}_1\cdot\mathbf{A}_3],$$

where we have assumed one of the two possible gauge invariant forms for the matrix element, and neglected possible numerical factors except the factors of π, which are easy to determine.

$$\sum M^2=\frac{8g^2e^6\kappa|\mathbf{k}_1|^2|\mathbf{k}_2|^3}{M^8|\mathbf{k}_3|^3}(1+2\cos^2\theta-5\cos^4\theta+2\cos^6\theta),$$

where $\cos\theta=\mathbf{k}_1\cdot\mathbf{k}_2/|\mathbf{k}_1||\mathbf{k}_2|$,

$$\tau^{-1}=\frac{8g^2e^6}{6\pi m^8}\int d\mathbf{k}_1\int d\mathbf{k}_2\int\frac{d\mathbf{k}_3}{(2\pi)^5}\delta_4(k_1+k_2+k_3-k)$$

$$\times\frac{k_1^3k_2^3}{k_3}(1+2\cos^2\theta-5\cos^4\theta+2\cos^6\theta)$$

$$\cong\frac{g^2e^6}{\pi}\left(\frac{\kappa}{m}\right)^8\kappa\times10^{-5}=5\times10^3g^2\text{ sec.}^{-1}.$$

This is a very long lifetime, about $(\kappa/m)^8$ longer than the previous result of Finkelstein.[10] In Finkelstein's calculation the questionable convergence of the integrals was put into the background. It is then not surprising that the result is not gauge invariant and certainly wrong.

For the vector meson with tensor coupling the lifetime should be of the same order of magnitude. For the pseudovector meson this process is forbidden by an analog of Furry's theorem. Since the two photon decay was already shown to be forbidden the first allowed transition is the 4 photon decay, with a somewhat longer lifetime than $10^{-3}\ g^{-2}$ sec.$^{-1}$.

(C) Decay of a Neutral Meson into Positron and Electron

A neutral meson may decay into a positron and electron by disintegrating into a virtual proton-antiproton pair. The pair annihilates with the emission of a virtual photon. The photon then disappears while creating the electron-positron pair. The processes are badly divergent, but made convergent by a liberal application of conditions 1–6. The results are given in Table I. It should be noted that the lifetime of the vector meson for this process is much shorter than its γ-decay lifetime, but that the pseudovector meson decay is forbidden. The most probable decay for the neutral pseudovector meson would seem to be into one quantum and an electron-positron pair.

IV. DECAY OF A CHARGED MESON INTO A NEUTRINO, AND EITHER ELECTRON OR SPIN ½(μ) MESON

Because of its coupling to the nucleon field, and the Fermi coupling of the nucleons to the electron neutrino fields, a π-meson should be unstable against β-decay. Furthermore, it is not known if the μ-meson is coupled to the π-meson directly, or through the mediation of a Fermi coupling of the μ-meson, neutrino fields to the nucleons. In the latter case the $\pi-\mu$, ν-decay lifetime should be calculable in terms of the nuclear force constant g and the rate of κ-capture of μ-mesons. Unfortunately, perturbation theory for these roundabout transitions yields infinite results. The method of subtraction fields has therefore been used to calculate the lifetimes of such decays of Bose particles into two Fermi particles via an intermediate Fermi-Dirac field. The results for several types of π-mesons and Fermi couplings are given in Table II.

V. DISCUSSION OF THE RESULTS

Since the validity of the method has already been analyzed, we confine ourselves here to a discussion of the results on the assumption that the method is correct, in order of magnitude.

The calculations on the γ-instability of neutral mesons show that both scalar and pseudoscalar mesons can decay very quickly ($10^{-10}-10^{-14}$ sec.) into two photons, but that vector mesons decay into three photons with a long lifetime ($\sim10^{-3}$ sec.) and that pseudovector meson decay into two or three photons is forbidden, and the 4 photon decay has an even longer lifetime. This should be compared with the observations on γ-rays at Berkeley.[14] Photons of energy in the

TABLE I. Two photon decay and electron-positron decay of neutral mesons.

Type of meson and coupling	Two-photon decay lifetime	Electron-positron decay lifetime
Scalar meson Scalar coupling	$\tau^{-1}=\frac{g^2e^4}{\pi^3}\left(\frac{\kappa}{12}\right)^2$ $=8\times10^{13}\ g^2$ sec.$^{-1}$	forbidden
Scalar meson Vector coupling	forbidden	$\tau^{-1}=e^4(\kappa f)^2\left(\frac{\kappa}{m}\right)^4\frac{\kappa}{450\times(2\pi)^2}$ $=8.7\times10^{10}(\kappa f)^2$ sec.$^{-1}$
Pseudoscalar meson Pseudoscalar coupling	$\tau^{-1}=\frac{g^2e^4}{\pi^3}\left(\frac{\kappa}{8m}\right)^2\kappa$ $=1.8\times10^{14}\ g^2$ sec.$^{-1}$	forbidden
Pseudoscalar meson Pseudovector coupling	$\tau^{-1}=\frac{g(\kappa f)^2}{\pi^3}e^4\left(\frac{\kappa}{m}\right)^4\frac{\kappa}{(24)^2}$ $=5.5\times10^{11}(\kappa f)^2$ sec.$^{-1}$	forbidden
Vector meson Vector coupling	forbidden	$\tau^{-1}=e^4g^2\left(\frac{\kappa}{m}\right)^4\frac{\kappa}{(2\pi)^5\times675}$ $=5.7\times10^{10}\ g^2$ sec.$^{-1}$
Pseudovector meson Pseudovector coupling	forbidden	forbidden

[14] H. York and B. Moyer, Phys. Rev. **76**, 187 (1949).

TABLE II. Lifetime for the decay of a meson of mass $300m_e$ into a meson of spin $\frac{1}{2}$ and mass 200, and a neutrino, or into an electron and a neutrino, via the fermi coupling of the nucleon. The value of g_f is taken in accord with the tritium-helium 3 β-decay. $\tau_{\mu\nu}$ = mean lifetime of the $\pi\to\mu$, ν-decay. $\tau_{e\nu}$ = mean lifetime of the $\pi\to e$, ν-decay $f=\frac{1}{2}-\frac{1}{2}\left(\frac{\kappa}{m_\mu \text{ or } m_e}\right)^2$.

Type of Fermi coupling				
Scalar	Vector	Tensor Scalar meson, scalar coupling	Pseudoscalar	Pseudovector
$\tau^{-1}=g^2g_f^2\left(\frac{\kappa}{m}\right)^4\left(\frac{\kappa}{2\pi}\right)^5\frac{f^2}{400}$	forbidden	$\tau^{-1}=g^2g_f^2\left(\frac{\kappa}{m}\right)^4\left(\frac{\kappa}{2\pi}\right)^5\frac{f^2}{25}$	forbidden	forbidden
$\tau_{e\nu}=0.16\ g^{-2}$ sec.		$\tau_{e\nu}=1.0\times10^{-2}\ g^{-2}$ sec.		
$\tau_{\mu\nu}=0.54\ g^{-2}$ sec.		$\tau_{\mu\nu}=3.3\times10^{-2}\ g^{-2}$ sec.		
Pseudoscalar meson, pseudoscalar coupling				
forbidden	forbidden	forbidden	$\tau^{-1}=g^2g_f^2\left(\frac{\kappa}{m}\right)^4\left(\frac{\kappa}{2\pi}\right)^5\frac{f^2}{3600}$	$\tau^{-1}=g^2g_f^2\left(\frac{\kappa}{m}\right)^2\frac{\kappa^5}{(2\pi)^5}\frac{(1-2f)}{36}f^2$
			$\tau_{e\nu}=1.5\ g^{-2}$ sec.	$\tau_{e\nu}=0.37\ g^{-2}$ sec.
			$\tau_{\mu\nu}=4.9\ g^{-2}$ sec.	$\tau_{\mu\nu}=3.1\times10^{-2}\ g^{-2}$ sec.
Pseudoscalar meson, pseudovector coupling				
forbidden	forbidden	forbidden	$\tau^{-1}=g^2g_f^2\left(\frac{\kappa}{m}\right)^2\frac{\kappa^7}{(2\pi)^5}\frac{f^2}{900}$	$\tau^{-1}=g^2g_f^2\left(\frac{\kappa}{m}\right)^4\frac{\kappa^7}{(2\pi)^5}f^2\frac{(1-2f)}{900}$
			$\tau_{e\nu}=.010/(\kappa g)^2$ sec.	$\tau_{e\nu}=3.3\times10^{-4}/(\kappa g)^2$ sec.
			$\tau_{\mu\nu}=.033/(\kappa g)^2$ sec.	$\tau_{\mu\nu}=2.8/(\kappa g)^2$ sec.
Vector meson, vector coupling				
forbidden	$\tau^{-1}=\frac{g^2g_f^2}{225}\left(\frac{\kappa}{m}\right)^4\left(\frac{\kappa}{2\pi}\right)^5f^2\frac{(3-2f)}{3}$	$\tau^{-1}=\frac{g^2g_f^2}{9}\left(\frac{\kappa}{m}\right)^2\frac{\kappa^5f^2}{(2\pi)^5}(3-4f)$	forbidden	forbidden
	$\tau_{e\nu}=0.32\ g^{-2}$ sec.	$\tau_{e\nu}=1.0\times10^{-4}$ sec.		
	$\tau_{\mu\nu}=0.73\ g^{-2}$ sec.	$\tau_{\mu\nu}=4.7\times10^{-4}$ sec.		

neighborhood of 70 Mev are observed to come from the target of the cyclotron. Now if the decay of a meson of mass $300m_e$ were into three or more photons, then the energy of each photon would be smaller on the average. Furthermore, the lifetime would be so great that the meson would decay at a great distance (many meters) from the target, and consequently not be observed. If these interpretations of the experiments and the theory are correct, one is led to conclude that these neutral mesons are either of the scalar or pseudoscalar type.

The disintegration of the π-meson into electron and neutrino or μ-meson and neutrino is also interesting in the light of recent experiments. It is known that the μ-decay of the π-meson proceeds at least by a factor $\sim$100 more rapidly than its β-decay. Now the two constants which enter into the π-meson β-decay are known approximately: g from the strength of the nuclear forces and g_f from the β-decay of light nuclei. Previously the calculations were hampered by the divergences, but conventional momentum cut-off procedures,[15] give a lifetime for the process about the same as the experimental $\pi-\mu$-decay time, 10^{-8} sec. However, the more definite calculations made here and listed in Table III give much longer values, therefore disposing of this difficulty.

In the case of the coupling of the π-meson to the μ-meson one has 3 experimental data: (1) the rate of $\pi-\mu$-decay (2) the rate of μ-capture from the κ-orbit of a nucleus (3) the strength of nuclear forces. Previously it has been considered possible to explain the experiments in two ways.

1. The π-meson is coupled to the nucleons, and the nucleons to the μ-meson-neutrino field. The π-meson then decays via intermediate nucleon pairs, and μ-capture is direct.

2. The π-meson is coupled to both nucleons and to the μ-meson-neutrino field. $\pi-\mu$, ν-decay is then a direct process, but μ-capture is via an intermediate π-meson field. The $\pi\to\mu$, ν-decay in case 1 suffers from the infinity difficulties, but its order of magnitude had been estimated by cutting off at large momenta. Because the value of the π-nucleon coupling constant g is so near to unity, both pictures had been about equally successful in agreeing with experiment. However, if one accepts the subtraction methods here described, the $\pi\to\mu$, ν-decay lifetime in picture 1 becomes much too long compared to μ-capture, and only picture 2 which contains no infinities and is unaffected by these results, is consistent.

I am in great debt to the physicists at the Institute for Advanced Study for their generous help, especially to Drs. K. M. Case, F. J. Dyson, N. Kroll, J. R. Oppenheimer, A. Pais, S. Power, F. Rohrlich and H. Yukawa. The investigation was materially advanced by a grant-in-aid from the Institute. The money for this grant comes from the AEC .

APPENDIX

1. Units, notation, equations of motion. Natural units are used.

$\hbar=c=1$; $e=1/(137)^{\frac{1}{2}}$.
M = matrix element.

[15] R. Christy, Seminar at the Institute for Advanced Study, April, 1949.

m = nucleon mass.
κ = mass of the decaying meson.
μ = mass of the product meson, if any.
$\psi(x)$ = nucleon wave function.
$\bar{\psi}(x)=\psi^*(x)\gamma_4$.
γ_μ, $\mu=1, 2, 3, 4=4$ Dirac matrices, $\gamma_5=\gamma_1\gamma_2\gamma_3\gamma_4$.
$\phi(x)$, $\phi^*(x)$ = meson wave functions.
$A_\mu(x)$ = electromagnetic 4 potential.
$k=4$ momentum.
$\mathbf{k}=3$ momentum.
$A_\mu(k)=1/V\int_V A_\mu(x)e^{-ik_\nu x_\nu}d_3x$,
= fourier component of vector potential.
$\partial_\mu=\partial/\partial x_\mu-ieA_\mu$.

The Lagrangians are the following

(a) Proton, field, $L=\bar{\psi}(x)(\gamma_\mu\partial_\mu+m)\psi(x)$.
(b) Free neutron field, $L=\bar{\psi}(x)(\gamma_\mu(\partial/\partial x_\mu)+m)\psi(x)$.
(c) Free electromagnetic field,

$$L=-\frac{1}{8\pi}\left(\frac{\partial A_\mu}{\partial x_\nu}-\frac{\partial A_\nu}{\partial x_\mu}\right)\left(\frac{\partial A_\mu}{\partial x_\nu}-\frac{\partial A_\nu}{\partial x_\mu}\right).$$

(d) Free neutral scalar or pseudoscalar meson field,

$$L=-\frac{1}{2}\left[\frac{\partial\phi}{\partial x_\mu}\frac{\partial\phi}{\partial x_\mu}+\kappa^2\phi^2(x)\right].$$

(e) Free neutral vector meson field,

$$L=-\frac{1}{2}\left[\frac{1}{2}\left(\frac{\partial\phi_\mu}{\partial x_\nu}-\frac{\partial\phi_\nu}{\partial x_\mu}\right)\left(\frac{\partial\phi_\mu}{\partial x_\nu}-\frac{\partial\phi_\nu}{\partial x_\mu}\right)+\kappa^2\phi_\mu\phi_\mu\right].$$

(f) Free charged scalar or pseudoscalar field,

$$L=-\left[\frac{\partial\phi^*}{\partial x_\mu}\frac{\partial\phi}{\partial x_\mu}+\kappa^2\phi^*\phi\right].$$

(g) Free charged vector field,

$$L=-\left[\frac{1}{2}\left(\frac{\partial\phi_\mu^*}{\partial x_\nu}-\frac{\partial\phi_\nu^*}{\partial x_\mu}\right)\left(\frac{\partial\phi_\mu}{\partial x_\nu}-\frac{\partial\phi_\nu}{\partial x_\mu}\right)+\kappa^2\phi_\mu^*\phi_\mu\right].$$

(h) Interaction between neutral scalar mesons and protons,

$$L=-g\phi(x)\bar{\psi}(x)\psi(x).$$

(i) Interaction between neutral pseudoscalar meson and proton,

$$L=-ig\phi(x)\bar{\psi}(x)\gamma_5\psi(x)-if(\partial\phi/\partial x_\mu)\bar{\psi}(x)\gamma_5\gamma_\mu\psi(x).$$
$$\gamma_5=\gamma_1\gamma_2\gamma_3\gamma_4.$$

(j) Interaction between neutral vector field and proton,

$$L=-g\phi_\mu(x)\bar{\psi}(x)\gamma_5\psi(x).$$

(k) Interaction between charged scalar meson and nucleon,

$$L=-g\phi(x)\bar{\psi}(x)\tau\psi(x)-g\phi^*(x)\bar{\psi}(x)\tau^*\psi(x).$$

(l) Interaction between charged pseudoscalar meson and nucleon,

$$L=-ig\phi(x)\bar{\psi}(x)\gamma_5\tau\psi(x)-ig\phi^*(x)\bar{\psi}(x)\gamma_5\tau^*\psi(x)$$
$$-if(\partial\phi/\partial x_\mu)\bar{\psi}(x)\gamma_5\gamma_\mu\tau\psi(x)$$
$$-if(\partial\phi^*/\partial x_\mu)(x)\bar{\psi}(x)\gamma_5\gamma_\mu\tau^*\psi(x).$$

(m) Interaction between charged vector meson and nucleon,

$$L=g\phi_\mu(x)\bar{\psi}\gamma_\mu\tau\psi-g\phi_\mu^*(x)\bar{\psi}(x)\gamma_\mu\tau^*\psi.$$

(n) Scalar Fermi interaction of nucleons,

$$L=g_f\bar{\psi}\tau\psi\vec{\phi}\tau^*\phi+g_f\bar{\psi}\tau^*\psi\vec{\phi}\tau\phi$$

Domain Structures and Phase Transitions in Barium Titanate*,**

P. W. FORSBERGH, JR.
Laboratory for Insulation Research, Massachusetts Institute of Technology, Cambridge, Massachusetts
(Received May 5, 1949)

The arrangements of domains that arise in single crystals of barium titanate in the ferroelectric tetragonal phase have been studied in detail. The domains are the result of tetragonal (101) twinning, and appear by the formation of wedge-shaped laminar domains between two converging (101) twin planes. The distance of penetration of thin wedge-shaped laminae into the crystal follows changes in an applied electric field reversibly. Often thin laminae extend through the thickness of a crystal plate at an angle of 45° to the surface. These laminae frequently advance in groups in the two perpendicular directions parallel to the edges of the rectangular plate. As a result of the intersections of these groups, the domain pattern becomes an array of laminated and unlaminated pyramids and tetrahedra, the birefringence properties of which give rise to net-like patterns of multicolored squares in polarized light. The evidence indicates that the square-net pattern is an arrangement of twinning reducing as much as possible the total energy of lattice strains. These strains are probably due to an inhomogeneous distribution of impurities causing a bending effect, as in a bimetallic disk.

A preliminary investigation of the phase transitions near 5°C and −70°C has been completed. Using clearly defined optical observations, we conclude that the crystal is orthorhombic *Cmm* between 5°C and −70°C, and trigonal *R3m* below −70°C, with the lattice stretched along the polar axis. The twinning is identified in terms of these lattices. It is maintained that the transitions near 5°C and −70°C can only be of the first order, in contrast with the λ-transition at 120°C. While a statistical mechanical treatment of the properties of barium titanate would be exceedingly difficult, a definite qualitative thermodynamic correlation of its properties has been made. Due to the piezoelectric "interaction," the free energy can be visualized in the ferroelectric states in terms of a simultaneous polarization and lattice deformation. The overall situation may be regarded as one in which a ferroelectric λ-transition from the (ordered) cubic phase can, in principle, take place along any direction of the highly symmetric cubic lattice, but subject to anisotropy effects which favor the [100] directions down to 5°C, the [110] directions between 5°C and −70°C, and the [111] directions below −70°C.

SINCE the peculiar dielectric behavior of barium titanate was first noticed by Wainer and Salomon[1] and the ferroelectric nature of the material established by research in this laboratory[2] and independently in Russia,[3] extensive progress has been made in the study and application of titanate ceramics. As important milestones may be mentioned: the determination of the Curie point at 120°C as a transition from cubic to pseudo-cubic and the discovery of two additional phase transitions near 5°C and −70°C[2]† (Fig. 1); the accurate determination of the temperature variation of the tetragonal c/a ratio between 120°C and 5°C by Megaw[4] (Fig. 2) showing that the change from cubic to tetragonal is a transition of the λ-type; and the inducement of a piezoeffect in the ceramic by a polarizing field, discovered by Roberts[5] in this laboratory.

The fundamental research efforts here then turned mainly to the study of single crystals, after a way of growing small crystals from ternary melts was found in Switzerland by Blattner, Matthias, Merz, and Scherrer.[6,7] Matthias and von Hippel[8] found that domains exist in the ferroelectric form of barium titanate. These domains could be seen in polarized and unpolarized light and changed in their number, size and orientation by electric fields, temperature, pressure and the prehistory of the crystal. An external field of sufficient intensity could produce a single domain. Lowering the temperature through the transitions near 5°C and −70°C did not affect the ferroelectric nature of the crystal, but seemed to affect the position of the optic axis. Minima were found in the piezoelectric resonances at the transitions, and the dielectric constant along the a-axis was found larger than along the c-axis.

The present writer then began the study of the structure and laws of formation of the various domain patterns, and the nature of the two lower phase transitions and pertinent properties of the crystal associated with them. These results have been reported, respectively, at the 1948 Conference of the International Union for Crystallography, at Harvard University, July, 1948, and at the 1948 Annual Meeting of the American Physical Society, at Columbia University, January, 1949.

I. THE DOMAIN STRUCTURE OF $BaTiO_3$ BETWEEN 120° AND 5°C

Identification of the Polar Axis

The basic lattice of barium titanate, existing above 120°C and slightly distorted below this temperature,

*The work reported in this paper was sponsored jointly by the ONR, the Army Signal Corps and the Air Force under contract N5ori-07801.

** From a thesis submitted in partial fulfillment of the requirements for the degree of Doctor of Philosophy in Physics at the Massachusetts Institute of Technology.

[1] E. Wainer and A. N. Salomon, Titanium Alloy Mfg. Company, Elec. Report **8** (1942), **9** and **10** (1943); E. Wainer, Trans. Electrochem. Soc. **89**, Preprint **3** (1946).

[2] A. von Hippel and co-workers, NDRC Reports 14-300 (1944), 14-540 (1945); von Hippel, Breckenridge, Chesley, and Tisza, J. Ind. Eng. Chem. **38**, 1097 (1946).

[3] B. M. Wul and I. M. Goldman, Comptes Rendus (USSR) **46**, 139 (1945); B. M. Wul and L. F. Vereschagen, Comptes Rendus (USSR) **48**, 634 (1945).

† The transition point near 5°C was established by thermal expansion and dielectric measurements, made by J. M. Brownlow and W. B. Westphal respectively; the transition point near −70°C was first seen clearly in hysteresis loops by A. P. de Bretteville, Jr.

[4] Helen D. Megaw, Proc. Roy. Soc. (London) **A189**, 261 (1947).

[5] S. Roberts, Phys. Rev. **71**, 890 (1947).

[6] Blattner, Matthias, and Merz, Helv. Phys. Acta. **20**, 225 (1947).

[7] Blattner, Matthias, Merz, and Scherrer, Experientia **3**, 4 (1947).

[8] B. Matthias and A. von Hippel, Phys. Rev. **73**, 1378 (1948).

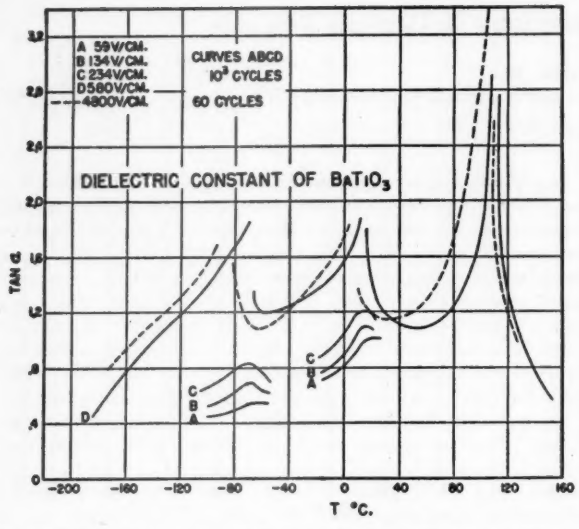

FIG. 1. Dielectric constant of the ceramic (according to von Hippel, Breckenridge, Chesley, and Tisza).

may be regarded as a simple cubic array of corner-sharing $Ti-O_6$ octahedra, with barium ions filling the holes between. This is the "perovskite" structure, of chiefly ionic nature: $Ba^{+2}Ti^{+4}O_3^{=}$. Between 120°C and 5°C, the lattice has a slight tetragonal distortion and a spontaneous polarization associated with a displacement of the Ti^{+4} ion away from the center of the unit cell. The temperature dependence of the c/a ratio is given in Fig. 2. X-ray data[9] shows the Ti ion to be off-center. The spontaneous polarization produces a bound surface charge of the order of 10^{-5} coulomb/cm².[8,10] This value is due partly to the displacement of the Ti ion with respect to its surroundings, and partly to the polarization of the highly polarizable oxygens resulting from the displacement of the Ti.

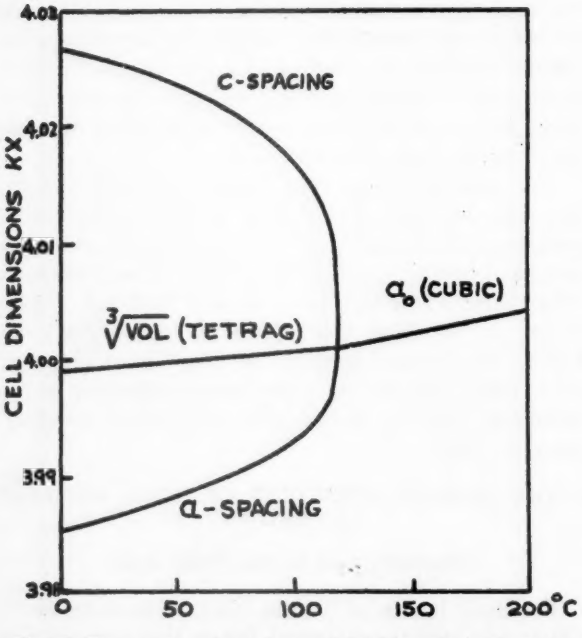

FIG. 2. Temperature dependence of axial lengths in the tetragonal phase (according to Megaw, see reference 4, see also Kay, reference 11).

[9] B. Matthias and G. Danielson, Phys. Rev. 74, 986 (1948).

The polar, optic and c-axes in the tetragonal crystal system are all in the same direction. In the tetragonal phase, one axis has expanded, forming the c-axis, and two have contracted to give the a-axis. At optical frequencies, then, the internal field associated with an induced polarization due to an applied field should be greater when the applied field is along the a-axis than when it is along the c-axis. The refractive index along the c-axis should then be lowest, and actually we find $n_c - n_a = -0.055$ for sodium light at room temperature. The optic ellipsoid is therefore uniaxial negative as verified optically.††

The domains in barium titanate are formed by twinning on a (101) or (011) face of the crystal[8,11] as shown in Fig. 5. A sufficiently high electric field orients all titanium ions into the same direction, resulting in a single domain. Due to the high symmetry of the cubic phase, twinning can occur only below 120°C, when the crystal symmetry is lowered from cubic to tetragonal. The birefringence of barium titanate makes the polarizing microscope the main tool for the investigation of domain patterns.

The value of the birefringence will be a good indication of the amount of deformation from cubic. We have measured this for sodium light from the separation of the fringes in a 45° wedge-shaped domain shown in Fig. 3, for both rising and falling temperatures to ascertain that pyroelectric effects did not enter. Alternately, by means of a quartz-wedge compensator, single-domain plates were used to measure the change in birefringence in sodium light from the calibration value 0.055 at room temperature, and the curves are in fairly good agreement with Fig. 3.

Wedge-Shaped Laminar Domains

It is often seen that 45°-lines (see Fig. 5) terminate in the crystal. Clearly a single twin plane cannot end in the middle of the crystal, so these particular lines must actually consist of two *converging* twin planes. Our supposition was verified upon finding examples such as that of Fig. 13 of the paper of Matthias and von Hippel,[8] and Fig. 4 here.

The distance of penetration of thin wedges is very sensitive and responds *smoothly* to a change in an applied electric field. If an alternating field is applied and a stroboscopic light source[8] used, the wedges move in and out over an appreciable distance in smooth response to the 60 cycle alternating field. This corre-

[10] J. K. Hulm, Nature 160, 126 (1947).

†† There is a hexagonal polymorph of barium titanate (R. D. Burbank and H. T. Evans, Jr.; Acta Cryst. 1, 330 (1948)) with refractive index 2.2 to 2.3 and a uniaxial positive birefringence of roughly 0.07 to 0.08.

[11] H. F. Kay, Acta Cryst. 1, 229 (1948).

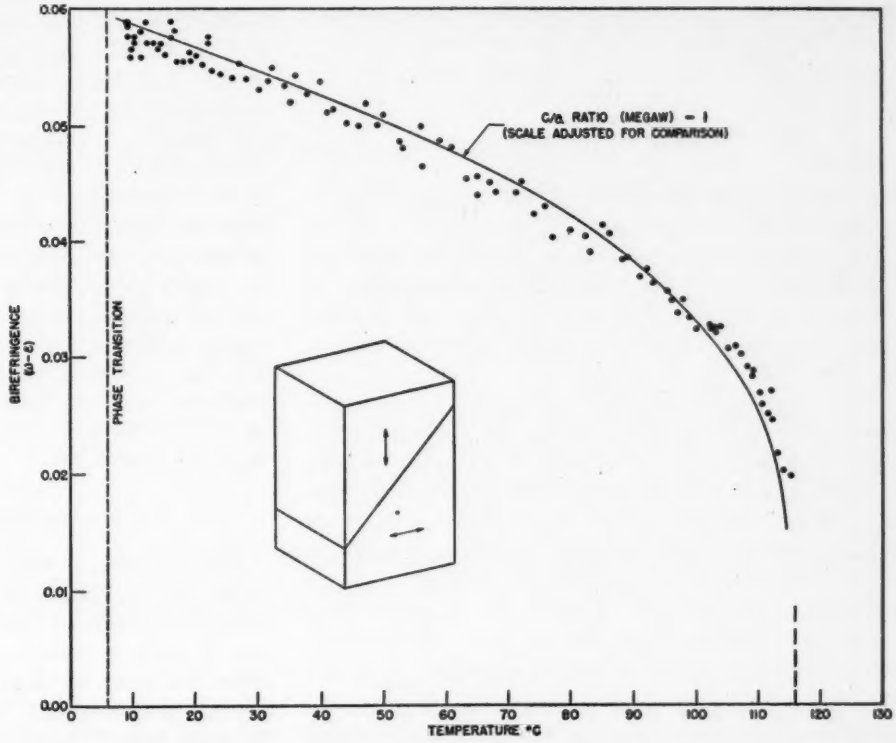

FIG. 3. Temperature dependence of Na_D birefringence in the tetragonal phase.

sponds to the *reversible* motion of domain boundaries in ferromagnetism, which make the major contribution to the initial magnetic susceptibility. These thin wedges also respond smoothly to changes in mechanical pressure.

The relation of the directions of the optic, polar and *c*-axes (all parallel to one another) inside and outside a wedge-shaped domain can be clearly demonstrated on the crystal of Fig. 4. When a birefringent plate is superposed, the wedges are of a different color from the surroundings in one 45° position (crystallographic axes at 45° to the polarization of the light) and the colors interchange in the other 45° position. The polar axes inside and outside the wedges are therefore perpendicular. Neither optical nor x-ray methods, however, can determine whether the polar arrows are in a "head-to-tail" relation across the twin plane as in Fig. 5 (normal rotation twinning), or whether similar ends of the polar arrow meet at the twin plane (reflection twinning). The great rapidity with which such wedges can move under the influence of an electric field is evidence for the former possibility, for here no surface polarization charge can exist at the twin plane, while in the case of similar ends of the polar arrows meeting at the twin plane a depolarizing field due to a surface polarization charge of $\sqrt{2}p^0$ (where p^0 is the spontaneous polarization) would exist until neutralized by electric conduction.

When the crystal of Fig. 4 is viewed near the normal parallel extinction position (crystal axes parallel or perpendicular to the plane of the polarized light) the extinction directions in the vicinity of the wedge are found to be slightly rotated toward the point of the wedge, inside and outside the wedge. This indicates a

FIG. 4. Wedge-shaped laminar domains in a single crystal.

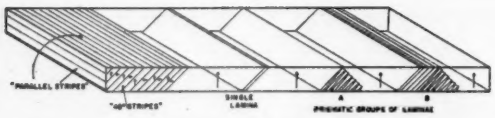

FIG. 5. Laminar twinning in a crystal plate.

state of strain in the lattice in this neighborhood. In regions of 45° stripes (see Fig. 5), rotations of the extinction positions as large as 45° have been observed. The lattice is clearly very sensitive to a shear about the *a*-axis. Such large rotations of the extinction position have never been observed in regions of parallel stripes (see Fig. 5).

Observing crystals under changing conditions of temperature, electric field, mechanical pressure, etc., make it appear that the advance of these thin wedge shaped laminar domains through the crystal is the sole manner in which domains are produced. A block-shaped domain can be formed by coalescence of such laminae.

In Fig. 5 there is illustrated a laminar domain extending through the thickness of a crystal plate having its optic axis normal to the plate. If the crystal is observed from above in crossed polarizers there will be seen a brightly luminous band due to the birefringence of the lamina, which has its optic axis across the line of sight. Such bands are shown in Fig. 6. The color of the band will be that of a thin plate of barium titanate having a thickness $\sqrt{2}$ times the thickness of the lamina, as experimentally verified. It is, in general, the birefringence of arrangements of thin laminae which gives rise to the colors often observed in barium titanate crystals in polarized light. If the crystal of Fig. 6 is tilted about an axis in the plane of the crystal plate (the plane of the photograph) and perpendicular to the direction of the bands, the extinct region will, of course, slowly become luminous. An angle of tilt is found, however, where the originally bright bands have for the most part become extinguished, for all rotations of the tilted crystal about the axis of the microscope. This is simply due to optical compensation of the lamina by the regions above and below it (see Fig. 5). It is for this reason that regions with a uniform distribution of very thin laminae, overlapping so as to give the crystal an overall birefringence color, have been supposed to be biaxial.

The "square-net" pattern

Figure 7 shows a square-net pattern of domains in a single crystal of barium titanate in crossed polarizers in monochromatic light. The two basic steps in the formation of such a pattern are: (1) the formation of a prismatic group of laminar domains as sketched in Fig. 5A (such a group of laminae is occasionally seen in the large faces of a crystal plate). (2) The intersection of two such groups, as illustrated in Fig. 8, forming a square pyramid at their intersection.

This process of formation can be observed by slowly

FIG. 6 Birefringent bands due to laminar domains (see also Kay, reference 11).

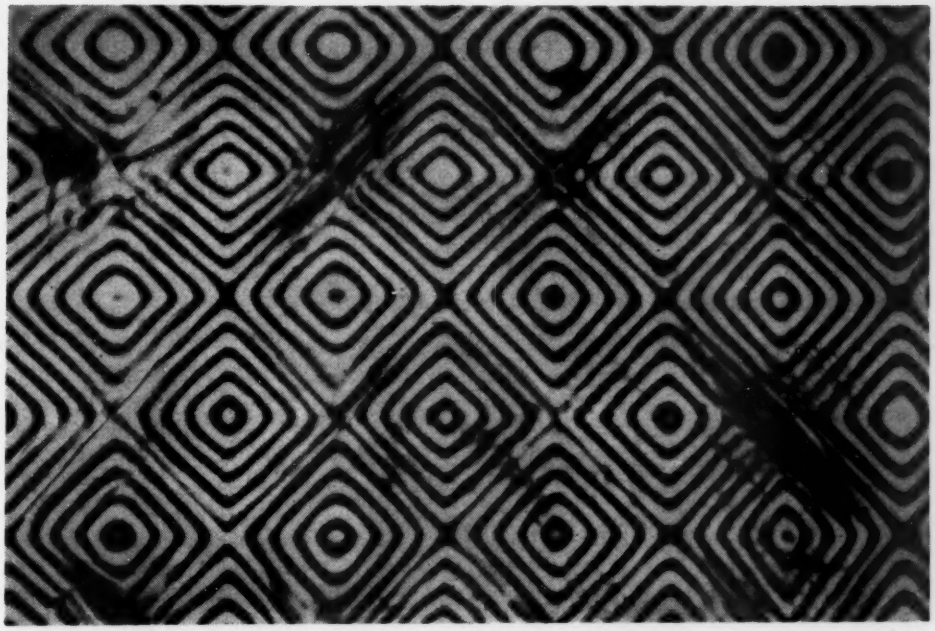

FIG. 7. Square-net domain pattern in a single crystal.

cooling an appropriate crystal through the region of the Curie point. White bands suddenly appear, spreading very rapidly over the complete length or breadth of the crystal plate. These bands grow in intensity and width in small jerks. Each time a new group of laminae appears, it intersects all the groups perpendicular to it, and at each intersection a little square of 45° stripes is formed. When the crystal is rotated into the parallel position, only these little squares do not extinguish.

Similarly, at room temperature, by applying an appropriate pressure to a single domain plate, groups of laminae can be made to appear, and again at the intersection of any two perpendicular groups appears a little square of 45° stripes. Upon relieving the pressure, these groups and their 45°-striped intersections promptly disappear. These 45° stripes correspond to vertical lamination of the pyramid of intersection (see Fig. 8).

The formation of a group of laminae will cause bending of the crystal plate. It seems reasonable that the $Ba-O_3$ part of the lattice remains completely linked through a twin plane,[11] the only change occurring in the direction of the displacement of the titanium ions. Along the *upper* face of the crystal of Fig. 9 the length is the axial length a times the number of unit cells along the length of the crystal, while along the *lower* surface the crystal has the same number of unit cells, but in some of them the longer c-axis lies in the surface. The lower surface is therefore elongated by the formation of the laminar group, and the crystal bent as in Fig. 9 in the vicinity of the group. In the intersection region of two laminar groups, the upper surface in the crystal of Fig. 8 will have to accommodate a stretch in *both* directions, which is best satisfied by a region of 45° stripes, as is demonstrated by the scheme of Fig. 10.

Figure 11 shows several vertical groups of laminae intersecting one perpendicular group. The right-hand picture shows the characteristic lack of extinction in the parallel position in the corresponding row of squares. Here one laminar group intersects a close succession of parallel laminar groups as schematized in Fig. 12. At each intersection there is formed a laminated pyramid, and *between* each intersection a laminated tetrahedron remains. For a succession of laminar groups in *both* directions of the crystal (a square-net pattern), there will remain of the original domain a series of square pyramids between the laminar groups. The square-net pattern, therefore, consists of an array of laminated pyramids (at the intersections of the laminar groups), laminated tetrahedra (remainder of the laminar groups between their intersections) and *un*laminated pyramids (remainder of the original domain after invasion by the laminar groups).

Thus three types of building blocks make up the domain structure of the crystals with the square-net pattern. These are shown schematically in Fig. 13. To build a square-net pattern from them, the laminated tetrahedra are arranged as in Fig. 14, where the lamination of the original groups is indicated. The laminated pyramids are then fitted in, apex up, from beneath, that is, at the intersections of the laminar groups. The *un*laminated pyramids are finally inserted, apex down,

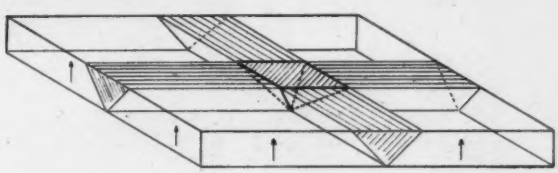

FIG. 8. The intersection of two perpendicular laminar groups.

FIG. 9. The bending of a crystal by a group of laminae.

from above, into the pyramidal holes left in between the laminar groups. We will show presently that the observed birefringence pattern corresponds to this arrangement. The direction of the polar axis in all the *un*laminated pyramids must be the same: in a crystal,

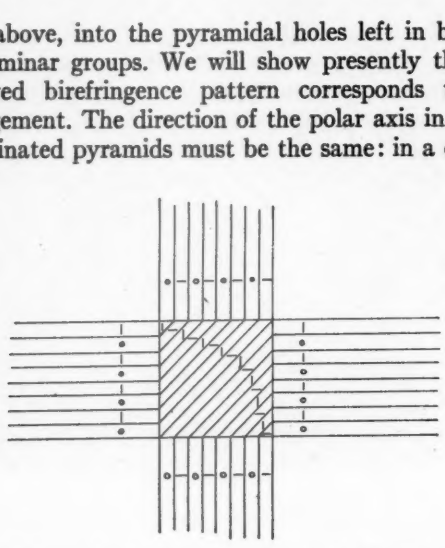

FIG. 10. Scheme showing that a region of "45°-stripes" is most likely to occur at an intersection of laminar groups.

upon cooling, a group of laminae divides a black region into two regions, which must then have the same direction of the polar axis. In thicker crystals the actual pyramidal shape of the intersection regions of the laminar groups can be observed: one face of the crystal plate, when exactly in the focus of the microscope, is covered with square regions of sharply distinct 45° stripes, the squares arranged as in a square-tiled floor; when, however, the focus of the microscope is slowly moved through the crystal toward the other face, the regions of sharp focus of the 45° stripes contract uniformly into the centers of the squares.

Some additional examples are shown in Figs. 15 and 16. The crystal of Fig. 15 shows one laminar group missing, and the corresponding row of non-extinct squares also missing. In Fig. 16 the horizontal groups are not as densely populated with laminae as the vertical groups, as can be seen from the number of orders of birefringence in each group.

It has been seen (see Fig. 9) that one laminar group will cause a bending of the crystal plate in its vicinity, with the "convex" face containing the base of the laminar group. A crystal with a whole succession of parallel laminar groups in only *one* direction of the plate, that is, forming a pattern of stairs, will then have a cylindrical shape, and a crystal with laminar groups in *both* directions (a square-net crystal) will have a spherical or "watch-glass" shape. This curvature, due to the fact that the c-axis exceeds the a-axis, should be roughly proportional to $(c/a)-1$. This has been confirmed: the convexity is in the correct face of the crystal and the curvature decreases in the general manner of $(c/a)-1$ when the temperature is raised.

If our interpretation of the square-net pattern is correct, all four edge-views should reveal a pattern of

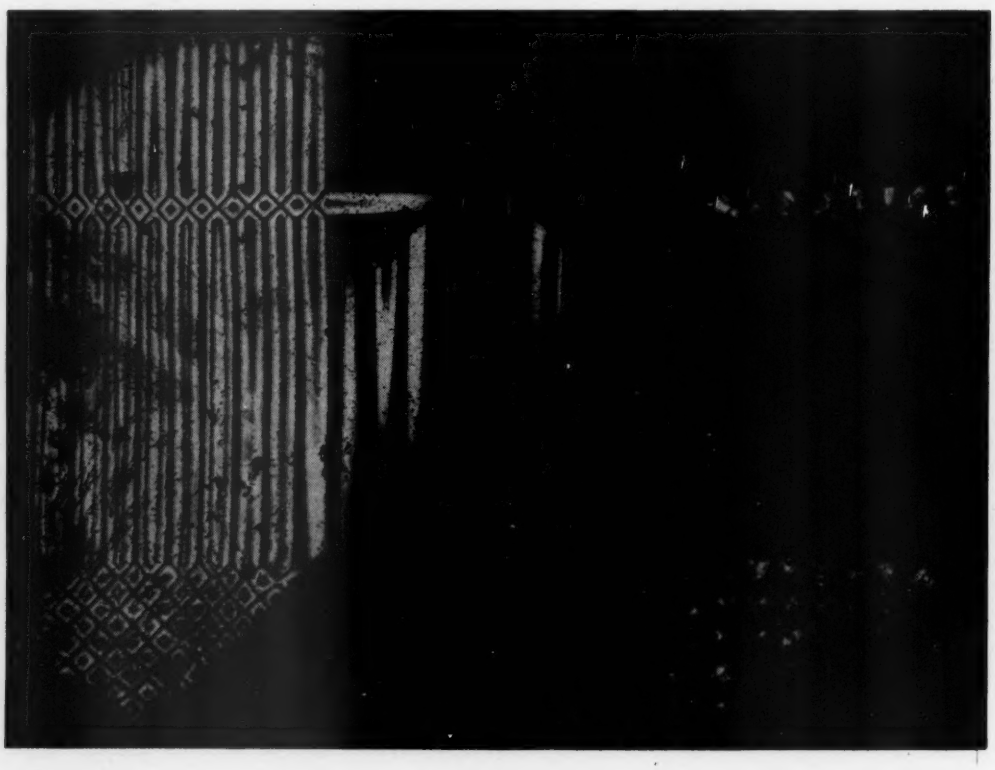

FIG. 11. A group of laminae intersecting a close succession of laminar groups. Left: 45° position. Right: parallel position.

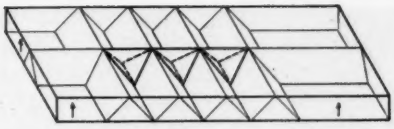

FIG. 12. Tetrahedra left between the intersections of laminar groups.

stairs. Figure 17 shows a crystal and all four edge-views in the 45° position (crystallographic axes at 45° to the plane of polarization of the light, incident from beneath), and in the parallel position it has the characteristic lack of extinction in squares corresponding to the bases of the laminated pyramids. In the light triangles in Fig. 17 the light is coming up through a series of *un*laminated pyramids and laminated tetrahedra, while in the dark triangles the light is going through laminated pyramids and laminated tetrahedra and so through many more twin planes, each of which reflects a certain amount of the light, and reduces the transmitted illumination. Figure 17 suggests that the "mesh-size" of a square-net pattern should be twice the crystal thickness. This is found true for over eighty samples ranging in thickness from 0.005 mm to 0.200 mm.

Finally, we come to an interpretation of the pattern of multicolored squares in the square-net crystal in polarized light. In white light the concentric squares in the crystal of Fig. 17 have a progression of colors similar to a birefringent wedge. In monochromatic light a relatively thick crystal is shown in Fig. 7. The arrangement of the laminated tetrahedra alone as in Fig. 14 should give the birefringence pattern of Fig. 7. When we insert the *un*laminated pyramids, apex down, from above, this birefringence pattern will not be altered, since these pyramids have their optic axes along the direction of vision. However, when the laminated pyramids are inserted, the pattern will be completely disturbed *unless* the birefringence of the material constituting the laminated pyramid is considerably lower than normal.

The abnormally low value of the birefringence in the laminated pyramids is corroborated by observation of specially selected crystals. If two laminar groups of the type of Fig. 5B intersect, the intersection will be a *truncated* laminated pyramid. There will then be a square, of the dimensions of the truncation, within which the optical behavior of the laminated pyramid is not masked by the optics of overlapping tetrahedra. Such regions are seen in Fig. 18. In the two largest truncations (the two largest regions of 45° stripes) the extinction positions are rotated 12° from normal, and in the next-to-largest two truncations they are rotated 43° from normal. The actual thickness of the crystal corresponds to about four orders of the birefringence of barium titanate, yet the truncated regions show at most half an order of birefringence, giving them a white or yellow appearance in crossed polarizers. Sometimes each truncation has several regions of 45° stripes, sloping toward the right or toward the left, and the

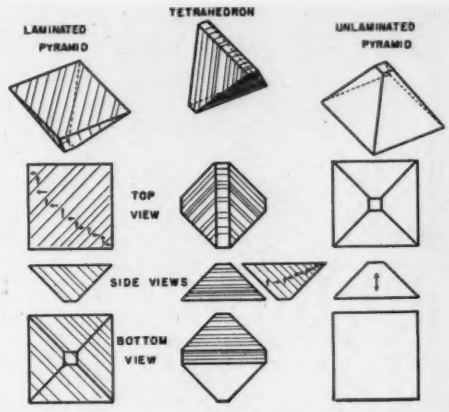

FIG. 13. The three types of building block in the square-net crystal.

over-all extinction position is rotated one way or the other from normal by an equal amount according as the 45° lines slope one way or the other. A few cases of 45° stripe crystals, not having any square-net pattern, have had this behavior over the entire area of the crystal, the abnormal rotation of the extinction positions becoming progressively less over a period of time in some cases.

The separation of the colored fringes in the squares of a square-net crystal is roughly that expected, and the number of fringes in each square decreases with increasing temperature in the same manner as the birefringence.

If one applies an electric field to a square-net crystal plate, the pattern changes from that of squares into one resembling the left-hand part of the crystal of Fig. 16, with the short diagonal of the lozenges in the field direction. It is clear that the field should favor the laminar groups perpendicular to it and depopulate those parallel to it.

Sometimes a succession of laminar groups intersects a region of uniform lamination as in the left-hand part of Fig. 5, instead of the usual succession of laminar groups. An example of this is shown in Fig. 19.

The origin of stable domain patterns

The very definite persistence of a particular type of domain pattern in a particular crystal, after heating

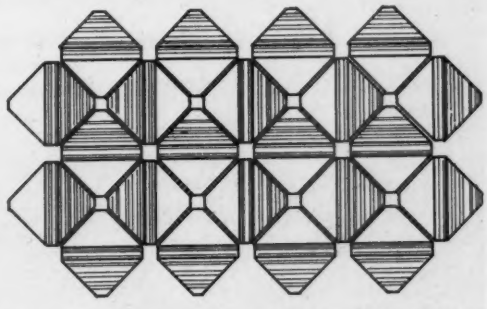

FIG. 14. Arrangement of tetrahedral building block in the square-net crystal.

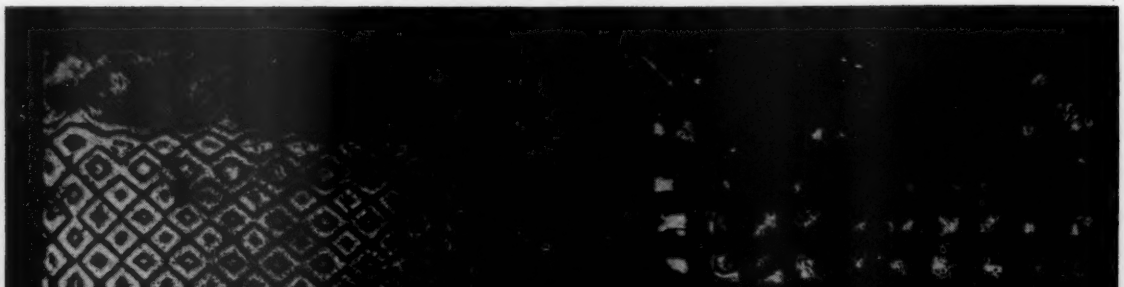

FIG. 15. Square-net pattern with one laminar group missing.

above the Curie point, clearly indicates that some condition characteristic of this particular type of pattern exists *above* the Curie point, where there are no domains. This could only be strains in the crystal.

The square-net crystal provides an excellent example of this state of affairs. Regardless of how many times the crystal is heated above the Curie point, the concave side of the crystal at room temperature is always the same face of the crystal, whichever way up the crystal was placed in the heating stage. *Above* the Curie point, say 30° above it, there is a small residual curvature in the crystal even though all the domains disappeared at the Curie point. This residual curvature is not observed in crystals that do not have the square-net peculiarity. In square-net crystals the transitions near 5°C and −70°C are found to require a wide range of temperatures for their completion, so wide that sometimes it is not possible to tell if the transitions have occurred.

The slight curvature of the square-net crystals above

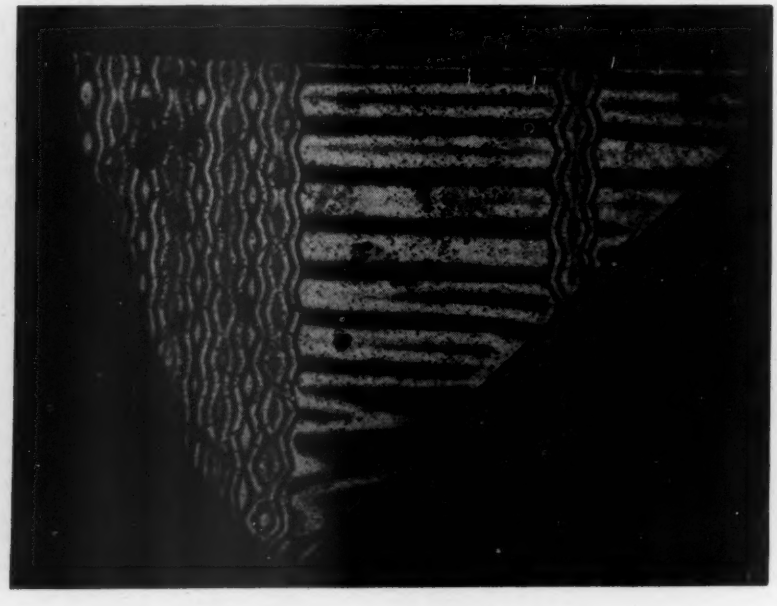

FIG. 16. Lightly populated groups intersecting heavily populated groups.

the Curie point can be explained very simply in terms of a greater concentration of impurities near one face of the plate than near the other face, which would cause the crystal to be strained in the manner of a bimetallic disk. This could happen when the crystal grows on the surface of the molten flux of $BaCl_2$, etc. The growing is done in a platinum crucible, and platinum is known to enter the lattice of barium titanate with some ease. Thus the square-net pattern appears to be a way of minimizing the total energy of lattice strain, and its remarkable regularity a result of the uniform degree of curvature produced above the Curie point by a distribution of impurities that varies only across the thickness of the crystal plate.

In some crystals, one could suppose that the rectangular edges of the plate contain a greater amount of impurities than the body of the crystal, as is suggested by appreciable birefringence near the edges above 120°C. If the impurities in the edges expand the lattice, the body of the crystal will be stretched in both directions, which we have seen in Fig. 10 to be best satisfied by a region of 45° stripes, the edges having another direction of lamination, giving rise to a picture-frame effect sometimes observed.

Conclusions

There is a good deal of justification for the ferroelectric-ferromagnetic analogy, for, in addition to their having in common the phenomena of spontaneous polarization, λ-type transition between polar and nonpolar phases, domains, and continuous linkage of the lattice across domain boundaries, we have found in barium titanate a type of domain motion analogous to the reversible motions of domain walls in ferromagnetism: the smooth way in which wedge-shaped laminar domains follow a rapidly varying electric field. The analogy, however, is incomplete in one important respect arising from the simple circumstance that while there is electric conduction, there is no magnetic conduction, as free magnetic poles do not exist. In a single-domain ferromagnet, the bound surface charge creates a depolarizing field, and domains form in such a way as to decrease this depolarizing field. In a single-domain ferroelectric in equilibrium (that is, after a sufficient length of time) the multidomain configuration

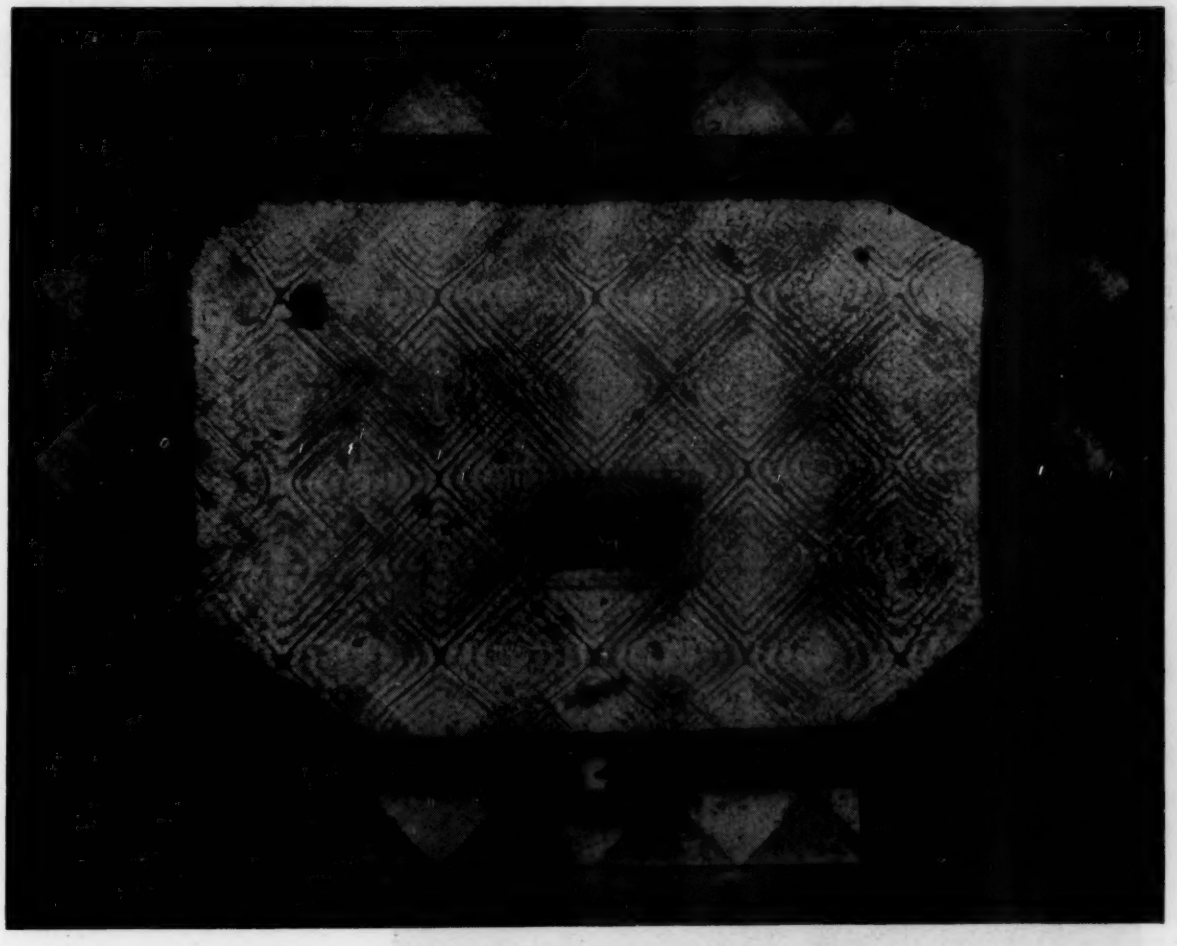

FIG. 17. Square-net pattern and edge-views of the crystal plate.

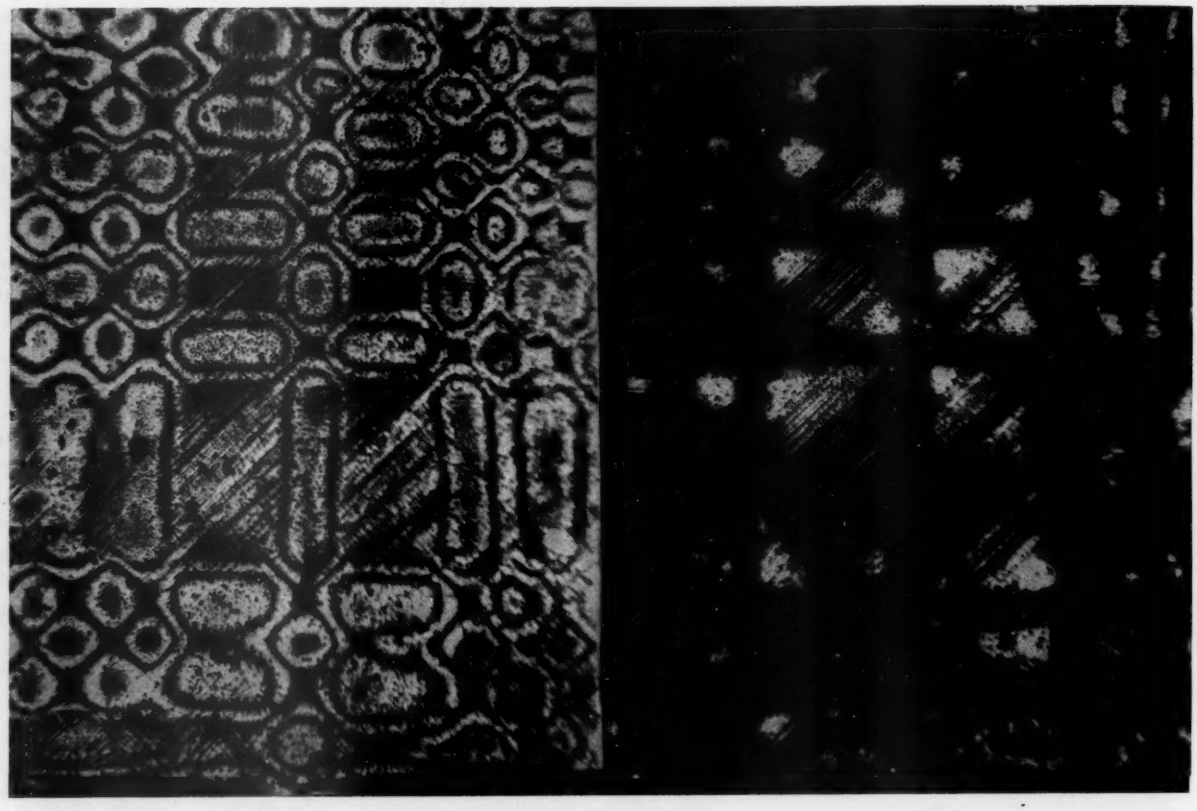

FIG. 18. Truncated laminated pyramids.

is not one of lower electrostatic energy, for electric conduction can neutralize surface polarization charges. However, when there are strains in the crystal, due to a mismatch of lattice dimensions caused by an inhomogeneous distribution of impurities, there exist stable multi-domain configurations having a lower total energy of lattice strain than the single domain.

However in the transient behavior, for instance as the temperature goes through a transition temperature, the conduction cannot immediately neutralize the

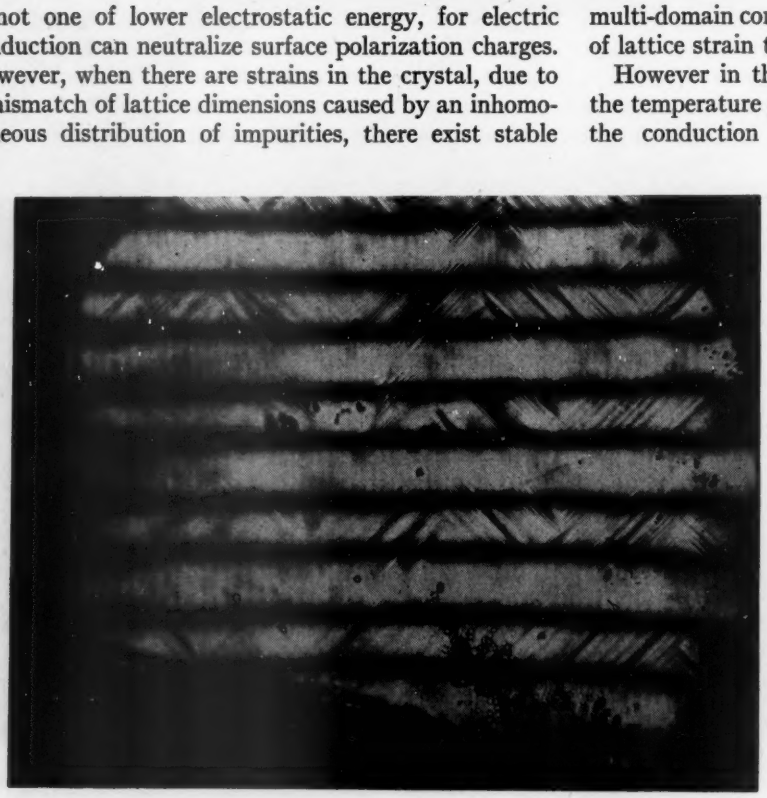

FIG. 19. Groups of laminae intersecting continuous lamination.

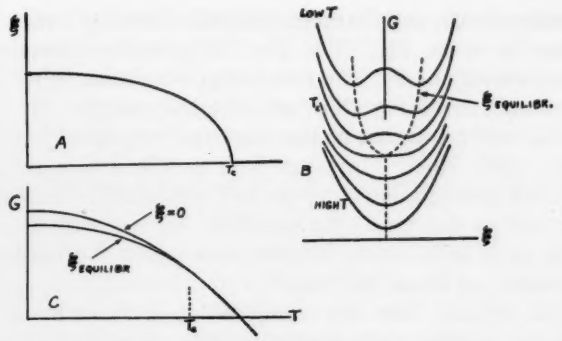

FIG. 20. Changes in configuration and free energy characteristic of a λ-transition.

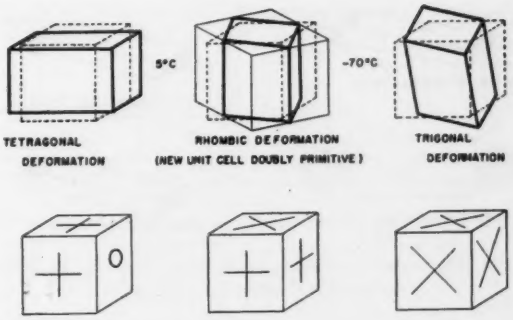

FIG. 22. Three deformations of the perovskite structure and the corresponding extinction directions in a single-domain cube.

surface polarization charges, and the domain formation must play an important role, as will be discussed in Part II in connection with the transitions near 5°C and −70°C. At any phase transition domains are of course formed by the mechanical strains existing in the lattice while the new phase is sweeping over the crystal.

II. THE PHASE TRANSITIONS IN $BaTiO_3$ NEAR 5°C AND −70°C

The Curie Point of $BaTiO_3$ at 120°C

This transition will be discussed first, as the lower two are connected with it in a fundamental way. The necessity of dividing λ-type transitions into two distinct classes, according to whether they involve order-disorder effects or take place between ordered phases, has recently been emphasized by Tisza.[12] Since disorder contributes a large entropy term, one basis for the classification is the entropy of transition $\Delta S=(1/T_c)\int c_p dT$. The ferroelectric transition in KH_2PO_4 is an order-disorder effect.[13] In the case of rochelle salt, the specific heat measurements are rather widely varying, although all indicate a low entropy of transition; we have applied Ehrenfest's relation to data in the literature[14,15] and find the computed specific heat jumps††† to be in best agreement with the measurements of Wilson.[16] The small entropy change can only be due to the changes in frequencies of the normal modes of lattice vibration of the crystal, when it acquires a minute monoclinic deformation[17] inside the ferroelectric region between 24°C and −18°C.

The Curie point of barium titanate has been classified as a transition between ordered phases.[2] The transition entropy is between six and forty times lower[2,18–20] than in KH_2PO_4. In spite of the relatively large value of Blattner and Merz[20] the possibility of order-disorder

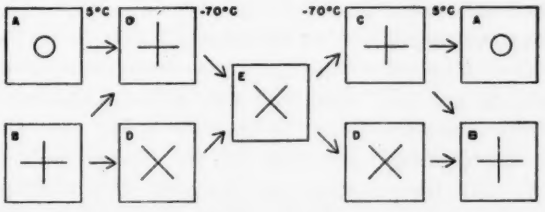

FIG. 21. Observed sequences of changes in extinction direction in crystal plates.

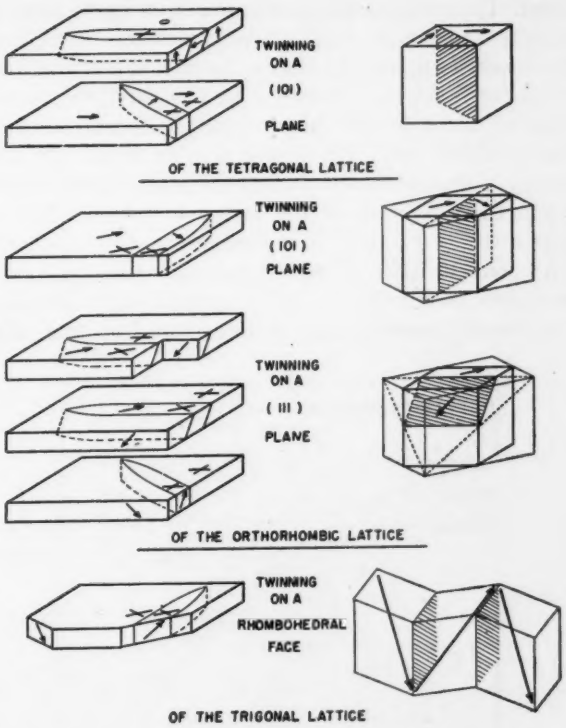
TWINNING ON A (101) PLANE
OF THE TETRAGONAL LATTICE
TWINNING ON A (101) PLANE
TWINNING ON A (111) PLANE
OF THE ORTHORHOMBIC LATTICE
TWINNING ON A RHOMBOHEDRAL FACE
OF THE TRIGONAL LATTICE

FIG. 23. The predominant twinning in the ferroelectric phases of $BaTiO_3$.

[12] L. Tisza, "On the General Theory of Phase Transitions" N.R.C. Symposium at Cornell University, Aug., 1948.
[13] J. C. Slater, J. Chem. Phys. **9**, 16 (1940).
[14] D. Bancroft, Phys. Rev. **53**, 587 (1938) (shift of transitions with hydrostatic pressure).
[15] W. P. Mason, Bell Sys. Tech. J. **26**, 80 (1947) (dilatometric experiments).
††† At 24°C an upward anomaly of $\Delta c_p=0.006$ jl/g/°$=\frac{1}{2}$ cal/mole/°; at −18°C, downward anomaly, $\Delta c_p=0.017$ jl/g/° $=1$ cal/mol/°.
[16] A. J. C. Wilson, Phys. Rev. **54**, 1103 (1938).
[17] H. Jaffe, Phys. Rev. **51**, 43 (1937).
[18] B. M. Wul, J. Phys. USSR **10**, 95 (1946).
[19] Harwood, Popper, and Rushman, Nature **160**, 58 (1947).
[20] H. Blattner and W. Merz Helv. Phys. Acta. **21**, 210 (1948)

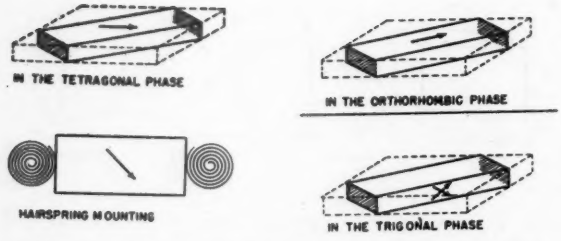

FIG. 24. Electrical detwinning experiment showing the lattice to be stretched along the polar axis.

still seems rather remote, for if there were six possible equilibrium positions for the Ti ion in each $Ti-O_6$ octahedron above 120°C[21] there would be 6^N possible complexions per mole as compared with 2^{2N} in KH_2PO_4, and it would be surprising if the restrictions on the complexions were as heavy as in KH_2PO_4. As the lattice deformation accompanying the ferroelectric state in $BaTiO_3$ is considerably larger than in rochelle salt, it would not be unreasonable for the entropy of lattice vibrations to change by an appreciably larger amount. Although the higher entropy of the cubic phase of $BaTiO_3$ would explain why it takes over at higher temperatures, this effect may only be secondary to more important effects.

The statistical problem in $BaTiO_3$ is very complicated. Thermodynamics however allows us to form a definite and simple qualitative framework correlating the observed properties. From the lattice deformations which we find in the phases of $BaTiO_3$, and the knowledge of the corresponding piezoelectric matrices, we can establish qualitatively the way in which the free energy G depends upon configuration and temperature. From thermodynamics, the dielectric susceptibility is high if the "curvature" in the minimum of $G(p)$ is low.[17] The configuration of the crystal may for qualitative purposes be referred to by a general configurational coordinate ξ representing the departure from the cubic phase ($\xi=0$); the characteristic behavior of a λ-transition is as in Fig. 20A, the configuration changing *continuously* at T_c. The free energy minimum shifts in the manner of Fig. 20B, and the free energies of the cubic and tetragonal phases converge tangentially as in Fig. 20C. Since ξ involves both a polarization and a lattice deformation (though not necessarily coupled, as will be discussed) the dielectric susceptibility along the polar axis has an infinite peak where the minima coalesce, as in rochelle salt.[17]

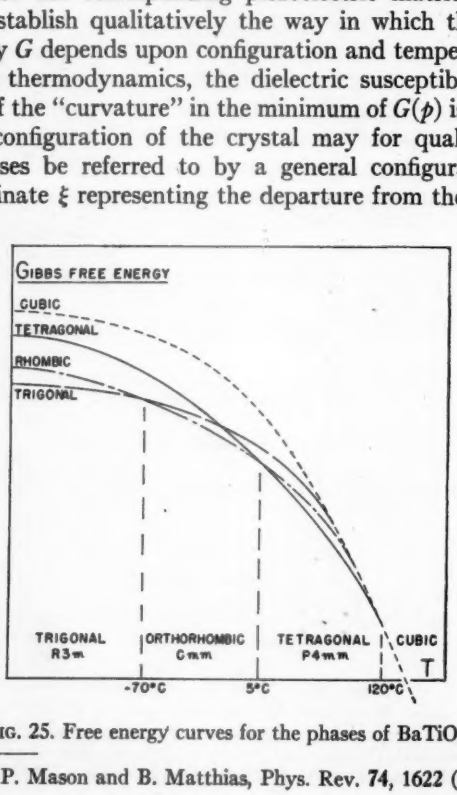

FIG. 25. Free energy curves for the phases of $BaTiO_3$.

In rochelle salt, the components p_x (polarization) and y_x (lattice deformation) of the configuration are closely interacting[22] or coupled at *all* temperatures through the piezoelectric coefficients g_{14} and e_{14}‡ of both the monoclinic (ferroelectric) and orthorhombic (non-ferroelectric) phases. However in the cubic phase of $BaTiO_3$ (above 120°C) the symmetry is such that *all* the piezoelectric coefficients vanish. In the tetragonal phase however, below 120°C, there will be piezoelectric coupling between the polarization along the polar axis and the tetragonal deformation through the coefficients g_{31}, g_{33} and e_{31}, e_{33}, and between polarization across the polar axis and shear z_x about an a-axis through g_{15} and e_{15}: a small change in polarization involves a proportional change in deformation through g, and a change in deformation involves a change in polarization through e, which is not the case above 120°C. Thus, qualitatively, a change in ξ in Fig. 20B implies a simultaneous polarization and lattice deformation, but only when the minimum in G is not at $\xi=0$. In rochelle salt, Mueller's theory[22] shows that clamping the lattice so as to prevent the shear accompanying the spontaneous polarization pushes the two Curie points so far together that they probably disappear, leaving only a high finite maximum in the susceptibility.

In ferroelectric crystals resting on a glass plate in vacuum, one would expect shape-dependent depolarizing conditions to exist; yet in the observations to be described there was no obvious dependence of the temperatures of the transitions on the directions of the polar axis with respect to the crystal plates. These temperatures showed no obvious difference from those in dielectric measurements, where depolarizing conditions do not exist. One may seek explanations in: (1) electric conductivity in the crystals, which neutralizes the depolarizing fields, and (2) the formation at the transition temperatures of domains which arrange themselves such as to minimize the depolarizing fields.

[21] W. P. Mason and B. Matthias, Phys. Rev. **74**, 1622 (1948).

[22] H. Mueller, Phys. Rev. **57**, 829 (1940); **58**, 565, 805 (1940).

‡ Using the variable p (polarization) instead of D (displacement), as p and D are practically equal when the dielectric constant is high, a transformation of thermodynamics allows us to use any two of the variables E, p, X, x (X, x, are the stress and strain tensors) as independent variables. The associated Maxwell relations are represented by:

$$(dE/dx)_p=-(dX/dp)_x=h \qquad -(dp/dX)_E=(dx/dE)_X=d$$
$$(dE/dX)_p=\quad(dx/dp)_X=g \qquad (dX/dE)_x=\ (dp/dx)_E=e$$

where the coefficients h, g, e, d, are those suggested by Mason (see reference 15).

In the following discussion we simply imagine the transitions to be discussed as taking place between different states of an unconstrained single-domain crystal enveloped in a conducting foil to remove depolarizing conditions.

The Optical Changes at the Transitions near 5°C and −70°C

A special vacuum microscope stage permitting high magnification observation of crystals down to −160°C was constructed. Crystal plates which are a single domain at room temperature occur with their optic axes either in the plane of the plate or perpendicular to it. Figure 21 shows the sequences of optical parallel extinction directions for over twenty rectangular plates of all sizes. The extinction directions are a property of the crystal *system* (of which there are seven) as they are in the directions of the principal axes corresponding to the dielectric tensor. If one imagines the unit cell of $BaTiO_3$ successively distorted as shown in Fig. 22, the extinction directions in a single-domain cube correspond exactly to those observed. The observation of electrical hysteresis[2] shows the crystal to be ferroelectric in these three systems. The orthorhombic crystal system has only one pyroelectric crystal class: *mm*, and this has the polar axis in the *Z*-direction and so in a [101] direction of the pseudo-cubic unit cell; the polar axis will therefore have twelve equivalent directions. The trigonal system has two pyroelectric classes: 3 and 3*m*, and the polar axis is along the trigonal *Z*-axis and so along a [111] direction of the pseudo-cubic unit cell; the polar axis will therefore have eight equivalent directions. A trigonal distortion of the perovskite structure has three planes of symmetry parallel to the polar axis, so the trigonal class is 3*m*. The orthorhombic class here is written *Cmm* (*C*=doubly primitive).

Presently it will be shown experimentally that, as in the tetragonal phase, the lattice deformation in the orthorhombic and trigonal phases is a *stretch* along the polar axis (as we have already indicated for the trigonal phase in Fig. 22). At a transition, the polar axis will most likely jump to an equivalent direction in the next phase that is nearest to its direction before the jump. Thus only the jumps actually observed (Fig. 21) will take place. The observed twinning in rectangular plates is interpreted in Fig. 23, and the optical extinction directions are shown.

The experimental demonstration that the lattice deformation is a *stretch* along the polar axis in the lower phases was made possible by a tiny crystal plate by chance broken roughly as shown in Fig. 24. With silver evaporated on its two smallest faces, the crystal was mounted between two hairsprings and placed in the chamber of a specially designed microscope stage for electro-optical work. In the orthorhombic temperature region, a sufficiently high electric field in either direction actually left, after removal, a single domain (except for a few very fine wedge-shaped domains). An optical

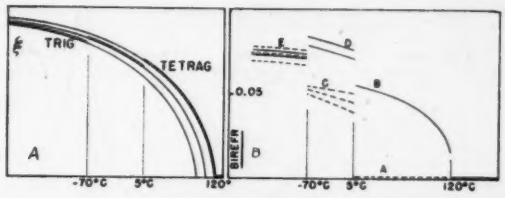

FIG. 26. A. Changes in configuration suggested by Fig. 25. B. Approximate birefringence as function of temperature for five crystals.

compensator then showed the *minor* axis of the optic ellipse to be along the polar axis. Thus the orthorhombic deformation is a *stretch* along the polar axis. In the *trigonal* phase however, none of the eight possible directions of the polar axis will be parallel to the field for the present set-up, although *two* directions as in Fig. 24 will be much nearer the field (making an angle 35° 15′ with it) than the other six. One might think that the field would produce, in general, a multi-domain configuration consisting of these two possibilities. The observed twinning however (Fig. 23) cannot accomplish this, nor could twinning on a prismatic face if it were possible. The field should therefore produce a single domain, and indeed does so, the domain remaining essentially single (except for a few fine wedges) after removal of the field. Again the

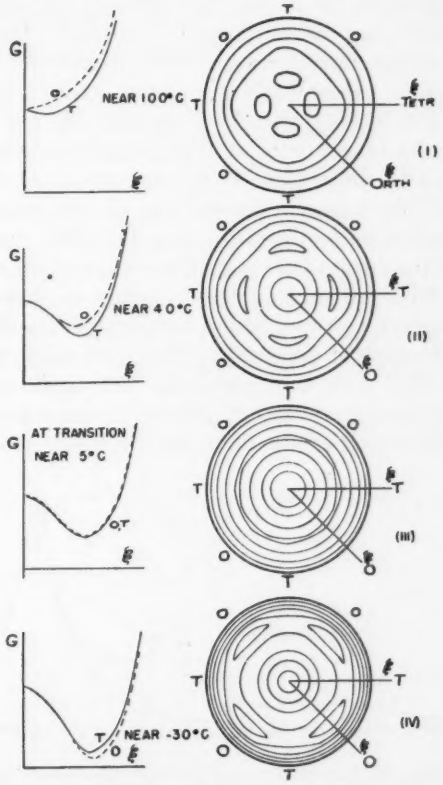

FIG. 27. Free energy surface for discussing the 5°C transition. Left: dependence of *G* on the tetragonal and orthorhombic configurations. Right: variation of *G* in a (100) plane of the pseudo-cubic lattice.

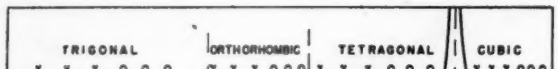

FIG. 28. Expected qualitative dependence of the principal dielectric susceptibilities on temperature (not necessarily equal on either side of the lower transitions).

minor axis of the ellipse is in the direction of the polar axis, so the lattice is *stretched* along the polar axis. As in the tetragonal phase, the thin wedge-shaped laminar domains observed in this experiment responded smoothly to changes in the electric field.

Interpretation of the Transitions near 5°C and −70°C

In the transition at 120°C the coordinates of the crystal structure change in a continuous manner as indicated in Fig. 20A. There is, however, a *finite* difference in the configurations of the tetragonal and orthorhombic phases. This finite change takes place abruptly at the transition temperature near 5°C, which must therefore be of the *first order* (a discontinuous transition) and not a λ-type transition. The same applies to the transition near −70°C from orthorhombic to trigonal. Accordingly we draw qualitatively the Gibbs free energy curves as in Fig. 25, the curves converging tangentially at the λ-transition, but intersecting at a finite angle at the transitions of the first order. This suggests dependence of the amount of deformation on temperature as in Fig. 26A, the heavy lines of the curves indicating the configuration actually selected by the minimum free energy condition. The birefringence as a function of temperature should show the same type of dependence: discontinuities near 5°C and −70°C and a progressively less rapid rise with falling temperature. In Fig. 26B are shown approximate measurements‡‡ of the birefringence below room temperature for sodium light for five thin crystals, the symbols *ABCDE* referring to Fig. 21. For all five crystals, the value is the same below −70°C, which is consistent with trigonality. Cubically clamping the crystal of barium titanate, that is preventing the lattice deformation which accompanies the ferroelectric state, would seriously alter the *G*-curves, and since these intersect at small angles the locations of the transitions near 5°C and −70°C would be seriously affected.

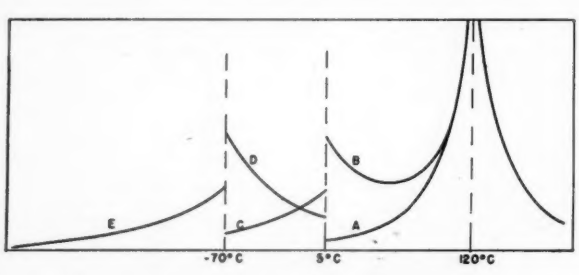

FIG. 29. Expected susceptibilities transformed to pseudo-cubic axes.

‡‡ Measured in Na light by the fringes in a chipped crystal, and followed with changing temperature in crystal plates using a compensator and white light.

Each of the curves in Fig. 25 corresponds to a situation as illustrated in Fig. 20, in the directions [100], [110], [111], of the pseudo-cubic lattice. Representing the direction and magnitude of the spontaneous polarization and accompanying lattice elongation by a vector ξ having the possibility of any direction in space, the transition near 5°C may be discussed by considering variations of this vector in a (100) plane of the pseudo-cubic lattice. The dielectric susceptibilities χ_{33} (along the *Z*- or polar axis) and χ_{11} (along the *X*-axis) and the associated deformations in the tetragonal and orthorhombic phases, correspond to variations taking place in this plane, and will be obtainable if the dependence of *G* is known. In Fig. 27 are shown (left) the dependence of *G* on the magnitude of ξ for the tetragonal and orthorhombic phases, according to Figs. 25, 20. At the transition temperature near 5°C the minima are at the same level, and nothing is lost qualitatively by putting them at the same magnitude of ξ; then when *G* is plotted in the (100) pseudo-cubic plane it must be as suggested in (iii) of Fig. 27 (right), for there is a free energy barrier between the tetragonal and orthorhombic positions (on the radii toward *T* and *O*) as there is no minimum between them. Such a free energy barrier is characteristic of a transition of the first order, and will produce *thermal hysteresis* in the experimental observations. As the temperature rises above the transition temperature near 5°C, the orthorhombic minima become higher than the tetragonal minima and the *G*-surface in (iii) must change into that in (ii). For temperatures falling below this the reverse is true, and (iii) changes into (iv).

A change in ξ from a minimum along the radius involves a change in polarization and lattice deformation that interact through the piezoelectric coefficients g_{31}, g_{33} and e_{31}, e_{33}. An angular change in ξ involves a change in polarization and lattice deformation interacting through g_{15} and e_{15}. As ξ involves the polarization, the dielectric susceptibility will be high if the curvature at the minimum in the appropriate direction is low. Extending this reasoning, we get the dielectric susceptibilities as shown in Fig. 28. Due to the piezoelectric coupling between the polarization and lattice deformation, the piezoelectric coefficients *d* and the mechanical compliances *s* of the unconstrained crystal will vary in a manner similar to the χ's in Fig. 28. For instance, in the tetragonal phase s_{44}, d_{15} and χ_{11} should all rise rapidly as the transition near 5°C is approached.

The piezoelectric and dielectric susceptibilities *d* and

χ are related by: $d=(dx/dE)_X=\chi_X(dx/dp)_X$, where χ_X is the susceptibility of the free crystal (Fig. 28) when the stress X is zero. If any idea of $(dx/dp)_X$ can be obtained from the relative variation in x and p as the temperature is changed, we expect at room temperature that $d_{31}\cong-\frac{1}{2}d_{33}$ and that d_{15}/d_{33} will be appreciably smaller than $\chi_{11}/\chi_{33}=\chi_a/\chi_c\cong 20$.[23] So far, electromechanical measurements have only been made on the barium titanate ceramic, in which the rearrangement of domains plays an important role.[24] This motion of domains can be identified with the reversible motion of fine wedge-shaped laminar domains (Part I). We have however observed a rather large electro-optical effect at room temperature corresponding to the d_{15} deformation.

To compare the expected dielectric susceptibility (Fig. 28) with measurements on the available thin rectangular crystal plates, the curves of Fig. 28 must be transformed to pseudo-cubic axes, as in Fig. 29, the labels *ABCDE* referring to Fig. 21. The most common sequences optically observable are *ACECA* and *BDEDB*. The expected behavior for these two sequences is shown in Fig. 30, A and B. Figure 31 shows actual measurements made by Merz[23] on thin crystal plates. The qualitative features are duplicated except that the lack of coincidence of his "e_c" and "e_a" curves below the transition near -70°C is inconsistent with trigonality. Domains and strains in the crystal no doubt influence the measurements, but we have as yet no satisfactory answer for the discrepancy. That there are strains of some sort even in plates that are a single-domain at room temperature is indicated by a strong tendency for the crystal to return to the configuration initially existing at room temperature.

In a ceramic, each crystallite is momentarily partially clamped until the mass adjusts itself to new imposed conditions. Since above 120°C the dielectric susceptibility is unaffected by clamping (a result of the thermodynamics of piezoelectricity) the peak at 120°C will not be suppressed, but those near 5°C and -70°C will be seriously suppressed. However near these transitions the coercive energy (height of free energy barrier between adjacent minima, see Fig. 27) is low, and higher fields will easily influence the domains and produce more pronounced peaks at 5°C and -70°C, as seen in Fig. 1.

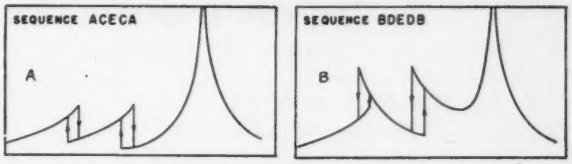

FIG. 30. Expected dielectric constant for rectangular single-domain crystal plates for sequences *ACECA* (A) and *BDEDB* (B) of Fig. 21.

ACKNOWLEDGMENT

The author wishes to thank Professor A. von Hippel for continued encouragement and many illuminating discussions during the course of the work. He also wishes to express his gratitude to Dr. Bernard Matthias for introducing him to many invaluable details concerning the crystals of barium titanate, and to Professor Laszlo Tisza for permitting him to read a copy of his manuscript on "The General Theory of Phase Transitions."

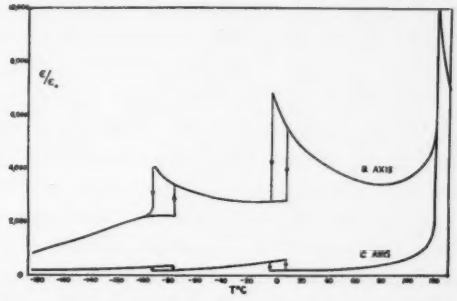

FIG. 31. Measurements of Merz on thin plates: upper curve for crystals initially in configuration *B*, lower curve initially in configuration *A*.

[23] W. Merz, Phys. Rev. **75**, 687 (1949).
[24] W. P. Mason, Phys. Rev. **74**, 1134 (1948).

The Dielectric Properties of Barium Titanate at Low Temperatures

R. F. BLUNT* AND W. F. LOVE
The Rice Institute, Houston, Texas

(Received July 5, 1949)

The complex dielectric constant of ceramic barium titanate has been measured as a function of temperature from 300°K down to 2.8°K. The large value of the slope of the real part of the dielectric constant, K', *versus* temperature curve in the 4°K region previously reported by Wul was observed in the measurements described here, and a large hump in the tanδ *versus* temperature curve was observed at low temperatures. Measurements were also made on barium titanate diluted with 15 percent and 30 percent strontium titanate. The dilution in both cases gave large slopes in the K' *versus* temperature curve at low temperatures. The measurements were made largely at 500 kilocycles per second.

INTRODUCTION

RECENTLY a great deal of interest has arisen in the dielectric properties of barium titanate and other compounds of titanium because they show such an enormous dielectric constant,[1,2] exhibit domain properties,[3] and may behave like transducers with modes of mechanical resonance to alternating electric fields.[3] Wul[1] reported studies of the dielectric constant as a function of temperature on barium titanate and found, at temperatures available with liquid helium, a remarkably large dependence of the dielectric constant on temperature. Considering the negligible expansion at these low temperatures and the inference from the third law of thermodynamics that such properties of matter as the dielectric constant should have zero temperature slope at 0°K, it was deemed important to repeat Wul's experiment on $BaTiO_3$ and measure both the real and imaginary parts of the dielectric constant. We have found complete agreement with Wul at 4°K on the temperature dependence of the real part, K'. Our studies show an interesting dependence of the imaginary part of the dielectric constant, K'', on temperature and on frequency.

It is generally believed that the high values of K' existing in the titanium compounds are due to the loose binding of the Ti ion in the unit crystalline cell. X-ray powder diffraction studies made by Megaw[4] reveal that the unit cell is tetragonal with the Ti ion shifted from its normal central position toward one of the oxygen atoms on the face of the cube. The unit cell is elongated about 1 percent in the direction of motion of the Ti ion, while the other dimensions are shortened by half this amount so as to keep the volume constant. Above 393°K, where the peak value of K' occurs, the tetragonal form goes into the cubic. The permanent dipole moment of the unit cell below the transition point suggests the possibility of a resultant macroscopic polarization and a domain structure analogous to ferromagnetic materials. Indeed, changes in the dielectric property, which are analogous to the Barkhausen jumps in ferromagnetic materials, have been observed by Matthias[5] and others. Thus it is inadequate to describe the motion of the Ti ion as a simple damped oscillator driven by an alternating electric field. Yet, as we shall show, such a theory may be useful in describing the experimental results on K', but cannot be used to explain the behavior of K''.

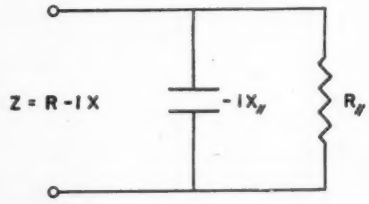

FIG. 1. Equivalent circuit of impedance of $BaTiO_3$ specimens.

EXPERIMENTAL

The experimental work was done in the Collins cryostat, which is capable of producing any temperature from room temperature down to 2°K. The ceramic specimens of barium titanate and barium titanate diluted with 15 percent and 30 percent strontium titanate were kindly supplied by the Bell Telephone Laboratories. They were in the form of parallel plate condensers consisting of ceramic disks about 25 mm in diameter and 1.6 mm thick on the average. The electrodes were silver and were applied by baking on silver paste. The leads were soldered directly onto the electrodes. Four pure specimens of barium titanate were labeled respectively: *A*, *B*, *C*, *D* and gave identical results. The disk which was diluted 15 percent with strontium titanate is specimen *E*, and the 30 percent diluted specimen *F*. Edge effects were neglected in all measurements for two reasons; first, the large value of K' reduces edge effects, and second, the electrodes were quite irregular in shape, making the measurement of electrode area difficult.

The electronic equipment used to measure the complex dielectric constant was of two types. During

* The author has been a Socony-Vacuum Fellow in Physics and has submitted this research as partial fulfillment of the requirements for the degree of Doctor of Philosophy.

[1] B. Wul, J. Phys. **10**, 95 (1946).

[2] Von Hipple, Breckenridge, Chesley, and Tisza, Ind. Eng. Chem. **38**, 1097 (1946).

[3] W. P. Mason, Phys. Rev. **74**, 1134 (1948).

[4] H. D. Megaw, Proc. Roy. Soc. London **A189**, 261 (1947).

[5] B. T. Matthias and A. von Hipple, Phys. Rev. **73**, 268 (1948).

the preliminary measurements a Boonton Type 160-A Q-meter was used. This is a calibrated radiofrequency oscillator which applies a regulated 0.02 volt r.m.s. signal across a 0.04 ohm non-inductive resistance which excites a series resonant circuit composed of a calibrated tuning condenser, standard inductance, and the unknown impedance of the test specimen. Frequencies of 50 kilocycles were used. Values of K' were obtained from the capacity value which the Q-meter indicated for the specimen. "Q" readings obtained indicated only roughly a high energy loss or a low energy loss in the test condenser. For this reason, a second piece of electronic equipment was introduced for measuring directly the real and imaginary parts of the dielectric constant. A radiofrequency signal generator, General Radio Type 805-C, was used to send signals at 500, 750, 1000, and 2000 kilocycles per second to an impedance bridge. General Radio Type 916-A. This impedance bridge measures directly the series resistance and reactance of the unknown impedance, which in these experiments, consists of the barium titanate condenser and the coaxial cable connecting it with the impedance bridge.

Small corrections for the impedance of the coaxial cable yielded the impedance of the specimen condenser. The calculation of the complex dielectric constant is made from the measured impedance as follows: Fig. 1 shows the specimen condenser considered as an equivalent circuit composed of a parallel capacitance and resistance. The parallel capacitive reactance, $X_{||}$ gives K', while the parallel resistance, $R_{||}$, gives K''.

TABLE I. Values of K', K'' and $\tan\delta$ for pure barium titanate, specimen C.

Temperature °K	Frequency kc	K'	$\tan\delta \times 10^3$	K''
298	1000	1164	3.78	4.4
297	500	1162	3.47	4.0
291	500	1227	4.91	6.0
287	500	1274	7.01	8.9
284	500	1320	8.30	11.0
281	500	1350	9.44	12.7
276	500	1351	10.4	14.1
270	500	1210	13.9	16.8
267	500	1121	13.1	14.8
264	500	1068	10.9	11.7
262	500	1050	8.38	8.8
248	500	956	15.5	14.8
227	1000	858	21.4	18.4
201	750	658	28.1	18.5
180	500	515	29.5	15.2
159	1000	431	32.6	14.1
145	500	390	35.1	13.7
125	1000	332	41.4	13.8
100	750	282	45.0	12.7
85	1000	240	48.6	11.7
64	750	193	47.5	9.2
39	500	150	43.3	6.2
25	500	129.3	37.7	4.9
17	500	111.6	30.4	3.4
8.0	2000	98.4	19.2	1.9
4.3	500	96.8	14.1	1.4
2.8	500	94.6	10.8	1.0

It follows from elementary a.c. circuit theory that

$$X_{||}=(R^2+X^2)/X \quad \text{and} \quad R_{||}=(R^2+X^2)/R.$$

Further, from the capacitive reactance $X_{||}=1/\omega C$ and the familiar parallel plate condenser formula $C=(\epsilon_0 K' A)/d$, where d is the distance between the electrodes, and A the area of each of the plates, we have

$$K'=(d/\epsilon_0 A)[X/\omega(R^2+X^2)].$$

Similarly, from $K''=(\sigma/\omega\epsilon_0)$ and $R_{||}=d/\sigma A$, where σ is the specific a.c. conductivity, we have

$$K''=(d/\epsilon_0 A)[R/\omega(R^2+X^2)].$$

Finally, we define the much used "loss factor,"

$$\tan\delta=K''/K'.$$

We have followed convention in plotting $\tan\delta$ in the figures representing our experimental results rather than K''.

Temperatures were measured by a series of overlapping thermometers consisting of thermocouples, constant volume thermometers, vapor pressure thermometers, and carbon resistance thermometers. By keeping the temperature drifts slow, temperatures are accurate to about $\frac{1}{10}$ of a degree at the extreme low

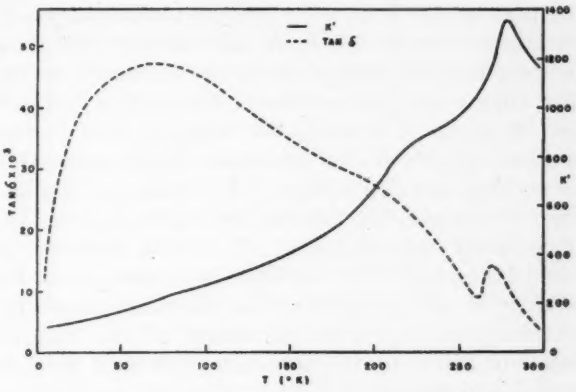

FIG. 2. K' and $\tan\delta$ of $BaTiO_3$ *versus* temperature.

temperatures, and to about $\frac{1}{2}$ degree at temperatures above 20°K.

RESULTS

Figure 2 shows the plot against temperature of K' and $\tan\delta$, for the four pure barium titanate specimens, A, B, C, D. Table I gives the values for specimen C at several temperatures and frequencies. Figure 3 shows the extreme low temperature portion of the curve so that some idea of the large slope may be obtained; the experimental points on all four pure specimens are plotted on this curve. In Fig. 4 the results of the studies on barium titanate diluted with a solid solution of 15 percent and 30 percent strontium titanate are shown as a function of temperature.

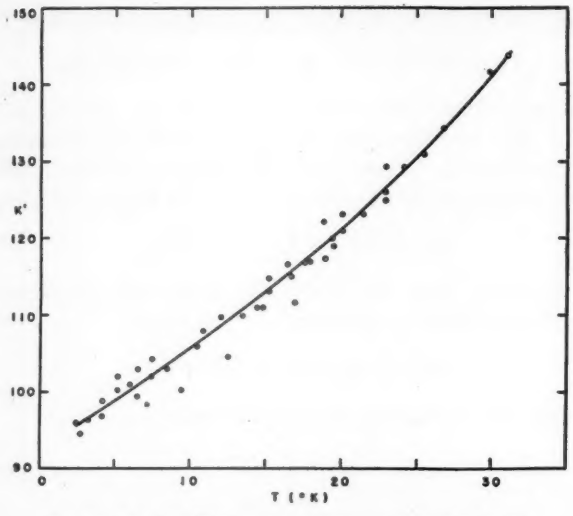

FIG. 3. K' of $BaTiO_3$ *versus* temperature below 30°K.

DISCUSSION

For the pure barium titanate the real part of the dielectric constant agrees in magnitude and in its temperature dependence with the work of Wul[1] and of von Hipple.[2] The peak at 280°K is not to be confused with the much larger peak found by many investigators at 393°K where there is a structure chance; possibly the peak at 280°K is to be identified with changes in domain size. Below 280°K, K' falls off with decreasing temperature to a value of about 100 in the 4°K region. The large slope gave a value of $1/K' \cdot dK'/dT$ of 0.01 per °K in the 4°K region for both the pure barium titanate and the diluted specimens. There appeared to be no frequency dependence of K' within experimental error over the entire temperature region studied. The temperature dependence of K' at low temperature could be explained on the basis of an increase in the binding of the titanium ion as the temperature decreases. Such a theoretical model of the damped oscillator driven by the periodic electric field gives an equation of motion:

$$m\ddot{x}+r\dot{x}+fx=eE_0e^{i\omega t}.$$

The well-known solution for the displacement, x, may be used to calculate the polarization $p=Nex$ for N oscillators per unit volume. From the relation $\epsilon_0 KE = \epsilon_0 E+P$, we obtain the complex dielectric constant

$$K=K'-iK''=1+\frac{Ne^2/m\epsilon_0}{(\omega_0^2-\omega^2)+ir\omega/m}.$$

For very low frequencies where $\omega \ll \omega_0$, the real part, K', is independent of the frequency of the electric field and depends on the force constant, f, in a way to satisfy the qualitative aspects of the experiments. Such a model predicts a dependence of K'' on the frequency and this has not been observed in our experiments.

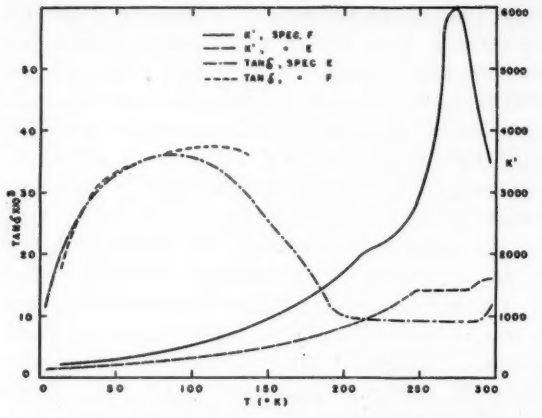

FIG. 4. K' and tanδ of diluted specimens *versus* temperature.

The large hump in tanδ at low temperatures observed on all specimens, pure and dilute, has not been observed previously. The values near room temperature are in agreement with those given by von Hipple[2] and by Roberts,[6] but disagree with their work at lower temperatures.

The effect of the dilution of barium titanate with 15 percent and 30 percent strontium titanate seems to have been a shifting of the normal barium titanate K' curve to lower temperatures. Thus the 30 percent dilution (specimen F) has its transition point peak of 6000 at 280°K and a value of 200 at 14°K. This shift in the transition point peak in K' is in agreement with the measurements reported by Jackson and Reddish.[7] The dilution with strontium ions in place of barium ions does very little to the temperature dependence of K''.

The theoretical interpretation presents a challenging problem both with respect to the surprisingly large dependence of K' on temperature at 4°K and with respect to the behavior of K'' with temperature and frequency. We suggest that the concept of domain growth must be introduced into the theory of K''.

ACKNOWLEDGMENTS

The authors would like to express their appreciation for the encouragement and guidance given them by Professor C. F. Squire, under whose direction this experimental investigation was made, and to Professor W. V. Houston for many interesting discussions on the interpretation of the results. Also we wish to acknowledge the discussions with Dr. John Richardson of the Bell Telephone Laboratories and thank him for supplying the specimens studied. One of us, R. F. Blunt, acknowledges with gratitude the Socony-Vacuum Fellowship. This work was supported in part by the Office of Naval Research (Navy Contract N6onr-224).

[6] Shepard Roberts, Phys. Rev. **71**, 890 (1947).
[7] W. Jackson and W. Reddish, Nature **156**, 717 (1949).

New Methods of Determining the Absolute Intensity of Cosmic Rays in the Atmosphere and the Residual Ionization in Ionization Chambers

VICTOR F. HESS AND ROGER P. VANCOUR
Fordham University, New York, New York

(Received July 5, 1949)

The portable Gish-Sherman ionization meter in connection with four geometrically similar cylindrical ionization chambers of different size was used for determining (1) the cosmic-ray intensity at sea level when the apparatus is completely shielded from local radiations by 10 cm of iron, and (2) at the same time a value for the residual ionization produced by spurious alpha-particles from the walls of the chambers. Two methods to obtain this end are described: one using all four chambers, and the other using the largest chamber and varying the pressure of the filling gas. Plotting the observed ionization *versus* the ratio of surface: volume gives a straight line which, when extrapolated for infinite volume leads to the value representing the ionization produced by cosmic rays without the secondaries from the wall.

THE "absolute intensity" of cosmic radiation at sea level (obtained in ionization chambers filled with air, reduced to normal temperature and pressure) reported by different authors varies within wide limits. For unshielded chambers at geomagnetic latitudes beyond the "knee" the values range from 1.9 to 2.8I. From the intensity *vs.* altitude curve a value of 2.08I was derived by Kolhoerster. In Holland J. Clay and P. H. Clay,[1] also using unscreened apparatus, found 1.63I for a vessel filled with air at atmospheric pressure and 15°C. This value is perhaps the most reliable one for the ionization by cosmic radiation at sea level, but even Clay did not take into account the increase of ionization by secondaries produced in the walls of the vessel. It is generally believed that the additional ion production by secondaries in a thin-walled brass chamber is quite small, perhaps only a few percent of the total effect. An experimental test for this contention would seem urgent.

The large discrepancies between the results of various authors may largely be due to the fact that the effects of local gamma-rays were not determined accurately enough. In some cases the residual ionization (due to radioactive impurities in the walls of the chamber) was over- or under-estimated; in other cases the reduction of observed ionization in high pressure chambers with argon or CO_2 to normal pressure in air may have been insufficiently accurate. In addition errors in the determination of small capacitances of some instruments or due to a lack of saturation in the ionization chambers may have been quite large.

One of us (V.F.H.) has made extensive studies of the ionization balance in the atmosphere at sea level[2] which is of fundamental importance for our knowledge of atmospheric electricity. The ionization of the atmosphere at sea level is produced by the alpha-, beta-, and gamma-rays from the radioactive products in the soil and in the atmosphere, and, to a lesser extent, by cosmic radiation. If we measure this ionization in a hermetically sealed vessel filled with a gas free of radon, the total ionization is due to: (1) occasional alpha-rays from radioactive impurities in the metal of the chamber (residual ionization, q_O), (2) gamma-rays from the radioactive substances in the soil (q_E), (3) gamma-rays from the radioactive decay products of radon, thoron, and actinon in the atmosphere (q_A), and (4) cosmic rays (q_C).

$$q=q_O+q_E+q_A+q_C.$$

If the ionization chamber is placed in an iron house with walls thick enough to absorb practically all gamma-rays (10 cm of iron) the total ionization is due to q_O and q_C. In this case we observe the effect of cosmic rays filtered through 10 cm of iron. If the apparatus is set up outdoors and the top of the iron house is left open, the ionization is due to unfiltered cosmic radiation and to the small gamma-ray component q_A which in most cases will not amount to more than 0.1I. The residual ionization (q_O) due to alpha-rays from the inner surface of the wall of the chamber can be kept at much less than 1I if the chamber walls are very carefully cleaned and the volume of the chamber is not too small. Since this residual ionization is proportional to the surface, while the other ionizing agencies are volume effects, it is advantageous to use chambers of fairly large size in which the ratio of surface area (A) to the volume (W) is rather small.

The total ionization as observed in the iron house (closed on top) is

$$q=q_O+q_C=Akn_\alpha+q_C, \quad (1)$$

TABLE I. Dimensions of the four chambers.

Chamber	Volume (W) cm³	Inner surface ($A=10r^2\pi$) cm²	Radius (r) cm	A/W
I	43680	7234	15.0	0.1656
II	13173	3247	10.16	0.249
III	4888	1675	7.30	0.348
IV	1645	811	5.08	0.504

[1] J. Clay and P. H. Clay, Physica 5, 898 (1938).
[2] V. F. Hess, *Die Ionisierungsbilanz der Atmosphäre* (Akademische Verlagsgesellschaft, Leipzig, 1934). V. F. Hess, Terr. Mag. 46, 409 (1941); Trans. Am. Geoph. Union 27, 670 (1946); Phys. Rev. 72, 609 (1947). V. F. Hess and J. D. Roll, Phys. Rev. 73, 592 (1948); Phys. Rev. 73, 916 (1948).

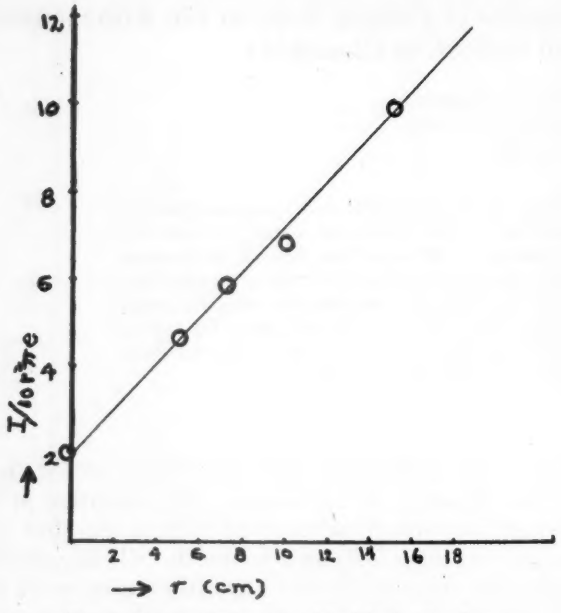

FIG. 1. Extrapolation of residual ionization from measurements of four chambers.

where n_α denotes the number of alpha-particles emitted from the wall per cm² per sec., A the surface area of the chamber wall, and k the average number of ion pairs produced by each alpha-particle.

The ionization produced by cosmic rays may also be considered partly as a surface effect since the secondaries produced in the walls of the chamber will increase (at constant thickness of the wall) with the area of the wall exposed to cosmic rays. Experiments to be discussed later will show that in thin-walled ionization chambers (as used by us) this effect of secondaries is very small. Therefore we can treat the cosmic-ray ionization as a volume effect, especially since the ranges of these secondaries are considerably longer than the diameter and height of our chambers.

We were using ionization chambers of cylindrical shape, made of yellow brass (wall thickness 2.5 mm) in conjunction with the ionization meter devised by O. Gish, K. L. Sherman and one of the authors which is described elsewhere.[3] The chambers were geometrically similar (height equal to twice the diameter of the chamber) with volumes 43.68, 13.17, 4.89, and 1.645 liters, and radii 15, 10.16, 7.30, and 5.08 cm respectively. All four cylinders were air-tight and could be evacuated or filled with any gas through a Hoke needle valve.

The amber-insulated inner electrode of each chamber is directly connected to the fiber system of a Lindemann electrometer which is mounted in a housing fitted exactly to the top of each of the chambers, which are used in a vertical position. The guard ring and the case of the electrometer are connected with a battery supplying 180 volts, and the center point of the quadrant battery is kept at the same potential. A needle contactor is used for connecting or disconnecting the fiber system from the battery with which the guard ring is permanently connected. The wall of each chamber is kept at ground potential. When the contactor is lifted the needle begins to float, and the rate of drift is a measure of the ionization in the vessel. We preferred to use the "null-method": a 3-volt auxiliary battery with a potentiometer and a precision voltmeter (range 3 volts) allowed us to add any voltage from 0 to −3 volts to the 180-volt sweep voltage, thus inducing an opposite charge on the floating system just enough to keep the electrometer needle always at or close to the zero point. When using this null-method, all corrections for insulation leakage of the electrometer are avoided. We found this method very reliable and practical even under very adverse atmospheric conditions. The reading of the compensating voltage at the end of each measurement (from 5 to 60 min. in duration) multiplied by a reduction factor, which is proportional to the induction coefficient between the guard ring system and the inner electrode for each chamber, gives the ionization (q) expressed in ion pairs per cm³ per sec.

The apparatus was built in the shop of the Department of Terrestrial Magnetism (Carnegie Institution), Washington, D. C. The fourth and largest chamber was constructed in 1947 and we are indebted to the Director, Dr. M. A. Tuve, for arranging this.

The capacitances and induction coefficients of all four chambers with the electrometer were redetermined in 1948 by means of a Wulf variable condenser calibrated with a G.E. capacitance bridge in the Department of Terrestrial Magnetism.

The residual ionization of the three smaller chambers was determined in 1947 by using them within the iron house in a subway tunnel under 210 ft. of solid rock where the cosmic-ray intensity is practically zero and local radiation was eliminated by the 10 cm iron wall around the apparatus. These direct measurements served as a control for determinations of the residual ionization with the two simpler methods to be described below.

We shall now first describe two methods used for the determination of the residual ionization and the intensity of cosmic rays in our brass chambers, and then proceed to the determination of the cosmic-ray intensity in the free atmosphere.

A. METHOD I

The method is based on the successive use of all four chambers in the iron house at the location where a determination of the cosmic-ray intensity is desired. To test this method we tried it first indoors, in the basement laboratory of the physics building at Fordham University. The cosmic rays measured there are filtered through four floors and ceilings and the additional 10 cm of iron (the top of the iron house). The experiments will be continued outdoors by setting up the iron house in a tent.

[3] V. F. Hess, Trans. Am. Geoph. Union **27**, 670 (1946).

The numerical values for the dimensions of the four chambers are listed in Table I.

The total ionization current in each chamber according to Eq. (1) is (in e.s.u.)

$$i=eAkn_\alpha+eWq_C. \tag{2}$$

Dividing by eA and inserting $A=10r^2\pi$ and $W=4r^3\pi$ (radius$=\frac{1}{4}$ of the height of each cylinder), we get

$$(i/10er^2\pi)=kn_\alpha+0.4rq_C. \tag{3}$$

This is a linear relationship between the total ionization observed and the radii of the chambers.

The experimental curve (Fig. 1) shows that such a relationship actually exists if all chambers show the same residual alpha-ray emission. Only chamber II shows a slight deviation. Extrapolation of the straight line to the value $r=0$ gives for $i/10er^2\pi$ the numerical value 2.00 which corresponds to our average value of ion production by alpha-ray emission from the walls of the brass chambers.

Taking for k a mean value of $1.5\times10^5 I$ per alpha-particle, the number of alphas emitted per cm² would be $n_\alpha=(2/1.5\times10^5)=1.33\times10^{-5}$ per sec., or 0.048 alpha-particles per hour for each cm² of brass. This figure may be a bit too low because some of the alpha-particles are coming not from the surface itself but from regions slightly below the surface. Taking $k=1.0\times10^5$ would probably be a better estimate, giving $n_\alpha=0.07$ alpha-particles per cm² per hour for our brass chambers. This shows that our chambers are practically free of radioactive impurities. The lowest alpha-ray emission reported so far is 0.03 per cm² per hour (for steel).*

We are now in a position to compute q_C. With nitrogen in the chambers at atmospheric pressure we got, for instance, for chamber I a total observed ionization $q=1.602I$, from which it follows that $I/10er^2\pi=9.89$. Inserting this value and the experimental value for kn_α (2.00) in Eq. (3)

$$0.4rq_C=9.89-2.00=7.89$$
$$q_C=1.315I.$$

This value of q_C is, of course, the cosmic-ray ionization actually produced within the brass chamber. Similar values were obtained with chambers II, III, and IV.

The residual ionization computed for the largest chamber is, therefore, $q_O=1.602-1.315=0.287I$. This value could not be checked directly by an underground experiment, because the underground station had to be discontinued before this particular chamber was constructed. For chambers III and IV such comparisons were made and gave satisfactory agreement within ±10 percent between experimental values (iron house in tunnel) and computed values of q_O.

* See J. A. Bearden Rev. Sci. Inst. 4, 271 (1933).

B. METHOD II

This method is based on the observation of the change of ionization with pressure in the largest chamber. It is well known that ionization increases almost linearly with pressure, but the curve flattens out at higher pressures except when very pure argon is used.[4] For this reason it seemed more appropriate to work at lower pressures, as C. T. R. Wilson did in his early experiments on penetrating radiation. We measured the ionization in the largest chamber (43.7 liters in volume) filled with either commercial nitrogen or argon at atmospheric pressure and at lower pressures by reducing the pressure in steps of 5 or 10 cm Hg down to about 7 cm. It was to be expected that the ionization *vs.* pressure curve would be linear as long as the pressure (p) was not lower than that at which the range of the alpha-particles is equal to the diameter of the chamber (15 cm). At still lower pressure the curve was expected to deviate downward toward zero. The slope of the linear part of the curve then would represent the actual value of the ionization produced by cosmic rays in the chamber (including secondaries), while the extrapolation of the linear part of the curve for $p=0$ would give the approximate value of the residual ionization.

Theoretically, the observation of just two points on the linear part of the ionization *vs.* pressure curve at $p=1$ atmos. and about $p'=0.5$ atmos. would give these results. If the saturation currents, i and i', are measured in the iron house at the pressures p and p',

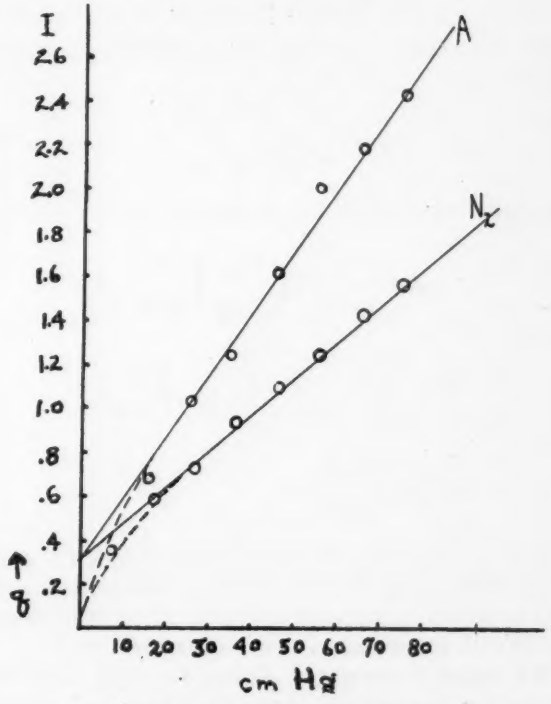

FIG. 2. Ionization by cosmic rays *vs.* pressure for argon and nitrogen.

[4] A. H. Compton and J. J. Hopfield, Rev. Sci. Inst. 4, 491 (1933).

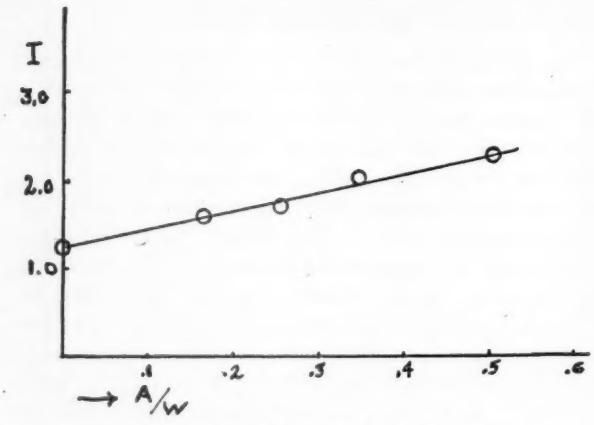

FIG. 3. Extrapolation of ionization by cosmic rays in the free atmosphere.

we have

$$i = Aekn_\alpha + Weq_C \cdot p$$

$$i' = Aekn_\alpha + Weq_C \cdot p'$$

$$i - i' = Weq_C(p - p')$$

$$q_C = \frac{1}{We} \cdot \frac{i-i'}{p-p'} = \frac{1}{We} \frac{di}{dp}.$$

For our cylindrical chambers (radius=$\frac{1}{4}$ of the height of the chamber)

$$i = 10r^2\pi ekn_\alpha + 4r^3\pi eq_C p,$$
$$i' = 10r^2\pi ekn_\alpha + 4r^3\pi eq_C p',$$

where kn_α and q_C are the two unknown quantities. Since

$$q_C = \frac{1}{4r^3\pi e} \frac{i-i'}{p-p'} = \frac{dq}{dp} \tag{4}$$

we obtain the residual ion production per cm² per sec.

$$kn_\alpha = \frac{i}{10r^2\pi e} - \left(\frac{i-i'}{p-p'}\right)\frac{p}{10r^2\pi e},$$

and

$$q_O = \frac{Akn_\alpha}{W} = \frac{i}{4r^3\pi e} - \left(\frac{i-i'}{p-p'}\right)\frac{p}{4r^3\pi e},$$

$$q_O = q - \frac{q-q'}{p-p'} \cdot p.$$

It is, of course, more accurate to determine the slope of the curve dq/dp from a number of points graphically and to obtain q_O from the intercept of the straight line dq/dp with the ordinate, as it is shown in Fig. 2.

We found it necessary always to begin with the readings at atmospheric pressure and to reduce pressure in steps instead of beginning at lower pressures, since filling the chamber with gas from a steel cylinder through a reduction valve is always accompanied by a spurious influx of ions, presumably Langevin ions, even when a cotton filter is inserted. It takes some time until this temporary ion cloud is removed. This effect is completely avoided when the readings are taken after each step of reduction in pressure.

Figure 2 gives two sample curves obtained with nitrogen and argon in the chamber. They show very clearly the linearity of the curves and the downward deviation of q at the lowest pressures used. The extrapolated value of $q_O = 0.32I$ is in good agreement with the value obtained with method I.

The values of cosmic-ray ionization $q_C = dq/dp$ for argon ($2.10I$) and nitrogen ($1.24I$) at atmospheric pressure are also in good agreement with the accepted figures; their ratio (1.69) is practically the same as was found by Hopfield.[4] It is to be kept in mind that these values of q_C represent the ionization by cosmic rays at sea level, geomagnetic latitude 51°N, in a large brass cylinder, after penetrating four ceilings and floors of our building and an additional screen of 10 cm of iron.

C. DERIVATION OF THE VALUE OF THE TRUE IONIZATION BY COSMIC RAYS WITHOUT SECONDARIES

In order to obtain the ionization without secondaries from the walls of the chamber, one can proceed as follows: we plot the observed values of $q = Akn_\alpha + q_C$ (total ionization in the iron house) *vs.* A/W. The extrapolated value of q for $A/W = 0$ (infinite volume) would indicate the ionization produced in a chamber of infinite volume filled with nitrogen at atmospheric pressure, at the point of observation. Figure 3 shows that the four chambers give a linear relationship q *vs.* A/W with an extrapolated value of $q_C = 1.23I$. This figure actually represents the true ion production in nitrogen without any secondaries emitted from the walls, since in a chamber of infinite volume any contribution of residual ionization (alpha-rays from the walls) as well as from electrons knocked out of the walls by cosmic rays would be negligible. If, therefore, similar experiments are performed outdoors, *we will be able to evaluate quite accurately the true ionizing effect of cosmic rays in the free atmosphere.*

The value obtained in a brass chamber, as derived in section *A*, $q_C = 1.315I$ is only 7 percent higher than the extrapolated value derived here. Therefore it is obvious that all measurements of cosmic-ray intensities with brass chambers are slightly too high. In other words, they do not represent the true ionization in the atmosphere at the point of observation. However, the difference is slight and certainly much smaller than many authors believed it would be sometime ago.

The senior author wishes to express his thanks to the American Philosophical Society for a grant supporting this work, and to Dr. J. A. Fleming and Dr. M. A. Tuve for arranging the construction of the four chambers in the shop of the Department of Terrestrial Magnetism in Washington, D. C.

Rollin Film Rates in Liquid Helium

HENRY A. FAIRBANK AND C. T. LANE
Sloane Physics Laboratory, Yale University, New Haven, Connecticut*
(Received July 11, 1949)

Quantitative measurements have been made on the flow of the Rollin film out of a cylindrical vessel containing liquid helium. The range of temperature studied extends from 1.34 K to the λ-point. It is found that the film transfer rate is somewhat greater than that observed for isothermal flow under a gravitational potential difference. Evidence is presented tending to show that the film can evaporate at temperatures near those of the parent liquid.

INTRODUCTION

IN 1936 Rollin[1] suggested that the observed high evaporation rate from vessels containing liquid helium II was due to a thin surface layer of liquid helium on the walls of the container. In subsequent experiments Rollin and Simon[2] established this high evaporation rate as due to an actual transport of the liquid, via the surface film, up the wall to the higher temperature region where evaporation of the film occurs. This type of film transport, referred to henceforth as Type A, is illustrated schematically in Fig. 1.

A similar transport of liquid by means of the film occurs from regions of higher to lower gravitational potential in the absence of any measurable temperature gradient. We shall call this case Type B. Thus in Fig. 1, the liquid level in the two impermeable beakers, partially immersed in liquid helium II, will assume the level of the outside bath due to this film transport process. This type of film transport was first studied systematically by Daunt and Mendelssohn[3] in 1939. The mass rate of flow of the film was found to be independent of the gravitational potential difference between the levels, and a function only of the temperature of the liquid and the minimum periphery in the connecting surface above the higher level. Recently Atkins,[4] using similar techniques, has reported experimental values of this film transport velocity several times larger than those of Daunt and Mendelssohn. In view of this wide disagreement, Webber and the authors[5] re-examined this case experimentally and found results in substantial agreement with the earlier work of Daunt and Mendelssohn. Bowers and Mendelssohn,[6] in a brief note recently received, present evidence that the high creep velocities such as those observed by Atkins are due to adsorbed or frozen air on the walls of the vessel over which the film creeps.

In view of the above discrepancies in experimental results in the B type of creeping film (Fig. 1) it seemed to us highly desirable to obtain more information about the behavior of the film under conditions represented in A (Fig. 1). The early work of Rollin and Simon[2] established the general character of the creeping film but did not give quantitative values of film transport velocity.

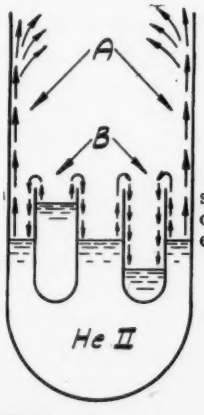

FIG. 1. A schematic representation of the two types of film transport phenomena.

EXPERIMENTAL PROCEDURE

The apparatus is shown schematically in Fig. 2. A 1.7-mm diameter U tube is immersed in a bath of liquid helium connected to a vacuum pump and manometer for control and measurement of the temperature. A

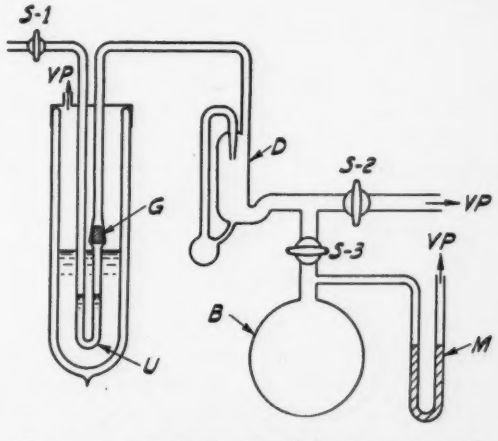

FIG. 2. A schematic drawing of the apparatus used in the present experiment.

* Assisted by the ONR.

[1] B. V. Rollin, Proc. VII Int. Congress of Refrigeration **1**, 187 (1936).

[2] B. V. Rollin and F. Simon, Physica **6**, 219 (1939).

[3] J. G. Daunt and K. Mendelssohn, Proc. Roy. Soc. **A170**, 423, 439 (1939).

[4] K. R. Atkins, Nature **161**, 925 (1948).

[5] Webber, Fairbank, and Lane, Phys. Rev. **76**, 609 (1949).

[6] R. Bowers a nd K. Mendelssohn, Nature **163**, 870 (1949).

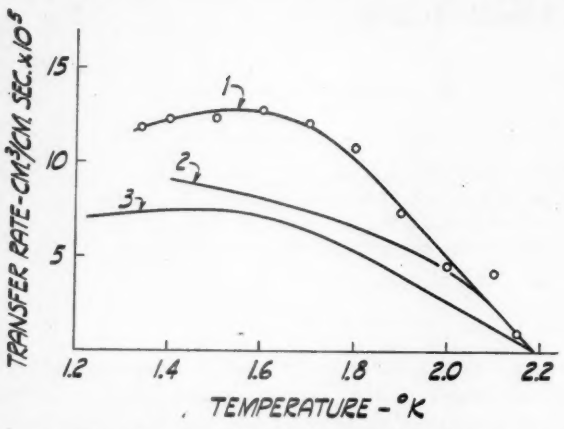

FIG. 3. The film transfer rate as a function of temperature. Curve 1 is the present experiment (Type A creep). Curves 2 and 3 give the results of Webber, Fairbank, and Lane and of Daunt and Mendelssohn, respectively, for gravitational film transport (Type B creep).

small amount of helium is condensed in the U tube via stopcock *S*-1. The tightly fitting ground glass plug *G* isolates the vapor space above the liquid in the tube from the rest of the system but the gap is large enough to allow the creeping film to pass the plug unhindered. Thus it is possible to pump off the gas from the evaporating film above the plug *G* with the mercury diffusion pump *D* without withdrawing any appreciable amount of the vapor from the vapor space below *G*. Hence the mass rate of flow of gas through the diffusion pump equals the mass rate of flow of the creeping film. This rate was measured by closing stopcock *S*-2 in the fore-pump line and measuring the rate of increase of pressure in the previously evacuated 2-liter bulb *B* by determining the time rate of fall of the oil manometer *M*. A simple calculation converts the rate of pressure increase into mass rate of flow from which the film transport velocity may then be found.

By measuring the rate of flow of vapor through the ground plug just above the λ-point, and using the equation for Poiseuille viscous flow through an annular gap given by Lamb,[7] the mean width of the channel was estimated to be of the order of a few microns, which is of the order of 100 times the film thickness as determined by Daunt and Mendelssohn.[3] The flow rate of the vapor past the plug was negligibly small compared to that of the film.

RESULTS

Film transfer rates were obtained at temperatures from 1.34°K to the λ-point. The average values of the measurements taken at each temperature are given in Table I, and represented graphically in Fig. 3, curve 1. Following Daunt and Mendelssohn we have given the creep velocities in the units cm³ of liquid flowing per cm of periphery per sec. For comparison purposes the transfer rate curves (smoothed values) for the gravitational case (*B* in Fig. 1) obtained by Daunt and Mendelssohn[3] and by Webber, Fairbank, and Lane[5] are included (curves 2 and 3).

In performing these measurements the following variations were made:

(a) At the start of the measurements the liquid level of the outside bath was even with the top of the ground plug *G* and about 13 cm above the liquid level inside the U tube. In the course of the experiment this outside level gradually dropped until it was even with the inside level. Within the accuracy of the measurements the transfer rates obtained at the same temperature under these changing conditions were identical. This would suggest that the transfer rate for a given surface depends primarily, and perhaps uniquely, on the temperature of the bath, which, as discussed below, is probably also the temperature of the film for a tube of this geometry.

TABLE I. Film transfer rate *versus* temperature (Type A creep).

Temperature (°K)	Film transfer rate (Cm²/cm sec.)
2.15	0.96×10^{-5}
2.1	4.1
2.0	4.5
1.9	7.3
1.8	10.7
1.7	12.0
1.6	12.7
1.5	12.3
1.4	12.3
1.34	11.8

(b) The previous experiments on Type A creep have given no clear indication as to the temperature of the film where final evaporation occurs. (See references 2 and 3.) In the present experiment we wound a small electrical heating coil on the outside of the U tube just below the glass plug and some distance above the surface of the liquid in this tube. With the bath temperature set at 1.5°K, we supplied various amounts of heat to this coil. With no heat applied the creep rate was 12.3×10^{-5} cm³/cm sec., but with 0.22 milliwatt the creep rate was found to decrease to 6.5×10^{-5} cm³/cm sec. Finally at 0.4-milliwatt heat input the creep rate was observed to vanish.

The plug permits only film, as such, to pass through it; vapor created by evaporating the film, or in any other way, cannot pass the plug. Hence the decreased creep rate with some heat supplied indicates that, while some evaporation has occurred, the remaining film continues to creep up the walls past the source of heat. This could happen only if the evaporation occurred below the λ-point and suggests that the film evaporates at a temperature near that of the liquid, i.e., the vapor pressure of the film is not drastically different from that of the parent liquid.

Returning to Fig. 3, there is seen to be a fair agreement between the film transfer velocities measured

[7] Horace Lamb, *Hydrodynamics* (Cambridge University Press, 1906), p. 545.

under the conditions A and B. The simplest conclusion that might be drawn would be that these cases are not fundamentally different and that the limiting film transfer velocity in all cases depends, for a given surface,

(1) on the temperature
(2) on the minimum periphery in the connecting surface above the higher level.

The suggestion of Bowers and Mendelssohn that adsorbed air on the surface is responsible for anomalously high transfer rates would not appear inconsistent with this picture.

Finally, we are grateful to Dr. C. A. Reynolds and Mr. E. A. Lynton for their assistance with the experiment.

Note added in proof.—Professor F. Simon, at the recent Conference on Low Temperatures at M.I.T., has kindly drawn our attention to the fact that an estimate of the Type A film transfer rate may be computed from data given in reference (2). These measurements extend down to about 1.6°K and give a transfer rate of approximately 8×10^{-5} cm³/cm·sec. at this temperature, which is somewhat less than the value observed by us above.

PHYSICAL REVIEW VOLUME 76, NUMBER 8 OCTOBER 15, 1949

Collision Theories of Pressure Broadening of Spectral Lines

J. H. Van Vleck
Harvard University, Cambridge, Massachusetts

AND

Henry Margenau
Yale University, New Haven, Connecticut*

(Received May 19, 1949)

It is shown that in the calculation of absorption in the Lorentz collision theory, it is essential to include the work done impulsively by the electric field during the sudden changes of position at collision. This work was implicitly included in the theory of Van Vleck and Weisskopf, but these authors did not give the breakdown into work done between and at collision. It is verified that the shapes of spectral lines for a classical harmonic oscillator and also a Debye slow rotator are the same in absorption and spontaneous emission, provided the energy density obeys the Rayleigh-Jeans law. The usual proofs of equilibrium simply establish equality of the integrated absorption and emission, without examining the detailed balancing at individual frequencies, not necessarily near resonance.

A COLLISION or impact theory of the width of spectral lines is one which conceives of the frequency distribution within a line as resulting from interruptions of the radiative process by collisions with molecules. The exact form of the resulting line width depends in a rather critical way on the detailed assumptions that are made about the nature of these interruptions, and there seems to be some confusion both as to concepts and terminology concerning the subject of impact broadening. The present paper attempts to clarify this situation.

A. LORENTZ THEORY OF SPONTANEOUS RADIATION

As it is usually understood, the Lorentz[1] formula for line breadths results from simple Fourier analysis of a finite wave train radiated by a harmonically moving charge. Let the radiative frequency be ω, and suppose that the radiation goes on for a time θ. Then, if the amplitude is x_0, the Fourier analysis of the displacement is

$$x(t)=\frac{1}{(2\pi)^{\frac{1}{2}}}\int_{-\infty}^{\infty}x(\omega')e^{i\omega' t}d\omega',$$

$$x(\omega')=\frac{1}{(2\pi)^{\frac{1}{2}}}\int_{0}^{\theta}x_0\cos(\omega\lambda+\phi)e^{-i\omega'\lambda}d\lambda.$$

When $|x(\omega')|^2$ is averaged over a random distribution in the arbitrary phase constant ϕ, the result is

$$|x(\omega')|^2=\frac{x_0^2}{4\pi}\left[\frac{1-\cos(\omega'-\omega)\theta}{(\omega-\omega')^2}+\frac{1-\cos(\omega'+\omega)\theta}{(\omega+\omega')^2}\right].$$

This expression must be integrated over all collision times θ with a weighting function $ae^{-a\theta}$, where a is the mean collision frequency. One thus obtains

$$|x(\omega')|^2=\frac{x_0^2}{4\pi}\left[\frac{1}{a^2+(\omega-\omega')^2}+\frac{1}{a^2+(\omega+\omega')^2}\right].$$

According to classical mechanics, the power radiated by a charge e oscillating in one dimension is

* Assisted by the ONR.

[1] H. A. Lorentz, Proc. Amst. Akad. Sci. 8, 591 (1906).

$\frac{2}{3}e^2c^{-3}(d^2x/dt^2)^2$. Our Fourier components are normalized in such a way that

$$\int_{-\infty}^{\infty}x(t)^2dt=\int_{-\infty}^{\infty}|x(\omega')|^2d\omega'=2\int_0^{\infty}|x(\omega')|^2d\omega'.$$

Hence the power emitted in the spectral interval ω', $\omega'+d\omega'$ is

$$P_E(\omega')d\omega'=(2e^2/3c^3)\cdot 2\omega'^4|x(\omega')|^2\cdot a\cdot d\omega'.$$

Here the factor a owes its origin to the fact that we have made the Fourier analysis of the displacement existing only in a single interval between two collisions, and in a very long time T there are aT such intervals. When we utilize our explicit formula for the mean square Fourier components, the expression for $P_E(\omega')$ becomes

$$P_E(\omega')=\frac{e^2x_0^2}{3\pi c^3}\omega'^4\left[\frac{a}{a^2+(\omega-\omega')^2}+\frac{a}{a^2+(\omega+\omega')^2}\right]. \quad (1)$$

B. LINE SHAPE IN ABSORPTION

The shape of the spectral line can also be studied by examining absorption rather than spontaneous radiation. We calculate the power absorbed by an oscillating charge of natural frequency ω from a light wave whose electric vector is $E\cos(\omega't+\phi)$. The oscillator is subject to collisions at times t_1, t_2, $\cdots$, and each collision is supposed by Lorentz to have the effect of making x and $\dot{x}$ zero abruptly at the instant of collision. The equation to be solved is then

$$\ddot{x}+\omega^2x=(eE/m)\cos(\omega't+\phi),$$

and the solution wanted here is

$$x=\begin{cases}x_1 \text{ for } t_1\leqslant t\leqslant t_2\\ x_2 \text{ for } t_2\leqslant t\leqslant t_3,\\ \text{etc.}\end{cases}$$

$$x_j=(eE/m\omega)\int_0^{t-t_j}\cos(\omega't-\omega'\lambda+\phi)\sin\omega\lambda d\lambda,$$

$$\dot{x}_j=(eE/m)\int_0^{t-t_j}\cos(\omega't-\omega'\lambda+\phi)\cos\omega\lambda d\lambda.$$

These integral forms, chosen to satisfy the conditions $x_j(t_j)=\dot{x}_j(t_j)=0$, are most convenient in calculations.

The work done by the field is

$$W=\sum_j\int_{t_j}^{t_{j+1}}eE\cos(\omega't+\phi)\dot{x}_jdt. \quad (2)$$

When the substitution for $\dot{x}_j$ is made and the difference $t_{j+1}-t_j$ is replaced by θ_j one obtains

$$W=(e^2E^2/m)\sum_j\int_0^{\theta_j}\cos(\omega't+\phi_j)\times dt\int_0^t\cos[\omega'(t-\lambda)+\phi_j]\cos\omega\lambda d\lambda, \quad (3)$$

with $\phi_j=\omega't_j+\phi$.

As to the distribution of collision times, we assume again that the number of intervals having duration between θ and $\theta+d\theta$ is $ce^{-a\theta}d\theta$, so that the total time of observation is

$$T=\int_0^{\infty}ce^{-a\theta}\theta d\theta=c/a^2.$$

Therefore, in Eq. (3), $\sum_j$ may be replaced by

$$a^2T\int e^{-a\theta}d\theta.$$

The presence of many absorbing atoms permits the assumption that the t_j, and hence the ϕ_j, are distributed at random. The expression for W may then be simplified by averaging over ϕ_j and it becomes

$$W=(e^2E^2/2m)aT\int_0^{\infty}e^{-a\theta}d\theta\int_0^{\theta}dt\int_0^t\cos\omega'\lambda\cos\omega\lambda d\lambda. \quad (4)$$

At this stage it is well to remember the formula:

$$a\int_0^{\infty}e^{-a\theta}d\theta\int_0^{\theta}f(\lambda)d\lambda=\int_0^{\infty}e^{-a\lambda}f(\lambda)d\lambda.$$

On using it one obtains for the average power absorbed per atom

$$\frac{W}{T}=\frac{e^2E^2}{4m}\left[\frac{a}{a^2+(\omega'-\omega)^2}+\frac{a}{a^2+(\omega'+\omega)^2}\right]. \quad (5)$$

The so-called "structure" factor, which is enclosed by square brackets, and which determines the dependence on frequency near resonance, agrees with that in (1).

C. CORRECTION OF LORENTZ FORMULA FOR WORK DONE DURING COLLISIONS

The preceding derivation, however, ignored the work done by the electromagnetic forces during collisions. As the oscillator displacement drops back from the value $x_j(t_{j+1})$ to zero at the time t_{j+1}, its velocity is momentarily infinite. Because of this, there is added to the work given by Eq. (2) the increment

$$\lim_{\delta\to 0}\sum_j\int_{t_{j+1}-\delta}^{t_{j+1}+\delta}eE\cos(\omega't+\phi)\dot{x}_jdt.$$

A partial integration converts each term of this sum-

mation into

$$[eE\cos(\omega' t+\phi)x]_{t_{j+1}-\delta}^{t_{j+1}+\delta}=-eE\cos(\omega' t+\phi)x_j(t_{j+1}),$$

plus an integral which vanishes in the limit.

To the right-hand side of (3) one must then add

$$(-e^2E^2/m\omega)\sum_j\cos(\omega'\theta_j+\phi_j)\times\int_0^{\theta_j}\cos[\omega'(\theta_j-\lambda)+\phi_j]\sin\omega\lambda d\lambda.$$

If the same assumptions as before are made about the distribution of the ϕ_j and θ_j, Eq. (4) takes on an additional term

$$(-e^2E^2aT/2m\omega)\int_0^\infty e^{-a\theta}d\theta\int_0^\theta\cos\omega'\lambda\sin\omega\lambda d\lambda,$$

and W/T, previously given by Eq. (5), increases by

$$\frac{e^2E^2a}{4m\omega}\left[\frac{\omega'-\omega}{a^2+(\omega'-\omega)^2}-\frac{\omega'+\omega}{a^2+(\omega'+\omega)^2}\right]. \quad (6)$$

This is the power spent against the forces during collisions. In the optical range of frequencies, where ω and ω' are nearly equal and both are very large, (6) is negligible in comparison with (5). It may also be noted that the power spent during collisions is abstracted from the light wave on one side of the spectral line, delivered to it on the other. When (5) and (6) are combined, the result is

$$(W/T)=\frac{e^2E^2\omega'}{4m\omega}\left[\frac{a}{a^2+(\omega'-\omega)^2}-\frac{a}{a^2+(\omega'+\omega)}\right]. \quad (7)$$

Van Vleck and Weisskopf[2] have derived Eq. (7) directly by computing the *mean* displacement of all oscillators and then differentiating it with respect to time to obtain the mean velocity. The work done at collisions is implicitly taken into account because the discontinuities at collision affect the time derivative of the mean displacement at any given instant even though they do not enter in the mean velocity of a particle between collisions. The significance of the procedure of Van Vleck and Weisskopf is made more explicit and clearer by the method of the present paper, which segregates the contributions of the work done between and at collisions, and which is therefore perhaps not entirely without interest. Van Vleck and Weisskopf call (7) the Lorentz formula. To what expression one attributes this name is to a large extent a matter of personal choice and opinion, as the calculations of Lorentz are many-sided. It is probably more customary to approach the problem of spectral distribution from the standpoint of spontaneous radiation rather than absorption; then one is led to regard (1) rather than (7) as the Lorentz formula.

As the structure factor is different in (1) and (7), it would at this stage appear that the shapes of emission and absorption lines are different, in violation of the thermodynamics of radiation. This dilemma, however, is removed when allowance is made for the fact that after collision the displacements should be taken as distributed according to the Boltzmann law rather than random, as Lorentz supposed. Van Vleck and Weisskopf show that a further contribution to W/T must be included if it is assumed that, after collision, an oscillator does not snap back to a zero (or mean zero) displacement, but to the value

$$(eE/m\omega^2)\cos\phi_j,$$

which is the mean of the displacement of all oscillators, computed with the Boltzmann weighting factor, in the field of the light wave at t_j. This requires a further addition to the power given by Eq. (7) of amount

$$\frac{e^2E^2a}{4m\omega^2}\left[\frac{\omega'^2-\omega'\omega}{a^2+(\omega'-\omega)^2}+\frac{\omega'^2+\omega'\omega}{a^2+(\omega'+\omega)^2}\right]. \quad (8)$$

(Van Vleck and Weisskopf do not give the breakdown of (8) in terms of work done between and at collisions; a simple calculation by the methods of the present paper shows that the contribution of the former to (8) just equals the expression (6) in value, and that the balance of (8) is accounted for by the impulsive work at collision.)

D. BALANCE BETWEEN EMISSION AND ABSORPTION

Formulas (7) and (8) relate to power absorbed from a monochromatic wave of amplitude E and frequency ω'. To study the spectral distribution of the absorption in a non-monochromatic radiation field, we must replace E^2 by $8\pi\rho(\omega')d\omega'/3$ and make some assumption concerning how the energy density $\rho(\omega')$ of radiation varies with frequency. When we make this replacement and add (8) to (7), we find that the energy absorbed in the interval ω', $\omega'+d\omega'$ is $P_A(\omega')d\omega'$ with

$$P_A(\omega')=\frac{2\pi e^2\omega'^2}{3m\omega^2}\left[\frac{a}{a^2+(\omega'-\omega)^2}+\frac{a}{a^2+(\omega'+\omega)^2}\right]\rho(\omega'). \quad (9)$$

Since our calculation is purely classical, we should expect equilibrium between absorption and spontaneous emission if the energy density has the Rayleigh-Jeans value

$$\rho(\omega')=kT\omega'^2/\pi^2c^3. \quad (10)$$

Indeed, the expression (9) just equals (1) if we use (10) and also employ, as we should, in (1) the equipartition value $x_0^2=2kT/m\omega^2$ for the statistical average of the square of the amplitude of a harmonic oscillator.

The literature is full of proofs that the total integrated

[2] J. H. Van Vleck and V. F. Weisskopf, Rev. Mod. Phys. 17, 227 (1947).

absorption and emission of a harmonic oscillator balance in a Rayleigh-Jeans radiation field. However, so far as we know, no explicit verification has previously been published that the shapes of the absorption and emission lines are the same.

It should be noted that our proof of the equilibrium required utilization of the correction (8) introduced by Van Vleck and Weisskopf to allow for the fact that after collisions the phases are distributed in accordance with the Boltzman law. Without this correction, balance between absorption and emission is not secured. It is true because of Eq. (5) that if one neglects the impulsive work done at collisions and assumes random phasing after collision, the absorbed energy will differ from the emitted only by a factor ω^2/ω'^2,—a distinction unimportant in the immediate vicinity of resonance, the case usually considered. Exact compensation at all frequencies is required, however, if detailed balancing is to hold. Accurate fulfillment of this requirement can be regarded as additional confirmation of the correctness of the Van Vleck-Weisskopf shape factor for absorption.

It should also be mentioned that in the calculation of spontaneous emission at the beginning of this paper, we implicitly took into account the sudden changes of position at collision, with attendant singularities in velocity and acceleration. For we made a Fourier analysis of the displacement, and multiplied by $-\omega'^2$ to obtain the Fourier components of the acceleration. If instead we made directly the Fourier analysis of an acceleration which is $-x_0\omega^2\cos(\omega t+\phi)$ over a time interval θ, and zero elsewhere, thus neglecting the infinite accelerations at collision, the Fourier components of the acceleration would differ by a factor ω^2/ω'^2 from those we use. Then a factor ω^4/ω'^4 would be introduced in (1), and the balance between emission and absorption spoiled.

E. THE SLOW ROTATOR

The need of considering the spontaneous radiation arising from the impulsive changes in position at collision becomes particularly clear if one utilizes the model employed by Debye[3] in studying absorption and dispersion at radiofrequencies in liquids. He takes the molecular system to be a rigid dumb-bell whose proper frequency of rotation is small compared with the collision parameter a. Except for vibrations forced by the applied field, the molecule thus is regarded as standing still between collisions. Hence no spontaneous radiation at all would be obtained if one tried to apply the Fourier analysis only to the acceleration for the interval between collisions. On the other hand, emission of the proper amount is obtained if (1) is used. In this connection, the proper frequency ω is to be taken as zero and the quantity $e^2x_0^2$ in (1) is to be replaced by $2\mu^2$ inasmuch as the circular rotation of a dipole of moment μ can be resolved into two simple harmonic motions of amplitude μ in two orthogonal directions. Various authors have shown that the absorption by the slow rotator is given by

$$P_A(\omega')=\frac{4\pi\mu^2\omega'^2}{3kT}\frac{a}{\omega'^2+a^2}\rho(\omega'). \tag{11}$$

There is exact agreement between (11) and (1) (with $\omega=0$, $e^2x_0^2=2\mu^2$) when the energy density has the Rayleigh-Jeans form (10).

In closing we should like to emphasize that the calculations of the present paper are based entirely on the Lorentz model of infinitely short collisions with no persistence in phase. For actual atomic systems, corrections for the finite length of collision may alter the line shape. Also, in quantum mechanics, where the Planck radiation law replaces that of Rayleigh-Jeans, the problem of the calculation of the shape of the absorption curve and verification of detailed balancing is far more difficult than in classical theory; we have not succeeded in solving it accurately even for collisions of the Lorentz type. In the microwave region, however, there is no difficulty, as ω' is small compared with kT/h, and the Planck formula reduces to that of Rayleigh-Jeans. In this region, the shape factor is therefore appropriately given by (1) or (9) for the Lorentz model of collisions even if quantum mechanics is used. In particular, a quantum-mechanical derivation of the Van Vleck-Weisskopf absorption formula has been given by Karplus and Schwinger.[4]

We wish to thank Professor D. M. Dennison for calling our attention to the desirability of studying line shapes simultaneously in absorption and emission.

[3] P. Debye, *Polar Molecules* (The Chemical Catalog Company, Inc., New York, 1929), Chapter V. For the calculation of the absorption with the Lorentz model of strong collisions, see especially Van Vleck and Weisskopf, reference 2.

[4] R. Karplus and J. Schwinger, Phys. Rev. 73, 1020 (1948).

Dielectric Constants and Polarizabilities of Ions in Simple Crystals and Barium Titanate

SHEPARD ROBERTS
Research Laboratory, General Electric Company, Schenectady, New York
(Received June 13, 1949)

The observed dielectric constants of alkali halides and certain other types of crystals coincide with a relatively simple interpretation of dielectric polarization which is based on the classical equation of Clausius and Mosotti. The polarizability of each elementary ion has only a small positive temperature coefficient and is invariant when the given ion is incorporated in different crystalline solids subject to certain symmetry requirements. The polarizabilities of the ions in cubic barium titanate, although normal, account quite satisfactorily for the high observed values of dielectric constant. A method of estimating dielectric constants from the known polarizabilities of ions is applied to several compounds for which dielectric data have not been reported.

I. INTRODUCTION

THE equation of Clausius and Mosotti,[1] relating the dielectric constant of a substance to the polarizability of the particles of which it is made has been known for a great many years and has been successfully applied to gases and non-polar liquids. The corresponding equation for optical index of refraction, attributed to Lorentz and Lorenz, has, in addition, been applied to simple ionic crystals of the alkali-halide type, but the results of this application were not originally viewed with satisfaction, since there were reported systematic deviations between theory and experiment.[2–4] This equation was later reviewed by Shockley[5] who found that values of polarizability could be assigned to individual ions in such a way that their sums coincided with the polarizabilities of compounds as calculated by the Lorentz-Lorenz formula. The deviations were found to be not greater than three percent.

The purpose of the present paper is to report the successful correlation of dielectric constants of ionic crystals by using the Clausius-Mosotti equation and to show in what types of crystals this relation may be expected to be valid. A brief résumé of the derivation of the fundamental equations is given. This is followed by a discussion of the experimental data in which polarizabilities of the individual ions are derived. The temperature coefficients of dielectric constant are analyzed, and it is shown that the polarizability changes only very slightly with temperature, even, as in barium titanate, when the temperature coefficient of dielectric constant is very high.

II. THEORY

The Clausius-Mosotti equation states a relation between the polarizability, α, per molecule of a substance and its dielectric constant K.

$$\alpha=3V(K-1)/(K+2), \tag{1}$$

where V is the volume of the unit cell in the crystal lattice divided by the number of molecules which it contains. A corollary of the Clausius-Mosotti equation is that the polarizability of a molecule is equal to the sum of polarizabilities of the ions which it contains. Thus, in a diatomic molecule

$$\alpha=\alpha_1+\alpha_2=3V(K-1)/(K+2). \tag{2}$$

This cannot be verified directly by experiment, since neither α_1 nor α_2 can be measured independently. But it can be checked indirectly, since it leads to an additivity relation between polarizabilities of the different compounds AC, AD, BC and BD of the same elements A, B, C, and D. Thus:

$$\alpha_{AC}+\alpha_{BD}=\alpha_{AD}+\alpha_{BC}=\alpha_A+\alpha_B+\alpha_C+\alpha_D. \tag{3}$$

Jonker and van Santen[6] have already demonstrated a special case of additivity in the example of several titanates, in which $\alpha_{MO}+\alpha_{TiO_2}=\alpha_{MTiO_3}$, M being an alkaline earth. We find that the experimental data not only confirm this result, but indicate that the more general additivity of separate ionic polarizabilities is valid to a good approximation in a large number of simple crystalline substances in accord with Eq. (3). On the other hand, this equation is not valid for a large number of less symmetrical crystals. These observations are consistent with a relatively simple theoretical interpretation.

The successful application of the additivity relation implies, first of all, that the total polarization, P, per unit volume (electronic and ionic) may be thought of as a sum of components of the form, P_i, each associated with a given ion, i. A definite non-linear relation may be conceived to exist between a given component P_i and the local field F_i which induces it. The analysis of the problem is greatly simplified by restricting its application to examples involving only relatively small values of F_i. If F_i is small enough, the relation between F_i and P_i may be represented by a linear approximation.

Fortunately, there are a great many compounds which crystallize in such a way that ions of one type are

[1] O. F. Mosotti, Mem. di Math. e di Fisica in Modena **24** (II), 49 (1850). R. Clausius, Die Mechanische Warmetheorie **II**, 62 (Vieweg) (1879).
[2] K. Spangenberg, Zeits. f. Krist **57**, 494 (1923).
[3] K. Fajans and G. Joos, Zeits. f. Physik **23**, 1 (1924).
[4] N. F. Mott and R. W. Gurney, *Electronic Processes in Ionic Crystals* (Oxford University Press, London, 1940), Chapter I.
[5] W. Shockley, Phys. Rev. **70**, 105 (1946).
[6] G. H. Jonker and J. H. van Santen, Chem. Weekblad **43**, 672 (1947).

symmetrically arranged around ions of another type. In these crystals, the coulomb forces on a given ion are normally in a state of balance, a fact which corresponds to a zero value of the field F_i. In these crystals, the value of the field F_i depends only on the applied field E and the polarization which it induces. Since these field components can be small compared to the coulomb forces between neighboring ions, the linear approximation can be used for P_i and the constant ratio so defined is a measure of the polarizability α_i.

$$\alpha_i = VP_i/\epsilon_0 F_i, \tag{4}$$

where ϵ_0 is the permittivity of free space and V is the volume per molecule in the crystal lattice as determined by x-ray diffraction or density measurements.

Owing to saturation effects in crystals in which an ion is normally subjected to strongly unbalanced coulomb forces ($F_i \neq 0$), one might expect the derivative dP_i/dF_i to be less than the value $\epsilon_0\alpha_i/V$, obtained by differentiating Eq. (4). This is closely related to the "deformation" effect discussed by Fajans and Joos[5] in connection with electronic (optical) polarizabilities, and is consistent with the observed non-linear dielectric properties of barium titanate.[7]

TABLE I. Dielectric constant, molecular volume and molecular polarizability of electrically balanced crystals.

Compound	K	V	α	$\Sigma\alpha_i$
LiF	9.27	16.21A³	35.7A³	37.5A³
LiCl	11.05	33.74	77.9	74.5
LiBr	12.1	41.36	97.6	92.7
LiI	11.03	54.00	124.7	121.1
NaF	6.0	24.65	46.2	46.0
NaCl	5.62	44.59	81.1	83.0
NaBr	5.99	52.95	99.3	101.2
NaI	6.60	67.46	131.7	129.6
KF	6.05	38.07	71.6	68.1
KCl	4.68	61.86	102.2	105.1
KBr	4.78	71.42	119.6	123.3
KI	4.94	87.67	149.4	151.7
RbF	5.91	44.85	83.6	83.9
RbCl	5.0	69.93	119.8	120.9
RbBr	5.0	80.50	137.9	139.1
RbI	5.0	98.30	168.4	167.5
CsCl	7.20	69.43	140.4	134.1
CsBr	6.51	78.95	153.2	152.3
CsI	5.65	94.94	173.2	180.7
MgO	9.8	18.52	41.4	41.4
CaO	11.8	27.65	64.9	64.9
SrO	13.3	33.16	79.9	79.1
BaO	14.4	41.59	102.0	100.6
CaF_2	8.43	40.47	86.5	86.5
SrF_2	7.69	48.27	99.9	100.7
BaF_2	7.33	59.29	120.8	122.2
$CaTiO_3$	165.0	54.8	161.5	160.4
$SrTiO_3$	275.0	59.55	176.5	174.6
$BaTiO_3$ (120°C)	5000.0	64.0	193.0	196.1
Cu_2O	10.5	38.44	87.8	84.4
CuCl	10.0	39.49	88.8	90.0
CuBr	8.0	45.83	96.2	108.2
Ag_2O	8.8	52.58	114.0	108.8
AgCl	12.3	42.67	101.0	102.2
AgBr	13.1	47.97	115.4	120.4
TlCl	31.9	56.36	154.0	152.9
TlBr	29.9	62.57	170.0	171.1

The local field F_i, effective in polarizing the ions in certain types of cubic crystals has been derived by Lorentz.[8]

$$F_i = E + P/3\epsilon_0. \tag{5}$$

His assumptions are appropriate for the so-called "diagonal cubic" crystals, including NaCl, CsCl, CaF_2 and ZnS. There is less theoretical support for the Lorentz value of the internal field in perovskite-type crystals, although the additivity relation is obeyed equally well by these. Since the Lorentz value of internal field is a necessary condition for deriving the Clausius-Mosotti equation, the success of the latter in interpreting the experimental results is cited as evidence that the Lorentz field is that which actually exists. No other value would give equally satisfactory results.

Since F_i is by definition the same for all ions, the total polarization P in symmetric crystals may be expressed in a way which involves only the sum of the polarizabilities ($\sum\alpha_i = \alpha$).

$$P = \sum P_i = \sum \frac{\epsilon_0 F_i \alpha_i}{V} = \frac{\epsilon_0 F_i \sum \alpha_i}{V} = \frac{\epsilon_0 F_i \alpha}{V}, \tag{6}$$

α is thus the polarizability per molecule, obtained by adding the polarizabilities of all the ions making up the molecule.

The molecular polarizability α can be determined directly from the measured dielectric constant, since

$$\begin{aligned} P &= \frac{\epsilon_0 F_i \alpha}{V} = \frac{\epsilon_0 \alpha E}{V} + \frac{\alpha P}{3V} = \frac{\epsilon_0 \alpha}{V-(\alpha/3)} E, \\ K &= \frac{D}{\epsilon_0 E} = 1 + \frac{P}{\epsilon_0 E} = \frac{V+(2\alpha/3)}{V-(\alpha/3)} = \frac{1+2\beta}{1-\beta}, \end{aligned} \tag{7}$$

in which $\beta = \alpha/3V$. In the above equation, D represents the electric displacement and K is the dielectric constant ($K = \epsilon/\epsilon_0$). Equation (7) may be alternatively expressed in a form more easily recognizable as the Clausius-Mosotti equation.

$$\alpha = 3V\beta, \text{ where } \beta = (K-1)/(K+2). \tag{8}$$

III. DIELECTRIC CONSTANTS AND POLARIZABILITIES

Table I gives experimental values for dielectric constant and molecular volume for a number of crystals which meet the requirement that each ion shall have a symmetrical environment. These include six different

[7] S. Roberts, Phys. Rev. 71, 890 (1947).
[8] H. A. Lorentz, "Theory of Electrons," Note 55, 308 (1916)

TABLE II. Polarizabilities of ions (cubic angstroms).

F^-	25.8	(7)	Li^+	11.7	(4)
Cl^-	62.8	(8)	Na^+	20.2	(4)
Br^-	81.0	(8)	K^+	42.3	(4)
I^-	109.4	(5)	Rb^+	58.1	(4)
			Cs^+	71.3	(3)
$O^=$	30.0	(9)			
			Mg^{++}	11.4	(1)
Cu^+	27.2	(3)	Ca^{++}	34.9	(3)
Ag^+	39.4	(3)	Sr^{++}	49.1	(3)
Tl^+	90.1	(2)	Ba^{++}	70.6	(3)
			Ti^{+4}	35.5	(3)

crystal types, all cubic, represented by NaCl, CsCl, CaF_2, CuCl, Cu_2O and $SrTiO_3$, respectively. The list is not believed to be exhaustive, although all symmetric crystals were included for which dielectric data were available.

The dielectric data in Table I are mostly drawn from a table compiled by Hojendahl.[9] The values of Cu_2O and Ag_2O were reported in another paper[10] by Hojendahl. The data for the titanates are given as reported by Wainer,[11] while the value for barium oxide is taken from a paper by Jonker and van Santen.[6] In checking the original sources of information, one finds rather large discrepancies in some cases. This is perhaps due to the fact that some substances could be obtained in the form of single crystalline plates large enough for accurate measurements, while other substances had to be measured in the form of a powder, or pellets formed from compressed powder.

The molecular volume, shown in the second column of Table II, is calculated from the dimensions of the crystal unit cell as determined by x-ray diffraction. The data compiled by Wyckoff[12] are used in this calculation. The molecular volume may alternatively be calculated from the density. In the alkali halides, the two results agree within a tolerance of about two percent.

The third column of figures in Table I gives the molecular polarizability as calculated by means of Eq. (8).

Taking the alkali halides as an example, one finds that the experimental data agree with the additivity relation to a good approximation.

For instance:

$$\alpha_{NaCl}=81.4, \quad \alpha_{NaI}=131.5,$$

$$\alpha_{RbI}=\frac{169.0}{250.4}, \quad \alpha_{RbCl}=\frac{121.7}{253.2}.$$

The polarizabilities of individual ions cannot be determined directly from dielectric constant measurements, although a series of sums and differences of polarizabilities can be derived from Table I so as to establish relative values for the polarizabilities of the different ions. In order to fix the absolute scale, the polarizability of oxygen is arbitrarily set equal to 30. When this is done, it is found that the resulting polarizabilities of the halide ions are nearly proportional to their volume. The average values of polarizability of the individual ions as determined in this way from the molecular polarizabilities in Table I are given in Table II. The numbers in parenthesis indicate the number of compounds in Table I which contain the given ion. The last column in Table I gives the values of molecular polarizability as calculated by adding the ionic values. No attempt has been made here to separate the total polarizabilities into electronic and ionic components.

The two values indicated for molecular polarizability in Table I check within a tolerance of five percent in every case except cuprous bromide. This is believed to be within the limits of experimental accuracy in view of the different sources of dielectric data and the slight differences between measured densities and x-ray densities. The deviations are not systematic.

Only one measurement has been reported for the

TABLE III. Dielectric constant, molecular volume and molecular polarizability of electrically unbalanced crystals.

Compound	K	V	α		$\Sigma\alpha_i$
		A			
TiO_2 (rutile)	114.0	29.2A³	85.3A³		95.5A³
anatase	31.0	33.7	92.2		95.5
brookite	78.0	30.2	87.2		95.5
$MgTiO_3$	18.0	52.5	133.8		136.9
PbO	25.9	44.0	117.8		121.8
$PbCl_2$	33.5	77.7	213.0		217.4
PbI_2	20.8	122.4	319.0		310.6
(assume α=	91.8 for Pb^{++})				
SiO_2 (α quartz)	4.5	37.3	60.2		62.2
fused	3.75	45.2*	64.2		62.2
(assume α=	2.2 for Si^{+4})				
		B			
$MgSO_4$	8.2	75.0*	158.5		147.1
$SrSO_4$	11.5	76.6	178.8		129.7
$BaSO_4$	9.32	83.4	184.0	$SO_4^=$	113.4
$PbSO_4$	36.5	78.7	218.0		126.2
Tl_2SO_4	25.5	123.8*	330.0		150.8
Li_2CO_3	4.9	58.1*	98.6		75.2
Na_2CO_3	8.75	70.1*	151.8		111.4
K_2CO_3	4.96	94.5*	161.8		77.2
$MgCO_3$	7.31	44.9	91.4	$CO_3^=$	80.0
$CaCO_3$ (calcite)	8.19	60.9	128.8		93.9
$SrCO_3$	8.85	65.8	143.0		93.9
$BaCO_3$	8.53	76.0	163.0		92.4
$NaNO_3$	6.85	62.3	123.5		103.3
KNO_3	4.37	80.3	127.9		85.6
$AgNO_3$	9.0	64.9	155.6		116.2
$TlNO_3$	16.5	75.3	189.0	NO_3^-	98.9
$Ca(NO_3)_2$	6.54	109.7	213.6		89.4
$Sr(NO_3)_2$	5.33	119.1	211.5		81.2
$Ba(NO_3)_2$	4.95	133.4	227.0		78.2
$Pb(NO_3)_2$	16.8	120.5	304.0		106.1

* Determined from density.

[9] K. Hojendahl, D. Kgl. Danske Vidensk. Selsk., Math. Fys. Medd. **16**, (2), 59 (1938).
[10] K. Hojendahl, Zeits. f. Physik. Chemie (B), **20**, 54 (1933).
[11] E. Wainer, Trans. Am. Electrochem. Soc. **89**, 47 (1946).
[12] R. W. G. Wyckoff, *Crystal Structures* (Interscience Publications, Inc., New York, 1948), Section I.

dielectric constant of cuprous bromide.[13] In this case, the samples were prepared in the form of disks of compressed powder and the dielectric measurements were corrected for the porosity as determined by comparing the measured density of the disks with the true density

TABLE IV. Temperature coefficients of dielectric constant, polarizability and thermal expansion of dielectric materials.*

Substance	K	$\frac{1}{K}\frac{dK}{dT}$ ($\times 10^{-6}$)	$\frac{1}{3V}\frac{dV}{dT}$ ($\times 10^{-6}$)	$\frac{1}{\alpha}\frac{d\alpha}{dT}$ ($\times 10^{-6}$)
LiF	9.27	37.5	3.5	21.7
NaCl	5.62	34.0	4.0	28.3
KCl	4.68	30.3	3.2	26.9
AgCl	12.3	140.0	3.0	41.0
AgBr	13.1	82.5	3.5	28.3
TlCl	31.9	−40.0	5.1	11.6
TlBr	29.9	−28.0	5.2	12.9
CuCl	10.0	250.0	—	>69.5
CuBr	8.0	160.0	1.9	60.6
$PbCl_2$	33.5	65.5	3.0	14.7
PbI_2	20.8	34.1	3.4	13.5
TiO_2 (rutile)	114.0	−70.0	0.73 0.91	0.36 0.90
$BaTiO_3$ (150°C)	4560.0	−2960.0	0.95	0.90

* *Note:* $1/T = 341 \times 10^{-5}$.

of the material. However, the value 4.72 generally quoted for the density of CuBr is incorrect, and it is conceivable that this value may have been used in the porosity calculation. The density determined from x-ray diffraction data is 5.20, and our experimental value for the density of CuBr powder is 5.15. According to our calculations, CuBr might be expected to have a dielectric constant of around 12 instead of 8. Thus, it would seem desirable to remeasure its dielectric constant in order to test this conclusion.

In discussing the meaning of the "polarizability" of an ion, it seemed natural to suppose that it might be somewhat less in electrically unbalanced crystals in view of saturation effects attributable to permanent local electrostatic fields. The degree to which this occurs will, of course, depend on the strength of the local field. Some crystals, for example ZnO, very nearly fulfill the requirements of an electrically balanced structure, while others, particularly those containing complex ions such as NO_3^-, etc., include atoms situated in positions where the local static fields are strongly unbalanced.

Dielectric constant, molecular volume and calculated molecular polarizability of a number of crystals having unbalanced Coulomb forces are shown in Tables IIIA and IIIB. The dielectric constants quoted for anisotropic crystals in these tables are obtained by averaging the values corresponding to the three axial directions, if known. In Table IIIA, the polarizability of the molecule is also calculated from the assumed polarizabilities of its ions. The experimental polarizabilities of the titanium compounds in this list are all smaller than the theoretical values, indicating a possible saturation effect. However, the results for anatase and magnesium titanate are well within the tolerance of five percent, showing that the electrostatic unbalance may be small in these materials. No anomalies are observed in the results for silica or the lead compounds.

Table IIIB gives similar results for a number of crystals containing complex ions. The last column shows the polarizability of the complex ion calculated from the experimental data and the previously determined polarizabilities of the metal ions. These results show so much variability that no definite values can be derived for the polarizability of these ions. This might be expected since the oxygen atoms are much more closely bound to the metalloid atom than to the rest of the crystal. Part of the variations observed in Table IIIB may be attributed to inaccuracy of the experimental values for dielectric constant and density since many of these compounds have not been studied as carefully as those listed in Table I.

IV. TEMPERATURE COEFFICIENTS

By differentiating Eq. (6) with respect to temperature, one obtains

$$\frac{1}{\alpha}\frac{d\alpha}{dT}=3\left(\frac{1}{3V}\frac{dV}{dT}\right)+\frac{3K}{(K+2)(K-1)}\cdot\frac{1}{K}\frac{dK}{dT}. \quad (9)$$

This equation expresses the temperature coefficient of the polarizability, $(1/\alpha)(d\alpha/dT)$, in terms of the linear expansion coefficient, $(1/3V)(dV/dT)$, and the T.C. of the dielectric constant, $(1/K)(dK/dT)$. Table IV shows experimental values of temperature coefficients for a number of materials taken from a table compiled by Eucken and Buechner.[13] The T.C. of dielectric constant for TiO_2 is taken from a paper by Bunting, Shelton, and Creamer,[14] while two values are given for the thermal expansion coefficient of the material as obtained by Jonker and van Santen[15] and by von Hippel[16] respec-

TABLE V. Estimated dielectric constants.

Substance	V	K
PbF_2	52.45	31.3
$SrCl_2$	85.75	7.3
K_2O	66.65	6.0
Li_2O	24.64	8.8
Na_2O	42.74	4.65
Rb_2O	76.55	6.2
AgF	29.77	9.1
TlI (cubic)	74.00	26.4
CuF	18.26	92.0
CuI	55.15	15.1
AgI (cubic)	67.80	9.1
$KMgF_3$	64.0	7.5

[13] A. Eucken and E. Buechner, Zeits. f. Physik. Chemie (B) **27**, 321 (1934).

[14] Bunting, Shelton and Creamer, J. Research Nat. Bur. of Stand. **38**, 337 (1947).

[15] J. H. van Santen and G. H. Jonker, Nature **159**, 333 (1947).

[16] A. von Hippel *et al.*, Ind. Eng. Chem. **38**, 1097 (1946).

tively. We measured the dielectric constant and its temperature coefficient of very pure sintered discs of barium titanate and made the appropriate correction for porosity.[17] The linear expansion coefficient of barium titanate was measured by Jonker and van Santen.[15] The last column in the table gives the T.C. of polarizability calculated from Eq. (9).

Some materials in Table IV have negative temperature coefficients of dielectric constant, although none of these has a negative T.C. of polarizability. Also the T.C. of polarizability is much smaller than that of the dielectric constant, especially when the latter T.C. is large to begin with. In the case of barium titanate, the T.C. of dielectric constant is more than 3000 times that of the polarizability, a fact which indicates that the polarizability is relatively much more nearly invariant. The temperature coefficients of polarizability of the titanium compounds do not vanish as reported by Jonker and van Santen,[15] yet the importance of thermal expansion in causing the large negative temperature coefficients of dielectric constant is correctly interpreted. A Curie-Weiss law can be derived from Eq. (9) which accurately describes the experimental results over a wide range of temperature if one assumes the thermal expansion and the T.C. of polarizability to be constant (linear).

V. DISCUSSION

The polarizabilities of molecules in symmetric types of ionic crystals as calculated by the Clausius-Mosotti equation have been shown to obey the rule of additivity to a very good approximation. This result implies the validity of the Lorentz value of the internal field, which is used in deriving the Clausius-Mosotti equation. Such a conclusion appears to be in contradiction to generally accepted theory.[4] In the particular case of alkali-halides, smaller values of internal field have been thought to be requisite in order to explain the experimentally observed frequencies of resonance in the infra-red range.[9] This subject will be discussed further in a forthcoming paper in which it is intended to show that the Lorentz value of internal field is reasonably consistent with all the experimental data, including the infra-red resonances.

In the case of cubic barium titanate, there is less theoretical justification for the Lorentz value of internal field. However, it may be worth while to point out some errors that have occurred in attempts to calculate the internal field of this material by making inappropriate use of the equations of ferromagnetism.

Mason and Matthias[18] have presented a theory of the dielectric behavior of barium titanate in which the total polarization is comprised of two parts:

$$P=P_e+P_d. \tag{10}$$

The first component, P_e, includes all polarization except that due to titanium dipoles. The second part P_d is that due to the dipoles caused by displacement of the titanium nuclei. For small field strengths and at temperatures above 130°C, where there is no spontaneous polarization, both components are proportional to the local field and P_d is inversely proportional to absolute temperature. Thus the polarizability may be expressed in the following form:

$$\alpha=\alpha_0+\alpha_1(\theta/T), \tag{11}$$

where α_0 and α_1 are parameters having the dimensions of polarizability and θ is the Curie temperature.

The internal field is expressed in a fashion similar to Eq. (5) in which the second component, calculated by Lorentz, is multiplied by an arbitrary factor γ.

$$F_i=E+\gamma P/3\epsilon_0. \tag{12}$$

The dielectric constant may then be calculated in a manner similar to Eq. (7):

$$K=1+\frac{3\alpha}{3V-\alpha\gamma}. \tag{13}$$

The experimental data fit a modified Curie-Weiss law,

$$K=K_0+C/(T-\theta), \tag{14}$$

where C is the Curie constant and θ is the Curie temperature. We find $C=154{,}000$°C and $\theta=118$°C (391°K).

Mason and Matthias have calculated γ from the following relation (in our notation),

$$\gamma=3\theta/C. \tag{15}$$

If one substitutes this expression for γ in Eq. (13) and solves Eqs. (13) and (14) for α, one obtains:

$$\alpha=V\frac{C+(K_0-1)(T-\theta)}{T+(\theta/C)(K_0-1)(T-\theta)}. \tag{16}$$

The experimental result[19] is that $|K_0-1|<10$, therefore:

$$\frac{C}{\theta}=\frac{154{,}000}{391}=393\gg|K_0-1|.$$

Then, especially at temperatures close to the Curie point:

$$\alpha\simeq VC/T. \tag{17}$$

This result is in contradiction with the original assumption (Eq. (10)) that a significant fraction of the total polarization is temperature independent. If this assumption is reasonable, then the internal field constant is not correctly given by Eq. (15). A further objection to the treatment by Mason and Matthias is that it does not take adequate account of thermal expansion.

The same authors have also calculated an internal field constant from the specific heat anomaly, making

[17] D. F. Rushman and M. A. Strivens, Proc. Phys. Soc. (London) 59, 1011 (1947).

[18] W. P. Mason and B. T. Matthias, Phys. Rev. 74, 1622 (1948).

[19] S. Roberts, Phys. Rev. 75, 989 (1949).

use of the equation:

$$\Delta Q=\frac{\gamma P_0^2}{6\epsilon_0}, \quad \text{or} \quad \gamma=\frac{6\epsilon_0\Delta Q}{P_0^2}, \tag{18}$$

where ΔQ is the energy required to release the spontaneous polarization P_0. This appears as an anomalous increase in the specific heat over a small range of temperature near the Curie point.

The correct formula is derived from an expression of the change in the total energy density of the system.

$$dU=TdS+EdD, \tag{19}$$

where S is the entropy.

The calculation of the difference in specific heats at constant electric displacement σ_D and at constant electric field σ_E from Eq. (19) is parallel to the corresponding calculation by Becker[20] of the analogous magnetic problem.

$$\sigma_D-\sigma_E=T(\partial E/\partial T)_D(\partial D/\partial T)_E. \tag{20}$$

The first derivative in Eq. (20) may be evaluated from the experimentally determined relation[7] between T, D and E, valid at temperatures above the Curie point.

$$E=[(T-\theta)/\epsilon_0 C]D+\beta D^3. \tag{21}$$

If this equation may be extrapolated below the Curie point and β may be considered constant,

$$\left(\frac{\partial E}{\partial T}\right)_D=\frac{D}{\epsilon_0 C} \tag{22}$$

and

$$\sigma_D-\sigma_E=\frac{T}{2\epsilon_0 C}\left(\frac{\partial D^2}{\partial T}\right)_E. \tag{23}$$

By integrating over a small range of temperature through the Curie point ($\Delta T\ll\theta$) and holding the field $E=0$, one obtains:

$$\Delta Q=\int(\sigma_D-\sigma_E)dT=\frac{\theta P_0^2}{2\epsilon_0 C}. \tag{24}$$

This is the result one would get by substituting Eq. (15) in Eq. (18). Therefore, since these equations are not independent, it is not surprising that they both give approximately the same value for γ, although neither result can be trusted as evidence that γ is different from one. A similar argument with similar shortcomings was presented in an earlier paper by Blattner and Merz,[21] however, their experimental values seem to be more precise and differ by a factor of three from the results of Mason and Matthias.

Following Jonker and van Santen,[15] we prefer the interpretation that the anomalous variations in dielectric constant of cubic barium titanate depend primarily on thermal expansion of the material,

$$V=V_0[1+3\delta(T-T_0)] \tag{25A}$$

with a simultaneous slight variation of polarizability with temperature.

$$\alpha=\alpha_0[1+\phi(T-T_0)], \tag{25B}$$

where V_0 and α_0 are the volume and polarizability at a specified temperature T_0; and δ and ϕ are the corresponding temperature coefficients.

By introducing Eqs. (25A) and (25B) in (7), and expressing the result in the form of (14) and by choosing $T_0=\theta$, one obtains

$$C=\frac{3}{3\delta-\phi}; \quad K_0=\frac{3\delta+2\phi}{3\delta-\phi}. \tag{26}$$

The experimental results indicate that both δ and ϕ are positive, as previously considered and indicated in Table IV. Thus, instead of being inversely proportional to temperature, the polarizability is viewed to be remarkably constant, increasing only slightly.

What is perhaps even more significant is, for example, that the value of α_i for the titanium ion is the same in different compounds and that the principle of additive polarizabilities seems to be generally applicable for a wide variety of substances. This principle can be used to advantage in predicting the approximate dielectric constant of new compounds and of compounds for which dielectric data are not available. A list of dielectric constants of such compounds estimated in this way is shown in Table V. Some of these dielectric constants, particularly those of the alkali oxides would be extremely difficult to measure directly owing to the great chemical activity of these compounds. It should be held in mind that the accuracy of these predicted dielectric constants is not too great if one recognizes an uncertainty of five percent in the values of polarizability.

The author wishes to acknowledge the encouragement and helpful advice of Drs. F. E. Williams and M. H. Hebb in the preparation of this paper.

[20] R. Becker, Theorie der Elektrizitat, II, Elektronentheorie, 6 Ed. (B. G. Teubner, 1933), p. 172.

[21] H. Blattner and W. Merz, Helv. Phys. Acta 21, 210 (1948).

The Electric and Optical Behavior of $BaTiO_3$ Single-Domain Crystals*

WALTER J. MERZ
Laboratory for Insulation Research, Massachusetts Institute of Technology, Cambridge, Massachusetts
(Received June 16, 1949)

The dielectric constants, the spontaneous polarization, and the optical properties of $BaTiO_3$ single-domain crystals have been measured as a function of temperature. It is shown that the deformation of the crystal in the tetragonal state is proportional to the square of the spontaneous polarization, in analogy to the behavior of the other ferroelectrics, and that the temperature dependence of the birefringence is proportional to the square of the spontaneous polarization. The change of the polarization at the two lower transition points is consistent with the assumption that the Ti ions in the oxygen octahedra are displaced from the [001] to the [011] and later to the [111] direction.

INTRODUCTION

SINCE the domain structure of $BaTiO_3$ and its response to electric fields, temperature and pressure[1,2] was discovered, the laws of formation of these domains have been clarified in detail.[3] Single-domain crystals have been grown, and their dielectric constants ϵ_c and ϵ_a, parallel and perpendicular to the polar axis, as well as their spontaneous polarization P_s and the optical properties (refractive index and birefringence), have been investigated over a wide temperature range. The results presented here are discussed in relation to the structure of the crystal, and furnish a basis for the comparison between $BaTiO_3$ and the two other groups of ferroelectrics.

INITIAL DIELECTRIC CONSTANTS

The single-domain crystals investigated were yellow, transparent plates of a few mm^2 in area and relatively high purity, with a Curie temperature of 120°C; their optical axis (c) was, in general, oriented perpendicularly to the plate surface.

Figure 1 shows the initial dielectric constants in the a- and c-directions as a function of temperature[4] and the three well-known transition points.[5] Above the Curie point the crystal is cubic ($\epsilon_a = \epsilon_c$), shifts then by a second-order transition from cubic to tetragonal,[6] while near 0° and −80°C the polar axis changes suddenly in two first-order transitions from the [001] to the [011] and later to the [111] positions of the original cubic system. Due to this shift of the Ti^{+4}-ions in the oxygen octahedra of the lattice, the crystal structure changes from the tetragonal class (C_{4v}), to the orthorhombic (C_{2v}), and later to the trigonal class (C_{3v}). At these two lower transitions internal strains cause the development of multi domain patterns which may differ from crystal to crystal. This causes variations in the dielectric con-

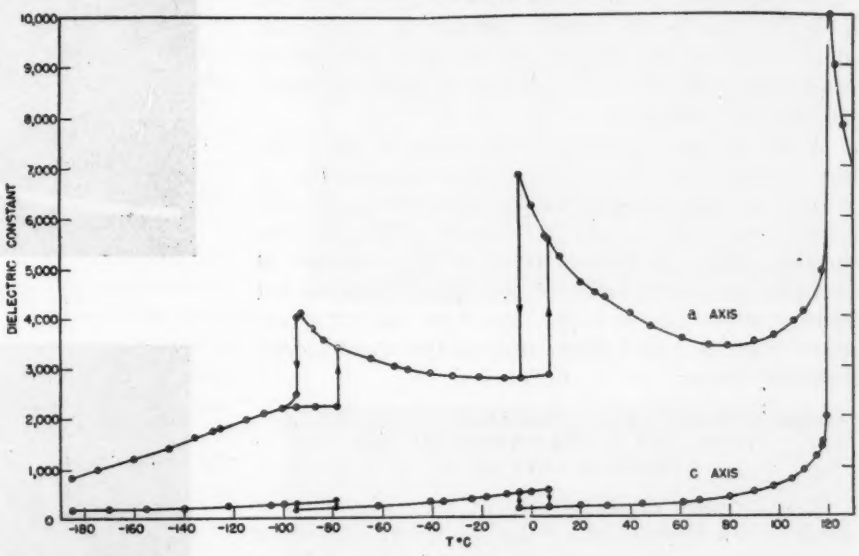

FIG. 1. Dielectric constants ϵ_a and ϵ_c as function of temperature.

* Sponsored by the ONR, the Army Signal Corps, and the Air Force under ONR Contract N5ori-07801.
[1] B. Matthias and A. von Hippel, Phys. Rev. **73**, 1378 (1948).
[2] Blattner, Matthias, Merz, and Scherrer, Experientia **3**, 148 (1947).
[3] P. Forsbergh, Technical Report XVIII, Laboratory for Insulation Research, M. I. T., 1949.
[4] W. Merz, Phys. Rev. **75**, 687 (1949).
[5] Von Hippel, Breckenridge, Chesley, and Tisza, J. Ind. Eng. Chem. **38**, 1097 (1946).
[6] H. Megaw, Proc. Roy. Soc. **A189**, 261 (1947).

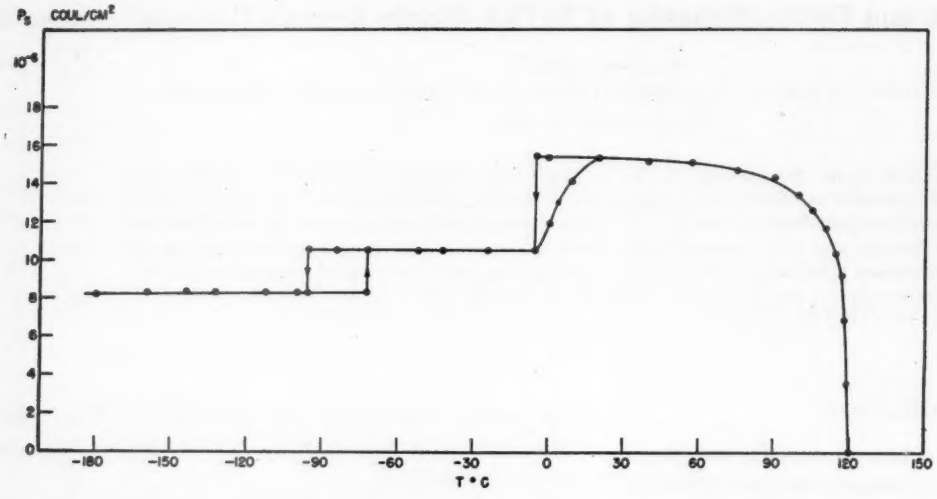

FIG. 2. Spontaneous polarization P_s as function of temperature.

stants below 0°C, and is the reason that $\epsilon_a \neq \epsilon_c$ below the transition near −80°C.

SPONTANEOUS POLARIZATION

The spontaneous polarization P_s was measured from the hysteresis loops by the modified method of Sawyer and Tower.[7] In contrast to the loops of multi-domain crystals, these loops can be easily saturated. However, some preconditioning is needed before satisfactory hysteresis loops are obtained. When the field is applied for the first time and the temperature raised, one often finds distorted loops, and the behavior of the spontaneous polarization as a function of temperature is not reproducible. These disturbances disappear after the loops have been taken through several heating cycles with systematically increased field strength. They are probably due to the initial existence of antiparallel domains, of which a smaller part is firmly anchored in its original orientation and can only be made to cooperate by such treatment.

At the two lower transition points near 0° and −80° the spontaneous polarization drops suddenly (Fig. 2) which, as will be explained later, follows from the shift of the polar axis from the [001] to the [011] and then to the [111] orientation. Due to the formation of domains the results below the tetragonal state are not quite reproducible, as in the case of the dielectric constant. Figures 3 to 7 show some of the characteristic hysteresis loops.

RELATION BETWEEN SPONTANEOUS POLARIZATION AND DEFORMATION OF THE CRYSTAL LATTICE

The structure of $BaTiO_3$ above the Curie point is cubic; at the Curie point a polar axis is formed and the crystal changes to tetragonal structure. Megaw[6] has determined the structure as a function of temperature; the relative change of the lattice constants is shown in Fig. 8 where the denominator of $\Delta a/a$ and $\Delta c/c$ refers to the extrapolated cubic value.

[7] C. Sawyer and C. Tower, Phys. Rev. **35**, 269 (1930).

It is known that the other two groups of ferroelectric crystals (light and heavy Rochelle salt and the alkali phosphates and arsenates) show, in the Curie region, an intimate relation between the spontaneous polarization and deformation of the crystal lattice, which can be discussed as follows:

Above the Curie point Rochelle salt belongs to the orthorhombic class ($V=D_2$), and has the following matrix of its piezoelectric constants:

$$\begin{matrix} 0 & 0 & 0 & d_{14} & 0 & 0 \\ 0 & 0 & 0 & 0 & d_{25} & 0 \\ 0 & 0 & 0 & 0 & 0 & d_{36} \end{matrix}. \qquad (1)$$

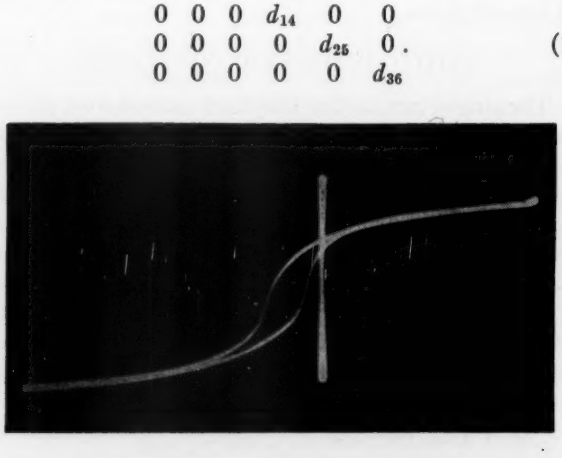

FIG. 3. Hysteresis loop at −100°C.

FIG. 4. Hysteresis loop at −70°C.

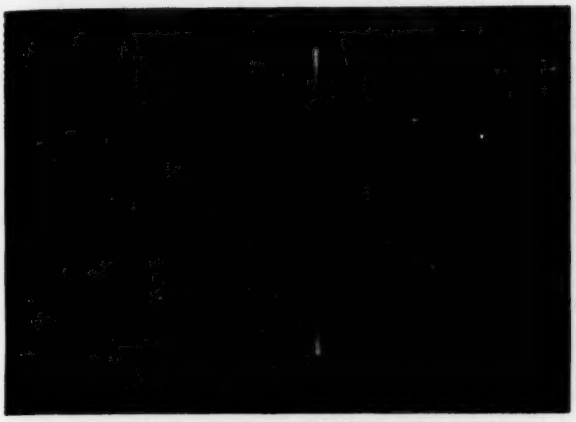

FIG. 5. Hysteresis loop at +20°C.

In the Curie region where the crystal has monoclinic symmetry (C_2) the matrix becomes:

$$\begin{matrix} d_{11} & d_{12} & d_{13} & d_{14} & 0 & 0 \\ 0 & 0 & 0 & 0 & d_{25} & d_{26}. \\ 0 & 0 & 0 & 0 & d_{35} & d_{36} \end{matrix} \qquad (2)$$

Because the a-axis is the polar axis in Rochelle salt, matrix (2) is written in a cyclical-changed form to allow comparison with matrix (1).

A spontaneous polarization in the x-direction produces corresponding deformations in the x-, y- and z-directions, and a shear in the y–z plane. As Mueller[8] has shown experimentally, the shear y_z is proportional to the spontaneous polarization. This can be understood as a continuation of the normal piezoelectric effect above the Curie point into the Curie region (d_{14}). On the other hand, Mueller found that the 3 normal strains x_x, y_y, z_z are proportional to P_s^2 and represent therefore a quadratic piezoeffect. As Jaffé[9] has pointed out, this can be understood by the fact that the piezoelectric constants d_{11}, d_{12}, d_{13} which appears now in the monoclinic system must be themselves proportional to the strain and polarization in a first approximation, so that

$$x_x \sim d_{11} P_s^2; \quad y_y \sim d_{12} P_s^2; \quad z_z \sim d_{13} P_s^2.$$

In the case of the alkali phosphates and arsenates the situation is quite analogous. The measurements of de Quervain[10] show that the shear x_y is proportional to the spontaneous polarization P_s in the z-direction, which again can be explained as a continuation of the piezoeffect (d_{36}), and the other strains are proportional to P_s^2.

For the cubic $BaTiO_3$ above the Curie point all the piezoelectric constants d_{ik} are zero. Below it, the crystal changes from cubic to tetragonal (C_{4v}) with the matrix:

$$\begin{matrix} 0 & 0 & 0 & 0 & d_{15} & 0 \\ 0 & 0 & 0 & d_{15} & 0 & 0. \\ d_{31} & d_{31} & d_{33} & 0 & 0 & 0 \end{matrix} \qquad (3)$$

[8] H. Mueller, Phys. Rev. **58**, 805 (1940).
[9] H. Jaffé, Phys. Rev. **51**, 43 (1937).
[10] M. de Quervain, Helv. Phys. Acta **17**, 509 (1944).

Consequently there must be strain components x_x, y_y and z_z caused by the spontaneous polarization P_s in the z-direction. In analogy to the other ferroelectrics one would expect that these normal strains are proportional to the square of P_s because the constants d_{31} and d_{33} should themselves be proportional to P_s.

The measurements of P_s (Fig. 2) and the values of $\Delta a/a$ and $\Delta c/c$ (Fig. 8), calculated with the aid of Megaw's measurements, show, in fact, the expected relation (Fig. 9)

$$(z_z)^{\frac{1}{2}} = (\Delta c/c)^{\frac{1}{2}} \sim P_s, \qquad (4)$$

$$(x_x)^{\frac{1}{2}} = (y_y)^{\frac{1}{2}} = (|\Delta a/a|)^{\frac{1}{2}} \sim P_s. \qquad (5)$$

This relation, however, was confirmed only from the Curie point (120°C) down to about 90°C. At lower temperatures the measured values of P_s are smaller than expected. It is found that this deviation decreases with increasing field strength, and with the temperature pretreatment at the high field strengths described above. One must therefore assume that this difference is, at least in part, due to the existence of domains oriented in other directions, especially the anti parallel, which at lower temperatures persist long enough at 60 cycles so that the crystal does not polarize completely. This makes it understandable that the absolute value of the spontaneous polarization at room temperature varies from crystal to crystal. As an average we mea-

FIG. 6. Hysteresis loop at a few degrees below the Curie point.

FIG. 7. Hysteresis loop at +120°C.

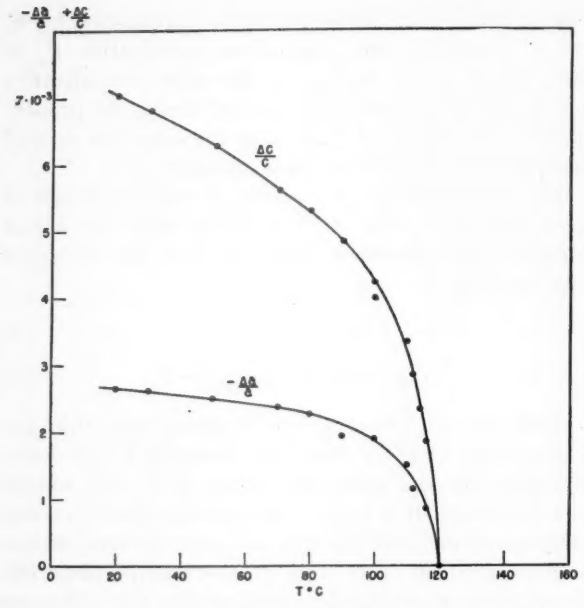

FIG. 8. $\Delta a/a$ and $\Delta c/c$ as function of temperature, calculated from Megaw's measurements.

sured the value

$$P_s = (15.5 \pm 1.5) \times 10^{-6} \text{ coulomb/cm}^2, \qquad (6)$$

in good agreement with Hulm's value[11] of 16×10^{-6} coulomb/cm² for multidomain crystals.

It is interesting to note that the curve of P_s/P_∞ plotted against the reduced temperature T/θ (θ = Curie temperature) for $BaTiO_3$ is about the same as that for KH_2PO_4, that is, it rises much more steeply than the Langevin theory would predict. In the ferroelectric region the polarization P is a function of the temperature and of the applied field strength E. With small values of E (less than the coercive field strength) P becomes very small and drops to zero with decreasing field. Besides this, one can observe a decrease of the polarization in the form of sudden jumps after the field is removed. These facts show that even the "single-domain" crystals split up into domains as soon as the external field approaches zero. These domains must be antiparallel because optically the crystal appears uniformly tetragonal. Thus there seem to exist crystals that are not really single-domain, but that contain only parallel and antiparallel domains, as in the cases of Rochelle salt and KH_2PO_4.

The behavior of the spontaneous polarization at the two lower transitions is characterized by sudden drops of P_s (Fig. 2). With the conclusion derived from optical and dielectric measurements one can understand this behavior. Since at the 0°C transition the [011] position of the polar axis becomes the most stable one, a drop of the spontaneous polarization perpendicular to the crystal face of the order of $1/\sqrt{2}$ should be expected. This value is, in fact, found (Fig. 2). At the second transition point at about −80°C a further drop should result because the polar axis moves into the [111] position. The measured change is larger than expected, which may be understood by the assumption that not only the direction changes but also the magnitude of the dipole moment decreases. However, it should be kept in mind that the values of P_s below the 0°C transition are never completely reproducible due to the formation of domains and consequently increasing internal strains.

Just as the d_{31} and d_{33} constants play an important part in the tetragonal region, the change to the orthorhombic and trigonal modification expresses itself in the high values and temperature dependence of the shear constants d_{15} and d_{24}.

THE OPTICAL BEHAVIOR OF $BaTiO_3$

We measured previously the refractive index of $BaTiO_3$ on thin crystal plates using Chaulnes's method to determine the ratio of the actual to the optical thickness.[12] At the Curie point one finds a peak in the

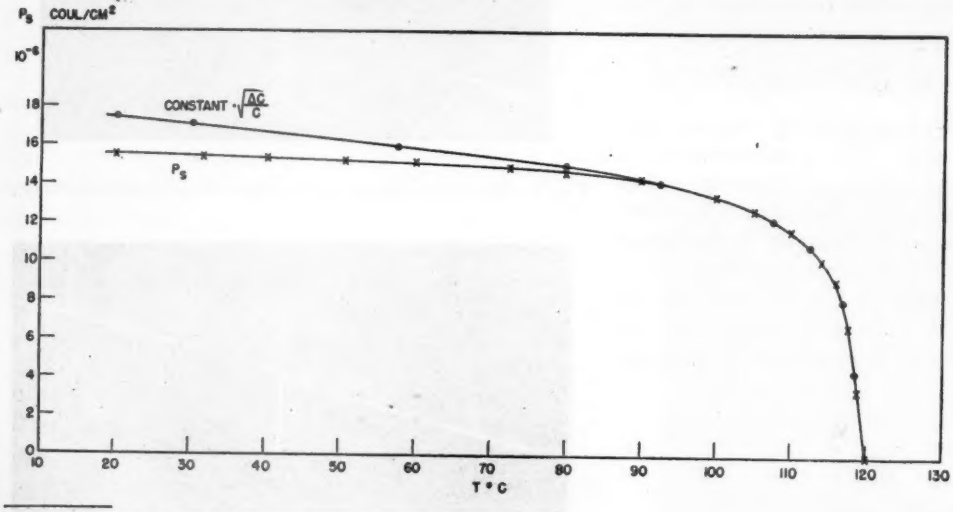

FIG. 9. P_s and constants $\times(\Delta c/c)^{\frac{1}{2}}$ as function of temperature.

[11] J. Hulm, Nature **160**, 127 (1947).
[12] Busch, Flury, and Merz, Helv. Phys. Acta **21**, 212 (1948).

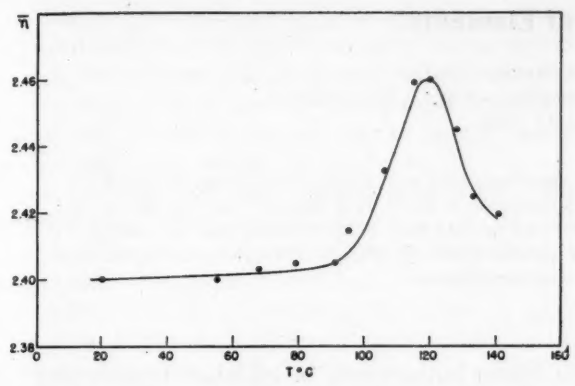

FIG. 10. Refractive index $\bar{n}$ as function of temperature.

curve of the refractive index (Fig. 10). It is interesting to note that the activation energy of the electrical conductivity is lowered in this region.[12] Besides the refractive index it was of interest to know the behavior of the birefringence of $BaTiO_3$ because it is related to the spontaneous polarization of the crystal. The birefringence Δn of $BaTiO_3$ was measured by Forsbergh[3] with the result shown in Fig. 11.

The theory of the electro-optical and elasto-optical effect gives, for the index ellipsoid, the form

$$\sum_{i,k=1}^{3} \frac{a_i' a_k'}{v_{ik}^2} = 1, \tag{7}$$

where for a piezoelectric crystal[13] v_{ik} has the value

$$\frac{1}{v_{ik}^2} = \frac{1}{n_{ik}^2} + \sum_{m=1}^{6} q_{ik,m} X_m + \sum_{l=1}^{3} f_{ik,l} E_l + \tfrac{1}{2} \sum_{l=1}^{3} \sum_{j=1}^{3} h_{ik,lj} E_l E_j, \tag{8}$$

where $q_{ik,m}$ represents piezo-optical constants, $f_{ik,l}$ represents electro-optical constants of the 1st order, and $h_{ik,lj}$ represents electro-optical constants of the 2nd order.

The measurements of Δn were made without external stresses ($X_m=0$) and without external fields. But the spontaneous polarization P_s in the z-direction is the reason for a spontaneous change in the birefringence (spontaneous Kerr effect). With the conditions $E_a=E_b=0$; $E_c\neq 0$; $n_1=n_2$ and $n_{ik}=0$ for $i\neq k$ and by using only the terms of first order Eq. (8) becomes, with the matrix of f_{kl}, that is, with

$$\begin{matrix} 0 & 0 & f_{13} \\ 0 & 0 & f_{13} \\ 0 & 0 & f_{33} \\ 0 & f_{51} & 0 \\ f_{51} & 0 & 0 \\ 0 & 0 & 0 \end{matrix} \tag{9}$$

[13] F. Pockels, *Lehrbuch der Kristalloptik* (B. G. Teubner, Leipzig, 1906).

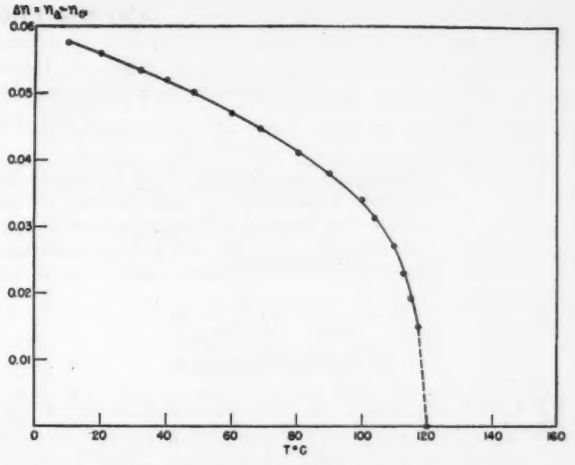

FIG. 11. Birefringence Δn as function of temperature.

as follows:

$$(a^2+b^2)[1/n_1^2 - f_{13}E_c] + c^2[1/n_3^2 + f_{33}E_c] = 1. \tag{10}$$

As in the case of Rochelle salt and KH_2PO_4, one must assume that the electro-optical constants of the first order (f_{kl}), which do not exist above the Curie point but arise below it due to the deformation of the crystal, behave quite analogously to those of the piezo-effect. Because the f_{kl}'s must be proportional to P_s in the Curie region, the spontaneous Kerr effect becomes proportional to P_s^2

$$\begin{aligned} \Delta n = n_c - n_a &= \frac{n_3}{(1+f_{33}E_c n_3^2)^{\frac{1}{2}}} - \frac{n_1}{(1-f_{13}E_c n_1^2)^{\frac{1}{2}}} \\ &= (n_3-n_1) - \tfrac{1}{2}E_c(f_{33}n_3^3 + f_{13}n_1^3) \\ &= \Delta n_0 + \text{const.} \times P_s^2, \end{aligned} \tag{11}$$

where $\Delta n_0 (= n_3 - n_1)$, the natural birefringence of $BaTiO_3$, is zero.

In fact, one finds good agreement between the measured value of Δn and of P_s^2, but again only at higher temperatures. On the other hand, in the whole tetragonal region, Δn is exactly proportional to $\Delta c/c$. That means that the measured values of P_s are too small at lower temperatures, which leads again to the conclusion that the crystal has the tendency to form parallel and antiparallel domains. This does not influence the birefringence and the x-ray measurements but only the values of P_s. In the tetragonal region, n_a^2 and n_c^2 have a similar temperature dependence as ϵ_a and ϵ_c. The dispersion of the refractive indices and of the birefringence is very strong. At both lower transition points one finds a sudden change in Δn due to the change of the crystal system.

The author is grateful to Professor A. von Hippel for many helpful discussions during the course of this work.

On the Origin of Elements

MARIA G. MAYER AND EDWARD TELLER
Institute for Nuclear Studies, The University of Chicago, Chicago, Illinois
(Received June 22, 1949)

The abundances of elements and of isotopes indicate that heavy and light elements have been produced by difference processes. The origin of heavy elements is discussed in detail. It is assumed that the heavy elements were formed by a fission process from a neutron-rich nuclear fluid. Simple assumptions are made about this fission process and isotopic abundances are calculated for $62 \leqq Z \leqq 78$. The properties of the neutron-rich liquid and possible details of the fission process are discussed.

I. INTRODUCTION

REGULARITIES in the abundances of nuclear species form the experimental evidence on which any theory of the origin of elements must be based. The data[1] on the abundance of chemical elements are shown in Fig. 1. The most striking feature of this figure is the different behavior of light and heavy elements. All the abundant elements are light. Furthermore, the abundances of light elements vary erratically. The last high abundance peak lies at Fe and within the next six or eight elements the abundance dips by a factor 10^4. Somewhat arbitrarily, the boundary between light and heavy elements shall be fixed at the end of this decrease, namely at $Z=34$. The abundance of heavy elements is low and roughly constant. The observed fluctuations seem mainly to be due to stability questions: odd Z-values have a small abundance, nuclei with closed shells[2] a high one.

Isotopic ratios also behave differently for light and heavy elements. This regularity shows up for even Z-values for which as a rule several isotopes are known. For high elements the lightest isotope is usually abundant, the heaviest is often rare. For the heavy elements there exists a dissymetry in the opposite sense. The lightest, and often also the next to lightest, isotope is rare, whereas the heaviest stable isotope is, as a rule, quite abundant. The first element to which this rule applies is Se, with $Z=34$. Its lightest isotope, Se^{74}, has an abundance of 0.9 percent, which is to be compared with 9.3 percent for the heaviest isotope. Among the other heavy elements the lightest isotopes are always less abundant than 1.4 percent with the exception of five cases. Four of these have closed neutron shells. The heaviest isotope is never rare.

The experimental evidence permits us to put forth a number of simple qualitative arguments.

A. Light and heavy elements differ markedly both in abundance and isotopic ratios.

B. The light elements may have been formed by thermonuclear reactions. The apparently greater abundance of lighter isotopes may be explained by assuming that the build-up process consisted in adding protons to already existing nuclei. The great differences between the abundances of light nuclei may be explained by the sensitive dependence of the effective cross sections on the temperature and by the great variability of cross sections for different kinds of processes.

C. There is conclusive evidence that at the time of production of the heavy nuclei, the proportion of neutrons considerably exceeded that which is now present in nuclei. Evidence for this neutron-excess comes from two sources: first, without such a neutron excess it is not possible to understand that the heavy isotopes of heavy elements are much more abundant than the lightest isotopes. Second, in absence of a neutron excess it is very hard to find any method by which the heavy nuclei could be built up at all. The only alternative would be to build up the heavy nuclei by reactions between charged particles. Such reactions would, however, require extremely high temperatures, and at these temperatures it is not possible to prevent disintegration of uranium and other fissionable nuclei. A neutron-excess within the heavy nuclei may stabilize them against fission.

Of the three statements proposed above, the last one seems inescapable. In fact, this last conclusion forms a part of every theory on the origin of heavy elements which so far has been proposed.[3] In the following we shall restrict our attention to the formation of heavy elements. In particular, we are going to explore the hypothesis that the heavy nuclei were formed by the disintegration of a "cold" nuclear fluid containing a great excess of neutrons.

II. THE BREAK-UP HYPOTHESIS

The breakup of a primordial nuclear fluid is in many respects similar to the fission process. We shall of course not limit ourselves to the neighborhood of uranium, but assume the presence, at that stage, of much heavier nuclei. These nuclei break up due to their

[1] The values used here have been given by Harrison S. Brown, Rev. Mod. Phys. (to be published), whose work was in many details based on the publication of V. M. Goldschmidt (Det Novske Videnskaps, Akademi i Oslo, I Mat.-Naturv. Klasse 1937, No. 4).

[2] M. G. Mayer, Phys. Rev. 74, 235 (1948).

[3] G. Gamow, Nature 162, 680 (1948); C. B. van Albada, Bull. Astr. Inst. Netherlands X, 374 (1946); and Astrophys. J. 105, 393 (1947); Klein, Beskow, and Treffenberg, Arkiv. f. Mat. Astr. o. Fys., Bd. 33B, No. 1 (1946). For further references see "On the abundance and origin of elements," by E. Teller and M. G. Mayer, Report to the Solvay Congress, Brussels (1948).

high charge. The fragments have an excess of neutrons and are highly excited, and thus, neutron evaporation follows. The number of neutrons evaporated is assumed much greater than in fission. The residual nuclei and their β-decay products are assumed to be the present heavy nuclei in the region beyond $Z=34$.

One might expect that elements with $Z>137$ are excluded since, in a Coulomb field with $Z>137$ the electron orbits with $j=\frac{1}{2}$ can no longer exist outside of the nucleus. This actually need not be considered as a difficulty if the finite extension of the nucleus is taken into account. We shall return to this question in the following section.

Let us consider a nuclear fragment, which, at the moment of the breakup has a charge Z. Even Z values are produced as fission fragments more frequently than odd Z values. This is so because at great neutron excesses pairs of protons are likely to form configurations similar to α-particles, while a single proton can be found in a configuration similar to that of a triton nucleus. These configurations are likely to be better approximations to the actual wave functions in a nuclear fluid rich in neutrons than they are in atomic nuclei. The great difference in binding energy between the α-particle and the triton then helps to explain why more fragments with even Z-values are formed. We shall assume that such fragments are produced exclusively.

The neutron number associated with the fragment of charge Z is not fixed, but its average is determined by the properties of the large nucleus before the break-up. It seems plausible to assume that the ratio of neutron- to proton-number does not vary over a wide range. In the break-up process, energy may be distributed over many degrees of freedom, with the result that the probability of finding the fragment with various internal energies can be represented by a smooth curve, probably a Gaussian. In the neutron evaporations varying amounts of energy will be lost as kinetic energy. After a number of such evaporation processes a resultant fixed (not yet stable) isotope will be left with energy whose probability distribution is most likely to be Gaussian. Finally, not enough energy will be left to evaporate another neutron, and the process will stop. The probability $P(Z, N)$ of the process terminating at a definite isotope with neutron number N is

$$P(Z,N)=K_Z(E_{N,Z}-E_{N-1,Z}) \times\exp[-(1/\alpha^2)(E_{N,Z}-E_0)^2]. \quad (1)$$

$E_{N,Z}$ is the binding energy of an isotope containing N neutrons; E_0 is the binding energy of the nucleus for which $P(Z, N)$ is a maximum. Both E_0 and α, the spread of isotopes, are functions of Z. K_Z is a normalization factor. The next factor, $E_{N,Z}-E_{N-1,Z}$ is the binding energy of the last retained neutron. Formula (1) is valid only if the spread, α, corresponds at least to several units, in which case the probability of evaporating down to N, but not to $N-1$ neutrons, is proportional to the binding energy of the last neutron.

Some of the isotopes produced will be unstable with respect to β-decay, and a chain of these events produces the final stable nuclei.

The nuclear energies were obtained from the semi-empirical formula for the mass of an atom.[4]

$$M=A-0.00081Z-0.00611A+0.014A^{\frac{2}{3}} +0.083\left(\frac{A}{2}-Z\right)^2 A^{-1}+0.000627Z^2A^{-\frac{4}{3}}+\delta, \quad (2)$$

where $\delta=0$ for A odd, $\delta=-0.036A^{-\frac{1}{2}}$ for A even Z even, $\delta=+0.036A^{-\frac{1}{2}}$ for A even Z odd. From this formula, the value of Z for which the energy is a minimum at constant A can be calculated. These points of Z and A will be referred to as the stability line. The observed asymmetric distribution of elements can be explained only if the maximum of the Gauss distribution lies at higher neutron numbers than correspond to the sta-

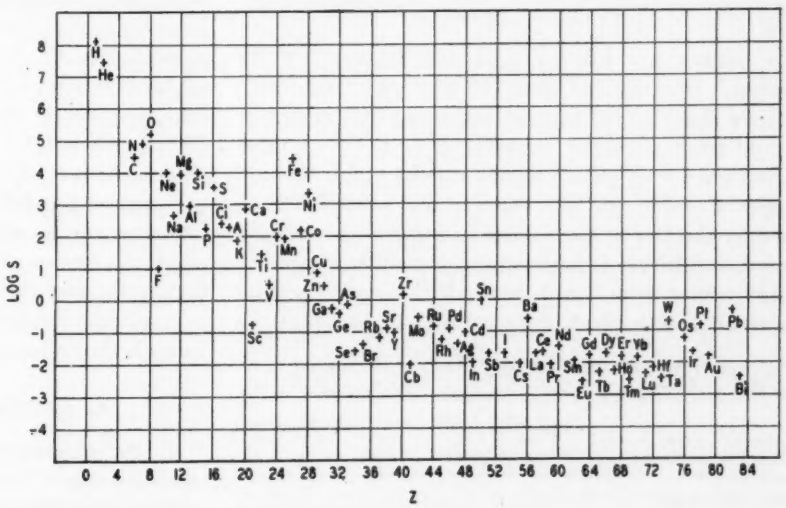

FIG. 1. Abundance of the chemical elements.

[4] N. Bohr and J. A. Wheeler, Phys. Rev. **56**, 426 (1939); von Albada, Astrophys. J. **105**, 393 (1947).

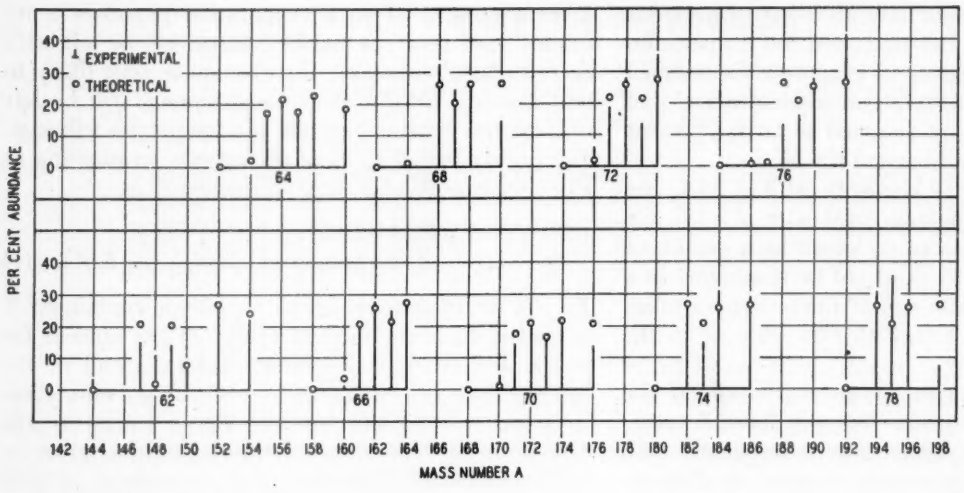

FIG. 2. Relative abundance of isotopes.

bility line. Formula (2) does not take into account fluctuations in binding energy. Such fluctuations occur near closed shells of 50, 82, or 126 like nucleons. In the range of nuclei $62 \leq Z \leq 78$ the influence of closed shells is minor. We have selected this region for a preliminary comparison. In order to fit the abundances with the minimum number of parameters, we assume that, if N, Z lies on the stability curve, $E_{N,Z} - E_0$ is a constant. In our calculations this constant was set equal to 0.03569 mass units.

The spread of the distribution, α, was chosen in such a way that the abundance of the lightest isotopes should agree as closely as possible with the actual abundances. In the calculations, $\alpha = 0.02415$ mass units was used.

As is seen from Fig. 2, there is a rough qualitative agreement between the calculated and observed isotopic distributions.

As a typical example we consider the case $Z = 62$. The agreement is satisfactory except for the isotopes of weight 144 and 148. The latter isotope is less abundant than the two neighboring odd isotopes. This remarkable behavior is reproduced and grossly exaggerated by theory.

The reason for this is that the isotope 148 is "shielded," whereas 147 and 149 are not. "Shielded" nuclei are those which cannot be formed by a chain of β-decays from elements containing 2, 4, 6, $\cdots$ less protons, since such chains would stop at stable isobars of lower Z value. In our theory, the isotope 148 is formed in the tail of the Gaussian for $Z = 62$, whereas the main contribution to the abundance of isotopes 147 and 149 comes from the β-decay of the corresponding isotopes of $Z = 60$, which are near the maximum of the Gaussian. The experimental abundance of the isotope 144 is 3 percent, whereas the calculation gives 0.0015 percent. This isotope has 82 neutrons and the relatively high abundance is connected with the stability of this shell.

TABLE I. Abundance of isotopes of odd mass number.

Range of nuclear charge (even Z-values only)	$Z=32$ to $Z=40$	$Z=42$ to $Z=50$	$Z=52$ to $Z=60$	$Z=62$ to $Z=70$	$Z=72$ to $Z=80$
Average percentage of odd mass-number isotopes	9%	25%	19%	33%	27%

One striking regularity in the isotopic ratios is the relatively small abundance of odd mass-number isotopes among the elements of even Z. This is partly due to the fact that practically all even mass-number nuclei have even Z-values while one may assume that odd mass-number elements are about equally divided between elements of even and odd charge. If this were the full explanation and if even and odd mass-numbers were equally abundant one should expect the average percentage of odd isotopes for even Z to be 33 percent.

The abundances of odd isotopes among the heavy elements of even Z vary considerably. Averages of the percentage of odd isotopes are given in Table I.

The value of 33 percent is reached only in rare earth region. This may be due to a fluctuation. For the heavy elements, the average percentage of odd mass-number isotopes is closer to 25 percent than to 33 percent. Assuming that there are as many odd mass-number nuclei for odd as for even Z, the ratio of the number of all heavy nuclei with odd mass-number to those of even mass-number is 0.671. The same ratio for the region $62 \leqq Z \leqq 78$ is 0.86. The calculated value is 0.80. This calculated ratio does not depend on an adjusted parameter but on the difference in binding energy of even and odd neutrons as given by (2) and on the assumption of original creation of fragments with even Z only. The latter assumption is, of course, essential.

A more complete calculation of abundances should include the following effects.

a. Fluctuation in Binding Energies

In the absence of accurate mass determinations one should correct formula (2) for the presence of closed shells. According to the experimental stability line a defect in binding energy exists for several neutrons fol-

lowing a closed shell; a corresponding excess of binding energy is indicated for the last neutrons of a closed shell. The same statement holds for protons. Such changes in binding energy would appear explicitly in (1) and they also influence the value of E_0.

b. Delayed-Neutron Emission

Experience with nuclear fission shows that in some cases β-processes are followed by further neutron evaporation. In the two identified cases the neutrons evaporated were the 51st and the 83rd. The reduced binding-energy of neutrons beyond the 50th and 82nd is a factor favoring delayed neutron emission. Nuclei further from the stability line have a higher β-energy, and for these nuclei delayed neutron emission may be even more probable.

c. Neutron Capture

Some of the neutrons evaporated from the nuclear fragments could be recaptured by nuclei. This process would deplete nuclei with high capture cross sections and enrich the next heavier isotope, provided this isotope has a lower neutron cross section. It happens to be a fact that all the known neutron absorption cross sections of nuclei with 50 or 82 neutrons are low.

III. THE POLYNEUTRON MODEL

In order to obtain a model of a nucleus which can serve as the starting point for the break-up process we shall assume that an assembly of neutrons forms a nuclear fluid which will not spontaneously disintegrate into neutrons. The only limitation imposed on the size of this polyneutron is that its total mass should not exceed the mass of a star. For bigger masses, effects of gravitation and general relativity would become decisive. These we do not propose to discuss.

The polyneutron is unstable with respect to β-decay. Such a decay transforms a neutron into a proton and liberates energy equal to the sum of the mass difference of neutron and proton and the binding energy of a triton. Added terms, due to interaction of the neutrons with the triton are assumed to be smaller. This means that for each β-decay an energy of about 9 Mev is obtained. A second β-decay can form an α-particle liberating an energy of about 20 Mev.

If the disintegration electrons left the polyneutron, Coulomb repulsion would soon make further β-decays energetically unfavorable. For a large polyneutron there is, however, no reason why the electrons should not remain in the nuclear liquid and neutralize the charge of the α-particles. If no other process intervenes, the disintegrations will proceed until the electron density has risen to the point where the zero point energy of the electrons is 9 Mev, making further triton formation impossible.

The maximum kinetic energy of the electrons is equal to the absolute value of their potential energy, $e\varphi$, and this quantity is connected to the number of electrons per unit volume n_e by the relativistic formula

$$n_e=(1/3\pi^2)(e\varphi/c\hbar)^3. \tag{3}$$

Near the surface of the polyneutron the electron distribution will protrude. The potential outside, φ, satisfies the relation

$$\Delta\varphi=-4\pi e n_e. \tag{4}$$

Using (3) we obtain the relativistic Thomas-Fermi equation

$$\Delta\varphi=(1/K^2e^2)\varphi^3. \tag{5}$$

Where K is a dimensionless number,

$$K=[(3\pi/4)(\hbar c/e^2)^3]^{\frac{1}{2}}=2462. \tag{6}$$

Assuming that φ depends only on the distance r from the surface of the polyneutron, neglecting effects of curvature, and assuming that the potential vanishes for $r\rightarrow\infty$, one obtains

$$\varphi=\sqrt{2}Ke/(r+r_0), \tag{7}$$

where the integration constant r_0 is determined by the condition of continuity at $r=0$. One obtains

$$r_0=(\sqrt{2}Ke/\varphi_i), \tag{8}$$

where φ_i is the constant value which the potential assumes in the interior of the polyneutron. If the β-decay has gone to completion, $\varphi_i=9$ million volts and $r_0=5.6\times10^{-11}$ cm. This thin layer of electrons is the rudiment of the extra-nuclear electrons in an atom.

The density of α-particles, n_α, inside the nucleus, is one-half that of the electrons.

$$n_\alpha=(1/6\pi^2)(e\varphi_i/c\hbar)^3=(2^{\frac{1}{2}}/4\pi)(K/r_0^3). \tag{9}$$

If φ_i is 9 million volts, $n_\alpha=1.60\times10^{+33}$ cm^{-3}.

The formation of the thin electron cloud near the surface lowers the surface energy σ of the polyneutron by the amount σ_e.

$$\sigma_e=-(1/6\pi)(K^2e^2/r_0^3), \tag{10a}$$

or

$$\sigma_e=-(\sqrt{2}K/12\pi)(\varphi_i e/r_0^2). \tag{10b}$$

Substituting the value $\varphi_i e=9$ Mev and using formulas (6) and (7) one obtains

$$\sigma_e=-4.24\times10^{17}\text{ erg cm}^{-2}=-0.265\text{ Mev barn}^{-1}. \tag{11}$$

This energy favors an increase in surface.

There will also be effects which tend to minimize the surface. For stable nuclei, these effects alone will be relevant. The corresponding surface tension σ_s can be obtained from the term proportional to $A^{\frac{2}{3}}$ in the semi-empirical formula (2). The assumptions that led to (2) give

$$\sigma_s=7.57\times10^{19}\text{ ergs cm}^{-2}=47.3\text{ Mev barn}^{-1}. \tag{12}$$

This surface tension is caused by the tendency of neutrons and protons to surround themselves with

other nucleons. A similar positive contribution to the surface tension must be expected in the case of the polyneutron. Such a contribution will decrease with decreasing neutron binding energy for two reasons. First, the energy needed to bring a neutron to the surface may be expected to be proportional to the binding energy. Second, the surface increase obtained in this way increases as the square of the average de Broglie wave-length of the neutron. If the kinetic energy of the neutron is assumed to be proportional to its binding energy, the surface increase is inversely proportional to the binding energy. Thus one is led to expect that σ_s of a polyneutron is proportional to the square of the binding energy of the neutrons within that structure. The positive surface tension σ_s will just balance the negative term σ_e if σ_s is about 180 times smaller than was calculated for stable nuclei. According to the above crude argument this will happen if the binding energy of a neutron in a polyneutron is 13.3 times smaller than that of a neutron in a stable nucleus. Using 8 Mev for the latter quantity one may estimate that 600,000 ev is this critical neutron binding energy for the polyneutron.

In order to investigate the surface stability, we shall briefly discuss the properties of surface waves. The frequency ω as a function of the wave-length λ, the density ρ, and the surface tension σ of the liquid is

$$\omega=(\sigma/\rho\lambda^3)^{\frac{1}{2}}. \tag{13}$$

The surface tension of the polyneutron, after the β-decay has proceeded for some time, is $\sigma=\sigma_s+\sigma_e$. We shall assume that from a certain point on the negative term σ_e is the bigger one of the two terms, that is, the total surface tension σ becomes negative. Surface waves will then no longer show a sinusoidal time dependence, but will grow exponentially as $e^{\omega t}$ with $\omega=(|\sigma|/\rho\lambda^3)^{\frac{1}{2}}$.

This statement is correct only for sufficiently long wave-lengths. For short wave-lengths, σ must be considered as a function of λ. In fact, if λ is small compared to r_0, the thickness of the electron cloud, the electronic energy does not contribute to the surface tension, and σ therefore is positive. The effective σ, to be inserted in (13), will be zero at an intermediate wave-length, which one would expect to be of the order r_0, unless the positive and negative parts of the surface tension are very closely balanced. The instability will lead to the fastest break-up of the surface where $\omega=(|\sigma|/\rho\lambda^3)^{\frac{1}{2}}$ has its maximum value. This will happen at a wave-length somewhat longer than that at which σ vanishes.

Because of this surface instability, droplets will break off. According to the above argument the order of magnitude of the droplet diameter is r_0. The charge Z_p contained in the droplet volume is, according to (9),

$$Z_p=\frac{\pi}{6}r_0^3 2n_\alpha=\frac{2^{\frac{1}{2}}}{12}K=\frac{1}{12}\left[\frac{3\pi}{2}\left(\frac{\hbar c}{e^2}\right)^3\right]^{\frac{1}{2}}=290. \tag{14}$$

The value of Z_p depends only on universal constants and not on the question of how far the β-decay has progressed before the break-up.

Formula (14), in addition to representing only a crude estimate, disregards the fact that our nuclear fluid carries a surface charge. This positive surface charge is equal to the charge of the electrons which protrude from the polyneutron. Substituting (7) into (3) and integrating over r from 0 to ∞, one gets for ξ, the surface charge per unit area

$$\xi=\frac{\sqrt{2}\,Ke}{4\pi r_0^2}. \tag{15}$$

A droplet of radius R will carry a part of this surface charge. One will expect, however, that its amount will be a fraction β of $4\pi R^2\xi$ because during the formation of the droplet the surface stretches and the same number of positive charges are spread over a larger area. One may assume $\frac{1}{4}<\beta<\frac{3}{4}$. The charge number $A_Z(R)$ as a function of the radius is, therefore,

$$Z_p(R)=2^{\frac{1}{2}}K[\tfrac{2}{3}(R/r_0)^3+\beta(R/r_0)^2]. \tag{16}$$

The energy released upon formation of a droplet consists of three terms. These are caused by the additional extrusion of electrons, by the increase in surface energy, and by Coulomb repulsion between positive charges. (For the low Z_p values to be considered the electrostatic term involving electron-electron interaction in the product nucleus is negligible.) It is probable that the β-decay will proceed beyond the point where the two surface energies balance and at the time of breakup one expects $\sigma_s<|\sigma_e|$. For the purpose of an estimate, we set, however, $\sigma_s=|\sigma_e|$. The total energy released in the droplet formation, $E(R, Z_p)$ is then

$$E(R,Z_p)=\frac{K^2e^2}{r_0}\left[2^{\frac{1}{2}}\frac{Z_p}{K}-\frac{2}{3}\left(\frac{R}{r_0}\right)^2-\frac{3}{5}\left(\frac{Z_p}{K}\right)^2\frac{r_0}{R}\right]. \tag{17}$$

The values of the charge, Z_p, the energy, the energy per unit charge and per unit volume are collected in Table II for different values of β and R. (The energy is given in units of $e\varphi_i$ and R in units of r_0.)

Assuming that a constant fraction of the energy appears as energy of translation, the droplet velocity

TABLE II. Values of the charge, Z_p, the energy, the energy per unit charge and per unit volume for different values of β and R. (The energy is given in units of $e\varphi_i$ and R in units of r_0.)

β	R/r_0	Z_p	$E/e\varphi_i$	$\frac{E}{Z_p(e\varphi_i)}$	$\frac{3r_0^3E}{4\pi R^3e\varphi_i}$
0.25	0.1	11	−0.79	−0.072	−188
0.25	0.2	53.4	+4.50	+0.084	+134
0.25	0.5	508	128.7	0.254	246
0.50	0.1	19.7	7.45	0.377	1784
0.50	0.2	88.2	35.1	0.398	1046
0.50	0.5	725	254	0.350	485
0.75	0.1	28.4	15.4	0.543	3690
0.75	0.2	123	63.6	0.517	1899
0.75	0.5	943	346	0.367	663

is proportional to the square root of the energy per unit volume. High-velocity droplets are formed faster and, therefore, in greater numbers. Table II shows that for small values of β the energy of formation of small droplets is negative, which means that such droplets would not form. For larger values of β greater velocities are obtained for smaller droplets. Thus, most droplets may be formed with charges smaller than those given in (14). The energy per unit volume does not depend sensitively on Z_p and so the whole range of known nuclear charges may be obtained. Charges smaller than 34 may be obtained but the great abundance of these light nuclei cannot be explained by this process. Nuclei with $Z_p>92$ are also formed. These will eventually decay, probably by fission, into known elements. For sake of definiteness we assume that the bulk of heavy elements is formed by neutron-evaporation from primary droplets.

In discussing formation of droplets we neglected motion of charges by exchange. No proof can be given that this motion is faster than the motion of the nucleons.

During the formation of droplets many neutrons are present for each pair of protons. Under these conditions groups resembling α-particles will be formed and it will take considerable energy to separate pairs of protons. Thus Z_p will be even and the final abundance for even and odd mass numbers will be different. The observed fission processes of uranium leads to equal abundances of even and odd mass numbers indicating that in this case fission products have even and odd Z values with roughly equal probabilities. This may be due to the fact that in uranium α-particles are less good sub-units.

The primary droplets evaporate neutrons. It is of interest to estimate the energy available for this process. In the fission of uranium considerably less than half of the available energy appears as internal energy of the fragments. Because of the looser structure of the droplets considered by us, a greater fraction of the energy given in (17) may appear as internal energy. We shall arbitrarily assume that the energy will be divided equally between translational motion and internal degrees of freedom.

In Section II it was assumed that neutrons are evaporated from the droplets until the internal energy is exhausted. We shall now compare the available internal energy with the binding energy of neutrons from the semi-empirical formula (2). For a given Z there exists a maximum neutron number $N_{\max}$ beyond which neutrons are no longer bound. Setting $A_{\max}=Z+N_{\max}$ we can determine $A_{\max}$ from

TABLE III. Values of neutron numbers $N_{\max}(Z)$ and of the energy required to evaporate neutrons from a nucleus with $N_{\max}$ neutrons until stability is reached. (All energies in Mev.)

Z	$N_{\max}(Z)$	$E(N_{\max})-E_{\text{stability}}(Z)$	$\frac{1}{2}E(Z_p)$ $\beta=0.25$	$\beta=0.5$	$\beta=0.75$
40	97.5	153	10	70	97
60	151.8	209	26	106	144
80	208.1	245	45	143	190
100	266	269	66	179	235

$$(Z/A_{\max})^2(0.083+0.000209A_{\max}^{\frac{1}{3}}) -0.0093A_{\max}^{-\frac{1}{3}}-0.00569=0. \quad (18)$$

As a crude estimate we assume that $E(N_{\max}, Z)-E(N, Z)$ is the energy needed to reach the nucleus N, Z by evaporation.

Table III contains, in column 2, the neutron-numbers $N_{\max}$. The following column gives the energy, according to formula (2), which is required to evaporate neutrons from a nucleus with $N_{\max}$ neutrons until the stability curve is reached. It is seen that these energies are somewhat greater than $\frac{1}{2}E(Z_p)$ obtained from (17) and (16). Thus it is plausible that the evaporation stops before the stability-line is reached. In fact, if $\beta=0.5$ or 0.25 is used, the evaporation would stop at a much greater distance from the stability curve than was assumed in Section II. The above results depend on many crude assumptions:

(1) Formula (2) has been used beyond its range of proved applicability. It has been assumed that for $N>N_{\max}$ the binding energy is zero.

(2) The primary droplets might have come off with $N<N_{\max}$.

(3) It was assumed in the calculation that at the time of break-up the maximum electronic energy in the polyneutron is 9 Mev.

(4) We have made specific assumptions about the surface energy, the value of β and the distribution of droplet energy between internal and kinetic energy.

All that can be stated is that the model here discussed is compatible with the assumption of Section II concerning the center of the Gaussian. The half-breadth of the Gaussian used in II corresponds to about 37 Mev. It seems likely that a considerable or even preponderant part of this is due to a variation of energy given to the primary droplets.

It is evident that the above proposals cannot be considered as proved. It seems, however, of interest that the assumption of a great and indefinite number of excess neutrons leads to a break-up process and to a distribution of isotopes which is consistent with our knowledge of isotopic abundances of heavy elements.

We wish to thank Robert W. Christy who carried out the calculations on which Fig. 2 has been based.

Crystal Statistics. II. Partition Function Evaluated by Spinor Analysis

BRURIA KAUFMAN*
Columbia University, New York City, New York
(Received May 11, 1949)

The partition function for a two-dimensional binary lattice is evaluated in terms of the eigenvalues of the 2^n-dimensional matrix V characteristic for the lattice. Use is made of the properties of the 2^n-dimensional "spin"-representation of the group of rotations in $2n$-dimensions. In consequence of these properties, it is shown that the eigenvalues of V are known as soon as one knows the angles of the $2n$-dimensional rotation represented by V.

Together with the eigenvalues of V, the matrix Ψ which diagonalizes V is obtained as a spin-representation of a known rotation. The determination of Ψ is needed for the calculation of the degree of order.

The approximation, in which all the eigenvalues of V but the largest are neglected, is discussed, and it is shown that the exact partition function does not differ much from the approximate result.

THE partition function for a 2-dimensional binary alloy has been evaluated exactly by Onsager,[1] using the approach introduced by Kramers and Wannier,[2] and Montroll.[3] According to this method, a matrix characteristic of the crystal is set up, and it is shown that the partition function is approximately equal to the largest eigenvalue of the characteristic matrix. The eigenvalue problem has been treated approximately by various authors.[4] Onsager has shown that the characteristic matrix is decomposable into a direct product of 2-dimensional matrices and so was able to find the exact eigenvalues through the solution of n-quadratic equations.

In this paper, a shorter method, though closely related, is employed to reduce the characteristic matrix, V. It is shown that V is a 2^n-dimensional "spin"-representative of a $2n$-dimensional rotation (i.e., orthogonal matrix), and that, as a consequence, its eigenvalues were known as soon as the eigenvalues of the rotation were given. Further considerations of symmetry reduce the $2n$-dimensional matrix into a product of n-plane rotations, so that again the eigenvalues are found from the solution of n-quadratic equations.

As a by-product of the solution of the eigenvalue problem, we are also able to find the matrix Ψ of eigenvectors of V. Since every operation in 2^n-space is mirrored in the $2n$-dimensional space, the operation of Ψ corresponds to the diagonalization of the $2n$-dimensional rotation. This latter operation is easy to carry out, again because of the symmetry of the $2n$-dimensional rotation.

As has been shown,[5] the knowledge of Ψ makes it possible to state the average probabilities of crystal configurations. In particular, it is possible to evaluate average correlations between pairs of atoms within the crystal. This will be done in III.

1. SETTING UP THE MATRIX PROBLEM

Our physical model is a rectangular lattice with m rows and n sites per row. These sites are to be occupied by two kinds of constituent atoms. We assume that interactions exist only between nearest neighbors, and that the energy of interaction is $+J$ between unlike neighbors in a row, and $+J'$ between unlike neighbors in a column; but that it is $-J$, $-J'$ between like neighbors in a row, or column, respectively. The total energy of a configuration of the lattice is found simply by counting the number of like neighbors in the lattice, and subtracting from it the number of unlike neighbors. (Since we distinguish between row and column interactions, this count has to be made separately for the J and the J' (see Fig. 1).)

The probability of finding the lattice in a given configuration, at the temperature T, is proportional to $\exp\{-E_c/kT\}$, where E_c is the total energy of the configuration. Clearly, the exponent which appears in the expression for the probability will always be of the form

$$(n_c\cdot J+n_c'\cdot J')/kT.$$

Here n_c, n_c' are integers which depend on the configuration of the lattice. It is convenient to introduce the variables $H\equiv J/kT$, $H'\equiv J'/kT$ instead of J, J'. And then the probability of a configuration is

$$(1/Z)\cdot\exp\{n_cH+n_c'H'\}.$$

Z is the "partition function" for the lattice,

$$Z=\sum_{\substack{\text{all}\\ \text{configurations}}} e^{n_cH+n_c'H'}.$$

The thermodynamic functions for the crystal can be

* Now at the Institute for Advanced Study, Princeton, New Jersey.

[1] L. Onsager, "Crystal statistics. I. A two-dimensional model with an order-disorder transition," Phys. Rev. **65**, 117 (1944). This paper, first in the present series, will be henceforth referred to as I.

[2] H. A. Kramers and G. H. Wannier, Phys. Rev. **60**, 252, 263 (1941).

[3] E. Montroll, J. Chem. Phys. **9**, 706 (1941).

[4] H. A. Kramers and G. H. Wannier (footnote 2); E. Montroll (footnote 3); E. N. Lassettre and J. P. Howe, J. Chem. Phys. **9**, 747 (1941); J. Ashkin and W. E. Lamb, Jr., Phys. Rev. **64**, 159 (1943).

[5] E. N. Lassettre and J. P. Howe, J. Ashkin and W. E. Lamb, Jr. (footnote 4).

found from a knowledge of Z, and, as can be seen from its definition, it is a simple matter to calculate Z for small crystals. However, since the number of terms in Z is $2^{m\cdot n}$, it is not feasible to carry out such a calculation except when m and n are of the order of unity. Nor is it necessary to proceed in such a tedious manner. It has been shown[2,3] that the terms in Z are members of the mth power of a matrix $\mathbf{V}$ which is characteristic for the lattice. Z is then seen to be the trace of $\mathbf{V}^m$.

To show this, it is convenient to introduce the fiction of spin attributed to each atom. All atoms of one kind will be given the spin $+1$, and the other kind -1. When this is done, the interaction between two neighboring atoms with spins μ, μ' is: $-\mu\mu'H$ (or $-\mu\mu'H'$) for row (or column) neighbors.

The configurations of the crystal can now be specified by stating the value of μ at each site of the crystal. However, it is more convenient to specify row-configurations. Since there are n atoms in a row, there are 2^n possible configurations, $1\leqslant\nu\leqslant 2^n$. And then the configuration of the crystal is given by the set $\{\nu_1, \nu_2, \cdots, \nu_m\}$.

The energy due to interactions within a row may be denoted by $E(\nu_i)$; the energy due to interaction between two adjacent rows—by $E(\nu_i, \nu_{i+1})$. As a result, the energy of a configuration of the crystal is

$$E_c=\sum_{i=1}^{m} E(\nu_i)+\sum_{i=1}^{m} E(\nu_i, \nu_{i+1}).$$

(Here it is assumed, for purposes of symmetry, that the mth row of the crystal interacts with the first row.) If we now make the abbreviations

$$(\mathbf{V}_1)_{\nu_i\nu_{i+1}}\equiv\exp\{-E(\nu_i, \nu_{i+1})/kT\}, \tag{1}$$

$$(\mathbf{V}_2)_{\nu_i\nu_i}\equiv\exp\{-E(\nu_i)/kT\}, \tag{2}$$

we see that the probability of a configuration is proportional to

$$e^{-E_c/kT}=(\mathbf{V}_2)_{\nu_1\nu_1}(\mathbf{V}_1)_{\nu_1\nu_2}(\mathbf{V}_2)_{\nu_2\nu_2}\times(\mathbf{V}_1)_{\nu_2\nu_3}\cdots(\mathbf{V}_2)_{\nu_m\nu_m}(\mathbf{V}_1)_{\nu_m\nu_1}.$$

We therefore get for the partition function

$$Z=\sum_{\nu_1,\nu_2,\cdots\nu_m}(\mathbf{V}_2)_{\nu_1\nu_1}(\mathbf{V}_1)_{\nu_1\nu_2}\cdots(\mathbf{V}_1)_{\nu_m\nu_1}\equiv\text{trace }(\mathbf{V}_2\mathbf{V}_1)^m. \tag{3}$$

Since for each i: $1\leqslant\nu_i\leqslant 2^n$, we see that $\mathbf{V}_1$ and $\mathbf{V}_2$ are 2^n-dimensional matrices, and $\mathbf{V}_2$ is diagonal. $\mathbf{V}_1$ and $\mathbf{V}_2$ have been given explicitly in I:

$$\mathbf{V}_2=\exp\{H'\cdot\sum_{r=1}^{n}\mathbf{s}_r\mathbf{s}_{r+1}\}\equiv\exp\{H'\cdot\mathbf{A}\},$$

$$\mathbf{V}_1=(2\sinh 2H)^{n/2}\cdot\exp\{H^*\cdot\sum_{r=1}^{n}\mathbf{C}_r\}. \tag{4}$$

Here $\mathbf{s}_r$ and $\mathbf{C}_r$ are 2^n-dimensional quaternion matrices,

$$\mathbf{s}_r\equiv 1\times 1\times\cdots\times\mathbf{s}\times 1\times\cdots\times 1$$
$$\mathbf{C}_r\equiv 1\times 1\times\cdots\times\mathbf{C}\times 1\times\cdots\times 1; \tag{5}$$

there are n factors in each direct-product, with $\mathbf{s}$ or $\mathbf{C}$ appearing in the rth position. $\mathbf{s}$ and $\mathbf{C}$ are generators of the Pauli matrices:

$$\mathbf{s}=\begin{pmatrix}1 & 0\\ 0 & -1\end{pmatrix},\quad \mathbf{C}=\begin{pmatrix}0 & 1\\ 1 & 0\end{pmatrix},\quad 1=\begin{pmatrix}1 & 0\\ 0 & 1\end{pmatrix}. \tag{6}$$

H^* is defined by

$$e^{-2H}\equiv\tanh H^*. \tag{7}$$

We may redefine $\mathbf{V}_1$ so as to remove from it the scalar coefficient:

$$\mathbf{V}_1\equiv\exp\{H^*\sum_{r=1}^{n}\mathbf{C}_r\}\equiv\exp\{H^*\cdot\mathbf{B}\}. \tag{8}$$

Then

$$Z=(2\sinh 2H)^{n/2}\cdot\text{trace }(\mathbf{V}_2\mathbf{V}_1)^m=(2\sinh 2H)^{n/2}\cdot\sum_{i=1}^{2^n}\lambda_i^m, \tag{9}$$

where λ_i are the eigenvalues of $\mathbf{V}\equiv\mathbf{V}_2\cdot\mathbf{V}_1$.

We now propose to show that matrices of the type $\exp(a\cdot\mathbf{s}_r\mathbf{s}_{r+1})$, $\exp\{b\cdot\mathbf{C}_r\}$, and their products, form a 2^n-dimensional representation of the group of rotations in $2n$-dimensions. Thus, the matrix $\mathbf{V}$ itself will be the representative of some such rotation.

We will further show that there is a very simple relationship between the eigenvalues of the rotation and the eigenvalues of its 2^n-dimensional representative. As a result, all our work will be reduced to finding eigenvalues in a $2n$-dimensional space.

2. ELEMENTS OF SPINOR ANALYSIS

The relation between the $2n$- and 2^n-spaces is best brought out by the study of sets of anticommuting matrices. The Pauli and Dirac matrices are examples of such sets. The general case was treated by Brauer and Weyl.[6] We will now derive those of their results which will be needed in what follows.[7]

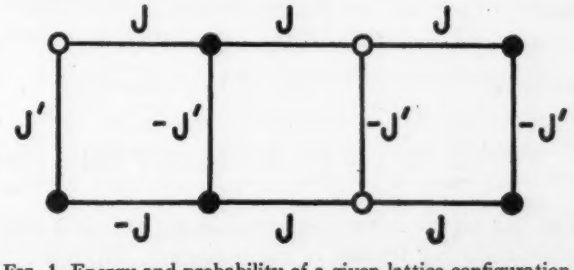

FIG. 1. Energy and probability of a given lattice configuration. The two kinds of atoms are denoted by ○ and ●.

[6] R. Brauer and H. Weyl, Am. J. Math. 57, 425 (1935). See also F. D. Murnaghan, *The Theory of Group Representations* (The Johns Hopkins Press, Baltimore, Maryland), Chapter 10.

[7] The discussion which follows is rather similar to that given by Pauli in treating the relativistic invariance of the Dirac wave-

We start out with a set of $2n$-quantities Γ_k which obey the commutation rules

$$\Gamma_k^2=1, \quad \Gamma_k\Gamma_l=-\Gamma_l\Gamma_k, \quad (1\leqslant k, l, \leqslant 2n). \tag{10}$$

These quantities may be realized by matrices. For example, for the case $n=1$, a possible realization is: $\Gamma_1=\mathbf{s}$, $\Gamma_2=i\mathbf{s}\mathbf{C}$. Γ_1 and Γ_2 are the generators of the set of Pauli spin matrices. That is to say, the complete set is formed by taking all products of the generators: $\mathbf{1}$, $\mathbf{s}$, $i\mathbf{s}\mathbf{C}$, $\mathbf{C}=i\Gamma_1\Gamma_2$.

Similarly, for the case $n=2$, a possible realization is given by the generators of the set of Dirac matrices:

$$\Gamma_1=\mathbf{s}\times\mathbf{1}, \quad \Gamma_2=i\mathbf{s}\mathbf{C}\times\mathbf{1}, \quad \Gamma_3=\mathbf{C}\times\mathbf{s}, \quad \Gamma_4=\mathbf{C}\times i\mathbf{s}\mathbf{C}.$$

In the general case we may choose for the Γ_k:

$$\begin{aligned}\Gamma_{2r-1}&\equiv\mathbf{C}\times\mathbf{C}\times\cdots\times\mathbf{s}\times\mathbf{1}\times\mathbf{1}\times\cdots\equiv\mathbf{P}_r,\\ \Gamma_{2r}&\equiv\mathbf{C}\times\mathbf{C}\times\cdots\times i\mathbf{s}\mathbf{C}\times\mathbf{1}\times\mathbf{1}\times\cdots\equiv\mathbf{Q}_r,\\ &\qquad\qquad 1\leqslant r\leqslant n,\end{aligned} \tag{11}$$

n factors appear in each product; $\mathbf{s}$ or $i\mathbf{s}\mathbf{C}$ appear in the rth place. The Γ_k are thus 2^n-dimensional matrices.

If we take all possible products of the Γ_k, we form a set of 2^{2n} matrices:

$$\mathbf{1}, \Gamma_1, \Gamma_2, \cdots, \Gamma_{2n}, \Gamma_1\cdot\Gamma_2, \Gamma_1\cdot\Gamma_3, \cdots, \Gamma_1\cdot\Gamma_2\cdot\Gamma_3, \cdots.$$

And now, any 2^n-dimensional matrix can be written as a linear combination of these "base matrices," just as any point in a vector space can be specified in terms of the "base vectors" which span that space. For this reason, the base matrices are said to span the complete algebra of 2^n-dimensional matrices.[8]

In particular, $\mathbf{V}_1$ and $\mathbf{V}_2$ are easily expressed in terms of the base matrices. We have:

$$\begin{aligned}\mathbf{C}_r&=i\mathbf{P}_r\mathbf{Q}_r=\mathbf{1}\times\mathbf{1}\times\cdots\times\mathbf{C}\times\mathbf{1}\times\cdots,\\ \mathbf{s}_r&=\mathbf{C}_1\mathbf{C}_2\cdots\mathbf{C}_{r-1}\mathbf{P}_r=\mathbf{1}\times\mathbf{1}\times\cdots\times\mathbf{s}\times\mathbf{1}\times\cdots.\end{aligned} \tag{12}$$

Therefore

$$\mathbf{V}_1=\prod_{r=1}^{n}\exp\{iH^*\mathbf{P}_r\mathbf{Q}_r\}. \tag{13}$$

On the other hand, since

$$\mathbf{s}_{r+1}\mathbf{s}_r=-i\mathbf{P}_{r+1}\mathbf{Q}_r \quad \text{for} \quad 1\geqslant r\geqslant n-1,$$

but

$$\mathbf{s}_1\mathbf{s}_n=+i\mathbf{P}_1\mathbf{Q}_n\cdot\mathbf{C}_1\mathbf{C}_2\cdots\mathbf{C}_n\equiv i\mathbf{P}_1\mathbf{Q}_n\cdot\mathbf{U},$$

we have[9]

$$\mathbf{V}_2=\prod_{r=1}^{n-1}\exp\{-iH'\mathbf{P}_{r+1}\mathbf{Q}_r\}\cdot\exp\{iH'\mathbf{P}_1\mathbf{Q}_n\mathbf{U}\}. \tag{14}$$

The end factor differs from the others. This is a somewhat annoying feature of the boundary, which will be treated in detail below. The new notation for $\mathbf{V}_1$, $\mathbf{V}_2$ reveals a striking similarity between these two matrices. $\mathbf{V}_2$ is obtained (except for its end factor) from $\mathbf{V}_1$ by replacing $\mathbf{P}_r$ by $\mathbf{P}_{r+1}$ in all its factors. Such a transformation (in $2n$-space) is the basic operation in spinor analysis, and it will be seen to have same effect as a similarity transformation in 2^n-space.

An Alternative Realization

In (11) we have given a particular matrix realization of the set of quantities Γ_k which obey the commutation rules

$$\Gamma_l\Gamma_k+\Gamma_k\Gamma_l=2\delta_{kl}. \tag{10}$$

Clearly, the commutation rules remain invariant if all the Γ_k undergo a similarity transformation in 2^n-space. Let $\Gamma_k^*=\mathbf{S}\Gamma_k\mathbf{S}^{-1}$ $(1\leqslant k\leqslant n)$. Then

$$\Gamma_k^*\Gamma_l^*+\Gamma_l^*\Gamma_k^*=2\delta_{kl}.$$

Thus we see that the set Γ_k^* provides another matrix realization obeying (10). For example, the set

$$\begin{aligned}\Gamma_{2k-1}^*&=\mathbf{s}\times\mathbf{s}\times\cdots\times\mathbf{C}\times\mathbf{1}\times\mathbf{1}\times\cdots\equiv\mathbf{P}_k^*,\\ &\qquad\qquad (1\leqslant k\leqslant n),\\ \Gamma_{2k}^*&=\mathbf{s}\times\mathbf{s}\times\cdots\times i\mathbf{C}\mathbf{s}\times\mathbf{1}\times\mathbf{1}\times\cdots\equiv\mathbf{Q}_k^*,\end{aligned} \tag{15}$$

is equally as good a realization as (11). It is obtained from (11) by a transformation which interchanges $\mathbf{C}$ and $\mathbf{s}$ in all operators. This realization is often easier to handle than (11), and we will use it upon occasion.

The transformation from Γ_k to the Γ_k^* given in (15) is effected by

$$\mathbf{g}=2^{n/2}(\mathbf{C}+\mathbf{s})\times(\mathbf{C}+\mathbf{s})\times\cdots\times(\mathbf{C}+\mathbf{s})=\mathbf{g}^{-1}$$

$$\mathbf{C}+\mathbf{s}=\begin{pmatrix}1 & 1\\ 1 & -1\end{pmatrix}. \tag{16}$$

(To see this, note that $\frac{1}{2}(\mathbf{C}+\mathbf{s})^2=\mathbf{1}$ and $\frac{1}{2}(\mathbf{C}+\mathbf{s})\cdot\mathbf{s}\cdot(\mathbf{C}+\mathbf{s})=\mathbf{C}$.) In this realization we have, of course, $i\mathbf{P}_r^*\mathbf{Q}_r^*=\mathbf{s}_r$, and thus

$$\mathbf{g}\cdot\mathbf{V}_1\cdot\mathbf{g}=\prod_{r=1}^{n}\exp\{iH^*\mathbf{P}_r^*\mathbf{Q}_r^*\}$$

is diagonal in this coordinate system. On the other hand, $-i\mathbf{P}_{r+1}^*\mathbf{Q}_r^*=\mathbf{C}_{r+1}\mathbf{C}_r$ and therefore $\mathbf{V}_2\rightarrow\mathbf{g}\mathbf{V}_2\mathbf{g}$, which is no longer diagonal.

The Spin-Representation of the Orthogonal Group

We have seen that if the set Γ_k is a matrix realization of the commutation rules (10), then all the sets $\mathbf{S}\Gamma_k\mathbf{S}^{-1}$ are also realizations of (10).

The converse of this statement is a very important theorem for our purpose: *If two sets of matrices, Γ_k and Γ_k^*, both obey the commutation rules (10), then a transformation $\mathbf{S}$ can be found such that $\Gamma_k^*=\mathbf{S}\Gamma_k\mathbf{S}^{-1}$.* If we agree to consider two sets of matrices which are related set-wise by a similarity transformation as being the same set, we can say simply: For a given n there is only

equation [*Handbuch der Physik* (Verlag. Julius Springer, Berlin), Vol. 24/1, second edition, pp. 219–224].

[8] The proof of the completeness of the algebra is given by Brauer and Weyl (footnote 6). See also I, p. 122.

[9] The operator $\mathbf{U}$ was denoted by $\mathbf{C}$ in I. See Eq. (32) in I.

one realization of the commutation rules. This theorem is not trivial. Its proof[9,10] rests upon the fact that the only possible automorphism of a complete matrix algebra is given by a similarity transformation.

In what follows, we will assume that we have already found one realization Γ_k (e.g., as in (11)). We will then show that certain linear combinations of the Γ_k will also obey the commutation rules. Therefore, according to the theorem above, these linear combinations (Γ_k^*) must be related to the Γ_k by a similarity transformation. This gives us two relations between the Γ_k and the Γ_k^*. One of these relations will be seen to be a "rotation" in $2n$-space, and the other will be referred to as the "spin-representation" in 2^n-space of the rotation in $2n$-space. Let the linear combinations be written as

$$\Gamma_k^*=\sum_{j=1}^{2n} o_{jk}\Gamma_j, \quad 1\leqslant k\leqslant 2n, \tag{17}$$

where o_{jk} are as yet arbitrary numbers, in general complex. Then:

$$(\Gamma_k^*)^2=(\textstyle\sum_j o_{jk}\Gamma_j)^2=\sum_i o_{ik}o_{jk}\Gamma_i\Gamma_j.$$

In this sum, terms will cancel in pairs. For $i\neq j$, $o_{jk}o_{ik}\Gamma_j\Gamma_i+o_{ik}o_{jk}\Gamma_i\Gamma_j=0$ because of (10). Only the terms $i=j$ have no partners and do not cancel. But by (10), $\Gamma_j\Gamma_j=\mathbf{1}$. Therefore:

$$(\Gamma_k^*)^2=\sum_{j=1}^{2n} o_{jk}^2.$$

If we now demand of the constants o_{jk} that they satisfy

$$\sum_{j=1}^{2n} o_{jk}^2=1, \quad (1\leqslant k\leqslant 2n),$$

we find that $(\Gamma_k^*)^2=\mathbf{1}$. Similarly, if we demand that

$$\sum_{j=1}^{2n} o_{jk}o_{jl}=0, \quad k\neq l, \quad (1\leqslant k,l\leqslant 2n),$$

we find $\Gamma_k^*\Gamma_l^*=-\Gamma_l^*\Gamma_k^*$. Thus the set Γ_k^* will form a realization of (10) if the o_{jk} fulfill:

$$\sum_{j=1}^{2n} o_{jk}o_{jl}=\delta_{kl}, \quad (1\leqslant k,l\leqslant 2n). \tag{18}$$

We may view the o_{jk} as members of a $2n$-dimensional matrix. From the restrictions on its members, this matrix is seen to be orthogonal. (If its members are real, it describes a rotation in $2n$-dimensional Euclidean space.) We then say that the rotation $\mathbf{o}$ operates on the $2n$ quantities Γ_k and sends them into Γ_k^*.

$$\mathbf{o}:\Gamma_k\rightarrow\Gamma_k^*=\sum_{j=1}^{2n} o_{jk}\Gamma_j, \quad (1\leqslant k\leqslant 2n). \tag{19}$$

[10] An elegant group-theoretical proof was also given by Jordan and Wigner, Zeits. f. Physik **47**, 631 (1928).

However, by the theorem, Γ_k^* is also related to Γ_k through a similarity transformation:[11]

$$\Gamma_k^*=\mathbf{S}(\mathbf{o})\cdot\Gamma_k\cdot\mathbf{S}(\mathbf{o})^{-1}, \quad 1\leqslant k\leqslant 2n. \tag{20}$$

We write $\mathbf{S}(\mathbf{o})$, to indicate that the similarity transformation depends on the orthogonal matrix $\mathbf{o}$, and proceed to discuss the nature of this dependence.

Consider the full group of orthogonal matrices $\mathbf{o}$ in $2n$-space. We show that the collection of matrices $\mathbf{S}(\mathbf{o})$ forms a 2^n-dimensional representation of the orthogonal group. That is to say: the correspondence between the $\mathbf{o}$ and $\mathbf{S}(\mathbf{o})$ matrices is such that $\mathbf{S}(\mathbf{o}'')$ which corresponds to the product $\mathbf{o}''=\mathbf{o}'\cdot\mathbf{o}$ is the product of the matrices corresponding to $\mathbf{o}$ and $\mathbf{o}'$:

$$\mathbf{S}(\mathbf{o}'')=\mathbf{S}(\mathbf{o}'\cdot\mathbf{o})=\mathbf{S}(\mathbf{o}')\cdot\mathbf{S}(\mathbf{o}). \tag{21}$$

To show this, let

$$\mathbf{o}:\Gamma_k\rightarrow\sum_{j=1}^{2n} o_{jk}\cdot\Gamma_j=\mathbf{S}(\mathbf{o})\cdot\Gamma_k\cdot\mathbf{S}(\mathbf{o})^{-1},$$

$$\mathbf{o}':\Gamma_k\rightarrow\sum_{l=1}^{2n} o_{lk}'\cdot\Gamma_l=\mathbf{S}(\mathbf{o}')\cdot\Gamma_k\cdot\mathbf{S}(\mathbf{o}')^{-1}.$$

Combining the two operations we have

$$\mathbf{o}''=\mathbf{o}'\cdot\mathbf{o}:\Gamma_k\rightarrow\sum_{l=1}^{2n}\sum_{j=1}^{2n} o_{jk}o_{lj}'\Gamma_j$$

$$=\sum_{l=1}^{2n} o_{lk}''\Gamma_l=\mathbf{S}(\mathbf{o}'')\cdot\Gamma_k\cdot\mathbf{S}(\mathbf{o}'')^{-1}.$$

But on the other hand

$$\mathbf{o}'\cdot\mathbf{o}: \quad \Gamma_k\rightarrow\mathbf{S}(\mathbf{o}')\cdot\mathbf{S}(\mathbf{o})\cdot\Gamma_k\cdot\mathbf{S}(\mathbf{o})^{-1}\cdot\mathbf{S}(\mathbf{o})^{-1}.$$

As a result

$$\mathbf{S}(\mathbf{o}'\cdot\mathbf{o})=\mathbf{S}(\mathbf{o}'')=\mathbf{S}(\mathbf{o}')\cdot\mathbf{S}(\mathbf{o}).$$

(It is important to notice that the Γ_k transform according to the transpose—or, what is the same here, the reciprocal—of $\mathbf{o}$, and *not* according to $\mathbf{o}$ itself.)

Every rotation in $2n$-space thus has a counterpart transformation, $\mathbf{S}(\mathbf{o})$, in 2^n-dimensional "spin" space. For example, the rotation referred to above, which sends $\mathbf{P}_r\rightarrow\mathbf{P}_{r+1}$, $\mathbf{Q}_r\rightarrow\mathbf{Q}_r$ and therefore sends $\mathbf{V}_1\rightarrow\mathbf{V}_2$, has a representative in spin space, and as a result we have $\mathbf{V}_2=\mathbf{S}\mathbf{V}_1\mathbf{S}^{-1}$ (if we disregard the difficulty with the end factor in $\mathbf{V}_2$).

Eigenvalues of the Spin-Representatives

While in principle it is possible to find $\mathbf{S}(\mathbf{o})$ explicitly for any rotation $\mathbf{o}$, this is quite a complicated job in general. Fortunately we shall need to know $\mathbf{S}(\mathbf{o})$ only for the very simple case where $\mathbf{o}$ is the product of commuting plane rotations. Consider first one plane rotation. It operates on a pair of Γ's, say Γ_k and Γ_l, and

[11] In the case of the Dirac wave equation, the matrix $\mathbf{o}$ is the Lorentz-transformation in $2n=4$ dimensional coordinate-space. The Lorentz-transformation induces a transformation in $2^n=4$-dimensional "spin space," so that $\psi\rightarrow\psi'=\mathbf{S}(\mathbf{o})\cdot\psi$, where $\mathbf{S}(\mathbf{o})$ is the spin-representative of $\mathbf{o}$, and ψ is the 4-component Dirac wave function. See Pauli, reference 7.

leaves the others unchanged. Thus

$$\mathbf{K}:\ \begin{matrix}\Gamma_k\to\cos\theta\cdot\Gamma_k-\sin\theta\cdot\Gamma_l\equiv\Gamma_k^*, & \Gamma_i\to\Gamma_i,\\ \Gamma_l\to\sin\theta\cdot\Gamma_k+\cos\theta\cdot\Gamma_l\equiv\Gamma_l^*, & i\neq k,\ l.\end{matrix} \tag{22}$$

We will verify that

$$\mathbf{S}(\mathbf{K})=\exp\{\theta/2\cdot\Gamma_k\Gamma_l\}, \tag{23}$$

or, using the series expansion of the right-hand term:

$$\mathbf{S}(\mathbf{K})=\cos(\theta/2)+\sin(\theta/2)\cdot\Gamma_k\Gamma_l, \tag{24}$$

(Γ_k, Γ_l are known 2^n-dimensional matrices; $\cos(\theta/2)$ stands for the 2^n-dimensional unit matrix multiplied by the scalar $\cos(\theta/2)$. Thus $\mathbf{S}(\mathbf{K})$ is given explicitly by (24)); and indeed,

$$\begin{aligned}&\mathbf{S}(\mathbf{K})\cdot\Gamma_k\cdot\mathbf{S}(\mathbf{K})^{-1}\\ &=\left(\cos\frac{\theta}{2}+\sin\frac{\theta}{2}\Gamma_k\Gamma_l\right)\Gamma_k\left(\cos\frac{\theta}{2}-\sin\frac{\theta}{2}\Gamma_k\Gamma_l\right)\\ &=\left(\cos^2\frac{\theta}{2}-\sin^2\frac{\theta}{2}\right)\Gamma_k-\left(2\cos\frac{\theta}{2}\sin\frac{\theta}{2}\right)\cdot\Gamma_l\\ &=\cos\theta\cdot\Gamma_k-\sin\theta\cdot\Gamma_l=\Gamma_k^*.\end{aligned}$$

Similarly $\mathbf{S}(\mathbf{K})\Gamma_l\mathbf{S}(\mathbf{K})^{-1}=\sin\theta\cdot\Gamma_k+\cos\theta\cdot\Gamma_l=\Gamma_l^*$. This proves the assertion about the explicit form of $\mathbf{S}(\mathbf{K})$.

The half-angle which appears in the explicit form of $\mathbf{S}(\mathbf{K})$ is a characteristic feature of the spin-representation. It shows that the group of matrices $\mathbf{S}(\mathbf{o})$ provides a double-valued representation for the orthogonal group. Clearly, if we add 2π to the angle θ in (22), the rotation $\mathbf{K}$ is unchanged, but $\mathbf{S}(\mathbf{K})$ is multiplied by -1 (see (24)).

Thus we find that $\mathbf{K}$ is represented by two inequivalent matrices, $\mathbf{S}(\mathbf{K})$ and $-\mathbf{S}(\mathbf{K})$. On the other hand, to any $\mathbf{S}(\mathbf{K})$ there corresponds only one rotation $\mathbf{K}$.

The angles of rotation in $\mathbf{K}$ (and in a general rotation $\mathbf{o}$) are not restricted to be real. They may be pure imaginary, or even complex numbers. In the next section it will be seen that the matrix $\mathbf{V}$ represents a rotation with pure imaginary angles. We may then write $\theta=i\gamma$ and obtain $\cosh\gamma$, $-i\sinh\gamma$ instead of $\cos\theta$, $\sin\theta$.

$\mathbf{S}(\mathbf{K})$ has a particularly simple form in the case that $\Gamma_k=\mathbf{P}_r^*$, $\Gamma_l=\mathbf{Q}_r^*$ (with the notation of (15)). We have then:

$$\begin{aligned}&\mathbf{S}(\mathbf{K})=\exp\{\theta/2\cdot\mathbf{P}_r^*\mathbf{Q}_r^*\}\\ &=\exp\{-i\theta/2\cdot\mathbf{s}_r\}=\cos\frac{\theta}{2}-i\sin\frac{\theta}{2}\cdot\mathbf{s}_r\\ &=1\times1\times\cdots\times\left(\cos\frac{\theta}{2}-i\sin\frac{\theta}{2}\cdot\mathbf{s}\right)\\ &\qquad\times1\times1\times\cdots\times1\\ &=1\times1\times\cdots\times\begin{pmatrix}e^{-i\theta/2}&0\\0&e^{i\theta/2}\end{pmatrix}\\ &\qquad\times1\times\cdots\times1.\end{aligned} \tag{25}$$

From this we see that the eigenvalues of $\mathbf{S}(\mathbf{K})$ are $e^{i\theta/2}$, $e^{-i\theta/2}$ with a 2^{n-1} fold degeneracy for each value. The rotation $\mathbf{K}$ itself has the eigenvalues: $e^{i\theta}$, $e^{-i\theta}$, and $+1$, the latter being $2(n-1)$-fold degenerate.

Consider now a product of n commuting plane rotations. The $2n$ Γ's are grouped into pairs, and each pair $(\Gamma_{r1}, \Gamma_{r2})$ is rotated by an angle θ_r, as in (22). We have

$$\mathbf{K}=\prod_{r=1}^{n}\mathbf{K}_r, \tag{26}$$

and the eigenvalues of $\mathbf{K}$ are

$$e^{\pm i\theta_1}, e^{\pm i\theta_2}, \cdots, e^{\pm i\theta_n}. \tag{27}$$

Since we know the representative of each factor in $\mathbf{K}$, we also know the representative of the product

$$\mathbf{S}(\mathbf{K})=\prod_{r=1}^{n}\mathbf{S}(\mathbf{K}_r)=\prod_{r=1}^{n}\exp\{\theta_r/2\cdot\Gamma_{r1}\Gamma_{r2}\}. \tag{28}$$

In the special case where $\Gamma_{r1}=\mathbf{P}_r^*$, $\Gamma_{r2}=\mathbf{Q}_r^*$, we have

$$\begin{aligned}&\mathbf{S}(\mathbf{K})=\prod_{r=1}^{n}\exp(\tfrac{1}{2}\theta_r\mathbf{P}_r^*\mathbf{Q}_r^*)\\ &=\begin{pmatrix}\exp[-(i/2)\theta_1]&0\\0&\exp[(i/2)\theta_1]\end{pmatrix}\\ &\times\begin{pmatrix}\exp[-(i/2)\theta_2]&0\\0&\exp[(i/2)\theta_2]\end{pmatrix}\times\cdots\\ &\times\begin{pmatrix}\exp[-(i/2)\theta_n]&0\\0&\exp[(i/2)\theta_1]\end{pmatrix},\end{aligned} \tag{29}$$

with the eigenvalues

$$\lambda=\exp[i/2(\pm\theta_1\pm\theta_2\pm\cdots\pm\theta_n)]. \tag{30}$$

All sign combinations are to be taken, giving the expected 2^n eigenvalues for $\mathbf{S}(\mathbf{K})$. Even for a more general choice of Γ_{r1}, Γ_{r2} we find the same eigenvalues for $\mathbf{S}(\mathbf{o})$. This is so because we can pass from any matrix base $\cdots, \Gamma_{r1}, \Gamma_{r2}, \cdots$ to the base $\cdots, \mathbf{P}_r^*, \mathbf{Q}_r^*, \cdots$ via a transformation in 2^n-space, according to the theorem on p. 1234. But this transformation does not change the eigenvalues of $\mathbf{S}(\mathbf{o})$.

To summarize, if the rotation $\mathbf{o}$ has the eigenvalues

$$e^{i\theta_1}, e^{-i\theta_1}, e^{i\theta_2}, e^{-i\theta_2}, \cdots, e^{i\theta_n}, e^{-i\theta_n},$$

then its spin-representative $\mathbf{S}(\mathbf{o})$ has the eigenvalues

$$\lambda=\exp[i/2(\pm\theta_1\pm\theta_2\pm\cdots\pm\theta_n)],$$

for any choice of axes in 2^n spin space.

Other Representations of the Orthogonal Group

Besides the spin-representation, the orthogonal group also has representations of dimension $\binom{2n}{f}$ $1\leqslant f\leqslant 2n$. These are easily found by considering the transformation of a product of f Γ's under the rotation $\mathbf{o}$. For

example (for $k\neq l$)

$$\mathbf{o}:\Gamma_k\Gamma_l\rightarrow(\sum_{i=1}^{2n} o_{ik}\Gamma_i)(\sum_{j=1}^{2n} o_{jl}\Gamma_j)=\sum_{i,j=1}^{2n} o_{ik}o_{jl}\Gamma_i\Gamma_j$$

$$=\sum_{1\leqslant i\leqslant j\leqslant 2n}(o_{ik}o_{jl}-o_{jk}o_{il})\cdot\Gamma_i\Gamma_j+\sum_{i=j=1}^{2n} o_{ik}o_{il}.$$

But the second sum vanishes, by (18), and so

$$\mathbf{o}:\Gamma_k\Gamma_l\rightarrow\sum_{i<j}\begin{vmatrix} o_{ik} & o_{jk}\\ o_{il} & o_{jl}\end{vmatrix}\Gamma_i\Gamma_j=\mathbf{S}(\mathbf{o})\cdot\Gamma_k\Gamma_l\cdot\mathbf{S}(\mathbf{o})^{-1}. \quad (31)$$

In general, the product $\Gamma_{r1}\cdot\Gamma_{r2}\cdots\Gamma_{rf}$ will be transformed into a linear combination of all products of the same rank. The coefficients in this linear combination will be the corresponding minors in the determinant of $\mathbf{o}$.

Particularly important is the product

$$\mathbf{U}\equiv\Gamma_1\cdot\Gamma_2\cdot\Gamma_3\cdots\Gamma_{2n}. \quad (32)$$

There is only one product of this rank. When the rotation $\mathbf{o}$ is applied to the Γ's, $\mathbf{U}$ is merely multiplied by the determinant of $\mathbf{o}$. Now, $\mathbf{o}$ is orthogonal, so that its determinant is either $+1$ (a proper rotation) or -1 (an improper rotation). Thus

$$\mathbf{o}:\quad \mathbf{U}\rightarrow\pm\mathbf{U}=\mathbf{S}(\mathbf{o})\cdot\mathbf{U}\cdot\mathbf{S}(\mathbf{o})^{-1}. \quad (33)$$

However, transformation by a matrix which is not a spin representative of any rotation will, in general, not leave $\mathbf{U}$ invariant. For example

$$\mathbf{g}\cdot\mathbf{U}\cdot\mathbf{g}\neq\pm\mathbf{U}.$$

3. THE EIGENVALUES AND EIGENVECTORS OF V

Dual Transformation

As was mentioned above, $\mathbf{V}_2$ is a transform of $\mathbf{V}_1$ through the rotation which sends $\mathbf{P}_r\rightarrow\mathbf{P}_{r+1}$, $\mathbf{Q}_r\rightarrow\mathbf{Q}_r$. This similarity between $\mathbf{V}_1$ and $\mathbf{V}_2$ was recognized by Onsager, who made use of a somewhat different transformation,[1] $\mathbf{D}$: $\mathbf{P}_r\rightarrow\mathbf{Q}_r$, $\mathbf{Q}_r\rightarrow\mathbf{P}_{r+1}$. As a result,

$$\mathbf{D}:\quad i\mathbf{P}_r\mathbf{Q}_r\rightarrow i\mathbf{Q}_r\mathbf{P}_{r+1}=-i\mathbf{P}_{r+1}\mathbf{Q}_r,$$
$$-i\mathbf{P}_{r+1}\mathbf{Q}_r\rightarrow -i\mathbf{Q}_{r+1}\mathbf{P}_{r+1}=i\mathbf{P}_{r+1}\mathbf{Q}_{r+1},$$

or, in the notation of I:

$$\mathbf{C}_r\rightarrow\mathbf{s}_r\mathbf{s}_{r+1},\quad \mathbf{s}_r\mathbf{s}_{r+1}\rightarrow\mathbf{C}_{r+1}.$$

Thus transformation by $\mathbf{D}$ interchanges $\mathbf{V}_1$ and $\mathbf{V}_2$. This provides the algebraic reason for the "dual transformation" found by Kramers and Wannier:[2] if $\mathbf{V}_1=\mathbf{V}_1(H^*)$ and $\mathbf{V}_2=\mathbf{V}_2(H')$, one has

$$\mathbf{D}:\quad \mathbf{V}_1(H^*)\cdot\mathbf{V}_2(H')\rightarrow\mathbf{V}_2(H^*)\cdot\mathbf{V}_1(H').$$

To each lattice there corresponds a "dual" lattice, in which the roles of H^* and H' are interchanged, and the partition function for the lattice described by $\mathbf{V}(H, H')$ is the same as the partition function of the dual lattice, with $\mathbf{V}(H'^*, H^*)$—except for a factor $(\sinh 2H\cdot\sinh 2H')^{-mn/2}$.

This fact enabled Kramers and Wannier to locate the critical temperature. In their model $H'\equiv H$, and the critical point occurs at the temperature where the equality $H=H^*$ is satisfied. In our model the critical point is at $H=H'^*$, or, in other words, at the temperature where

$$\sinh 2H\cdot\sinh 2H'=1.$$

Procedure for Diagonalizing V

The similarity between $\mathbf{V}_1$ and $\mathbf{V}_2$ may be utilized in order to decompose $\mathbf{V}$ into a direct product of simple components. It is possible to show that the transformation $(\mathbf{P}_r\rightarrow\mathbf{P}_{r+1},\ \mathbf{Q}_r\rightarrow\mathbf{Q}_r)$, which sends $\mathbf{V}_1$ into $\mathbf{V}_2$, can be written, in 2^n-space, as a direct product of two-dimensional matrices. And since $\mathbf{V}_1$ is also such a direct product (although $\mathbf{V}_2$ is not), the eigenvalue problem is reduced to the solution of n quadratic equations.

However, a much more direct approach is based on the fact that $\mathbf{V}_1$ and $\mathbf{V}_2$ are themselves spin representatives of certain rotations in $2n$-space, say $\mathbf{R}_1$ and $\mathbf{R}_2$. $\mathbf{V}$ is then a representative of $\mathbf{R}_1\cdot\mathbf{R}_2$, and its eigenvalues are known as soon as we know the eigenvalues of the $2n$-dimensional matrix $\mathbf{R}_1\cdot\mathbf{R}_2$. Now, the similarity between $\mathbf{V}_1$ and $\mathbf{V}_2$ implies that there is a similarity between $\mathbf{R}_1$ and $\mathbf{R}_2$; and, indeed, we will see that $\mathbf{R}_2$ is obtained from $\mathbf{R}_1$ by a permutation of rows and columns. As a result, it is quite an easy matter to find the eigenvalues of $\mathbf{R}_1\cdot\mathbf{R}_2$.

One preparatory step has to be taken: From (28) it follows that

$$\mathbf{V}_1=\sum_{r=1}^{n}\exp(iH^*\cdot\mathbf{P}_r\mathbf{Q}_r)$$

is the representative of a rotation with $\frac{1}{2}\theta_r=iH^*$, $1\leqslant r\leqslant n$. Similarly in $\mathbf{V}_2$, all factors except the last are representatives of plane rotations: $\exp(-iH'\cdot\mathbf{P}_{r+1}\mathbf{Q}_r)$. In order to bring this last "boundary" factor into line with the others, we note that

$$\begin{aligned}(1+\mathbf{U})\cdot i\mathbf{U}\cdot\mathbf{P}_1\mathbf{Q}_n&=(1+\mathbf{U})\cdot i\mathbf{P}_1\mathbf{Q}_n,\\ (1-\mathbf{U})\cdot i\mathbf{U}\cdot\mathbf{P}_1\mathbf{Q}_n&=-(1-\mathbf{U})\cdot i\mathbf{P}_1\mathbf{Q}_n.\end{aligned} \quad (34)$$

We can therefore write[12]

$$\mathbf{V}=\tfrac{1}{2}(1+\mathbf{U})\cdot\mathbf{V}+\tfrac{1}{2}(1-\mathbf{U})\cdot\mathbf{V}$$

$$=\tfrac{1}{2}(1+\mathbf{U})\cdot\{\prod_{r=1}^{n}\exp(iH^*\mathbf{P}_r\mathbf{Q}_r)$$

$$\cdot\prod_{r=1}^{n-1}\exp(-iH'P_{r+1}\mathbf{Q}_r)\cdot\exp(iH'\mathbf{P}_1\mathbf{Q}_n)\}$$

$$+\tfrac{1}{2}(1-\mathbf{U})\cdot\{\prod_{r=1}^{n}\exp(iH^*\mathbf{P}_r\mathbf{Q}_r)$$

$$\cdot\prod_{r=1}^{n}\exp(-iH'\mathbf{P}_{r+1}\mathbf{Q}_r)\}$$

$$\equiv\tfrac{1}{2}(1+\mathbf{U})\cdot\mathbf{V}^{+}+\tfrac{1}{2}(1-\mathbf{U})\cdot\mathbf{V}^{-}. \quad (35)$$

[12] As noted in footnote 9, $\mathbf{U}$ is identical with the operator $\mathbf{C}$ in I, and fulfills the same function of splitting the space into two disjoint subspaces. Kramers and Wannier operate only in the subspace of the projection $\frac{1}{2}(1+\mathbf{U})$.

It is seen that not $\mathbf{V}$ itself, but $\mathbf{V}^+$ and $\mathbf{V}^-$ are representatives of rotations in $2n$-space.

Selection of the Eigenvalues in the Two Subspaces

To indicate that $\mathbf{V}^+$ and $\mathbf{V}^-$ are spin-representatives, we write $\mathbf{V}^+=\mathbf{S}(\mathbf{R}^+)$ and $\mathbf{V}^-=\mathbf{S}(\mathbf{R}^-)$. We will proceed to find the eigenvalues of each of these separately, and will take into account the effect of the factors $\frac{1}{2}(1+\mathbf{U})$, $\frac{1}{2}(1-\mathbf{U})$ by selecting half of the eigenvalues of $\mathbf{V}^+$ and half of those of $\mathbf{V}^-$. The two half-sets together will then constitute the full set of eigenvalues of $\mathbf{V}$. The justification for this procedure may perhaps be best seen in a different coordinate system from the one in which we have been working. Suppose that we change from our original coordinate system by transforming with the matrix

$$\mathbf{g}=2^{n/2}\cdot(\mathbf{C}+\mathbf{s})\times(\mathbf{C}+\mathbf{s})\times\cdots\times(\mathbf{C}+\mathbf{s}). \tag{16}$$

This interchanges $\mathbf{s}$ and $\mathbf{C}$ in all operators. Then (in the notation of (4))

$$\mathbf{B}\rightarrow\sum_1^n \mathbf{s}_r={}^t\mathbf{B},\quad \mathbf{A}\rightarrow\sum_1^n \mathbf{C}_r\mathbf{C}_{r+1}={}^t\mathbf{A},$$
$$\mathbf{U}\rightarrow\mathbf{s}\times\mathbf{s}\times\cdots\times\mathbf{s}={}^t\mathbf{U}. \tag{36}$$

${}^t\mathbf{U}$ is a diagonal matrix in which only $+1$ and -1 appear along the diagonal. Imagine that we rearrange the order of the base vectors of our new coordinate system in such a way that first come all the $+1$ members of ${}^t\mathbf{U}$ and then all the -1's. Then ${}^t\mathbf{U}$ is merely a unit matrix in a subspace (a half) of the 2^n-dimensional space, and it is the negative of a unit matrix in the other half. ${}^t\mathbf{U}$ commutes with ${}^t\mathbf{A}$:

$$(\mathbf{s}\times\mathbf{s}\times\cdots\times\mathbf{s})\cdot(\sum_1^n \mathbf{C}_r\mathbf{C}_{r+1})$$
$$=(\sum_1^n \mathbf{C}_r\mathbf{C}_{r+1})\cdot(\mathbf{s}\times\mathbf{s}\times\cdots\times\mathbf{s}).$$

And, of course, it commutes with ${}^t\mathbf{B}$; it therefore commutes with ${}^t\mathbf{V}$. (In general, ${}^t\mathbf{U}$ commutes with any operator which is a product of an even number of $\mathbf{\Gamma}_k$; it anticommutes with products of an odd number of $\mathbf{\Gamma}_k$.) However, if any matrix $\mathbf{X}$ commutes with ${}^t\mathbf{U}$, it must be of the form

$$\mathbf{X}=\begin{pmatrix}\times & 0\\ 0 & \times\end{pmatrix}.$$

Thus ${}^t\mathbf{V}$ is of this form too. On the other hand, if $\mathbf{Y}$ anticommutes with ${}^t\mathbf{U}$, it has the form

$$\mathbf{Y}=\begin{pmatrix}0 & \times\\ \times & 0\end{pmatrix}.$$

$\frac{1}{2}(1+{}^t\mathbf{U})$ is a projection of the unit matrix on one of the halves of our total space. $\frac{1}{2}(1-{}^t\mathbf{U})$ is the complementary projection; that is:

$$\tfrac{1}{2}(1+{}^t\mathbf{U})+\tfrac{1}{2}(1-{}^t\mathbf{U})=1,\quad \tfrac{1}{2}(1+{}^t\mathbf{U})\cdot\tfrac{1}{2}(1-{}^t\mathbf{U})=0.$$

Also:

$$[\tfrac{1}{2}(1+{}^t\mathbf{U})]^2=\tfrac{1}{2}(1+{}^t\mathbf{U});$$

similarly for $\frac{1}{2}(1-{}^t\mathbf{U})$. As a result,

$$\tfrac{1}{2}(1+{}^t\mathbf{U})\cdot{}^t\mathbf{V}=\tfrac{1}{2}(1+{}^t\mathbf{U})\cdot{}^t\mathbf{V}\cdot\tfrac{1}{2}(1+{}^t\mathbf{U})$$
$$=\tfrac{1}{2}(1+{}^t\mathbf{U})\cdot{}^t\mathbf{V}^+\cdot\tfrac{1}{2}(1+{}^t\mathbf{U})$$

is the upper square of ${}^t\mathbf{V}$ (also of ${}^t\mathbf{V}^+$), whereas $\frac{1}{2}(1-{}^t\mathbf{U})\cdot{}^t\mathbf{V}$ is the lower square of ${}^t\mathbf{V}$ (or ${}^t\mathbf{V}^-$):

$${}^t\mathbf{V}=\begin{pmatrix}\times & 0\\ 0 & \times\end{pmatrix}\equiv\begin{pmatrix}\times & 0\\ 0 & 0\end{pmatrix}+\begin{pmatrix}0 & 0\\ 0 & \times\end{pmatrix}.$$

Now, we may diagonalize the upper and lower squares of ${}^t\mathbf{V}$ independently of each other. That is to say, we apply a transformation to $\frac{1}{2}(1+{}^t\mathbf{U})\cdot{}^t\mathbf{V}^+$ which brings it into diagonal form, and another transformation—to diagonalize $\frac{1}{2}(1-{}^t\mathbf{U})\cdot{}^t\mathbf{V}^-$.

It will be seen below, when the actual transformations are constructed, that both of these will be representatives of orthogonal rotations. But while the rotation $\mathbf{T}^+$ involved in diagonalizing $\mathbf{V}^+$ is a proper rotation, the other one, $\mathbf{T}^-$, is improper. As we have seen (Eq. (33)), this means that

$$\mathbf{T}^+\colon {}^t\mathbf{U}\rightarrow+{}^t\mathbf{U},\quad \mathbf{T}^-\colon {}^t\mathbf{U}\rightarrow-{}^t\mathbf{U}.$$

Therefore

$$\mathbf{S}(\mathbf{T}^+)\cdot\{\tfrac{1}{2}(1+{}^t\mathbf{U})\cdot{}^t\mathbf{V}^+\}\cdot\mathbf{S}(\mathbf{T}^+)^{-1}$$
$$=\tfrac{1}{2}(1+{}^t\mathbf{U})\cdot\mathbf{S}(\mathbf{T}^+)\cdot({}^t\mathbf{V}^+)\cdot\mathbf{S}(\mathbf{T}^+)^{-1}$$
$$=\tfrac{1}{2}(1+{}^t\mathbf{U})\cdot\mathbf{S}[(\mathbf{T}^+)\cdot(\mathbf{R}^+)\cdot(\mathbf{T}^+)^{-1}];$$

but

$$\mathbf{S}(\mathbf{T}^-)\cdot\{\tfrac{1}{2}(1-{}^t\mathbf{U})\cdot{}^t\mathbf{V}^-\}\cdot\mathbf{S}(\mathbf{T}^-)^{-1}$$
$$=\tfrac{1}{2}(1+{}^t\mathbf{U})\cdot\mathbf{S}(\mathbf{T}^-)\cdot({}^t\mathbf{V}^-)\cdot\mathbf{S}(\mathbf{T}^-)^{-1}$$
$$=\tfrac{1}{2}(1+{}^t\mathbf{U})\cdot\mathbf{S}[(\mathbf{T}^-)\cdot(\mathbf{R}^-)\cdot(\mathbf{T}^-)^{-1}]. \tag{37}$$

Suppose that we had already found the $2n$-eigenvalues of $\mathbf{R}^-$, and we denoted them by $\exp(\pm\gamma_{2r})$, $1\leqslant r\leqslant n$. By (29) this means that

$$\mathbf{S}(\mathbf{T}^-)\cdot({}^t\mathbf{V}^-)\cdot\mathbf{S}(\mathbf{T}^-)^{-1}=\mathbf{S}(\mathbf{K})$$
$$=\prod_{r=1}^n \exp\left(\frac{i}{2}\gamma_{2r}\mathbf{P}_r{}^*\mathbf{Q}_r{}^*\right)\equiv\mathbf{\Lambda}^-.$$

This is a diagonal matrix with components (eigenvalues):

$$\exp[\tfrac{1}{2}(\pm\gamma_2\pm\gamma_4\pm\cdots\pm\gamma_{2n})].$$

The particular combination of plus and minus signs appearing in each eigenvalue depends on the value of the components of $(\mathbf{P}_r{}^*\mathbf{Q}_r{}^*)$. Now, the factor $\frac{1}{2}(1+{}^t\mathbf{U})$ eliminates half of these eigenvalues, keeping only those which fall into the upper square. In that square

$${}^t\mathbf{U}_{ii}=+1=\prod_{r=1}^n(\mathbf{P}_r{}^*\mathbf{Q}_r{}^*)_{ii}.$$

On the other hand $(\mathbf{P}_r{}^*\mathbf{Q}_r{}^*)_{ii}$ may be either $+1$ or -1 for any $1 \geqslant r \geqslant n$. In order to maintain ${}^\dagger\mathbf{U}_{ii}$ equal to $+1$, only an *even* number of factors $(\mathbf{P}_r{}^*\mathbf{Q}_r{}^*)_{ii}$ may equal -1. That is to say, only those eigenvalues remain in which an *even* number of angles appear with a minus sign.

The same considerations apply to ${}^\dagger\mathbf{V}^+$. Let the eigenvalues of $\mathbf{R}^+$ be denoted by $\exp(\pm\gamma_{2r-1})$ $(1 \leqslant r \leqslant n)$. Then the eigenvalues of $\mathbf{V}^+$ are $\exp[\frac{1}{2}(\pm\gamma_1 \pm \gamma_3 \pm \cdots \pm \gamma_{2n-1})]$. But from (37), only those eigenvalues occur which fall into the subspace $\frac{1}{2}(1+{}^\dagger\mathbf{U})$. So that again we must take only such sign combinations in the eigenvalues in which an even number of angles appear with minus signs.

To summarize: Half of the 2^n eigenvalues of $\mathbf{V}$ are of the form $\exp[\frac{1}{2}(\pm\gamma_2 \pm \gamma_4 \pm \cdots \pm \gamma_{2n})]$; the other half are of the form $\exp[\frac{1}{2}(\pm\gamma_1 \pm \gamma_3 \pm \cdots \pm \gamma_{2n-1})]$. In each eigenvalue an *even* number of minus signs appears in the exponent. The γ_{2r} are the angles of rotation in $\mathbf{R}^-$, the γ_{2r-1}—those of $\mathbf{R}^+$, and they are found by diagonalizing the respective $2n$-dimensional matrices.

Inasmuch as diagonalization of $\mathbf{R}^-$ and $\mathbf{R}^+$ does not uniquely determine the order of their eigenvalues, the question might arise whether or not the selection of eigenvalues in the subspaces $\frac{1}{2}(1+{}^\dagger\mathbf{U})$ and $\frac{1}{2}(1-{}^\dagger\mathbf{U})$ is unambiguous. And indeed, in the equation $(\mathbf{T}^+)\cdot(\mathbf{R}^+)\cdot(\mathbf{T}^+)^{-1}=\mathbf{K}$, one may replace $\mathbf{T}^+$ by the transformation $\mathbf{P}\cdot\mathbf{T}^+$, where $\mathbf{P}$ is any permutation, which interchanges the order of eigenvalues in $\mathbf{K}$, provided it leaves $\mathbf{K}$ in canonical form (i.e., $\mathbf{P}$ may interchange the pair $\gamma_r, -\gamma_r$ with the pair $\gamma_s, -\gamma_s$, or it may interchange γ_r with $-\gamma_r$).

However, if $\mathbf{P}$ is an odd permutation (i.e., $|\mathbf{P}| = -1$), we have $\mathbf{PT}$: ${}^\dagger\mathbf{U} \rightarrow -{}^\dagger\mathbf{U}$, since $\mathbf{T}^+$ was a proper rotation. Then:

$$\mathbf{S}(\mathbf{PT}^+)\cdot\{\tfrac{1}{2}(1+{}^\dagger\mathbf{U})\cdot{}^\dagger\mathbf{V}^+\}^*\cdot\mathbf{S}(\mathbf{PT}^+)^{-1} = \tfrac{1}{2}(1-{}^\dagger\mathbf{U})\cdot\mathbf{S}[(\mathbf{PT}^+)\cdot(\mathbf{R}^+)\cdot(\mathbf{PT}^+)^{-1}],$$

so that we must take those eigenvalues which fall into the subspace $\frac{1}{2}(1-{}^\dagger\mathbf{U})$. There is nevertheless no difference between the set of eigenvalues selected by $\frac{1}{2}(1+{}^\dagger\mathbf{U})$ out of $\mathbf{S}[(\mathbf{T}^+)\cdot(\mathbf{R}^+)\cdot(\mathbf{T}^+)^{-1}]$ and the set selected by $\frac{1}{2}(1-{}^\dagger\mathbf{U})$ out of $\mathbf{S}[(\mathbf{PT}^+)\cdot(\mathbf{R}^+)\cdot(\mathbf{PT}^+)^{-1}]$.

This is so, because the odd $\mathbf{P}$, which is an improper rotation, will interchange an *odd* number of γ_r with $-\gamma_r$; but this interchange is counteracted by the selection operator $\frac{1}{2}(1-{}^\dagger\mathbf{U})$, which keeps only those sign combinations which have an *odd* number of minus signs,

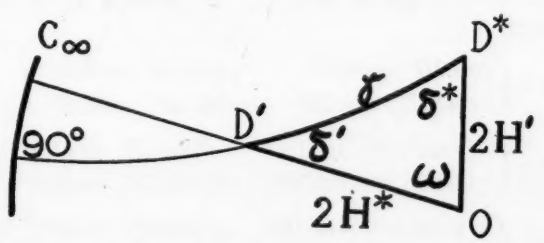

FIG. 2. Hyperbolic triangle. Stereographic projection, conformal. (Circles are represented by circles, geodetics by circles invariant toward inversion in the limiting circle C_∞ of the projection.)

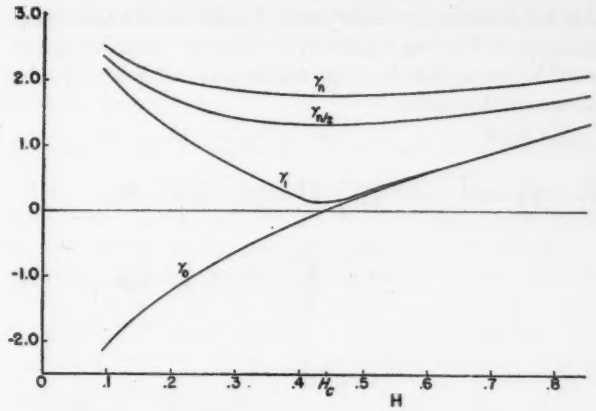

FIG. 3. Dependence of the angles γ_r on temperature. For $H<H_c$ (high temperatures) $\gamma_1 \sim -\gamma_0$. For $H>H_c$ (low temperatures) $\gamma_1 \sim +\gamma_0$.

so that finally we get again our old angles with an *even* number of minus signs. If $\mathbf{P}$ were a proper rotation, it would interchange an even number of γ_r with $-\gamma_r$, and would remain in the subspace $\frac{1}{2}(1+{}^\dagger\mathbf{U})$, so that once more we have our old angles with an *even* number of minus signs.

Thus we see that any choice of transformation, $\mathbf{PT}^+$, will give the same selection of eigenvalues, provided we take the appropriate subspace to go with $\mathbf{PT}^+$. Similar considerations apply of course to $\mathbf{V}^- = \mathbf{S}(\mathbf{R}^-)$.

The Complete Partition Function

The complete partition function for the lattice can now be formally written down:

$$Z=(2\sinh 2H)^{mn/2}\cdot\sum_{i=1}^{2^n}\lambda_i{}^m=(2\sinh 2H)^{mn/2}\cdot\{\sum\exp[m/2(\pm\gamma_2\pm\gamma_4\pm\cdots)]+\sum\exp[m/2(\pm\gamma_1\pm\gamma_3\pm\cdots)]\}. \quad (38)$$

The summations are performed over the permitted sign combinations. A more compact form is:

$$Z=\tfrac{1}{2}(2\sinh 2H)^{mn/2}\cdot\left\{\prod_{r=1}^{n}\left(2\cosh\frac{m}{2}\gamma_{2r}\right)+\prod_{r=1}^{n}\left(2\sinh\frac{m}{2}\gamma_{2r}\right)+\prod_{r=1}^{n}\left(2\cosh\frac{m}{2}\gamma_{2r-1}\right)+\prod_{r=1}^{n}\left(2\sinh\frac{m}{2}\gamma_{2r-1}\right)\right\}. \quad (39)$$

The Rotation Represented by $\mathbf{V}^-$, its Eigenvalues and Eigenvectors

We now proceed to determine explicitly the eigenvalues and eigenvectors of $\mathbf{V}^+$ and $\mathbf{V}^-$. $\mathbf{V}^-$ is the easier one to handle from the point of view of notation, and we will treat it first. It is convenient to deal with the symmetrical operator

$$\mathbf{V}_0 \equiv \mathbf{V}_1{}^{\frac{1}{2}}\cdot\mathbf{V}_2\cdot\mathbf{V}_1{}^{\frac{1}{2}}=\mathbf{V}_1{}^{-\frac{1}{2}}\cdot\mathbf{V}\cdot\mathbf{V}_1{}^{\frac{1}{2}}.$$

We will find the eigenvectors of $\mathbf{V}_0$ and obtain the eigenvectors of $\mathbf{V}$ from these by a further transformation with $\mathbf{V}_1^{\frac{1}{2}}=\exp(\frac{1}{2}H'\mathbf{A})$. The eigenvalues of $\mathbf{V}$ and $\mathbf{V}_0$ are of course the same.

We have

$$\mathbf{V}_0^-\equiv\prod_{r=1}^{n}\exp\left(\frac{i}{2}H^*\mathbf{P}_r\mathbf{Q}_r\right)\cdot\prod_{r=1}^{n}\exp(-iH'\mathbf{P}_{r+1}\mathbf{Q}_r)\cdot\prod_{r=1}^{n}\exp\left(\frac{i}{2}H^*\mathbf{P}_r\mathbf{Q}_r\right)\equiv\mathbf{S}(\mathbf{R}_0^-). \quad (41)$$

$$\begin{pmatrix}\cosh 2H' & & & & \\ & \cosh 2H' & i\sinh 2H' & & \\ & -i\sinh 2H' & \cosh 2H' & & \\ & & & & \\ i\sinh 2H' & & & & \end{pmatrix}$$

Each of these $2n$-dimensional matrices is "cyclic" in two-row strips. Their product, $\mathbf{R}_0^-$, is therefore also cyclic. Cyclic matrices have very convenient properties which permit the determination of eigenvalues and eigenvectors without much difficulty. More complicated matrices than $\mathbf{R}^-$ (corresponding to different physical models) can also be handled in the same way.

We start with the simple n-dimensional cyclic matrix

$$\alpha=\begin{pmatrix}a & b & c & d & \cdots & & g & h\\ h & a & b & c & \cdots & & & g\\ g & h & a & b & \cdots & & & \\ \cdots & \cdots & \cdots & \cdots & \cdots & \cdots & \cdots & \cdots\\ b & c & d & \cdots & & & & a\end{pmatrix}, \quad (44)$$

where a, b, c, $\cdots h$ are any n scalar numbers. The normalized eigenvectors of this matrix are

$$1/(n)^{\frac{1}{2}}\begin{pmatrix}\epsilon^{2r}\\ \epsilon^{4r}\\ \cdot\\ \cdot\\ \cdot\\ \epsilon^{2(n-1)r}\\ 1\end{pmatrix}, \quad \text{where} \quad \epsilon\equiv e^{i(\pi/n)}, \quad 1\leqslant r\leqslant n. \quad (45)$$

The corresponding eigenvalues are

$$a+\epsilon^{2r}\cdot b+\epsilon^{4r}\cdot c+\cdots+\epsilon^{2(n-1)r}\cdot h. \quad (46)$$

This can be verified by construction.

In the general case, the members of α may themselves be matrices, say of dimension f. α is now $n\cdot f$-dimensional. Its eigenvectors will be of the form

$$\begin{pmatrix}\epsilon^{2r}\cdot\mathbf{W}_{2r}\\ \epsilon^{4r}\cdot\mathbf{W}_{2r}\\ \cdot\\ \cdot\\ \cdot\\ \epsilon^{2nr}\cdot\mathbf{W}_{2r}\end{pmatrix}, \quad (47)$$

where $\mathbf{W}_{2r}$ is an eigenvector of the f-dimensional matrix

$$\alpha_{2r}=\mathbf{a}+\epsilon^{2r}\cdot\mathbf{b}+\epsilon^{4r}\cdot\mathbf{c}+\cdots+\epsilon^{2(n-1)r}\cdot\mathbf{h}. \quad (48)$$

If λ_{2r} is an eigenvalue of α_{2r} then it is also an eigenvalue of α. Thus the eigenvalue problem for the matrix α is only f-dimensional, instead of being $n\cdot f$-dimensional.

In applying the above to our matrix $\mathbf{R}_0^-$, we see that $f=2$. Upon multiplying the three factors of the rotation $\mathbf{R}_0^-$ (see (42), (43)), we find that $\mathbf{R}_0^-$ can be written schematically as

$$\mathbf{R}_0^-=\begin{pmatrix}\mathbf{a} & \mathbf{b} & 0 & 0 & \cdots & & 0 & 0 & \mathbf{b}^*\\ \mathbf{b}^* & \mathbf{a} & \mathbf{b} & 0 & 0 & \cdots & 0 & 0 & 0\\ 0 & \mathbf{b}^* & \mathbf{a} & \mathbf{b} & 0 & \cdots & & & \\ \cdots & \cdots & \cdots & \cdots & \cdots & \cdots & & & \\ \mathbf{b} & 0 & \cdots & & & & 0 & \mathbf{b}^* & \mathbf{a}\end{pmatrix},$$

where

$$\mathbf{a}=\begin{pmatrix}\cosh 2H'\cdot\cosh 2H^* & -i\cosh 2H'\cdot\sinh 2H^*\\ i\cosh 2H'\cdot\sinh 2H^* & \cosh 2H'\cdot\cosh 2H^*\end{pmatrix},$$

$$\mathbf{b}=\begin{pmatrix}-\frac{1}{2}\sinh 2H'\cdot\sinh 2H^* & i\sinh 2H'\cdot\sinh^2 H^*\\ -i\sinh 2H'\cdot\cosh^2 H^* & -\frac{1}{2}\sinh 2H'\cdot\sinh 2H^*\end{pmatrix},$$

$$\mathbf{b}^*=\begin{pmatrix}-\frac{1}{2}\sinh 2H'\cdot\sinh 2H^* & i\sinh 2H'\cdot\cosh^2 H^*\\ -i\sinh 2H'\cdot\sinh^2 H^* & -\frac{1}{2}\sinh 2H'\cdot\sinh 2H^*\end{pmatrix}.$$

The $2n$-eigenvalues of $\mathbf{R}_0^-$ are the eigenvalues of the

The first (and last) product represents the rotation:

$$\begin{pmatrix}\cosh H^* & i\sinh H^* & & & \\ -i\sinh H^* & \cosh H^* & & & \\ & & \cosh H^* & i\sinh H^* & \\ & & -i\sinh H^* & \cosh H^* & \\ & & & & \cdot\\ & & & & \cdot\\ & & & & \cdot\end{pmatrix}. \quad (42)$$

The middle product represents the rotation:

$$\begin{pmatrix} & & & & -i\sinh 2H'\\ & & & & \\ \cosh 2H' & i\sinh 2H' & & & \\ -i\sinh 2H' & \cosh 2H' & & & \\ & & \cdot & & \\ & & & \cdot & \\ & & & \cdot & \\ & & & & \cosh 2H'\end{pmatrix}. \quad (43)$$

n 2-dimensional matrices

$$\alpha_{2r}=\mathbf{a}+\epsilon^{2r}\cdot\mathbf{b}+\epsilon^{2(n-1)r}\cdot\mathbf{b}^*. \tag{50}$$

The determinant of this matrix is $+1$. Its eigenvalues may therefore be written as $\exp(\pm\gamma_{2r})$, and γ_{2r} is determined by[13]

$$\begin{aligned}\tfrac{1}{2}\,\text{trace}\,(\alpha_{2r})&=\tfrac{1}{2}(e^{\gamma_{2r}}+e^{-\gamma_{2r}})\\&=\cosh\gamma_{2r}=\cosh 2H^*\cdot\cosh 2H'\\&\quad-\sinh 2H^*\cdot\sinh 2H'\cdot\cos(2r\pi/n).\end{aligned} \tag{51}$$

Geometrically, γ_{2r} is the third side of a hyperbolic triangle whose other two sides, $2H'$ and $2H^*$, include the angle $\omega_{2r}=(2r\pi/n)$. Introducing the angle δ_{2r}' (between $2H^*$ and γ_{2r}), we can simplify the matrix α_{2r}. (See Fig. 2.)

We have from the geometry:

$$\begin{aligned}\sinh 2H^*\cdot\cosh 2H'-\cosh 2H^*\cdot\sinh 2H'\cdot\cos\omega&=\sinh\gamma\cdot\cos\delta',\\ \sinh 2H'\cdot\sin\omega&=\sinh\gamma\cdot\sin\delta'.\end{aligned} \tag{52}$$

Thus

$$\begin{aligned}\alpha_{2r}&=\cosh\gamma_{2r}\cdot\begin{pmatrix}1&0\\0&1\end{pmatrix}\\&\quad+\sinh\gamma_{2r}\cdot\begin{pmatrix}0&\sin\delta_{2r}'-i\cos\delta_{2r}'\\ \sin\delta_{2r}'+i\cos\delta_{2r}'&0\end{pmatrix}\\&=\cosh\gamma_{2r}-i\sinh\gamma_{2r}\cdot\begin{pmatrix}0&e^{i\delta_{2r}'}\\-e^{i\delta_{2r}'}&0\end{pmatrix}.\end{aligned}$$

The normalized eigenvectors of α_{2r} are

$$1/(2)^{\frac{1}{2}}\begin{pmatrix}e^{(i/2)\delta_{2r}'}\\ ie^{-(i/2)\delta_{2r}'}\end{pmatrix},\quad 1/(2)^{\frac{1}{2}}\begin{pmatrix}ie^{(i/2)\delta_{2r}'}\\ e^{-(i/2)\delta_{2r}'}\end{pmatrix}, \tag{53}$$

corresponding to the eigenvalues $\exp(\gamma_{2r})$, $\exp(-\gamma_{2r})$. By (47), the $2n$-normalized eigenvectors of $\mathbf{R}_0^-$ are

$$\mathbf{u}_{2r}\equiv 1/(2n)^{\frac{1}{2}}\begin{pmatrix}e^{i(\omega_{2r}+\frac{1}{2}\delta_{2r}')}\\ ie^{i(\omega_{2r}-\frac{1}{2}\delta_{2r}')}\\ e^{i(\omega_{4r}+\frac{1}{2}\delta_{2r}')}\\ ie^{i(\omega_{4r}-\frac{1}{2}\delta_{2r}')}\\ \cdot\\ \cdot\\ \cdot\\ ie^{i(\omega_{2nr}-\frac{1}{2}\delta_{2r}')}\end{pmatrix}$$

and

$$\mathbf{v}_{2r}\equiv 1/(2n)^{\frac{1}{2}}\begin{pmatrix}ie^{i(\omega_{2r}+\frac{1}{2}\delta_{2r}')}\\ e^{i(\omega_{2r}-\frac{1}{2}\delta_{2r}')}\\ ie^{i(\omega_{4r}+\frac{1}{2}\delta_{2r}')}\\ \cdot\\ \cdot\\ \cdot\\ e^{i(\omega_{2nr}-\frac{1}{2}\delta_{2r}')}\end{pmatrix}. \tag{54}$$

Let the matrix of these eigenvectors be denoted by $\mathbf{t}$, so that

$$\mathbf{t}\cdot\mathbf{R}^-\cdot\mathbf{t}^{-1}=\lambda^-, \tag{55}$$

where λ^- is the diagonal form of $\mathbf{R}_0^-$. Neither λ^- nor $\mathbf{t}$ are orthogonal, and so they cannot be represented in spin space. We therefore apply a transformation $\mathbf{I}$ to both sides of (55):

$$(\mathbf{It})\cdot\mathbf{R}^-\cdot(\mathbf{t}^{-1}\mathbf{I}^{-1})\equiv\mathbf{T}\cdot\mathbf{R}^-\cdot\mathbf{T}^{-1}=\mathbf{I}\cdot\lambda^-\cdot\mathbf{I}^{-1}\equiv\mathbf{K}. \tag{56}$$

$\mathbf{I}$ is so chosen that it brings λ^- into its canonical form, and at the same time makes $\mathbf{T}=\mathbf{I}\cdot\mathbf{t}$ orthogonal. The spin-representative of the canonical form $\mathbf{K}$ is given by (28). We shall not need to know the spin-representative of $\mathbf{T}$ explicitly, but we must make sure that $\mathbf{T}$ is orthogonal, so that it possesses a spin-representative.

When this is carried through, we find that the transformation $\mathbf{T}$ is given by

$$\begin{aligned}\mathbf{T}\colon\ \mathbf{P}_a&\rightarrow\sum_{r=1}^{n}\sigma_{ra}\mathbf{P}_r+\sum_{r=1}^{n}\tau_{ra}\mathbf{Q}_r,\\ \mathbf{Q}_a&\rightarrow\sum_{r=1}^{n}\sigma_{ra}'\mathbf{P}_r+\sum_{r=1}^{n}\tau_{ra}'\mathbf{Q}_r,\end{aligned} \tag{57}$$

with

$$\begin{aligned}\sigma_{ra}&=\frac{1}{n^{\frac{1}{2}}}\cos\left(\frac{2ra\pi}{n}+\tfrac{1}{2}\delta_{2r}'\right),\\ \tau_{ra}&=\frac{-1}{n^{\frac{1}{2}}}\sin\left(\frac{2ra\pi}{n}+\tfrac{1}{2}\delta_{2r}'\right),\\ \sigma_{ra}'&=\frac{1}{n^{\frac{1}{2}}}\sin\left(\frac{2ra\pi}{n}-\tfrac{1}{2}\delta_{2r}'\right),\\ \tau_{ra}'&=\frac{-1}{n^{\frac{1}{2}}}\cos\left(\frac{2ra\pi}{n}-\tfrac{1}{2}\delta_{2r}'\right).\end{aligned} \tag{58}$$

$\mathbf{T}$ is now orthogonal,[14] and possesses a spin-representative, so that the equation

$$\mathbf{T}\cdot(\mathbf{R}^-)\cdot\mathbf{T}^{-1}=\mathbf{K} \tag{56}$$

leads to

$$\mathbf{S}(\mathbf{T})\cdot(\mathbf{V}_0^-)\cdot\mathbf{S}(\mathbf{T})^{-1}=\mathbf{S}(\mathbf{K})=\prod_{r=1}^{n}\exp[(i/2)\gamma_r\mathbf{P}_r\mathbf{Q}_r]. \tag{59}$$

Diagonalization of $\mathbf{V}^-$

$\mathbf{S}(\mathbf{K})$ is still not diagonal, because in our coordinate system $i\mathbf{P}_r\mathbf{Q}_r=\mathbf{C}_r$. However, this is as close as we can come to the diagonal form of $\mathbf{V}_0^-$ as long as we make transformations in $2n$-space. In order to diagonalize $\mathbf{S}(\mathbf{K})$ we have to use the transformation

$$\begin{aligned}\mathbf{g}=2^{n/2}\cdot(\mathbf{C}+\mathbf{s})\times(\mathbf{C}+\mathbf{s})\times\cdots\times(\mathbf{C}+\mathbf{s})=\mathbf{g}^{-1},\\ \mathbf{g}\mathbf{C}_r\mathbf{g}=\mathbf{s}_r,\end{aligned}$$

which is not the spin-representative of any rotation. Then we find

$$\mathbf{g}\cdot\mathbf{S}(\mathbf{T})\cdot(\mathbf{V}_0^-)\cdot\mathbf{S}(\mathbf{T})^{-1}\cdot\mathbf{g}=\mathbf{g}\cdot\mathbf{S}(\mathbf{K})\cdot\mathbf{g}=\mathbf{A}^-. \tag{60}$$

[13] These are the γ_r given in I, Eq. (89). Figure 2 is the same as Fig. 4 of I.

[14] The determinant of $\mathbf{T}$ is -1, so that it is an improper rotation.

Since $\mathbf{V}_0=\mathbf{V}_1^{-\frac{1}{2}}\cdot\mathbf{V}^-\cdot\mathbf{V}_1^{\frac{1}{2}}\equiv\mathbf{S}(\mathbf{H})\cdot(\mathbf{V}^-)\cdot\mathbf{S}(\mathbf{H})^{-1}$, we have

$$\mathbf{g}\cdot\mathbf{S}(\mathbf{TH})\cdot(\mathbf{V}^-)\cdot\mathbf{S}(\mathbf{TH})^{-1}\cdot\mathbf{g}\equiv\mathbf{\Psi}_-\cdot(\mathbf{V}^-)\cdot\mathbf{\Psi}_-^{-1}=\mathbf{\Lambda}^-, \quad (61)$$

with

$$\mathbf{\Psi}_-=\mathbf{g}\cdot\mathbf{S}(\mathbf{TH}). \quad (62)$$

Here $\mathbf{H}$ stands for the rotation represented by $\mathbf{V}_1^{-\frac{1}{2}}$ (the reciprocal of the rotation in (42)):

$$\mathbf{H}: \quad \begin{aligned}\mathbf{P}_r&\rightarrow\cosh H^*\cdot\mathbf{P}_r-i\sinh H^*\cdot\mathbf{Q}_r,\\ \mathbf{Q}_r&\rightarrow i\sinh H^*\cdot\mathbf{P}_r+\cosh H^*\cdot\mathbf{Q}_r.\end{aligned} \quad (63)$$

Although the rotations involved in $\mathbf{\Psi}_-$ are completely known, it is nevertheless not feasible to write down explicitly the components of $\mathbf{\Psi}_-$ because of the complexity of $\mathbf{S}(\mathbf{T})$.

On the other hand, we can, without much difficulty, evaluate quantities of the form $\{\mathbf{\Psi}_-\cdot\mathbf{X}\cdot\mathbf{\Psi}_-^{-1}\}_{11}$ which will be seen in Section III to have important physical significance.

Analogous Results for $\mathbf{V}^+$

We still have to find the eigenvalues and eigenvectors of

$$\mathbf{V}^+=\prod_{r=1}^{n}\exp(iH^*\mathbf{P}_r\mathbf{Q}_r)\cdot\prod_{r=1}^{n-1}\exp(-iH'\mathbf{P}_{r+1}\mathbf{Q}_r)\cdot\exp(iH'\cdot\mathbf{P}_1\mathbf{Q}_n)=\mathbf{S}(\mathbf{R}^+). \quad (64)$$

$\mathbf{R}^+$ is identical with $\mathbf{R}^-$ except for a few sign changes. Schematically $\mathbf{R}_0^+$ is of the form

$$\begin{pmatrix}\mathbf{a}&\mathbf{b}&0&0&\cdot&\cdot&\cdot&0&-\mathbf{b}^*\\ \mathbf{b}^*&\mathbf{a}&\mathbf{b}&0&0&\cdot&\cdot&&0\\ 0&\mathbf{b}^*&\mathbf{a}&\mathbf{b}&0&\cdot&\cdot&&0\\ \cdot&\cdot&\cdot&\cdot&\cdot&\cdot&\cdot&&0\end{pmatrix}. \quad (65)$$

The eigenvectors are:

$$1/(2n)^{\frac{1}{2}}\begin{pmatrix}\epsilon^{2r-1}\cdot\mathbf{W}_{2r-1}\\ \epsilon^{2(2r-1)}\cdot\mathbf{W}_{2r-1}\\ \cdot\\ \cdot\\ \cdot\\ \epsilon^{n(2r-1)}\cdot\mathbf{W}_{2r-1}\end{pmatrix}, \quad (66)$$

where $\mathbf{W}_{2r-1}$ is an eigenvector of the 2-dimensional matrix

$$\boldsymbol{\alpha}_{2r-1}=\mathbf{a}+\epsilon^{2r-1}\cdot\mathbf{b}-\epsilon^{(n-1)(2r-1)}\cdot\mathbf{b}^*=\mathbf{a}+\epsilon^{2r-1}\cdot\mathbf{b}+\epsilon^{-(2r-1)}\cdot\mathbf{b}^*. \quad (67)$$

The eigenvalues of $\boldsymbol{\alpha}_{2r-1}$ (and of $\mathbf{R}^+$) may be denoted by $\exp(\pm\gamma_{2r-1})$ and

$$\cosh\gamma_{2r-1}=\cosh 2H^*\cdot\cosh 2H'-\sinh 2H^*\cdot\sinh 2H'\cdot\cos((2r-1)\pi/n). \quad (68)$$

Thus, γ_{2r} and γ_{2r-1} are covered by the same formula (as can also be seen from the similarity between $\boldsymbol{\alpha}_{2r}$ and $\boldsymbol{\alpha}_{2r-1}$).

Again, if we introduce the angles δ'_{2r-1}, with the help of which the eigenvectors are expressed, we find just as in the case of $\mathbf{V}^-$

$$\mathbf{\Psi}_+=\mathbf{g}\cdot\mathbf{S}(\mathbf{TH}), \quad (69)$$

where $\mathbf{T}$ now involves the odd-indexed angles δ'_{2r-1} and $\omega_{2r-1}=[(2r-1)\pi/n]$.

4. DISCUSSION OF THE PARTITION FUNCTION

Comparison of the relative magnitudes of the eigenvalues of $\mathbf{V}$ yields important qualitative results about the behavior of the partition function. Since we have

$$Z=\sum_{i=1}^{2^n}\lambda_i^m,$$

we find for very large m

$$Z\sim f\cdot\lambda_{\max}{}^m, \quad (70)$$

where f is the degree of degeneracy of $\lambda_{\max}$.

We have two sets of eigenvalues,

$$\log\lambda^-\equiv\tfrac{1}{2}(\pm\gamma_2\pm\gamma_4\pm\cdots\pm\gamma_{2n}), \quad (71)$$

and

$$\log\lambda^+\equiv\tfrac{1}{2}(\pm\gamma_1\pm\gamma_3\pm\cdots\pm\gamma_{2n-1}), \quad (72)$$

with the permissible sign combinations. The largest eigenvalue in each set is the one in which all signs are positive. The two maximal eigenvalues are, then,

$$\lambda_{\max}{}^+=\exp[\tfrac{1}{2}(\gamma_1+\gamma_3+\cdots+\gamma_{2n-1})], \quad (73)$$

and

$$\lambda_{\max}{}^-=\exp[\tfrac{1}{2}(\gamma_0+\gamma_2+\cdots+\gamma_{2n-2})], \quad (74)$$

(we write γ_0 instead of γ_{2n}).

Since, from its definition, $\gamma_{2r}\sim\gamma_{2r-1}$ for large n, these two eigenvalues are almost equal for low temperatures, up to the critical point. However, γ_0 falls off very rapidly in comparison with γ_1, and, as a result, $(\lambda_{\max})^m$ becomes negligible compared to $(\lambda_{\max}{}^+)^m$, for temperatures higher than the critical point. This can be readily seen in the case of the quadratic crystal, where $J'=J$ or $H'=H$. There we have:

$$\cosh\gamma_r=\cosh 2H^*\cdot\cosh 2H-\sinh 2H^*\cdot\sinh 2H'\cdot\cos(r\pi/n)=\coth 2H\cdot\cosh 2H-\cos(r\pi/n), \quad (75)$$

since from the definition of H^*, $\sinh 2H^*\cdot\sinh 2H=1$. All the γ_r have a minimum at the point $H=H_c$ given by

$$\coth 2H_c\cdot\sinh 2H_c-\frac{\cosh 2H_c}{\sinh^2 2H_c}=0, \quad (76)$$

or

$$\sinh^2 2H_c=1. \quad (77)$$

H must be positive, and therefore $H_c=0.4407\cdots$.

However, γ_0 behaves differently from the other γ_r. From

$$\cosh\gamma_0=\cosh 2H^*\cdot\cosh 2H-\sinh 2H^*\cdot\sinh 2H=\cosh 2(H^*-H), \quad (78)$$

we see that γ_0 changes sign[15] at the critical point $H=H_c$. Figure 3 shows the behavior of γ_r as a function of $H=(J/kT)$. All the γ_r are more or less symmetrical about the critical point, except for γ_0, which changes sign there. This causes λ_{max}^- to fall off very rapidly in comparison with λ_{max}^+ for temperatures above the critical point.

$$\frac{\lambda_{max}^-}{\lambda_{max}^+}=\begin{cases}1 & \text{for } H>H_c,\ T<T_c\\ e^{2(H-H^*)} & \text{for } H<H_c,\ T>T_c.\end{cases} \tag{79}$$

The existence of a degenerate eigenvalue implies long-range order:[5] this occurs for the low temperature range (twofold degeneracy) up to the critical point T_c. For the partition function we have approximately

$$\begin{aligned}&(2\sinh 2H)^{-mn/2}\cdot Z\sim 2\lambda_{max}{}^m\\ &\equiv 2\exp\left[\frac{m}{2}(\gamma_1+\gamma_3+\cdots+\gamma_{2n-1})\right]\\ &\qquad\text{when}\quad H>H_c,\\ &(2\sinh 2H)^{-mn/2}\cdot Z\sim\lambda_{max}{}^m\\ &=\exp\left[\frac{m}{2}(\gamma_1+\gamma_3+\cdots+\gamma_{2n-1})\right]\\ &\qquad\text{when}\quad H<H_c.\end{aligned} \tag{80}$$

The exact partition function, which takes into account all eigenvalues, does not differ much from the approximate result. In the exact solution we have

$$\begin{aligned}Z=&\tfrac{1}{2}(2\sinh 2H)^{mn/2}\\ &\cdot\left\{\prod_{r=1}^{n}\left(2\cosh\frac{m}{2}\gamma_{2r-1}\right)+\prod_{r=1}^{n}\left(2\sinh\frac{m}{2}\gamma_{2r-1}\right)\right.\\ &\left.+\prod_{r=1}^{n}\left(2\cosh\frac{m}{2}\gamma_{2r}\right)+\prod_{r=1}^{n}\left(2\sinh\frac{m}{2}\gamma_{2r}\right)\right\}.\end{aligned} \tag{39}$$

Everywhere, except in the immediate vicinity of the critical point, we may take $\gamma_{2r}=\gamma_{2r-1}$ $(1\leqslant r\leqslant n-1)$ for large enough n, and

$$\gamma_0=\begin{cases}\gamma_1 & \text{for } T<T_c\\ -\gamma_1 & \text{for } T>T_c.\end{cases}$$

Therefore the two products containing $\cosh(m\gamma/2)$ as factors may be taken as equal; while the two products with $\sinh(m\gamma/2)$ are equal below the critical temperature, but cancel each other above $T=T_c$. We have then:

$$\begin{aligned}&(2\sinh 2H)^{-mn/2}\cdot Z\cong\prod_{r=1}^{n}(2\cosh(m/2)\gamma_{2r-1}),\\ &\qquad\text{for}\quad T>T_c,\\ &(2\sinh 2H)^{-mn/2}\cdot Z\\ &\cong\prod_{r=1}^{n}(2\cosh(m/2)\gamma_{2r-1})+\prod_{r=1}^{n}(2\sinh(m/2)\gamma_{2r-1})\\ &=\prod_{r=1}^{n}(2\cosh(m/2)\gamma_{2r-1})\cdot\{1+\prod_{r=1}^{n}(\tanh(m/2)\gamma_{2r-1})\}\\ &\qquad\text{for}\quad T<T_c.\end{aligned} \tag{81}$$

Furthermore, since m is very large,

$$2\cosh(m/2)\gamma_{2r-1}\sim\exp[(m/2)\gamma_{2r-1}],$$

except for temperatures very near T_c ($\cosh x\sim e^x/2$ as soon as $x\sim 5$). Therefore, above the critical temperature

$$\begin{aligned}&(2\sinh 2H)^{-mn}/2\cdot Z\\ &\sim\exp[(m/2)(\gamma_1+\gamma_3+\cdots+\gamma_{2n-1})]\equiv\lambda_{max}{}^m.\end{aligned} \tag{82}$$

Below the critical temperature we find

$$(2\sinh 2H)^{-mn}/2\cdot Z\sim\eta\cdot\lambda_{max}{}^m, \tag{83}$$

where

$$\eta=1+\prod_r(\tanh(m/2)\gamma_{2r-1}).$$

The product of the factors $\tanh(m\gamma/2)$ is never larger than 1, so that $1<\eta<2$; and with large m, $\eta\sim 2$ rather close to T_c. The appearance of η here is equivalent to the twofold degeneracy of λ_{max} for $T<T_c$ in the approximate solution of Z.

The writer is grateful to Professor Lars Onsager for his constant interest and advice in the course of this work.

[15] (75) and (78) do not determine the sign of γ_r. To do this one must actually apply the chosen transformation **T** to **R**. With our choice, and the suitable selection operators (see p. 1239), we find easily that all $\gamma_r>0$, $(r\geqslant 1)$, and $2\gamma_0\equiv H-H^*$.

Crystal Statistics. III. Short-Range Order in a Binary Ising Lattice

BRURIA KAUFMAN
The Institute for Advanced Study, Princeton, New Jersey

AND

LARS ONSAGER
Yale University, New Haven, Connecticut

(Received May 11, 1949)

The degree of order in a binary lattice is described in terms of a family of "correlation" functions. The correlation function for two given lattice sites states what is the probability that the spins of the two sites are the same; this probability is, of course, a function of temperature, as well as of the distance and orientation of the atoms in the pair. It is shown that each correlation function is given by the trace of a corresponding 2^n-dimensional matrix. To evaluate this trace, we make use of the apparatus of spinor analysis, which was employed in a previous paper to evaluate the partition function for the lattice. The trace is found in terms of certain functions of temperature, Σ_a, and these are then calculated with the aid of an elliptic substitution.

Correlations for the five shortest distances (without restriction as to the orientation of the pair within the plane) are plotted as functions of temperature. In addition, the correlation for sites lying within the same row is given to any distance. For the critical temperature this correlation is plotted as a function of distance. It is shown that the correlation tends to zero as the distance increases, that is to say: there is no long-range order at the critical temperature.

1. DEFINITION OF THE DEGREE OF ORDER

THE "degree of order" in a crystal composed of several kinds of atoms is an observable, as is shown by x-ray diffraction studies.[1] Several attempts[2] have been made to interpret the degree of order quantitatively, so that a functional dependence of order upon temperature could be stated. In this paper we use a statistical approach to find the average, taken over all configurations of the crystal, of the correlation between a pair of atoms within the crystal. This correlation will be a function of the temperature, and will depend on the relative position of the atoms in the pair. Since only relative positions enter here, we may keep one of the atoms fixed and consider the family of correlation curves for all pairs in which our fixed atom is a member. This family of curves will describe the degree of order within the crystal.

In order to define, and evaluate, the correlation functions in a formal way, we must rely upon the results of previous papers, I and II;[3] we will make use of the spinor-analysis method introduced in II.

The model we use is, as in the previous papers, a two-dimensional rectangular lattice, with a spin variable $\mu=\pm1$ at each lattice site. It is assumed that only nearest neighbors interact, and that at zero temperature the perfectly ordered crystal has all its spins aligned in one direction (either $\mu=+1$ for all lattice sites, or $\mu=-1$ for all sites). It has been shown[4] that all the information about probabilities of configurations could be presented in a compact way with the help of a matrix $\mathbf{V}$ having 2^n rows and columns, such that for example the partition function for the lattice becomes

$$Z=\sum_{\substack{\text{all}\\ \text{configurations}}}(\text{probability of configuration})$$

$$=\sum_{1,2,\cdots}\mathbf{V}_{\nu_1\nu_2}\mathbf{V}_{\nu_2\nu_3}\cdots\mathbf{V}_{\nu_m\nu_1}=\text{trace}\mathbf{V}^m. \quad \text{(II. 3)}$$

Here ν_i is the configuration of the ith row, that is to say, the specification of the values of μ for all the n atoms in this row ($1\leqslant\nu_i\leqslant2^n$ for all $1\leqslant i\leqslant m$).

Using the matrix $\mathbf{V}$, we can also write the average values of various functions of the configurations of the lattice. Such functions must be weighted in each configuration by the probability of the configuration, and so we find that the average of the function $f_{\nu_1\nu_2}\cdots$ is

$$\bar{f}=\frac{1}{Z}\sum_{\nu_1,\nu_2,\cdots}f_{\nu_1\nu_2}\cdots\mathbf{V}_{\nu_1\nu_2}\mathbf{V}_{\nu_2\nu_3}\cdots\mathbf{V}_{\nu_m\nu_1}. \quad (1)$$

The Correlation Functions

The spin of the jth site in any given row (say row k) is clearly a function of the configuration of the lattice. It depends only on the configuration of its own row, i.e., on ν_k. And it is easy to see that as ν_k goes through its range of values ($1\leqslant\nu_k\leqslant2^n$), the spin under consideration takes on the values $+1$ or -1 in a particular order, which is the order of the diagonal elements in the (diagonal) matrix $\mathbf{s}_j\equiv\mathbf{1}\times\mathbf{1}\times\cdots\times\mathbf{s}\times\mathbf{1}\times\mathbf{1}\cdots$ (n factors). (The notation is as in I:

$$\mathbf{1}\equiv\begin{pmatrix}1&0\\0&1\end{pmatrix},\quad \mathbf{s}\equiv\begin{pmatrix}1&0\\0&-1\end{pmatrix},\quad \mathbf{C}\equiv\begin{pmatrix}0&1\\1&0\end{pmatrix}$$

are the Pauli matrices; $\times$ stands for direct product of

[1] G. C. Nix and W. Shockley, Rev. of Mod. Phys. **10**, 1 (1938).
[2] W. L. Bragg and E. J. Williams, Proc. Roy. Soc. London **145A**, 699 (1934); **151A**, 540 (1935); **152A**, 231 (1935). H. A. Bethe, Proc. Roy. Soc. **150A**, 552 (1935).
[3] L. Onsager, Phys. Rev. **65**, 117 (1943) will be referred to as I. B. Kaufman, Phys. Rev. **76**, 1232 (1949) (preceding paper) will be referred to as II.
[4] H. A. Kramers and G. H. Wannier, Phys. Rev. **60**, 252, 263 (1941); E. N. Lassettre and J. P. Howe, J. Chem. Phys. **9**, 747 (1941).

matrices). As an example, consider the simple case $n=2$. ν_k has $2^2=4$ possibilities: $++$, $+-$, $-+$, $--$. Correspondingly, the spin of the left-hand site is: $+1$, $+1$, -1, -1. But these are the diagonal elements (in that order) of $\mathbf{s}\times\mathbf{1}$. The spin of the right-hand site is: $+1$, -1, $+1$, -1, which can be read off the diagonal of the matrix $\mathbf{1}\times\mathbf{s}$. In general the spin of the jth site in the kth row, when the crystal is in configuration $\{\nu_1, \nu_2, \cdots, \nu_m\}$, is $(\mathbf{s}_j)_{\nu_k\nu_k}$.

We can now find the average value of this spin:

$$\begin{aligned}\bar{s}_j &= 1/Z \sum_{\nu_1,\nu_2,\cdots} (\mathbf{s}_j)_{\nu_k\nu_k}\mathbf{V}_{\nu_1\nu_2}\mathbf{V}_{\nu_2\nu_3}\cdots \\ &\qquad \times\mathbf{V}_{\nu_{k-1}\nu_k}\mathbf{V}_{\nu_k\nu_{k+1}}\cdots\mathbf{V}_{\nu_m\nu_1} \\ &= 1/Z \sum_{\nu_1,\nu_2,\cdots} \mathbf{V}_{\nu_1,\nu_2}\mathbf{V}_{\nu_2\nu_3}\cdots \\ &\qquad \times\mathbf{V}_{\nu_{i-1}\nu_1}(\mathbf{s}_j)_{\nu_k\nu_k}\mathbf{V}_{\nu_k\nu_{k+1}}\cdots\mathbf{V}_{\nu_m\nu_1} \\ &= 1/Z\cdot\text{trace}\{\mathbf{V}^{k-1}\mathbf{s}_j\mathbf{V}^{m-k+1}\}. \qquad (2)\end{aligned}$$

Since the trace is invariant with respect to cyclic changes in the order of factors we have

$$\bar{s}_j = (1/Z)\ \text{trace}(\mathbf{s}_j\mathbf{V}^m). \qquad (3)$$

This result is independent of k, as it should be. It will be seen later that $\bar{s}_j$ vanishes identically for every j, and this is not surprising because *a priori* every site has the same probability of being occupied by a positive spin as by a negative one, at all temperatures.

The situation is different for the correlation between two sites. Consider the product of the spins of site k in row j and site b in row a. The average of this product will be:

$$\begin{aligned}\langle s_{jk}s_{ab}\rangle_{Av} &= (1/Z) \sum_{\nu_1,\nu_2,\cdots} \mathbf{V}_{\nu_1\nu_2}\cdots\mathbf{V}_{\nu_{j-1}\nu_j}(\mathbf{s}_k)_{\nu_j\nu_j}\mathbf{V}_{\nu_j\nu_{j+1}}\cdots \\ &\qquad \times\mathbf{V}_{\nu_{a-1}\nu_a}(\mathbf{s}_b)_{\nu_a\nu_a}\mathbf{V}_{\nu_a\nu_{a+1}}\cdots \\ &= (1/Z)\ \text{trace}\{\mathbf{V}^{j-1}\mathbf{s}_k\mathbf{V}^{a-j}\mathbf{s}_b\mathbf{V}^{m-a+1}\} \\ &= (1/Z)\ \text{trace}\{\mathbf{s}_k\mathbf{V}^{a-j}\mathbf{s}_a\mathbf{V}^{m-a+j}\}. \qquad (4)\end{aligned}$$

This average value will not vanish. At zero temperature, all spins are aligned, so that $(\mathbf{s}_k)_{\nu_j\nu_j}=(\mathbf{s}_b)_{\nu_a\nu_a}=+1$ and therefore $(\mathbf{s}_k)_{\nu_j\nu_j}(\mathbf{s}_b)_{\nu_a\nu_a}=+1$. As a result

$$\langle s_{jk}s_{ab}\rangle_{Av} = 1/Z\cdot Z = +1$$

for all pairs of sites. This is the state of perfect order. At higher temperatures $\langle s_{jk}s_{ab}\rangle_{Av}$ decreases, and tends to zero for very high T.

We will refer to $\langle s_{jk}s_{ab}\rangle_{Av}$ as the *correlation* between the two sites (j, k) and (a, b), and will take the set of all these functions to be a measure of the degree of order within the crystal. Short-range order is described by the correlations for finite (small) distances between the sites. Long-range order is the limit for great distances, and will be discussed in Part IV.

In what follows, we will show how to evaluate the correlations as functions of temperature for successive distances between pairs of sites. Part of the work in the evaluation of these averages is algebraic: it is necessary to find the trace of the appropriate matrices, as given in (4). This will be simple for $a-j=0, 1$. For larger distances between rows the procedure, while still straightforward, is quite tedious. The algebraic work will give the correlation in terms of sums of the form

$$\frac{1}{n}\sum_{s=1}^{n}\cos(a(s\pi/n)+\delta_s') \equiv \Sigma_a \quad (a=0, 1, 2, \cdots).$$

These sums are then evaluated (with the help of an elliptic substitution) for the case of a quadratic crystal: $H=H'$. A particularly simple result obtains at the critical temperature, where $\Sigma_a \sim [-2/\pi(2a-1)]$. The value of $\langle s_{1,1}s_{1,k}\rangle_{Av} \equiv \langle s_1 s_k\rangle_{Av}$ can then be computed to any desired distance. It is found that

$$\lim_{k\to\infty}\langle s_1 s_k\rangle_{Av} = 0,$$

but this limit is approached very slowly.

2. PROCEDURE FOR EVALUATING AVERAGES

In our basic Eq. (4) we will employ an approximation: we will neglect all eigenvalues of $\mathbf{V}$ as compared with the largest one, when the power of the eigenvalues is high enough. (This approximation was justified in II, in the discussion of the partition function.) In order to make use of the approximation we transform (4) by $\mathbf{\Psi}$, which brings $\mathbf{V}$ to its diagonal form:

$$\langle s_{1,1}s_{1+a,b}\rangle_{Av} = \left\{\sum_{i=1}^{2^n}\lambda_i{}^m\right\}^{-1} \cdot\left\{\sum_{i=1}^{2^n}\lambda_i{}^{m-a}\cdot(\mathbf{\Psi}\mathbf{s}_1\mathbf{V}^a\mathbf{s}_b\mathbf{\Psi}^{-1})_{ii}\right\}. \qquad (5)$$

It was shown (see I.101) that for $T>T_c$ the largest eigenvalue, $\lambda_{\max}=\exp\{\frac{1}{2}(\gamma_1+\cdots+\gamma_{2n-1})\}$ is non-degenerate. On the other hand, for $T<T_c$ there is a twofold degeneracy:

$$\lambda^+{}_{\max}\simeq\lambda^-{}_{\max}=\exp\{\tfrac{1}{2}(\gamma_0+\cdots+\gamma_{2n-2})\}.$$

If we write, for both cases, $\lambda^+{}_{\max}\equiv\lambda$, we have above the critical temperature

$$\langle s_{1,1}s_{1+a,b}\rangle_{Av}\simeq\lambda^{-a}\{\mathbf{\Psi}_+\mathbf{s}_1\mathbf{V}^a\mathbf{s}_b\mathbf{\Psi}_+{}^{-1}\}_{11}, \qquad (6)$$

and below the critical temperature

$$\langle s_{1,1}s_{1+a,b}\rangle_{Av}\simeq\tfrac{1}{2}\lambda^{-a}[\{\mathbf{\Psi}_+\mathbf{s}_1\mathbf{V}^a\mathbf{s}_b\mathbf{\Psi}_+{}^{-1}\}_{11} + \{\mathbf{\Psi}_-\mathbf{s}_1\mathbf{V}^a\mathbf{s}_b\mathbf{\Psi}_-{}^{-1}\}_{11}]. \qquad (7)$$

$\mathbf{\Psi}_+$ and $\mathbf{\Psi}_-$ differ only in that $\mathbf{\Psi}_+$ involves the even-indexed angles $\omega_{2r}=(2r\pi/n)$ and δ_{2r}', while $\mathbf{\Psi}_-$ contains the odd-indexed ones. For simplicity of notation, we will no longer differentiate between odd- and even-indexed angles, but will use the neutral index t, which is to take on the values $2r$ or $2r-1$ as needed for the evaluation

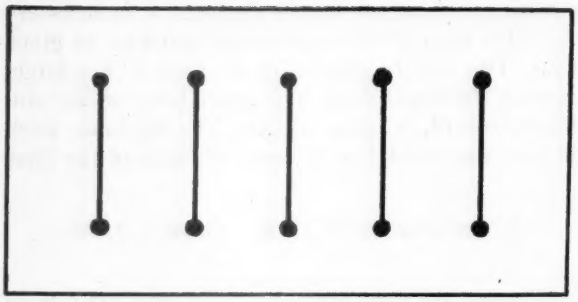

FIG. 1. Correlation of nearest neighbors in adjacent rows.

of the averages (6) and (7). Later on it will be seen that for large n, m both terms in (7) are equal, so that (6) may be used at *all* temperatures.

The quantity Ψ is completely known in terms of the rotation which it induces in the spinor base $\mathbf{P}_1$, $\mathbf{Q}_1$, $\mathbf{P}_2$, $\cdots$, $\mathbf{P}_n$, $\mathbf{Q}_n$. We had

$$\Psi=\mathbf{g}\cdot\mathbf{S}(\mathbf{TH}), \qquad \text{(II. 62, 69)}$$

where

$$\mathbf{H}: \quad \begin{aligned} &\mathbf{P}_r\rightarrow\cosh H^*\cdot\mathbf{P}_r-i\sinh H^*\cdot\mathbf{Q}_r \\ &\mathbf{Q}_r\rightarrow i\sinh H^*\cdot\mathbf{P}_r+\cosh H^*\cdot\mathbf{Q}_r \end{aligned} \qquad (1\leqslant r\leqslant n), \quad \text{(II. 63)}$$

$$\mathbf{T}: \quad \mathbf{P}_a\rightarrow\sum_{r=1}^{n}\sigma_{ra}\mathbf{P}_r+\sum_{r=1}^{n}\tau_{ra}\mathbf{Q}_r \qquad (1\leqslant a\leqslant n), \quad \text{(II. 57)}$$

$$\mathbf{Q}_a\rightarrow\sum_{r=1}^{n}\sigma_{ra}'\mathbf{P}_r+\sum_{r=1}^{n}\tau_{ra}'\mathbf{Q}_r$$

with

$$\begin{aligned} \sigma_{ra}&=\frac{1}{n^{\frac{1}{2}}}\cos\left(\frac{la\pi}{n}+\tfrac{1}{2}\delta_l'\right), \\ \tau_{ra}&=\frac{-1}{n^{\frac{1}{2}}}\sin\left(\frac{la\pi}{n}+\tfrac{1}{2}\delta_l'\right), \\ \sigma_{ra}'&=\frac{1}{n^{\frac{1}{2}}}\sin\left(\frac{la\pi}{n}-\tfrac{1}{2}\delta_l'\right), \\ \tau_{ra}'&=\frac{-1}{n^{\frac{1}{2}}}\cos\left(\frac{la\pi}{n}-\tfrac{1}{2}\delta_l'\right). \end{aligned} \qquad \text{(II. 58)}$$

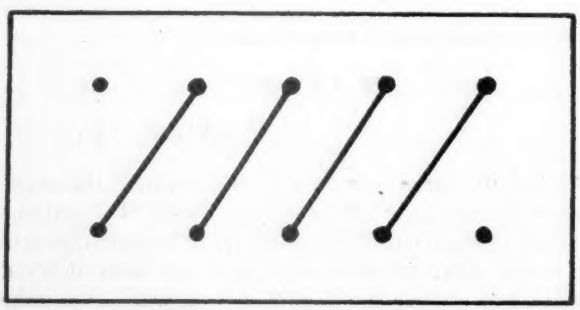

FIG. 2. Correlation of next-nearest neighbors.

(l is $2r$ or $2r-1$, as explained above). Finally

$$\mathbf{g}=\mathbf{g}^{-1}=2^{-n}\cdot\begin{pmatrix}1 & 1\\ 1 & -1\end{pmatrix}\times\begin{pmatrix}1 & 1\\ 1 & -1\end{pmatrix}\times\cdots \quad (n \text{ factors}), \qquad \text{(II. 16)}$$

and $\mathbf{g}$ has the property that $\mathbf{g}\mathbf{s}_r\mathbf{g}=\mathbf{C}_r$, $\mathbf{g}\mathbf{C}_r\mathbf{g}=\mathbf{s}_r$.

Since $\mathbf{S}(\mathbf{T})$ is a complicated matrix we do not give its components, and so we cannot write Ψ explicitly. Nevertheless, it will be seen that the $\{\ \}_{11}$ member of matrices transformed by Ψ can be found without much difficulty if we study the effect of the successive operations: $\mathbf{S}(\mathbf{H})$, $\mathbf{S}(\mathbf{T})$ and $\mathbf{g}$ on $(\mathbf{s}_1\mathbf{V}^a\mathbf{s}_b)$.

3. AVERAGES FOR 2-SPINOR MATRICES

Consider first $a=0$, $b=2$. We have then $\mathbf{s}_1\mathbf{V}^a\mathbf{s}_b=\mathbf{s}_2\mathbf{s}_1=-i\mathbf{P}_2\mathbf{Q}_1$. The average of this quantity will give us the correlation between two neighbors in a row. However, it is useful for the following problems to treat the more general 2-spinor quantities $\mathbf{X}=\mathbf{P}_k\mathbf{P}_l$, $\mathbf{P}_k\mathbf{Q}_l$, or $\mathbf{Q}_k\mathbf{Q}_l$. We will therefore investigate $\{\mathbf{g}\cdot\mathbf{S}(\mathbf{TH})\cdot\mathbf{X}\cdot\mathbf{S}(\mathbf{TH})^{-1}\mathbf{g}\}_{11}$, where $\mathbf{X}$ is a 2nd rank spinor. Clearly, transformation by $\mathbf{S}(\mathbf{TH})$ will send $\mathbf{X}$ into a linear combination of 2-spinor quantities. These are still to be transformed by $\mathbf{g}$, and the $\{\ \}_{11}$ member has to be taken. However, we know that the only matrices which have diagonal elements are the matrices $\mathbf{s}_r$ (or their products, which, as we shall see, do not enter here). Therefore, $\{\ \}_{11}=0$ unless the bracketed quantity is a product of $\mathbf{s}_r$ matrices. But this means that before transformation by $\mathbf{g}$ the bracketed quantity was a product of $\mathbf{C}_r$ matrices. Now $\mathbf{C}_r=i\mathbf{P}_r\mathbf{Q}_r$ is already a 2-spinor quantity so that no products of $\mathbf{C}_r$ matrices appear. We thus have the following result: In the transform of $\mathbf{X}$ by $\mathbf{S}(\mathbf{TH})$ only the terms of the form $\mathbf{P}_r\mathbf{Q}_r$ will contribute to the average.

Up to now we have not yet made use of the special properties of the rotation $\mathbf{T}$. These will lead to further simplifications. Choose for example $\mathbf{X}=\mathbf{P}_k\mathbf{Q}_l$. By (II. 63), cited above,

$$\begin{aligned} \mathbf{H}: \quad \mathbf{P}_k\mathbf{Q}_l\rightarrow&\cosh^2H^*\mathbf{P}_k\mathbf{Q}_l+i\cosh H^* \\ &\times\sinh H^*(\mathbf{P}_k\mathbf{P}_l-\mathbf{Q}_k\mathbf{Q}_l)-\sinh^2H^*\mathbf{P}_l\mathbf{Q}_k \\ &=\mathbf{S}(\mathbf{H})\cdot\mathbf{P}_k\mathbf{Q}_l\cdot\mathbf{S}(\mathbf{H})^{-1}. \end{aligned} \qquad (8)$$

This linear combination must now be transformed by $\mathbf{S}(\mathbf{T})$. Consider the term $\mathbf{P}_k\mathbf{P}_l$.

$$\mathbf{T}: \quad \mathbf{P}_k\mathbf{P}_l\rightarrow\sum_{r=1}^{n}\begin{vmatrix}\sigma_{rk} & \tau_{rk}\\ \sigma_{rl} & \tau_{rl}\end{vmatrix}\cdot\mathbf{P}_r\mathbf{Q}_r+\text{other terms}. \qquad (9)$$

The "other terms" are of the form $\mathbf{P}_r\mathbf{P}_s$ or $\mathbf{Q}_r\mathbf{Q}_s$ or $\mathbf{P}_r\mathbf{Q}_s$, and we have seen above that they will not contribute to the average. Now we put in the values of σ_{rk} etc., from (II. 58), and we get:

$$\mathbf{T}: \quad \mathbf{P}_k\mathbf{P}_l\rightarrow\frac{1}{n}\sum_{r=1}^{n}\sin(k-l)\frac{l\pi}{n}\cdot\mathbf{P}_r\mathbf{Q}_r+\text{other terms}.$$

Therefore

$$\mathbf{g}\cdot\mathbf{S}(\mathbf{T})\cdot\mathbf{P}_k\mathbf{P}_l\cdot\mathbf{S}(\mathbf{T})^{-1}\cdot\mathbf{g}$$
$$=-\frac{i}{n}\sum_{r=1}^{n}\sin(k-l)\frac{t\pi}{n}\cdot(\mathbf{s}_r)+\text{other terms.}$$

Finally, we have to take the $\{\ \}_{11}$ member of this matrix. But $\{\mathbf{s}_r\}_{11}=1$ for all r, so that

$$\{\mathbf{g}\cdot\mathbf{S}(\mathbf{T})\cdot\mathbf{P}_k\mathbf{P}_l\cdot\mathbf{S}(\mathbf{T})^{-1}\mathbf{g}\}_{11}=-\frac{i}{n}\sum_{t}\sin(k-l)\frac{t\pi}{n}=0. \quad (10)$$

In exactly the same way we find that

$$\{\mathbf{g}\cdot\mathbf{S}(\mathbf{T})\cdot\mathbf{Q}_k\mathbf{Q}_l\cdot\mathbf{S}(\mathbf{T})^{-1}\mathbf{g}\}_{11}=0. \quad (11)$$

On the other hand, for $\mathbf{P}_k\mathbf{Q}_l$ we have

$$\mathbf{T}:\quad \mathbf{P}_k\mathbf{Q}_l\rightarrow\frac{1}{n}\sum_{r=1}^{n}\cos\left[(k-l)\frac{t\pi}{n}+\delta_t'\right]\cdot\mathbf{P}_r\mathbf{Q}_r+\text{other terms.}$$

As a result

$$\{\mathbf{g}\cdot\mathbf{S}(\mathbf{T})\cdot i\mathbf{P}_k\mathbf{Q}_l\cdot\mathbf{S}(\mathbf{T})^{-1}\cdot\mathbf{g}\}_{11}$$
$$=\frac{1}{n}\sum_{t}\cos\left[(k-l)\frac{t\pi}{n}+\delta_t'\right]\equiv\Sigma_{k-l}. \quad (12)$$

Thus we see that we could disregard, in (8), all the terms in the transform of $\mathbf{X}$ which did not have the form $\mathbf{P}_k\mathbf{Q}_l$, and then we read off the average of $\mathbf{X}$ directly from (8):

$$i\bar{\mathbf{X}}=\langle i\mathbf{P}_k\mathbf{Q}_l\rangle_{Av}=\{\mathbf{g}\cdot\mathbf{S}(\mathbf{TH})\cdot i\mathbf{P}_k\mathbf{Q}_l\cdot\mathbf{S}(\mathbf{TH})^{-1}\cdot\mathbf{g}\}_{11}$$
$$=\cosh^2H^*\cdot\Sigma_{k-l}-\sinh^2H^*\cdot\Sigma_{l-k}. \quad (13)$$

In particular

$$\bar{\mathbf{C}}_k=\langle i\mathbf{P}_k\mathbf{Q}_k\rangle_{Av}=\Sigma_0. \quad (14)$$

Similarly, one finds

$$\langle\mathbf{P}_k\mathbf{P}_l\rangle_{Av}=\tfrac{1}{2}\sinh2H^*\cdot(\Sigma_{k-l}-\Sigma_{l-k}), \quad (15)$$

$$\langle\mathbf{Q}_k\mathbf{Q}_l\rangle_{Av}=-\tfrac{1}{2}\sinh2H^*\cdot(\Sigma_{k-l}-\Sigma_{l-k}). \quad (16)$$

The Σ_a can be evaluated exactly for large n, when the sum may be replaced by an integral. See below for the calculation of the Σ_a, and the derived results.

We are now in position to find the three simplest correlation functions.

Neighboring atoms in a row:

$$\langle s_1s_2\rangle_{Av}=\langle\mathbf{s}_1\mathbf{s}_2\rangle_{Av}=\langle-i\mathbf{P}_2\mathbf{Q}_1\rangle_{Av}$$
$$=-\cosh^2H^*\cdot\Sigma_1+\sinh^2H^*\cdot\Sigma_{-1}. \quad (17)$$

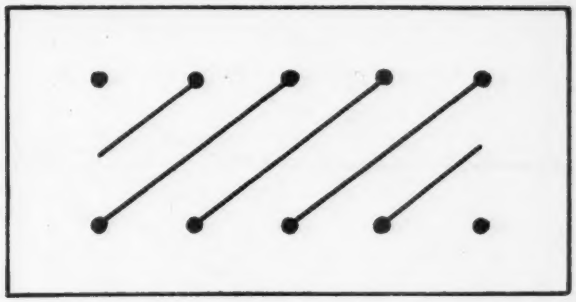

FIG. 3. Correlation between the sites (1, 1) and (2, 3).

(17) may also be written in the following useful form:

$$\langle s_1s_2\rangle_{Av}=-\cosh^2H^*\cdot\frac{1}{n}\sum_{t}\cos\left(\frac{t\pi}{n}+\delta_t'\right)$$
$$+\sinh^2H^*\cdot\frac{1}{n}\sum_{t}\cos\left(-\frac{t\pi}{n}+\delta_t'\right)$$
$$=-\frac{1}{n}\sum_{t}\left(\cos\frac{t\pi}{n}\cos\delta_t'-\sin\frac{t\pi}{n}\sin\delta_t'\right.$$
$$\left.\cdot\cosh2H^*\right)\equiv-\frac{1}{n}\sum_{t}\cos\delta_t^*. \quad (18)$$

(We recognize, from its definition, that δ^* is the third angle in the hyperbolic triangle of Fig. 4 in I.)

Neighboring atoms in adjacent rows are shown in Fig. 1. We need

$$\langle s_{1,1}s_{2,1}\rangle_{Av}=\lambda^{-1}\{\Psi^*\mathbf{s}_1\mathbf{V}\mathbf{s}_1\Psi^{*-1}\}_{11}.$$

Now

$$\mathbf{s}_1\mathbf{V}\mathbf{s}_1=\mathbf{s}_1\cdot\exp(H^*\mathbf{B})\cdot\exp(H'\mathbf{A})\cdot\mathbf{s}_1$$
$$=\mathbf{s}_1\cdot\exp(H^*\Sigma\mathbf{C}_r)\cdot\exp(H'\Sigma\mathbf{s}_r\mathbf{s}_{r+1})\cdot\mathbf{s}_1$$
$$=\exp(-2H^*\mathbf{C}_1)\cdot\mathbf{V}.$$

This is a result of the fact that all factors in $\mathbf{V}$ commute with $\mathbf{s}_1$, except for $\exp(H^*\mathbf{C}_1)$. Therefore

$$\langle s_{1,1}s_{2,1}\rangle_{Av}=\cosh2H^*-\sinh2H^*\cdot\Sigma_0. \quad (19)$$

Next-nearest neighbors are shown in Fig. 2.

$$\langle s_{1,1}s_{2,2}\rangle_{Av}=\lambda^{-1}\{\Psi^*\mathbf{s}_1\mathbf{V}\mathbf{s}_2\Psi^{*-1}\}_{11}.$$

Here

$$\mathbf{s}_1\mathbf{V}\mathbf{s}_2=\mathbf{s}_1\mathbf{s}_2\exp(-2H^*\mathbf{C}_2)\cdot\mathbf{V}$$
$$=(\cosh2H^*\cdot\mathbf{s}_1\mathbf{s}_2-\sinh2H^*\cdot\mathbf{s}_1\mathbf{s}_2\mathbf{C}_2)\mathbf{V},$$

and

$$\mathbf{s}_1\mathbf{s}_2\mathbf{C}_2=\mathbf{Q}_2\mathbf{Q}_1,$$

so that

$$\langle s_{1,1}s_{2,2}\rangle_{Av}=\cosh2H^*\cdot\langle s_1s_2\rangle_{Av}-\tfrac{1}{2}\sinh^22H^*(\Sigma_1-\Sigma_{-1}). \quad (20)$$

Several remarks may be made here:

(a) $\langle s_{1,1}s_{2,1}\rangle_{Av}$ must, of course, equal $\langle s_1s_2\rangle_{Av}$ in the case of a crystal with $H=H'$. Comparing (17) and (19), we

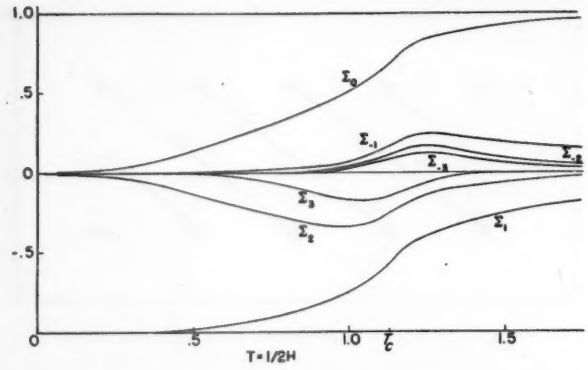

FIG. 4. Dependence of the functions Σ_a upon temperature. At low temperatures all Σ_a are negligible, except for Σ_1 which is $\sim+1$. At high temperatures only Σ_0 is significant.

see that this cannot be a term-by-term equality. But it it is to be expected that the complete expressions will equal one another. And indeed, this will be shown to be the case when the Σ_a are evaluated. See Section 5.

(b) $mn\langle s_1s_2\rangle_{Av}$ is, by its meaning, the average energy of a quadratic crystal (if J be normalized to unity). It should therefore equal the logarithmic derivative of the partition function, Z, with respect to H. Now

$$dZ/dH=d/dH\sum_i\lambda_i{}^m=m\sum_i(d\lambda_i/dH)\lambda_i{}^{m-1}; \quad (21)$$

but

$$\frac{d\lambda_i}{dH}=\frac{d}{dH}\exp[\tfrac{1}{2}(\cdots\pm\gamma_t\pm\gamma_{t+2}\pm\cdots)]$$

$$=\tfrac{1}{2}\lambda_i\frac{d}{dH}(\cdots\pm\gamma_t\pm\gamma_{t+2}\pm\cdots)=\tfrac{1}{2}\lambda_i\sum_t(\pm)\frac{d\gamma_t}{dH}. \quad (22)$$

(The sign-combination is determined by i; for $i=1$ we know that all signs are $+$.)

Furthermore, we have, from the definition of γ (see I. 89 and I. 112)

$$(d\gamma_t/dH)=2\cos\delta_t{}^*. \quad (23)$$

Combining the last three expressions, we get:

$$dZ/dH=m\sum_i\lambda_i{}^m\cdot\{\sum_t\pm\cos\delta_t{}^*\}_i. \quad (24)$$

Using only the largest eigenvalue, we have

$$1/Z\cdot dZ/dH\sim m\sum_t\cos\delta_t{}^*\sim mn\langle s_1s_2\rangle_{Av}. \quad (25)$$

These two entirely different methods of obtaining the average energy in the crystal have thus been shown to check with each other.

(c) An even closer analysis can be made, which will at the same time check the result for

$$\overline{\mathbf{C}}_a=\Sigma_0=(1/n)\sum_t\cos\delta_t'.$$

Taking the general case, $H\neq H'$, we will express $\partial Z/\partial H'$ and $\partial Z/\partial H^*$ in terms of the angles δ^* and δ', respectively.

$$\frac{\partial Z}{\partial H'}=\frac{\partial}{\partial H'}\operatorname{trace}(\mathbf{V}^m)$$

$$=\frac{\partial}{\partial H'}\operatorname{trace}\{(\exp(H^*\mathbf{B})\cdot\exp(H'\mathbf{A}))^m\}$$

$$=\operatorname{trace}\{\mathbf{AV}^m+\mathbf{VAV}^{m-1}+\mathbf{V}^2\mathbf{AV}^{m-2}+\cdots\}$$

$$=m\operatorname{trace}\{\mathbf{AV}^m\}=m\operatorname{trace}\{\mathbf{\Psi A\Psi}^{-1}\cdot\mathbf{\Lambda}^m\}$$

$$=m\sum_i\lambda_i{}^m\{\mathbf{\Psi A\Psi}^{-1}\}_{ii}=mn\sum_i\lambda_i{}^m\{\mathbf{\Psi s_1s_2\Psi}^{-1}\}_{ii}.$$

This can now be compared by term with (24), giving

$$\{\mathbf{\Psi s_1s_2\Psi}^{-1}\}_{ii}=(1/n)\{\sum_t\pm\cos\delta_t{}^*\}_i. \quad (26)$$

For the special case $i=1$ we rederive (18).

Consider how the derivative of Z with respect to H^*.

$$\partial Z/\partial H^*=m\operatorname{trace}\{\mathbf{BV}^m\}=mn\textstyle\sum_i\lambda_i{}^m\{\mathbf{\Psi C_a\Psi}^{-1}\}_{ii}; \quad (27)$$

but we also have, as in the case of $\langle s_1s_2\rangle_{Av}$,

$$\partial Z/\partial H^*=\partial/\partial H^*\textstyle\sum_i\lambda_i{}^m, \quad (28)$$

and (see I. 112)

$$\partial\gamma_t/\partial H^*=2\cos\delta_t'. \quad (29)$$

Therefore

$$\partial Z/\partial H^*=m\sum_i\lambda_i{}^m\{\sum_t\pm\cos\delta_t'\}_i. \quad (30)$$

Comparing the two expressions for $\partial Z/\partial H^*$ we find

$$\{\mathbf{\Psi C_a\Psi}^{-1}\}_{ii}=1/n\{\sum_t\pm\cos\delta_t'\}_{ii}. \quad (31)$$

For $i=1$, then, all signs are $+$, and $\overline{\mathbf{C}}_a=\Sigma_0$, as should be.

4. EXTENSION TO GREATER DISTANCES

The next farthest correlation introduces a new type of problem. In $\langle s_1s_3\rangle_{Av}$ we find that we need the transform of $\mathbf{P_3Q_2P_2Q_1}$. There is no difficulty in applying $\mathbf{H}$, especially since $\mathbf{P_2Q_2}$ remains invariant under $\mathbf{H}$. However, we must investigate the effect of the other operations on a 4-spinor matrix, say $\mathbf{P}_a\mathbf{Q}_b\mathbf{P}_c\mathbf{Q}_d$.

It will be helpful here to introduce a notation for an intermediate step in the averaging procedure. Let $\mathbf{X}$ be the quantity to be averaged, i.e., we want to evaluate $\overline{\mathbf{X}}=\{\mathbf{gS(T)\cdot S(H)XS(H)}^{-1}\cdot\mathbf{S(T)}^{-1}\mathbf{g}\}_{11}$. Denote by $\mathbf{Y}$ the the result of transforming $\mathbf{X}$ by $\mathbf{S(H)}$: $\mathbf{Y=S(H)XS(H)}^{-1}$. Then $\overline{\mathbf{X}}=\{\mathbf{gS(T)\cdot YS(T)}^{-1}\cdot\mathbf{g}\}_{11}\equiv\langle\{\mathbf{Y}\}\rangle_{Av}$. This notation is useful because the transformation by $\mathbf{S(T)}$ is the main step, whereas $\mathbf{S(H)}$ can be performed by inspection for the quantities $\mathbf{X}$ with which we will be dealing.

In this new notation we can rewrite (10), (11) and (12):

$$\langle\{\mathbf{P}_k\mathbf{P}_l\}\rangle_{Av}=\langle\{\mathbf{Q}_k\mathbf{Q}_l\}\rangle_{Av}=0, \quad (32)$$

$$\langle\{i\mathbf{P}_k\mathbf{Q}_l\}\rangle_{Av}=\Sigma_{k-l}. \quad (33)$$

We will now show that

$$\langle\{\mathbf{P}_a\mathbf{Q}_b\mathbf{P}_c\mathbf{Q}_d\}\rangle_{Av}=\langle\{\mathbf{P}_a\mathbf{Q}_b\}\rangle_{Av}\cdot\langle\{\mathbf{P}_c\mathbf{Q}_d\}\rangle_{Av}$$
$$+\langle\{\mathbf{P}_a\mathbf{P}_c\}\rangle_{Av}\cdot\langle\{\mathbf{Q}_b\mathbf{Q}_d\}\rangle_{Av}+\langle\{\mathbf{P}_a\mathbf{Q}_d\}\rangle_{Av}\cdot\langle\{\mathbf{Q}_b\mathbf{P}_c\}\rangle.$$
$$+\text{a negligible correction term.} \quad (34)$$

Reasoning as in Section 3, we know that $\mathbf{T}$ sends $\mathbf{P}_a\mathbf{Q}_b\mathbf{P}_c\mathbf{Q}_d$ into a linear combination of 4-spinor matrices, but that only those which are of the form

$$\mathbf{P}_r\mathbf{Q}_r\mathbf{P}_u\mathbf{Q}_u=-\mathbf{s}_r\mathbf{s}_u$$

can contribute to $\langle\{\mathbf{P}_a\mathbf{Q}_b\mathbf{P}_c\mathbf{Q}_d\}\rangle_{Av}$.

Now

$$\mathbf{T}:\quad \mathbf{P}_a\mathbf{Q}_b\rightarrow 1/n\sum_t\cos[(a-b)t\pi/n+\delta_t']\mathbf{P}_r\mathbf{Q}_r$$
$$+\text{other terms,} \quad (35)$$

$$\mathbf{P}_c\mathbf{Q}_d\rightarrow 1/n\sum_v\cos[(c-d)v\pi/n+\delta_v']\mathbf{P}_u\mathbf{Q}_u$$
$$+\text{other terms.} \quad (36)$$

If we multiply the $\mathbf{P}_r\mathbf{Q}_r$ terms in (35) by the $\mathbf{P}_u\mathbf{Q}_u$ terms in (36) we get a set of matrices all having the desired form $\mathbf{P}_r\mathbf{Q}_r\mathbf{P}_u\mathbf{Q}_u$. The products in which $r=u$ (and, therefore, $\mathbf{P}_r\mathbf{Q}_r\mathbf{P}_u\mathbf{Q}_u=-1$) must be excluded, since the transform of $\mathbf{P}_a\mathbf{Q}_b\mathbf{P}_c\mathbf{Q}_d$ must contain only 4-spinor matrices.

We will therefore have, as a set of contributing matrices:

$$\{1/n\sum_t\cos[(a-b)t\pi/n+\delta_t']\cdot\mathbf{P}_r\mathbf{Q}_r\}$$
$$\cdot\{1/n\sum_v\cos[(c-d)v\pi/n+\delta_v']\mathbf{P}_u\mathbf{Q}_u\}$$
$$-1/n^2\sum_t\cos[(a-b)t\pi/n+\delta_t']$$
$$\cdot\cos[(c-d)t\pi/n+\delta_t']\cdot\mathbf{P}_r\mathbf{Q}_r\mathbf{P}_r\mathbf{Q}_r, \quad (37)$$

and its contribution will be

$$\langle\{\mathbf{P}_a\mathbf{Q}_b\}\rangle_{Av}\langle\{\mathbf{P}_c\mathbf{Q}_d\}\rangle_{Av}+1/n^2\sum_t\cos[(a-b)t\pi/n+\delta_t']$$
$$\cdot\cos[(c-d)t\pi/n+\delta_t']. \quad (38)$$

However, this set does not exhaust all contributing matrices in the transform of $\mathbf{P}_a\mathbf{Q}_b\mathbf{P}_c\mathbf{Q}_d$. (For example, a $\mathbf{P}_k\mathbf{Q}_l$ matrix in (35) when multiplied by $\mathbf{P}_l\mathbf{Q}_k$ in (36), is also of the desired form.) The reason for this is that we had restricted the pair $\mathbf{P}_r\mathbf{Q}_r$ to be taken from the transform of $\mathbf{P}_a\mathbf{Q}_b$, and $\mathbf{P}_u\mathbf{Q}_u$ to be taken from the transform of $\mathbf{P}_c\mathbf{Q}_d$. Two other possibilities are:

$\mathbf{P}_r\mathbf{Q}_r$ from the transform of $\mathbf{P}_a\mathbf{P}_c$ and $\mathbf{P}_u\mathbf{Q}_u$ from the transform of $\mathbf{P}_b\mathbf{Q}_d$,

$\mathbf{P}_r\mathbf{Q}_r$ from the transform of $\mathbf{P}_a\mathbf{Q}_d$ and $\mathbf{P}_u\mathbf{Q}_u$ from the transform of $\mathbf{Q}_b\mathbf{P}_c$.

There are no other possibilities, and the three given ones contain no common terms, except for the matrices $\mathbf{P}_r\mathbf{Q}_r\mathbf{P}_r\mathbf{Q}_r$, which are everywhere to be excluded, as in (37). When n is very large, the sum of the excluded terms is negligible compared to all the rest, and will henceforth be neglected. We have thus proved (34). Making use of (32) and (33), we get finally:

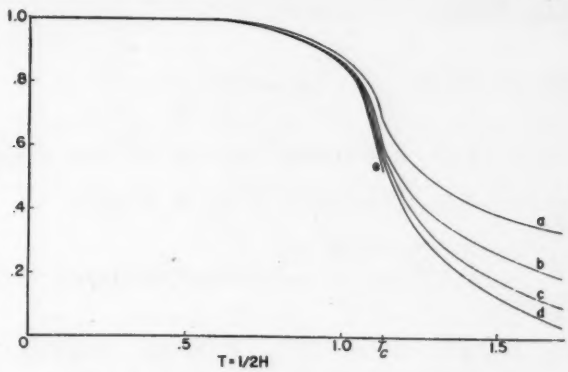

FIG. 5. Correlations for small distances, as functions of temperature. (a) $\langle s_1s_2\rangle_{Av}$; (b) $\langle s_{1,1}s_{2,2}\rangle$; (c) $\langle s_1s_3\rangle_{Av}$; (d) $\langle s_{1,1}s_{2,2}\rangle_{Av}$; (e) $\langle s_1s_4\rangle_{Av}$.

$$\langle\{\mathbf{P}_a\mathbf{Q}_b\mathbf{P}_c\mathbf{Q}_d\}\rangle_{Av}=\Sigma_{a-b}\Sigma_{c-d}-\Sigma_{a-d}\Sigma_{c-b}$$
$$=\begin{vmatrix}\Sigma_{a-b} & \Sigma_{a-d}\\ \Sigma_{c-b} & \Sigma_{c-d}\end{vmatrix}. \quad (39)$$

From (32) there results the further useful simplification that $\langle\{\mathbf{X}\}\rangle_{Av}=0$ for $\mathbf{X}=\mathbf{P}_a\mathbf{P}_b\mathbf{P}_c\mathbf{P}_d$, $\mathbf{P}_a\mathbf{P}_b\mathbf{P}_c\mathbf{Q}_d$, etc., i.e., whenever it is impossible to group all factors in $\mathbf{X}$ into $\mathbf{P}-\mathbf{Q}$ pairs. Therefore $\mathbf{X}$ must contain equal numbers of $\mathbf{P}$'s and $\mathbf{Q}$'s.

Equation (39) can be generalized to any number of factors:

If $\mathbf{X}=\mathbf{P}_{a_1}\mathbf{Q}_{b_1}\mathbf{P}_{a_2}\mathbf{Q}_{b_2}\cdots\mathbf{P}_{a_f}\mathbf{Q}_{b_f}$ $(a_i, b_i=1, 2, \cdots n)$, *then* $\langle\{\mathbf{X}\}\rangle_{Av}$ *is equal to an* f*-rowed determinant whose* (k, l)*-member is* $\Sigma_{a_k-b_l}$. (40)

Further Correlations

Returning to the correlation functions, we have:

$$\langle s_1s_3\rangle_{Av}=-\langle\{\mathbf{S}(\mathbf{H})\mathbf{P}_3\mathbf{Q}_2\mathbf{P}_2\mathbf{Q}_1\mathbf{S}(\mathbf{H})^{-1}\}\rangle_{Av}.$$
$$\mathbf{H}:\quad -\mathbf{P}_3\mathbf{Q}_2\mathbf{P}_2\mathbf{Q}_1\rightarrow\cosh^2H^*\cdot\mathbf{P}_3\mathbf{Q}_2\mathbf{P}_2\mathbf{Q}_1$$
$$-\sinh^2H^*\mathbf{P}_1\mathbf{Q}_2\mathbf{P}_2\mathbf{Q}_3+\text{other terms.}$$

The "other terms" here do not contain equal numbers of $\mathbf{P}$'s and $\mathbf{Q}$'s, and will therefore not contribute to

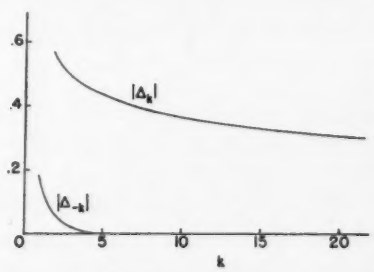

FIG. 6. The quantity $|\Delta_k|$ is proportional to the correlation $\langle s_1s_{1+k}\rangle_{Av}$ at the critical temperature. Δ_k tends to zero as $k\rightarrow\infty$. There is no long-range order at T_c.

$\langle s_1 s_3\rangle_{Av}$. Hence:

$$\langle s_1 s_3\rangle_{Av}=\cosh^2 H^*\begin{vmatrix}\Sigma_1 & \Sigma_2\\ \Sigma_0 & \Sigma_1\end{vmatrix}+\sinh^2 H^*\begin{vmatrix}\Sigma_{-1} & \Sigma_{-2}\\ \Sigma_0 & \Sigma_{-1}\end{vmatrix}$$
$$\equiv\cosh^2 H^*\cdot\Delta_2+\sinh^2 H^*\cdot\Delta_{-2}. \quad (41)$$

For the correlation indicated in Fig. 3, we have:

$$\langle s_{1,1}s_{2,3}\rangle_{Av}=\lambda^{-1}\{\Psi\mathbf{s}_1\mathbf{V}\mathbf{s}_3\Psi^{-1}\}_{11}$$
$$=\cosh 2H^*\langle s_1 s_3\rangle_{Av}+i\sinh 2H^*\{\Psi\dot{\mathbf{Q}}_1\mathbf{P}_2\mathbf{Q}_2\mathbf{Q}_3\Psi^{-1}\}_{11};$$

but

$$\mathbf{H}:\ \mathbf{Q}_1\mathbf{P}_2\mathbf{Q}_2\mathbf{Q}_3\to i/2\sinh 2H^*(-\mathbf{P}_1\mathbf{Q}_2\mathbf{P}_2\mathbf{Q}_3+\mathbf{P}_3\mathbf{Q}_2\mathbf{P}_2\mathbf{Q}_1)\cdot$$
$$+\text{other terms.}$$

Hence:

$$\langle s_{1,1}s_{2,3}\rangle_{Av}=\cosh 2H^*\langle s_1 s_3\rangle_{Av}+\tfrac{1}{2}\sinh^2 2H^*(\Delta_2-\Delta_{-2}). \quad (42)$$

It is not necessary to evaluate $\langle s_{1,1}s_{3,2}\rangle_{Av}$, for this is equal to $\langle s_{1,1}s_{2,3}\rangle_{Av}$; also $\langle s_{1,1}s_{3,1}\rangle_{Av}$ equals $\langle s_{1,3}\rangle_{Av}$.

It is easy to generalize (41) and (42) to any distance. One finds:

$$(-1)^k\langle s_1 s_{1+k}\rangle_{Av}=\cosh^2 H^*\Delta_k+\sinh^2 H^*\Delta_{-k}, \quad (43)$$

and

$$\langle s_{1,1}s_{2,1+k}\rangle_{Av}=\cosh 2H^*\cdot\langle s_1 s_{1+k}\rangle_{Av}$$
$$-(-1)^k/2\sinh^2 2H^*\cdot(\Delta_k-\Delta_{-k}), \quad (44)$$

where

$$\Delta_k=\begin{vmatrix}\Sigma_1 & \Sigma_2 & \Sigma_3 & \Sigma_4 & \cdots & \Sigma_k\\ \Sigma_0 & \Sigma_1 & \Sigma_2 & \Sigma_3 & \cdots & \Sigma_{k-1}\\ \Sigma_{-1} & \Sigma_0 & \Sigma_1 & \Sigma_2 & \cdots & \Sigma_{k-2}\\ \cdot & \cdot & \cdot & \cdot & \cdot & \cdot\\ \Sigma_{-k+2} & \cdot & \cdot & \cdot & \cdot & \Sigma_1\end{vmatrix},$$

$$\Delta_{-k}=\begin{vmatrix}\Sigma_{-1} & \Sigma_{-2} & \Sigma_{-3} & \Sigma_{-4} & \cdots & \Sigma_{-k}\\ \Sigma_0 & \Sigma_{-1} & \Sigma_{-2} & \Sigma_{-3} & \cdots & \Sigma_{-k+1}\\ \Sigma_1 & \Sigma_0 & \Sigma_{-1} & \Sigma_{-2} & \cdots & \Sigma_{-k+2}\\ \cdot & \cdot & \cdot & \cdot & \cdot & \cdot\\ \Sigma_{k-2} & \cdot & \cdot & \cdot & \cdot & \Sigma_{-1}\end{vmatrix}. \quad (45)$$

5. EVALUATION OF THE Σ_a

For large n, the sum in Σ_a may be replaced by an integral;

$$\Sigma_a=\frac{1}{n}\sum_{r=1}^{n}\cos\left[a\frac{2r\pi}{n}+\delta_{2r}'\right]$$
$$\simeq\frac{1}{\pi}\int_0^{\pi}\cos[a\omega+\delta'(\omega)]d\omega. \quad (46)$$

(It obviously makes no difference now if one replaces the even-indexed angles in Σ_a by odd-indexed ones. This justifies the statements made on p. 1245–6.)

δ' is a function of H and ω through the relations (for the case $H=H'$; see (I. 89)):

$$\sin\delta'=\sinh 2H(\sin\omega/\sinh\gamma), \quad (47)$$

$$\sinh\gamma\cos\delta'=(\cosh 2H/\sinh 2H)-\cosh 2H\cdot\cos\omega, \quad (48)$$

and

$$\cosh\gamma=(\cosh^2 2H/\sinh 2H)-\cos\omega. \quad (49)$$

An elliptic substitution[5] is now made separately for values of H below and above the critical point. (The critical point itself occurs at $\sinh 2H_c=1$.) The variable u_1 is introduced, and both ω and δ' are expressed in terms of this variable.

Below the critical temperature ($T<T_c$, $H>H_c$). First choose for the elliptic modulus

$$k\equiv\sinh^{-2}2H<1 \quad (50)$$

and

$$\cos\delta'\equiv cn(u,k),\quad \sin\delta'\equiv sn(u,k). \quad (51)$$

As a result (see I. 2.4),

$$\cos\omega=k^{\frac{1}{2}}\frac{(1+k)sn^2u-dnu\,cnu}{1+k\,sn^2u}. \quad (52)$$

The limits of integration in (46) become: 0 to $2K(k)$, where K is the complete elliptic integral of the first kind. Now make one further substitution,[6] which serves to eliminate the denominator in (52):

$$u_1\equiv u(1+k),\quad k_1\equiv 2k^{\frac{1}{2}}/1+k. \quad (53)$$

Then we have

$$cn(u_1,k_1)=\frac{cn(u,k)\,dn(u,k)}{1+k\,sn^2(u,k)},$$
$$dn(u_1,k_1)=\frac{1-k\,sn^2(u,k)}{1+k\,sn^2(u,k)} \quad (54)$$

and

$$K_1\equiv K(k_1)=K(k)\cdot(1+k). \quad (55)$$

As a result, we get

$$\cos\omega=\frac{1}{k_1}[1-dn(u_1,k_1)]-cn(u_1,k_1), \quad (56)$$

and the limits of integration become: 0 to $2K_1$. Since the integrals of powers of *dnu* and *cnu* are all known, it is now possible to evaluate any integral of the form

$$\int_0^{2K_1}\cos^a\omega\cdot du_1. \quad (57)$$

In order to express δ' in terms of u_1, we make use of the relationship (see I. 2.4 and I. 2.5)

$$\partial\omega/\partial u=-\sinh\gamma/k^{\frac{1}{2}}. \quad (58)$$

This we insert into $\cos\delta'\cdot d\omega$:

$$\cos\delta'\cdot d\omega=\cos\delta'\cdot\partial\omega/\partial u\cdot du$$
$$=-(\cos\delta'\sinh\gamma/k^{\frac{1}{2}})du. \quad (59)$$

[5] See I, especially Section 2 of the Appendix.

[6] See, for example, E. Jahnke and F. Emde, *Tables of Functions* (B. G. Teubner, Leipzig and Berlin, 1933).

We now use (48) and (50), and get

$$\cos\delta' \cdot d\omega = (1+k)^{\frac{1}{2}}(k^{\frac{1}{2}} - \cos\omega)\cdot du. \tag{60}$$

Finally we replace u by u_1:

$$\cos\delta' \cdot d\omega = \frac{1}{(1+k)^{\frac{1}{2}}}(k^{\frac{1}{2}} - \cos\omega)\cdot du_1. \tag{61}$$

Similarly we get for $\sin\delta'$:

$$\sin\delta' d\omega = \sin\omega\, du = \frac{\sin\omega\, du_1}{(1+k)}. \tag{62}$$

And now, we can apply these results to the integrand of Σ_a:

$$\cos(a\omega+\delta')d\omega = \cos a\omega\cdot\cos\delta' d\omega - \sin a\omega\,\sin\delta' d\omega$$

$$= \frac{1}{(1+k)^{\frac{1}{2}}}\sum_{s=1}^{a} \alpha_s \cdot \cos^s\omega (k^{\frac{1}{2}} - \cos\omega) du_1$$

$$= \frac{1}{1+k}\sum_{s=1}^{a-1} \beta_s \cos^s\omega \sin^2\omega \cdot du_1,$$

where we have expanded $\cos a\omega$ and $\sin a\omega$ into polynomials in $\cos\omega$. The integral of $\cos(a\omega+\delta')$ now involves only integrals of the form (57). Thus the procedure for evaluating any Σ_a is completed.

As an example we will now give the details of the computation for Σ_0.

$$\Sigma_0 = \frac{1}{\pi}\int_0^{\pi} \cos\delta' d\omega = \frac{1}{\pi(1+k)^{\frac{1}{2}}}\int_0^{2K_1} (k^{\frac{1}{2}} - \cos\omega) du_1$$

$$= \frac{1}{\pi}\left(\frac{k}{1+k}\right)^{\frac{1}{2}} 2K_1 - \frac{(1+k)^{\frac{1}{2}}}{\pi}\int_0^{2K_1} \cos\omega du_1.$$

And from (56):

$$\int_0^{2K_1} \cos\omega\, du_1 = \int_0^{2K_1}\left[\frac{1}{k_1}(1 - dn u_1) - cn u_1\right] du_1 = \frac{2K_1 - \pi}{2k^{\frac{1}{2}}}.$$

Altogether

$$\Sigma_0 = 1/\pi(1+k/k)^{\frac{1}{2}}\{\pi/2 - (1-k)K\} \quad (T<T_c). \tag{63}$$

(This result is the same as that already obtained in (I. 5.1).)

Above the critical temperature ($T>T_c$, $H<H_c$). Choose

$$k = \sinh^2 2H < 1, \tag{64}$$

$$\cos\delta' = dn u, \quad \sin\delta' = k\, sn u. \tag{65}$$

And find, as above:

$$\cos\delta' d\omega = \frac{1}{(1+k)^{\frac{1}{2}}}(1 - k^{\frac{1}{2}}\cos\omega) du_1, \tag{66}$$

$$\sin\delta' d\omega = \frac{k}{1+k}\sin\omega \cdot du_1. \tag{67}$$

(52) and (56) hold at all temperatures. Applying to Σ_0 we find:

$$\Sigma_0 = (1+k)^{\frac{1}{2}}/\pi\{\pi/2 + (1-k)K\} \quad (T>T_c). \tag{68}$$

Σ_0 is continuous and bounded at the critical point. The reason for this is that, although $K\to\infty$ as $k\to 1$, $(1-k)K\to 0$. At the critical point then,

$$\Sigma_0 = 1/\sqrt{2}. \tag{69}$$

In the same way we find:

$$\pi\Sigma_{\pm 1} = \begin{cases} (1+k)^{\frac{1}{2}}/k\{(\pi/2) - k(1-k)\cdot K - (1+k)E_1\} \\ \quad \mp(1+k/k)\{(\pi/2) - E_1\} \quad \text{for } T<T_c \\ (1+k/k)^{\frac{1}{2}}\{k(\pi/2) + (1-k)\cdot K - (1+k)E_1\} \\ \quad \mp(1+k)\{(\pi/2) - E_1\} \quad \text{for } T>T_c. \end{cases} \tag{70}$$

Here E_1 is an abbreviation for $E(2k^{\frac{1}{2}}/(1+k))$. Graphs of Σ_0, $\Sigma_{\pm 1}$, $\Sigma_{\pm 2}$, $\Sigma_{\pm 3}$ are shown in Fig. 4. It is seen that, for $|a|>2$, all Σ_a are very small except in the immediate neighborhood of the critical point.

At the critical temperature. A fairly good approximation[7] gives $\delta' \sim \pi/2 - \omega/2$ at the critical point, so that

$$\Sigma_a \sim 1/\pi\int_0^{\pi} \cos(a\omega + \pi/2 - \omega/2) = -2/[\pi(2a-1)]. \tag{71}$$

Exact values at the critical point are

$$\Sigma_0 = 1/\sqrt{2} = 0.7070,$$

$$\Sigma_{\pm 1} = \sqrt{2}\left(\frac{1}{2} - \frac{2}{\pi}\right) \mp \left(1 - \frac{2}{\pi}\right) = \begin{cases} -0.5566 \\ 0.1702, \end{cases}$$

$$\Sigma_{\pm 2} = \sqrt{2}\left(\frac{5}{2} - \frac{8}{\pi}\right) \mp \left(4 - \frac{12}{\pi}\right) = \begin{cases} -0.2461, \\ 0.1145 \end{cases}$$

$$\Sigma_{\pm 3} = \sqrt{2}\left(\frac{25}{2} - \frac{118}{3\pi}\right) \mp \left(19 - \frac{178}{3\pi}\right) = \begin{cases} -0.1421 \\ 0.0853. \end{cases}$$

The Correlation Curves

A few qualitative statements can be made immediately about the behavior of the correlation curves at the ends of their range, i.e., for very low and very high temperatures. As $T\to 0$, $\delta' \sim \pi - \omega$, therefore

$$\cos(a\omega + \delta') = -\cos(a-1)\omega;$$

as a result $\Sigma_a = 0$ for all a, except that $\Sigma_{+1} = -1$. On the other hand, as $T\to\infty$, $\delta'\sim 0$, therefore $\cos(a\omega+\delta') = \cos a\omega$. This gives $\Sigma_a = 0$ for all a, except that $\Sigma_0 = +1$. Thus $\langle s_1 s_k\rangle_{av} = 1$ at low temperatures, and $=0$ at high ones, for all k. This results from the fact that we chose a model in which the energy of like neighbors, $-J$, is lower than that of unlike neighbors, $+J$. In other words, the completely ordered state, at absolute zero temperature, is a configuration with all spins alike; it is left unstated whether these spins are all + or all

[7] It can be shown that $\delta' = \pi/2 - \omega/2$ at the critical temperature for correlations along a 45° diagonal of the lattice.

$-$. The model with the opposite assignment of interaction energies would give $\langle s_1 s_k\rangle_{Av}=0$ in the completely ordered state (0°K).

Figure 5 shows exact curves for $\langle s_1 s_2\rangle_{Av}$, $\langle s_{1,1} s_{2,2}\rangle_{Av}$, $\langle s_1 s_3\rangle_{Av}$, $\langle s_{1,1} s_{2,3}\rangle_{Av}$, $\langle s_1 s_4\rangle_{Av}$ which correspond to the geometric distances 1, $2^{\frac{1}{2}}$, 2, $5^{\frac{1}{2}}$, 3, respectively. It is seen that the curve for $\langle s_{1,1} s_{2,2}\rangle_{Av}$ lies between $\langle s_1 s_2\rangle_{Av}$ and $\langle s_1 s_3\rangle_{Av}$: similarly $\langle s_{1,1} s_{2,3}\rangle_{Av}$ lies between $\langle s_1 s_3\rangle_{Av}$ and $\langle s_1 s_4\rangle_{Av}$. At the critical point the values have been computed exactly for the first few correlations of the type $\langle s_1 s_k\rangle_{Av}$, and, for the ones farther out, the approximation $\Sigma_a\sim -2/[\pi(2a-1)]$ was used. With these values for Σ_a one has[8]

$$|\Delta_k|=-\frac{2}{\pi}\prod_{s=1}^{k}\frac{\Gamma(s+1)\Gamma(s+1)}{\Gamma(s+\frac{1}{2})\Gamma(s+\frac{3}{2})}$$

and

$$|\Delta_{-k}|=-\frac{2}{\pi}\prod_{s=1}^{k}\frac{\Gamma(s+1)\Gamma(s+1)}{\Gamma(s+\frac{3}{2})\Gamma(s+(5/2))}. \tag{72}$$

Both Δ_k and Δ_{-k} tend to zero as $k\to\infty$, although Δ_k approaches this limit very slowly.[8] The quantities $|\Delta_k|$ and $|\Delta_{-k}|$ are plotted as functions of k in Fig. 6. Since Δ_{-k} is negligible compared to Δ_k, certainly for $k\geqslant 4$, we have from (43) and (44) at the critical point:

$$(-1)^k\langle s_1 s_{1+k}\rangle_{Av}=(1+\sqrt{2}/2)\Delta_k,$$
$$(-1)^k\langle s_{1,1} s_{2,1+k}\rangle_{Av}\cong(1+\sqrt{2}/2)\Delta_k=(-1)^k\langle s_1 s_{1+k}\rangle_{Av},$$

which is to be expected, since the geometrical distances are almost equal. Finally, it is of interest to verify the statement made on p. 1247 that $\langle s_1 s_2\rangle_{Av}=\langle s_{1,1} s_{2,1}\rangle_{Av}$.

[8] T. Muir, *A Treatise on the Theory of Determinants*, revised and enlarged by W. H. Meltzer (private publication, Albany, New York, 1930), p. 437.

From (17) we have:

$$\langle s_1 s_2\rangle_{Av}=-\tfrac{1}{2}(\cosh 2H^*+1)\Sigma_1+\tfrac{1}{2}(\cosh 2H^*-1)\Sigma_{-1}$$
$$=\tfrac{1}{2}\cosh 2H^*(\Sigma_1-\Sigma_{-1})-\tfrac{1}{2}(\Sigma_1+\Sigma_{-1}).$$

Also

$$\cosh 2H^*=\coth 2H=\begin{cases}(1+k)^{\frac{1}{2}} & \text{for } T<T_c,\\ (1+k/k)^{\frac{1}{2}} & \text{for } T<T_c.\end{cases}$$

Therefore, by (70),

$$\langle s_1 s_2\rangle_{Av}=\begin{cases}\dfrac{(1+k)^{\frac{1}{2}}}{\pi k}\left\{\dfrac{\pi}{2}-E_1\right\}-\dfrac{(1+k)^{\frac{1}{2}}}{\pi k}\\ \times\left\{\dfrac{\pi}{2}-k(1-k)K-(1+k)E_1\right\} \text{ for } T<T_c\\ \dfrac{(1+k)^{\frac{1}{2}}}{\pi k^{\frac{1}{2}}}\left\{\dfrac{\pi}{2}-E_1\right\}-\dfrac{(1+k)^{\frac{1}{2}}}{\pi k^{\frac{1}{2}}}\\ \times\left\{\dfrac{\pi}{k}\dfrac{}{2}+(1-k)K-(1+k)E_1\right\} \text{ for } T>T_c.\end{cases}$$

On the other hand, from Eqs. (19), (63), and (68) we have:

$$\langle s_{1,1} s_{2,1}\rangle_{Av}=\cosh 2H^*-\sinh 2H^*\Sigma_0$$
$$=\begin{cases}(1+k)^{\frac{1}{2}}-\dfrac{(1+k)^{\frac{1}{2}}}{\pi}\left\{\dfrac{\pi}{2}-(1-k)K\right\} \text{ for } T<T_c\\ \left(\dfrac{1+k}{k}\right)^{\frac{1}{2}}-\dfrac{1}{\pi}\left(\dfrac{1+k}{k}\right)^{\frac{1}{2}}\left\{\dfrac{\pi}{2}+(1-k)K\right\}\\ \qquad\qquad \text{for } T>T_c.\end{cases} \tag{74}$$

Equations (73) and (74) are identical except for their algebraic form.

Letters to the Editor

PUBLICATION of brief reports of important discoveries in physics may be secured by addressing them to this department. The closing date for this department is five weeks prior to the date of issue. No proof will be sent to the authors. The Board of Editors does not hold itself responsible for the opinions expressed by the correspondents. Communications should not exceed 600 words in length.

The Possible Existence of the $4n+1$ Radioactive Series in Chloritized Ytterby Mica

J. H. J. POOLE, C. F. G. DELANEY, AND R. C. MCCORMICK
Physical Laboratory, Trinity College, Dublin, Ireland
August 22, 1949

THE late Professor Joly discovered many years ago certain pleochroic halos in chloritized ytterby mica of whose origin he was uncertain.[1] The most striking feature of these halos is a bleached or reversed belt or ring, the bleaching being so complete in some cases that the original color of the mica has been destroyed. They differ strikingly in appearance from any known type of uranium or thorium halo, but are common in both ytterby and arendal micas, which are both of Archaean Age. It seems certain that they cannot be thorium halos, since no trace of a ring large enough to be produced by ThC′ can ever be detected. Joly, on the whole, was inclined to attribute their origin to an unknown radioactive series, and referred to them as X halos. It may be remarked that in the same mica he first found the so-called hibernium halos, which were shown many years later to be probably samarium halos, the radioactivity of samarium being unknown at that date (1923).

The possibility that X halos may be due to the recently artificially produced neptunion or $4n+1$ radioactive series naturally arises. The first known member of the series is $^{94}Pu^{241}$, a β-emitter of half-life ten years, and the longest lived member is $^{93}Np^{237}$, an α-emitter of half-life 2.3×10^{6} years. It is accordingly clear that if the $4n+1$ series is present in the mica the series must have an unknown long-lived progenitor, which would very probably be an α-emitter, and must accordingly have an atomic weight of at least 245. No elements as heavy as this have been, as yet, artificially produced and hence nothing is known experimentally of their characteristics.

The simplest method of identifying a fully developed halo is by measurement of its outer diameter. We have applied this method to some of Joly's original material. If the X halos were due to the $4n+1$ series, they should be intermediate in outer diameter to uranium and thorium halos, the relevant α-ray ranges in air being: RaC′, 6.97 cm; $^{84}Po^{213}$, 7.89 cm; and ThC′, 8.62 cm. Since uranium halos are also present in the mica, the diameters of uranium and X halos could be directly compared. This method eliminates to some extent the error due to the uncertain value of the stopping power of the mica. The average diameter of the uranium halo was 0.057 mm. If we assume, as an approximate figure, that the diameter of a halo is proportional to the range of the generating α-ray, this gives that the diameter of a $4n+1$ halo should be 0.0645 mm. The average measured diameter of the X halos was however only 0.061 mm. It must be pointed out, however, that exact measurements on these halos are very difficult, as the mica itself is very opaque, and the position of the outer edge of the halo largely a matter of the personal opinion of the observer. On the whole the tendency would be to exaggerate the diameter of the X halo, which was usually stronger in contrast than the uranium halo. Our results, however, show only about half the anticipated increase in diameter for a $4n+1$ halo, and some of this increase may also be due to the X halos having abnormally large nuclei, since the size of their nuclei cannot be measured owing to the great blackening of the central pupil. We would therefore consider that our results would, on the whole, indicate that the X halos are not due to the $4n+1$ or neptunium series. This leaves the problem of the real origin of the X halos still unsolved.

It is unfortunate that the nature of the radioactivity of a halo nucleus cannot be investigated conveniently by the nuclear plate technique, owing to the very slow emission rate of the α-rays from the nucleus. Joly and Rutherford showed that about four α-rays per year would produce a fully developed halo in Ballyellen, Ireland, mica of age about 400 million years,[2] and as the X halos are probably at least five times greater in age, their emission rate would probably be considerably lower.

An Ilford nuclear plate Type C2, when exposed to some of the ytterby mica, showed, however, that the whole surface of the mica was highly radioactive. The α-ray count amounted to $800\alpha/cm^2/hr.$ which may be compared with a count of about $1.5\alpha/cm^2/hr.$ from a typical basalt. Fergusonite, a rare earth uranium-columbate tantalate is known to occur at ytterby, and may contain from one to two percent UO^2, so that evidently uranium is fairly common in the district. An attempt was made to investigate the nature of the radioactivity of the mica by measuring the ranges of the longer α-ray tracks in the emulsion, and then plotting the number of tracks V-range histogram. Lattes, Fowler, and Cuer[3] have measured the range energy relationship for the Ilford emulsion, and their figures were used in interpreting the histogram. The shape of histogram obtained was not all what would have been expected from a thick source of uniformly distributed radioactive matter. It corresponded rather better to a fairly thin surface distribution of thorium, but showed a pronounced peak at a range of about 44 microns. The range of ThC′ in the emulsion is 47.5 microns, whereas that of $^{84}Po^{213}$, from the $4n+1$ series, is 43.9 microns. This again suggested the possible existence of this series in the mica, but further investigation seems again to have disproved this idea.

The radium isotope, $^{88}Ra^{225}$, in the $4n+1$ series is a β-emitter of half-life 14 days. It decays into $^{89}Ac^{225}$, which is an α-emitter of half-life ten days. Thus, if a $^{88}Ra^{225}$ source could be obtained, its α-ray activity would depend nearly entirely on the initial growth and subsequent decay of $^{89}Ac^{225}$, reaching a maximum in about 17 days from the date of the preparation of the source and then falling away again. An ordinary radium source would however grow in activity to a nearly constant maximum value; whereas a Th X source would start at maximum activity and decay gradually to zero.

It was found possible to separate enough of the radium isotopes from six grams of the mica to provide us with reasonably active sources. This was done by precipitating these isotopes as sulfates from an acid solution of the mica, obtained by first fusing the mica with mixed alkali carbonates. Barium sulfate was used as a carrier, following the usual chemical method for the separation of radium The α-ray activity of these sources was investigated by means both of an ionization chamber α-ray counter and also by the nuclear plate technique. The maximum rate of count with the α-ray counter varied for various sources from about 100 to 300α per minute, the background count being about 5α per minute. Using both methods, all sources showed an increase of activity with time to a maximum value which was constant within the limits of experimental error, and gave no evidence of the presence of the $4n+1$ series. The activity of the sources was measured up to periods exceeding 60 days.

It is clear that this method would reveal the presence of the $4n+1$ series only if its total activity in the mica was comparable to that of the uranium and thorium series also present. The chemical method depends on the bulk radioactive content of the mica, whereas the original histogram depended apparently on a surface distribution. Hurley[4] of the Massachusetts Institute of Technology has recently found that for some granites a large portion of the radioactivity is present as a surface film on small granules, and may be removed by dilute hydrochloric acid. If this

result proves to be also true for the mica, it may enable us to investigate the nature of the surface distribution apart from the bulk distribution.

A more detailed account of the work to date will be published later.

[1] J. Joly, Proc. Roy. Soc. A102, 682 (1923).
[2] J. Joly and E. Rutherford, Phil. Mag. 25, 644 (1913).
[3] Lattes, Fowler, and Cuer, Proc. Phys. Soc. (London) 59, 883 (1947).
[4] P. M. Hurley (private communication).

Infra-Red Color Center Bands in the Alkali Halides

E. Burstein and J. J. Oberly
Crystal Branch, Naval Research Laboratory, Washington, D. C.
September 1, 1949

NEW color center bands in the near infra-red have been observed in alkali halides irradiated with x-rays from a beryllium window tube with a tungsten target[1] and subsequently irradiated with white light. In agreement with the results of earlier investigators, the F- and M-bands formed by relatively small x-ray exposures (10^5 roentgens/cm^2) are completely bleached without appreciable R-band formation. However, after greater x-ray exposures (10^6 roentgens/cm^2) the F- and M-bands are only partially bleached by irradiation with white light. Under these conditions there is appreciable R-band formation and, in addition, new bands are observed in the near infra-red beyond the M-bands. Additional prolonged irradiation with white light produced relatively little effect on the appearance of the various bands. Visual examination of the partially bleached specimens showed that the residual color was located in a thin section at the surface of the crystal entered by the x-rays. At liquid nitrogen temperatures the various bands narrowed, shifted to shorter wave-lengths, and showed additional structure. The various color center bands are shown in Fig. 1 for KCl after a dosage of 600×10^6 roentgens/cm^2 and subsequently irradiation with white light. Preliminary measurements on additively colored crystals of KCl which were exposed to white light revealed that the new bands are also present in these crystals. Similar results were obtained for KBr and NaCl.[2]

The nature of the new near infra-red bands ("N-bands") and the factors leading to their formation are being investigated further. At present, it may be supposed that the N-bands correspond either to electrons trapped at specific clusters of vacancies in a manner analogous to that suggested by Seitz for the R- and M-bands[3] or to two-dimensional aggregates of F-centers as suggested by Mitchell for the color center bands in the silver halides.[4] The inability to bleach the color center bands indicates that the positive holes formed during irradiation have diffused away from the surface regions of the crystal. A loss of atomic halogen from the surface of the crystal during x-irradiation is highly probable and may, in fact, account for part of the decrease in density observed in KCl on prolonged x-irradiation.[5] Regardless of the exact mechanism for the decrease in density, it is reasonable to assume that the x-irradiated crystal contains a larger concentration of vacancies than is normally present. Partial bleaching increases the concentration of negative ion vacancies still further so that conditions are favorable for the aggregation of vacancies or F-centers. Measurements are being carried out on the changes in ionic conductivity and dielectric loss to obtain further information about the mechanism of vacancy formation during x-irradiation.

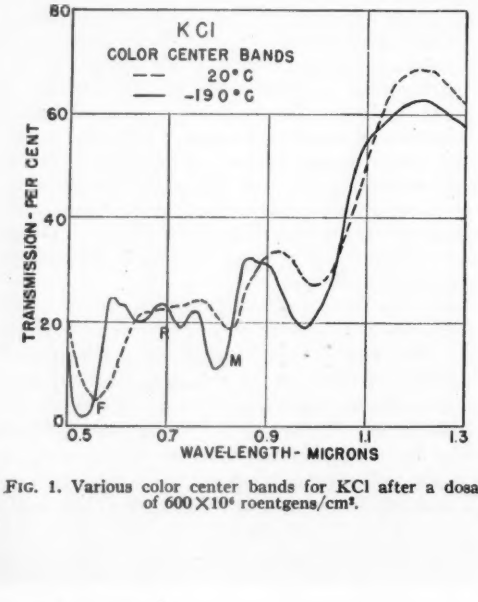

Fig. 1. Various color center bands for KCl after a dosage of 600×10^6 roentgens/cm^2.

[1] A Machlett AEG-50A tube operated at 50 kv and 20 ma was used in this work.
[2] A color center band in NaCl corresponding to the N-band was reported by Molnar in his thesis (M.I.T. 1942).
[3] F. Seitz, Rev. Mod. Phys. 18, 348 (1946).
[4] J. W. Mitchell, Phil. Mag. 40, 249 (1949). We are grateful to Dr Mitchell, who pointed out this possibility to us.
[5] Estermann, Leivo and Stern, Phys. Rev. 75, 627 (1949).

The S-Matrix for Meson-Nucleon Interactions

P. T. Matthews
Clare College, Cambridge, England
September 2, 1949

DYSON[1] has given a set of simple rules for writing down the integrals for the matrix elements for transitions in electrodynamics. These rules have since been extended to cover the more general meson-nucleon interactions which may include differentials.[2] With the use of his rules Dyson[3] has proved that the consistant renormalization of mass and charge will remove all the divergences from the S-matrix for scattering processes in electrodynamics. Dyson starts by proving that there are only four types of primitive divergents in the theory. One of these—the scattering of light by light, to be referred to as a "square" part—is then shown by arguments of gauge invariance to introduce, in fact, no new divergences. For (pseudo-)scalar meson scalar-interactions with nucleons the primitive divergents are the same as in electrodynamics, but the attempt to obtain a finite S-matrix fails because genuine divergences arise from square parts.[4] In all the other meson-nucleon interactions the occurrence of extra differentials allows for an infinite number of primitive divergents and Dyson's method appears to fail completely. However, the (pseudo-)vector meson vector-interactions are peculiar in that the differentials occur in the commutation relations, not in the interactions. It will be shown below that in the single case of the neutral vector meson vector-interaction the differentials do not contribute to the matrix elements and a finite S-matrix can be obtained by Dyson's method.

The vector meson field $\varphi_\mu(x)$ with positive definite energy can be expressed in terms of two subsidiary fields,[5] a vector field $A_\mu(x)$ and a scalar field $B(x)$, where

$$\varphi_\mu(x)=A_\mu(x)+(1/\kappa)(\partial B/\partial x_\mu). \tag{1}$$

The wave function satisfies the subsidiary condition

$$(\partial A_\mu/\partial x_\mu+\kappa B)\Psi=0. \tag{2}$$

The Hamiltonian for the vector-interaction in the interaction representation is[6]

$$H(x)=(1/c)j_\mu(x)(A_\mu(x)+(1/\kappa)\partial B/\partial x_\mu)+(1/2c^3\kappa^3)(j_\mu(x)n_\mu)^2, \tag{3}$$

where n_μ is the normal to the general space-like surface. The components of $A_\mu(x)$ and $B(x)$ commute like independent scalar fields so that the differentials in the commutation relations of $\phi_\mu(x)$ arise from the differential of $B(x)$ in the definition of $\phi_\mu(x)$.

Now $B(x)$ occurs in $H(x)$ as a scalar meson vector-interaction. If we perform the transformation[7]

$$\Psi = e^{-iS}\Psi', \tag{4}$$

where

$$S = (1/\hbar c\kappa)\int j_\mu(x)B(x)d\sigma_\mu, \tag{5}$$

on the generalized Schrödinger equation in the Schrödinger representation,[8] the total Hamiltonian is unaltered except for the removal of the last two terms in (3). In this form the free field Hamiltonians can be removed by a transformation to the interaction representation to give the Hamiltonian

$$H(x) = (1/c)j_\mu(x)A_\mu(x) = ig\bar{\psi}(x)\gamma_\mu\psi(x)A_\mu(x) \tag{6}$$

from which differentials of Δ_F-functions will not arise in the S-matrix. Since (5) commutes with the operator in (2), the subsidiary condition will not be altered by the transformation. Just as in electrodynamics, the suffix μ can take all four values in virtual effects but for real mesons it is restricted by the supplementary condition. This restriction will be automatically satisfied if the free meson lines are made to correspond to factors $\phi_\mu(x)$ in the integrals. Thus the Hamiltonian can be taken to be

$$H_1(x) = (1/c)j_\mu(x)\phi_\mu(x) - \hbar c\delta\kappa_0\bar{\psi}(x)\psi(x) - \tfrac{1}{2}\delta\kappa^2\phi_\mu^2(x) \tag{7}$$

in the calculation of the S-matrix provided internal meson lines correspond to factors

$$\langle P(A_\mu(x), A_\nu(y))\rangle_0 = \tfrac{1}{2}\hbar c\delta_{\mu\nu}\Delta_F(x-y). \tag{8}$$

The extra terms in $H_1(x)$ allow for the renormalisation of both nucleon and meson masses. The possible primitive divergents are the same as in electrodynamics. The integrals from square parts are also the same and thus introduce no new divergences. Hence a finite S-matrix can be obtained. If the mesons are charged there is an extra term in (6)[7] which cannot be treated by these methods.

A similar treatment is not possible for the pseudo-vector meson because the corresponding transformation does not remove the subsidiary pseudo-scalar field, but introduces a complicated interaction involving the subsidiary field in the power of an exponential.[7]

It is hoped to publish elsewhere a more detailed discussion of the derivation of (7) and the failure of Dyson's method in the other cases.

[1] F. J. Dyson, Phys. Rev. **75**, 486 (1949).
[2] P. T. Matthews, Phys. Rev. **76**, 684 (1949).
[3] F. J. Dyson, Phys. Rev. **75**, 1736 (1949).
[4] I am indebted to Mr. F. J. Dyson for pointing out a fundamental error in my original (unpublished) deduction on this point.
[5] E. C. G. Stückelberg, Helv. Phys. Acta. **11**, 225 (1938).
[6] Y. Miyamoto, Prog. Theor. Phys. **3**, 124 (1948).
[7] F. J. Dyson, Phys. Rev. **73**, 929 (1948); K. M. Case, Phys. Rev. **76**, 14 (1949).
[8] P. T. Matthews, Phys. Rev. **75**, 1270 (1949).

Electric Quadrupole Moments of Nuclei

G. J. Bene, P. M. Denis, and R. C. Extermann
Université de Genève, Geneva, Switzerland
August 29, 1949

THE rule, given by Gordy[1] in order to estimate the electric quadrupole moments Q for isotopic pairs having the same spin may be extended to isotopic pairs having different spin and to nuclei with Z values nearly equal.

The magnetic moment is a function of atomic number, spin, and quadrupole electric moment, other things being equal: (1) the spin decreases with a decrease of the magnetic moment; (2) the magnetic moment increases with Z; (3) if the quadrupole moment becomes more positive (or less negative for flattened nuclei), the magnetic moment appears to decrease.

With these rules, we can obtain further Q-values, absolute or relative. All the quadrupole electric moments as estimated by Gordy are in good agreement with these rules, which are cumulative. For instance, going from Ga^{71} to As^{75}, Z grows by two units, the spins remain the same, and the magnetic moment gets smaller. Therefore, we expect the nuclear quadrupole moment of As^{75} to be more positive, which turns out to be true.

According to these rules, the following Q-values can be expected:

Zn^{67} nucleus is less flattened than Cu^{65} and $Q(Zn^{67}) \sim = 0$,
Co^{59} nucleus is less flattened than Mn^{55} and $Q(Co) > Q(Mn)$,
Rb^{85} nucleus is less flattened than Rb^{87} and $Q(Rb^{85}) \sim = +30 \times 10^{-26}$ cm^2,
Sb^{123} nucleus is less flattened than Sb^{121} and $Q(Sb^{123}) \sim = -60 \times 10^{-26}$ cm^2.

[1] W. Gordy, Phys. Rev. **76**, 139 (1949).

On the Delayed Neutron Emitter $_7N^{17}$ *

R. A. Charpie, Kuan-Han Sun, and B. Jennings
Westinghouse Research Laboratories, East Pittsburgh, Pennsylvania
and
J. F. Nechaj
University of Pittsburgh, Pittsburgh, Pennsylvania
August 24, 1949

IT has been found by E. O. Lawrence and his associates[1] at California that when O and the elements immediately above it in atomic number are bombarded with 195-Mev deuterons, a delayed neutron emitter with a 4.14 ± 0.04 sec. half-life is formed. Alvarez[2] identified this delayed neutron emitter as N^{17} and Alvarez[3] and Hayward[4] determined the energy relationships in the β–n decay process. The production of N^{17} by bombarding elements of higher atomic number than fluorine with 195-Mev deuterons probably takes place by a spallation process. It is known that the yield of the delayed neutron emitter decreases with increasing atomic number of the target material.[5] The same nuclide was also produced by the $C^{14}(\alpha,\dot{p})N^{17}$ process by Sun, Jennings, Shoupp, and Allen[6] who found an upper limit of the $(\alpha,\dot{p})$ threshold of 16 Mev in agreement with Alvarez's measurements.

We may calculate the Q-values of the possible simple nuclear reactions by which N^{17} may be formed. Using Bethe's[7] value for the mass of O^{17} and Alvarez's value[3] for the $(N^{17}-O^{17})$ mass difference one obtains the mass of N^{17} to be 17.01385 a.m.u. Using Bethe's values for the other atomic masses, the Q-values for these reactions are given in Table I.

Because of the short half-lives of N^{16} and F^{20}, it is reasonable to consider the stable, although rare, nuclides O^{17} and O^{18} as the starting elements for the production of N^{17}. The following experiment was performed to determine whether N^{17} can be made by the $O^{17}(n,\dot{p})N^{17}$ process. Neutrons of known maximum energy were produced by bombarding a thick LiF or C target with a 14-Mev 2μa external deuteron beam from the University of Pittsburgh cyclotron. (Q-values are 15.0 Mev for Li^7, 10.7 Mev for F and -0.28 Mev for C.) Our previous measurements of neutron fluxes from various targets in this cyclotron indicate that the total number of neutrons produced per μa by the LiF and C targets is about the same and that only the energy of the neutrons, as inferred from the Q-values, is different. Thus it follows that the number of neutrons with energy above 8 Mev is greater for LiF than C targets. Neutrons from these sources were used to bombard 500 g of water containing O^{17} in its natural isotopic proportion.

TABLE I. Q-values of various reactions by which N^{17} is formed.

Reaction	Q-value
$N^{16}(n,\gamma)N^{17}$	5.9 Mev[a]
$O^{17}(n,\dot{p})N^{17}$	-7.9 Mev
$O^{18}(n,d)N^{17}$	-13.7 Mev
$N^{16}(d,\dot{p})N^{17}$	3.7 Mev
$O^{18}(\gamma,\dot{p})N^{17}$	-15.9 Mev
$F^{20}(n,d)N^{17}$	> -4.3 Mev and < 0.4 Mev

[a] The mass of N^{16} is taken as 16.01121 after L. D. Wyly, Phys. Rev. **76**, 462 (1949).

An enriched $B^{10}F_3$ proportional counter, surrounded with 2 inches of paraffin was placed immediately behind the water container. The delayed neutrons from the reaction were counted by this counter, the pulses from which were amplified by an Atomic Instrument Company linear amplifier and recorded as a function of time by a Brush pen recorder connected through the scaling elements of a Tracerlab auto scaler. Selection of the scaling factor provided either fast or slow recording. The water was bombarded by neutrons from the LiF or the C source for about 20 sec., after which the cyclotron was shut off. The delayed neutron intensity was recorded. A half-life of 4.5 ± 1.0 sec. was found, indicating the existence of N^{17}.

The delayed neutron count without the water target was about one-third of that observed when the water target was in position. This high background is probably due to the cooling water in the cyclotron itself. However, when neutrons of lower maximum energy from C were used to bombard the water, the number of delayed neutrons was reduced by a factor of about 15 because of the smaller number of high energy neutrons from the C source. It should be noted that the reaction energy of the $O^{17}(n,p)N^{17}$ process is 8 Mev.

The reaction $O^{18}(\gamma,p)N^{17}$ is unlikely, even though the isotopic content of O^{18} is five times that of O^{17} in normal water, because the cross section for a (γ,p) process is, in general, much smaller than that for an (n,p) process. However, to test the possibility of the formation of N^{17} by an $O^{18}(\gamma,p)N^{17}$ process in our experimental conditions, a four-inch lead shield was placed between the LiF and the water target. The reduction of about 35 percent in the number of delayed neutrons from the water target due to the absorption of primary neutrons in the lead was the same as the measured absorption of the primary neutron beam itself. This indicates that the number of atoms of N^{17} formed is proportional to that of the incident neutrons and that neutrons rather than γ-rays are responsible for the production of N^{17}.

The average cross section for the process has been roughly estimated to be 10^{-26} cm^2. This figure may be off by a factor of 10, but it does serve to illustrate that the order of magnitude of the cross section of the process is comparable with other (n,p) reactions.

It is suggested that the reaction $O^{18}(\gamma,p)N^{17}$ may be induced in a similar fashion where strong γ-ray sources of over 16 Mev are available.

* Partially assisted by the Joint Program of ONR and AEC.
[1] Knable, Lawrence, Leith, Moyer, and Thornton, Phys. Rev. **74**, 1217A (1948).
[2] L. W. Alvarez, Phys. Rev. **74**, 1217A (1948).
[3] L. W. Alvarez, Phys. Rev. **75**, 1127 (1949).
[4] E. Hayward, Phys. Rev. **75**, 917 (1949).
[5] W. E. Chupp and E. M. McMillan, Phys. Rev. **74**, 1217A (1948).
[6] Sun, Jennings, Shoupp, and Allen, Phys. Rev. **75**, 1302A (1949).
[7] H. A. Bethe, *Elementary Nuclear Theory* (John Wiley and Sons, Inc., New York, 1947), except that the mass of neutron is taken as 1.00899.

New Radioactive Isotopes of Dysprosium*

B. H. KETELLE
Oak Ridge National Laboratory, Oak Ridge, Tennessee
September 6, 1949

ALTHOUGH two isomers of Dy^{165} have been established by the studies of several investigators,[1] no activities have been assigned definitely to other dysprosium isotopes.

A sample of dysprosium oxide,[2] highly purified by ion exchange techniques, was irradiated with slow neutrons in the Oak Ridge National Laboratory reactor. The decay curve of the induced activity was resolved into three components with periods of 138 min., 81 hr., and 146 days. The 138-min. activity is known to belong to Dy^{165}. Feather analysis of aluminum absorption curves showed that there were two beta-groups with maximum energies of 0.4 Mev and 1.8 Mev associated with the decay of the 81-hr. activity. The 146-day activity appeared to decay largely by orbital electron capture.

Because of the difficulty of preparing pure rare earths and the prevalence of high activation cross sections among these elements, it is essential to make chemical separations before assigning activities. Therefore an ion exchange column separation[3] was performed on another sample of the dysprosium oxide which had been irradiated for five months. The conditions were such that holmium, dysprosium, and terbium would be separated. The presence of the 27.3-hr. activity of Ho^{166} was demonstrated. Since the dysprosium which was irradiated was known to be extremely pure, it was suspected that the holmium activity was produced by double neutron capture as represented by either or both of the following two series of reactions:

$$Dy^{164} \xrightarrow{n\gamma} Dy^{165} \xrightarrow[138\text{ min.}]{\beta} Ho^{165} \xrightarrow{n\gamma} Ho^{166} \xrightarrow[27.3\text{ hr.}]{\beta-} Er^{166}, \quad (1)$$

$$Dy^{164} \xrightarrow{n\gamma} Dy^{165} \xrightarrow{n\gamma} Dy^{166} \xrightarrow{\beta} Ho^{166} \xrightarrow[27.3\text{ hr.}]{\beta} Er^{166}. \quad (2)$$

The dysprosium fraction from which the holmium had been removed showed growth rather than decay. Therefore it appears certain that at least part of the holmium activity observed had been formed according to Eq. (2). In order to verify this hypothesis a second chemical separation of holmium from the dysprosium was made. Again Ho^{166} was identified. The analysis of the growth curve of the holmium deficient dysprosium sample showed that an activity with an 80-hr. half-life was decaying to a daughter whose half-life was 27 hr. Furthermore, it was possible to obtain an aluminum absorption curve on the freshly purified dysprosium. Feather analysis of this curve showed that the 80-hr. activity emits a beta whose maximum energy is 0.4 Mev. After equilibrium had been established between the 80-hr. parent and the 27-hr. daughter, an aluminum absorption curve indicated the presence of the 0.4-Mev beta and also a 1.8-Mev beta. Since both the half-life and the energy of the daughter activity agree with those of Ho^{166}, we conclude that the 80-hr. parent is Dy^{166}.

After the 80-hr. activity had decayed out of these dysprosium samples, there was a residual activity with a half-life of 140 ± 10 days. Since absorption curves in copper and tantalum show that this activity decays by orbital electron capture, it must belong to Dy^{157} or Dy^{159}. The decay has not been followed sufficiently long to ascertain whether there is a longer lived activity of Tb^{157} present.

From the ratio of 80-hr. activity to 140-min. activity in a sample of dysprosium which had undergone no chemical separation after irradiation, an approximate value of the neutron activation cross section of Dy^{165} was computed to be 5000 barns.

A detailed discussion of these studies is being prepared for publication in the near future.

* This document is based on work performed under Contract Number W-7404 eng 26 for the Atomic Energy Project at Oak Ridge National Laboratory.
[1] Summarized by G. T. Seaborg and I. Perlman, Phys. Rev. **20**, 585 (1948).
[2] The author wishes to thank Mr. D. H. Harris who kindly supplied this extremely pure material.
[3] B. H. Ketelle and G. E. Boyd, J. Am. Chem. Soc. **69**, 2800 (1947).

Detection of Antiferromagnetism by Neutron Diffraction*

C. G. SHULL
Oak Ridge National Laboratory, Oak Ridge, Tennessee
AND
J. SAMUEL SMART
Naval Ordnance Laboratory, White Oak, Silver Spring, Maryland
August 29, 1949

TWO necessary conditions for the existence of ferromagnetism are: (1) the atoms must have a net magnetic moment due to an unfilled electron shell, and (2) the exchange integral J relating to the exchange of electrons between neighboring atoms

must be positive. This last condition is required in order that spin states of high multiplicity, which favor ferromagnetism, have the lowest energy. It seems certain that for many of the non-ferromagnetic substances containing a high concentration of magnetic atoms the exchange integrals are negative. In such cases the lowest energy state is the one in which the maximum number of antiparallel pairs occur. An approximate theory of such substances has been developed by Néel,[1] Bitter,[2] and Van Vleck[3] for one specific case and the results are briefly described below.

Consider a crystalline structure which can be divided into two interpenetrating lattices such that atoms on one lattice have nearest neighbors only on the other lattice. Examples are simple cubic and body-centered cubic structures. Let the exchange integral for nearest neighbors be negative and consider only nearest neighbor interactions. Theory then predicts that the structure will exhibit a Curie temperature. Below the Curie temperature the spontaneous magnetization *vs.* temperature curve for one of the sub-lattices is that for an ordinary ferromagnetic material. However, the magnetization directions for the two lattices are antiparallel so that no net spontaneous magnetization exists. At absolute zero all of the atoms on one lattice have their electronic magnetic moments aligned in the same direction and all of the atoms on the other lattice have their moments antiparallel to the first. Above the Curie temperature the thermal energy is sufficient to overcome the tendency of the atoms to lock antiparallel and the behavior is that of a normal paramagnetic substance.

Materials exhibiting the characteristics described above have been designated "antiferromagnetic." Up to the present time the only methods of detecting antiferromagnetism experimentally have been indirect, e.g., determination of Curie points by susceptibility and specific heat anomalies. It has occurred to one of us (J.S.S.) that neutron diffraction experiments might provide a direct means of detecting antiferromagnetism. In an antiferromagnetic material below the Curie temperature a rigid lattice of magnetic ions is formed and the interaction of the neutron magnetic moment with this lattice should result in measurable coherent scattering. Halpern and Johnson[4] have shown that the magnetic and nuclear scattering amplitudes of a paramagnetic atom should be of the same order of magnitude and this result has been qualitatively verified by experimental investigators.[5] At the time of the above suggestion, an experimental program on the determination of the magnetic scattering patterns for various paramagnetic substances (MnO, MnF_2, $MnSO_4$ and Fe_2O_3) was underway at Oak Ridge National Laboratory and room temperature examination had shown (1) a form factor type of diffusion magnetic scattering (no coupling of the atomic moments) to exist for MnF_2 and $MnSO_4$, (2) a liquid type of magnetic scattering (short-range order coupling of oppositely directed magnetic moments) to exist for MnO and (3) the presence of strong coherent magnetic diffraction peaks at forbidden reflection positions for the α-Fe_2O_3 lattice. The latter two observations are in complete accord with the antiferromagnetic notion since the Curie points for MnO and α-Fe_2O_3 are respectively[6] 122°K and 950°K.

Figure 1 shows the neutron diffraction patterns obtained for powdered MnO at room temperature and at 80°K. The room temperature pattern shows coherent nuclear diffraction peaks at the regular face-centered cubic reflection positions and the liquid type of diffuse magnetic scattering in the background. It should be pointed out that the coherent nuclear scattering amplitudes for Mn and O are of opposite sign so that the diffraction pattern is a reversed NaCl type of pattern. The low temperature pattern also shows the same nuclear diffraction peaks, since there is no crystallographic transition in this temperature region,[7] and in addition shows the presence of strong magnetic reflections at positions not allowed on the basis of the chemical unit cell. The magnetic reflections can be indexed, however, making use of a magnetic unit cell twice as large as the chemical unit cell. A complete description of the magnetic structure will be given at a later date.

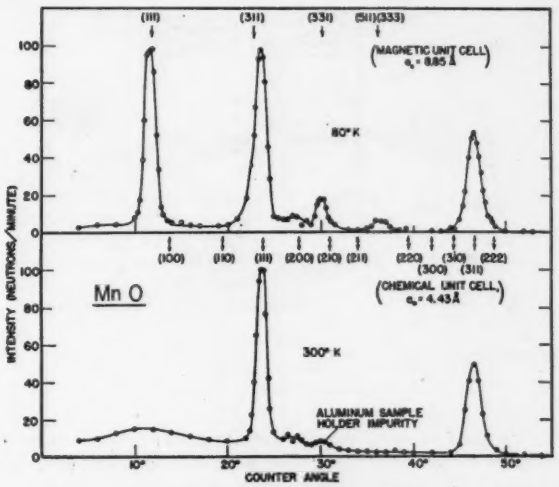

FIG. 1. Neutron diffraction patterns for MnO at room temperature and at 80°K.

In conclusion it appears that neutron diffraction studies of antiferromagnetic materials should provide a new and important method of investigating the exchange coupling of magnetic ions.

* This work was supported in part by the ONR.

[1] L. Néel, Ann. de physique **17**, 5 (1932).
[2] F. Bitter, Phys. Rev. **54**, 79 (1938).
[3] J. H. Van Vleck, J. Chem. Phys. **9**, 85 (1941).
[4] O. Halpern and M. H. Johnson, Phys. Rev. **55**, 898 (1939).
[5] Whittaker, Beyer, and Dunning, Phys. Rev. **54**, 771 (1938); Ruderman, Havens, Taylor, and Rainwater, Phys. Rev. **75**, 895 (1949); and also unpublished work at Oak Ridge National Laboratory.
[6] Bizette, Squire, and Tsai, Comptes Rendus **207**, 449 (1938).
[7] B. Ruhemann, Physik. Zeits. Sowjetunion **7**, 590 (1935).

Imprisonment of Resonance Radiation in Mercury Vapor

D. ALPERT, A. O. MCCOUBREY, AND T. HOLSTEIN
Westinghouse Research Laboratories, East Pittsburgh, Pennsylvania
August 29, 1949

THE term "imprisonment of resonance radiation" describes the situation wherein resonance radiation emitted in the interior of a gas-filled enclosure is strongly absorbed by normal gas atoms before it can get out; the eventual escape of a quantum of radiation then takes place only after a number of successive atomic absorptions and emissions. The phenomenon was first observed by Zemansky[1] who measured the time of decay, T, of diffuse resonance radiation from an enclosure of optically excited mercury vapor, after the exciting beam of 2537A light was cut off. T was found to depend upon gas density and enclosure geometry; at densities around 10^{15}/cc, T attained values of the order of 10^{-4} sec., a thousand times greater than the natural lifetime of an excited 6^3P_1 atom.

On the theoretical side, a number of treatments[2-6] have been presented. The early work[2-4] is reviewed in reference 6. In the latter paper (as well as in that of Bieberman[5]), the transport of resonance quanta is described by a Boltzmann-type integro-differential equation for the density of excited 6^3P_1 atoms; the solution of this equation by the Ritz variational method gives accurate values for the decay time, T. It was found that T depends not only on vapor density and enclosure geometry, but also on the spectral line shape of the resonance radiation, as pointed out earlier by Kenty;[4] explicit results were obtained for the case of Doppler broadening and plane-parallel enclosure geometry. Most recently, unpublished calculations have extended the analysis to enclosures of the form of infinite circular cylinders and to a variety of line shapes.

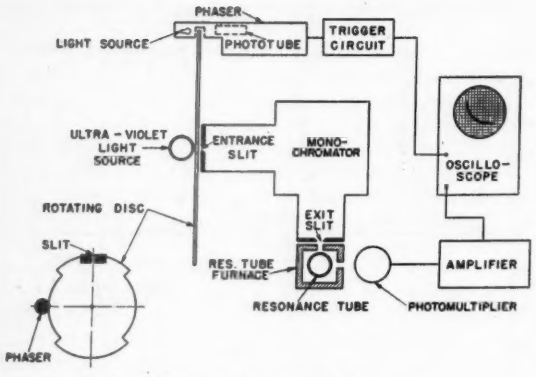

FIG. 1. Schematic diagram of apparatus.

With regard to the comparison of the theory with Zemansky's results, we may remark that, while order-of-magnitude agreement is obtained, the quantitative comparison is not altogether satisfactory. Actually, as pointed out in reference 6, both the geometry of the enclosures, as well as the limited pressure range over which the measurements were taken, are not very suitable for comparison purposes. For these reasons and because of the considerable advances in experimental techniques—i.e., in the preparation of impurity-free gas systems, in the measurement of radiation intensities by use of the photo-multiplier tube, and in the measurement of time by synchroscope techniques—we have performed a modernized version of Zemansky's experiment under conditions of vapor density and enclosure geometry appropriate for comparison with theory.

The apparatus is shown schematically in Fig. 1. The 2537A light is obtained from a mercury discharge source and isolated by a monochromator. The light is turned on and off by a sectored disk rotating (at about 10,000 r.p.m.) past the entrance slit of the monochromator. It is then incident on the resonance tube, a carefully evacuated and sealed-off silica glass cylinder containing a small quantity of mercury. A phaser is used to synchronize the triggering of the oscilloscope sweep circuit with the rotation of the disk. To adjust the pressure of mercury vapor, which is in equilibrium with the liquid mercury, the resonance tube (1.3 cm in diameter, 13.5 cm long) is placed in a specially designed furnace whose temperature can be varied at will. The diffuse radiation coming from the resonance tube is incident on a photo-multiplier, and the resulting signal is amplified and displayed on an oscilloscope. Observation of the decay trace for various furnace temperature gives directly the decay time T as a function of vapor density N.

The experimental results are indicated by the black circles in Fig. 2. For N less than 1.5×10^{16}/cc, the line shape is determined predominantly by Doppler broadening; for this case the theory has been worked out[7] and is represented by the solid curve. For N greater than 1.5×10^{16}/cc, the dual complications of pressure broadening and hyperfine structure render the calculations more difficult; in this region, upper and lower limits to the theory are given. Agreement between measurements and theory is seen to be quite satisfactory. Zemansky's observation that the time

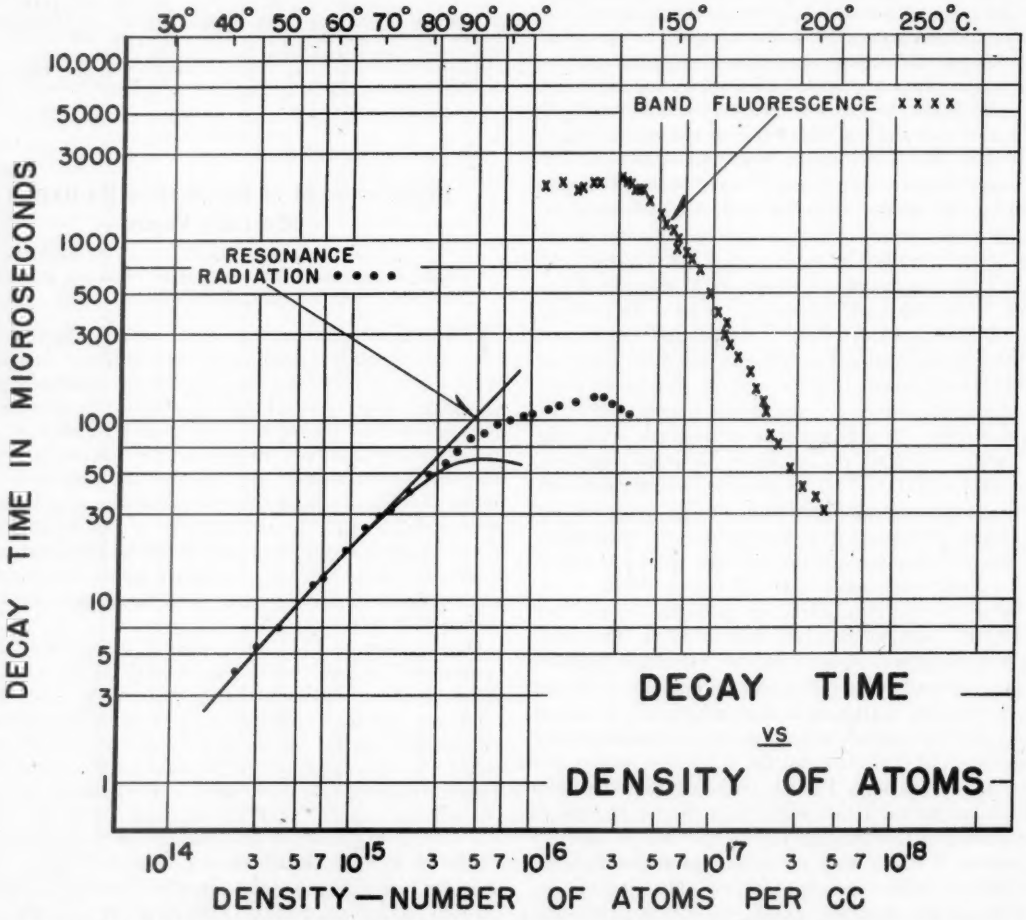

FIG. 2. Black circles represent experimental measurements of decay time of resonance radiation; the solid curves, the upper and lower limits of the theoretical prediction. The crosses represent measurements of the band fluorescence of Hg_2, which is discussed in the following letter.

constant is appreciably lowered for N greater than 7×10^{15}/cc is not confirmed. Further experimental details and results will be presented in a later publication.

[1] M. W. Zemansky, Phys. Rev. 29, 513 (1927).
[2] K. T. Compton, Phys. Rev. 20, 283 (1922).
[3] E. A. Milne, J. Math. Soc. London 1, 1 (1926).
[4] C. Kenty, Phys. Rev. 42, 823 (1932).
[5] L. M. Bieberman, J. Exper. Theor. Phys. U.S.S.R. 17, 416 (1947). The analysis of this paper is based on the same integro-differential equation as that of reference 6. Since it is applied only to the steady-state case of a continuously incident beam, the results cannot be used in the evaluation of decay experiments.
[6] T. Holstein, Phys. Rev. 72, 1212 (1947).
[7] The formula used is: $T=\frac{1}{2}k_0R(\pi\log k_0R)^{\frac{1}{2}}$, where R is the cylinder radius and k_0 the absorption coefficient at the center of a Doppler broadened line. For mercury vapor k_0 is given in terms of vapor density N and absolute temperature θ by the expression: $k_0=(2.19\times10^{-12}N)/\theta^{\frac{1}{2}}$ cm^{-1}.

Persistence of Band Fluorescence in Mercury Vapor

T. Holstein, D. Alpert, and A. O. McCoubrey
Westinghouse Research Laboratories, East Pittsburgh, Pennsylvania
August 29, 1949

When mercury vapor is excited with 2537A resonance radiation it emits not only the resonance line itself but also a continuous spectrum[1] whose main constituents are two bands in the visible and near ultraviolet regions. The visible band extends from 4000A to 5300A with a maximum intensity at 4850A; the near ultraviolet band is contained in a range from 3000A to 3700A with maximum intensity at 3350A.

The persistence of this band fluorescence after the removal of the exciting light, first discovered by Phillips,[2] was investigated rather extensively by Lord Rayleigh with the aid of a moving-vapor-stream technique. In an experiment[3] in which the pressure, although not measured, was presumably kept at a minimum, this author observed a decay time of 1.8 millisec. for the fluorescence.

Interpretations of the different observations in terms of excited states of Hg_2 have been advanced by a number of authors. Of these, the most recent, due to Mrozowski,[4] is illustrated in Fig. 1. Optical transitions from the excited levels to the ground state give rise to the two bands previously mentioned, as well as to the 2540A band, closely adjacent to the resonance line. Two of these transitions, ($^3\Pi_u-{}^1\Sigma_g^+$) and ($^3O_u^+-{}^1\Sigma_g^+$), are presumed to occur with a probability of the same order as that of the corresponding atomic transitions ($^3P_1-{}^1S_0$), i.e., $\sim10^7$ sec.$^{-1}$. The transition ($^3O_u^--{}^1\Sigma_g^+$) is forbidden for pure Case c classification of the molecular levels; the experimentally observed presence of the 4850A band is to be attributed to a small deviation from Case c, presumably in the direction of Case b. Rough estimates indicate that the lifetime of the $^3O_u^-$ state may well be of the order of the persistence time (1.8 millisec.) observed by Lord Rayleigh. One is thus led to assume that the $^3O_u^-$ state acts as the primary reservoir of long-lived molecular excitation; the identity of decay times of both the visible and near ultraviolet bands is explained as arising from the continual replenishment of the $^3\Pi_u$ level from the $^3O_u^-$ level by collisions of the second kind.

In our experiment on imprisoned resonance radiation, described in the preceding letter, band fluorescence first showed up at densities of about $N=10^{16}$/cc, giving rise to a composite trace on the oscilloscope. From this trace one could discern two decay processes, the shorter of which we associated with resonance radiation, the longer with molecular fluorescence. This interpretation was confirmed by the use of glass transmission filters with which we could eliminate resonance radiation and observe a simple exponential decay of the fluorescence alone; the near ultraviolet and visible bands were found to decay at the same rate. Measured values of the common time constant are given in Fig. 2 of the preceding letter. We note that the low pressure limit of T agrees quite well with Lord Rayleigh's value (1.8 millisec.).

It might be supposed that the decrease in T with increasing density is actually due to the simultaneous increase of temperature according to the saturated vapor pressure curve of mercury.[5] The absence of such an effect was demonstrated in a preliminary experiment in which, at a given pressure, two different observation temperatures were provided by the use of two furnaces of somewhat differing design. It was found that, at constant pressure, the time constant actually *increases* with temperature. This observation is in sharp disagreement with the interpretations based in Fig. 1, according to which a rise in temperature would enhance the probability of jumps from the $^3O_u^-$ level to the $^3\Pi_u$ level by collisions of the second kind. An effect of this type would shorten the observed time constant since the $^3\Pi_u$ state is presumed to decay immediately (10^{-7} sec.), emitting the 3350A band.

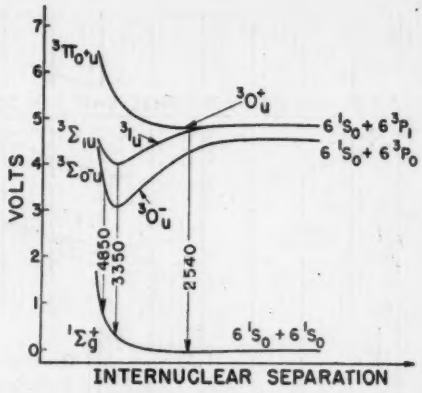

FIG. 1. Energy level diagram of Hg_2 according to Mrozowski (see reference 4(b), Fig. 1), with slight alterations. For large internuclear distances, the levels are described in terms of states of the separated atoms; for intermediate and small internuclear distances, this classification is replaced by those of Hund's Cases c and a, respectively.

According to Fig. 1, we would also expect the ratio of the intensities of the two bands, I_{4850}/I_{3350}, to decrease with increasing temperature. This has indeed been observed by Lord Rayleigh[3] and by Mrozowska.[6] The latter author, in addition, observed I_{4850}/I_{3350} to increase with pressure at constant temperature. In our experiments, in which the pressure and temperature varied interdependently according to the saturated vapor curve, an increase in I_{4850}/I_{3350} was also observed with increasing furnace temperature. The effect of pressure variation on the intensity ratio has not been explained in terms of the energy level scheme in Fig. 1.

Further experiments in which the pressure and temperature can be varied independently are now in progress.

[1] See, for example, W. Finkelnburg, *Kontinuerliche Spektren* (Verlag. Julius Springer, Berlin, 1938), Section 60, for a short survey and bibliography.
[2] F. S. Phillips, Proc. Roy. Soc. 89, 39 (1913).
[3] Lord Rayleigh, Proc. Roy. Soc. 114, 620 (1927).
[4] S. Mrozowski, (a) Zeits. f. Physik 106, 458 (1937); (b) Rev. Mod. Phys. 16, 153 (1944), especially pp. 160, 161.
[5] Actually, the temperature of the furnace in the region of observation is somewhat higher than the temperature where the liquid mercury condenses.
[6] I. Mrozowska, Acta Phys. Polonica 2, 81 (1933).

Nuclear Magnetic Resonance Shift in Metals*

W. D. Knight**
Brookhaven National Laboratory, Upton, Long Island, New York
September 1, 1949

The purpose of this letter is to report the observation of a shift in the nuclear magnetic resonance frequencies from expected values in five metals, Li, Na, Al, Cu, and Ga, in magnetic fields ranging from five to ten thousand gauss, using an automatic search type radiofrequency spectrometer.[1] The magnitudes of the signals observed were in all cases at least twenty times noise amplitude, and in all cases the resonance frequencies, for constant magnetic field, were higher by tenths of a percent than the resonance frequencies observed in salts of the corresponding metals. The absolute accuracy of the frequency measurements was about 0.01

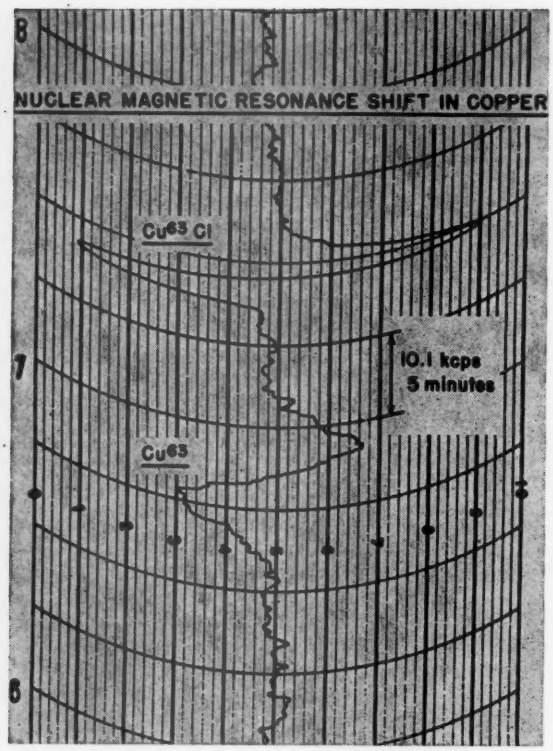

FIG. 1. The resonances are both due to the Cu^{63} isotope. The more intense line is due to CuCl powder. The broader line occurs in Cu metal powder at a frequency higher by about 25 kc.p.s. at a resonance frequency of about 10 mc.p.s. The two dry powders are mixed in the proportion of 100 parts CuCl to 64 parts Cu by weight.

percent, while small frequency differences were accurate to about 0.002 percent of the average frequency.

The lithium and sodium resonances were observed in shavings of the respective metals in kerosene, while the copper and aluminum resonances occurred in metal powders which had been suspended in melted paraffin and subsequently cooled in a mold. The gallium metal was sealed in several capillary tubes, each about one millimeter in diameter. These tubes were placed in the r-f coil with their axes parallel to the coil. The ambient temperature in the case of gallium was above the melting point of that metal. The gallium resonance was not observed when the temperature was lowered below the melting point.

This shift has been observed in separate samples of a particular metal and its salts and in samples of a metal mixed with its salt. In the latter situation, one could be certain that the resonances occurred in exactly the same applied field. Observations have been made on separate runs for precise frequency comparisons, and on single continuous runs (see Fig. 1) in order to display the effect qualitatively. The shift for a given isotope is proportional to the resonance magnetic field (or frequency) within the limits of error stated above. Values of the observed shifts and line widths are given in Table I. It is to be noted that the shift is greater in the heavier metals, a trend which follows qualitatively that of the known values for hyperfine structure splitting.

TABLE I. Values of the observed shifts and line widths.

Isotope	Salt*	Resonance frequency in salt (mc.p.s.)	Frequency shift in metal (kc.p.s.)	Line width in metal (kc.p.s.)	Line width in salt (kc p.s.)
Li^{7}	LiCl	9.436	$+3.4\pm0.2$	1.4 ± 0.2	1.2 ± 0.2
Na^{23}	NaCl	10.123	+10.5	0.5	1.4
Al^{27}	$AlCl_3$	10.145	+16.2	9.3	0.8
Cu^{63}	CuCl	10.321	+23.7	7.4	2.6
Cu^{65}	CuCl	11.050	+25.6	5.8	2.6
Ga^{71}	$GaCl_3$	7.409	+33.3	1.5	3.0

* With the exception of CuCl, which was compressed powder, the samples were in aqueous solution.

C. H. Townes has suggested that the shift may be due to the paramagnetic effect of the conduction electrons in the vicinities of the metal nuclei. If this is true, the shift in the metal should be proportional to the hyperfine splitting of the ground state of the free atom. Suppose, then, for sodium that: 1. There is one conduction electron per nucleus on the average in the metal; 2. the value at the metal nucleus of the wave function of this average conduction electron is the same as of the valence electron of the normal free atom; 3. the bulk susceptibility (corrected to give the net paramagnetic part)[2] divided by the average density of conduction electrons is a measure of the number of conduction electrons which contribute to the shift. Then the product of the susceptibility per electron and the applied magnetic field should give the average effective magnetic moment per electron. The ratio of this quantity to the Bohr magneton should be equal to the ratio of the observed shift in the metal to the hyperfine splitting in the free atom, taken in energy units. Here it is to be noted that the total hyperfine splitting[3] should be modified before making the above comparison. First, for the sodium nucleus, three equal transitions are possible in the applied magnetic field, and, second there is a complete Paschen-Back effect when the field is applied to the metal. The effect of these considerations is to reduce the hyperfine splitting by a factor of four before comparing the above ratios.

The results of this simple calculation show that the predicted value of the shift in sodium to be larger than that observed by about fifty percent. A more detailed analysis is being made in an effort to improve this calculation. It is thought that a closer examination of the respective wave functions (see 2, above) will yield information which leads to a closer agreement.

Further experimental work is being done to determine the magnitude of this effect in these and other metals and alloys at varying temperatures, and to determine the possible existence of a shift in resonance frequency when comparing two or more salts of the same metal. Preliminary measurements show that the latter shift, if it exists, is certainly less than 0.001 percent among similar salts of a given metal (CuCl, CuBr, CuI). More accurate measurements are under way to confirm the existence of shifts of about 0.01 percent among some phosphorous compounds. The magnitude of this shift is of the order of the line width or slightly larger.

The author's thanks are due Dr. V. W. Cohen, who has directed this work, and Dr. C. H. Townes for many helpful discussions.

* Work performed at Brookhaven National Laboratory under contract with the AEC.
** Permanent address: Physics Department, Trinity College, Hartford, Connecticut.
[1] R. V. Pound, Phys. Rev. **72**, 527 (1947).
[2] F. Seitz, Phys. Rev. **58**, 633 (1940).
[3] M. Fox and I. I. Rabi, Phys. Rev. **48**, 746 (1935).

A New Determination of the Relative Abundance of Rhenium in Nature*

HARRISON BROWN AND EDWARD GOLDBERG
Institute for Nuclear Studies, University of Chicago
AND
Argonne National Laboratory, Chicago, Illinois
August 29, 1949

IT has become generally recognized that a most peculiar discontinuity exists at $A=185$ and $A=187$ in the curve representing the relative abundances of nuclear species as a function of mass number.[1-3] It is of interest to determine whether the observed low abundances of Re^{185} and Re^{187} are real, or whether the discontinuity is the result of faulty determinations of rhenium concentrations in meteorites by previous investigators.[4]

In view of the chemical properties of rhenium, one would expect the element to be concentrated primarily in the metal phase of the earth and in the metal phase of meteoritic matter. Conse-

TABLE I. The rhenium contents of five iron meteorites.

Meteorite	Class	Rhenium content (parts per million)
Altonah	Off	0.87
Henbury	Om	1.4
Goos Lake	Og-Om	0.28
Canyon Diablo	Og	0.28
Xiquipilco	Om	0.25
Average		0.62

quently, five iron meteorites have been examined for rhenium utilizing the neutron activation method of analysis described elsewhere.[5,6] The results of the new determinations are given in Table I.

Each of the individual determinations is precise to about ten percent. The average of only five meteorite specimens has poor statistical precision, and as a result the value for the rhenium abundance in iron meteorites may be given as 0.6 ± 0.2 part per million. Nevertheless, it can be seen that the abundance of rhenium is probably at least 50 times greater than the abundance as reported by the Noddacks.

It is of interest to compare the abundances of odd nuclear species, of the sequence beginning with rhenium, all of which are associated with elements which concentrate in the metal phase. The figures are shown in Table II, and are taken from a recent compilation by one of us.[7]

TABLE II. The abundances of several odd heavy nuclear species.

Species	Re^{185}	Re^{187}	Os^{189}	Ir^{191}	Ir^{193}	Pt^{195}	Au^{197}
Abundance (atoms/10^7 atoms Si)	1.1	1.9	5.6	5.4	8.6	29	8.2

The platinum value is probably too high, but the osmium and gold values should be quite reliable. It appears that in this region of the abundance curve, the abundance increases significantly with increasing mass number.

* Declassified April 13, 1949, Unclassified Areas Committee, Argonne National Laboratory, #UAC-82.

[1] V. M. Goldschmidt, Geochem. Verteilungs. Elemente Atom-arten. Oslo, IX (1938).
[2] H. Suess, Zeits. f. Naturforschung 2a, 606 (1947).
[3] F. C. Frank, Proc. Phys. Soc. London 60, 211 (1948).
[4] I. and W. Noddack, Naturwiss. 35, 59 (1930).
[5] H. Brown and E. Goldberg, Science 109, 347 (1949).
[6] E. Goldberg and H. Brown, *Analytical Chemistry* (in press).
[7] H. Brown, Rev. Mod. Phys. (to be published).

Cloud-Chamber Study of High Energy Positrons from Na^{22} *

KENNARD H. MORGANSTERN AND KARL P. W. WOLF
Washington University, St. Louis, Missouri
August 26, 1949

THE radioactivity of Na^{22} has been investigated by a number of physicists. It has been found to have a half-life of 3.0 yr., to give a positron spectrum whose end point is at 0.56 Mev, and to have gamma-photons of 1.3 Mev energy.[1-3] The transition to the ground state is found to be highly forbidden empirically. However, there are slight indications of very weak, high energy tails to the regular positron spectrum indicating the possibility of the presence of a higher energy positron spectrum.[4]

Feenberg[5] concludes from a comparison of the Ne^{22} to Na^{22} transition with that of Be^{10} and B^{10} that a weak, high energy positron spectrum should be present and that its ratio to that of the normal positron spectrum should be of the order of one to ten thousand.

An investigation was made in a cloud chamber to determine the energy and frequency of the higher energy positrons. The chamber employed was 25 cm in diameter and filled with a mixture of hydrogen and alcohol vapor. A weak source of Na^{22} was placed on a thin aluminum backing and suspended in the chamber. A glass baffle also was suspended in the chamber to help distinguish positron tracks from tracks of electrons ejected by gamma-rays at the source holder. The chamber was in a pulsed magnetic field of 700 gauss.

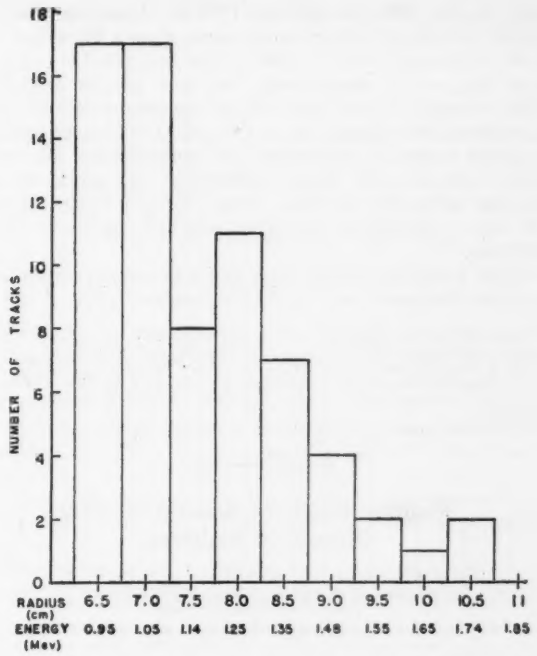

FIG. 1. Histogram of higher energy positron tracks from Na^{22}.

Approximately 6000 pictures were taken with sources of varying intensities. Sixty-nine tracks were definitely identified as high energy positron tracks. Their histogram is given in Fig. 1. No significance can be attached to the shape of the histogram because of many difficulties in the method (thick sources, poor resolution, poor geometry). However, the histogram does indicate the presence of a high energy positron spectrum, and the end point agrees satisfactorily with what would be expected in a transition of the Na^{22} directly to the ground state of Ne^{22}.

At best only a rough estimate could be made of the probability of this occurrence. A very weak source was used to determine the total number of tracks in a single expansion. Comparing then the activity of the weak source with the stronger ones by use of an auxiliary Geiger counter, the number of tracks from the latter could be estimated. It was then calculated that the aggregate of

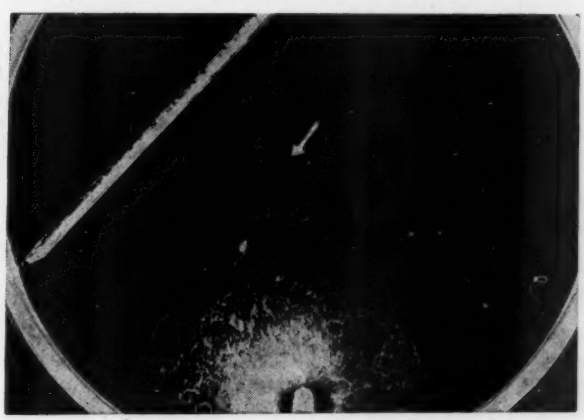

FIG. 2. Typical cloud-chamber photograph of high energy positron track. Arrow indicates positron track whose radius is 7.5 cm and energy 1.14 Mev.

tracks in the 6000 pictures was 1.8×10^6. Comparison of this number with the 69 higher energy tracks gives a branching ratio of one to an upper limit of 26,000. It was only possible to give an upper limit to this phenomenon; the total number of positron tracks belonging to the higher energy spectrum would be higher than the number counted for two reasons. First, tracks emerging at certain angles are obscured by the dense cloud of low energy tracks. Secondly, only those of sufficiently high energy to reach the glass baffle were included. Those tracks of energy less than 0.95 Mev could not be identified positively as tracks due to positrons.

Figure 2 exhibits a typical case of a high energy positron originating at the source and stopping in the glass baffle.

* Assisted by the Joint Program of the ONR and AEC.
[1] Good, Peasles, and Deutsch, Phys. Rev. **69**, 313 (1946).
[2] G. T. Seaborg and I. Perlman, Rev. Mod. Phys. **20**, 585 (1948).
[3] F. Oppenheimer and E. P. Tomlinson, Phys. Rev. **56**, 858 (1939).
[4] Private communication with G. Owen and J. Townsend of this laboratory.
[5] E. Feenberg and K. C. Hammack, Phys. Rev. **75**, 1877 (1949).

Positive Particles Associated with Beta-Ray Emitters

K. L. Erdman, G. T. Kokotailo,* and D. B. Scott
Department of Physics, University of Alberta, Edmonton, Alberta, Canada
August 29, 1949

In a nine-inch cloud chamber using air at atmospheric pressure, a search has been made for the positive particles reported to accompany the decay of certain beta-ray sources.[1,2] Stereoscopic photographs of sources S^{35}, UX, $Ra(D+E)$ and P^{32} were taken, the chamber being illuminated by a beam of light approximately one inch in height. A lead foil, 34 mg/cm² was stretched across the chamber ten cm from the source. Collimated and uncollimated sources were used.

An initial count with an uncollimated UX source giving approximately 50 tracks per picture produced 0.1 positive tracks per electron. Count of apparent pairs produced by electrons in the lead foil gave a cross section of the order of 10^{-23} cm². Both figures disagree with theory.[3,4]

The confusion resulting from large number of tracks and reflections from every surface in the chamber made these results untrustworthy. Accordingly, a source of reduced strength was collimated so that emergent particles were limited to the illuminated part of the chamber. With these modifications many of the "positive" tracks were seen to be reflections back to the source. Only positive tracks which showed no indication of being reflections were counted.

In Table I appear the counts made on this basis with collimated sources of UX, $Ra(D+E)$, and P^{32}, with the recent results of other workers where available.

It is possible that even these so-called positive particles were reflections back to the source, of electrons for which part of the track was outside the illumination. A count was therefore taken of the number of definite reflections from all surfaces. Considering the relative source and chamber diameters, the ratio of the number of tracks which could be reflected back to the source, to the number of electron tracks, has the following values for UX, $Ra(D+E)$, and P^{32}, respectively: 0.01, 0.003, and 0.003. These figures are greater than the corresponding values of N^+/N^- in Table I.

TABLE I. Maximum possible positive particle count with UX, $Ra(D+E)$, and P^{32}.

	Approximate number of tracks per picture	Total number of electrons (N^-)	Total number of positive particles (N^+)	N^+/N^-	N^+/N^- observed by others recently
UX	31	5340	8	0.0013	—
$Ra(D+E)$	17	3490	6	0.0017	0.001[a]
P^{32}	13	6100	6	0.0010	0.0011[b]

[a] C. B. A. McCusker, Nature 161, 564 (1948).
[b] T. H. Pi and C. V. Chao, Phys. Rev. **72**, 638 (1947).

The majority of the positive tracks included in the counts were of the order of 0.1 Mev, judging by their curvature. Bethe's scattering formula[5] shows that for electron energies less than about 0.1 Mev, the scattering radius of curvature is of the same order as that due to the magnetic field (250 gauss) used in this work. In confirmation of this, photographs of S^{35} (maximum energy 0.12 Mev) showed tracks which were completely disordered. It was quite impossible to determine the direction of the magnetic field from the photographs.

From these results, one may conclude that the positive particles which have been reported are one of the (a) electrons which have been reflected back to the source, (b) electrons whose tracks are nearly closed circles, part of the track being out of the illumination or obscured by other tracks, or (c) electrons of low energy with "positive" curvature due to scattering.

It is worth noting that the theoretical work of Arley and Møller[4] gives N^+/N^- a value of zero for internal pair conversion by electrons from sources whose end-point energy is less than 4 Mev.

Numerous apparent pairs produced in the lead foil by incident electrons were found. Upon examination however, these were seen to be one of the (a) electrons which penetrated the foil and curved back to strike the foil again in the same vertical line as another electron which had penetrated the foil, or (b) electrons which penetrated the foil and curved back to the foil, being reflected at a point in the same vertical line as another electron whose track could be distinguished only up to the foil.

From the results of these experiments it seems unnecessary to propose either the existence of positive particles of lighter mass than the electron[1] or positive particles of greater mass than the electron.[6]

Groetzinger *et al.*[6] have reported four cases of positive particles branching from tracks of electrons with a P^{32} source. In two cases, a change of curvature of the electron track appeared at the branch point, but in no case was there a change in direction. The experiments here reported included a careful search for such events. None were found.

This work was supported by grants from the National Research Council of Canada.

* Now with Socony-Vacuum, Paulsboro, New Jersey.
[1] Bradt, Heine, and Scherrer, Helv. Phys. Acta **16**, 491 (1943).
[2] L. Smith and G. Groetzinger, Phys. Rev. **70**, 96 (1946).
[3] J. R. Oppenheimer, Phys. Rev. **47**, 146 (1935).
[4] N. Arley and C. Møller, Kgl. Danske Vid. Sels. Math.-fys. Medd. **XV**, 9 (1938).
[5] H. A. Bethe, Phys. Rev. **70**, 821 (1946).
[6] Groetzinger, Ribe, and Smith, Phys. Rev. **75**, 342 (1949).

A Precise Determination of the Proton Magnetic Moment in Bohr Magnetons*

J. H. Gardner and E. M. Purcell
Lyman Laboratory of Physics, Harvard University, Cambridge, Massachusetts
August 26, 1949

We have completed an experimental determination of the ratio of the precession frequency of the proton, $\omega_p=\gamma_p H_0$, to the cyclotron frequency $\omega_e=eH_0/mc$ of a free electron in the same magnetic field. The result, ω_p/ω_e, is the magnitude of the proton magnetic moment μ_p, in Bohr magnetons, since $\gamma_p=2\mu_p/\hbar$.

The proton resonance absorption in mineral oil was observed by the bridge technique[1] at a frequency of 14.24 Mc/sec. The electron resonance, at approximately 9360 Mc/sec., was obtained as follows. An evacuated rectangular wave guide, its broad dimension parallel to H_0, is traversed by a beam of slow electrons which originate outside the wave guide, enter the guide through a 2.0×0.1-mm slit in the narrow wall, and drift across the guide in the direction of the magnetic field. The field prevents the ribbon-shaped beam from spreading, so the electrons can pass through a similar slit in the opposite wall of the guide, to be collected. If

now the guide is excited by a source of frequency ω_s, the oscillating electric field expands the helical trajectories of the electrons. We had intended originally to recognize this condition by the decrease in collector current resulting from the failure of the expanded beam to get through the second slit. The effect was indeed observed and it behaved as predicted by an analysis of the electron trajectories. It was found, however, that when the beam current was limited by a space-charge potential minimum within the wave guide and when a very weak microwave field was applied, a peak in the collected current appeared at resonance, owing to the expansion of the electron cloud at the minimum with a consequent reduction in the depth of the minimum. Because the depth of the minimum is very sensitive to the presence of those electrons that nearly stop there and are exposed for an unusually long time to the oscillating field, this resonance effect is very sharp. It was used for the determination of ω_s/ω_p. The full width of the current peak, at half-maximum, was about 1 in 10^4.

The electron beam and the proton sample were about 1.5 cm apart; their positions could be interchanged to eliminate the effect of field inhomogeneity. The two resonances were displayed simultaneously on an oscilloscope while the magnetic field was modulated at 60 c.p.s. After adjustment for symmetry and coincidence, the ratio of the frequencies was determined by comparing the 657th harmonic of the proton frequency with the electron frequency ω_s. As the difference was only a few megacycles, the error introduced in this step was negligible.

Nine complete experiments were carried out, over a period of a month. The mean value of the ratio ω_s/ω_p, uncorrected for diamagnetism, was 657.4752 with a mean deviation of 0.0037 and a maximum deviation of 0.0056. The accuracy of the result depends, however, on the extent to which systematic errors can be excluded. We have carefully investigated possible sources of systematic error (magnetic field of filament, magnetic contamination of parts, effect of space charge on ω_s, etc.) and we believe that the true ratio, uncorrected for diamagnetism, lies within the range:

$$\omega_s/\omega_p = 657.475 \pm 0.008.$$

The diamagnetic correction to the field at the proton is 1.8×10^{-5} in the case of atomic hydrogen.[2] If we apply the same correction here, the proton moment, on Bohr magnetons, becomes:

$$\mu_p = (1.52100 \pm 0.00002)\times10^{-3}(e\hbar/2mc).$$

This is to be compared with the result $(1.52106\pm0.00007)\times10^{-3}$ obtained by Taub and Kusch.[3] The agreement may be regarded as further confirmation of the correction[4,5] to the spin-moment of the electron, for our experiment amounts to a comparison of the orbital g-factor (n very large!) of the electron with the proton g-factor, whereas Taub and Kusch compared the proton g-factor and the g-factor of a $^3S_1$ state, applying the factor $2(1+\alpha/2\pi)$ to obtain the number just quoted.

Our result, like that of Taub and Kusch,[3] can be combined with the absolute γ_p measured by Thomas, Driscoll, and Hipple,[6] to yield e/mc, and with cR_∞ and the hydrogen h.f.s. splitting[7] to yield α. The accuracy of e/mc is still limited by the uncertainty in γ_p. The value of α is improved to the point where the present uncertainties in c and in the theoretical formula become important.

* Assisted by the Joint Program of the ONR and the AEC.
[1] Bloembergen, Purcell, and Pound, Phys. Rev. **73**, 679 (1948).
[2] W. E. Lamb, Jr., Phys. Rev. **60**, 817 (1941).
[3] H. Taub and P. Kusch, Phys. Rev. **75**, 1481 (1949).
[4] P. Kusch and H. M. Foley, Phys. Rev. **74**, 250 (1948).
[5] J. Schwinger, Phys. Rev. **73**, 416 (1948).
[6] Thomas, Driscoll, and Hipple, Phys. Rev. **75**, 992 (1949).
[7] J. E. Nafe and E. B. Nelson, Phys. Rev. **73**, 718 (1948).

Gamma-Radiation from Br^{82}

KAI SIEGBAHN, ARNE HEDGRAN, AND MARTIN DEUTSCH*
Nobel Institute for Physics, Stockholm, Sweden
July 13, 1949

THE γ-radiation from Br^{82} has been re-examined in this laboratory using higher resolution than in the previously published investigation.[1] The radiation was studied in a double-focusing spectrometer ($\rho=50$ cm) with the resolution of the instrument set to ~one percent. The radiation was earlier thought to consist of three γ-rays of equal intensity emitted in cascade after a simple β-spectrum. The result of the present investigation show that the disintegration is more complicated. The spectrum is complex and there are seven γ-rays of different intensities. We have found the photoelectron lines from a lead converter corresponding to these γ-rays and also the internal conversion lines in the β-spectrum. The internal conversion spectrum (all K lines) is shown in Fig. 1.

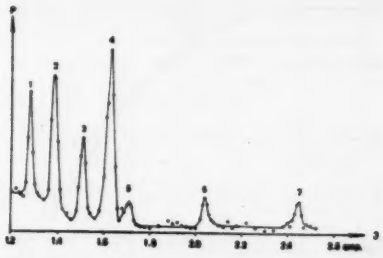

FIG. 1. Internal conversion spectrum of Br^{82}.

The energies of the γ-lines as obtained from the photo and internal conversion line spectrum are given in Table I together with the relative intensities of the corresponding internal conversion lines.

TABLE I. Energies of the γ-lines as obtained from the photo and internal conversion line spectrum of Br^{82}.

No. of γ-ray	1	2	3	4	5	6	7
Hr. from secondary electron spectrum (Mev)	0.553	0.613	0.685	0.772	0.826	1.045	1.317
Hr. from internal conversion spectrum (Mev)	0.547	0.608	0.692	0.766	0.823	1.031	1.312
Relative intensities of the conversion lines	0.68	0.78	0.42	*1.00*	0.13	0.18	0.14

A complete description of the experiments is planned together with a discussion of the disintegration scheme.

* On leave from Massachusetts Institute of Technology, Cambridge, Massachusetts.
[1] Roberts, Downing, and Deutsch, Phys. Rev. **60**, 544 (1941).

The Transformation between One- and Three-Dimensional Power Spectra for an Isotropic Scalar Fluctuation Field

LESLIE S. G. KOVASZNAY, MAHINDER S. UBEROI, AND STANLEY CORRSIN
Department of Aeronautics, The Johns Hopkins University, Baltimore, Maryland
September 2, 1949

WE should like to call attention to a mathematically simple result that may have some significance in the (still unformulated) theory of the relative behaviors of vector and scalar quantities in the incompressible turbulent flow of a continuum.

W. Heisenberg[1] has shown that in isotropic turbulence the one-dimensional velocity power spectrum can be expressed in terms of the three-dimensional power spectrum as follows:

$$F_1(k_1) = \tfrac{1}{2}\int_{k_1}^{\infty} [F(k)/k][1-(k_1^2/k^2)]dk, \qquad (1)$$

where k is the magnitude of the radius vector in the wave number space and k_1 is a coordinate. The $[1-(k_1^2/k^2)]$ factor arises from the fact that the velocity spectral vector is always perpendicular to the wave number vector (due to continuity), whereas $F_1(k_1)$ is proportional to the energy in a differential slab perpendicular to the k_1 axis.

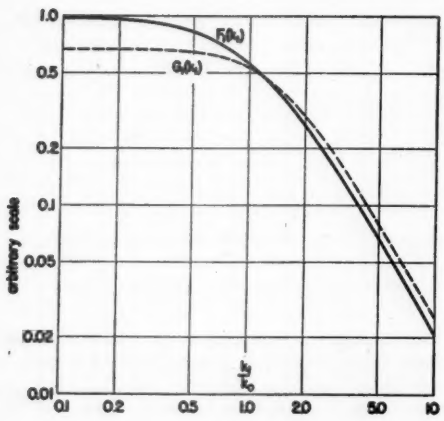

FIG. 1.

In an isotropic scalar fluctuation field (e.g., temperature fluctuations) the corresponding transformation can, of course, be derived in the same way. This is simply a special case in which no vector component need be taken, and the above factor does not enter. The result is

$$G_1(k_1)=\tfrac{1}{2}\int_{k_1}^{\infty}[G(k)/k]dk. \tag{2}$$

The inverse formulas are easily found to be

$$F(k_1)=2k_1[k_1F_1''(k_1)-F_1'(k_1)] \tag{3}$$

and

$$G(k_1)=-2k_1G_1'(k_1). \tag{4}$$

To see the physical consequences of the difference between (1) and (2), suppose an isotropic turbulence field with both vector (velocity) and scalar (e.g., temperature) fluctuations present, and suppose that their three-dimensional power spectra are proportional. Purely for the sake of computation, we assume that in the low wave numbers range they both follow the von Kármán interpolation formula[2] proposed for three-dimensional velocity spectrum:

$$F(k)\sim(k/k_0)^4/[1+(k/k_0)^2]^{17/6}. \tag{5}$$

Then the resulting one-dimensional spectra differ basically as shown in Fig. 1.

The integral scales are proportional to the ordinate intercepts of the one-dimensional power spectra:

$$L_x=C\cdot F_1(0);\quad \Lambda_x=C\cdot G_1(0). \tag{6}$$

In this case $L_x/\Lambda_x=1.50$. Furthermore, for isotropic turbulence, the lateral integral scales are related to the longitudinal ones by

$$L_y=\tfrac{1}{2}L_x;\quad \Lambda_y=\Lambda_x. \tag{7}$$

Hence

$$L_y/\Lambda_y=0.75.$$

If some appropriate high wave number extrapolation for the three-dimensional spectra is postulated, the microscale relation can be deduced in similar fashion.

[1] W. Heisenberg, Zeits. f. Physik 124, 628 (1948).
[2] Th. Von Kármán, Proc. Nat. Acad. Sci. 34 (11), pp. 530–539.

Erratum: Determination of Nuclear Gyromagnetic Ratios I

[Phys. Rev. 76, 350 (1949)]

JOHN R. ZIMMERMAN AND DUDLEY WILLIAMS
Mendenhall Laboratory of Physics, Ohio State University, Columbus, Ohio

THE following typographical error has been noted in the above paper:

Page 354, the first expression of Eq. (6) should read

$$(k+1)^2=(\nu_A{}^r\nu_A{}^s/\nu_B{}^r\nu_B{}^s).$$

A New Gamma-Ray Resonance in the Reaction $C^{12}(p,\gamma)N^{13}$ *

D. M. VAN PATTER
Laboratory for Nuclear Science and Engineering, Massachusetts Institute of Technology, Cambridge, Massachusetts

August 24, 1949

A PREVIOUSLY unreported gamma-ray resonance has been found for the reaction $C^{12}(p,\gamma)N^{13}$. It was first located by the measurement of the gamma-rays from a thick graphite target bombarded by protons. The detector consisted of thin-walled beta-counters in coincidence, which measured the secondary electrons from a thick aluminum converter. The resonance was definitely assigned to the reaction $C^{12}(p,\gamma)$ by taking a thick-target excitation curve of the N^{13} positron activity which showed the same resonance. A thin-target excitation curve for the N^{13} positron activity was also measured, using a 7-kv Formvar target, and the experimental points agreed with a symmetrical Breit-Wigner curve. The different excitation curves gave a resonance at an average proton bombarding energy of 1.697 ± 0.012 Mev with a half-width of 74 ± 9 kev. The absolute voltage scale was established from known $F^{19}(p\alpha',\gamma)$ resonances and also from measurements of the energy of elastically scattered protons and deuterons by deflection in the field of a 180-degree focusing magnet (using the energy of polonium alphas as a standard).

The ratio of thick-target yields from the 1.70, 0.456-Mev $C^{12}(p,\gamma)$ resonances was measured as 1.3 ± 0.2 from the N^{13} activity. Assuming the value of Fowler and Lauritsen[1] for the thick-target yield of the 0.456-Mev resonance as 7.2×10^{-10} quanta per incident proton, we obtain $9.4\pm1.4\times10^{-10}$ quanta per incident proton for the thick-target yield of the 1.70-Mev resonance. This thick-target yield gives a value for the radiation breadth Γ_γ of 1.3 ± 0.2 ev.

A search was made for additional resonances, using a 50-kev lampblack target but without success. In the energy range 0.95- to 1.6-Mev proton bombarding energy, no resonance was found with a peak intensity greater than 0.04 of the peak intensity of the 1.70-Mev resonance. From 1.6 to 2.1 Mev, no resonance occurred greater than 0.12 of the maximum intensity of the 1.70-Mev resonance.

In order to determine the position of the energy level of N^{13} corresponding to this gamma-ray resonance, it is necessary to know the mass difference $C^{12}+p-N^{13}$ given by Hornyak and Lauritsen[2] as 1.92 Mev, which they calculated by using Bethe's mass values. Analysis of more recent data indicates that this value should be altered. Let us first make use of the $C^{12}(d,n)N^{13}$ reaction as measured by Bennett and Richards.[3]

$$C^{12}+d=N^{13}+n+Q_1,\quad C^{12}+p-N^{13}=(p+n-d)+Q_1,$$
$$Q_1=-0.27\pm0.02\text{ Mev}^3,\quad (p+n-d)=2.237\pm0.005\text{ Mev}^4.$$

We obtain $C^{12}+p-N^{13}=1.967\pm0.025$ Mev.

It is also possible to use the two following reactions:

$$C^{12}+d=C^{13}+p+Q_2,\quad N^{13}=C^{13}+Q_3,$$
$$C^{12}+p-N^{13}=(p+n-d)-(n-p)+Q_2-Q_3,$$
$$Q_2=2.729\pm0.009\text{ Mev}^5,\quad (n-p)=0.782\pm0.002\text{ Mev}^6.$$

The latest value for the maximum energy of the N^{13} positrons is 1.202 ± 0.005 Mev[7], so that

$$Q_3=1.202\pm0.005+2m_0c^2=2.223\pm0.005\text{ Mev}.$$

We obtain

$$C^{12}+p-N^{13}=1.961\pm0.021\text{ Mev}.$$

The weighted average of the two determinations of $C^{12}+p-N^{13}$ is 1.963 ± 0.015 Mev. We find, then, corresponding to gamma-ray resonances at 0.456 ± 0.002[1] and 1.697 ± 0.012 Mev, energy levels in N^{13} at 2.383 ± 0.018 and 3.53 ± 0.027 Mev.

Grosskreutz[8] has just recently measured the energy of the neutron groups from the $C^{12}(d,n)N^{13}$ reaction using 10-Mev deuterons. In addition to the ground-state neutrons, he finds only two other groups which go to energy levels in N^{13} measured at

2.29±0.12 and 3.48±0.12 Mev. These results are in complete agreement with the energy levels in N^{13} found by the $C^{13}(p,\gamma)$ reaction, which is a strong indication that there are no additional levels in N^{13} below 3.8 Mev.

It is of theoretical interest to compare these energy levels of N^{13} to those of the mirror nucleus C^{13}. The first three levels of C^{13} known at present are at 0.9±0.2 Mev,[9-11] 3.098±0.008 Mev[5], and 3.91 Mev.[12] The existence of the lowest level is not yet firmly established. However, it is evident that the energy levels of these mirror nuclei do not correspond, as would be expected for equal neutron-neutron and proton-proton forces.

The author is indebted to Professor W. W. Buechner and to Dr. John Blatt for their invaluable guidance, and to A. Sperduto for the measurement of the energy of elastically scattered protons.

* This work has been supported by the Joint Program of the ONR and the AEC.

[1] W. A. Fowler and C. C. Lauritsen, Phys. Rev. 76, 314 (1949).
[2] W. F. Hornyak and T. Lauritsen, Rev. Mod. Phys. 20, 191 (1948).
[3] W. E. Bennett and H. T. Richards, Phys. Rev. 71, 565 (1947).
[4] R. E. Bell and L. G. Elliot, Phys. Rev. 74, 1552 (1948).
[5] Buechner, Strait, Sperduto, and Malm (to be published shortly).
[6] Taschek, Argo, Hemmendinger, and Jarvis, Phys. Rev. 76, 325 (1949).
[7] Hornyak, Dougherty, and Lauritsen, Phys. Rev. 74, 1727 (1948).
[8] J. C. Grosskreutz, Phys. Rev. 76, 482 (1949).
[9] R. R. Roy, Phys. Rev. 75, 1775 (1949).
[10] O. Merhaut, Physik. Zeits. 41, 528 (1940).
[11] W. Jentschke, Physik Zeits. 41, 524 (1940).
[12] Heydenberg, Inglis, Whitehead, and Hafner, Phys. Rev. 75, 1147 (1949).

On the Double Beta-Process

MARK G. INGHRAM AND JOHN H. REYNOLDS
University of Chicago and Argonne National Laboratory, Chicago, Illinois
August 31, 1949

A STUDY has been made of the isotopic constitution of xenon extracted from a pre-Cambrian tellurium ore, in order to determine the half-lives of the double beta-transitions $Te^{128} \rightarrow Xe^{128}$ and $Te^{130} \rightarrow Xe^{130}$. In this ore, measurable amounts of these two isotopes of xenon should have accumulated during geological time if the transitions take place at a rate comparable to that reported by Fireman[1] for the similar transition $Sn^{124} \rightarrow Te^{124}$. The importance of double beta-studies lies in the fact that the half-lives calculated from the Majorana theory of the neutrino[2] and the Dirac theory of the neutrino[3] differ by a large factor. Table I gives half-lives

TABLE I. Theoretical half-lives for allowed double beta-disintegrations.

Transition	$Te^{128} \rightarrow Xe^{128}$	$Te^{130} \rightarrow Xe^{130}$
Atomic mass difference in Mev	0.5	1.6
Majorana half-life in years	2×10^{16}	6.0×10^{14}
Dirac half-life in years	3×10^{27}	1.1×10^{26}

so calculated; the energies available for the transitions have been estimated from the decay schemes of the intermediate nuclei and from considerations of the nuclear energy surface[4] and are conservative.

The ore used for this study was the mineral tellurobismuthite (Bi_2Te_3) in andalusite and sericite rock blasted from an outcrop in Mángfallberget, near Boliden, Sweden. This telluride deposit has been described in detail by Grip and Ödman.[5] A rough estimate by Dr. K. Rankama places the age of the original sulfide mineralization at 1500±500 million years.

TABLE III. Measured minimum half-lives based on crystal age of 1.5×10^9 years.

Transition	$Te^{128} \rightarrow Xe^{128}$	$Te^{130} \rightarrow Xe^{130}$
Max. no. radiogenic xenon atoms per atom of Xe^{134}	0.07	0.014
Max. no. radiogenic xenon atoms in sample	3.0×10^{12}	5.0×10^{11}
No. of parent atoms in sample	3.8×10^{23}	4.2×10^{22}
Minimum half-life in years	1.3×10^{19}	8.0×10^{19}

The sample (430 grams containing 6 percent tellurium) was crushed in an iron mortar and transferred to a quartz bottle which was then evacuated and heated to well above the melting point of Bi_2Te_3. The gas evolved was collected and purified in an apparatus patterned closely after that of Epstein and co-workers[6] in their experiments with fission xenon. The final rare gas mixture was analyzed in a conventional 60° single-focusing mass spectrometer. By calibrating with artificially prepared mixtures of argon and xenon, it was possible to measure both the chemical composition and the isotopic constitution of the gas.

The mixture was found to consist of $1.3\pm0.3\times10^{-5}$ cc S.T.P. xenon plus $1.3\pm0.3\times10^{-2}$ cc S.T.P. argon. The results of the isotopic analysis are represented in Table II together with Nier's values[7] for normal xenon. All abundances are referred to mass 134. It will be noted that the only evidence for the presence of radiogenic xenon occurs at mass 130. For this minute sample of xenon, however, the accuracy of the measurements is such that the apparent excess xenon at this mass can only be viewed as intriguing (even though a measurement of normal xenon immediately thereafter checked Nier's value of 0.386 exactly). At masses 124, 126 and 128 the recorder peaks were so close to background level that only upper limits for these abundances can be given.

These data can be used, however, to place lower limits on the half-lives of the double beta-transitions. The results are presented in Table III. A corresponding calculation for the energetically questionable transition $Te^{126} \rightarrow Xe^{126}$ gives a minimum half-life of 6×10^{19} years.

On comparison with the half-lives presented in Table I, it appears that these results support the Dirac antineutrino theory. However, the values are subject to qualification on two counts. First, the possibility exists that radiogenic xenon may have escaped from the crystals of ore since the time of the original mineralization, either by simple diffusion or during later alteration of the mineral. Considering the retentivity of helium by various minerals,[8,9] it appears that the former possibility is remote. A hydrothermal alteration of the telluride, on the other hand, would certainly result in loss of xenon, and this possibility cannot be dismissed for the present ore. If this has occurred, the accumulation of daughter xenon dates only from the time of alteration and the half-lives in Table III must be reduced in proportion. Secondly, the theoretical half-lives presented in Table I are essentially minimum values; favorable forms of the interaction terms have been assumed and the calculations have been made for completely allowed transitions. As a result, the Majorana half-lives may be longer in the particular transitions we have investigated, due, for example, to a possible difference in parity between the ground states of Te^{130} and Xe^{130}. That these two effects, acting in combination, could overpower the factor of 10^5 by which the measured minimum half-life exceeds the calculated Majorana half-life in the transition at mass 130 is improbable, but it must be admitted as a possibility.

TABLE II. Relative abundances of the xenon isotopes.

Mass	124	126	128	129	130	131	132	134	136
Present study	<0.015	<0.018	<0.25	2.47 ±0.03	0.394 ±0.004	2.00 ±0.02	2.55 ±0.02	1.000	0.847 ±0.008
Normal xenon*	0.0089	0.0083	0.180	2.49	0.386	2.009	2.558	1.000	0.849

* See reference 7.

These results are preliminary to more extensive investigations of the matter.

The writers take pleasure in acknowledging helpful discussions with Professors W. H. Newhouse and K. Rankama of the Geology Department and A. J. Dempster and E. Fermi of the Physics Department of the University of Chicago.

[1] E. L. Fireman, Phys. Rev. **75**, 323 (1949).
[2] W. H. Furry, Phys. Rev. **56**, 1184 (1939).
[3] M. G. Mayer, Phys. Rev. **48**, 512 (1935).
[4] E. Feenberg, Rev. Mod. Phys. **19**, 239 (1947).
[5] E. Grip and O. Ödman, Sveriges Geologiska Undersökning **36**, No. 4 (1942).
[6] S. Epstein, Proc. Conf. on Nuclear Chem., McMaster University, pp. 108–116 (May 1947).
[7] A. O. Nier, Phys. Rev. **52**, 933 (1937).
[8] P. M. Hurley and C. Goodman, Bull. Geol. Soc. Am. **54**, 305 (1943).
[9] N. B. Keevil, Proc. Am. Acad. **73**, 311 (1940).

On the Negative Proton*

KUAN-HAN SUN
Westinghouse Research Laboratories, East Pittsburgh, Pennsylvania
August 24, 1949

THE possible existence of negative proton has been speculated on by various investigators.[1] The initial and final nuclei involved in the delayed neutron emission (or preferably the β–n decay process) are the same as that for a hypothetical process of negative proton emission. Equations (1), (2) and (3) illustrate this point and also yield a value of the reaction energy for the negative proton emission.

$$ {}_zX^A = {}_{z+1}Y^{A-1} + \beta^- + {}_0n^1 + Q_1, \tag{1} $$

$$ {}_zX^A = {}_{z+1}Y^{A-1} + {}_{-1}H^1 - 2e + Q_2, \tag{2} $$

$$ Q_2 = Q_1 + 1.826 \text{ in Mev}. \tag{3} $$

Equation (3) is obtained on the assumption that the negative proton has the same mass as the positive proton.

For a process that involves delayed neutron emitters, Q_1 is always positive. Q_2, then, is also positive which means that reaction (2) is possible, at least from energy considerations. The emission of negative protons if further favored on account of the negative potential barrier involved.

The delayed neutron emitter, N^{17}, was first discovered by the University of California group.[2] It was produced by bombarding oxygen or elements immediately above it in atomic number with 200-Mev deuterons. The group at Westinghouse Research Laboratories and the University of Pittsburgh have induced the reactions, $C^{14}(\alpha,p)N^{17}$, by means of 16 to 30 Mev α-particles, and $O^{17}(n,p)N^{17}$ by means of the cyclotron-produced fast neutrons on the O^{17} in natural water.[3,4] The reaction energy for the β–n decay of N^{17} was measured by Alvarez[5] to be 4.58 Mev. This yields reaction energy of 6.41 Mev for the emission of a negative proton from N^{17}.

It is possible to produce N^{17} in the order of one millicurie strength from the large California cyclotron[6] or from the University of Pittsburgh cyclotron by the $C^{14}(\gamma,p)N^{17}$ method, if a few hundred millicurie of C^{14} are used.

It should not be difficult to detect negative proton emission with a cloud chamber in a magnetic field even if the probability of negative proton decay is only one in 10^7. A cyclotron producing 200-Mev deuterons would be particularly suitable for this experiment. Because of the high penetrating power of deuterons, N^{17} may be made inside a cloud chamber. If the intense ionizations from other radioactive products cause difficulty in the cloud-chamber operation, a magnetic spectrometer with a proportional counter as the detector may be used.

An alternative way of detecting the presence of negative protons is to observe the annihilation radiations which should be present. If a pair of γ-rays is produced for each annihilation, their energy would be about 10^9 ev. These may be detected by observing showers produced by the powerful γ-rays in a cloud chamber or in some device composed of lead sheets and Geiger counters. This method is convenient to be carried out because the N^{17} or other delayed neutron emitters may be produced in a separate container from that of the detecting device, and also because a thick target may be used in the production of N^{17}. Since intense delayed neutron emitters can also be produced in a fission reactor, this method may also be easily applied.

It is, perhaps, also advisable to look for mesons in N^{17} or other delayed neutron emitters, since it has been postulated[7] that mesons may be produced during the annihilation process.

* Assisted by the Joint Program of the ONR and the AEC.
[1] See for examples, L. Rosenfeld, *Nuclear Forces, I* (1948), p. 8, and G. Gamow, *Structure of Atomic Nuclei and Nuclear Transformations* (1937), p. 14.
[2] Knable, Lawrence, Leith, Moyer, and Thornton, Phys. Rev. **74**, 1217 (1948).
[3] Sun, Jennings, Shoupp, and Allen, Phys. Rev. **75**, 1302 (1949).
[4] Charpie, Sun, Jennings, and Nachaj, Phys. Rev. (to be published).
[5] L. W. Alvarez, Phys. Rev. **75**, 1127 (1949); E. Hayward, Phys. Rev. **75**, 917 (1949).
[6] L. W. Alvarez, private communication at Washington Meeting of the American Physical Society, 1949.
[7] J. McConnell and L. Janossy, Nature **159**, 335 (1947).

Erratum: The Chi-Square Test as a Criterion for Testing Halogen-Filled Geiger Tubes

[Phys. Rev. **75**, 1461 (1949)]

A. B. WILLOUGHBY
Naval Radiological Defense Laboratory, San Francisco, California

THE second sentence in the abstract should read: "Many of the early halogen-quenched tubes exhibited slopes of six percent or more, although Liebson* has reported that it is possible to produce tubes with one or two percent slopes."

Since the time of this report Lieutenant Commander F. W. Brown III of this laboratory has also obtained halogen-quenched tubes with slopes of a few percent.

* S. H. Liebson, Rev. Sci. Inst. **19**, 303 (1948).

Spontaneous Decay Rate of Heavy Mesons. II

L. I. SCHIFF AND D. L. WEISMAN
Stanford University, Stanford, California
September 6, 1949

IN a recent note of the same title,[1] it was shown that either a coupling between heavy (π) and light (μ) mesons or a coupling between μ-mesons and nucleons can lead to both the observed rate of π–μ-decay and the observed rate of capture of negative μ-mesons by nuclei. It was also shown that neither a coupling between π-mesons and electrons (e) nor a coupling between electrons and nucleons can lead to rates of both π–e decay and nuclear beta-decay in agreement with observation. It was assumed there that π-mesons are scalar particles, μ-mesons, electrons, neutrinos (ν), neutrons (N), and protons (P) are all Dirac particles, and that all couplings are of the scalar type that involve the Dirac β-operator. A divergent integral that appears in the calculation

$$ I = \int_0^\infty P^4 dP / (P^2 + M^2 c^2)^{\frac{1}{2}}, \tag{1} $$

where M and P are the nucleon mass and momentum, was interpreted both by taking the upper limit to be roughly equal to Mc, and by setting the self-energy of the π-meson (which involves I) equal to mc^2. The two interpretations of I give approximately the same values, the latter being

$$ I = 3\pi m^3 c^3, \tag{2} $$

when the π–N coupling constant has the magnitude

$$ |G| = (4\pi\hbar c^3/3)^{\frac{1}{2}} $$

obtained from the strength of nuclear forces.

Steinberger[2] has attempted to resolve the discrepancy noted above by using Pauli's regulator formalism[3] to so interpret the integral (1) that it is negligibly small in comparison with the value (2). Since this application of regulators to an integral that is not even conditionally convergent makes it so small that the sum over intermediate states characteristic of second-order per-

turbation theory ceases to have any meaning, it seems worth while to consider other possibilities. Thus if the existence of antinucleons is denied, I is identically zero since the intermediate nucleon states do not occur. Then agreement with experiment could be attained by assuming appropriate values for the π–μ- and N–e coupling constants.[2] Alternatively, nuclear beta-decay could perhaps be explained in terms of a very short-lived intermediate meson of much greater mass ($\sim 1000 m_e$) that is strongly coupled to nucleons, which might then also be responsible for initiating soft cosmic-ray showers.

Another possibility, investigated here, assumes both π–e and N–e couplings, so that there is interference between first- and second-order processes in both π–e decay and nuclear beta-decay. The pertinent interaction terms in the Hamiltonian are

$$G\int \psi_\pi(\psi_P^*\beta\psi_N)d\tau+\gamma\int \psi_\pi(\psi_e^*\beta\psi_\nu)d\tau + g_e\int(\psi_\nu^*\beta\psi_e)(\psi_P^*\beta\psi_N)d\tau+\text{c.c.}$$

Then the ratio of the rate of π–e decay to the rate of free neutron decay is

$$\frac{w_{\pi e}}{w_{Ne}}=\frac{45\pi}{8f(\Delta/m_e)}\left(\frac{m}{\Delta}\right)^5\left|\frac{1-(G\mathcal{g}_e/\gamma)(I/\pi^2\hbar^3c)}{1-(G\mathcal{g}_e/\gamma)(3m^2c/4\pi\hbar^3)}\right|^2, \quad (3)$$

where

$$f(x)\equiv\left(1-\frac{9}{2x^2}-\frac{4}{x^4}\right)\left(1-\frac{1}{x^2}\right)^{\frac{1}{2}}+\frac{15}{2x^4}\ln(x+(x^2-1)^{\frac{1}{2}}),$$

and Δ is the neutron-proton mass difference. The experimental upper limit for this ratio is roughly $10^7/6\times10^{-4}$, so that the squared bracket in (3) is less than about 0.02. This is so small that the quantity $G\mathcal{g}_e/\gamma$ must be mainly real and positive with not more than a small imaginary part, if the evaluation (2) for I is assumed. Then $|g_e|$ must have about one-third the value usually assumed to account for nuclear beta-decay, and the ratio $|\gamma/G|$ of π–e to π–N coupling constants is approximately equal to 1.3×10^{-7}.

It is interesting to note that the magnitude of the π–μ-coupling constant required to explain π–μ-decay as a pure first-order process is very nearly equal to the value of $|\gamma|$ obtained above.

[1] L. I. Schiff, Phys. Rev. 76, 303 (1949).
[2] J. Steinberger, Phys. Rev. 76, 1180 (1949).
[3] W. Pauli and F. Villars, Rev. Mod. Phys. 21, 434 (1949).

A Note on the Infra-Red Spectra of the Deutero-Ammonias

JOHN S. BURGESS
Mendenhall Laboratory of Physics, Ohio State University, Columbus, Ohio
August 29, 1949

MIGEOTTE and Barker[1] measured the fundamental vibration-rotation bands of the ND_3 molecule but were bothered some by contaminations of ND_2H and NDH_2, as well as CO_2 and possibly D_2O. An attempt has been made to remeasure these bands at higher resolution with the vacuum grating spectrometer of the laboratory. However, the gas obtained was not of sufficiently high purity to make an accurate analysis of the ND_3 fundamental bands, but was found to contain a considerable amount of the mixed ammonias. During the course of these measurements, high resolution data were recorded from about 790 cm^{-1} to 1800 cm^{-1} and in the region 2350–2600 cm^{-1} and several Q-branches were observed which undoubtedly belong to the mixed ammonia molecules. This data is included as part of a dissertation by the author.[2]

TABLE I. Observed and calculated fundamental frequencies in cm^{-1} for the ammonia molecules.*

Molecule		ν_2	ν_4	ν_1	ν_3
NH_3	calc.	1010	1631	3355	3470
	obs.	966 933	1631	3335.9 3337.5	3407
NH_2D	calc.	1025	1385a 1600s	3400	2510s 3470a
	obs.	894** 874**	1592		
NHD_2	calc.	925	1230s 1460a	2455	2565a 3435s
	obs.	818** 808**	1234 1464	2418	2556
ND_3	calc.	840	1180	2405	2565
	obs.	749.2** 745.8**	1191.2	2420,4	2555.6

Howard[3] calculated the fundamental frequencies for the various ammonia molecules on the basis of valence forces using values of the force constants which gave the proper values of ν_3 and ν_4 for NH_3. By a comparison with these calculated frequencies, the various Q-branches observed have been assigned in Table I.

* The letter, a or s, after a frequency of NH_2D or NHD_2 indicates that it corresponds to a vibration which is antisymmetric or symmetric, respectively, with respect to reflection through a plane passing through the figure axis and the hydrogen isotope differing from the other two.
** Values obtained from data of Migeotte and Barker (see reference 1).
[1] M. V. Migeotte and E. F. Barker, Phys. Rev. 50, 418 (1936).
[2] J. S. Burgess, "Infra-red Spectra of Methane and Deutero-ammonia," Dissertation, Ohio State University (1949).
[3] J. B. Howard, J. Chem. Phys. 3, 207 (1935).

On the Latitude Dependence of the Absolute Neutron Intensities in Cosmic Radiation*

LUKE C. L. YUAN**
Palmer Physical Laboratory, Princeton University, Princeton, New Jersey
August 25, 1949

THIS is a preliminary report on some of the results obtained on the study of the latitude dependence of slow neutron intensities in the free atmosphere carried out by means of a B-29 plane. Two identical proportional counters filled with boron trifluoride of 96 percent B^{10}, similar to those employed in our earlier experiments,[1] were placed in the pressurized cabin of the tail gunner's compartment of the plane. They were suspended two feet apart near the center of the cabin with all hydrogenous material and heavy equipment removed from the compartment and its vicinity. Furthermore, the plastic bubble was replaced by a thin Duralumin plate. Thus the counters would not be appreciably affected by their surroundings in the plane and should measure essentially the slow neutron intensity in the free atmosphere. This conclusion is borne out by the fact that the measurements obtained in the plane agree well with our free balloon results for the absolute intensity.[2]

Each counter output was fed directly to a cathode follower which was placed inside one end of the counter shield. Both counter shields were pressurized to prevent corona. The output leads from the cathode followers as well as the high voltage cable from the counters were fed through a long pressurized duct to the rear compartment of the plane where all the electronic circuits and high voltage supplies were located. The rear compartments was located about 35 feet away from the counters.

Figure 1 shows the results of the flight from McArthur Field,

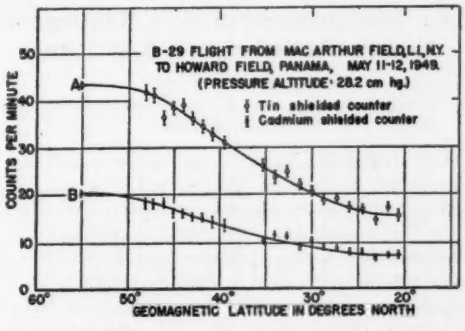

FIG. 1. Counts per minute as a function of geomagnetic latitude obtained at an altitude of 25,000 feet, with a tin-shielded counter (upper curve), and with a cadmium-shielded counter (lower curve).

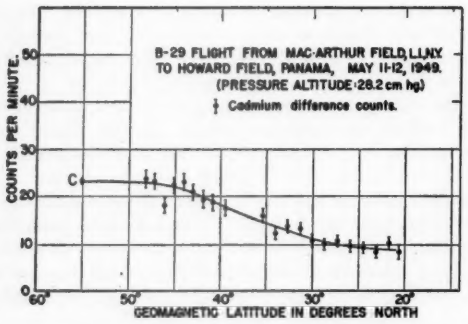
B-29 FLIGHT FROM MAC-ARTHUR FIELD, L.I.,N.Y.
TO HOWARD FIELD, PANAMA, MAY 11-12, 1949.
(PRESSURE ALTITUDE-28.2 cm hg)
† Cadmium difference counts.
COUNTS PER MINUTE.
C
GEOMAGNETIC LATITUDE IN DEGREES NORTH

FIG. 2. Cadmium difference counts as a function of geomagnetic latitude.

Long Island, New York (geomagnetic latitude 52°N) to Tampa, Florida (38°30′N) and then to Howard Field, Panama (20°42′N). The altitude of the flight was maintained at 25,000 throughout the entire flight. Readings were taken every 10 minutes and the mean counting rates were plotted as a function of the geomagnetic latitude. The top curve shows the counting rates obtained in the tin-shielded counter and the lower curve those obtained in the cadmium-shielded one. The points *A* and *B* are the more accurate measurements obtained from constant latitude flights at Rome, New York (55°8′N). Figure 2 shows the cadmium difference counts plotted similarly to Fig. 1. Point *C* is a more accurate value of the cadmium difference value obtained at Rome, New York. There seems to be a knee at about 47°N for the slow neutron latitude curve. The ratio of the neutron intensities

$$n(55°\text{N})/n(20°\text{N})=2.9$$

at the altitude of 25,000 feet (28.2 cm Hg pressure altitude). These results agree well with those obtained by Simpson *et al.*[3]

As described in another paper,[4] the effective response cross section for the counter used in this experiment was determined to be 10.6 cm² and the air mass equivalent thus calculated is 52.0 g of air.

The absolute number, *s*, of slow neutrons absorbed in one g of air per minute at any latitude, can be obtained simply by dividing the air mass equivalent for this counter into the appropriate counting rates given in Fig. 2.

The author wishes to express his appreciation to the officers and men of the 3171st Electronics Squadron, U. S. Air Force, for their full cooperation in making the experiment successful.

* Assisted by the joint program of the AEC and the ONR.
** Now at Brookhaven National Laboratory, Upton, Long Island, New York.
[1] Luke C. L. Yuan, Phys. Rev. **74**, 504 (1948). Luke C. L. Yuan and R. Ladenburg, Bull. Am. Phys. Soc. **23**, No. 2, 21 (1946).
[2] Luke C. L. Yuan, Phys. Rev. **76**, 1268 (1949).
[3] J. A. Simpson, Jr., Phys. Rev. **73**, 1389 (1948). Simpson, Baldwin, and Vretz, Phys. Rev. **76**, 165 (1949).
[4] Luke C. L. Yuan (to be published).

On the Measurement of Slow Neutrons in the Cosmic Radiation on a B-29 Plane*

LUKE C. L. YUAN**
Palmer Physical Laboratory, Princeton University, Princeton, New Jersey
August 25, 1949

OUR first extensive measurements of the cosmic-ray neutron intensities at medium high altitudes (around 30,000 ft.) were made in 1947, and a preliminary report of these results was given.[1] In this experiment, two identical proportional counters filled with enriched boron trifluoride, one bare and one shielded with cadmium, were installed in the navigator's cabin (the front pressurized compartment) of the plane. In spite of the good agreement between our results on the absorption depth, λ, ($N=N_0\exp(-x/\lambda)$) and that obtained by Agnew, Bright, and Froman,[2] Simpson,[3] and Yuan (balloon measurements),[4] the cadmium difference counts thus obtained were much higher than the free-space measurements carried out by means of free balloons. Tests were made during flight, but no appreciable effect on the slow neutron intensity was found that could be attributed to the gasoline tanks in the wings of the plane. Further tests on the possible influence of other materials present inside the cabin, such as Kapok insulation, etc., also proved to be negligible.

Since the measurements of Agnew *et al.* were made at the tail end of a B-29 plane and their cadmium ratio was considerably lower than ours, it seemed necessary to check our measurements at the tail section which unfortunately was unavailable to us at the time of the first experiment. Consequently, more recent results[5] were obtained by installing the counters in the pressurized cabin of the tail gunner's compartment of a B-29 plane. All hydrogeneous material and heavy equipment were removed from the cabin and its vicinity to reduce as much as possible the effect of the airplane surroundings on the counters. High voltage supplies as well as electronic equipment were installed at least 30 feet away from the counters and they were fed via long cables. The results thus obtained agree very well in their absolute values with the free-space measurements.[4] For example: At 20.1-cm Hg pressure, the cadmium difference counting rate obtained in Rome, New York (geomagnetic latitude 55°8′ N) on a B-29 plane was 44.3 ± 0.7 counts per minute; and that obtained in Princeton (geomagnetic latitude 51°46′ N) on free balloons was 42 ± 4 counts per minute after taking into account the respective air mass equivalent of the counters.[4]

From these results and from the fact that the nose wheel of the plane, when folded up during flight, was actually less than one foot away from the counters placed in the navigator's cabin, it seems to point to the massive rubber tire of the nose wheel as the probable source of excessive slow neutrons obtained in the earlier B-29 measurements. Presumably, a considerable fraction of fast neutrons in the atmosphere was slowed down by the rubber and was consequently detected by the slow neutron counters.

Since the measurements at the tail of a B-29 agree well with the free-space measurements, we may thus conclude that absolute measurement of the slow neutron intensities in the cosmic radiation can be justifiably made in the tail gunner's compartment of a B-29 plane with proper precautions.

The author wishes to thank Professor R. Ladenburg for suggesting this paper for the purpose of calling the attention of other workers who are interested in making absolute measurements of cosmic-ray neutrons on a B-29 plane.

* Assisted by the Joint Program of the AEC and the ONR.
** Now at Brookhaven National Laboratory, Upton, Long Island, New York.
[1] Luke C. L. Yuan and R. Ladenburg, Bull. Am. Phys. Soc. **23**, No. 2, 21 (1948).
[2] Agnew, Bright, and Froman, Phys. Rev. **72**, 203 (1947).
[3] J. A. Simpson, Jr., Phys. Rev. **73**, 1389 (1948).
[4] Luke C. L. Yuan, Phys. Rev. **74**, 504 (1948); Luke C. L. Yuan (to be published).
[5] Luke C. L. Yuan, Phys. Rev. **76**, 1267 (1949).

A Theory of Pressure Absorption

MASATAKA MIZUSHIMA
Physics Department, Faculty of Science, Tokyo University, Tokyo, Japan
August 31, 1949

SYMMETRICAL diatomic molecules, such as H_2, O_2, N_2, have no dipole moment both in static and vibrating states, so they are not expected to have infra-red absorption due to vibration and rotation. But recently Herzberg[1] succeeded in obtaining a very weak absorption line in the near infra-red with H_2 gas, which is, according to his view, the quadrupole absorption. After that, Crawford, Welsh, and Locke[2] obtained the infra-red absorption with O_2 and N_2 at 1556 and 2331 cm^{-1}, respectively. When they changed the pressure of the gases, they found that the absorption intensity is proportional to the square of the pressure, so they suggested that these absorptions are induced by inter-

molecular forces. In this note a theoretical formula for the absorption of the latter kind is given.

When a molecule is under an electrostatic field $\mathbf{E}$ and a radiation field $\mathbf{E}_r \cos\omega t$, the perturbation Hamiltonian which makes the molecule absorb light quanta is $\boldsymbol{\mu}(\mathbf{E}+\mathbf{E}_r\cos\omega t)$, where $\boldsymbol{\mu}$ is the dipole moment of this molecule. In our problem, the external field $\mathbf{E}$ is due to the molecules surrounding the one under consideration. Thus, if the ith molecule has dipole moment $\boldsymbol{\mu}_i$ and quadrupole moment $\mathbf{Q}_i$ (which is represented by $Q_{zz}=2P$ and $Q_{xx}=Q_{yy}=-P$ for the above type molecules), and is at a distance $\mathbf{R}_i$ from the central molecule, then

$$\mathbf{E}=\sum_i \mathbf{E}_i=\sum_i\left\{\frac{2\mu_i\cos\theta_i}{R_i^4}+\frac{3P_i(3\cos^2\theta_i-1)}{2R_i^5}+\cdots\right\}\mathbf{R}_i, \quad (1)$$

where θ_i is the angle between $\mathbf{R}_i$ and the axis of ith molecule.

If ψ_i is the wave function of ith molecule, the absorption coefficient of the transition $\psi_0\rightarrow\psi_0^*$ at the resonance frequency ν is

$$\frac{8\pi^3\nu}{3hc}\left\{\sum_{**}\frac{\left(\int\psi_0\cdots\psi_N\boldsymbol{\mu}_0\mathbf{E}\psi_0^{**}\cdots\psi_N d\tau\right)\times\left(\int\psi_0^{**}\cdots\psi_N\boldsymbol{\mu}_0\psi_0^{*}\cdots\psi_N d\tau\right)}{W_0-W_0^{**}}\right\}^2 n$$

$$=\frac{8\pi^3\nu}{3hc}\left\{\sum_{**}\frac{\int\psi_0\boldsymbol{\mu}_0\psi_0^{**}d\tau'\int\psi_0^{**}\boldsymbol{\mu}_0\psi_0^{*}d\tau'}{W_0-W_0^{**}}\right\}^2\times\left(\int\psi_1\cdots\psi_N\mathbf{E}\psi_1\cdots\psi_N d\tau''\right)^2 n$$

$$=\frac{8\pi^3\nu}{3hc}\left(\int\psi_0\boldsymbol{\alpha}\psi_0^*d\tau'\right)^2\left\{\sum_i\left[\frac{2\bar{\mu}_i\cos\theta_i}{R_i^4}+\frac{3\bar{P}_i(3\cos^2\theta_i-1)}{2R_i^5}+\cdots\right]\mathbf{R}_i\right\}^2 n, \quad (2)$$

where $\boldsymbol{\alpha}$ is the polarizability tensor, and n is the number of molecules in unit volume. It must be remembered that only the diagonal elements (permanent moments) $\bar{\mu}_i$ and $\bar{P}_i$ appear in (2). The matrix elements of $\boldsymbol{\alpha}$ have already been obtained.[3]

We will calculate the sum of $\mathbf{E}_i$, assuming the so-called statistical theory.[4] When the molecules are randomly distributed, the $\mathbf{E}_i$'s are also spherically distributed. To sum these electric field vectors is equivalent to searching for the position of a Brownian particle whose unit displacement is spherically distributed. The solution of the latter problem is obtained by Markoff's method;[5] thus, the probability that the summed field has an absolute value between E and $E+dE$ is given by the formula

$$W(E)dE=\frac{4\pi\exp(-3E^2/2\langle\Sigma_i E_i^2\rangle)}{(2\pi\langle\Sigma_i E_i^2\rangle/3)^{\frac{3}{2}}}E^2dE, \quad (3)$$

where $\langle\Sigma_i E_i^2\rangle$ is the average of $\Sigma_i E_i^2$, which is

$$\langle\Sigma_i E_i^2\rangle=\int_{R_0}^{\infty}\int_0^{\pi}\left\{\frac{2\bar{\mu}\cos\theta}{R^3}+\frac{3\bar{P}(3\cos^2\theta-1)}{2R^4}+\cdots\right\}^2\times 2\pi\sin\theta d\theta R^2dRn$$

$$=4\pi n\left\{\frac{4\bar{\mu}^2}{9R_0^3}+\frac{9\bar{P}^2}{25R_0^5}+\cdots\right\}. \quad (4)$$

The absorption coefficient of gas is

$$\frac{8\pi^3\nu}{3hc}\left(\int\psi_0\boldsymbol{\alpha}\psi_0^*d\tau'\right)^2\int_0^{\infty}E^2W(E)dEn=\frac{16\pi^3\nu}{3hc}\left(\int\psi_0\boldsymbol{\alpha}\psi_0^*d\tau'\right)^2\langle\Sigma_i E_i^2\rangle n. \quad (5)$$

For the Q-branch of symmetric diatomic molecules at room temperature this formula is reduced to

$$\frac{192\pi^4\nu n^2}{25hcR_0^5}\bar{P}^2\left(\beta^2+\frac{11}{30}\gamma^2\right), \quad (6)$$

where

$$\beta=\int\psi\tfrac{1}{2}(\alpha_{xx}+\alpha_{yy}+\alpha_{zz})\psi^*d\tau,$$

$$\gamma=\int\psi(\alpha_{zz}-\alpha_{xx})\psi^*d\tau.$$

In the paper of Crawford, Welsh, and Locke,[2] the intensity curve for the vibration line of O_2 near 1556 cm^{-1} is given, from which the absorption coefficient of the Q-branch is calculated to be 4.0×10^{3} cm^{-1} sec.$^{-1}$ at 1 atmos.

In this case, n is 2.72×10^{19} cm^{-3}, R_0 may be considered to be equal to twice the interatomic distance of O_2, thus $R_0=2.4$A. For $\bar{P}$, there are no experimental data, but, from the curve of Lassettre and Dean,[6] we can estimate it to be 3.4×10^{-28} cm^3. In order to explain the experimental result with these values, $\beta^2+(11/30)\gamma^2$ must be 2.1×10^{-60} cm^4. Although no direct measurements of the latter exist, at least the order of this value is certainly valid. (An estimation with classical model yields 6.6×10^{-60} cm^4 for it.) Thus we may consider that the experimental result was explained by our formula (6).

By (6) we can estimate the contribution of the pressure absorption in the Herzberg's experiment.[1]

If we assume that the change of P during the vibration is nearly equal to $\bar{P}$ in the static state, the proportion of quadrupole absorption to pressure absorption is about

$$1:\frac{n}{R_0^5}\left(\beta^2+\frac{11}{30}\gamma^2\right)\doteqdot 1:10^{10}$$

at 10 atmos. (his experimental condition); thus the pressure absorption is predominant.

I wish to thank Professor M. Kotani and Dr. M. Usui for advice and encouragement.

[1] G. Herzberg, Nature **163**, 170 (1949).
[2] Crawford, Welsh, and Locke, Phys. Rev. **75**, 1607 (1949).
[3] C. M. Lewis and W. V. Houston, Phys. Rev. **44**, 903 (1933).
[4] H. Margenau and W. W. Watson, Rev. Mod. Phys. **8**, 22 (1936).
[5] S. Chandrasekhar, Rev. Mod. Phys. **15**, 1 (1943).
[6] E. N. Lassettre and L. B. Dean, Jr., J. Chem. Phys. **17**, 317 (1949).

Experimental Study of the Compton Effect at 1.2 Mev

ROBERT HOFSTADTER AND JOHN A. MCINTYRE
Palmer Physical Laboratory, Princeton University, Princeton, New Jersey
September 6, 1949

SINCE the Compton effect represents one of the most fundamental interactions between radiation and matter, it is desirable that the theory be compared carefully with experiment. The angular distribution of the scattered gamma-rays has been predicted by Klein and Nishina,[1] and while it is true that the total cross sections have been well checked by many investigators,[2] search of the literature reveals that angular distribution studies have been relatively neglected. Angular investigations in the x-ray region show reasonably good agreement with theory,[3] and Chao,

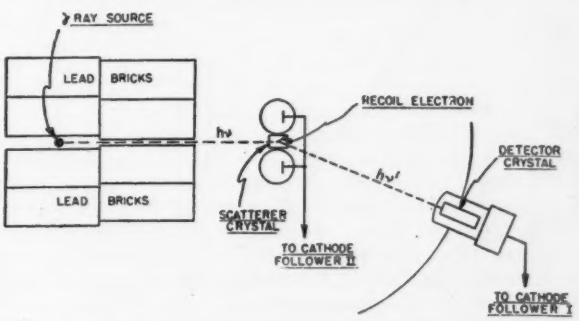

FIG. 1. Compton scattering apparatus for 1.24-Mev gamma-rays.

Bay and Szepesi, and Jordan[4] have been experimental studies in the gamma-ray region. However, these latter results are not sufficiently accurate to provide a conclusive test of the Klein-Nishina formula. Recent developments in counting gamma-rays with scintillations make possible a more accurate experimental investigation of the angular scattering in the Compton effect. The preliminary results of such a study are presented below.

The apparatus used in this experiment has been briefly described previously.[5] A sketch of the main features appears in Fig. 1. The quantity measured in the experiment is the number of coincidences between the recoil electron (counted by the "scatterer") and the scattered photon (counted by the "detector"). The number of coincidences has been studied as a function of the angular position of the detector. This number is corrected for the detector's efficiency and may be directly compared with the theoretical functions.

The source in this experiment has been a 20-millicurie Co^{60} rod of dimensions $\frac{1}{4}$ inch diameter, $\frac{3}{8}$ inch length. Co^{60} gamma-ray lines are present in equal strength and are of energies 1.169 and 1.331 Mev. The collimating channel is 10 inches long and of $\frac{1}{4}$-inch $\times\frac{1}{4}$-inch cross section in lead. A $\frac{1}{2}$-inch stilbene cube serves as scatterer and the detector is a block of stilbene $\frac{1}{2}$ inch$\times\frac{1}{2}$ inch $\times 1$ inch. In this experiment the distance between scatterer and detector is 11.6 cm. The crystals as well as the 1P21 photo-multipliers are carefully selected, and in operation the detector photo-multipliers are cooled to dry ice temperature. A $\frac{1}{16}$-inch aluminum sheet is placed between the scatterer and detector to isolate the detector from any scatterer recoil electrons. The coincidence method uses an oscilloscope viewed by an auxiliary counting photo-multiplier (not shown) and will be described elsewhere.

Forty-eight measurements of the number of coincidences per 200 seconds were made at each angular position examined. Plateaus in counting rate indicated that all scattering events were counted at each angular position except 20° and 15° where plateaus were not obtained. The number of events missed at 20° was probably not greater than 10 percent, however. In Fig. 2, which shows results obtained, the counting rates were corrected for the efficiency of the stilbene detector crystal which varies with the energy of the scattered photon. The well-established experimental total cross sections were used to make this correction. Other corrections applied to the experimental points in Fig. 2 have been made for: (*a*) the varying amount of absorption in the scatterer crystal which depends on the path traversed and photon energy and, hence, on the angular position of the detector; (*b*) the absorption of the scatterer photo-multiplier (glass envelope and contents) also in the path traversed by the scattered gamma-ray in some angular positions; and (*c*) the absorption of the thin-walled aluminum housings surrounding scatterer and detector photo-multipliers as well as the absorption of the $\frac{1}{16}$-inch aluminum sheet isolating the detector from scatterer electrons. The sum of corrections (*a*), (*b*), and (*c*) amounts to 9 percent at 20°, 21 percent at 50°, and 30 percent at 90°.

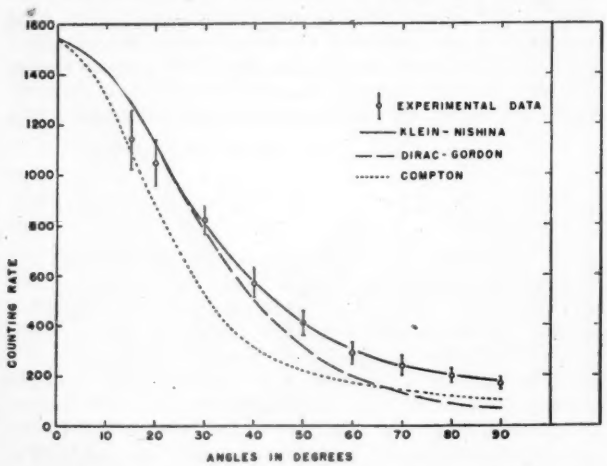

FIG. 2. Comparison of experimental and theoretical curves.

The theoretical curves plotted in Fig. 2 are the sums of the angular distributions of scattered photons for each of the two Co^{60} gamma-rays. The strength of the source is known to only about 15 percent, and the normalization of the experimental curve has, therefore, been made with the closest theoretical Klein-Nishina curve within this 15 percent range. The Klein-Nishina curve is seen to fit the data much better than the older Compton and Dirac-Gordon curves. Further improvements in the experiment which will eliminate corrections (*b*) and (*c*) and determine absolute source strength are contemplated. The former improvements will reduce the total corrections to 9 percent at 50° and 11 percent at 90°.

This work received partial support from the joint program of the ONR and the AEC.

[1] O. Klein and Y. Nishina, Zeits. f. Physik **52**, 853 (1928).
[2] L. Meitner and H. Hupfeld, Zeits. f. Physik **67**, 147 (1930); G. T. B. Tarrant, Proc. Roy. Soc. **128**, 345 (1930) and others.
[3] W. Friedrich and G. Goldhaber, Zeits. f. Physik **44**, 700 (1927); G. E. M. Jauncy and G. G. Harvey, Phys. Rev. **37**, 698 (1931).
[4] C. Y. Chao, Phys. Rev. **36**, 1519 (1930); Z. Bay and Z. Szepesi, Zeits. f. Physik **112**, 20 (1939); W. H. Jordan, thesis, Cal. Inst. Tech. (1934).
[5] R. Hogstadter and J. A. McIntyre, Phys. Rev. **76**, 172 (1949).

The Electromagnetic Separation of the Isotopes of Mercury

C. P. KEIM*
Carbide and Carbon Chemicals Corporation, Y-12 Plant, Oak Ridge, Tennessee
August 29, 1949

THE natural isotopes of mercury have been enriched successfully in the mass spectrographs (calutrons) at the electromagnetic separation plant, Oak Ridge, Tennessee. Effort has been directed toward obtaining an enriched even-mass isotope with low odd-mass contamination, to minimize the isotope wave-length shift in the mercury spectrum, particularly the 5461A line. For this purpose the enriched sample of Hg 202, shown in Table I, has been obtained. In this product the sum of the odd mass isotopes is 0.478 percent and the sum of the even mass isotopes is 99.522 percent.

TABLE I. Enriched and natural abundances of Hg isotopes in the sample of Hg 202.

Isotope	Enriched abundance	Natural abundance
Hg 196	0.014 percent	0.16 percent
Hg 198	0.092	10.02
Hg 199	0.113	16.92
Hg 200	0.781	23.10
Hg 201	0.365	13.22
Hg 202	98.06	29.72
Hg 204	0.574	6.84

In addition to the Hg 202 collection, Hg 198 has been enriched to >60 percent, Hg 199 to >70 percent, Hg 200 to >75 percent, and Hg 204 to >92 percent. Hg 196 and Hg 201 are still in process at this writing. Isotopic mixtures of high single isotope concentration are available on allocation from the Isotopes Division, Atomic Energy Commission, Oak Ridge, Tennessee.

The high purity Hg 202 reported in this letter has been examined in our spectroscopy laboratory by J. R. McNally, P. M. Griffin, and L. E. Burkhart and its characteristics are being discussed in a companion Letter to the Editor of the Journal of the Optical Society of America.

The successful enrichment of these mercury isotopes is the result of the cooperative efforts of the personnel of the Isotope Development Department. The contribution of the calutron crews, engineers, and shops are appreciated. These groups most directly

associated with isotope production problems are under the supervision of H. W. Savage, B. S. Weaver, and P. J. Hagelston. W. E. Leyshon and L. O. Love deserve particular credit for their contributions to the solution of the difficult calutron problems. All isotopic analyses on natural and enriched mercury were done in the mass spectrometer laboratory under the direction of R. F. Hibbs and J. W. Redmond.

This document is based on work performed under Contract No. W-7405-eng-26 for the Atomic Energy Commission at the Carbide and Carbon Chemicals Corporation, Y-12 Plant, Oak Ridge, Tennessee.

* Superintendent, Isotope Development Department, Y-12 Plant, Carbide and Carbon Chemicals Corporation, Oak Ridge, Tennessee

A Preliminary Note on Nuclear Periodic Scheme in Three Dimensions

S. PODGOR
NEPA Division, Fairchild Engine and Airplane Corporation, Oak Ridge, Tennessee
August 19, 1949

IT appears to be well established that 2, 8, 20, 50, 82 numbers of neutrons or protons and 126 neutrons form particularly stable configurations.[1,2] In order to illustrate better how the properties of nuclei vary and to aid in discovering periodicities that exist, it seems worth while to arrange a nuclear periodic scheme analogous to the atomic periodic chart. However, since in the ordinary nuclear chart the isotopes proceed along two dimensions, the nuclear periods will have to advance along the third dimension.

It might be well to emphasize at this point that the properties of a nucleus are functions of two variables: Z, the number of protons, and N, the number of neutrons. Any particular nucleus, for instance, may have a complete shell in Z, but not necessarily in N, and conversely. Within limitations, there is then some independence in the variation of Z and N, and in the completion of shells in each of these variables.

We can build up the system with the assistance of a Segré chart, as illustrated in Fig. 1. It consists of successive planes; each plane starts with nuclei having a complete shell in either neutrons or protons, and ends with nuclei of the next complete shell in either nucleon. Only the first three planes are shown on the diagram.

Stable nuclei are indicated by cross-hatching; radioactive nuclei have the half-life on clear background; nuclei with a complete shell in either neutrons or protons are enclosed in heavy lines. Nuclei that are complete in both neutrons and protons ($_2He^4$, $_8O^{16}$, $_{20}Ca^{40}$) are darkened.

The complete scheme can be outlined as follows:

Plane I.—This consists of all nuclei up to those having a complete 2-shell in either neutrons or protons, or including the isotopes of He.

Plane II.—This starts with nuclei having 2 neutrons or 2 protons, and ends with a complete 8-shell in either nucleon, or including the isotopes of oxygen and F^{19}.

Plane III.—Similarly, this starts with all nuclei with 8 neutrons or protons, and ends with a complete 20-shell in either nucleon. After this, the neutron and proton periods proceed independently.

Plane IV.—This goes from nuclei with 20 nucleons of either type to nuclei with 50 protons, or the isotopes of Sn.

Plane V.—From nuclei with 50 neutrons to those with 82 neutrons.

Plane VI.—From the isotopes of Sn to nuclei with 82 protons or 126 neutrons (the isotopes of Pb and all nuclei with 126 neutrons).

Plane VII.—This goes from 82 protons or 126 neutrons, and includes all the remaining radioactive nuclei.

This arrangement should be very suggestive in bringing together species that have similar properties since it will tend to line up nuclei that are at the same stage of starting or completing a shell

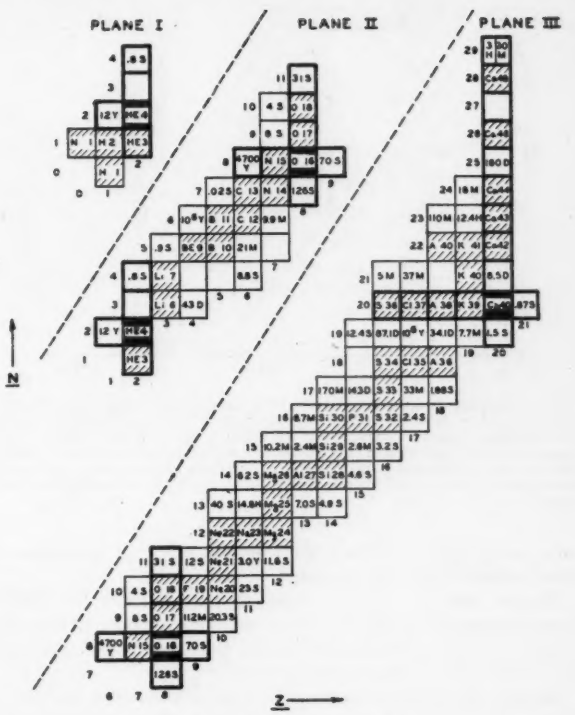

FIG. 1. Nuclear periodic scheme.

in either neutrons or protons. For instance, nuclei lacking one neutron to form a complete shell should have related properties; similarly for nuclei with one neutron more than a complete shell.

As an example of the use of this scheme, we may consider the following: $_8O^{17}$,[3] $_{36}Kr^{87}$,[1] $_{54}Xe^{137}$ [1] are known delayed neutron emitters. They have 9, 51, 82 neutrons, respectively, or one neutron more than a closed shell. They decay by neutron emission to $_8O^{16}$, $_{36}Kr^{86}$, $_{54}Xe^{136}$ all with closed shells in neutrons, $N=8$, 50, 82.

In our scheme they appear on Planes II, IV, VI, respectively. One would expect that there should be a neutron emitter in a corresponding place on Plane III at $N=21$. This might perhaps be $_{16}S^{37}$, decaying to $_{16}S^{36}$, ($N=20$). It would then be analogous to $_{36}Kr^{87}$ and $_{54}Xe^{137}$ since they decay to stable nuclei of lowest Z consistent with a complete neutron shell.

[1] M. G. Mayer, Phys. Rev. **74**, 235 (1948).
[2] E. Feenberg and K. C. Hammack, Phys. Rev. **75**, 1877 (1949); L. W. Nordheim, Phys. Rev. **75**, 1894 (1949).
[3] Luis W. Alvarez, Phys. Rev. **75**, 1127 (1949).

The Beta-Spectrum of Be^{10}

H. W. FULBRIGHT AND J. C. D. MILTON
Palmer Physical Laboratory, Princeton University, Princeton, New Jersey
August 30, 1949

THE beta-decay of Be^{10} has a particular interest at this time because the transition $Be^{10} \rightarrow B^{10}$ is now known almost certainly to involve a spin change of three units, so that the transition is highly forbidden according to the Fermi theory of beta-decay. Marshak has shown[1] that the Fermi theory predicts an energy spectrum for the Be^{10} beta-rays which is substantially different from the allowed form. He gives a set of curves of correction factors for converting the allowed spectrum into other forms corresponding to the different types of transitions which theoretically might apply to this case. By arguments based on the half-life, he narrows the choice down to one curve (D_3). The D_3 curve corresponds to second- or third-forbidden tensor or second-forbidden axial vector type transitions if Gamow-Teller selection

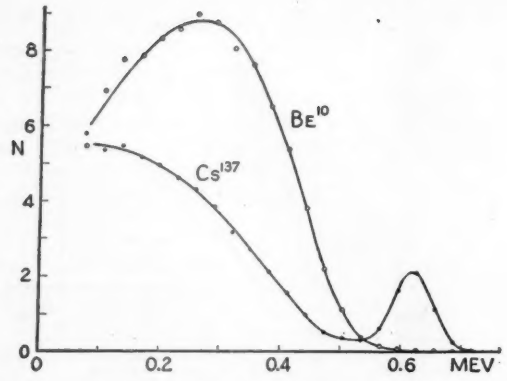

FIG. 1 Energy distributions of the beta-rays of Cs^{137} and Be^{10} as determined by means of a high pressure proportional counter. The energy scale was obtained from the known (see reference 4) 0.626 Mev energy of the metastable Ba^{137} conversion line. Ordinates are proportional to ten channel discriminator readings less backgrounds. The three lowest energy points are good to only about twelve percent because of the high background in that region.

rules are accepted, or to a third-forbidden vector transition if Fermi selection rules are accepted.

Hughes and co-workers[2] have estimated from absorption measurements that Be^{10} has an allowed type spectrum. Bell and Cassidy,[3] using a scintillation counter, have found some evidence for deviation from the allowed spectrum.

We have recently determined the shape of the Be^{10} spectrum by means of a high pressure proportional counter in which the sample was mounted on a 0.2 m/cm^2 aluminum foil suspended between two tungsten collector wires, so that all electrons emitted would be observed. This arrangement has a number of other advantages, among them the fact that primary electrons scattered through the foil will, if their energy is not too low, give secondary electron current pulses of about the correct size. Actually, two identical counters of this type were mounted inside the same high pressure vessel filled with argon at a pressure of 700 p.s.i. Be^{10} was placed in one; Cs^{137} was placed in the other. The amplifier could be switched from one side to the other. A calcium purifier was operated continuously. As the counter voltage was raised, saturation of the ionization electron current was observed before appreciable gas multiplication appeared. Approximately twofold gas multiplication was used. Use of greater gas multiplication would improve the resolving power at the expense of stability.

The Cs^{137} was deposited carrier-free by evaporation The Be^{10} in the form of BeO powder was deposited by evaporation of an amyl acetate suspension to which a trace of wax had been added to act as a binder. Three different samples of beryllium were used, having thicknesses ranging from 0.5 to 3.5 m/cm^2. All gave very similar results.

Typical results are shown in Figs. 1 and 2. The conversion line of metastable Ba^{137} has an energy spread at half-maximum of about 70 kilovolts. It was used for calibrating the system. Curves *a* and *b* of Fig. 2 are allowed spectrum plots of Be^{10} and Cs^{137}, respectively. Curve *a* has a marked bond, while curve *b* shows the slight bend expected from previous work.[5,6] The high energy tailing is due to the inherent limited resolving power of the system.

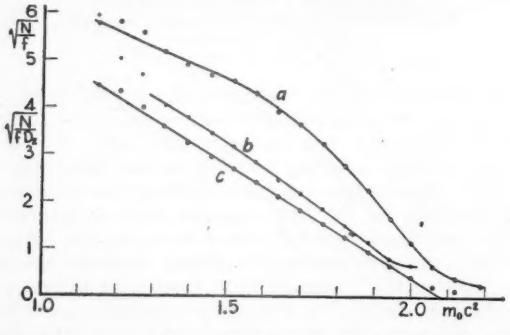

FIG. 2. Curves *a* and *b* are allowed spectrum plots of Be^{10} and Cs^{137}, respectively. Curve *c* is the result of transforming the ordinates of curve *a* by use of Marshak's D_2 correction curve. The end point of the Be^{10} spectrum is at 0.553±0.015 Mev.

Curve *c* of Fig. 2 shows the Be^{10} spectrum plotted as a forbidden spectrum by use of Marshak's D_2 correction curve. The points lie very nearly on a straight line, supporting the validity of the D_2 curve, hence supporting the Fermi theory. The other D_1 do not give satisfactory plots.

We wish to thank Professor W. E. Stephens for generously giving us the Be^{10} sample used in this work. We also wish to acknowledge the assistance of Mrs. Elizabeth Karplus and Mr. R. Chalmers.

This work was assisted by the joint program of the ONR and the AEC.

[1] R. E. Marshak, Phys. Rev. **75**, 513 (1949).
[2] Hughes, Eggler, and Huddleston, Phys. Rev. **75**, 515 (1949).
[3] P. R. Bell and J. M. Cassidy, Phys. Rev. **76**, 183A (1949).
[4] Townsend, Owen, Cleland, and Hughes, Phys. Rev. **74**, 99 (1948).
[5] C. L. Peaock and A. C. G. Mitchell, Phys. Rev. **75**, 1272 (1949).
[6] J. S. Osoba, Phys. Rev. **76**, 345 (1949).

The Disintegrations of Sn^{121} and Sn^{123} *

R. B. DUFFIELD** AND L. M. LANGER***
Los Alamos Scientific Laboratory, Los Alamos, New Mexico
September 1, 1949

THE 39.5-min. activity of Sn^{123} and the 28-hr. activity Sn^{121} were studied by means of a magnetic lens spectrometer.[1] Sources were prepared by irradiating metal foils of separated isotopes in the thermal column of a nuclear reactor. The separated isotopes**** contained 70.7 percent Sn^{122} and 95.4 percent Sn^{120}, respectively. The times of irradiation and measurement were selected so as to avoid interference from the activation of other periods. Decay rates were checked in the spectrometer and also directly. The sources were about 0.5 in. in diameter. The Sn^{120} sample was rolled at 7.5 mg/cm^2. The Sn^{122} sample was 6.2 mg/cm^2 thick. Calibration of the spectrometer was in terms of the 0.663-Mev gamma-ray which follows the decay of Cs^{137}. Most of the measurements were made with a resolution of 6.4 percent. The internal conversion line found in Sn^{123} was also investigated with a resolution of 2.4 percent in an attempt to resolve the *K* and *L* lines. However, the broadening of these low energy lines because of the thickness of the source prevented their separation. Detection was by means of a 3.5-mg/cm^2 mica end-window counter.

Figure 1 shows the momentum distribution of the electrons emitted by the 39.5-min. period of Sn^{123}. In addition to the beta-

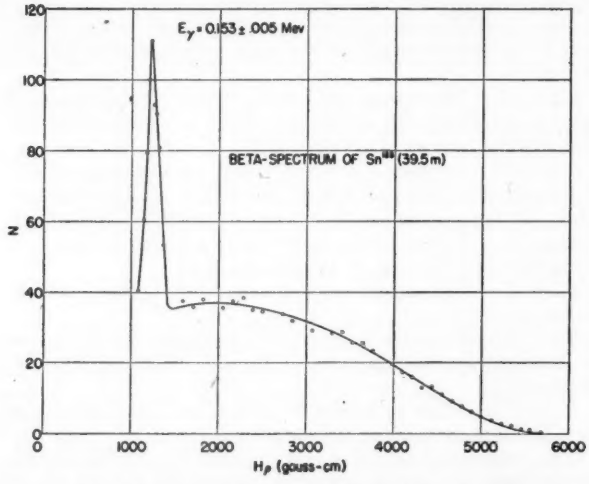

FIG. 1. Beta-spectrum of Sn^{123}. Ordinate is counting rate divided by current.

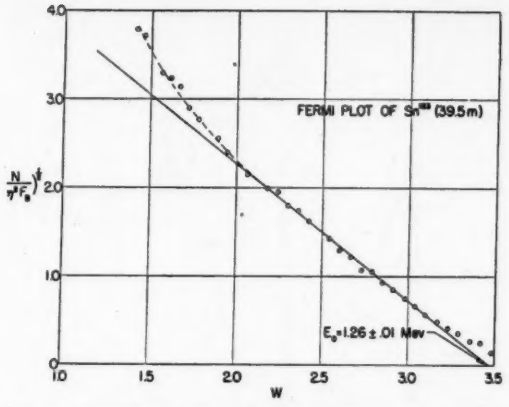

FIG. 2. Fermi plot of Sn^{123} data. F_B is the Coulomb factor calculated by means of Bethe's formula.

spectrum, there is the line of internal conversion electrons corresponding to a gamma-ray energy of 0.153±0.005 Mev. The decay period of this line was followed and found to be 39.5 min. In a separate experiment, coincidences were observed between the internal conversion electrons and the beta-particles. The existence of such coincidences eliminates the possibility that the 0.153-Mev gamma-ray might correspond to a transition feeding the 130-day isomeric state of Sn^{123}. Instead, the gamma-ray apparently follows the beta-decay and corresponds to an undelayed transition to the ground state of Sb^{123}. Although some uncertainty exists because of absorption in the counter window and in the source, from the relative areas under the momentum distribution curve, one obtains for the ratio of internal conversion electrons to beta-disintegrations a value of 0.12. From the coincidence measurements, using a U_3O_8 standard to determine counter efficiency and geometry, the ratio was found to be 0.11.

Figure 2 shows a Fermi plot of the beta-spectrum of Sn^{123}. The deviation from a straight line at low energies arises from the use of a relatively thick source. The extrapolated end point is 1.26 ±0.01 Mev. The data in the immediate vicinity of the end point would have to be corrected for the resolution in order to fall on the straight line.

The momentum distribution of the beta-rays of Sn^{121} is shown in Fig. 3. No internal conversion electrons were observed. Absorption measurements also indicated that there is no gamma-radiation present. It appears, therefore, that the beta-transition is directly to the ground state of Sb^{121}. Figure 4 shows a Fermi plot of the data obtained with two different resolutions of the spectrometer. The extrapolated end point is 0.383±0.005 Mev. The fall-off at low energy is, of course, due to the absorption in the counter window.

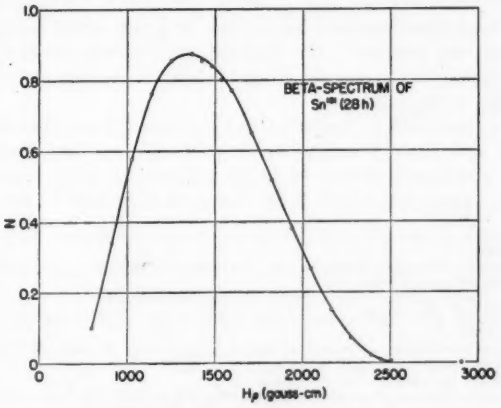

FIG. 3. Beta-spectrum of Sn^{121}.

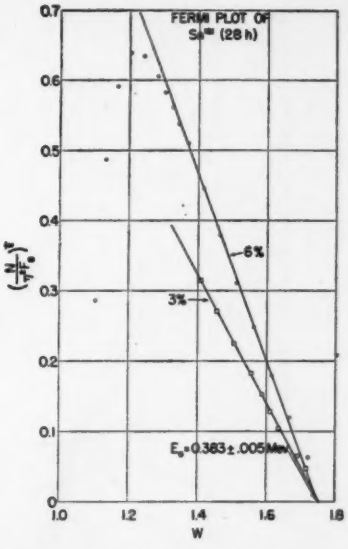

FIG. 4. Fermi plot of Sn^{121}.

We should like to thank Mr. R. J. S. Brown and Mr. L. M. Baggett for assisting with the measurements.

* This document is based on work performed under government contract number W-7405-Eng-36 for the Los Alamos Scientific Laboratory of the University of California.

** University of Illinois, Urbana, Illinois.
*** Indiana University, Bloomington, Indiana.

[1] Data to support the isotopic assignment of the periods will be published later by Duffield and Knight.

**** The separated isotopes used in this investigation were obtained from the Y-12 Plant of the Carbide and Carbon Chemical Corporation on allocation from the U. S. AEC.

The ν_3-Fundamental of Nitrous Oxide

K. B. RHODES AND E. E. BELL
Mendenhall Laboratory of Physics, Ohio State University, Columbus, Ohio
August 31, 1949

THE infra-red spectrum of the previously unresolved ν_3-fundamental of nitrous oxide has been recorded with a self-recording grating spectrometer which was operated in a vacuum. High resolution of the rotational fine structure was obtained using a 10-centimeter cell with the gas at a pressure of 2 centimeters of Hg.

The line frequencies were determined and combination relations used to evaluate the band center and rotational constants. The band center was found to be 2224.4 cm^{-1} and the difference between the rotational constants, $B'-B''$, was evaluated as -0.00343 cm^{-1}. Combination relations also yielded a value of 0.4200 cm^{-1} for B''.

The intensity pattern of the spectrum was uneven. This unevenness was thought to be caused by the superposition of an upper stage band, i.e., one which arose from absorption by molecules which were initially in the energy level $v_2=1$.

Two Kinds of Very High Energy Cosmic-Ray Stars

L. LEPRINCE-RINGUET, F. BOUSSER, HOANG-TCHANG-FONG, L. JAUNEAU, AND D. MORELLET
Laboratoire de l'Ecole Polytechnique, Paris, France
September 6, 1949

WE shall describe two very characteristic nuclear cosmic-ray stars obtained at high altitude (about 100,000 feet) with Ilford G5 emulsions. Stars with relativistic prongs have already been observed at various heights.[1-3] Each of the stars described here has more than 50 prongs, and the energy involved is larger than 12 Bev. However, the explanation is very different in the two cases.

Star No. 1 (Fig. 1). This star has 27 ionizing prongs, corresponding to the usual type of nuclear fragments (protons, α-par-

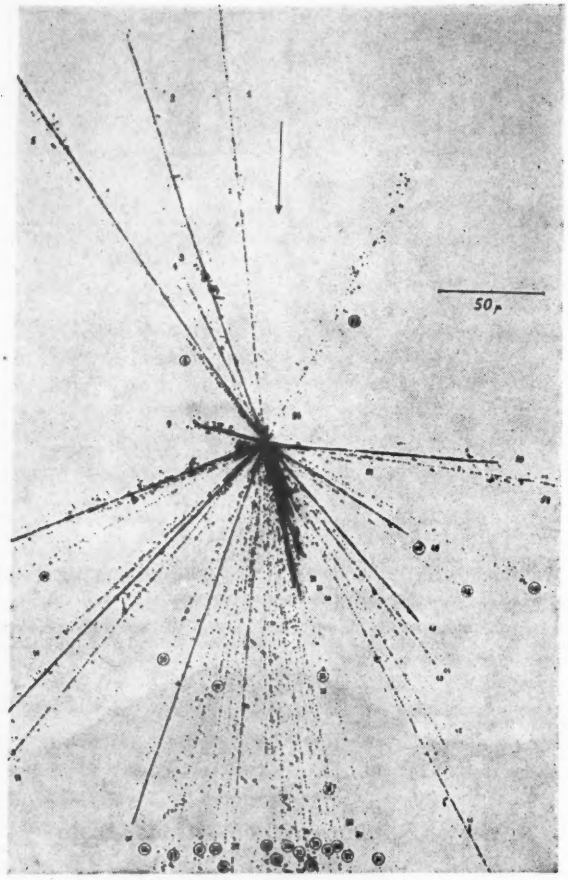

FIG. 1. Star No. 1. No incident primary particle has been observed.

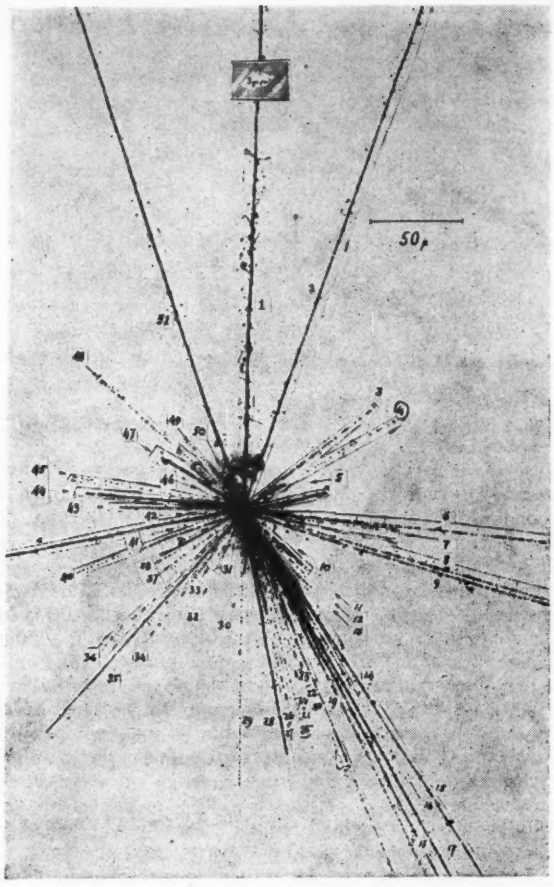

FIG. 2. Star No. 2. Produced by a heavy primary with Z between 14 and 20.

ticles, etc.). It also has 27 relativistic prongs which are well collimated. Sixteen of these prongs are emitted within a cone of 30°; the others, except for three, within a cone of 60°. No incident ionizing primary particle has been observed.

The first question is the nature of the 27 relativistic particles. Our conclusion is in favor of a mixture of mesons and energetic protons. We are led to this conclusion by the following considerations:

A first hypothesis, that all the relativistic particles are mesons created in a single act during a nucleon-nucleon interaction process, can hardly be acceptable. This follows if we consider the relation between the maximum of the half-angle of the meson shower and the number of mesons created.[4] This conclusion must be modified, however, if the most scattered relativistic particles are protons ejected by the primary from the silver nucleus after the shower production.

A second hypothesis is that approximately five to eight mesons are created in a first multiple production, followed by a small number of other processes in the same nucleus involving fewer multiplicities of mesons. This hypothesis of plural-multiple production of mesons involves the ejection of a certain number of fast nucleons, the number of which will increase if the multiplicity becomes less, and the direct ejection of some fast nucleons by the collision. The discussion[5] leads us to divide the 27 relativistic tracks into ten protons and 17 mesons.

The hypothesis of such a process seems in good agreement with the result of Butler[6] (large proportion of positive relativistic particles in penetrating showers observed with his experimental set-up). It also agrees with the theoretical results of Lewis, Oppenheimer, and Wouthuysen,[7] if one considers the mesons to be pseudoscalar.

Star No. 2 (Fig. 2). A heavy primary nucleus produces the star of 51 prongs, 17 of which are relativistic. The heavy track is visible on four neighboring plates; it is nearly at the minimum of ionization. Its charge can be determined by the method indicated by Bradt and Peters[8] and by Freier *et al.*,[9] and is found to be between 14 and 20 while its energy is more than 12 Bev. The relativistic prongs are not well collimated.

If we assume that the charge of the incident particle is 17 and that the star corresponds to the total disintegration of a silver nucleus, and if we take into account the proportion of α-particles observed and the fact that a small number of relativistic particles can escape observation, we must consider the star as being due to the total disintegrations of the incident heavy particle and of the struck silver nucleus. No mesons, or a very small number of mesons, are produced; the probability of meson production is quite small, for the energies of the nucleons of the incident nucleus are only 0.5 to 1 Bev.

Stars produced by heavy nuclei have already been observed by Bradt and Peters,[8] and by Freier *et al.*[9] We see that these two stars correspond to very different phenomena which have one characteristic in common: Their energy is more than 12 Bev.

[1] Brown, Camerini, Fowler, Muirhead, Powell, and Ritson, Nature **163**, 47 (1949).
[2] Cosins, Dilworth, Goldschmidt, Occhialini, Schönberg, and Vermaezen (private communication).
[3] H. Bradt and B. Peters, Phys. Rev. **75**, 1179 (1949).
[4] Peyrou, d'Espagnat, and Leprince-Ringuiet, Comptes Rendus **228**, 1777 (1949).
[5] Leprince-Ringuet, Bousser, Hoang-Tchang-Fong, Janeau, and Morellet, Comptes Rendus **229**, 163 (1949).
[6] Butler (private communication).
[7] Lewis, Oppenheimer, and Wouthuysen, Phys. Rev. **73**, 127 (1948).
[8] H. Bradt and B. Peters, Phys. Rev. **74**, 1828 (1948).
[9] Freier, Lofgren, Ney, and Oppenheimer, Phys. Rev. **74**, 1818 (1948).